IDŐJÁRÁS

QUARTERLY JOURNAL
OF THE HUNGARIAN METEOROLOGICAL SERVICE

Special Issue: Application of remote sensing and geoinformatics in environmental sciences and agriculture

Guest Editor: **Kálmán Kovács**

CONTENTS

****

http://www.met.hu/Journal-Idojaras.php

VOL. 116 * NO. 1 * JANUARY – MARCH 2012

IDŐJÁRÁS

Quarterly Journal of the Hungarian Meteorological Service

Editorial Office: Kitaibel P.u. 1, H-1024 Budapest, Hungary
P.O. Box 38, H-1525 Budapest, Hungary
E-mail: journal.idojaras@met.hu
Fax: (36-1) 346-4669

Indexed and abstracted in Science Citation Index Expanded™ and Journal Citation Reports/Science Edition
Covered in the abstract and citation database SCOPUS®

Subscription by

mail: IDŐJÁRÁS, P.O. Box 38, H-1525 Budapest, Hungary
E-mail: journal.idojaras@met.hu

Editorial

Application of remote sensing and geoinformatics in environmental sciences and agriculture

At the beginning of the third millennium, the extensive variability of weather has become the most significant risk factor for a number of social-economic areas. This can be particularly seen in the state of the environment and in agriculture, which makes the research of these impacts a priority task. Reasonably, fast advancing scientific areas as space science and information technology play major roles in these research fields. As Chair of the Hungarian Space Board, a former minister of building the Hungarian information society, leader of certain environmental and sustainability research projects, and the member of several international bodies since the '90s, I have an overview of the development taking place in the areas of research and application of remote sensing and geoinformatics (GIS). In the present Special Issue of Időjárás, a segment of the research is presented targeting the correlation between weather and environmental and agricultural issues underlining the applications of remote sensing and geoinformatics.

Hungary has numerous achievements in atmospheric and hydrological researches in the areas of analyzing climate changes and their impacts. The Faculty of Civil Engineering of the Budapest University of Technology and Economics, where the education of geodesy was initially started in Hungary more than two hundred years ago, and where a PhD school was first established in the subject, is an outstandingly significant research workshop. During the past two decades, I saw numerous internationally acknowledged applications of their excellent research results. The first paper contains the results of the study of five Hungarian research institutes (Department of Geodesy and Surveying the Budapest University of Technology and Economics; Department of Meteorology of the Eötvös Loránd University; the Satellite Geodetic Observatory of the Institute of Geodesy, Cartography and Remote Sensing; the Hungarian Meteorological Service, and the Geodetic and Geophysical Research Institute) on the application of GNSS observations in the estimation of atmospheric water vapor. The Hungarian Active Global Navigation Satellite Systems (GNSS) Network consists of 35 continuously operating reference stations (CORS), which collect the observations in real-time for surveying applications. In recent years, important atmospheric studies have been started using this network. This paper shows, that the introduced approach is suitable to estimate the precipitable water vapor (PW) content of the atmosphere with the temporal resolution of one hour or better in 35 points over the country with sufficient accuracy. Thus, this technique could be a complementary tool of the radiosonde observations in the measurement of precipitable water vapor. In the second paper, I would like to illustrate this statement with post doctorate research of a young colleague. This paper presents the efficiency of satellite images and Geographic Information Systems (GIS) for assisting disaster management before and during catastrophic events. Specially, it describes application of remote sensing in monitoring hydrological cycle not only in Hungary, but also in arctic and subarctic regions. Observations of continental hydrological processes reveal the impact of climate change on these cold regions.

We have achieved similarly outstanding results in the scientific foundation of rational land use, landscape planning, formation of sustainable farming conforming to soil protection regulations, and environmentally friendly farming taking variable weather into account.

The next three papers are a selection from the achievements of one of the most significant Hungarian agricultural research workshops. The Centre for Agricultural and Applied Economic

Sciences of the University of Debrecen (Agricultural Centre in short) has been performing researches into the impact and correlations of ecological, biological, and agronomical factors in the field for several decades. The objective is to form balanced and stable land use structures, to disseminate, in wide range, the environmentally friendly production methods, to preserve and improve the status of landscape, soil, and water resources. The agrometeorological measurements now collected for 60 years at the Agrometeorological Observatory as part of the Agricultural Centre, and the increasingly efficiently processed remote sensed data offer excellent basis for a more detailed understanding of changes in climate relations, for the determination of components making up the energy balance of the soil surface, for the research of regularities of energy and water flow. Based on the results – especially in maize production – , the agronomical and economical efficiency of production technologies can be improved, while the interventions comply with the requirements of sustainable farming.

The third paper analyzes the joint effect of fertilization and precipitation in maize production. The research was able to verify significant statements on the basis of data from a long-term (17 years) multifactorial field experiment program: Fertilization explains nearly twice the share of crop dispersion than the amount of precipitation does. At the same time, fertilizer nutrient utilization is determined by the amount of precipitation: in dry years, smaller fertilizer doses (60 kg N/ha) were utilized, bigger doses are not justified, while in wet years larger (120 kg N/ha) doses reliably resulted in larger crop, larger nutrient utilization. The next paper focuses on examining maize production in stress situations (e.g., atmospheric drought). By applying as foliar fertilizer, we achieved more favorable crop increase in drought years as in year 2008 that was more favorable for fertility, which leads to the conclusion that the yield increasing effect of algae and algae extract based foliar fertilizers is due to their plant conditioning effect, more articulate in stress situations than under optimal circumstances. It follows that cost efficiency of treatments may be more favorable in stress situations. In the fifth paper, weather dependencies of the increasingly used optical measurement results were examined. The efficiency of optical measurements may be influenced by the change of weather parameters; therefore, practical application must know the correlations between measurement results and weather parameters. The statistical evaluation of results showed that the results of NDVI measurements were primarily biased by the relative atmospheric water vapor, secondarily by air temperature, thirdly by wind speed. Taking these into account it is important, for example, in the case of quick nitrogen supply measurement of the crop and in the determination of area specific intervention.

It has been my hope to compile state-of-the-art testing tools and methods in the area of weather correlations of environmental and agricultural issues in present Special Issue.

I am very grateful to the Editor-in-Chief of IDŐJÁRÁS to be open to put forward this Special Issue. I thank the authors of the articles for the high level of their scientific work, and for the TÁMOP 4.2.1./B-09/1/KMR-2010-0002 EU operative program and numerous other programs, funds, and grants detailed in the papers to support these researches. I also give thanks the reviewers for their comments and recommendations keeping the high standards of the journal. Finally I express our thanks together with the authors of the papers for the hard work of the Executive Editor of the journal.

Kálmán Kovács
Guest Editor

Director, Federated Innovation and Knowledge Centre
Budapest University of Technology and Economics, Hungary
kovacsk@mail.bme.hu

IDŐJÁRÁS

Quarterly Journal of the Hungarian Meteorological Service
Vol. 116, No. 1, January–March 2012, pp. 1–20

The role of GNSS infrastructure in the monitoring of atmospheric water vapor

Szabolcs Rózsa[1*], **Tamás Weidinger**[2], **András Zénó Gyöngyösi**[2], and **Ambrus Kenyeres**[3]

[1] *Department of Geodesy and Surveying, Budapest University of Technology and Economics, Muegyetem rkp. 3, H-1111 Budapest,Hungary*

[2] *Department of Meteorology, Eötvös Loránd University, Pázmány P. sétány 1/A, H-1117 Budapest, Hungary*

[3] *Satellite Geodetic Observatory, Institute of Geodesy, Cartography and Remote Sensing, P.O. Box 585, H-1592 Budapest, Hungary*

[*] *Corresponding author; E-mail: szrozsa@agt.bme.hu*

(Manuscript received in final form December 12, 2011)

Abstract—The observations of the Global Navigation Satellite Systems (GNSS) are affected by various systematic error sources. These effects are usually eliminated in positioning applications using a suitable processing technique. With the emerging active GNSS networks, it became possible to use the GNSS infrastructure for monitoring various parameters of the atmosphere. One of these error sources is the delaying effect of the troposphere due to the atmospheric masses including the water vapor, too. The observed tropospheric delays can be used for monitoring the water vapor content of the troposphere. In several regions of the world GNSS derived products are already used on a routine basis for numerical weather prediction.

With the establishment of the active, GNSS network in Hungary, it became feasible to quantify and monitor the precipitable water vapor (PW) in the atmosphere. The advantage of this solution is the high spatial (approx. 60 km) and temporal (hourly, sub-hourly) resolution of the observations.

This paper introduces the near real-time processing system of GNSS observations in Hungary. The hourly observations of 35 Hungarian permanent GNSS reference stations are processed. This network is extended beyond the territory of Hungary with some 50 stations covering Eastern and Central Europe. The estimation of the PW from the zenith wet tropospheric delay (ZWD) is carried out in near-real time. Firstly, the zenith

hydrostatic delays are subtracted from the estimated total delays. Afterwards, the wet delays are scaled to precipitable water vapor content. Among the well known global models, some local models are also introduced to compute the scaling factor between the zenith wet delay and the PW.

The GPS derived PW values are validated by radiosonde observations over Central Europe, and they are also compared with some numerical weather model estimations, too.

The results show, that the estimated PW values agree with the radiosonde observations with the accuracy of slightly more than 1 mm in terms of standard deviation and a bias of 1 mm.

Key-words: precipitable water, tropospheric water vapor, GNSS/GPS, numerical weather prediction, radiosonde observations

1. Introduction

The atmospheric water vapor plays an important role in many meteorological applications. It is used for numerical weather predictions as well as for climatic studies, since the water vapor is one of the most significant greenhouse gases. Atmospheric water vapor content is measured by radiosondes, microwave radiometers, and some meteorological satellites, too (*Niell et al,* 2001; *Li et al.,* 2003). This paper focuses on a relatively new technique: the atmospheric remote sensing with the Global Positioning System (or more broadly with the Global Navigation Satellite Systems - GNSS). Although the Global Positioning System is available since the early 1980s for positioning purposes, its application for atmospheric studies started in the last decades, because a dense GNSS network is needed for these applications (*Rothacher* and *Beutler*, 1998; *Moore* and *Neilan*, 2005; *Plag* and *Pearlman*, 2009; *Igondova* and *Cibulka*, 2010).

Fortunately, in the last decade the Hungarian Active GNSS Network has been established, and it is continuously maintained by the Satellite Geodetic Observatory of the Institute of Geodesy, Cartography and Remote Sensing. This network consists of 35 continuously operating reference stations (CORS), which collect the GNSS observations in real-time for surveying applications. Since all of the stations have accurate geodetic coordinates, they can be used as the pillars of the process of the estimation of atmospheric water vapor. Similar studies are carried out in other Central-European countries (*Karabatic et al.*, 2011; *Bosy et al.*, 2010).

This paper focuses on the estimation of atmospheric water vapor using GNSS observations. Although some prior studies have already been published in this field by *Borbás* (2000) and *Bányai* (2008), at that time the active GNSS network was not fully developed to assist the estimation of precipitable water vapor.

In the next sections, the theoretical background is shortly discussed and the developed near-realtime processing system is introduced. Moreover, some preliminary results are also shown, based on the validation with radiosonde observations.

2. *Application of GNSS in Meteorology*

The Global Navigation Satellite Systems are widely used for positioning applications. These GNSS receivers can be found in many cars to assist the drivers in the navigation, they are also used for monitoring the migration of wild birds, for assisting precise farming in the agriculture, or they can be even used on GPS buoys to predict tsunamis on the oceans. The global GNSS network operated by the International GNSS Service of the International Association of Geodesy is a backbone of many geodetic and geophysical applications. These observations are used for the determination of tectonic displacements, for the study of the ionosphere, as well as for the precise orbit determination of low Earth orbiting satellites, which measure and monitor the magnetic and gravity field of the Earth (*Reigber et al.*, 2005).

GNSS positioning is based on range observations, which is carried out by the measurement of the travel time of a signal emitted from a satellite and received by a GNSS receiver (*Hoffmann-Wellenhof et al.*, 2008). The range can be computed with the product of the travel time and the speed of the signal. Since the signal travels through the atmosphere (except for space applications), the speed of the signal is delayed due to the atmospheric masses. The atmospheric effect can be split into two parts. The ionospheric delay is caused by the free electron content of the ionosphere, while the tropospheric delay is caused by the atmospheric masses including the hydrostatic part and the wet part of the troposphere (*Ádám et al.*, 2004):

$$ZTD = ZHD + ZWD\,, \tag{1}$$

where *ZTD* is the total tropospheric delay in the zenith direction, *ZHD* and *ZWD* are hydrostatic and 'wet' parts, respectively. Although these values include the effect of stratospheric masses, the term 'tropospheric delay' is used in the literature, since the majority of the delay is caused by the troposphere (2.5 metres) and not the stratosphere (approx. 3–5 cm).

These delays are systematic error sources in the positioning applications. The observation equation of the phase ranges is:

$$\begin{aligned} \Phi_{k,L_1}^{j}(t_i) = \rho_k^j\left(t_i - \tau_k^j, t_i\right) - c\delta t_k(t_i) + c\delta t^j\left(t_i - \tau_k^j\right) + \lambda_{L_1} N_{k,L_1}^{j} + \\ + T_k^j(t_i) - I_k^j(t_i) + v_{\Phi_{k,L_1}^{j}}(t_i) \end{aligned}\,, \tag{2}$$

where Φ_{k,L_1}^{j} is the observed phase range, ρ_k^j is the geometrical distance between the satellite j and the groundpoint k, c is the speed of light, δt_k is the

receiver clock error, δt^j is the satellite clock error, λ_{L_1} is the wavelength of the carrier signal, N^j_{k,L_1} is the phase ambiguity, T^j_k is the tropospheric delay, I^j_k is the ionospheric delay, and v is the random error of the observation. In precise positioning applications the receiver and satellite clock errors are eliminated with the differencing technique. The ionospheric delay is either eliminated by forming the ionosphere free linear combination of phase ranges measured in the two carrier frequencies. The phase ambiguities are resolved during the processing, and the tropospheric delays and the coordinates of the stations are estimated from the observations.

Assuming that the positions (coordinates) of the receivers are known in Eq. (2), the inverse problem can be formulated, leaving only the tropospheric delays as unknowns. This ground based remote sensing of the atmospheric water vapor can be carried out in two ways: estimating the precipitable water vapor above the reference station in the zenith direction; or estimating the slant wet delays and create a 4D (space + time) water vapor model using a tomographic approach (*Braun et al.*, 2001; *Bi et al.*, 2006).

The simplest way is to estimate the tropospheric delay in the zenith direction. In order to achieve this, an appropriate mapping function must be used to map the zenith tropospheric delay to the raypath of the incoming satellite signal:

$$T^j_k = f_d ZHD + f_w ZWD \,, \tag{3}$$

where f_d and f_w are the values of the hydrostatic and wet mapping functions.

The *Niell* (1996) mapping function is a widely used mapping function:

$$f_d = \frac{1 + \dfrac{a}{1 + \dfrac{b}{1 + c}}}{\sin E + \dfrac{a}{\sin E + \dfrac{b}{\sin E + c}}} + \delta f_d(H, E) \,, \tag{4}$$

where E is the elevation angle of the satellite the a, b, c variables are the functions of the latitude and the day of the year, and H is the elevation of the station. δf_d is the elevation dependent correction value.

Since each reference station observes approximately 10–20 satellites in every second, a large number of phase range observations can be evaluated to estimate the zenith tropospheric delays (*ZTD*).

The atmospheric water vapor is highly correlated with the wet part of the tropospheric delay and it can be computed from the zenith wet delays with a simple regression model:

$$PW = Q \cdot ZWD \ , \tag{5}$$

where Q is a scale factor, that depends on the surface air temperature (measures at the weather station in 2 m height). A large number of slightly different mathematical models exist to compute the value of Q. One of them is the model proposed by *Emardson* and *Derks* (2000):

$$Q = \frac{1}{a_0 + a_1\left(T_s - \overline{T}\right) + a_2\left(T_s - \overline{T}\right)^2} , \tag{6}$$

where T_s is the surface temperature, a_0=6.458 m^3/kg, a_1=–1.78×10^{-2} m^3/kg/K, a_2=–2.2×10^{-5} m^3/kg/K, $\overline{T}$=283.49 K.

Another widely used model is proposed by *Bevis et al.* (1992), where the scale factor is computed in two steps. Firstly the weighted mean temperature of the troposphere is computed:

$$T_m = 70.2 + 0.72 T_s , \tag{7}$$

and the scale factor Q is determined from the following equation:

$$Q(T_m) = \frac{10^6}{R_v\left(-\frac{R_d}{R_v}k_1 + k_2 + \frac{k_3}{T_m}\right)} , \tag{8}$$

where R_d and R_v are the specific gas constant of dry air and water vapor respectively, and k_1, k_2, and k_3 are empirical constants, which describe the refractivity of the air as a function of the temperature, partial water vapor pressure, and air pressure using the *Essen-Froome* equation (*Ádám et al.*, 2004). The values of the constants can be found in *Thayer* (1974).

Summarizing the computational approach, the precipitable water vapor can be estimated using the following procedure:

- the total zenith tropospheric delays (*ZTD*) are estimated from the phase range observations based on the accurate coordinates of the GNSS reference stations,
- the zenith wet delays (*ZWD*) are computed by subtracting the hydrostatic delay from the total delay,

- the Q scale factor is computed using surface temperature values (at each reference station), and
- the precipitable water vapor is computed as the product of the *ZWD* and the Q scale factor.

It must be noted that these estimations can be carried out on an hourly or even on a sub-hourly basis. Thus, the precipitable water vapor can be estimated with the frequency of 15–60 minutes at all of the stations of the GNSS network (35 points over the territory of Hungary).

The tomographic method estimates the slant tropospheric delays instead of the vertical ones. The number of the observed satellites is approximately 10–20 at each station, therefore, a set of 350–700 rays cross the troposphere in each hour over Hungary. Since the slant wet delays are estimated along these rays, therefore a three dimensional block model of the tropospheric water vapor can be created using the tomographic approach in each processing step (in every hour). Although this approach is more sophisticated than the previous one, it highly depends on the satellite and the network configuration, and additional observations or assumptions might also be necessary to solve the tomographic equations.

Although it is not the scope of this paper, it must also be noted that vertical humidity profiles can be extracted from GPS radio occultation observations on the Low-Earth Orbiters (LEOs). Based on the bending angle of the signal emitted by the occulting GPS satellite, the refractivity profile of the atmosphere can be determined. Depending on the altitude, this refractivity is related to the total electron content of the ionosphere or the density of the dry air and the water vapor in the troposphere. Thus, GPS radio occultations are used to study the upper atmosphere as well as the lower atmosphere. Unfortunately the spatial resolution of occultation observations is quite low, therefore, these observations can be used for continental or global investigations (*Yahya et al.*, 2008; *Reigber et al.*, 2005).

3. The estimation of precipitable water vapor over Hungary

In order to study the application of GNSS observations in the estimation of atmospheric water vapor, five Hungarian research institutes (the Department of Geodesy and Surveying of the Budapest University of Technology and Economics; the Satellite Geodetic Observatory of the Institute of Geodesy, Cartography and Remote Sensing; the Hungarian Meteorological Service; the Department of Meteorology of the Loránd Eötvös University; and the Geodetic and Geophysical Research Institute) started a research programme in 2011 funded by the Hungarian Research Fund. The first objective was to create the near real-time processing system, which is capable to process the GNSS

observations on a regular hourly basis, and it produces the *ZWD* estimates in each hour with an average latency of 1.5 hours.

The block diagram of the processing system can be seen in *Fig. 1.* The left part of the figure shows the GNSS data processing, including the data collection phase, the processing phase, and the estimation phase. The right part of the figure contains the meteorological data collection system, which collects radiosonde observations for validation purposes and surface meteorological data used for the estimation of *PW*.

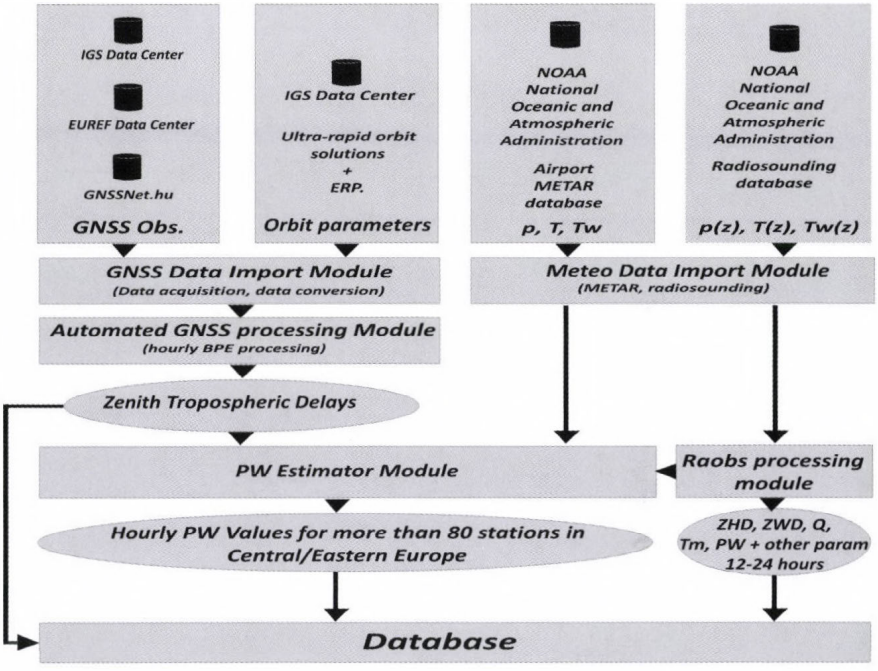

Fig. 1. The block diagram of the near real-time processing system (IGS – International GNSS Service; EUREF – European Reference Network; ERP – Earth Rotation Parameters; METAR – Meteorological Aviation Report; BPE – Bernese Processing Engine).

The automated processing system collects the hourly GNSS observations from all the Hungarian Active GNSS Network (www.GNSSNet.hu). In order to extend the network beyond the borders of Hungary, additional stations have been introduced from the IGS and the EUREF Permanent Network. This extension is necessary to estimate the absolute value of the tropospheric delays. Since the GPS processing is realized using the relative positioning technique, a small network would be suitable for the estimation of relative tropospheric delays differences between the stations. Therefore, altogether 86 stations (*Fig. 2.*) are processed on a regular basis using the Bernese V 5.0 Software (*Dach et al.*, 2007).

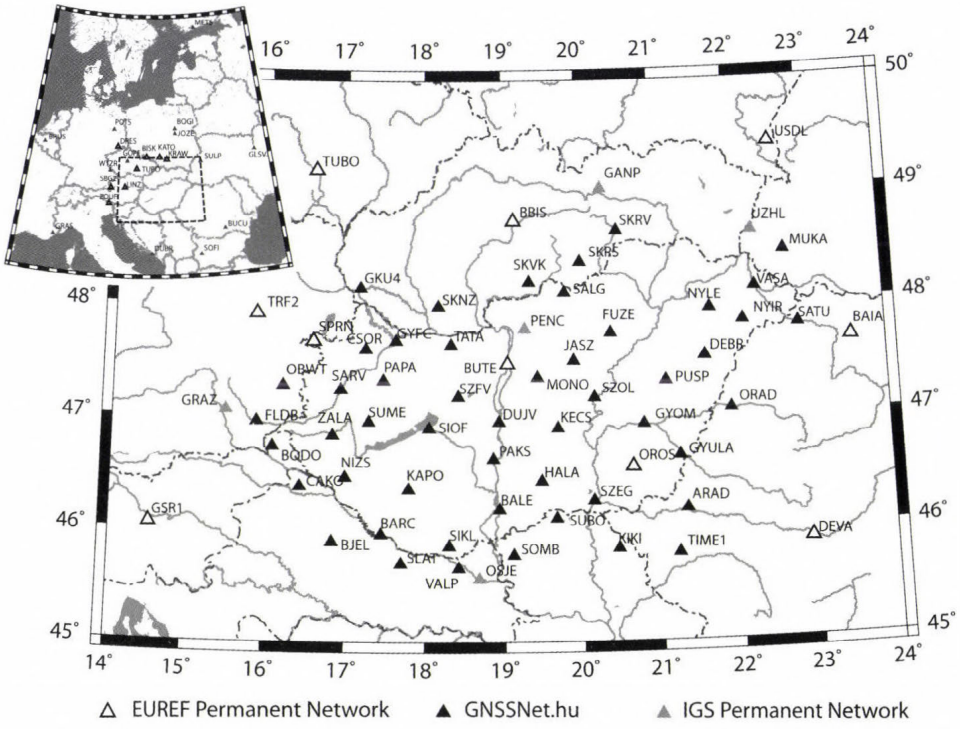

Fig. 2. The location of GNSS stations in the network.

In order to validate the estimations, radiosonde observations were collected from the National Oceanic and Atmospheric Administration (NOAA). All the available observations in Central Europe from 23 radiosounding stations were downloaded from the NOAA RAOBS server. These observations were processed, and the precipitable water vapor and various tropospheric delays were computed from the temperature, humidity, and pressure profiles. Thus, these data sets are suitable for not only the validation of the *PW* estimates, but also for the evaluation of the various mathematical models applied in the computations.

4. Methodology

The following section introduces the computational algorithms of the precipitable water vapor estimations. Various computational methods are studied and evaluated using independent *PW* observations.

4.1. Computation of the zenith wet delays

The zenith total delays (*ZTD*) values can be estimated from the GNSS observations with the accuracy of 5–7 mm. Since the *PW* is correlated with the wet delays, therefore the hydrostatic delays should be modeled and subtracted from the estimated total delays. There are various models to describe the hydrostatic part of the tropospheric delay (*Saastamoinen*, 1972 a,b; *Hopfield*, 1969). In this study, two global tropospheric models and two locally fitted models have been compared to the hydrostatic delays estimated from the radiosonde observations.

The global models were the Saastamoinen and the modified Hopfield models. *Saastamoinen* (1972 a,b) proposed the following equation to compute the slant hydrostatic delay (*SHD*):

$$SHD = \frac{0.002277}{\cos z} p \quad , \tag{9}$$

where z is the zenith angle of the satellite and p is the surface air pressure in mbar.

Hopfield (1969) proposed a different idea to model the zenith hydrostatic delays:

$$ZHD = \frac{10^{-6}}{5} N_{d,0} h_d \ , \tag{10}$$

where $N_{d,0}$ is the refractivity at the sea level ($h = 0$) and h_d is the height of the troposphere.

Both the Saastamoinen and Hopfield models were derived from radiosonde observations. Thus, similar models could be fitted to Central-European radiosonde observations. Therefore, two fitted models have been computed using a linear regression between the surface air pressure and the zenith hydrostatic delays computed from the radiosonde observations. The second locally fitted model contains an additional bias correction, too.

It must be noted, that the radiosonde observations are not suitable to account for the whole delay caused by the neutral atmosphere, since the observations are usually taken up to the altitude of 33–35 km. Therefore, the effect of the higher levels of the neutral atmosphere must be added to the *ZHD* computed from the radiosonde observations. This correction can be computed from the International Standard Atmosphere (*ISO 2533:1975*). *Fig. 3* shows the value of the correction depending on the highest observation level of the radiosonde. It can be seen, that the correction reaches the level of 1.4 cm in the altitude of 35 km. The neglection of this effect would correspond to a systematic bias of more than 2 mm in the *PW* estimates, since the *PW* is approximately one sixth of the zenith wet delay.

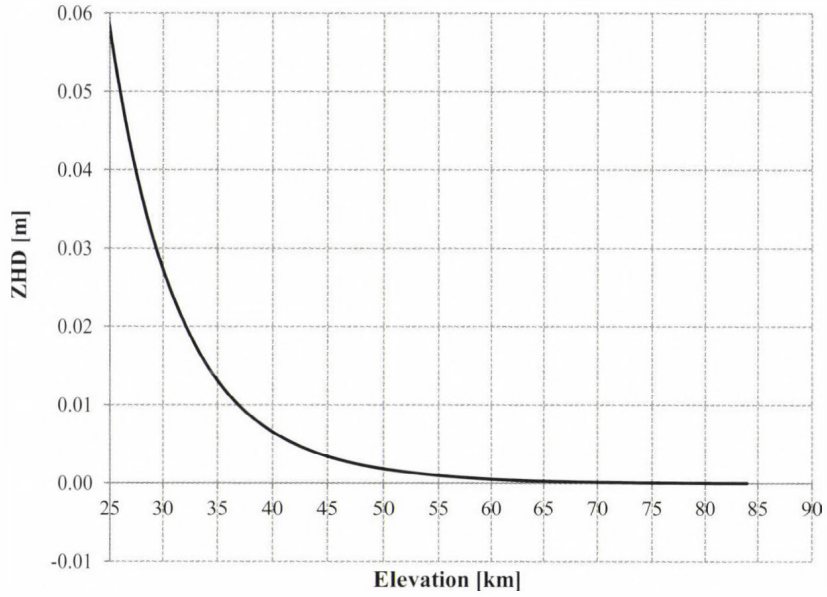

Fig. 3. Zenith hydrostatic delays as a function of the altitude.

In order to derive the regression parameters of the locally fitted models, the zenith hydrostatic delays were computed from the radiosonde observations. The hydrostatic part of the refractivity can be computed from the density of the air at the various observation levels (*Rózsa et al.*, 2010):

$$N_h = k_1 R_d \rho, \tag{11}$$

where ρ is the density of the air (including dry air and water vapor), k_1 is the empirical constant used in Eq. (8), and R_d is the specific gas constant of dry air.

The total zenith hydrostatic delay can be computed from the Thayer-integral (*Thayer,* 1974):

$$ZHD = 10^{-6} \int_{h_s}^{h_{top}} N_h ds, \tag{12}$$

where h_s is the elevation of the station and h_{top} is the topmost level of the radiosonde observations.

After the application of the *ZHD* corrections computed from the standard atmosphere (*Fig. 3*), the regression model parameters could be derived from more than 10 years of radiosonde observations in the Central-European region. Thus, the following locally fitted models have been derived. The linear model (CE linear) is:

$$ZHD = 0.0022766\,p\ . \tag{13}$$

The fitted model including the bias correction (CE linear + bias) is:

$$ZHD = 0.0022790p - 0.0027\,. \tag{14}$$

In Eqs. (13) and (14), p is the atmospheric pressure in mbar units. Since our aim is to compute the zenith wet delays with the utmost accuracy, the aforementioned four models have been validated with radiosonde observations between April 14 – May 31, 2011.

The results of the statistical comparisons can be found in *Table 1*. The results show that the Saastamoinen model outperforms the Hopfield model in terms of standard deviation. The locally fitted Saastamoinen models showed a slight improvement in terms of the bias, but no improvement could be detected in terms of standard deviation.

Table 1. Statistical properties of the *ZHD* residuals [mm]

	Minimum [mm]	**Maximum [mm]**	**Mean [mm]**	**Standard deviation [mm]**
Saastamoinen	–4.1	2.3	–1.4	1.2
Hopfield	–4.5	5.6	–0.6	2.0
CE linear	–3.7	2.7	–1.0	1.2
CE linear + bias	–3.4	3.0	–0.7	1.2

It must also be noted, that 1 mm error in the *ZHD* determination corresponds to approximately 0.15 mm error in the *PW* values. Thus, the various models cause a bias in the *PW* estimates in the order of 0.1–0.2 mm only.

4.2. Computation of the scale factor between the ZWD and PW

When the *ZWD* estimates are computed, the scale factor Q must be determined to compute the *PW* values according to Eq. (7). This scale factor can be computed using the Emardson-Derks model (*Emardson-Derks,* 2000), which was derived from more than 100,000 European radiosonde observations, or using the Bevis model (*Bevis et al.*, 1992), which relies on the results of some 10,000 radisonde observations in the United States. Since both the *ZWD* and *PW* values can be computed from radiosonde observations, the accuracy of these models can be investigated and some local models could also be developed for Central and Eastern Europe.

The first set of the local models follow the approach of *Bevis et al.* (1992). Thus annual and monthly regression parameters were derived between the weighted mean temperature of the troposphere and surface temperature (*Fig. 4.*) using more than 10.000 radiosonde observations launched from Budapest and Szeged (*Rózsa et al.,* 2009). The annual model is defined by the following equation:

$$T_m = 75.99 + 0.70 T_s, \tag{15}$$

where T_s is the surface temperature in Kelvin.

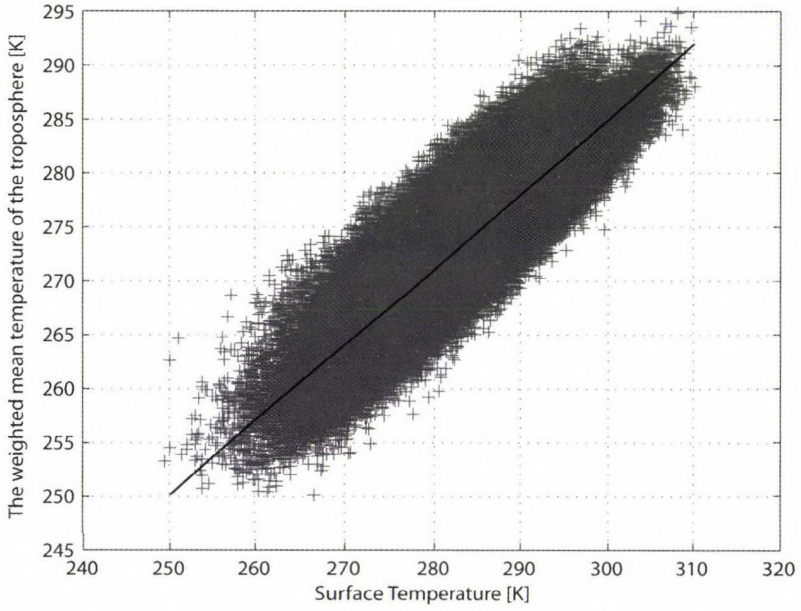

Fig. 4. The linear regression between T_s and T_m.

Since the automated processing system collects not only Hungarian but Central-European radiosonde observations from 23 stations, a second order polinomial equation could also be built between the surface temperature and the scale factor Q. The *ZWD* and *PW* values were computed from more than 152,000 Central-European radiosonde observations, and the scale factor has been computed from:

$$Q = \frac{PW}{ZWD}. \tag{16}$$

Finally, a second order polinomial was fit to the dataset of the surface temperature and the scale factor (*Fig. 5*):

$$Q(T_s) = \frac{1}{a_0 + a_1(T_S - \overline{T}) + a_2(T_S - T)^2}, \tag{16}$$

where $a_0 = 6.39 \pm 0.0003$,
$a_1 = -1.75\times10^{-2} \pm 2.7\times10^{-5}$ (1/K),
$a_2 = 7.5\times10^{-5} \pm 2.5\times10^{-6}$ (1/K^2) and
$T = 283.17$ (K).

It must be noted that the polinomial coefficients a_0 and a_1 are quite similiar to the original Emardson-Derks model, however the coefficient a_2 has a different sign.

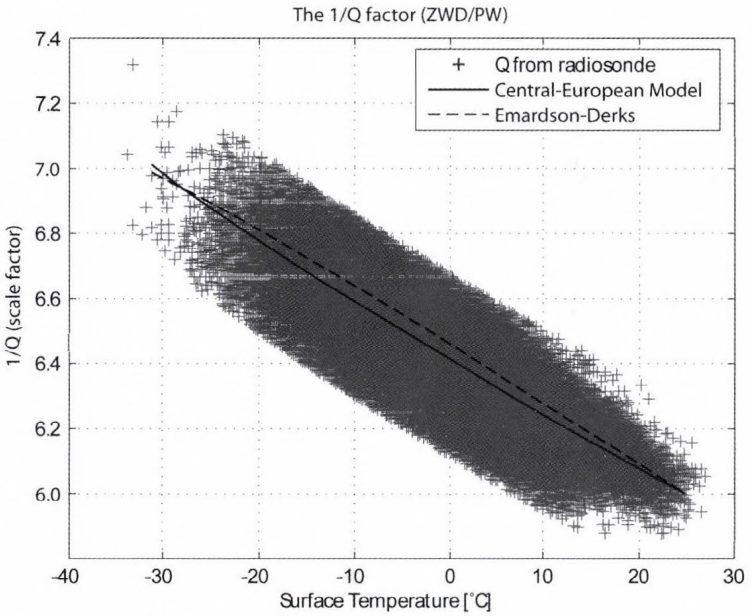

Fig. 5. 2nd order polinomial fit of the ratio between the *ZWD* and *PW* with respect to the surface temperature.

In order to compare the original Emardson-Derks model with the one fitted to the Central-European observations, the Q factors were computed from the surface temperatures. Afterwards, these values were compared with the factors computed from the radiosonde observations. The statistical properties of the residuals can be found in *Table 2*.

Table 2. The statistics of the residual of the scale factor ($1/Q$)

	Minimum	Maximum	Mean	Standard deviation
Emardson-Derks	–0.344	0.289	0.061	0.092
2nd order fitted	–0.277	0.277	0.000	0.092

4.2.1. Comparison of the direct and indirect approaches

The scale factor Q can be computed based on the aforementioned direct approach using the surface temperature, and using an indirect approach proposed by *Bevis et al.* (1992), too. In the indirect approach, the weighted mean temperature of the troposphere is computed from the observed surface temperature based on a linear regression model, and the scale factor is computed by Eq. (9).

The efficiency of the direct and indirect approaches has been compared. The scale factor Q has been computed according to both of the approaches and the values were compared with the reference values stemming from the radiosonde observations. The results (*Table 3*) show that the indirect approach causes a systematic bias in the computation of the Q factor in the order of 0.3%, which would lead to a similar systematic bias in the *PW* estimations. Although the indirect approach is more popular in the international practice, the direct approach provides slightly better results. It must also be noted, that the second order polinomial model fitted to the observed values with the standard deviation of approximately 1.5%.

Table 3. The statistics of the residual of the scale factor ($1/Q$) computed by the direct and indirect approaches

	Minimum	Maximum	Mean	Standard deviation
$Q(T_m)$	–0.311	0.317	–0.020	0.092
$Q(T_s)$	–0.277	0.277	0.000	0.092

5. Results

The automated processing system has been collecting and processesing the GNSS observations since April 14, 2011. In order to validate the results, the precipitable water vapor estimates were compared to radiosonde observations and the *PW* estimates stemming from ECMWF analysis. Although *PW* estimates

are available in 86 stations over Central Europe, comparisons could have been made at the 23 radiosonde sites. The results obtained in Budapest can be seen in *Fig. 6*, while the statistical properties can be found in *Table 4*. The residuals show that the ECMWF slightly underestimates the precipitable water vapor, while the GNSS overestimates it.

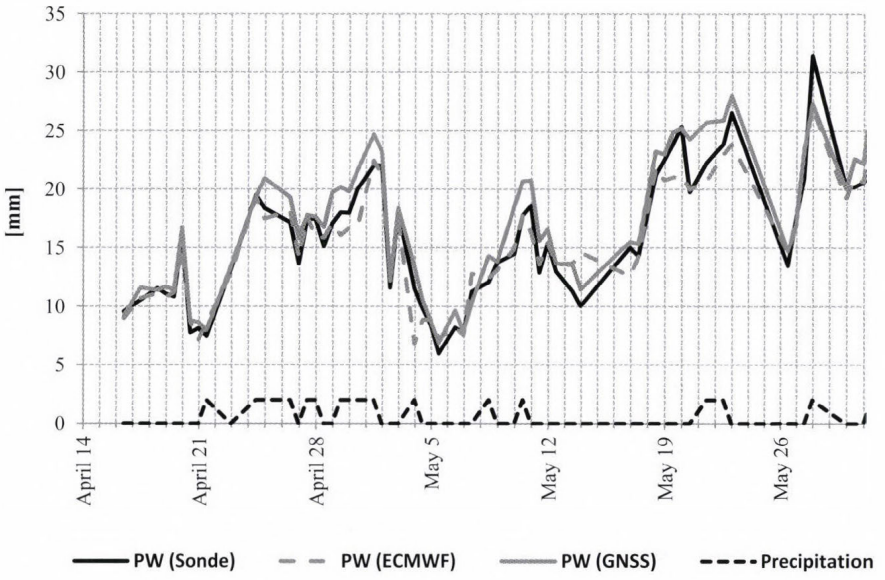

Fig. 6. Comparison of GNSS-derived *PW* with ECMWF analysis and radiosonde observations in Budapest (April 14 – May 31, 2011).

Table 4. Statistics of the fit between the precipitable water vapor from radiosonde and ECMWF analysis/GNSS estimations

	Minimum [mm]	**Maximum [mm]**	**Mean [mm]**	**Standard deviation [mm]**
PW(Sonde) –*PW*(ECMWF)	–4.6	4.7	0.4	± 1.6
PW(Sonde) –*PW*(GNSS)	–4.5	4.1	–1.2	± 1.3

Fig. 6 shows that in some intervals the *PW* estimates derived from the GNSS observations (grey continuous line) do not fit nicely to the radiosonde

observations (black continuous line). This is the case for the periods April 25 – April 26, April 29 – May 1, May 21 – May 22, and for May 28. In order to find the reason for this misfit, the radar images obtained during the study period were checked and a simple function was created, which reflects the intensity of precipitation in the vicinity of the radiosonde station. The dashed black line at the bottom of *Fig. 6* shows this function. Zero values mean no significant precipitation in the vicinity of Budapest, while the value of 1 denotes significant precipitation seen on the radar images. Despite this categorization is rather simple, the majority of misfits coincide with the periods, where significant precipitation could be observed. In these cases the GNSS derived *PW* values overestimate the precipitable water vapor with respect to the radiosonde observations.

Comparing the hourly *PW* estimates from GPS with the radiosonde observations, altogether 59 *PW* estimate residuals can be computed in the study period. Out of these, 19 had a higher absolute value than 2 mm, and in 15 cases significant precipitation could be observed on the radar images, which also show the relationship between the performance of *PW* estimates and the stability of the *PW* values around the GNSS station.

In order to find the reason for this deviation, various parameters, such as the zenith hydrostatic delay, zenith wet delay, and *1/Q* factor have been compared with their counterparts computed from the radiosonde observations. The results can be seen in *Fig 7*, *Fig 8* and *Fig 9* respectively. *Fig. 9* clearly shows that the estimation of the *1/Q* factor does not cause large discrepancies in the *PW* estimates. The absolute values of the residuals are smaller than 0.2, which corresponds to the maximal error of 3% (approximately 0.6 mm) in the *PW* values.

The estimation of the zenith hydrostatic delays is not a key issue either. The maximal residual reached the level of −4 mm, which corresponds to approximately 0.6 mm in the *PW* values. However a systematic bias can clearly be seen in *Fig. 7*, which needs further investigations.

The large discrepancies in the estimated *PW* values are most probably caused by the estimation of the zenith wet delays. Since zenith wet delays are estimated in the GNSS processing, the troposphere mapping functions need further investigations to improve the quality of *ZWD* estimates. *Fig. 8* shows that the *ZWD* residuals vary in time with an order of magnitude larger amplitudes than the *ZHD*, reaching the level of 30 mm. This corresponds to 4.5 mm in terms of precipitable water vapor.

Since the estimation of the zenith wet delays is done using isotropic mapping functions, these estimates are likely to be less accurate when the precipitable water vapor content varies greatly in the vicinity of the GNSS stations. Thus the estimated *PW* values can be interpreted as mean *PW* values for an area with the radius of approximately 60 km.

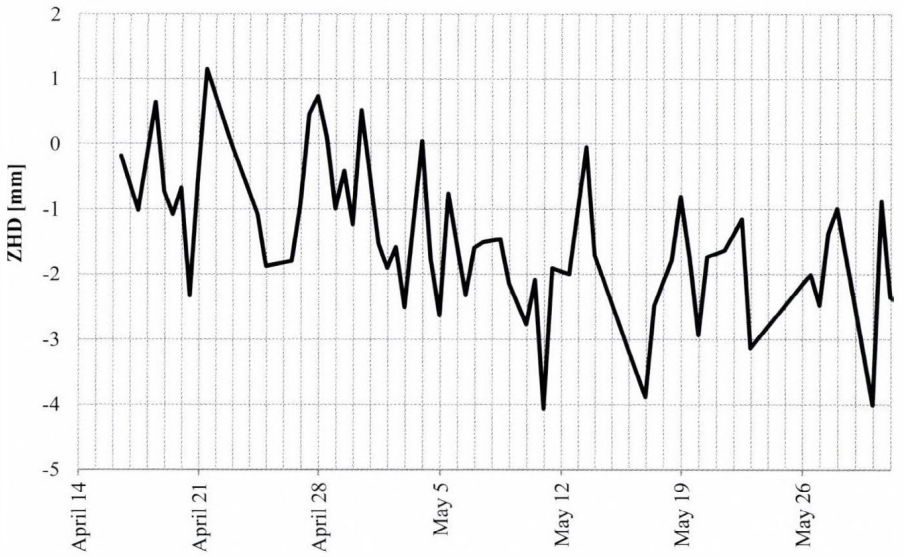

Fig. 7. Residuals of the *ZHD* values computed from the Saastamoinen model.

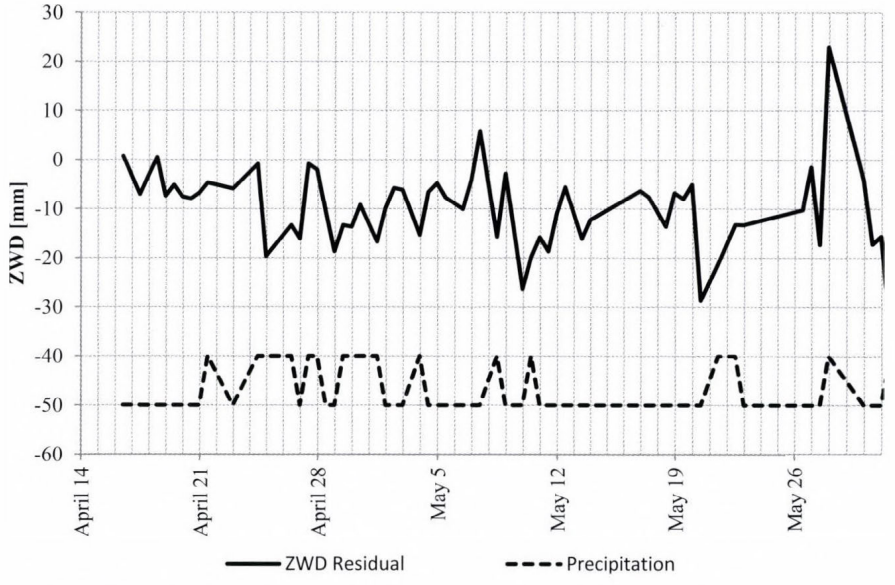

Fig. 8. Residuals of the *ZWD* values estimated from GNSS observations.

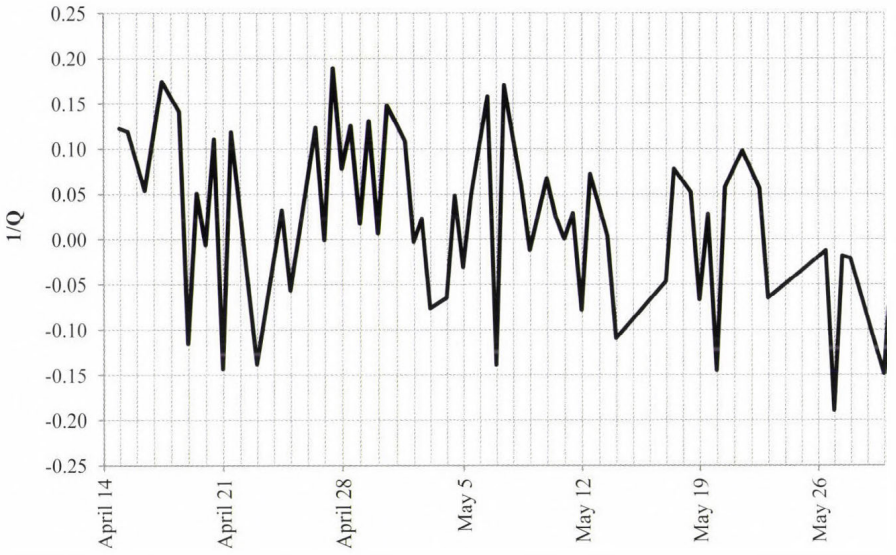

Fig. 9. Residuals of the *1/Q* factor estimated from the surface temperature.

6. Conclusions and outlook

Our investigations showed that the estimation of precipitable water vapor is possible using the Hungarian Active GNSS Network (*GNSSNet.hu*). The near real-time processing system has been developed to process the GNSS data and collect the meteorological data sets for the estimation and validation of the precipitable water vapor.

Various mathematical models have been studied, too. A new polynomial model of the scale factor Q has been determined, which fits slightly better to the Central Europen radiosonde observations than the original Emardson-Derks model. Moreover, numerical studies prove that the direct computation of the Q factor is better than the indirect approach proposed by *Bevis et al.* (1992).

The results of the *PW* estimations agreed with the radiosonde observations at the level of ±1.3 mm in terms of standard deviation. However, large discrepancies have been found, when precipitation was observed in the vicinity of the GNSS stations. A reason for this could be the application of isotropic mapping functions, therefore, the application of advanced mapping functions should be investigated in the future.

The estimated *PW* values showed a systematic bias of 1.2 mm compared to the radiosonde observations. This systematic bias is most likely caused by

seasonal effects in the GNSS coordinates, which were neglected in this processing. Therefore, further adjustments in the GNSS processing strategy must be made to minimize the effect of these seasonal coordinate variations on the precipitable water vapor estimates.

Acknowledgements—The authors would like to thank the financial support of the Hungarian Research Fund (OTKA) in the frame of the project *K-83909*.
This work has been done in the frame of the „Development of quality-oriented and harmonized R+D+I strategy and functional model at BME" project. This project is supported by the New Hungary Development Plan (*Project ID: TÁMOP-4.2.1/B-09/1/KMR-2010-0002*).
The authors would also like to thank the funding of the European Union and the co-financing of the European Social Fund in the frame of the project *TÁMOP 4.2.1./B-09/1/KMR-2010-0003*.
Special thanks for *István Ihász* (Hungarian Weather Service) for preparation of ECMWF precipitable water vapor dataset.

References

Ádám, J., Bányai, L., Borza, T., Busics, Gy., Kenyeres, A., Krauter, A., Takács, B., 2004: *Satellite positioning* (in Hungarian). Műegyetemi Kiadó, Budapest, 458.

Bányai L., 2008: The application of Global Positioning System in Earth Sciences (in Hungarian). *Geomatikai Közlemények XI*, Sopron, 1–181.

Bevis, M., Businger, S., Herring, T.A., Rocken, C., Anthes, A., Ware, R., 1992: GPS meteorology: Remote sensing of atmospheric water vapor using the global positioning system. *J. Geophys. Res. 97*, 15 787–15 801.

Bi, Y., Mao, J., Li, C., 2006: Preliminary results of 4-D water vapour tomography in the troposphere using GPS. *Adv. Atmos. Sci. 23*, 551–560.

Borbás, É, 2000: A new source of meteorological observations: the Global Positioning System. *PhD thesis*, Loránd Eötvös University, Budapest.

Bosy, J., Rohm, W., Sierny, J., 2010: The concept of near real time atmpshere model based on the GNSS and meteorological data from the ASG-EUPOS reference stations. *Acta Geodyn. Geomater. 7*, 253–263.

Braun, J., Rocken, C., Ware, R., 2001: Validation of line-of-sight water vapour measurements with GPS. *Radio Sci. 36*, 459–472.

Dach, R, Hugentobler, U., Fridez, P., Meindl, M., 2007: Bernese GPS Software, Version 5.0. Astronomical Institute, University of Bern.

Emardson, T.R., Derks, H.J.P., 2000: On the relation between the wet delay and the integrated precipitable water vapour in the European atmosphere. *Meteorol. Appl.* 7, 61–68.

Hoffmann-Wellenhof, B., Lichtenegger, H., Wasle, E., 2008: GNSS – Global Navigation Satellite Systems. Springer Verlag, 516.

Hopfield, H.S., 1969: Two-quartic tropospheric refractivity profile for correcting satellite data. *J. Gephys. Res. 74*, 4487–4499.

Igondova, M., Cibulka, D., 2010: Precipitable Water Vapour and Zenith Total Delay time series and models over Slovakia and vicinity. *Contrib. Geophys. Geod. 40*, 299–312.

Karabatic, A., Weber, R., Haiden, T., 2011: Near real-time estimation of tropospheric water vapour content from ground based GNSS data and its potential contribution to weather now-casting in Austria. *Adv. Space. Res. 47*, 1691–1703.

Li, Z., Muller, J.-P., Cross, P., 2003: Comparison of precipitable water vapor derived from radiosonde, GPS and Moderate Resolution Imaging Spectroradiometer measurements. *J. Geophys. Res. 1008(D20)*, 4651.

Moore, A.W., Neilan, R.E., 2005: The International GPS Service tracking network: Enabling diverse

studies and projects through international cooperation. *J. Geodyn. 40,* 461–469.
Niell, A.E., 1996: Global mapping functions for the atmosphere delay at radio wavelengths. *J. Geophys. Res. 101(B2),* 3227–3246.
Niell, A.E., Coster, A.J., Solheim, F.S., Mendes, V.B., Toor, P.C., Langley, R.B., Upham, C.A., 2001: Comparison of Measurements of Atmospheric Wet Delay by Radiosonde, Water Vapor Radiometer, GPS and VLBI. *J. Atmos. Ocean Tech. 18,* 830–850.
Plag, H.-P., Pearlman, M. (eds.), 2009: *The Global Geodetic Observing System: Meeting the Requirements of a Global Society on a Changing Planet in 2020.* Springer, Doldrecht Heidelberg, London, New York, 325.
Reigber, C., Lühr, H., Schwintzer, P., Wickert, J., 2005: *Observations with CHAMP. Results from Three Years in Orbit.* Springer Verlag Berlin-Heidelberg-New York, 630.
Rothacher, M., Beutler, G., 1998:The role of GPS in the study of global change. *Phys. Chem. Earth 23,* 1029–1040.
Rózsa, Sz., Dombai, F., Németh, P., Ablonczy, D., 2009: The estimation of integrated water vapor from GPS observations. *Geom. Közl., XII(1),* 187–196.
Rózsa, Sz., Kenyeres, A., Weidinger, T., Gyöngyösi, A.Z., 2010: The near realtime processing of GNSS observations for meteorological applications. *Geom. Közl., XIII(2),* 55–65.
Saastamoinen, J., 1972a: Contributions to the theory of atmospheric refraction. *B. Géodes. 105,* 279–298.
Saastamoinen, J., 1972b: Contributions to the theory of atmospheric refraction. *B. Géodes. 105,* 383–397.
Thayer, G. D., 1974: An improved equation for the radio refractive index of air. *Radio Sci. 9,* 803–807.
Yahya, M. H., Kamarudin, M.N., Lim, S., Rizos, C. 2008: The potential of Global Positioning System in weather and environmental studies. *9th SENVAR & 2nd ISESEE 2008 Conference,* Shah Alam, Malaysia, 1–3 December, 527–534.

IDŐJÁRÁS

Quarterly Journal of the Hungarian Meteorological Service
Vol. 116, No. 1, January–March 2012, pp. 21-38

Remote sensing for natural hazard mitigation and climate change impact assessment

Zsófia Kugler

Department of Photogrammetry and Geoinformatics
Budapest University of Technology and Economics
Műegyetem rkp. 3, H-1111 Budapest, Hungary
E-mail: zsofia.kugler@mail.bme.hu

(Manuscript received in final form December 16, 2011)

Abstract—Geographic data and remote sensing have become sophisticated tools for obtaining knowledge on natural hazards of meteorological origin. In many cases the impact of disasters can not be prevented, however, efficient mitigation strategy and rapid response can reduce losses and damages in emergency situations. In addition, climate change is expected to increase the magnitude and frequency of natural hazards like extreme precipitation, floods, hurricanes, droughts. This paper aims at demonstrating the potential of satellite image analysis and Geographic Information Systems (GIS) for assisting disaster management before and during catastrophic events. Furthermore, it describes application of remote sensing to support climate change impact assessment on hydrological cycle in sensitive arctic regions. Divers applications in Hungary and around the world will illustrate the capabilities of the technology. Operational and scientific advantages of the practice will justify the use of geographical data in managing natural hazards with origin in meteorology. Not only for analyzing the hazard with an element at risk method but also for estimating the vulnerability factor accounting for physical and socio-economic resilience of the affected area.

Key-words: natural hazards, satellite imagery, GIS, flood mapping, flood detection, arctic region, climate change impact, river ice break-up

1. Introduction

The rapid economical and social development of our ages appears to increase the number of total deaths caused by natural disasters of meteorological origin. Hydrological hazards are causing 40% of the damages globally each year. Although some catastrophes can not be avoided, the social-economic impact of natural risk may be reduced by enhancing the effectiveness of disaster management. The security of the residents on floodplains is highly determined

by finding the appropriate mitigation approach to reduce vulnerability. The state-of-the-art technology of remote sensing and Geographic Information Systems (GIS) can respond to this need by delivering accurate spatial information before, during, and after the disaster (*Kovács*, 2010).

During a natural disaster of meteorological origin, great amount of spatial information need rises. Where did the disaster strike? What is the extent of the disaster, what is the magnitude of the event? Who was affected? Where and how to execute emergency operations? Where to set up evacuation shelters? Traditionally, all these questions may be answered by extracting information from analogue printed maps. However, the state-of-the-art technology of GIS and remote sensing can respond more sophistically to this spatial information need. For this reason during the last decade, several Earth observation satellite sensors were launched with the specific aim to assist disaster management and hazard awareness. Not only to improve knowledge of the flood hazard before the disaster happens but also to assist disaster response when the disaster strikes.

A great number of advantages are related to the use of satellite imagery in disaster management:

- far, inaccessible areas can be monitored without the need of field observations;
- images can be acquired with high revisit frequency – in specific cases almost in near real-time;
- data can be obtained large-scale with a unique observation method.

All these advantages facilitate the technology to play a significant contribution in fulfilling the geographic information need of hazard assessment and disaster management. Remote sensing not only plays a role after the disaster strikes, but assists research to reduce the negative effect of flood hazard in a pre-disaster situation too.

In this paper, first, an application will be described in details assisting flood disaster response. Then the use of satellite technology for flood hazard mitigation and climate change impact assessment will be discussed.

2. Flood disaster response with satellite imagery and GIS

The use of remote sensing tools for flood disaster mapping dates back to the early years of the first optical satellite systems like the Multi-Spectral Scanner (MMS) in the 1970` and 1980`. With the technical development of our age, several satellite systems were put on orbit lately with the aim to assist not only Earth observation but, especially, to obtain information during crisis situations. The Moderate Resolution Imaging Spectroradiometer (MODIS), a low

resolution (250 m) NASA satellite is playing a key contribution in disaster applications. The two platforms carrying MODIS sensor on board the Aqua (launched in 2002) and Terra (launched in 1999) platforms are monitoring the Earth every day with an almost full coverage of its complete surface. It has the significant potential to enable observing and updating information on crisis situations every day. Data can be obtained on no charge basis. Furthermore, near real-time data is available some hours after acquisition, which can assist rapid response to crisis situations. Orbital swath images are available approximately 2.5 hours after observation from NASA's LANCE data centre (*LANCE*, 2011).

For all the above advantages, MODIS is playing a unique contribution to map natural disasters, especially to monitor the evolution of floodplain flooding from day to day. Therefore, numerous applications have flourished in the past using MODIS images to assist disaster mapping (*Zhan et al.*, 2002; *Thenkabail et al.*, 2005; *Sakamoto et al.*, 2007). One of the major contributors of flood mapping is the Dartmouth Flood Observatory (*Brakenridge et al.*, 2005). A global flood atlas has been developed at DFO for major floods from 2000 to recent based on optical MODIS imagery.

During the large-scale inundation in Southern Africa at the beginning of the year 2001, flood mapping was carried out with the assistance of the author at the German Aerospace Center (DLR) too. Heavy long lasting rainy season starting in early January lasting several months was causing above normal flood peaks in the River Zambezi in Mozambique. The serious flood disaster was leading to over 100 deaths and 90 000 displaced people in the river basin. Information on flood hazard from satellite sensors was combined with spatial data on vulnerability. Resulting maps could assess the magnitude of damages and losses in the disaster. Consequently, they could help to reduce uncertainties in problem solving and improve decision making for stakeholders involved in the emergency response.

The assessment of the crisis situation in the Zambezi valley is a good example of how spatially related information combined with satellite images and digital maps can help in emergency situations. MODIS imagery was used to obtain information on the inundation extent (*Fig. 1*). After acquiring satellite data, geometric distortion was corrected using orbital reference data. Classification of inundated areas was carried out using the 250 m highest resolution spectral band of the visible red (0.620–0.670 μm) and the near-IR (0.841–0.876 μm) channels. According to the spectral reflectance characteristics of water surfaces, the two bands were suitable for classifying water bodies. From several multispectral image transformation methods, best results were obtained when using a simple arithmetic subtraction of the two available bands as follows:

$$Floodmask = R - NIR \ . \tag{1}$$

Near-IR was subtracted from red band, where resulting images showed an enhanced contrast between land and water. Finally, a threshold value has been set up on empirical basis to divide water from land. The only feature type of the image that had unfortunately the same spectral characteristic and could not be divided from water, was cloud shadow. Flood maps were derived for the Zambezi River valley in Mozambique resulting in more 12 000 km^2 of area under water cover (*Fig. 1*).

In a next step, spatial analysis was performed in GIS environment combining the flood extent maps and spatial data on administrative entities plus the number of inhabitants. As a result information on the effected inhabitants could be extracted. In the example showed in lower *Fig. 1*, the number of affected inhabitants was weighted by the proportion of flooded and non-flooded area in each administrative entity. As a result, seriously hit regions could be revealed, like the province at the confluence of the Shire and Zambezi rivers, where large lakes were formed between the two rivers.

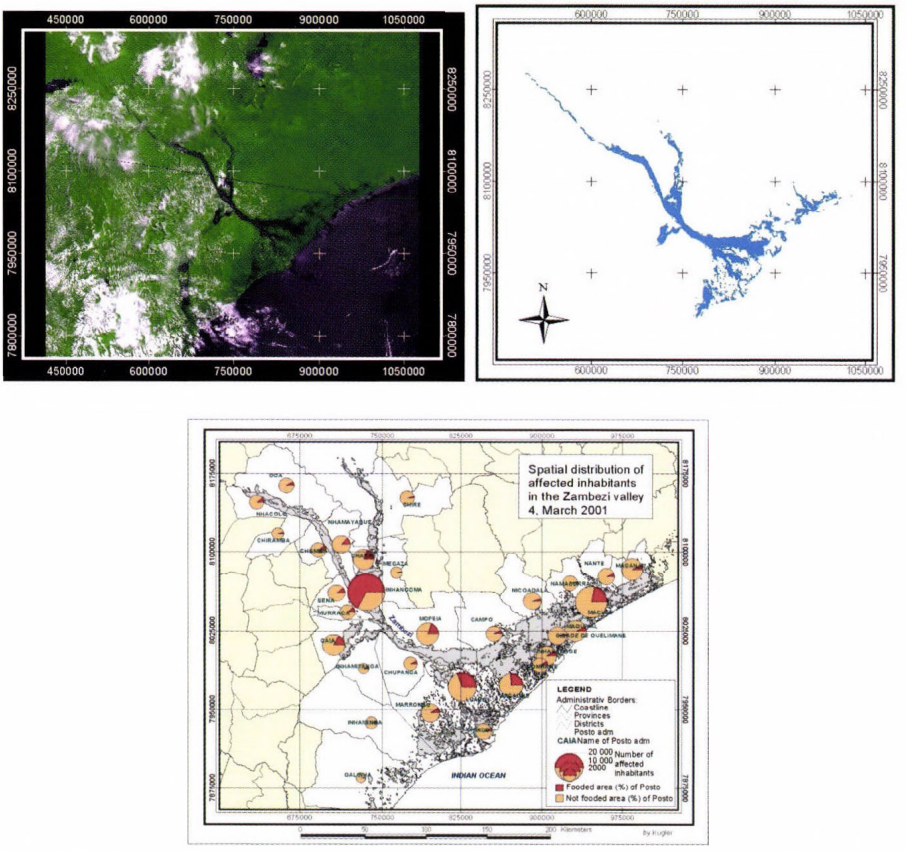

Fig. 1. Flood mapping from MODIS images along the River Zambezi in Mozambique, 2001, and the spatial analysis of the disaster situation by GIS. (*Kugler*, 2004/1)

Beyond obtaining data, the dissemination of the acquired information is crucial in disaster situations. In many cases Internet is used to target end-users. Interactive Web GIS systems – similarly to GoogleMap – can serve not only as a platform of data exchange, but as a possibility to visualize and transmit geographic data for a world-wide audience. For the demonstrated application in Mozambique, a Web GIS system of the freeware UMN MapServer was developed as one possibility to disseminate and publish geographic information about the flood crisis through the World Wide Web.

Further to this, a mobile GIS application was developed as a source of interactive spatial data on-site, for the case when communication with an online server storing the spatial database is interfered or completely cut (*Fig. 2*). It stores its own spatial database locally at the client's side, thus, the system does not have to connect trough the Internet to the central database – like the Web GIS applications described above – in order to display geographic information at the client's side. However, a central database is still a substantial part of the system, since it may serve as a platform of data exchange between the client and the central data server. Moreover, updates of geographic data captured by clients working on-site may be uploaded to the central database. Then spatial data can be downloaded to online. Consequently, the exchange of updated information can be carried out through the central database communicating both with mobile clients and Web GIS systems. The developed system was assisting flood mitigation efforts in Mozambique, yet it can be implemented to any further region.

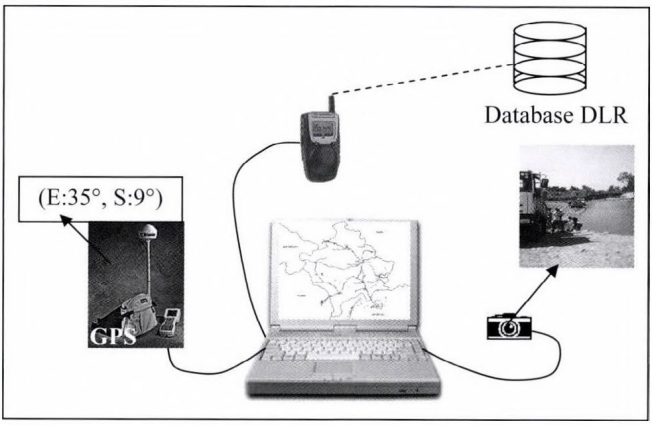

Fig. 2. Architecture of mobile mapping system connected to a central database for on-site disaster data acquisition and update. (*Kugler*, 2004/2)

In lack of spatial data to support risk modeling and calculation of meteorological hazards, historical maps of past events can be processed too. The combination of satellite based information and GIS can not only provide updates

on current disaster situations but is also able to handle historical data about past events to assess their former impact. This allows a better understanding of natural hazards and their possible future impact based on historical events.

An example of that was the detailed analysis of the well documented great flood in 1838 in Budapest, Hungary, where the River Danube flooded almost 80% of the city in March. Historical maps recorded the extent of the flood event, from which spatial information could be collected. Historical maps were acquired by the crisis management team of the Department of Photogrammetry and Geoinformatics at the Budapest University of Technology and Economics. After a geometrical transformation of the map, inundation extent was collected and combined with current maps in a GIS environment (*Fig. 3*).

Historical flood extent shows that only a minor part of the city centre was saved on the Pest side, while the Buda side was affected less. The reason for that is obvious when further combining the flood extent data with topographic information. The Pest side of the riverbank is flat, the Buda side is more hilly.

The acquisition of spatial information on historical disaster events can help to obtain a primarily assessment of possible future impact.

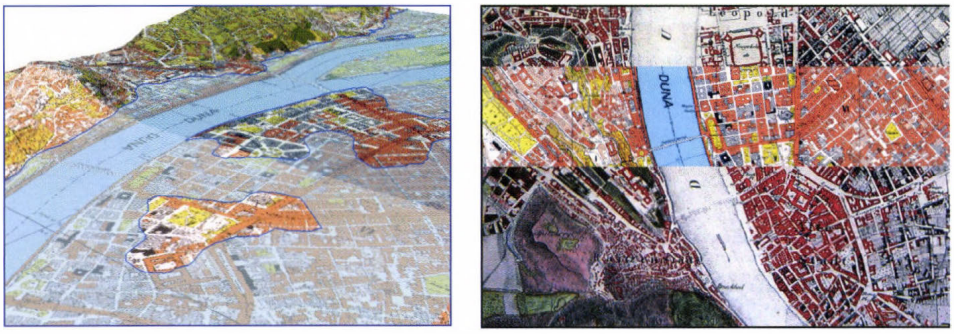

Fig. 3. Virtual view of the great flood in 1838 along the River Danube in Budapest from historical maps (left). Historical map combined with current maps shows structural changes of the channel geometry after the great flood (right). (*Ládai et al.*, 2004)

3. Satellite detection of flood events

Remote sensing and GIS can contribute to the mitigation of emergency situations as discussed in the previous chapters. Furthermore, the technology also enables to provide early detection of major flood disasters. Generally, emergency alerting relies on national or global network of in-situ river gauging measures or on international media reports of disaster events. However, in lack of in-situ measurements, satellite data can play a key contribution in detecting major flood disasters around the globe. To fill this lack, a space-borne methodology was developed using AMSR-E passive microwave data providing near real-time, systematic detection of river floods around the world.

Observing hydrological conditions of river reaches from space dates back to the earlier decades. The use of optical sensors in the visible or infrared portion of the spectrum introduced in the previous chapters can be limited due to cloud cover. Thus, the systematic tracking of river reaches is not feasible in constant time intervals. To overcome this, active satellite systems, penetrating cloud cover, were used for monitoring river hydrology. Besides inundation area delineation (*Hess et al.*, 1995), radar altimetry was applied in different studies to measure stage elevation or water surface level change directly (*Brikett*, 1998; *Koblinsky et al.*, 1993). The renowned scientific study of *Alsdorf et al.* (2000) describes water level measurement based on interferometic radar data acquired by the SRTM mission over the Amazon basin. Still, the mentioned NASA topographic mission was providing observations only over a short time period, thus the technology could not be implemented on an operational basis.

Other studies were using passive microwave emission of the Earth's surface to estimate flooded area from space. The first pioneer study of using passive microwave sensors to estimate inundated area was set up by *Stippel et al.* (1994) in the Amazon basin using the Scanning Multichannel Microwave Radiometer (SMMR). The NASA sensor was providing measurements from 1978 to 1987 and has been used to measure time series of water levels on very large rivers, such as the Amazon. Nevertheless, the measurements of the SMMR instrument were only available in weekly intervals.

Yet, all these applications did not support operational daily observations of river gauging in near real-time with global coverage. For this reason, a system has been developed to monitor river conditions using passive microwave observations of Advanced Microwave Scanning Radiometer (AMSR-E). The system set-up at the Joint Research Center with the assistance of the author (*Kugler et al.*, 2007) is based on the methodology developed by *Brakenridge et al.* (2007) at the Dartmouth Flood Observatory. The aim of the Global Flood Detection System (GFDS) is to monitor river sites and detect flooding by using the radiation difference of land and water on passive microwave images. The operational system is acquiring, updating, and providing data every day on a global scale not restricted by cloud cover. With current fast internet technologies data is delivered to the users in less than half a day after the acquisition (http://www.gdacs.org/flooddetection/).

The technique uses AMSR-E microwave remote sensing data of the descending orbit, H polarization, 36 GHz frequency band which is sensitive to water surface changes. Brightness temperature measured by the sensor onboard is related to the physical temperature (T) and the emissivity (ε) of an object:

$$T_b = \varepsilon T. \tag{2}$$

Due to the different thermal inertia and emission properties of land and water, the observed microwave radiation, in general, accounts for a lower

brightness temperature (T_b) for water and higher for land (*Fig. 4*). During a river condition change, the increased water surface of the inundated area will cause a decrease in the brightness temperature value. Observations are influenced by many factors including physical temperature (T), permittivity (P), surface roughness (R), and soil moisture (θ) as follows:

$$T_b = f(T, P, R, \theta) . \tag{3}$$

Whereas the relative contribution of these factors can not be easily measured, they are assumed to be constant over a larger area. Therefore, by dividing the measurement $T_b(M)$ received over the river channel (measurement pixel) by the calibration or comparison signal $T_b(C)$ not influenced by water change (calibration pixel), the mentioned influences can be minimized in a consistent way. Thus, a ratio was set up defined by the relationship:

$$M / C = T_b(M) / T_b(C), \tag{4}$$

where $T_b(M)$ and $T_b(C)$ are the brightness temperatures of the measurement and calibration pixel, respectively.

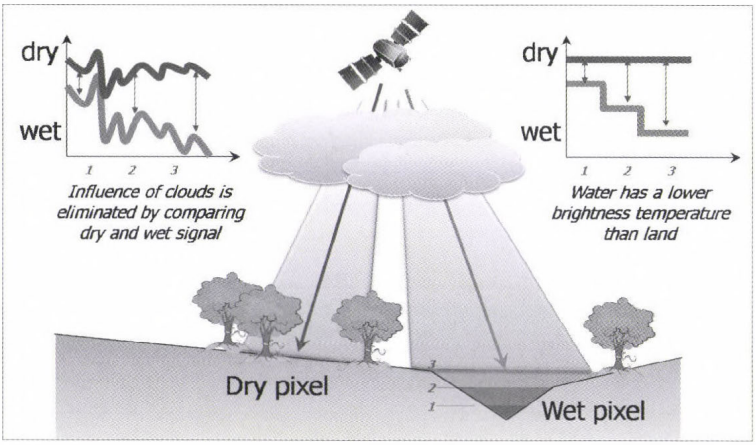

Fig. 4. GFDS is monitoring river gauging from space, based on thermal inertia and emission differences of inundated/wet and dry observations. (*Kugler et al.*, 2007)

The time series of the extracted *M/C* ratio provides operational gauging hydrographs for a selected river site from space with a daily temporal resolution (*Fig. 5*). Following the technique, the detection of flood events in ungauged and inaccessible remote river channels is feasible from space on a near real-time, operational basis. The system observes more than 3000 locations over various rivers valleys around the world. The time series of the *M/C* signal from AMSR-E

data reaches from the launch of the system in June 2002 to the present. Observations and flood alerts are summarized in a database and visualized in form of maps on the GFDS web page distributing information on the internet.

Orbital gauging was validated by in-situ river stage measurements and was compared with flood maps of the corresponding events (*Fig. 5*, right). Although significant correlation was proved between the orbital gauging signals and the on-site stage hydrographs, the *M/C* signal was found to be noisy when comparing to daily discharge data measured on-site. For this reason, a temporal averaging was introduced to reduce disturbing factors. The signal for a given day was averaged from the signal of the last 3 days and the signal for the current day. This 4 days temporal averaging stabilized the signal more effectively than the spatial filtering.

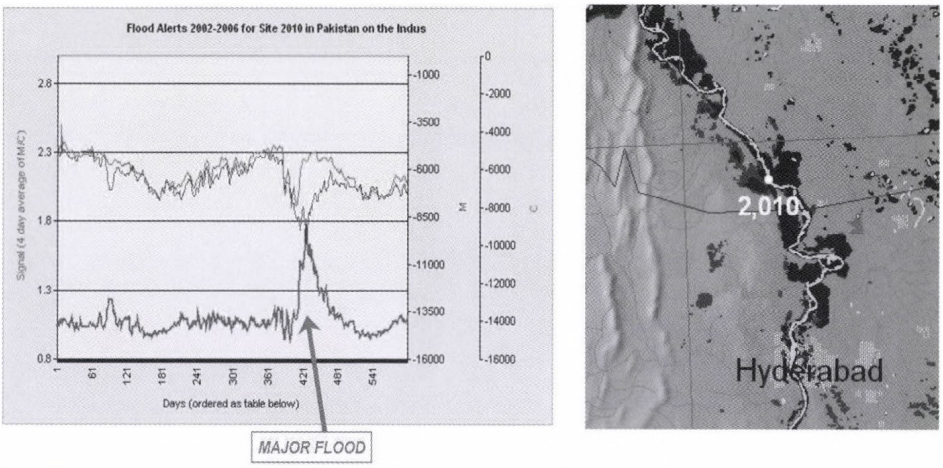

Fig. 5. Orbital gauging hydrograph from space for a selected river site in Pakistan (left) and inundation map of the corresponding event for validation (right).

River flooding is defined when the *M/C* signal is higher than 80% of the signal's cumulative frequency over its complete time series. Major flood is the 95% percentile, flood is the 80% percentile, and normal flow is below the 80% percentile of its cumulative histogram.

The first operational implementation of the GFDS methodology was during the devastating flood crisis in Bolivia at the beginning of the year 2007. Harsh rainy season due to El Nino was causing flooding throughout the country, 8 provinces out of 9 were severely hit, 350 000 people were affected. New observation sites were set every 50 km over the River Mamore to ensure the spatial continuity of the measurement. Orbital hydrographs were extracted for all 14 sites from upstream to downstream along the river channel.

Additionally to orbital hydrographs, inundation mapping was performed from optical satellite resource of MODIS during the disaster event. Comparing the flood maps obtained in February and March, we can observe that the flood extent decreased at the southern upstream end of the river reach, while increased in the northern downstream area reflecting the flood wave propagation in time along the river (*Fig. 6*).

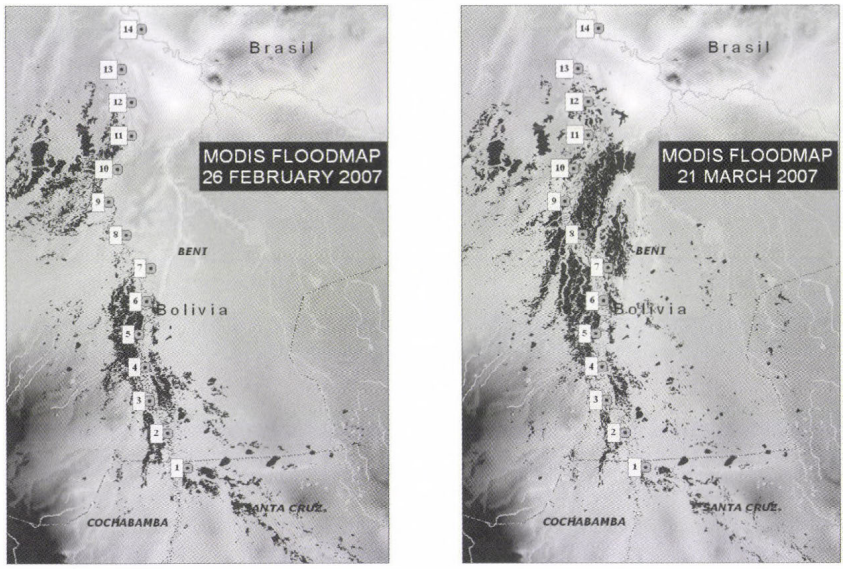

Fig. 6. Optical satellite flood maps along the River Mamore in Bolivia in 2007. (*Kugler et al.*, 2007).

During the event, inundation mapping was limited by clouds in the region, thus AMSR-E microwave observations were playing a key role in providing situation overview along the river on a daily basis. The 3D graph in *Fig. 7* illustrates the *M/C* ratios in time and space. Axis x refer to river gauging sites numbered sequentially along to reach from upstream to downstream. Axis y presents the time scale during the flooding from January 1, 2007 to March 22, 2007 and axis z dimension refers to the *M/C* gauging values.

The propagation of the flood wave is visible on the gauging peaks of the graph that run diagonally both to distance along the river (x axis) and time measured in days (y axis). Thus, while optical flood maps can only be produced on cloud free days, the propagation of the flood wave can be monitored every day from AMSR-E images. Further to this, it gives a good estimation and possibility to forecast the arrival of the floodpeak to downstream areas.

Summarizing the founding it can be concluded, that both optical and microwave satellite data can contribute to the acquisition of spatial information

in flood disasters. Yet microwave data has the significant advantage of not being hindered by cloud cover during the event.

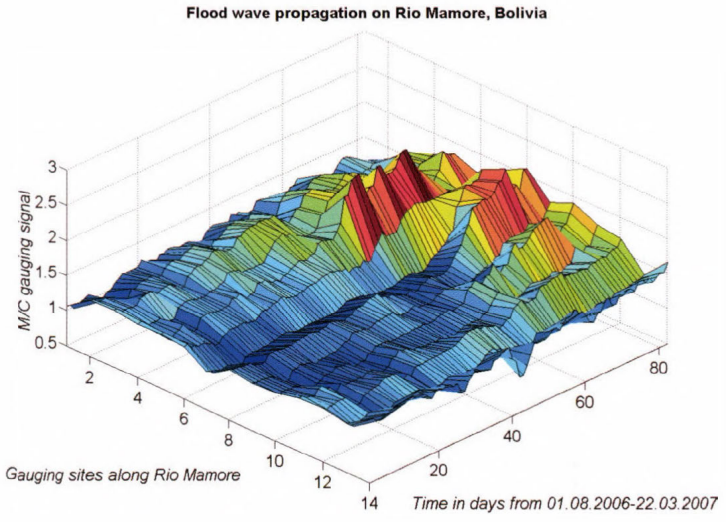

Fig. 7. Orbital gauging measurements in time and space along the Mamore River in Bolivia during the great flood event of 2007. Flood wave propagation is remarkably visible from 3D graph both in time and space. (*Kugler*, 2007).

4. Effects of global climate change on arctic river hydrology

Orbital GFDS technology allows not only the monitoring of flood events but also observing other changes in hydrological conditions. Using the GFDS methodology, river ice freezing and melting can be monitored in arctic regions without the need of in-situ measurements. The extent of polar sea ice cover and ice shield is a well-known indicator of global climate change. Satellite observations have been used for long time to operationally monitor sea ice cover and its changes in the past decades (*Maslanik et al.*, 1999; *Cavalieri et. al.*, 2003; *Rodrigues et al.*, 2008; and *Kwok et al*, 2009). Yet no regular observations are carried out on continental arctic rivers, even though their annual spring ice break-up and freezing would also serve as a notable sign for climate change processes. The lack of traditional hydrological measurements in those remote inaccessible regions makes the use of satellite data a key technique in obtaining information on their hydrological cycle. The analysis of arctic regions can contribute to the quantitative and qualitative estimations of the global impact.

For this reason, satellite data was used to estimate spatial and temporal patterns of arctic river ice from satellite sources like MODIS and AVHRR

(*Pavelsky*, 2004). Using optical resources has the significant disadvantage of being dependent on cloud cover conditions negatively influencing the continuity of its time series. Yet no passive or active microwave data was used so far to monitor the annual timing of the river condition change. For this reason, a study was carried out at the Department of Photogrammetry and Geoinformatics, Budapest University of Technology and Economics, based on GFDS technology to obtain information about remote, inaccessible areas in northern polar and subpolar river systems like the Lena, Yenisey, Ob, Kolyma, and Mackenzie. Using the time series of GFDS, seasonal changes in annual river ice was detectable (*Fig. 8*).

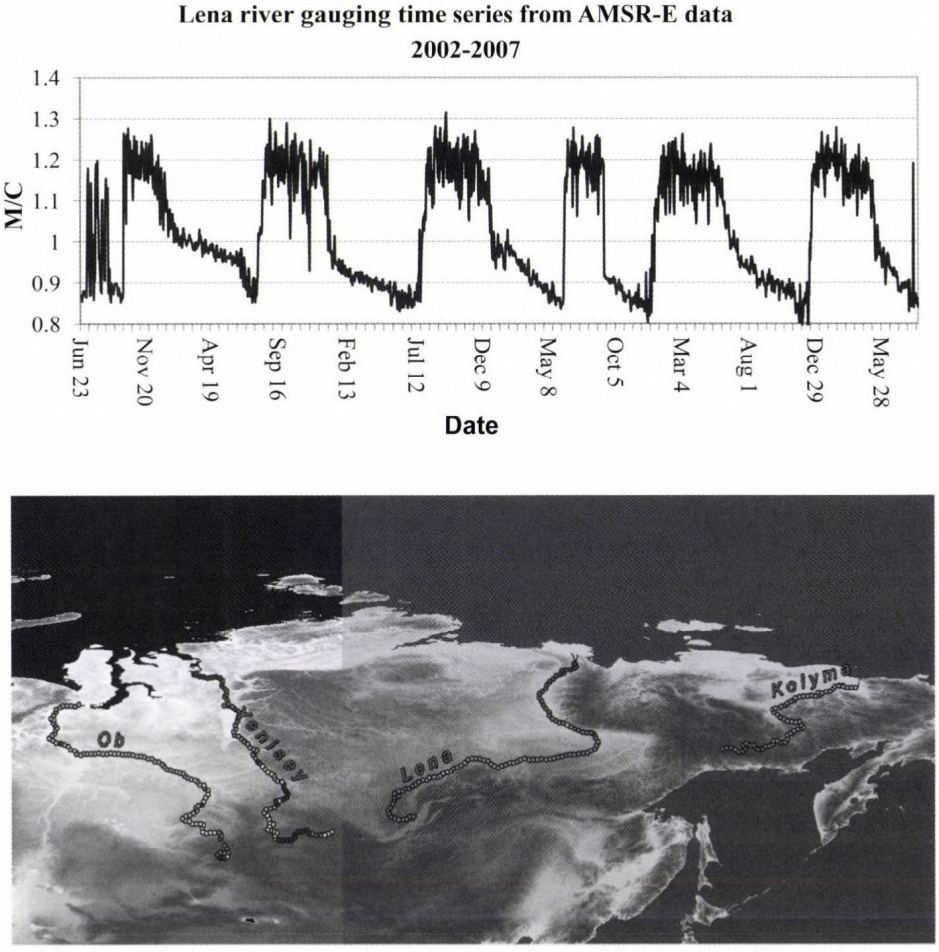

Fig. 8. Seasonal changes in ice-melting and freezing is detectable from *M/C* signal (upper graph). Orbital gauging measurement sites set every 50 km along selected subarctic rivers in Siberia (lower image).

The aim was to reveal possible effects of global climate change on arctic rivers. Anomalies in the period of seasonal river ice melting in spring were analyzed in detail. Orbital gauging observations were set every 50 km in the selected large river valleys to obtain high spatial resolution of the analyses.

The selected rivers generally run from south to north crossing different climate zones. For this reason, melting in spring starts in the lower latitudes and propagates downstream to the north with time. Further to this, there is a strong drift of climatic origin from the most west river of Ob starting to melt at the begin of May to the most east river of Kolyma, where ice break-up starts only at the end of May.

A pilot study has been carried out to extend AMSR-E time series with Special Sensor Microwave/Imager (SSM/I) passive microwave satellite data. Both sensors have similar properties, and images are free of charge. Likewise AMSR-E data *M/C* signal was extracted from 37 GHz, H polarization band of the SSM/I sensor. During the SSM/I mission, several sensors were launched into orbit starting from F8 series in 1987 to F11, 13, 17 satellite missions acquiring data till present. Based on their images, ice melting time series from AMSR-E data was extended with 14 additional years. *M/C* signal was obtained for selected river sites, and orbital gauging was used to detect changes during the investigated years reaching from 1989 to 2010.

To detect the timing of the ice break-up at a given river site, statistical parameters of its complete time series were calculated and defined as magnitude:

$$Magnitude = \frac{M/C - mean(W/C)}{stand.dev.(s)} . \quad (5)$$

As a result, the *M/C* signal was normalized to a value that enables comparison of different sites in various river valleys. Magnitude was below 0 during the winter freezing period and increased to above 0 when spring ice break-up started.

To assess preliminary performance of the techniques, 5 orbital gauging sites were selected and analyzed in detail for the River Lena. Sites were located 1–200 km apart from each other along the river. The day of the ice break-up was extracted and plotted for each studied year demonstrated in *Fig. 9*. Applying a simple linear regression model, lines were fitted to the timing curves to give a preliminary assessment of the changes in the last two decades. Estimations revealed a negative shift over the investigated gauging sites, thus, river ice appeared to break earlier with time. In average, sites were having from –2 to –6 days changes/decade in the timing of their ice-breaking during the past two decades.

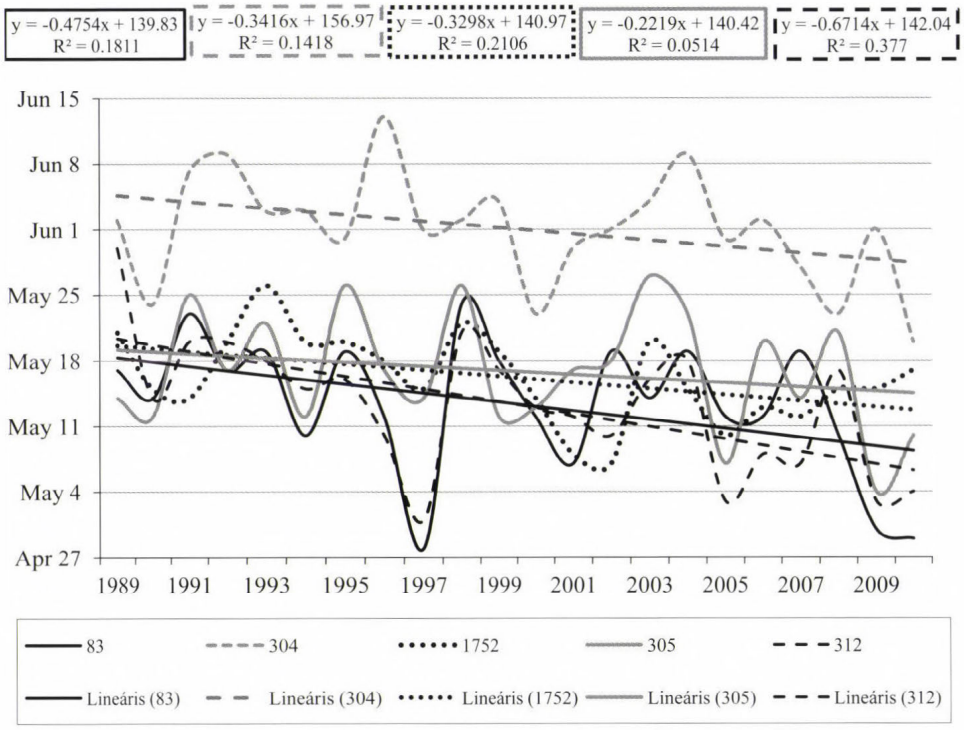

Fig. 9. Ice break-up extracted from orbital gauging measurements from 1989 to 2010 in selected sites along the subarctic River Lena.

Besides the River Kolyma, 4 additional arctic rivers the Ob, Yenisey, Lena in Siberia and the Machenzie in North-America were put under similar investigation. Ice break-up was extracted using the magnitude of the signal (Eq. (5)). Relationship between the day of the ice break-up and the different years was estimated using linear regression approach described above. From 50 to 80 orbital gauging sites were investigated per river valley depending on the length of the reach. The slope of the linear regression line was calculated for each site along the river. The histogram of the slopes for each river is illustrated in *Fig. 10*.

The peak of the distribution lays in negative values meaning that the linear regression lines have a negative direction for the majority of the investigated sites. Thus, the majority of the river sites show a change towards earlier ice break-up in time. The quantitative estimation of the trends may have unexpected uncertainties, but the direction of the changes shows similar trends in the majority of the investigated arctic river valleys.

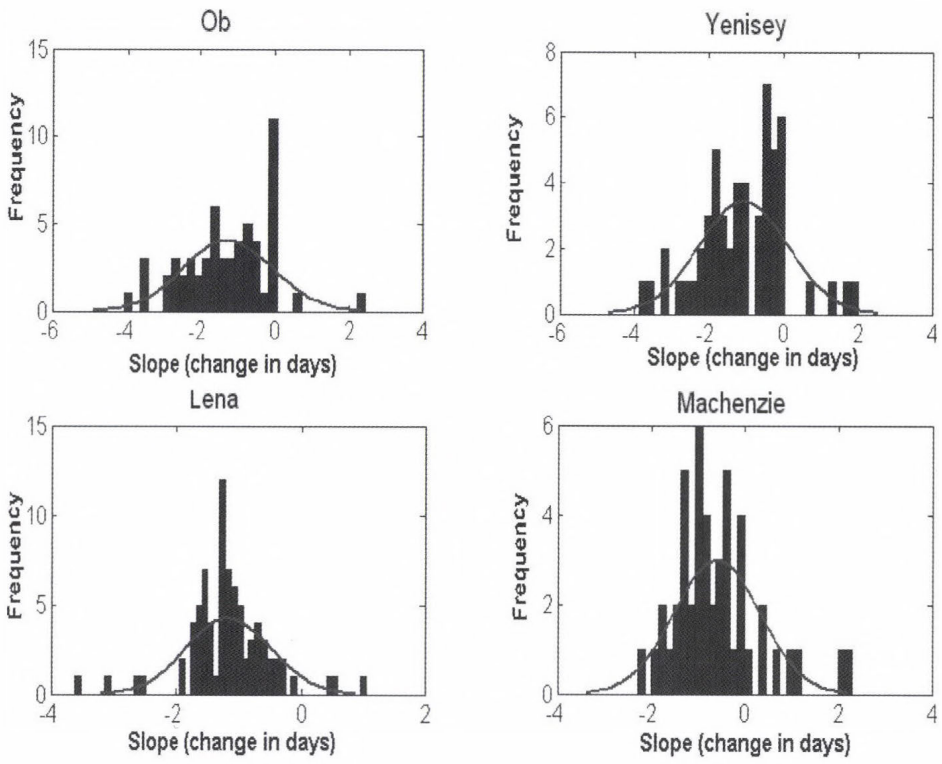

Fig. 10. Histogram of regression line slopes calculated for changes in annual timing of river ice break-up. Results show a negative trend indicating an earlier seasonal ice break-up in the majority of the investigated arctic river sites.

To assess the performance of the described investigation, in-situ gauging measurements were compared with satellite data. Unfortunately, no parallel data was found to the orbital measurement, since arctic hydrometeorological monitoring network drastically declined after 1986 (*Shiklomanov et al.*, 2002). The nearest measurement on the River Lena was found at the station Kusur (70°41`N, 127°24`E) upstream from the orbital site numbered 304. Observations started in 1955 and ended in 1991 (*Vuglinsky*, 2000). Linear regression analysis showed an almost 1 day / decade change in the past half century (*Fig. 11*).

Further to this, orbital results were compared to studies investigating surface air temperature anomalies in the past decade. *Overland et al.* (2008) concludes that the past decade showed a drastic warming in the northern arctic region, especially in Siberia. Consequently, the changes calculated from river ice break-up seems to underline the direction of both the surface temperature changes and the trends in the ice break-up in the past century.

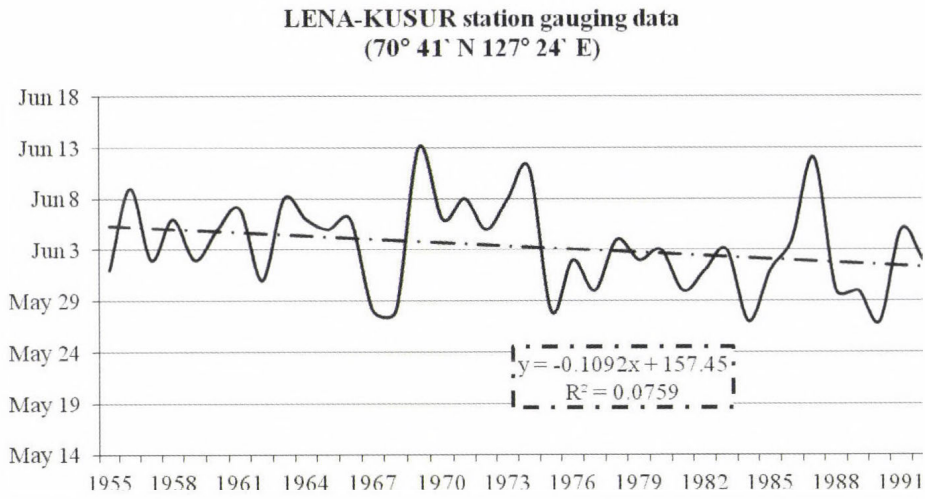

Fig. 11. In-situ gauging measurement of ice break-up along the River Lena at Kusur station (70°41`N 127°24`E), Siberia. Regression analysis shows negative trend. (*Vuglinsky*, 2000).

5. Conclusions

This paper demonstrated the operational use of satellite technology and GIS for hazard assessment. Satellite resources were demonstrated for flood disaster mapping, and in lack of available data, historical maps were introduced for obtaining information on risk and possible future scenarios. Satellite data was also proved to be suitable for operational daily observation of river gauging from space. Further to investigating the possible impact of natural hazards, the quantitative influence of climate change was studied in arctic regions.

Selecting the most appropriate sensor for hazard mapping is depending on many factors. The major limitation of optical satellite systems is cloud cover, even if sensors have appropriate resolution and revisit capability to support operational daily, global observations. Cloud cover plays a significant hindering affect so that passive and active microwave satellite sensors have to be considered. Active systems have no daily global coverage, for this reason the continuous monitoring of flood events is not feasible on a daily basis. For this reasons the GFDS system using passive microwave data is a good alternative to optical systems. Since the emitted energy from the surface is low, the spatial resolution of passive microwave systems is coarse. Still, GFDS applications demonstrated good results even in sub-pixel dimension. For this reason both optical and microwave sensors have great importance in hazard mitigation considering their above mentioned limitations.

Global climate change is expected to increase the magnitude and frequency of natural hazards. The influence of the global change can be measured on

sensitive areas such as polar and subpolar regions. For this reason, the paper also discussed the results from the study analyzing changes in the seasonal ice break-up along arctic rivers. Results concluded an anomaly towards earlier ice melting in the majority of the analyzed river sections in Siberia and Northern America. Even though the quantitative output of the anomalies may have high standard deviation and unexpected inaccuracies, the direction of the change was found to be the same over all investigated river sites.

Acknowledgement—Part of the work presented was supported by *Magyary Zoltán* Postdoctoral Fellowship, Budapest with the grant of the EEA and the Norwegian Financial Mechanism, and by the TÁMOP-4.2.1/B-09/1/KMR-2010-0002 Project was partly supported by the EU.

References

Alsdorf, D.E., Melack, J.M., Dunne, T., Mertes, L.A.K., Hess, L.L., Smith, L.C., 2000: Interferometric radar measurements of water level changes on the Amazon floodplain. *Nature 404,* 174–177.

Birkett, C.M., 1998: Contribution of the TOPEX NASA radar altimeter to the global monitoring of large rivers and wetlands. *Water Resour. Res. 34,* 1223–1239.

Brakenridge, G.R., Anderson, E., 2005: MODIS-based flood detection, mapping, and measurement: the potential for operational hydrological applications. In *Transboundary Floods, reducing risks through flood management NATO Science Series* (eds.: J. Marselek, G. Stacnalie, G. Bálint): IV Earth and Environmental Scineces 72, Springer, The Netherlands, 1–12.

Brakenridge, G.R., Nghiem, S.V., Anderson, E., Mic, R., 2007: Orbital microwave measurement of river discharge and ice status. *Water Resour. Res. 43,* W04405, 16 pp., doi:10.1029/2006WR005238

Cavalieri, D.J., Parkinson, C.L., Vinnikov, K.Y., 2003: 30–year satellite record reveals contrasting Arctic and Antarctic decadal sea ice variability. *Geophys. Res. Lett. 30*(18), 4 pp., doi:10.1029/2003GL018031.

Hess, L.L., Melack, J.M., Filoso, S., Wang, Y., 1995: Delineation of inundated area and vegetation along the Amazon floodplain with SIR-C synthetic aperture radar. *IEEE Trans. Geosci. Remote Sens. 33,* 896–904.

Koblinsky, C.J., Clarke, R.T., Brenner, A.C., Frey, H., 1993: Measurement of river level variations with satellite altimetry. *Water Resour.Res. 29*(6), 1839–1848.

Kovács, K.I., 2010: Spatial information systems for emission reduction. *Clean Technol. Environ Policy 12,* 647–651.

Kugler, Zs., 2004/1*:* The Use of GIS and Remote Sensing in Flood Disaster Management in Mozambique. In: *II. PhD CivilExpo Symposium Proceedings: BUTE Dept. of Highway and Railway Engineering* (eds.: *Barna Zs., Fenyős D.*), Budapest, Hungary, 84–88., ISBN: 963-421-600-5.

Kugler, Zs., 2004/2*:* A 2001. évi mozambiki árvízkatasztrófa felmérése és koordinálása a távérzékelés és térinformatika segítségével. *Geometriai Közlemények VII,* 139–148.

Kugler, Zs., De Groeve, T., Brakenridge, G.R., Anderson, E., 2007: Towards Near real-time Global Flood Detection System. *Int. Arch. Photogramm. Rem. S. XXXVI:*(PART 7/C50), 1–8.

Kwok, R., Rothrock, D.A., 2009: Decline in Arctic sea ice thickness from submarine and ICESat records: 1958-2008. *Geophys. Res. Lett. 36,* L15501.

Ládai, A.D., Kugler, Zs., Tóth, Z., Barsi, Á., 2004: A pest-budai nagy árvíz térinformatikus szemmel. *Térinformatika XVI* (7), 16–18.

LANCE (Land Atmosphere Near Real-time Capability for EOS), 2011: Rapid Response system, Near Real Time (Orbit Swath) Images. [Online] available*: http://lance-modis.eosdis.nasa.gov/cgi-bin/imagery/realtime.cgi*, last access: 2011-09-16

Maslanik, J.A., Serreze, M.C., Agnew, T., 1999*:* On the record reduction in 1998 western Arctic sea-ice cover. *J. Geophys. Res. 26,* 1905–1908.

Overland, E., Wang, M. Salo S., 2008: The recent Arctic warm period. *Tellus A 60,* 589–597.
Pavelsky, T.M., Smith, L.,C., 2004: Spatial and temporal patterns in Arctic river ice breakup observed with MODIS and AVHRR time series, *Remote Sensing of Environment, Volume: 93,* 328–338.
Rodrigues, J., 2008: The rapid decline of the sea ice in the Russian Arctic. *Cold Reg. Sci. Technol. 54,* 124–142.
Sakamoto, T., Nguyen, N.V., Kotera, A., Ohno, H., Ishitsuka, N., Yokozawa, M., 2007: Detecting temporal changes in the extent of annual flooding within the Cambodia and the Vietnamese Mekong Delta from MODIS time-series imagery. *Remote Sens. Environ. 109,* 295–313.
Shiklomanov, A.I., Lammers, R.B., Vörösmarty, C.J., 2002: Widespread Decline in Hydrological Monitoring. Threatens Pan-Arctic Research. EOS Transactions, *American Geophysical Union 83(2)*, 13–17.
Sippel, S.J., Hamilton, S.K., Melack, J.M., Choudhury, B.J., 1994: Determination of inundation area in the Amazon River floodplain using SMMR 37 GHz polarization difference. *Remote Sens. Environ. 48,* 70–76.
Thenkabail, P.S., Schull, M., Turral, H., 2005: Ganges and Indus river basin land use/land cover (LULC) and irrigated area mapping using continuous streams of MODIS data. *Remote Sens. Environ. 95,* 317–341.
Vuglinsky, V., 2000: Russian river ice thickness and duration. Boulder, CO: National Snow and Ice Data Center/World Data Center for Glaciology. Digital media.
Zhan, X., Sohlberg, R.A., Townshend, J.R.G., DiMiceli, C., Carroll, M.L., Eastman, J.C., 2002: Detection of land cover change using MODIS 250 m data. *Remote Sens. Environ. 83,* 336–350.

IDŐJÁRÁS

Quarterly Journal of the Hungarian Meteorological Service
Vol. 116, No. 1, January–March 2012, pp. 39–52

The effect of fertilization and precipitation on the yield of maize (*Zea mays* L.) in a long-term experiment

János Nagy

Centre for Agricultural and Applied Economic Sciences,
University of Debrecen,
Böszörményi út 138, H-4032 Debrecen, Hungary
Email: nagyjanos@agr.unideb.hu

(Manuscript received in final form February 22, 2012)

Abstract—This study examines how the amount of precipitation, the NPK fertilizer treatment and their interaction affects maize yield. The measurements were carried out at the Látókép experiment site of the University of Debrecen (Debrecen, Hungary N: 47°33', E: 21°27', 113–118 metres above sea level) on mid-heavy calcareous chernozem soil in a multifactoral long-term field experiment established in 1984. 17-year-long data series were used (1990–2008) in the study. We examined how the precipitation during the growing season and the winter period affected maize yield and demonstrated into that there was a strong positive correlation ($r=0.710$; $p<0.01$) between the amount of precipitation during the growing season and yield. Based on the effective heat units (EH) and the potential evapotranspiration (PET) values, the growing seasons of the long-term experiment were separated to dry and wet years. The difference between the average yields of dry and wet years was significant ($p<0.05$). Significant difference was obtained ($p<0.05$) between the non-fertilized and fertilized treatments (60 and 120 kg N ha^{-1}). The 120 kg N ha^{-1} treatment did not significantly increase the maize yield in comparison with the 60 kg N ha^{-1} treatment. The evaluation of the joint effect of fertilization and precipitation on yield showed that fertilization is responsible for nearly twice as much of the standard deviation of yield as the amount of precipitation. In dry years, there was a significant difference only between the non-fertilized and fertilized treatments, whereas in wet years, we even found a statistical difference between fertilizer doses. As regards fertilizer treatments, higher yields were obtained in wet years than in dry ones. Altogether, statistical evaluations showed that the nutrient utilization of the applied fertilizer is determined by precipitation supply. In dry years, only smaller fertilizer doses (60 kg N ha^{-1}) were utilized, higher doses were not necessary. In wet years, higher doses (120 kg N ha^{-1}) induced significantly higher yield and higher extent of nutrient utilization.

Key-words: maize, precipitation, fertilization, long-term field experiment

1. Introduction

The high variability of climate is one of the biggest risk factors of production and agricultural producers have to continuously consider this factor. Over many years, differences in temperature and precipitation, as well as their distribution, significantly affect yield and yield quality, even in the case of very similar production technologies.

In the last century, the proportion of drought or extremely wet years significantly increased. Both have a negative effect on maize production and its predictability. *Barrov et al.* (2000) reached a similar conclusion when they determined the change of the quantity of precipitation in winter (0.4–3.6%) and summer ((–0.5)–3.7%) periods between 1961–1990. *Láng* (1976) and *Márton* (2002) showed the significant effect of weather on yield. *Berényi* (1956) established that natural water supply determined 55–75% of yield.

Water has multiple and rather complex roles in the life and metabolism of plants. The rate of growth of maize reacts in a much more sensible and much quicker way to the change of water supply than any other change in the environmental factors. Water stress during vegetative development reduces the growth of stem and leaf cells, which then leads to the decrease of crop height and leaf area (*Lauer,* 2003). Drought during tasselling could result in 40–50% yield loss (*Claassen* and *Shaw,* 1970). Water shortage during tasselling and flowering reduce the grain number per row, whereas water stress after pollination decreases grain weight, thereby causing a significant yield drop (*Shaw,* 1977; *Westgate* and *Boyer,* 1986; *Lauer,* 2003). *Kiesselbach* (1950) states that temperature and water supply have significant effects during grain filling. Drought during grain filling usually results in the development of smaller grains (*Smith et al.*, 2004). As a result of unfavourable water supply, the speed and duration of dry matter incorporation decreases (*Quattar et al.,* 1987). *Westgate* and *Garnt* (1989) pointed out that even a shorter period of water shortage caused a significant drop in the water content of grains.

Besides the level of water and nutrient supply, the efficiency of maize production is also determined by the date of fertilization and its distribution. Therefore, professional fertilization is the basic requirement of optimal crop production. During the determination of the optimal date of fertilization and the optimal fertilizer dose, producers have to consider the transformation, leaching and fixing processes in the soil, the nutrient absorption ability and fertilizer reaction of the produced hybrid, as well as the effect of precipitation (*Hansen* and *Djurhuus,* 1996; *Delphin,* 2000; *Ichir et al.,2003; Nakamura et. al.,* 2004; *Körschens,* 2006).

The results of long-term fertilization field experiments provide an opportunity to evaluate multifactoral interactions in crop production and environmental protection research projects (*Körschens,* 2006; *Nagy,* 2008). The aim of this study was to examine the effect of precipitation – as an independent

variable – during winter and the growing season, as well as the effect of NPK fertilization on yield. Furthermore, we examined the effect of the interaction of these two factors on maize yield.

2. *Materials and methods*

The measurements were carried out at the Látókép experiment site of the University of Debrecen (Debrecen, Hungary N: 47°33', E: 21°27', 113–118 metres above sea level) in a multifactoral long-term field experiment established in 1984. 17 year long data series were used (1990–2008) in the study.

Soil properties of the field experiment:

The experiment was carried out on mid-heavy calcareous chernozem soil. Based on the soil analysis results obtained in 2008, the average pH_{KCl} of the soil was 6.6 (slightly acidic), which is optimal from the aspect of the nutrient uptake of the crop. The physical type of the soil was mid-heavy adobe. The soil plasticity of the upper (0.2 m) layer was 39 (*Arany*'s number). The total soil water-soluble salt content (anions and cations) was 0.05% (low salt content soil). The calcium carbonate content in the upper 0.8 m of soil was 0% (i.e. there is a chalk deficiency), but it gradually increased between 1 m and 1.6 m, reaching 11% (i.e. moderately chalky). The organic matter of the soil was 2.4% in the upper 0.2 m of soil, whereas it did not exceed 1% at a depth of 1.2 m. The soil nitrogen and potassium supply was good and the phosphorous content was average.

Fertilizer treatments:

The basic dose was 30 kg N ha^{-1}, 23 kg P_2O_5 ha^{-1}, 27 kg K_2O ha^{-1}. Fertilizer treatments of 1, 2, 3, 4 and 5 times higher than this dose were applied and a non-fertilized treatment was also included. we examined the results of the non-fertilized treatment and the 60 kg N ha^{-1}, 46 kg P_2O_5 ha^{-1}, 54 kg K_2O ha^{-1} (indication: 60 kg N ha^{-1}), 120 kg N ha^{-1}, 90 kg P_2O_5 ha^{-1}, 106 kg K_2O ha^{-1} (indication: 120 kg N ha^{-1}) treatments. The entire quantity of fertilizers was applied in spring. The experiment had a strip plot design, with the 30 hybrid and fertilizer treatments located crosswise in four replications. The plant density was 70 thousand plants ha^{-1}. In order to determine the nitrate N content of the soil, soil samples were taken twice a year in spring (one week before sowing) and after harvest from the 0–200 cm soil layer.

Weather parameters:

Environmental parameters at the Research Plant of the University were continuously measured and logged by an automatic data-logging station. Air temperature (°C) at heights of 0.5, 1 and 2 m, relative humidity (%) soil

temperature (°C) at depths of 50, 250 and 500 mm, incoming radiation (W m^{-2}) and the amount of precipitation (mm) were measured every sixth second. The statistical parameters derived from the data (average, standard deviation) were stored every 15 minutes. Basic data are accompanied by pheno- and phytometric observations and soil analyses. we used the following equation to calculate heat units – one of the most important criteria in maize growing – over the entire growing season (*Table 1*):

$$HU = \sum_{i=1}^{n} \frac{(T_{max} - T_{min})}{2} - T_{basis}, \quad (1)$$

where HU indicates the heat unit,

T_{max} indicates maximum daily temperature,

T_{min} stands for minimal daily temperature,

T_{basis} indicates the base temperature for crop development, which is 10°C in the case of maize (*Davidson* and *Campbell,* 1983; *Gallagher,* 1979; *Nield* and *Seeley,* 1977).

Table 1. Precipitation, effective heat sum and potential evapotranspiration (Debrecen, 1990–2008)

Years	Precipitation during the growing season (mm)	Heat unit (°C)	Potential evapotranspiration (mm day^{-1})
1990	202	1175	625
1992	180	1531	693
1993	253	1381	665
1994	240	1461	681
1996	428	1336	655
1997	248	1424	672
1998	472	1420	671
1999	389	1537	691
2000	196	1502	687
2001	402	1380	666
2002	256	1288	650
2003	219	1439	679
2004	343	1168	624
2005	499	1302	649
2006	326	1414	670
2007	284	1573	704
2008	484	1475	680

There are numerous methods for the determination of potential evapotranspiration (*PET*), some of which are empirical correlations, others are multivariate functions calculated with statistical methods, whereas the most recently applied formulae are derived from the most important thermodynamic parameters. Among others, these are the methods of *Penman* (1948), *Thornthwaite* (1948), *Mckenny* and *Rosenberg* (1993) and *Szász* (1977). We used the method of *Szász* (1977) to determine the value of *PET*. This method provides a highly accurate estimation and it considers the atmospheric elements and processes significantly determining the evaporation of water – air temperature, the relative moisture content of water vapour, wind speed and microadvection effects.

$$PET = \beta\left[0.0095\,(T-21)^2\,(1-R)^{2/3}\,f(v)\right] , \tag{2}$$

where PET is the potential evapotranspiration (mm day^{-1}),
T is the daily mean temperature (°C),
R is the degree of saturation,
$f(v)$ is the effect function of wind speed,
β is the coefficient for the expression of the oasis effect.

The oasis effect is the quotient of the environment and the evaporating water.

$$\beta = \frac{(c\rho)_{soil}}{(c\rho)_{water}} \tag{3}$$

The numerator covers the heat capacity of the environment and the soil and the denominator is the heat capacity of water. The heat capacity of water is 4.19 J cm^{-3}.

The heat capacity of wet soil:

$$c_v = 0.84\,\gamma + 4.2N_{tf} + 0.0012L_{tf} , \tag{4}$$

where γ is the volume mass (g cm^{-3}),
N_{tf} is the moisture content (cm^3 cm^{-3}),
L_{tf} is the air content (cm^3 cm^{-3}).

Statistical procedures:

In order to examine the effect of precipitation during the winter period and the growing season on yield, we determined the coefficient of correlation between the variables. Based on the available weather data, we separated the examined years into groups by using hierarchical cluster analysis. We used variance analysis to examine whether there is any difference between the two

groups as independent variables identified by the cluster analysis from the aspect of the effect on yield. We ran a *Kruskal-Wallis* non-parametric test generally used for the comparison of the means of three or more samples concerning the whole sample to examine the effect of fertilization on maize yield. We applied paired *Mann-Whitney* U test with *Bonferroni* correction to examine the differences between treatment means.

We analysed the common effect of dry and wet years and fertilizer treatments as independent variables on maize yield. We separately evaluated the differences between fertilizer effects in dry and wet years, as well as the effect of precipitation on different fertilizer levels. Following this, we categorized the examined years from the aspect of yield using hierarchical cluster analysis (very low, low, high, very high).

3. *Results and conclusions*

3.1. The effect of precipitation during the winter period and the growing season on maize yield

Based on the value of Pearson's correlation coefficient (using a paired test), it was shown that there is a strong positive correlation between the precipitation in the growing season and yield ($r=0.718$, $p<0.01$) at 1% level of significance (*Fig. 1*), similar to the results of *Aguilar et al.* (2007).We could not show any correlation between the amount of precipitation in the winter period and the yield, therefore, we only analysed the correlation between the data during the growing season and yield.

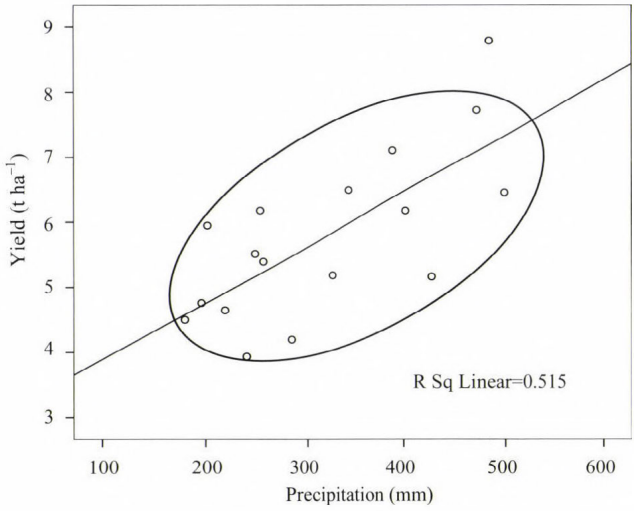

Fig. 1. Correlation between the precipitation during the growing season and yield (Debrecen, 1990–2008).

In itself, the amount of precipitation does not determine the amount of water available for maize. Using the data available at the meteorological station of the university, we calculated the values of the effective temperature (*ET*) and potential evapotranspiration (*PET*) for the entire growing season (*Table 1*). Based on the amount of precipitation during the growing season, the *ET* and *PET* values, we used hierarchical cluster analysis to classify the years into groups. One of the groups was named dry years and the other one was named wet years. Of the 17 experimental years, the following ones were dry: 1990, 1992, 1993, 1994, 1997, 2000, 2002, 2003, 2007; wet years: 1996, 1998, 1999, 2001, 2004, 2005, 2006, 2008. (The years 1991 and 1995 were excluded from the analysis, due their extreme values and the „sensitivity" of the statistical analyses.) The average amount of precipitation in the growing season (April-September) was 231 mm in dry years and 418 mm in wet years. The potential evapotranspiration was 673 mm on average in dry years during the growing season and 626 mm in wet years.

The results of the variance analysis showed that there is a significant difference ($p<0.05$) between the average maize yields of wet and dry years. The average yield was 6.96 t ha^{-1} in dry years and the water supplied by precipitation significantly increased maize yield (by 2.19 t ha^{-1}). Every millimeter of precipitation in the growing season was associated with 34 kg grain yield in dry years and 45 kg in wet years.

During the 17 years of the long-term experiment, yields varied greatly from year to year. The lowest maize yield was obtained in 2007 (5.21 t ha^{-1}), whereas the highest yield was harvested in 2008 (11.41 t ha^{-1}) (*Fig. 2* and *3*).

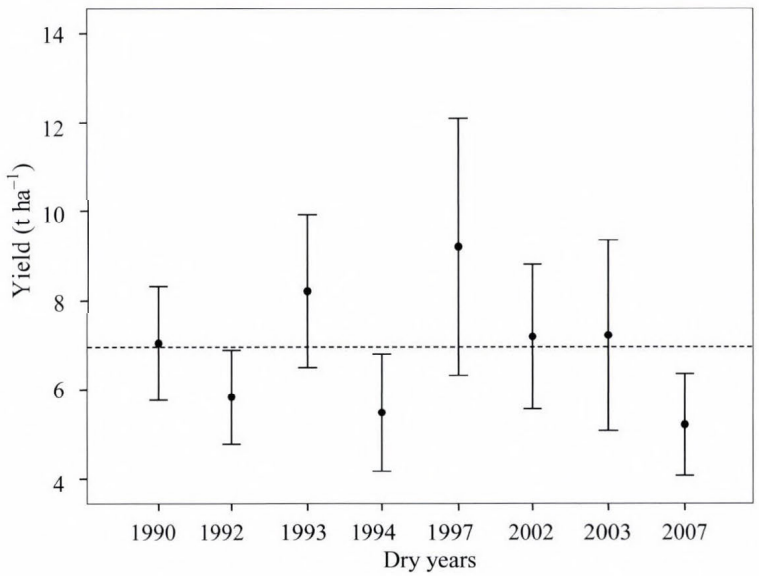

Fig. 2. Average yield of maize in dry years.

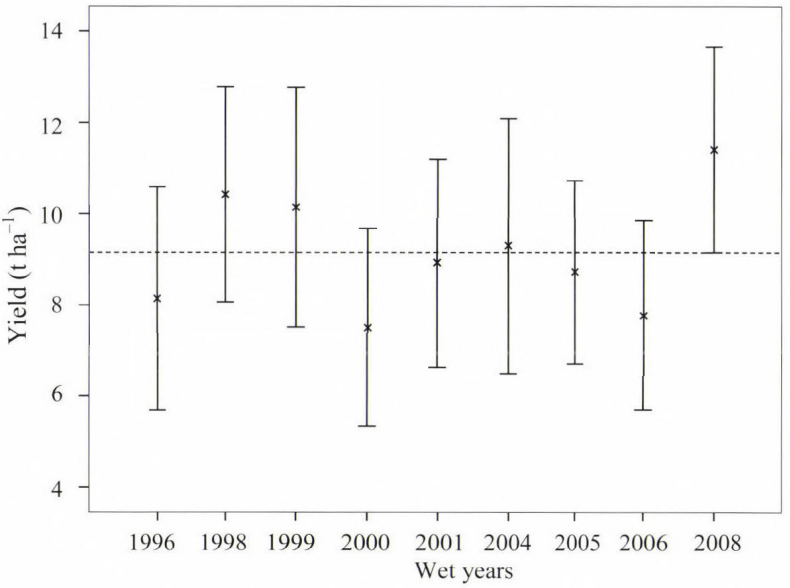

Fig. 3. Average yield of maize in wet years.

3. 2. Evaluation of the effect of fertilization

Precipitation during the growing season greatly determines the leaching of nitrogen forms and the utilization of the nitrogen active ingredient. Only a part of the active ingredient content of the applied N fertilizer is present in the yield, the rest is leached out, it denitrificates or is transformed in other ways (*Kavlen et al.,* 1998; *Díez et al.,* 2008). Due to the high amount of precipitation and the high dose of applied nitrogen fertilizer, significant nitrate contamination can be observed in the soil water on certain areas (*Ordofiez et al.,* 1990; *Ramos* and *Varela*, 1990). These phenomena caused serious problems in the recent years. Before evaluating the effect of fertilization on yield, we examined the 1990–2008 nitrate N content of the 0–200 cm soil profile of the experimental plots that have different levels of nutrient supply. In the non-fertilized treatments, the amount of nitrate N found in the examined layers of the soil was rather low, reaching only 2–7 mg. Its distribution within the profile was even, we observed a slight increase from the surface soil to the deeper layers. In the period of examination, there was no difference in the amount of nitrate N and its distribution within the layer. Depending on the dose of fertilizer and the given year, there were differences in the entire depth of the soil profile. The nitrogen in the fertilizer applied after harvest during the autumn was accumulated in the upper layer of the soil at the time of measurement. The zone of accumulation was at the same depth in the case of both the 60 kg N ha^{-1} and the 120 kg N ha^{-1} fertilizer doses (*Fig. 4*).

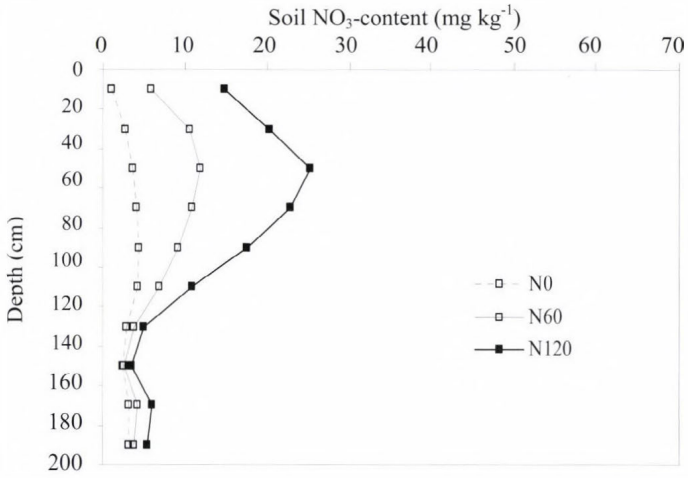

Fig. 4. The nitrate N content of soil in different fertilization treatments before sowing (Debrecen, 2008)

Under the zone of accumulation, the nitrate N content of the soil profile significantly decreases,we measured 5–12 mg kg^{-1} in the 100–130 cm depth, depending on the amount of fertilizers and the years. In the 140–200 cm deep soil layer, the nitrate N content that accumulated due to each fertilizer treatment did not significantly differed from the data of the non-fertilized control plots.

Every year, there was significant difference (0.1%) between the non-fertilized and the fertilized treatments (60 and 120 kg N ha^{-1}) from the aspect of maize yield (independently of whether it was a wet or dry year). The 120 kg N ha^{-1} fertilizer treatment significantly increased maize yield in comparison with the 60 kg N ha^{-1} treatment (*Fig. 5*).

The difference between 60 and 120 kg N ha^{-1} treatments was significant on a 0.01% level in four years (1997, 1999, 2000, 2005) and on 1% level in one year (2006), 5% level in four years (1996, 1998, 2003, 2008), whereas the difference was not significant in eight years (1990, 1992, 1993, 1994, 2001, 2002, 2004, 2007).

By using the yearly data of the yield reaction measured in the experiment, *Fig. 6* shows the cumulative effect of fertilizer treatments on the grain yield of maize.we chose the treatments 60 kg N ha^{-1}, 46 kg P_2O_5 ha^{-1}, and 54 kg K_2O ha^{-1} as a basis treatment the various treatments show the cumulated difference in yield in comparison with the basis treatment. The non-fertilized control treatment causes a higher and higher yield drop from year to year, its value is 54.5 t ha^{-1} in the 17th year, compared to the basis treatment. Two sections can be identified in the temporal dynamics of cumulated yield differences. In the first five years of the experiment, the treatment 120 kg N ha^{-1}, 90 kg P_2O_5 ha^{-1}, 106 kg K_2O ha^{-1} had hardly any effect on the cumulated yield. Following this,

yield increased from year to year, and the yield surplus was 10.8 t ha^{-1} in the 17th year of the experiment, compared to the basis treatment.

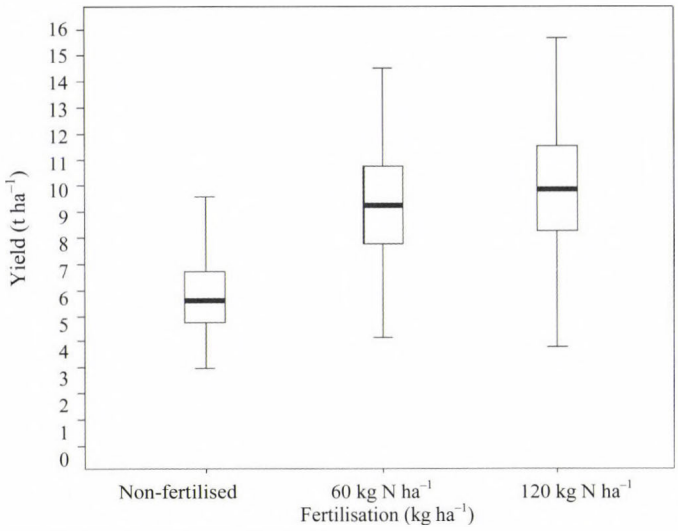

Fig. 5. The effect of fertilization on maize yield (Debrecen, 1990–2008).

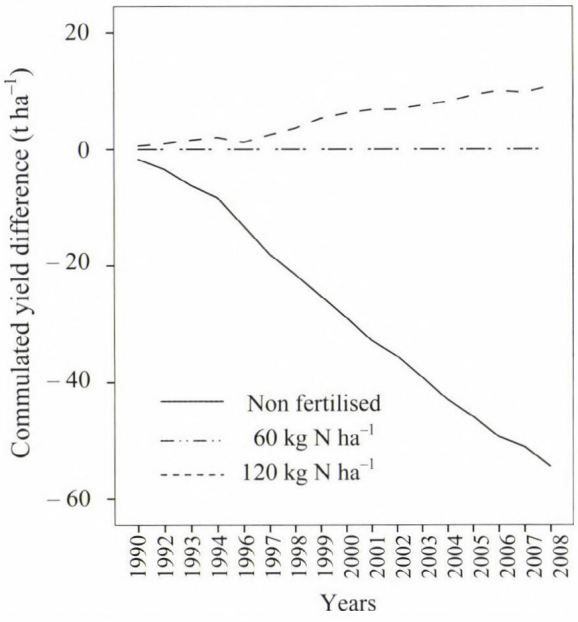

Fig. 6. Cumulated yield difference of the various treatments in comparison with the basis treatment (Debrecen, 1990–2008)

3.3. Effect of fertilization and precipitation on maize yield

Multifactoral analysis of variance of yield

During the joint analysis of variance,we examined the effect of the two independent variables (1: fertilization, 2: precipitation) on yield at the same time. Based on the significance levels, both factors had significant effects on yield ($p<0.001$) and the interaction of the two factors was also significant ($p<0.05$). Fertilization is responsible for nearly twice as much of the standard deviation of yield as precipitation, that is the effect of fertilization treatments on maize yield is much more significant than that of precipitation (*Table 2*). Based on the value of R^2, independent variables are 56.8% responsible for the variance of the dependent variable.

Table 2. The (combined) variance analysis of the effect of fertilization and precipitation, also considering years, yield t ha^{-1} (Debrecen, 1990–2008)

Factors	Mean Square	Degrees of Freedom	F value	Sig
Fertilization	706,9	2	237,7	0,000
Precipitation	363,8	1	122,3	0,000
Fertilization × Precipitation	11,7	2	3,9	0,049
Error	3,0	486		

R squared = 0,568 (Adjusted R Squared = 0,523)

Effect of fertilizer treatments in dry and wet years

In dry years,we analysed the effect of fertilizer treatments on the dependent variable by the non-parametric equivalent of one-way ANOVA (*Kruskal-Wallis*) andwe established that the effect was significant ($p<0.01$). The non-fertilized and fertilized (60 and 120 kg N ha^{-1}) treatments significantly differed from each other: at the 60 kg N ha^{-1} fertilizer level, the average yield obtained was higher by 2.82 t ha^{-1} than in the case of non-fertilized treatments, whereas if 120 kg N ha^{-1} is applied, the yield obtained was higher by 3.25 t ha^{-1} ($p<0.001$) in comparison with non-fertilized conditions.we compared median values by *Mann-Whitney* test and found that there was no significant difference between 60 and 120 kg N ha^{-1} treatments.

In wet years,we used variance analysis to show that different fertilizer treatments have different effects on maize yield ($p<0.01$). As for the 60 kg N ha^{-1} fertilizer treatment, the utilization of fertilizer was significantly higher by 3.69 t ha^{-1} than in the case of the non-fertilized treatment, whereas this value was 4.46 t ha^{-1} when 120 kg N ha^{-1} was applied ($p<0.001$). No statistical difference could be shown between the 60 and 120 kg N ha^{-1} fertilizer treatments.

The effect of precipitation in different fertilizer treatments

After examining the normality of yield in every fertilizer treatment,we established that the variable has a normal distribution on two fertilizer levels. Concerning these treatments,we performed variance analysis to examine the effect of precipitation on yield, whereaswe applied a non-parametric test in the case of non-fertilized treatment.

As for the non-fertilized treatment and the two different NPK effects, the amount of precipitation significantly affected yield ($p<0.001$) and significantly higher yields were obtained in years when there was more precipitation. In the non-fertilized treatment, the yield was 1.50 t ha^{-1} higher in wet years, whereas it was 2.36 t ha^{-1}higher in the case of the fertilizer treatment 60 kg N ha^{-1} and by 2.70 t ha^{-1} in the case of the fertilizer treatment 120 kg N ha^{-1} than in dry years.

During the wet years, the yield increasing effect of fertilization is higher than in dry years. The yield increment was 0.86 t ha^{-1} in the case of non-fertilized treatments and the 60 kg N ha^{-1} treatment, whereas it was 1.21 t ha^{-1} in the case of 120 kg N ha^{-1}.

I classified the years by average yield into four groups using a hierarchic cluster analysis based on combination. Of the examined 17 years, very low yields were obtained in three years, low yields were obtained in seven years, whereas there were high yields in three years and very high yields in three years (*Fig. 7*).

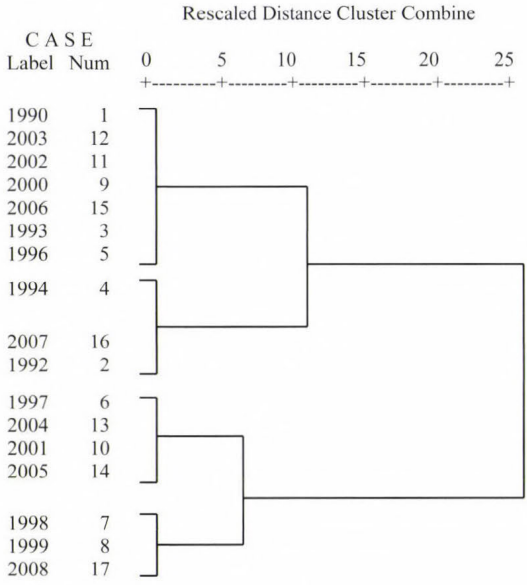

Fig. 7. Hierarchical cluster analysis based on combination on the basis of the average maize yield (Debrecen, 1990–2008).

Acknowledgement—This work was supported by the National Office for Research and Technology NKTH 00210/2008, TÁMOP 4.2.1./B–09/1/KONV–2010–0007 and TÁMOP 4.2.2./B–10/1-2010-0024.

References

Aguilar, M., Borjas, F., Espinosa, M., 2007: Agronomic response of maize to limited levels of water under furrow irrigation in southern Spain. *Spanish Agric. Res. 5*, 587–592.

Barrov, E.M., Hulme, M., Semenov, M.A., Brooks, R.J., 2000: Climate change scenarios. In: Climate Change, Climatic Variablility and Agriculture in Europe (eds.: Downing, T.E., Harrison, P.A., Butterfield, R.E., Londsdale, K.G.) Europcan Commision, Brussel.

Berényi, D., 1956: A cukorrépa termésátlaga és az időjárási elemek közötti összefüggés. *Acta Univ. Debr. 3*, 229–249.

Claassen, M.M., Shaw, R.H., 1970: Water deficit effects on corn. II. Grain components. *Agron. J. 62*, 652–655.

Davidson, H.R., Campbell, C.A., 1983: The effect of temperature, moisture and nitrogen on the rate of development of spring wheat as measured by degree days. *Can. Plant Sci. 63*, 833–846.

Delphin, J-E., 2000: Estimation of nitrogen mineralization in the field from an incubation test and from soil analysis. *Agron. Sustain. Dev. 20*, 349–361.

Díez-López J.A., Hernaiz-Algarra, P., Arauzo-Sánchez, M., Carrasco-Martín, I., 2008: Effect of a nitrification inhibitor (DMPP) on nitrate leaching and maize yield during two growing seasons. *Spanish Agric. Res. 6*, 294–303.

Gallagher, J.N., 1979: Field studies of cereal leaf growth: I. Initation and expansion in relation to temperature and ontogeny. *J. Exp. Bot. 30*, 625–636.

Hansen, E.M., Djurhuus, J., 1996: Nitrate leaching as affected by long-term N fertilization on a coarse sand. *Soil Use Manage. 12*, 221–228.

Ichir, L.L., Ismaili, M., Hofman, G., 2003: Recovery of 15N labeled wheat residue and residual effect of N fertilization in a wheat-wheat cropping system under Mediterranean conditious. *Nutr.Cycl. Agroecosys. 66*, 201–207.

Kavlen, D.L., Kramer, L.A., Logsdon, S.D., 1998: Field-scale nitrogen balances associated with long-term continous corn production. *Agron. J. 90*, 644–650.

Kiesselbach, T.A., 1950: Progressive development and seasonal variation of corn crop. *Univ. Nebraska Bull.*, 166.

Körschens, M., 2006: The importance of lond-term experiments for soil science and environmental research – a review. *Plant Soil Environ.* 52, *(Special Issue)* 1–8.

Láng, G., 1976: Szántóföldi növénytermesztés. Mezőgazdasági Kiadó, Budapest.

Lauer J., 2003: What happens within the corn plant when drought occurs. *Univer. Wisconsin Ext.*, http://www.uwex.edu/ces/ag/issues/drought2003/corneffect.html

Márton, L., 2002: Az évhatás elemzése az északkelet-magyarországi, nyírlugosi műtrágyázási tartamkísérletben. A természetes csapadék és a tápanyagellátottság hatása a burgonya (*Solanum tuberosum* L.) termésére. *Növénytermelés 51*, 71–87.

Mckenney, M.S., Rosenberg, N.J., 1993: Sensitivity of some potential evapotranspiration estimation methods to climate change. *Agric. Forest Meteorol. 64*, 81–110.

Nagy, J., 2008: Maize production. Akadémiai Kiadó, Budapest, 391.

Nakamura, K., Harter, T., Hirono, Y., Hirono, H., Mitsuno, T., 2004: Assessment of root zone nitrogen leaching as affected by irrigation and nutrient management practices. *Vadose Zone J. 3*, 1353–1366.

Nield, R.E., Seeley, M.W., 1977: Growing degree days predictions for corn and sorghum development and some applications to crop production in Nebraska. *Nebr. Agric. Exp. Stn. Res. Bull. 280.* Lincoln, Ne.

Ordofiez, R., Giraldez, J.V., Gonziiez, P., 1990: Nitrogen use on irrigated farms in the Guadalquivir Valley: approach to a rational design after soil column leaching experiments. *International Symposium, Nitrate-Agriculture-Eau. Proc.* (ed. :*R. Calvet*), Paris, 437–443.

Penman, H.L., 1948: Natural evaporation from open water, bare soil and grass. *Proc. R. Soc. Lond. 193*, 120–145.

Quattar, S., Jones, R.J., Crookston, R.K., Kajelou, M., 1987: Effects of water deficit during grain filling on the pattern of maize kernel growth and development. *Crop Sci. 27*, 730–735.

Ramos, C., Varela, M., 1990: Nitrate leaching in two irrigated fields in the region of Valencia (Spain). *International Symposium, Nitrate-Agriculture-Eau. Proc.* (ed.: *R. Calvet*), Paris, 335–345.

Shaw, R.H., 1977: Climatic requirement. In: *Corn and corn improvement* (ed.: *Sprague, G.F.*), Amer.Soc.Agron.Inc. Publisher, Madison, Wisconsin, 774.

Smith, W.C., Betrán, J., Runge, E.C.A. (eds), 2004: Corn. Origin, History, Technology, and Production. Hoboken, NJ: John Wiley, 949.

Szász G., 1977: Formulae of Calculating Evapotranspiration and their Application in the Practice of Hungary. *I.C.I.D., Internat round Table conf. On „Evapotranspiration". Question 3*, 1–13.

Thornthwaite, C.W., 1948: An approach toward a rational classification of climate. *Geogr. Rev. 38*, 5–94.

Westgate, M.E., Boyer,J.S., 1986: Reproduction at low silk and pollen water potentials in maize. *Crop Sci. 26,* 951–956.

Westgate, M.E., Grant, D.L.T., 1989: Water deficits and reproduction in maize responses of the reproductive tissues to water deficits at anthesis and mid-gain fill. *Plant Physiol. 91*, 862–867.

IDŐJÁRÁS

Quarterly Journal of the Hungarian Meteorological Service
Vol. 116, No. 1, January–March 2012, pp. 53–64

The efficiency of natural foliar fertilizers

Róbert Víg[1*], Attila Dobos[1], Krisztina Molnár[2], and János Nagy[1]

[1]*Research Group of Cultivation and Regional Development, Hungarian Academy of Sciences, University of Debrecen Böszörményi út 138.H-4032 Debrecen, Hungary*

[2]*Institute for Land Utilisation, Technology and Regional Development, Center of Agricultural Sciences and Engineering, University of Debrecen Böszörményi út 138, H-4032 Debrecen, Hungary*

[*]*Corresponding author; E-mail: vr.esoxipmail.hu*

(Manuscript received in final form February 3, 2012)

Abstract—In the light of the agricultural development, microbiological products have increasing significance, since it is possible to improve soil fertility and tolerance of cultivated crops, and the use of chemical fertilizer can be reduced.

The efficiency of natural foliar fertilizers was examined in a three-year long analysis (2006–2008) in the southern production area of Hajdúszoboszló on meadow chernozem soil. During the examinations, the primary question was whether the foliar fertilizers Natur Vita (*Chlorella vulgaris* and *Spirulina platensis*), Natur Plasma (*Chlorella spp.*), and Amalgerol Premium (alginate, mannitol, laminarin etc.) provide further yield increase on top of basic fertilisation in maize population and stubble field treatments. The efficiency of products was tested in hybrid seed production, and the examinations were extended to potato production, too.

During the statistical evaluation of the research results, it was established that the use of the tested foliar fertilizers improve the vital conditions of the hybrid seed production. Depending on the applied treatment, foliar fertilizers provide further yield increase on top of basic fertilization, and their combined use does not result in significantly higher yield than in the case of applying products individually.

Key-words: maize, SPAD, foliar fertilizer, efficiency

1. Introduction

One of the key issues of sustainable agriculture is the maintenance of soil fertility (*Reeves,* 1997; *Arshad* and *Martin,* 2002; *Gosling* and *Shepherd,* 2005), but the strongly chemicalized farming method which neglects production site

conditions could lead to harmful processes in the soil that results in the reduction of soil fertility (*Schwab,* 1990; *Kim et al.,* 2000; *Nagy,* 2006, 2007). Such negative effects are the deterioration of the fertile soil (erosion, deflation) (*Evans,* 2005; *Deumlich et al.,* 2006), soil contamination (*Hansen et al.,* 2000), reduction of the organic matter content and biological activity of the soil (*Dawe et al.* 2003; *Loveland* and *Webb,* 2003), salinification (*Liang et al.,* 1996), and deterioration of the soil structure (*Lupwayi et al.,* 2001; *Bronick and Lal,* 2005).

Biofertilizers could have significant role in sustainable agroecosystems, as they help to maintain soil fertility (*Kannaiyan,* 2002; *Wu et al.,* 2005; *Kincses et al.,* 2009), and they can contribute to yield increase without imposing a chemical load on the environment (*Gould,* 1990).

Biofertilizers are the products which contain microorganisms that have a beneficial effect on the nutrient extraction, plant growth, and development (*Vessey,* 2003). These products could either be plant growth-promoting rhizobacteria (PGPR) (*Kloepper et al.,* 1989; *Döbereiner,* 1997; *Cong et al.,* 2009), arbuscular mycorrhizal fungi (AMF) (*Duffy* and *Cassells,* 2000; *Douds et al.,* 2006), and algae (*Nisha et al.,* 2007).

The bacteria living in the soil (PGPR) have a beneficial effect on crops and they play a significant role in the protection against phytopathogens, nitrogen fixation, nutrient extraction (*Vessey,* 2003), improve the development of the favorable soil structure (*Kohler et al.,* 2006), and increase the resistance of crops to environmental stress factors (*Sturz* and *Nowak,* 2000; *Gajdos,* 2009). The mycorrhizal fungi that live in symbiosis with plant roots make immobile elements available to plants, they help water uptake and increase resistance to pathogens (*Smith* and *Read,* 1997).

Algae have outstanding nitrogen fixation ability which makes it possible to use them as a fertilizer. Similarly to farmyard manure, the proportion of organic matter is high in algae (400 units), while the ratio of potassium is satisfactory (27 units) and that of phosphorus is small (2 units); therefore, algae fertilization needs to be supplemented with phosphorus. In addition to the favorable nitrogen supply ability, the yield increasing efficiency is also due to the microelements (Fe, Cu, Mn, Zn), vitamins auxins and gibberellins, which can be found in algae (*Péterfi,* 1977). The algae varieties tested as biofertilizers primarily belong to the branch of blue-green algae (*Cyanophyta*) and green algae (*Chlorophyta*) (*Tripathi et al.,* 2008; *Hernandez et al.,* 2009).

2. Material and methods

The selected plots were uniform from the aspect of soil characteristics. The localization of experimental areas was performed with Trimble GPS Pathfinder ProXH and ArcPad 7.0 software, and the polygons of the plots were aligned to a digitalized genetic soil map in ArcGis 9.1. The range of plots suitable for the

examination was determined on the basis of the number of soil types and subtypes on the plot, as well as their regional distribution. Examinations were established on chernozem soil in all cases.

In the area selected for the examination, the soil sampling was done by using an Eikelkamp manual borer on every 4 hectares, in average in the upper 0–30 cm layer of the soil, using Trimble GPS Pathfinder ProXH and ArcPad 7.0 software based on a genetic soil map in the spring and autumn of 2006.

The soil of the examined plots belongs to the clayey adobe physical soil group. The soil is slightly acidic, it is moderately chalky and it has low salt content, adequate humus content, average nitrogen content and low zinc content. The area of maize production in 2006 and 2007 was moderately supplied with phosphorus and potassium, while the plot used for hybrid seed production in 2008 was poorly supplied with these two elements (*Table 1*).

In all three years, the examinations were performed in hybrid seed production area on which basic fertilisation was applied. Interplanting was used. The previous crop was maize in all cases. The vegetable remains were chopped by stem crushing and disking (early-mid September), and the crushed stem remains were incorporated into the soil in the autumn (mid-late September) with 35 cm deep ploughing at the early stage of seedbed preparation with a compactor in early April. Sowing took place in late April – early May by interplanting technique. Female rows were sown with a Monosem sowing machine, while we used an Optima sowing machine in the case of male rows.

130–160 kg ha^{-1} nitrogen, 80–85 kg ha^{-2} phosphorus and 70–80 kg ha^{-1} potassium were applied as basic fertilizer. 10–15% of phosphorus, potassium, and nitrogen were applied in the autumn in the form of complex fertilizer and 85–90% of nitrogen was applied in the spring before seedbed preparation.

Table 1. Mean values of the soil analysis results of the experimental areas

Soil parameters	Year of examination		
	2006	2007	2008
pH(H_2O)	8.3	8.2	8.1
$CaCO_3$ (mg kg^{-1})	$3.1 \cdot 10^4$	$2.2 \cdot 10^4$	$1.6 \cdot 10^4$
Total water-soluble salt content (mg kg^{-1})	130	130	130
Humus (mg kg^{-1})	$3.11 \cdot 10^4$	$3.12 \cdot 10^4$	$2.92 \cdot 10^4$
Total nitrogen (mg kg^{-1})	1750	1814	1701
AL-P_2O_5 (mg kg^{-1})	161	169	84
AL-K_2O (mg kg^{-1})	287	286	218
KCl-EDTA Zn (mg kg^{-1})	1.45	1.62	1.17

The treated and the control plots were planned to be 12 m wide, and the sampling points were selected in four replications with ArcGis 9.1 software.

During the examinations, the efficiency of foliar fertilizers containing algae and algae extracts was evaluated. Natur Plasma is a microbiological product which contains living *Chlorella spp.* species (3×10^7 per ml) (*Haller,* 2009). This

foliar fertilizer contains 0.3 w w^{-1}% dry matter, 550 mg l^{-1} nitrogen, 150 mg l^{-1} phosphorus, 1146 mg l^{-1} magnesium, and 70 mg l^{-1} zinc. The variant of Natur Plasma enriched with zinc was also used, as its zinc content is 530 mg l^{-1} higher. Natur Vita contains *Chlorella vulgaris* and *Spirulina platensis* in powdered form (*Haller,* 2009). This foliar fertilizer contains 90 w w^{-1}% dry matter, 15 g 100 g^{-1} nitrogen, and 1.3 g 100g^{-1} phosphorus and potassium. Furthermore, the foliar fertilizer called Amalgerol Premium was also tested. This product contains algae extracts (alginate, mannitol, laminarin), and it contains 17.2 ww^{-1}% dry matter, 5550 mg l^{-1} nitrogen, 614 mg l^{-1} phosphorus, and 3649 mg l^{-1} potassium.

250 g ha^{-1} Natur Vita, 6.4 l ha^{-1} Natur Plasma and Natur Plasma enriched with zinc, and 2.5 l ha^{-1} Amalgerol Premium were used with 250 l ha^{-1} water in population treatment. The products were applied on two occasions (at the 5–8 leaf stages and 1–1.5 weeks before tasseling) in similar doses by using a Berthoud Boxer 3000 sprayer. In the third year (2008), Amalgerol Premium (5.0 l ha^{-1}) was applied in combined treatment at the 2–3 leaf stages and Natur Plasma (5.0 l ha^{-1}) was applied at the 5–8 leaf stages one week before tasseling.

Examined products:

- Natur Plasma (Chlorella algae concentrate enriched with nutrients)
- Natur Vita (Powdered version of Chlorella algae concentrate)
- Amalgerol Premium (vegetable volatile oils, alginate, mannitol, laminarin, algae extract, macro- and microelements)

In the stubble field treatment (October 2006), Amalgerol Premium was applied in 2.0% concentration (6.0 l ha^{-1} with 300 l ha^{-1} water) and Natur Plasma was applied in 3.2% concentration (10 l ha^{-1} with 300 l ha^{-1} water). The treatment was carried out on a maize stubble field ,and it was preceded by stem crushing and disking. The application of products was performed directly onto the soil surface which was then followed by shallow (5–10 cm) disking. The effect of stubble field treatment was evaluated in a hybrid seed production in 2007.

Before harvesting, yield samples were collected in four replications per treatment from 10 plants per replication, then the efficiency of foliar fertilizers was evaluated on the basis of fertility (number of grains per stem) and yield (g per stem).

The chlorophyll content of leaves provides information about the physiological condition of plants, since the different natural and anthropogenic stress factors affect the amount of chlorophyll (*Carter* 1994). The amount of chlorophyll can be easily measured in the visible and ultraviolet range with non-destructive optical methods (*Markwell et al.,* 1995; *Sims et al.,* 1995; *Cartelat et al.,* 2005). The Minolta SPAD-502 chlorophyll meter determines the relative chlorophyll content of leaves by means of the absorption of 650 nm wavelength light. In order to do that, the SPAD-502 meter uses infrared light in the

940 nanometer wavelength range as reference. The device expresses the relative chlorophyll content in SPAD values which is calculated from the intensity of the red and infrared light transmitted through the leaf (*Minolta Camera Co. Ltd.,* 1989). In order to evaluate the effect of treatments on the crop condition, SPAD measurements were performed with the Minolta SPAD-502 meter in 2008. Ten measurement points were proportionally divided along the entire leaf-blade on the left and right sides (5–5 points), using the 6^{th}–7^{th} leaves on 10 stems per sampling point. The measurements were carried out on three occasions; before the first treatment (June 5, 2008), between the two treatments (July 11, 2008), and after the second treatment (August 6, 2008).

During the statistical evaluation of the foliar fertilizer treatments, the normality of the distribution of fertility, yield, and SPAD values were examined by the Kolmogorov-Smirnov test, and the identity of variances was evaluated by the Levene's test. The examination of normality showed normal distribution in all cases; therefore, a parametric test was selected to compare means. The simultaneous comparison of mean values was done by the Duncan's test at a 5% inaccuracy level).

Of the years of examination, 2006 and 2007 were too dry for maize, while 2008 was favorable. The number of sunny hours in the growing season (1618–1779 hours), its effective heat sum (1437–1660 °C), average temperature (17.6–18.7 °C), rainfall (348–406 mm) and the annual precipitation (545–629 mm) was favourable for maize. The distribution of rainfall was unfavourable in all three years at the time of tasseling (July). The monthly amount of precipitation (61–65 mm) was in the optimal range for maize (50–80 mm), but 82% (50 mm) of the monthly precipitation in 2006 was measured in one day (July 22, 2006), 72% (47 mm) of the rainfall in July 2007 was measured in two days (July 4 and 5, 2007), while 68% (29 mm) of the monthly precipitation in 2008 was measured in two days (July 4, 2008 and July 7, 2008).

The average 14-hour relative atmospheric humidity at the time of pollen spreading (July) was 46% in 2006, 44% in 2007, 59% in 2008. In 2006 and 2007, the number of days with relative humidity under 45% in July was high (19–21 days); therefore, 2006 and 2007 were less favorable than 2008 from the aspect of fertility. The differences in yield of the various crop years were evaluated with Welch and t tests, depending on whether the Levene's test showed the identity or difference of the variances.

3. Results of the experiments

In the first year of the examination (2006), the yield increasing efficiency of Natur Plasma was examined in population treatment on four treated and four control plots. During the evaluation of efficiency, the effect on yield was examined as expressed in grains per stem (number of grains per stem) and g per

stem. As a result of the treatment, the number of grains improved by 59 grains per stem and yield increased by 14.2 g per stem (0.9 $t\,ha^{-1}$) in comparison with the control.

The normality of the fertility and yield of the control and treated plots was examined with the Kolmogorov-Smirnov test and the identity of variances was checked with the Levene's test. The examined variables had normal distribution and the same variance; therefore, an independent two-sample t-test was used. The t-test showed significant differences ($p < 0.05$) in the number of grains per crop and yield between the treated and control populations; therefore, the Natur Plasma treatment had a favorable effect on the fertility and yield on the hybrid seed production (*Table 2*).

Table 2. Results of the t-test concerning grain number per plant (number per stem) and yield (g per stem) (2006)

	Grain number (number per stem)			**Yield (g per stem)**		
	Mean	**t value**	**df**	**Mean**	**t value**	**df**
Natur Plasma	149	3.25*	78	35.7	3.26*	78
Control	90			21.5		

* $p < 0.15$, df = number of degrees of freedom

In the second year of examination (2007), the efficiency of natural foliar fertilizers (Natur Plasma, Natur Plasma enriched with zinc, Natur Vita, Amalgerol Premium) was examined in population treatment and stubble field treatment. During the evaluation of efficiency, the effect of these fertilizers on the number of grains per plant (number of grains per stem) and yield (g per stem) was evaluated.

The average number of plant was lower on the control plot than in the population treatments, and the number of grains measured in the stubble field treatments was similar to that of the control plots. Among the different population treatments, the highest grain number was observed on the areas treated with Natur Plasma and Natur Plasma enriched with zinc. In comparison with the control plot, the number of grains per plant increased by 0–26 grains per stem in the stubble field treatments, while it increased by 41–48 grains per stem in population treatments. Based on the Duncan's test, the number of grains per plant measured in the stubble field treatments did not differ significantly from the control population, but significantly higher ($p < 0.05$) grain number was observed in all population treatments than in the control population and the Amalgerol Premium stubble field treatment. In the population treatments with Natur Plasma and Natur Plasma enriched with zinc, the number of grains per stem was significantly higher ($p < 0.05$) than in the case of areas sprayed with Natur Vita and Amalgerol Premium. There was no significant difference between the population treatments with Natur Plasma, Natur Plasma enriched

with zinc, the population treatment with Natur Vita and Amalgerol Premium, and the stubble field treatment with Natur Plasma (*Table 3*).

The average yield was the lowest in the Natur Plasma stubble field treatment (2.0 t ha^{-1}) and in the control population (2.2 t ha^{-1}), while the highest values were observed in the areas treated with Natur Plasma enriched with zinc (2.9 t ha^{-1}), Natur Vita (2.8 t ha^{-1}), and Natur Plasma (2.7 t ha^{-1}). The population treatment with Amalgerol Premium (2.5 t ha^{-1}) and the stubble field treatment with the same fertilizer (2.5 t ha^{-1}) had nearly similar results, but they were below those that were measured in the population treatments of the other examined products. In comparison with the control population, the stubble field treatments resulted in 0.1–4.7 g per stem (0.1–0.3 t ha^{-1}), while the population treatments increased the yield by 5.4–11.9 g per stem (0.3–0.7 t ha^{-1}). Based on the significance results of the Duncan's test, it was established that the yield obtained in population treatments and the yield measured in the stubble field treatment with Amalgerol Premium were significantly higher ($p<0.15$) than the yield measured in the control population, while the stubble field treatments done with Natur Plasma is not significantly different from that of the control population. Based on the significance results, there were no obvious differences between the treatments. The yield obtained in the stubble field and population treatments with Amalgerol Premium did not differ significantly from those of the population treatments with Natur Vita and Natur Plasma. The yield obtained in the treatment with Natur Plasma enriched with zinc was significantly higher ($p<0.05$) than the yield of the control population and the stubble field treatment, but its yield was the same as that of the population treatments with Amalgerol Premium, Natur Plasma, and Natur Vita (*Table 3*).

Based on the results obtained in 2007, the population treatments had a favorable effect on the fertility and yield of the hybrid seed production, while the differences between the effects of stubble field treatments and population treatments were not clearly expressed; therefore, further examinations are necessary.

Table 3. The effect of treatments on the grain number per plant (number per stem) and yield (g per stem) (2007)

Treatments	Grain number	Yield	n
Control	149 c	33.3 c	40
Amalgerol Premium (s)	143 c	38.1 b	40
Natur Plasma (s)	175 bc	31.1 c	40
Natur Plasma (p)	233 a	42.1 ab	40
Natur Plasma enriched with zinc (p)	224 a	45.2 a	40
Natur Vita (p)	190 b	42.7 ab	40
Amalgerol Premium (p)	191 b	38.7 ab	40
F value	9.10 *	4.94 *	

* $p < 0.15$, p = population treatment, s = stubble treatment, n = element number

In the third year of the examination (2008), the efficiency of natural foliar fertilizers (Natur Plasma, Natur Vita, Amalgerol Premium) was examined in population treatment. During the evaluation of efficiency, the effect of these fertilizers on the SPAD values, the number of grains per plant (number of grains per stem), and the yield (g per stem) were evaluated.

The differences between the selected plant populations expressed in SPAD values were evaluated before the first spraying. The lowest average SPAD value was measured in the population selected for combined treatment, while the highest average value was obtained in the second control population. The SPAD value of the plot to be treated with Amalgerol Premium and the first control was above 32.0, but it was lower than the average values measured in the areas selected for Natur Vita and Natur Plasma treatments. Based on the Duncan's test, it was established, that the SPAD values measured in the second control population were significantly higher ($p<0.05$) than in the other areas, but the SPAD values of the first control area and the plots selected for treatments were shown to be identical; therefore, the effects of treatments were evaluated in comparison with the first control (*Table 4*).

Table 4. The effect of treatments on the SPAD value of maize leaves (2008)

Treatments	Before the 1st treatment	After the 1st treatment	After the 2nd treatment	n
Control 1	32.9 b	47.1 b	35.8 c	48
Control 2	36.1 a	-	-	48
Natur Plasma	33.8 b	50.2 a	38.5 b	48
Natur Vita	33.1 b	49.6 a	38.4 b	48
Amalgerol Premium	32.8 b	50.5 a	38.8 b	48
Combined treatment	31.8 b	50.9 a	41.3 a	48
F value	4.46 *	5.34 *	5.38 *	

* $p < 0.05$, n = element number

After the first treatment, the lowest average SPAD value was measured in the control population, while the highest value was obtained in the combined treatment. There was only a slight difference (0.4–1.3) between the values measured in the population treatments. After the first treatment, the Duncan's test showed significant difference ($p<0.05$) between the SPAD results of the control population and the treatments, while there was no significant difference between the SPAD values of the treatments (*Table 4*).

After the second treatment, the lowest average SPAD value was measured in the control plot, while the highest one was obtained in the combined treatment. The average SPAD values of the plots treated with Natur Vita, Natur Plasma, and Amalgerol Premium did not reach 40.0. The Duncan's test showed that the SPAD measurements performed in the treatments were significantly higher ($p<0.05$) in comparison with the control plot. There was no significant

difference between the treatments with Natur Vita, Natur Plasma, and Amalgerol Premium, but their average SPAD values were significantly lower ($p<0.05$) than the average SPAD value of the combined treatment (*Table 4*).

The lowest grain number per stem was counted in the control population and the Natur Vita treatment, while the highest average value was obtained in the combined treatment. The extent of fertility in the case of Natur Plasma and Amalgerol Premium was lower than the average values in the combined treatment. In comparison with the control plot, the number of grains per plant increased by 9–39 grains per stem, but the Duncan's test did not show any significant difference between the treated and non-treated populations (*Table 5*).

The lowest average yield was obtained in the control population (3.2 $t ha^{-1}$), while the highest value was measured in the combined treatment (3.9 $t ha^{-1}$). The average yield of the plots treated with Natur Vita (3.7 $t ha^{-1}$), Natur Plasma (3.8 $t ha^{-1}$), and Amalgerol Premium (3.8 $t ha^{-1}$) exceeded the average yield of the control population, but they were lower than the value measured in the combined treatment. The Duncan's test showed significant differences ($p<0.05$) between the yield of the control population and the treatments, but it did not show any significant difference in the average yield of the different treatments. Fertilization with the examined products resulted in 8.1–11.3 g per stem (0.5–0.7 $t ha^{-1}$) yield increase in comparison with the control population (*Table 5*).

During the statistical evaluation of the examination results, it was established that the natural foliar fertilizers had a favorable effect on the SPAD values of the hybrid seed production, and this effect was even more expressed after the second treatment. In contrast with 2007, the treatments did not increase the grain number significantly in 2008, but they resulted in significant yield increase in comparison with the control population.

Table 5. The effect of treatments on the grain number per plant (number per stem) and yield (g per stem) (2008)

Treatments	Grain number (number per stem)	Yield (g per stem)	n
Control 1	251 a	49.2 b	40
Natur Plasma	272 a	57.7 a	40
Natur Vita	260 a	57.3 a	40
Amalgerol Premium	283 a	58.9 a	40
Combined treatment	290 a	60.5 a	40
F value	1.59 $^{n.s}$	2.95 *	

* $p < 0.05$, n.s. = no significant difference, n = element number

2006 and 2007 were unfavorable years from the aspect of fertility, while 2008 was a favorable year. The average 14-hour relative atmospheric humidity at the time of pollen spreading (July) was lower in 2006 and 2007 (44–46%)

than in 2008 (59%), while the number of days in July with the relative humidity below 45% were more in 2006 and 2007 (19–21 days) than in 2008.

Comparing the results of 2006 and 2007 with those of 2008, it was established that the number of grains per plant and yield obtained in the control populations and the treated populations in the drought years (2006, 2007) were significantly lower ($p<0.001$) than in the year which was more favorable from the aspect of fertility (2008), and the increase in grain number and yield in comparison with the control population was larger than in 2008 (*Table 6*).

Table 6. The effect of treatments in different crop years

Years of examination	M_c	df	t value	M_{pt}	df	t value	MD_c
Grain number (number per stem) (3)							
2006-2007	120	116	9.13*	180	358	9.43*	60
2008	251			276			25
Yield (g per stem) (4)							
2006-2007	27.4	116	7.82*	39.0	358	10.42*	11.6
2008	49.5			58.6			9.1

* $p < 0.05$, M_k = mean of control populations, M_{pt} = mean of population treatments, MD_c = average difference in comparison with the control, df = number of degrees of freedom

4. Conclusions

During the statistical evaluation of the examination results, it was established that the use of the tested foliar fertilizers improved the condition of the crop population. Depending on the applied treatment, they provide further yield increase in addition to the basic fertilization, and their combined use does not result in significantly higher yield than the individual application of each product. Based on the results, it is assumed that natural foliar fertilizers are able to substitute basic fertilization to a certain extent; therefore, it is necessary to examine this issue under small and large plot conditions.

The application of the examined products as foliar fertilizers resulted in more favorable yield increase in the drought years than in 2008, which was a less favorable year from the aspect of fertility. This result leads to the conclusion that the yield increasing effect of algae- and algae extract-based foliar fertilizers is a result of their crop conditioning effect, which is more expressed in stress (e.g. atmospheric drought) than under optimal conditions. Consequently, the cost-effectiveness of these treatments could be more favorable in stress.

Field experiments on foliar fertilization are more difficult to carry out because sometimes the treated and the control plots are not uniform even before the treatment. Based on the results of the SPAD measurements performed before the first foliar fertilizer treatment, it can be examined whether the conditions of

the crop populations selected as control or treated populations are identical or different. Therefore, during the evaluation of the obtained yield and based on the preliminary SPAD measurements, it is possible to compare the treatments to the control population in which the plant condition was identical to the populations selected for treatment even before the treatment itself. The advantage of this method is that the yield increasing potential of foliar fertilizers can be accurately evaluated, which provides an opportunity to compare foliar fertilizers in a rational way. The disadvantage of this method is that the obtained results are slightly higher than the yield increase which can be expected under controlled field trial conditions that results from the fact that the yield loss resulting from the heterogeneity of the crop population is excluded during the examination; therefore, the cost-efficiency based examination of the large-scale use of these products is indispensable.

Acknowledgements—We would like to thank *István Farkas, Sándor Bartha, Csaba Varga,* and *Szabolcs Munkácsi* for their help in establishing the experiments.

Refrences

Arshad, M.A. and *Martin S.,* 2002: Identifying critical limits for soil quality indicators in agro-ecosystems. *Agr. Ecosyst. Environ. 88*, 153–160.

Bronick, C.J. and *Lal, R.,* 2005: Soil structure and management: a review. *Geoderma 124*, 3–22.

Cartelat, A., Cerovic, Z.G., Goulas, Y., Meyer, S., Lelarge, C., Prioul, J.L., Barbottin, A., Jeuffroy, M.H., Gate, P., Agati, G., Moya, I., 2005: Optically assessed contents of leaf polyphenolics and chlorophyll as indicators of nitrogen deficiency in wheat (Triticum aestivum L.). *Field Crops Res. 91*, 35–49.

Carter, G.A., 1994: Ratios of leaf reflectances in narrow wavebands as indicators of plant stress. *Int. J. Remote Sens. 15*, 697–703.

Cong, P.T., Dung, T.D., Hien, T.M., Hien, N.T., Choudhury, A.T.M. A., Kecskés, M.L., and *Kennedy, I.R.,* 2009: Inoculant plant growth-promoting microorganisms enhance utilisation of urea-N and grain yield of paddy rice in southern Vietnam. *Eur. J. Soil Biol. 45*, 52–61.

Dawe, D., Dobermann, A., Ladha, J.K., Yadav, R.L., Bao, *L., Gupta, R.K., Lal, P., Panaullah, G., Sariam, O., Singh, Y., Swarup, A.,* and *Zhen, Q.X.,* 2003: Do organic amendments improve yield trends and profitability in intensive rice systems? *Field Crop. Res. 83,* 191–213.

Deumlich, D., Funk, R., Frielinghaus, M., Schmidt, W.A., and *Nitzsche, O.,* 2006: Basics of effective erosion control in German agriculture. *J. Plant Nutr. Soil Sc. 169,* 370–381.

Douds Jr., D.D., Nagahashi, G., Pfeffer, P.E., Reider, C., and *Kayser, W.M.,* 2006: On-farm production of AM fungus inoculum in mixtures of compost and vermiculite. *Bioresource Technol. 97*, 809–818.

Döbereiner, J., 1997: Biological nitrogen fixation in the tropics: Social and economic contributions. *Soil Biol. Biochem. 29*, 771–774.

Duffy, E.M. and *Cassells, A.C.,* 2000: The effect of inoculation of potato (*Solanum tuberosum L.*) microplants with arbuscular mycorrhizal fungi on tuber yield and tuber size distribution. *Appl. Soil Ecol. 15,* 137–144.

Evans, R., 2005: Reducing soil erosion and the loss of soil fertility for environmentally sustainable agricultural cropping and livestock production systems. *Ann. Appl. Biol. 146,* 137–146.

Gajdos É., 2009: Baktérium alapú bio-trágya hatása a kukorica és a napraforgó kadmium toleranciájára vízkultúrás kísérletekben. *Agrártudományi Közlemények (Acta Agraria Debreceniensis) 35*, 15–21.

Gould, W.D., 1990: Biological control of plant root diseases by bacteria. In *Biotechnology of Plant-Microbe Interactions* (eds.: *Nakas, J.P., Hagedorn C.*). McGraw-Hill, New York, 287–372.

Gosling, P. and *Shepherd, M.,* 2005: Long-term changes in soil fertility in organic arable farming systems in England, with particular reference to phosphorus and potassium. *Agr. Ecosys. Environ. 105,* 425–432.

Haller G., 2009: Növényvédőszerek, termésnövelő anyagok 2009 II. Földművelésügyi és Vidékfejlesztési Minisztérium, Budapest.

Hansen, B., Kristensen, E.S., Grant, R., Hogh-Jensen, H., Simmelsgaard, S.E., and *Olesen, J.E.,* 2000: Nitrogen leaching from conventional versus organic farming systems - a systems modelling approach. *Eur. J. Agron. 13,* 65–82.

Hernandez, J.P., de-Bashan, L.E., Rodriguez, D.J., Rodriguez, Y., and *Bashan, Y.,* 2009: Growth promotion of the freshwater microalga Chlorella vulgaris by the nitrogen-fixing, plant growth-promoting bacterium Bacillus pumilus from arid zone soils. *Eur. J. Soil Biol. 45,* 88–93.

Kannaiyan, S., 2002: Biofertilizers for sustainable crop production. In: *Biotechnology of biofertilizers* (ed.: Kannaiyan, S.). Narosa Publishing House, New Delhi, India, 9–49.

Kim, K., Barham, B.L., and *Coxhead, I.,* 2000: Recovering soil productivity attributes from experimental data: a statistical method and an application to soil productivity dynamics. *Geoderma 96,* 239–259.

Kincses, I., Nagy, P.T., Sipos, M., 2009: Effect of bacteria fertilizers on plant extracted Zn and Cu content of ryegrass (*Lolium perenne*) at different types of soil. In *Trace elements in the food chain, Vol. 3. Deficiency or excess of trace elements in the environment as a risk of health.* (eds.: Szilágyi, M., Szentmihályi, K.) Hungarian Academy of Sciences, Chemical research Center, Budapest, 357–361.

Kloepper, J.W., Liftshitz, K., Zablotowitcz, R.M., 1989: Free-living bacterial inocula for enhancing crop productivity. *Trends Biotechnol. 7,* 39–43.

Kohler, J., Caravaca, F., Carrasco, L., and *Roldán, A.,* 2006: Contribution of Pseudomonas mendocina and Glomus intraradices to aggregates stabilisation and promotion of biological properties in rhizosphere soil of lettuce plants under field conditions. *Soil Use Manage. 22,* 298–304.

Liang, Y.C., Shen, Q.R., Shen, Z.G., and *Ma, T.S.,* 1996: Effects of silicon on salinity tolerance of two barley cultivars. *J. Plant Nutr. 19,* 173–183.

Loveland, P. and *Webb, J.,* 2003: Is there a critical level of organic matter in the agricultural soils of temperate regions: a review. *Soil Till. Res. 70,* 1–18.

Lupwayi, N.Z., Arshad, M. A., Rice, W.A., and *Clayton, G.W.,* 2001: Bacterial diversity in water-stable aggregates of soils under conventional and zero tillage management. *Appl. Soil Ecol. 16,* 251–261.

Markwell, J., Osterman, J.C., and *Mitchell, J.L.,* 1995: Calibration of the Minolta SPAD-502 leaf chlorophyll meter. *Photosynth. Res. 46,* 467–472.

Minolta Camera Co. Ltd., 1989: Chlorophyll meter SPAD-502. *Instruction Manual.* Radiometric Instruments Divisions, Osaka, Minolta.

Nagy, J., 2006: Effect of tillage on the yield of crop plants. *Cereal Res. Commun. 34,* 255–258.

Nagy, J., 2007: Evaluating the effect of year and fertilisation on the yield of mid ripening (FAO 400–499) maize hybrids. *Cereal Res. Commun. 35,* 1497–1507.

Nisha, R., Kaushik, A., Kaushik, and *C.P.,* 2007: Effect of indigenous cyanobacterial application on structural stability and productivity of an organically poor semi-arid soil. *Geoderma 138,* 49–56.

Péterfi, I., 1977: Az algák biológiája és gyakorlati jelentősége. Ceres Könyvkiadó, Bukarest.

Reeves, D. W., 1997: The role of soil organic matter in maintaining soil quality in continuous cropping systems. *Soil Till. Res. 43,* 131–167.

Schwab, A.P., 1990: Changes in soil chemical properties due to 40 years of fertilization. *Soil Sci. 149,* 35–46.

Sims, J.T.,Vasilas, B.L., Gartley, K.L., Milliken, B., and *Green, V.,* 1995: Evaluation of soil and plant nitrogen tests for maize on manured soils of the Atlantic coastal plain. *Agron. J. 87,* 213–222.

Smith, S.E. and *Read, D.J.,* 1997: Mycorrhizal Symbiosis. Academic Press, San Diego, CA.

Sturz, A.V. and *Nowak, J.,* 2000: Endophytic communities of rhizobacteria and the strategies required to create yield enhancing associations with crops. *Applied Soil Ecol. 15,* 183–190.

Tripathi, R.D., Dwivedi, S., Shukla, M.K., Mishra, S., Srivastava, S., Singh, R., Rai, U.N., and *Gupta D.K.,* 2008: Role of blue green algae biofertilizer in ameliorating the nitrogen demand and fly-ash stress to the growth and yield of rice (*Oryza sativa* L.) plants. *Chemosphere 70,* 1919–1929.

Vessey, J.K., 2003: Plant growth promoting rhizobacteria as biofertilizers. *Plant Soil 255,* 571–586.

Wu, S.C., Cao, Z.H., Li, Z.G., Cheung, K.C., and *Wong, M.H.,* 2005: Effects of biofertilizer containing N-fixer, P and K solubilizers and AM fungi on maize growth: a greenhouse trial. *Geoderma 125,* 155–166.

IDŐJÁRÁS

Quarterly Journal of the Hungarian Meteorological Service
Vol. 116, No. 1, January–March 2012, pp. 65–75

Evaluation of the correlation between weather parameters and the normalized difference vegetation index (NDVI) determined with a field measurement method

Attila Dobos[1*], **Róbert Vig**[1], **János Nagy**[2], and **Kálmán Kovács**[3]

[1]*Research Group of Cultivation and Regional Development, Hungarian Academy of Sciences, University of Debrecen Böszörményi út 138, H-4032 Debrecen, Hungary*

[2]*Institute for Land Utilisation, Technology and Regional Development, Center of Agricultural Sciences and Engineering, University of Debrecen Böszörményi út 138, H-4032 Debrecen, Hungary*

[3]*Department of Telecommunications, Faculty of Electrical Engineering and Informatics, Budapest University of Technology and Economics Egry József u. 18, H-1111 Budapest, Hungary*

[*]*Corresponding author; E-mail: dobosa@gmail.com*

(Manuscript received in final form February 3, 2012)

Abstact—The level of nitrogen supply of a plant population can be quickly measured with non-destructive optical measurement devices and the differentiated determination of nitrogen shortage, while the replenishment of nitrogen can also be carried out. The level of nitrogen supply is based on the fact that the chlorophyll content of crops is in close correlation with nitrogen content and that the amount of chlorophyll can be easily measured on the basis of the light absorption of chlorophyll molecules. The successfulness of optical measurements can be influenced by the change of weather parameters; therefore, it is important to know the correlations between the measurement results and weather parameters when it comes to practical use.

The GreenSeeker Model 505 measurement device determines the relative chlorophyll content in the form of the normalized difference vegetation index (NDVI) calculated on the basis of the intensity of the reflected red and infrared rays of light from the crop population. The measurements were performed in alfalfa population with 10 replications at five measurement heights and four measurement times. The weather parameters were measured by a weather station located in the middle of the alfalfa population, and the correlations between the meteorological data and the NDVI values were examined.

During the statistical evaluation of the results, it was established that the NDVI measurement is primarily influenced by the relative humidity of the air, secondly by air temperature, and thirdly by wind speed. Relative humidity was in strong correlation with the NDVI values which were also influenced by the measurement height and time.

Regression was not significant in the case of the 20 cm measurement height, but the measurements above 40 cm height showed significant correlations. The correlation was shown to be strong at each measurement time, but the influence of humidity was the lowest at 11:00 and 14:00 in local time.

Key-words: alfalfa, NDVI, GreenSeeker, measurement height, measurement time, humidity

1. Introduction

In the vegetation period, the nitrogen demand of plants can be satisfied based on the actual nitrogen need of plants (*Fox et al.,* 1986; *Lemaire et al.,* 2008) determined by destructive laboratory analyses, or with non-destructive optical measurements (*Justes et al.,* 1997; *Feibo et al.,* 1998). The advantage of non-destructive optical measurement methods in comparison with laboratory analyses is that they are less expensive, quicker, and they have less labor need; therefore, it is worth using optical measurement methods in practice (*Blackmer* and *Schepers,* 1994; *Chapman* and *Barreto,* 1997; *Justes et al.,* 1997).

Optical measurement methods are based on the phenomenon that chlorophyll molecules absorb light in the visible red range, while they transmit light in the infrared range (*Brown,* 1969; *Murata* and *Sato,* 1978; *Yadava,* 1986); therefore, the indexes formed by proportionating infrared and red light intensities are in close correlation with chlorophyll content (*Roderick et al.,* 1996; *Zhang et al.,* 2009). The chlorophyll content is also in close correlation with the nitrogen content of leaves (*Evans,* 1983, 1989; *Houlès et al.,* 2007); therefore, the indexes calculated on the basis of the intensity of red light absorbed by chlorophyll molecules make it possible to conclude to the level of nitrogen supply of crops (*Iida et al.,* 2000; *Freeman et al.,* 2007; *Wright et al.,* 2007).

One of the most frequently used indexes is the normalized difference vegetation index (NDVI) which is determined by the following formula:

$$\mathrm{NDVI} = (NIR - RED)/(NIR + RED) \tag{1}$$

where *NIR* is the intensity of infrared light and *RED* is the intensity of red light (*Rouse et al.,* 1973). NDVI can either be determined by the spectral analysis of satellite images which makes it possible to perform regional examinations (*Szabó et al., 1998*; *Wang* and *Tenhunen,* 2004; *Knight et al.,* 2006; *Ren et al.,* 2008), and by using optical measurement devices used in the field that makes it possible to carry out plot-scale evaluation (*Hancock* and *Dougherty,* 2007; *Rambo et al.,* 2010).

The normalized difference vegetation index is in close correlation with the development of the plant population (*Aparicio et al.,* 2000; *Nambuthiri,* 2010), its chlorophyll content (*Roderick et al.,* 1996; *Cui et al.,* 2009), nitrogen content

(*Iida et al.,* 2000; *Wei et al.,* 2010), biomass production (*Hong et al.,* 2007, *Hancock* and *Dougherty,* 2007), and yield (*Teal et al.,* 2006; *Chung et al.,* 2008), therefore, NDVI measurements have practical forms of use. By temporally and spatially determining the normalized difference vegetation index, it is possible to monitor the development of the plant population (*Viña et al.,* 2004; *Martin et al.,* 2007), to survey the health status and level of nitrogen supply of the population (*Boegh et al.,* 2002; *Nambuthiri,* 2010), to determine the nitrogen shortage and replenish nitrogen in a differentiated way (*Singh et al.,* 2006), as well as to estimate the expected yield (*Teal et al.,* 2006).

The measurement results could be affected by the extent of plant coverage which results from the lower or higher reflectance of the soil (*Aparicio et al.,* 2002); therefore, it is important to examine the measurement methods in hoed and closed crop cultures. The primary objective of this research is to find the measurement method that can be used to determine the correlation between NDVI and nitrogen supply most accurately in closed canopy crop cultures. In our previous publications, we described the correlations between NDVI, measurement height, and measurement times (*Víg et al.,* 2010), while in this study, we evaluate the influence of weather parameters on NDVI measurements.

2. Material and methods

The examinations were carried out in the demonstration garden of the Institute of Horticulture of the University of Debrecen on chernozem soil. The measurement location was an alfalfa field of 729.8 m^2 (17.8 m × 41.0 m) in which 10 measurement points were determined by using Trimble GPS Pathfinder ProXH and ArcPad 7.0 software. Within the alfalfa population, 5–5 measurement points were selected with 1.2 m long bamboo sticks on the two sides of the plot, 2 meters from the edge of the plot and 7 meters from each other.

NDVI measurements were performed with GreenSeeker Model 505 on six occasions at four times (08:00, 11:00, 14:00, and 17:00 in local time) per occasion between May 27, 2010 and September 21, 2010 in the vegetation period. All measurements were performed in the previously selected measurement points, 20, 40, 60, 80, and 100 cm above the crop population.

A weather station was placed in the middle of the alfalfa population in order to measure weather parameters. The components of this station are: CR 1000 data logger and memory (Campbell Scientific Ltd., UK), 52202 rain-gauge (R. M. Young Co., USA), CS215 temperature and moisture meter (Campbell Scientific Ltd., UK), 05103-5 wind speed and wind direction meter (R. M. Young Co., USA), CMP3 radiation meter (Kipp & Zonen Inc., USA), LWS leaf moisture meter (Decagon Devices Inc., USA), CS616 soil moisture probe (Campbell Scientific Ltd., UK), and Model 107 soil temperature meter (Campbell Scientific Ltd., UK).

The examination site (Debrecen) is located in the northeastern part of the climate zone 9/a by the classification of *Ángyán* (1985). In the examination year (2010), the mean temperature of the spring-summer season was similar to the typical value of the climate zone (17.8 °C). The mean temperature in July was 0.8 °C higher than the 80-year average, while that of April was 0.9 °C higher. The amount of rainfall over the year (Oktober 1, 2009 – September 30, 2010) was 70% (377 mm) higher than the average value of the climate zone, while that of the autumn-winter period (Oktober 1, 2009 – March 31, 2010) was 44% (100 mm) higher, that of the spring-summer period (April 1, 2010 – September 30, 2010) was 88% (277 mm) higher, and the amount of precipitation during the hottest month of the year was 43% (29 mm) higher than the average of the climate zone.

The evaluation of the measurement results was done with SPSS for Windows 14.0. The correlation between NDVI values, mean difference in NDVI measurements ($MD_{\%}$), the variability of the measurement results ($CV_{\%}$) and various weather parameters were evaluated by using linear, quadratic, third degree exponential and logarithmic regression analyses at the 0.1%, 1.0% and 5.0% levels of significance, of which only the regression equations showing the strongest correlation are published.

The mean difference of the measurement results were expressed in percentages based on the following formula:

$$MD_{\%} = \sum[(M_x - M_y)/(M_y/100)], \tag{2}$$

where $MD_{\%}$ is the mean difference, M_x is the mean of the results measured at x height, M_y is the mean of the results measured at y height, and $M_x > M_y$. The variability of measurement results were characterized by the coefficient of variation; therefore, standard deviation was expressed as a percentage of the mean value:

$$CV_{\%} = Sd/(M/100), \tag{3}$$

where $CV_{\%}$ is the coefficient of variation, Sd is the standard deviation, M is the mean (*Senders,* 1958).

3. Experimental results

During the examination and evaluation of the correlations between the daily mean NDVI values determined in the various measurement points and the daily mean weather values, it was established that the daily mean NDVI values are in close positive correlation with the daily mean humidity. The correlation could be determined most accurately with a significant ($p < 0.01$), third degree regression equation which showed a 96.5% correlation between the daily mean NDVI values and the daily mean humidity. This correlation is strong; therefore, the

results of the NDVI measurements can significantly differ from the real values depending on the humidity values. The other examined weather parameters (daily mean temperature, total global solar radiation, daily mean wind speed, evapotranspiration) did not influence the daily mean NDVI value (*Table 1*).

The respective weather parameters were assigned to the NDVI values measured at the various times (08:00, 11:00, 14:00, and 17:00 in local time), then the strength and nature of correlations were determined with regression analysis. There was no significant difference between the actual global solar radiation (measured at the time of the NDVI measurement) and the normalized difference vegetation index (*Table 1*), which reinforces the statement of the GreenSeeker Model 505 developers about the fact that light conditions do not influence the success of the measurement (*NTech Industries Inc.*, 2007). The actual humidity, temperature, and wind speed showed average-strong correlation with the results of the NDVI measurement. The actual humidity and the actual temperature also had significant ($p<0.001$), close correlation with the normalized difference vegetation index. The value of the quadratic regression was 58.0% between the NDVI values and the actual humidity, and it was 53.3% between the actual temperature and the NDVI values. There was a significant ($p<0.05$), third degree correlation between the actual wind speed and the NDVI values which shows that wind speed had a 43.5% influence on the success of measurements (*Table 1*).

Table 1. Evaluation of the correlations between NDVI and weather parameters

Weather parameters	R^2	R	F	Regression equation
Correlations between the daily mean NDVI values and the weather parameters				
NAP	0.956	0.978	32.9^{**}	$y = 0.091 + 0.015x - 9*10^{-7}x^3$
NÁH	0.344	0.587	0.787^{n}	–
NÖGN	0.168	0.410	0.304^{n}	–
NÁSZ	0.073	0.270	0.052^{n}	–
EPT_P	0.257	0.507	0.230^{n}	–
EPT_{SZ}	0.164	0.405	0.130^{n}	–
Correlations between NDVI values determined at different times and the respective weather parameters				
P	0.580	0.762	13.1^{***}	$y = 0.806 + 5.46*10^{-5}x^2 - 6.10*10^{-7}x^3$
H	0.533	0.730	10.8^{***}	$y = 0.588 + 0.024x - 4.8*10^{-4}x^2$
GS	0.077	0.277	0.5^{n}	–
SZ	0.435	0.660	4.6*	$y = 0.734 + 0.351x - 0.278x^2 + 0.068x^3$

n = no significant correlation, $^{*}p<0.05$, $^{**}p<0.01$, $^{***}p<0.001$, R^2 = coefficient of determination, R = coefficient of correlation, F = F–test statistics, *NAP* = Daily mean humidity (%), *NÁH* = Daily mean temperature (°C), *NÖGN* = Daily total global solar radiation (KJ m^{-2}), *NÁSZ* = Daily mean wind speed ($m\,s^{-1}$), EPT_P = Evapotranspiration ($mm\,day^{-1}$) calculated with Penman's formula, EPT_{SZ} = Evapotranspiration ($mm\,day^{-1}$) calculated with *Szász*'s formula, *P* = Humidity measured at the time of the NDVI measurement (%), *H* = Temperature measured at the time of the NDVI measurement (°C), *GS* = Global radiation measured at the time of the NDVI measurement ($KJ\,m^{-2}$), *SZ* = Wind speed measured at the time of the NDVI measurement ($m\,s^{-1}$)

A contradiction was found in relation to the fact that NDVI measurements were influenced by the actual humidity to a 58.0% extent, while actual temperature had a 53.3% influence and wind speed had a 43.5% influence. According to our hypothesis, there is an overlap between the correlations due to the fact that weather parameters are not independent of each other. In order to support this hypothesis, a one-way ANOVA was performed to determine the difference shown by the various weather parameters at different measurement times, and a main component analysis was also carried out to determine the correlations between the weather parameters. Significant correlations ($p < 0.001$) were found between the values measured at the four measurement times in the case of humidity, temperature and wind speed. Humidity decreased between 08:00 and 14:00 in local time and then it slightly increased, while temperature and wind speed changed inversely, so that they increased from 08:00 to 14:00 and then started to decrease. The significantly highest humidity was measured at 08:00 and the significantly lowest value was obtained at 04:00. The values logged at 11:00 and 17:00 were significantly higher than the value measured at 14:00 and they were significantly lower than the data measured at 08:00. There was no significant difference between the air temperature measured at 17:00 and 14:00 and the data obtained at 08:00 and 11:00 were significantly lower than the values at 14:00 and 17:00. The significant differences in wind speed measured at different times had the following rank: 14:00 > 11:00 > 08:00 > 17:00 (*Table 2*).

In the main component analysis of the correlations between humidity, air temperature, and wind speed, one component was determined. Based on that, by considering the sign of the main components, it was established that humidity had a negative correlation with temperature and wind speed. The main component weights showed that humidity was closely correlated with wind speed and temperature (*Table 2*).

Table 2. Evaluation of the differences between the weather parameters measured at different times and the correlation between weather parameters

Measurement time (hour in local time)	Relative humidity (%)	Air temperature (°C)	Wind speed ($m\ s^{-1}$)
	Measured values		
08:00	70.6 ± 11.5 a	21.7 ± 5.0 c	0.87 ± 0.43 d
11:00	54.8 ± 2.5 b	25.9 ± 4.2 b	1.45 ± 0.46 b
14:00	48.4 ± 4.6 d	28.1 ± 4.7 a	1.52 ± 0.36 a
17:00	50.5 ± 6.8 c	27.5 ± 4.3 a	1.08 ± 0.36 c
$F(5)$	539.2^{***}	112.6^{***}	159.9^{***}
	Main component weights (8)		
1st main component	–0.899	0.849	0.663

$^{***}p < 0.001$, F = F-test statistics

During the evaluation of the correlations between NDVI and weather parameters (humidity, temperature, wind speed) with a regression analysis and that of the correlation between humidity, air temperature and wind speed with a main component analysis, we came to a conclusion that NDVI measurements are influenced by humidity, temperature and wind speed. Based on the main component analysis, it was shown that humidity is negatively correlated with temperature and wind speed, therefore, air temperature and wind speed affect the results of NDVI measurements through the relative humidity. Based on the coefficients of correlation which were the result of the evaluation of the regression between NDVI values and the examined weather parameters, it can be stated that NDVI values were primarily influenced by the relative humidity (R=762), secondly by air temperature (R=0.730) and thirdly by wind speed (R=0.660).

The correlations between NDVI measurements and humidity were examined against different measurement heights and times, since our previous examinations led us to conclude that the NDVI value is significantly different as a function of the measurement height and time (*Víg et al.,* 2010). During the examination of the correlations between NDVI values and relative humidity by linear, quadratic, third degree, exponential and logarithmic regression analyses, it was established that the closest correlations were described by quadratic and third degree regression equations. There was no significant regression between the NDVI values and humidity at the 20 cm measurement height, while there were significant correlations ($p<0.01$ and $p<0.001$) between NDVI values and humidity at the 40, 60, 80 and 100 cm measurement heights. Depending on the measurement height, humidity was shown to be a strong factor (R=0.819–0.873) and it had a 67.0–76.3% influence ($R^2=0.670–0.763$) on NDVI measurement. As regards the various measurement times, significant ($p<0.01$ and $p<0.001$) and strong (R=0.828–0.986) correlations were shown in all cases. The influence of humidity on NDVI measurement was the strongest ($R^2=0.972$) at 08:00 and it was the weakest ($R^2=0.686$) at 14:00 (*Table 3*).

Table 3. Correlations between the relative humidity and the NDVI values at different measurement heights and times

Measurement height (cm)	R^2	R	F	**Regression equation**
20	0.065	0.255	0.7^{n}	–
40	0.755	0.869	29.2^{***}	$y = 0.738 - 0.003x - 3.4*10^{-7}x^3$
60	0.763	0.873	30.5^{***}	$y = 0.792 + 6.2*10^{-5}x^2 - 7.0*10^{-7}x^3$
80	0.734	0.857	26.3^{***}	$y = 0.779 + 7.4*10^{-5}x^2 - 8.3*10^{-7}x^3$
100	0.670	0.819	8.4^{**}	$y = 0.783 + 6.9*10^{-5}x^2 - 7.7*10^{-7}x^3$
Measurement time (hour)	R^2 **(2)**	R **(3)**	F **(4)**	**Regression equation**
08:00	0.972	0.986	52.8^{***}	$y = 0.590 - 1.5*10^{-6}x^3$
11:00	0.744	0.863	29.8^{***}	$y = -3.735 + 0.168x - 0.002x^2$
14:00	0.686	0.828	10.3^{**}	$y = -0.770 + 0.66x - 0.001x^2$
17:00	0.850	0.922	46.7^{***}	$y = 0.168 + 0.027x - 2.0*10^{-4}x^2$

n = no significant correlation, $^{**}p<0.01$, $^{***}p<0.001$, R^2 = coefficient of determination, R= correlation of coefficient, F = F-test statistics

In one of our previous publications, it was established that the mean difference ($MD_{\%}$) values determined in relation to the NDVI values measured at different heights are different at the various measurement times and the variability of the measurement results ($CV_{\%}$) depends on the applied measurement height (*Víg et al.,* 2010). In this study, it is shown that the change in the examined parameters is in correlation with the relative humidity.

By evaluating the correlations between the mean difference ($MD_{20\text{-}100}$) of the NDVI values measured at different heights and the variability ($CV20–100_{\%}$) of the values measured at different heights and humidity by quadratic, third degree, exponential and logarithmic regression analyses, it was established that the correlations can be most accurately described with quadratic and third degree regression equations. There was significant ($p<0.001$) and strong correlation between the mean difference and humidity, showing that the relative humidity had a 68.1% influence on the mean difference between NDVI values measured at different heights. There was no significant correlation between the variability of the measurements performed at 20 and 40 cm ($CV20_{\%}$, $CV40_{\%}$) and the relative humidity, while there were average correlations in relation to the coefficients of variation of the other measurement heights ($CV60_{\%}$, $CV80_{\%}$, $CV100_{\%}$). The correlations determined at 60 and 80 cm measurement heights are also significant ($p<0.05$) and the value of the regression coefficient was nearly 0.6, while the significance was $p<0.01$ and the regression coefficient was above 0.6 in the case of measurements performed at 100 cm. Based on the coefficient of determination, humidity had 35.4% and 35.3% influence the variability of NDVI values at 60 and 80 cm measurement heights, respectively, while the extent of this influence was 38.8% in the case of 100 cm measurement height (*Table 4*).

Table 4. Correlations between the mean difference ($MD_{20\text{–}100}$) and variability ($CV20$–100%) and the relative humidity

Examined parameters	R^2	R	F	Regression equation
$MD_{20\text{-}100}$	0.681	0.825	20.3^{***}	$y = 5.376 - 0.003x^2 - 4.06*10^{-5}x^3$
$CV20_{\%}$	0.087	0.295	0.905^{n}	–
$CV40_{\%}$	0.232	0.482	2.9^{n}	–
$CV60_{\%}$	0.354	0.595	5.2^{*}	$y = 3.478 - 0.002x^2 + 1.59*10^{-5}x^3$
$CV80_{\%}$	0.353	0.594	5.2^{*}	$y = 4.407 - 0.075x + 7.29*10^{-6}x^3$
$CV100_{\%}$	0.388	0.623	6.0^{**}	$y = 8.574 - 0.221x + 0.002x^2$

n = no significant correlation, $^{*}p<0.05$, $^{**}p<0.01$, $^{***}p<0.001$, R^2 = coefficient of determination, R = coefficient of correlation, F = F–test statistics, $MD_{20\text{–}100}$ = Mean difference between the NDVI values measured at different heights, $CV20_{\%}$ = Variability of NDVI values measured at 20 cm, $CV40_{\%}$ = Variability of NDVI values measured at 40 cm, $CV60_{\%}$ = Variability of NDVI values measured at 60 cm, $CV80_{\%}$ = Variability of NDVI values measured at 80 cm, $CV100_{\%}$ = Variability of NDVI values measured at 100 cm.

4. Conclusions

The obtained research results led to the conclusion that the results of the field NDVI measurement are primarily influenced by the relative humidity. Secondly and thirdly, air temperature and wind speed also influence NDVI values, as temperature and wind speed are negatively correlated to humidity. The effect of humidity on NDVI measurement depends on the measurement height and time. In the case of the 20 cm measurement height, the effect of humidity on NDVI measurement cannot be detected, while if the measurement is carried out above 40 cm, the distortion effect of humidity is strong. The correlation between humidity and NDVI values is the strongest in the case of the measurements performed at 08:00 and 17:00, while it was the weakest at 11:00 and 14:00 in local time. Consequently, by increasing the measurement height and performing measurements in the morning and late in the afternoon, the distortion effect of humidity on NDVI measurements becomes stronger.

It was shown in our previous examinations that the increase of measurement height results in the decrease of the variability of the measurement results (*Víg et al.,* 2010), but the effect of humidity on variability increases with the increase of the measurement height.

In order to more accurately determine the nitrogen supply on the basis of the NDVI value, we consider it necessary to examine the correlations between humidity, NDVI values, and the leaf nitrogen content with the aim to find the correction factors needed for the more accurate determination of nitrogen shortage on the basis of the NDVI values.

Acknowledgements—The preparation of this paper was supported by the National Technology Program (NKTH 00 210/2008), the Research Group of Cultivation and Regional Development of the Hungarian Academy of Sciences, and the TÁMOP 4.2.1./B–09/1/KONV–2010–0007 operative program.

References

Ángyán J., 1985: Nagyüzemi árukukorica-termesztés - A kukoricatermesztés területi elhelyezése. In *A kukoricatermesztés kézikönyve* (ad.: Menyhért, Z.), Mezőgazdasági Kiadó, Budapest, 199–228.

Aparicio, N., Villegas, D., Casadesus, J., Araus, J.L., and *Royo, C.,* 2000: Spectral vegetation indices as nondestructive tools for determining durum wheat yield. *Agron. J. 92,* 83–91.

Aparicio, N., Villegas, D., Arausb, J. L., Casadesus, J., and *Royo, C.:* 2002. Relationship between growth traits and spectral vegetation indices in durum wheat. *Crop Sci. 42,* 1547–1555.

Blackmer, T. M. and *Schepers, J.S.,*1994: Techniques for monitoring crop nitrogen status in corn. *Commun. Soil Sci. Plan. 25,* 1791–1800.

Boegh, E., Soegaard, H., Broge, N., Hasager, C.B., Jensen, N.O., Schelde, K., and *Thomsen, A.,* 2002: Airborne multispectral data for quantifying leaf area index, nitrogen concentration, and photosynthetic efficiency in agriculture. *Remote Sens. Environ. 81,* 179–193.

Brown, J.S., 1969: Absorption and fluorescence of chlorophyll *a* in particle fractions from different plants. *Biophys. J. 9,* 1542–1552.

Chapman, S.C., Barreto, H.J., 1997: Using a chlorophyll meter to estimate specific leaf nitrogen of tropical maize during vegetative growth. *Agron. J. 89,* 557–562.

Chung, B., Girma, K., Martin, K.L., Tubaña, B.S., Arnall, D.B., Walsh, O., and *Raun, W.R.,* 2008: Determination of optimum resolution for predicting corn grain yield using sensor measurements. *Arch. Agron. Soil Sci. 54,* 481–491.

Cui, D., Li, M., and *Zhang, Q.,* 2009: Development of an optical sensor for crop leaf chlorophyll content detection. *Comput. Electron. Agric. 69,* 171–176.

Evans, J.R., 1983: Nitrogen and photosynyhesis in the flag leaf of wheat (*Triticum aestivum* L.). *Plant Physiol. 72,* 297–302.

Evans, J.R., 1989: Photosynthesis and nitrogen relationships in leaves of C3 plants. *Oecologia 78,* 9–19.

Feibo, W., Lianghuan, W., and *Fuhua, X.,* 1998: Chlorophyll meter to predict nitrogen sidedress requirements for short-season cotton (*Gossypium hirsutum* L.). *Field Crop. Res. 56,* 309–314.

Fox, R.H., Kern, J.M., and *Piekielek, W.P.,* 1986: Nitrogen fertilizer source, and method and time of application effects on no-till corn yields and nitrogen uptake. *Agron. J. 78,* 741–746.

Freeman, K.W., Girma, K., Arnall, D.B., Mullen, R.W., Martin, K. L., Roger K., Teal, R.K., and *Raun, W.R.,* 2007: By-plant prediction of corn forage biomass and nitrogen uptake at various growth stages using remote sensing and plant height. *Agron. J. 99,* 530–536.

Hancock, D.W. and *Dougherty, C.T.,* 2007: Relationships between blue- and red-based vegetation indices and leaf area and yield of alfalfa. *Crop Sci. 47,* 2547–2556.

Hong, S.D., Schepers, J.S., Francis, D.D., and *Schlemmer, M.R.,* 2007: Comparison of ground-based remote sensors for evaluation of corn biomass affected by nitrogen stress. *Commun. Soil Sci. Plan. 38,* 2209–2226.

Houlès, V., Guérif, M., and *Mary, B.,* 2007: Elaboration of a nitrogen nutrition indicator for winter wheat based on leaf area index and chlorophyll content for making nitrogen recommendations. *Eur. J. Agron. 27,* 1–11.

Iida, K., Suguri, M., Umeda, M., and *Matsui, T.,* 2000: Estimation of nitrogen content using machine vision in a paddy field. In *2000 ASAE Annual International Meeting,* 9–12 July 2000, Milwaukee, Wisconsin, USA, 1–21.

Justes, E., Jeuffroy, M.H., and *Mary, B.,* 1997: Wheat, barley, and durum wheat. In *Diagnosis of the nitrogen status in crops* (ed.: Lemaire, G.), Springer-Verlag, Berlin, 73–91.

Knight, J., Lunetta, R., Ediriwickrema, J., and *Khorram, S.,* 2006: Regional scale land cover characterization using MODIS-NDVI 250 m Multi-Temporal Imagery: A phenology-based approach. *GISci. Remote Sens. 43,* 1–23.

Lemaire, G., Jeuffroy M.H., and *Gastal, F.,* 2008: Diagnosis tool for plant and crop N status in vegetative stage: Theory and practices for crop N management. *Eur. J. Agron. 28,* 614–624.

Martin, K.L., Girma, K., Freeman, K.W., Teal, R.K., Tubaña, B., Arnall, D.B., Chung, B., Walsh, O., Solie, J.B., Stone, M.L., and *Raun, W.R.,* 2007: Expression of variability in corn as influenced by growth stage using optical sensor measurements. *Agron. J. 99,* 384–389.

Murata, N. and *Sato, N.,* 1978: Studies on the absorption spectra of chlorophyll *a* in aqueous dispersions of lipids from the photosynthetic membranes. *Plant Cell Physiol.* 19, 401–410.

Nambuthiri, S.S., 2010: Soil water and crop growth processes in a farmer's field. *PhD Dissertation.* College of Agriculture at the University of Kentucky, Lexington, Kentucky, USA.

NTech Industries Inc., 2007: Operating Manual of GreenSeeker Model 505. Ukiah, California, United States of America.

Rambo, L., Mal, B.L., Xiong, Y., and *da Silvia, P.R.F.,* 2010: Leaf and canopy optical characteristics as crop-N-status indicators for field nitrogen management in corn. *J. Plant Nutr. Soil Sci. 173,* 434–443.

Ren, J., Chen, Z., Zhou, Q., and *Tang, H.,* 2008: Regional yield estimation for winter wheat with MODIS-NDVI data in Shandong, China. *Int. J. Appl. Earth Observ. Geoinf. 10,* 303–413.

Roderick, M., Smith, R., and *Cridland, S.,* 1996: The precision of the NDVI derived from AVHRR observations. *Remote Sens. Environ. 56,* 57–65.

Rouse, J.W., Haas, R.H., Schell, J.A., and *Deering, D.W.,* 1973: Monitoring vegetation systems in the Great Plains with ERTS. In *Proceedings of the Third Earth Resources Technology Satelite-1 Symposium, NASA SP-351 I.* December 10–14, 1973, Washington, 309–317.

Senders, V.L., 1958: Measurement and statistics. Oxford University Press, New York.

Singh, I., Srivastava, A.K., Chandna, P., and *Gupta, R.K.,* 2006: Crop sensors for efficient nitrogen management in sugarcane: potential and constraints. *Sugar Tech. 8,* 299–302.

Szabó J., Pásztor, L., Suba, Z., and *Várallyay, Gy.,* 1998: Integration of remote sensing and GIS techniques in land degradation mapping. *Agrokémia és Talajtan. 47,* 63–75.

Teal, R.K., Tubana, B., Girma, K., Freeman, K.W., Arnall, D.B., Walsh, O., and *Raun, W.R.,* 2006: In-season prediction of corn grain yield potential using Normalized Difference Vegetation Index. *Agron. J. 98,* 1488–1494.

Viña, A., Gitelson, A.A., Rundquist, D.C., Keydan, G., Leavitt, B., and *Schepers, J.,* 2004: Monitoring maize (*Zea mays* L.) phenology with remote sensing. *Agron. J. 96,* 1139–1147.

Víg, R., Dobos, A., Nagy, J., 2011: A normalizált vegetációs index (NDVI) mérésének módszertani vizsgálata lucernában (*Medicago sativa* L.). *Növénytermelés 60,* 111–126.

Wang, Q., Tenhunen, J.D., 2004: Vegetation mapping with multitemporal NDVI in North Eastern China Transect (NECT). *Int. J. Appl. Earth Observ. Geoinf. 6,* 17–31.

Wei, Y., Minzan, L., and *Sigrimis, N.,*2010: Estimating nitrogen content of cucumber leaves based on NIR spectroscopy. *Sensor Lett. 8,* 145–150.

Wright, D.L., Rasmussen, V.P., Ramsey, R.D., Baker, D.J., Ellsworth, J.W., 2007: Canopy reflectance estimation of wheat nitrogen content for grain protein management. *GISci. Remote Sens. 41,* 1548–1603.

Yadava, U L., 1986: A rapid and nondestructive method to determine chlorophyll in intact leaves. *HortScience. 21,* 1449–1450.

Zhang, J., Han, C., Li, D., 2009: New vegetation index monitoring rice chlorophyll concentration using leaf transmittance spectra. *Sensor Lett. 7,* 1–6.

INSTRUCTIONS TO AUTHORS OF *IDŐJÁRÁS*

The purpose of the journal is to publish papers in any field of meteorology and atmosphere related scientific areas. These may be

- research papers on new results of scientific investigations,
- critical review articles summarizing the current state of art of a certain topic,
- short contributions dealing with a particular question.

Some issues contain "News" and "Book review", therefore, such contributions are also welcome. The papers must be in American English and should be checked by a native speaker if necessary.

Authors are requested to send their manuscripts to

Editor-in Chief of IDŐJÁRÁS
P.O. Box 38, H-1525 Budapest, Hungary
E-mail: journal.idojaras@met.hu

including all illustrations. MS Word format is preferred in electronic submission. Papers will then be reviewed normally by two independent referees, who remain unidentified for the author(s). The Editor-in-Chief will inform the author(s) whether or not the paper is acceptable for publication, and what modifications, if any, are necessary.

Please, follow the order given below when typing manuscripts.

Title page: should consist of the title, the name(s) of the author(s), their affiliation(s) including full postal and e-mail address(es). In case of more than one author, the corresponding author must be identified.

Abstract: should contain the purpose, the applied data and methods as well as the basic conclusion(s) of the paper.

Key-words: must be included (from 5 to 10) to help to classify the topic.

Text: has to be typed in single spacing on an A4 size paper using 14 pt Times New Roman font if possible. Use of S.I. units are expected, and the use of negative exponent is preferred to fractional sign. Mathematical formulae are expected to be as simple as possible and numbered in parentheses at the right margin.

All publications cited in the text should be presented in the *list of references*, arranged in alphabetical order. For an article: name(s) of author(s) in Italics, year, title of article, name of journal, volume, number (the latter two in Italics) and pages. E.g., *Nathan, K.K.,* 1986: A note on the relationship between photo-synthetically active radiation and cloud amount. *Időjárás 90,* 10-13. For a book: name(s) of author(s), year, title of the book (all in Italics except the year), publisher and place of publication. E.g., *Junge, C.E.,* 1963: *Air Chemistry and Radioactivity.* Academic Press, New York and London. Reference in the text should contain the name(s) of the author(s) in Italics and year of publication. E.g., in the case of one author: *Miller* (1989); in the case of two authors: *Gamov* and *Cleveland* (1973); and if there are more than two authors: *Smith et al.* (1990). If the name of the author cannot be fitted into the text: *(Miller,* 1989); etc. When referring papers published in the same year by the same author, letters a, b, c, etc. should follow the year of publication.

Tables should be marked by Arabic numbers and printed in separate sheets with their numbers and legends given below them. Avoid too lengthy or complicated tables, or tables duplicating results given in other form in the manuscript (e.g., graphs).

Figures should also be marked with Arabic numbers and printed in black and white or color (under special arrangement) in separate sheets with their numbers and captions given below them. JPG, TIF, GIF, BMP or PNG formats should be used for electronic artwork submission.

Reprints: authors receive 30 reprints free of charge. Additional reprints may be ordered at the authors' expense when sending back the proofs to the Editorial Office.

More information for authors is available: journal.idojaras@met.hu

Published by the Hungarian Meteorological Service

Budapest, Hungary

INDEX 26 361

HU ISSN 0324-6329

IDŐJÁRÁS

QUARTERLY JOURNAL
OF THE HUNGARIAN METEOROLOGICAL SERVICE

CONTENTS

****

http://www.met.hu/Journal-Idojaras.php

VOL. 116 * NO. 2 * APRIL – JUNE 2012

IDŐJÁRÁS

Quarterly Journal of the Hungarian Meteorological Service

Editorial Office: Kitaibel P.u. 1, H-1024 Budapest, Hungary
P.O. Box 38, H-1525 Budapest, Hungary
E-mail: journal.idojaras@met.hu
Fax: (36-1) 346-4669

Indexed and abstracted in Science Citation Index Expanded™ and Journal Citation Reports/Science Edition
Covered in the abstract and citation database SCOPUS®

Subscription by

mail: IDŐJÁRÁS, P.O. Box 38, H-1525 Budapest, Hungary
E-mail: journal.idojaras@met.hu

IDŐJÁRÁS

Quarterly Journal of the Hungarian Meteorological Service
Vol. 116, No. 2, April–June 2012, pp. 77-91

Convective systems and periods with large precipitation in Hungary

Ákos Horváth[1*], **András Tamás Seres**[2], and **Péter Németh**[3]

[1]*Hungarian Meteorological Service,*
Vitorlás u. 17, H-8600 Siófok, Hungary,
E-mail: horvath.a@met.hu

[2]*Hungarian Defence Forces Geoinformation Service,*
Szilágyi E. fasor 7-9, H-1024 Budapest, Hungary
E-mail: seres.andrastamas@upcmail.hu

[3]*Hungarian Meteorological Service,*
Kitaibel P. u. 1, H-1024 Budapest, Hungary,
E-mail: nemeth.p@met.hu

**Corresponding author*

(Manuscript received in final form January 10, 2012)

Abstract—This paper presents a study describing the synoptic scale meteorological conditions and the mesoscale structures of phenomena which can cause large amounts of convective precipitation and often flash floods in Hungary. This examination is based on radar observations, 24-hour rain gauge precipitation measurements, model analyses and forecasts in the six-year period of 2003–2010. For the investigated precipitation period, an objective procedure was applied to decide whether convection had determining role in producing of precipitation. The procedure used radar based precipitation measurements and ECMWF precipitation forecasts. ECMWF analyses and forecasts were also applied to determine the representative synoptic scale weather patterns. Based on observed radar image structures and movements of radar echoes, the mesoscale structures were identified. Studies show that most of the cases can be classified into three main clusters: events with (1) convective chains (squall lines) in the warm sector of a cyclone; (2) convective lines with related cold front; and (3) convective lines in occluded cyclones. These most common types are demonstrated by case studies. This study may help to recognize weather conditions and patterns that are responsible for flash flood events in the Carpathian Basin.

Key-words: radar, large precipitation, convection, flash flood, Hungary.

1. Introduction and background

Climate research revealed that a number of extremely rainy days had significantly grown in the last quarter of the 20th century in Hungary (*Bartholy* and *Pongrácz*, 2005), and the chance of flash floods had increased, too. The aim of this study is to describe the meteorological conditions and the structures of phenomena which can cause flash floods. This examination is based on Hungarian radar observations, rain gauge measurements, and numerical model analyses.

Investigation of flash floods has a long history, especially in the United States. One of the most severe flash floods happened in the Big Thomson Canyon (USA) in 1976, where 143 people were killed (*Caracena et. al.*, 1979). Intensive research in connecting with these phenomena started after this tragedy. Several examinations investigated flash floods and their hydrological aspects (for example run-off simulations) in the USA and Europe (*Maddox*, 1979; *Hansen et al.*, 1982; *Browning,* 1986; *Doswell et al.*, 1996; *Warner et al.,* 2000; *Yates et al.*, 2000; *Davis*, 2001; *Rigo* and *Liasat* ,2002; *Blöschl et al.,* 2008; *Déqué* and *Somot*, 2008).

Marshall and *Palmer* (1948) introduced the so-called Z-R relation between radar reflectivity and precipitation intensity, which is still used with little modifications for precipitation estimation.

The main advantage of radars is that the time and spatial resolution of data are much higher than that of the ground observations. However, radar measurements may have many errors and precipitation data are provided indirectly (*Lombardo* and *Baldini*, 2010). In the last few decades, radar precipitation measurements were used for meteorological and hydrological modeling and forecasts (*Kessler* and *Wilk*, 1968; *Wilson* and *Brandes,* 1979; *Mimikou* and *Baltas*, 1996; *Smith et al.,* 2007; *Rossa et al.,* 2010).

In Hungary, the mesometeorological research started at the beginning of the 1960s. Early studies dealt with the structure and dynamics of convective systems and used data obtained by synoptic scale measurements and observations (*Bodolai*, 1954; *Götz* and *Bodolainé*, 1963a, 1963b, *Bodolainé et al.,* 1967). From the early 1980s, researches started to use remote sensing (radar, satellite, later lightning) data (*Bodolainé*, 1980; *Kapovits*, 1986; *Boncz et al.,* 1987; *Bodolainé* and *Tänczer,* 1991). The examination of weather situations with heavy precipitation, focusing on extreme floods became more common (*Bodolainé,* 1983; *Bodolainé* and *Homokiné*, 1984; *Bonta* and *Takács*, 1988, 1989, 1990; *Takács et al.*, 2000; *Geresdi et. al*, 2004). Floods of river Tisza in 1998 and 2001 were described by *Homokiné* (1999, 2001) from a synoptic meteorological point of view. Nowadays, flash floods can be detected by satellite observations (*Kerényi* and *Putsay*, 2005), and case studies using nowcasting models appeared, too (*Horváth* and *Geresdi,* 2003; *Horváth et al.*, 2007).

Mesoscale convective complexes (MCCs) are circular mesoscale convective systems which produce large amount of precipitation. These phenomena were firstly described by *Maddox* (1980), and in Hungary by *Bodolainé* and *Tänczer* (2003). MCC-s are very rare in Hungary.

In Hungary, *linear mesoscale convective systems* are more common than circular ones. Convective systems have two main parts: the strongest, mature (thunderstorm) cells which have the highest radar echoes, and the weaker, stratiform zone which consists of dissipating cells with less intense radar echoes. These systems were classified into three main clusters by *Parker* and *Johnson* (2000): the *TS (trailing stratiform),* the *PS (parallel stratiform)*, and the *LS (leading stratiform)* types. In the TS and LS systems, the heaviest thunderstorms move (almost) perpendicular to the convergence (instability) line, and the weaker, stratiform parts move behind (trailing) or ahead (leading) of the thunderstorm zone. In this paper TS and LS systems are referred to as *convective chains* or *squall lines*. In the PS types *(convective lines)*, the strongest cells move (almost) parallel to the convergence line. In this study it was found that the TS and PS systems were common, while LS was very rare in Hungary. All of these systems can produce large precipitation. In Hungary, many squall lines come from southwest, and these phenomena are called *Slovenian instability lines* (*Bodolainé et al.,* 1967).

In this paper, the most significant synoptic patterns and mesoscale precipitation structures responsible for large precipitation are coupled to each other, and large precipitation cases are classified into ascertained types.

2. Methodology

The investigation focused on 24-hour periods (from 06 UTC to 06 UTC next day) from 2003 to 2010. In our work, the following data were applied: daily, 24-hour (from 06 UTC to 06 UTC next day) precipitation amounts provided by the Hungarian rain gauge measurement network, composite radar images (resolution is 2 × 2 km in space and 15 minutes in time), 24-hour precipitation estimated by radars, and ECMWF (European Centre for Medium-Range Weather Forecast) analysis or 36-hour forecasts (resolution is 30 × 30 km in space and 3 hours in time). Note that the calculations were based on an area covered by the HMS's (Hungarian Meteorological Service) radar system which is much greater than Hungary (245 116 km^2 vs. 93 030 km^2).

A 24-hour period was considered as a *convective period with large precipitation*, when the following conditions were satisfied:

(1) Two or more stations of the Hungarian rain gauge measurement network reported at least 50 mm precipitation.

(2) At least 60% of the forecasted precipitation was convective in the ECMWF model forecast during the period.

(3) There were one or more pixels (2×2 km areas) with at least 50 mm precipitation measured by radar.

(4) At least 60% of the radar cells with large precipitation had strong echo (intensity ≥ 40 dBz).

To check the realization of the second condition, the ECMWF convective precipitation and the total precipitation were compared for the whole domain at every grid point for the entire precipitation period.

To test the third and fourth conditions, a radar based precipitation estimation procedure, named TREC, was applied. Using this procedure, it was possible not only to estimate the amount of precipitation in all radar pixels but estimate the rate of intensive convective rainfall, separately. A short description of TREC is given in the Appendix.

In the next step, the most significant mesoscale structures of the precipitation period were examined. The *TITAN-method* (Thunderstorm Identification Tracking Analysis and Nowcasting, *Dixon* and *Weiner*, 1993; *Horváth et al.*, 2008) was applied to detect the existence of intensive convective echoes in an objective way. It is important to emphasize that the heavy precipitation falls both from the strong cells (intensity > 40 dBz) and from the weaker trailed or associated stratiform zone. Considering the structure based on movement, the convective precipitation systems were divided into three main clusters:

A. disorganized or weakly organized convective patches (mainly thunderstorms),

B. convective lines (LS systems, mainly thunderstorm lines), where movements of individual cells along the line are more significant than the replacement of the line, and

C. convective chains or squall lines (TS systems) where cells move perpendicular to the thunderstorm line.

The appearance of convective precipitation systems was also classified from a synoptic aspect. For this investigation ECMWF analyses were used. The model fields were visualized by the HAWK-2 (Hungarian Advanced WorKstation) application. Three main synoptic classes were found:

(1) cold front (both slow and fast),

(2) convergence-line of cyclone or cyclone cloud band, and

(3) sporadic cells in weak pressure depression with featureless distributions of values about the mean-sea-level pressure.

The first type is associated with a cold front, it refers to mostly pre-frontal, frontal, rarely post-frontal synoptic situations. The second cluster contains the precipitation zones which form along the convergence-lines of an (occluded) cyclone. The third type represents those situations, when on the ground there is weak pressure gradient with an upper cold and low trough.

Except for one case, all 24-hour periods were classified into these clusters, and combined categories were created as follows:

A1: cold front with sporadic thunderstorms;

A2: sporadic thunderstorms with a convergence line in a cyclone;

A3: sporadic thunderstorms in a weak depression;

B1: convective lines related to a cold front;

B2: convective lines along the convergence zones of a cyclone;

B3: convective lines in weak depression;

C1: squall lines related to a cold front;

C2: squall lines in a cyclone;

C3: weak squall lines in a depression.

If more than one convective system were detected in a 24-hour period, the most significant was considered.

3. Results

Altogether 56 convective periods with large precipitation were found between 2003 and 2010. As it was expected, most of the convective periods appeared between May and September. Concerning their distribution in time the maximum was in 2010 (*Fig. 1*) and in June (*Fig. 2*). Note that one period was found in March.

In the eight-year period, the most frequent combined types were C1 (squall lines related to a cold front), B2 (convective lines along the convergence zones of a cyclone), and B1 (convective lines related to a cold front). The fourth pattern was A3 (low pressure gradient field with disorganized thunderstorms), followed by C2 (squall lines in cyclone). Frequencies of the other types are only 0 or 1 (*Fig. 3*). Note that periods with squall lines (C1 and C2 types) or situations with cold fronts (A1, B1, C1 patterns) appeared more often than the lines (B1 and B2 patterns) or cyclonic situations (B2, C2 combinations). One situation (May 26, 2003) could not be clustered into this classification. On this day, strong squall lines formed and moved from east to west in the central and western parts of Hungary.

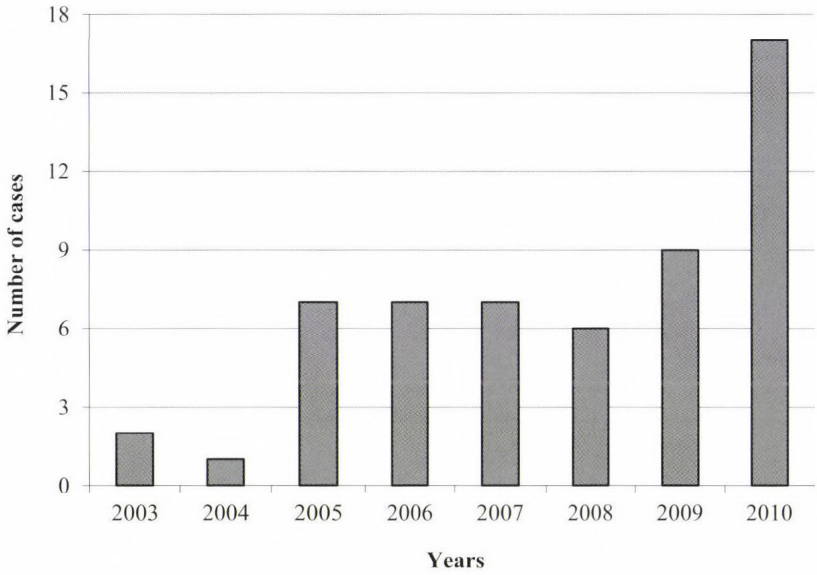

Fig. 1. Frequency distribution of 24-hour periods with large precipitation by year.

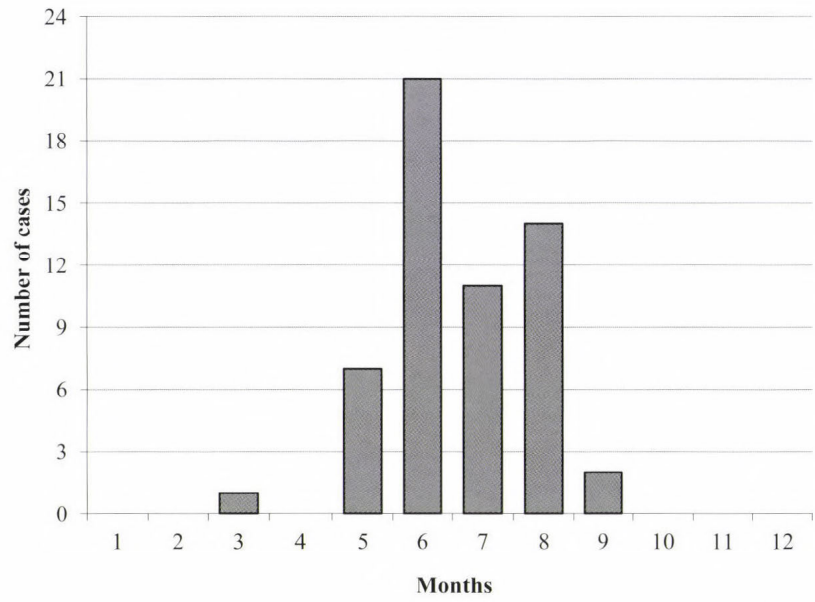

Fig. 2. Frequency distribution of 24-hour periods with large precipitation by month.

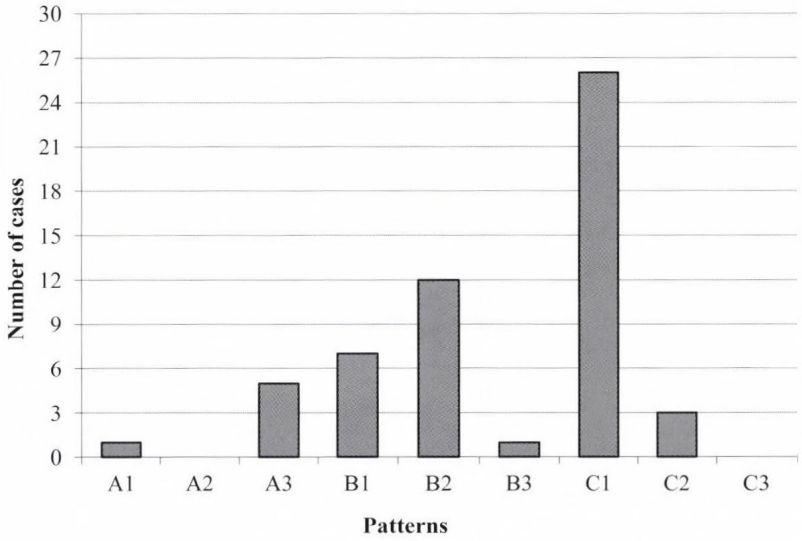

Fig. 3. Frequency distribution of 24-hour periods with large precipitation by combined patterns.

Considering all case studies, it was found that in average, the amount of radar estimated precipitation was larger than 50 mm only on 0.23% of the entire area (that means 564 km^2 of 245 116 km^2). In the large precipitation areas, 18% of the precipitation arose from echoes with reflectivity $\geq$40 dBz (this was the so-called *convective part*). Meanwhile, nearly at about 50% of all cases, the rate of convective precipitation was higher than 60% in large precipitation areas. It was also found that there was at least one strong echo (intensity $\geq$40 dBz) in about 92% of areas with large precipitation. Average characteristics of the most frequent five types as well as the average values for all the seven types are shown in *Table 1.*

3.1. C1 type (Squall line related to cold front)

On August 20, 2007, a cold front reached Hungary from north-west (*Fig. 4*). Thunderstorms developed in front of the cold front, and formed an extended squall line. Behind the intensive cells, a massive stratiform zone was forming. In advance of the squall line, in the prefrontal zone (in the Great Plain), isolated convective systems developed. In the western part of Hungary (Transdanubia), large amounts of precipitation fell both from the intensive cells and from the trailed stratiform regions of the squall line, while in south-east the precipitation fell mainly from the most intensive parts. There was strong contrast in temperature at 850 hPa level, while at 700 hPa wet airmasses were advected. In the mid-troposphere region (at 500 hPa), Hungary was situated in front of a cold low. There was strong, southerly wind, and the cold advection was just

beginning from south-west in the afternoon. This case can be considered as a type of large precipitation with intensive, fast moving thunderstorms.

Table 1. Average characteristics of the most frequent patterns and for all cases. Rows mean:
Note: the last column shows the average values for all (seven) cases.

	A3	B1	B2	C1	C2	All
1	0.04	0.20	0.14	0.30	0.37	0.23
2	6.57	26.21	7.45	26.75	26.32	17.92
3	45.34	52.50	43.02	57.08	54.03	50.34
4	90.87	91.88	85.66	97.40	95.59	91.94

1 Ratio of areas with large precipitation (where the calculated 24-hour amount is above 50 mm). Total area: 245116 km^2.

2 Rate (in percentage) of convective (calculated only from echoes above 40 dBz) and total precipitation in areas with large precipitation.

3 On areas with large precipitation ratio of pixels where the convective part reached at least 60 % of the total amount.

4 On areas with large precipitation percentage of pixels where at least one strong echo (intensity $\leq$ 40 dBz) appeared.

Case studies also show that for types C1 or C2, greater amount of the large precipitation originated from strong echoes, and the convective activity was heavier having more cells with large precipitation as compared to other types.

Short case studies of the three most frequent combinations are described below.

3.2. B2 combination (Convective lines along the convergence zones of cyclone)

On August 11–12, 2007, a shallow, occluded cyclone could be analyzed on surface weather maps *(Fig. 5)*. In the upper levels, the synoptic scale vorticity was more significant, especially at 500 hPa, where a cut-off low zone could be detected. The relative humidity analyses on the 700 hPa level marked the wet convergence lines (so-called cyclone arms). One of these convective lines is shown in the radar image. The higher reflectivity echoes, surrounded by less intensive but still convective-derived areas, move almost in parallel to the curved convective line. This is a typical PS system (convective line). The maxima of the 24-hour precipitation are organized almost in lines in Transdanubia. This situation is a good example of a decaying, occluded cyclone, which can stay in the region of the Carpathian Basin for several days. In the upper levels, the cold, cut-off low and the stronger (but not jet-stream) winds guarantee the convective instability. The convergence lines ('arms') of the cyclone collect the humidity, and developing thunderstorms propagate slowly along these lines, producing large amounts of precipitation. This case can be considered as a type of large precipitation with less intensive thunderstorms.

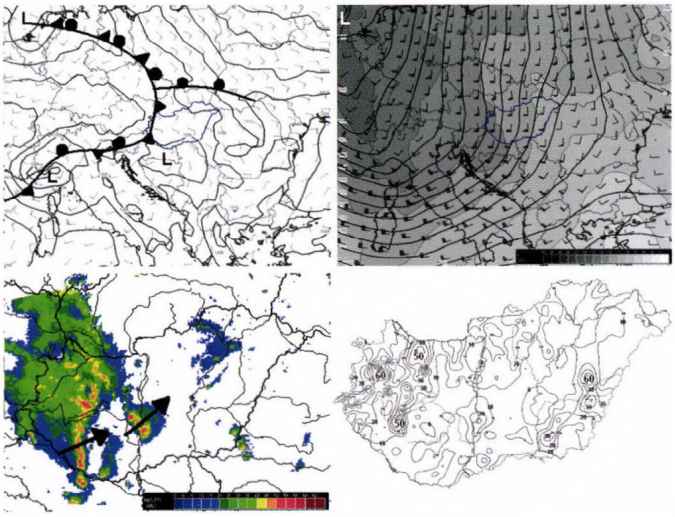

Fig. 4. Top: ECMWF analyses for August 20, 2007, 12:00 UTC.
Top left: MSL pressure (isobars by 2 hPa) wind field at the 925 hPa level and fronts. *Top right*: geopotential heights (lines by 20 gpm), temperature (monochrome shades by 2 °C) and wind field at 500 hPa level. *Bottom left*: composite radar image on August 20, 2007, 14:45 UTC. The arrows show the motion of the most intensive cells. *Bottom right*: Spatial distribution of 24-hour precipitation from August 20, 2007, 06:00 UTC to August 21, 2007, 06:00 UTC.

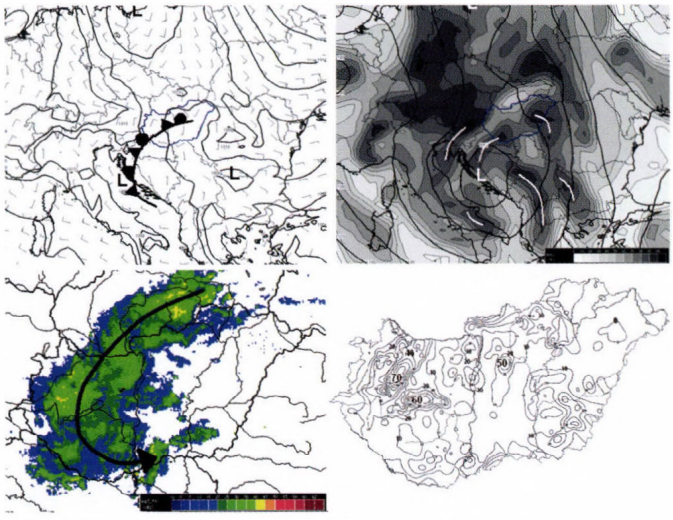

Fig. 5. Top: ECMWF analyses for August 11, 2007, 12:00 UTC.
Top left: MSL pressure (isobars by 2 hPa) at the 925 hPa level wind field and fronts. *Top right*: geopotential heights (lines by 20 gpm), 700 hPa humidity (monochrome shades) and wind. Convergence lines are drawn by white, curved lines. *Bottom left*: mosaic radar image on August 12, 2007, 03:30 UTC. The arrow marks the convective line. *Bottom right*: spatial distribution of 24-hour precipitation from August 11, 2007, 06:00 UTC to August 12, 2007, 06:00 UTC.

3.3. B1 type (Convective lines with cold front)

On July 14, 2008, a cold front was located over Hungary (*Fig. 6*). The front came from north-west and was moving slowly to south-east. Heavy thunderstorms developed ahead of it; some of them were long-living supercells. The most intensive storms were moving along lines from south-west to north-east, almost parallel to the front-line (*Csonka* and *Kolláth*, 2008). At the 500 hPa level, on the prefrontal side of the cold low (situated west of Hungary), cold advection could be observed, while on lower levels, the colder air reached only the north-western parts of Hungary. Strong upper winds generated significant shear, while at 700 hPa, from south-west humid airmasses were approaching. The maxima of 24-hour precipitation marked the path of the strongest cells. This case can be considered as the type of relative slow moving, sometimes extremely strong severe thunderstorms with supercells.

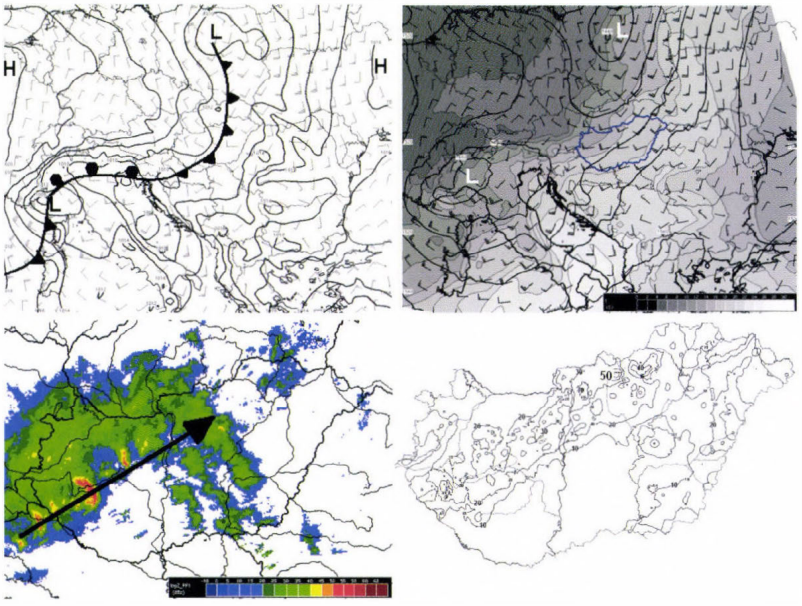

Fig. 6. Top : ECMWF analyses for July 14, 2008, 00:00 UTC
Top left: MSL pressure (isobars by 2 hPa) and the wind fields at the 925 hPa level and the front lines. *Top right*: geopotential heights (lines by 20 m), temperature (monochrome shades by 2 °C) and wind field of the 850 hPa level. *Bottom left*: composite radar images on July 14, 2008, 06:00 UTC. The arrow indicates the tracks of the most intensive storms. *Bottom right*: spatial distribution of 24-hour precipitation from July 14, 2008, 06:00 UTC to July 15, 2008, 06:00 UTC.

4. Conclusions

This paper presents the results of a study of large amount precipitation events in Hungary for the eight-year period of 2003–2010. The aim of this study was to describe these phenomena (which may cause flash flood) and to cluster them from synoptic and mesoscale points of view. Following this objective, 24-hour precipitation data, composite radar images, radar precipitation measurements, and ECMWF analyses and forecasts were applied. Nine combined patterns were created by considering mesometeorological, phenomenological, and synoptic points of view. The most frequent three types were demonstrated with case studies.

The main results of the research are as follows:

- 56 convective periods with large precipitation were found, and 55 were classified into 7 combined clusters.
- Most of the periods appeared in summer, the maxima were in June and in 2010.
- The most frequent combined types were squall lines with cold front (C1), convective lines along the convergence zones of a cyclone (B2), and convective lines with cold front (B1).
- Periods of convective squall lines with cold fronts appeared more often than convective lines in cyclonic situations.
- In each period, pixels with large precipitation (the calculated 24-hour amount is above 50 mm) appeared in about 0.23% of the total area (which is 564 km^2) on the average.
- Considering the large precipitation areas, the average ratio of convective precipitation (calculated only from strong echoes with reflectivity higher than 40 dBz) was approximately 18% in each period, but in about 50% of these cases the convective part was at least 60%.
- Periods with squall lines have higher convective activities and more cells with large precipitation than periods with lines or disorganized/weakly organized convective patches, because greater part of the large precipitation was produced by strong echoes.

In the future, this examination will be extended by focusing on regions endangered by flash floods involving more hydrological aspects.

Acknowledgements—This research was supported by the Jedlik Ányos Program 2005, identification number: OM-00103/2005.

Appendix

Calculation of motion vectors and accumulated precipitation using time series of radar reflectivity

HMS radar network collects data in 15-minute cycles, which can result in significant under-sampling in both space and time. A typical 12-hour accumulation precipitation field based on HMS radar network observation is shown in *Fig. 7*. The under-sampling strongly depends on the velocity of the radar cells, and can result in serious underestimation of the surface accumulated precipitation in the case of the fast moving squall lines.

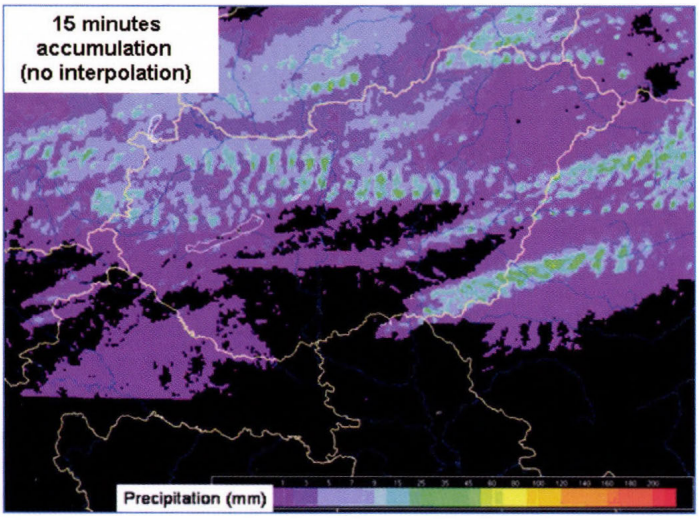

Fig. 7. 12-hour accumulated precipitation calculated by radar images with 15-minute time resolution.

The error caused by the under-sampling was reduced by using correlation tracking method (TREC, Tracking Radar Echoes by Correlation). During the TREC procedure, the radar grid was divided into so-called macro grids, and the calculation of motion vectors was based on maximum correlations for the macro grids. After quality control to filter out noisy vectors on macro grids, fine resolution motion vectors were interpolated for all grid points of the original radar grid. Once a motion vector field belonging to radar images at times T2 and T1 is available, interpolation of the radar reflectivity can be done at any time between T1 and T2. Echoes from T1 are moved forward and echoes from T2 moved backward by motion vectors, and the reflectivity of a given pixel is

interpolated between the forward and backward moving reflectivity values as shown in *Fig. 8.*

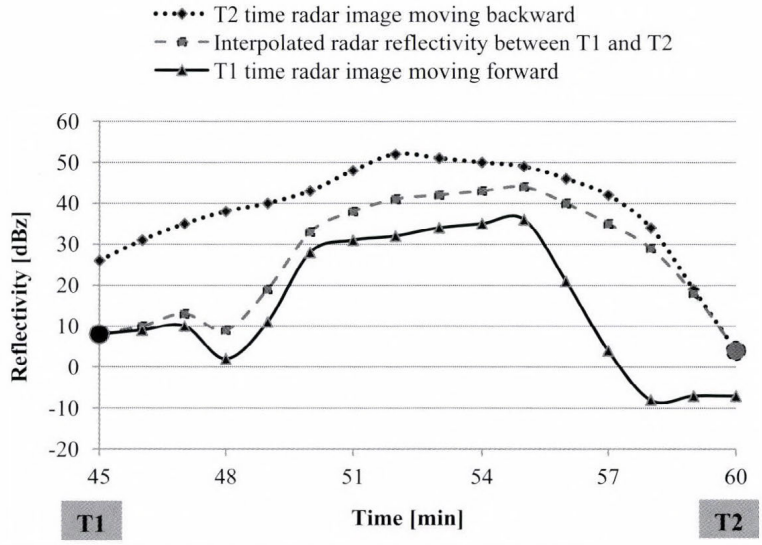

Fig. 8. Interpolation of radar reflectivity using motion vectors.

The application of the TREC method offers a more realistic accumulated precipitation field (*Fig. 9*). The 12-hour precipitation field in *Fig. 9* is calculated from 15-minute sampling cycle data. The optimal interpolation time step for precipitation calculation was found to be 1 minute.

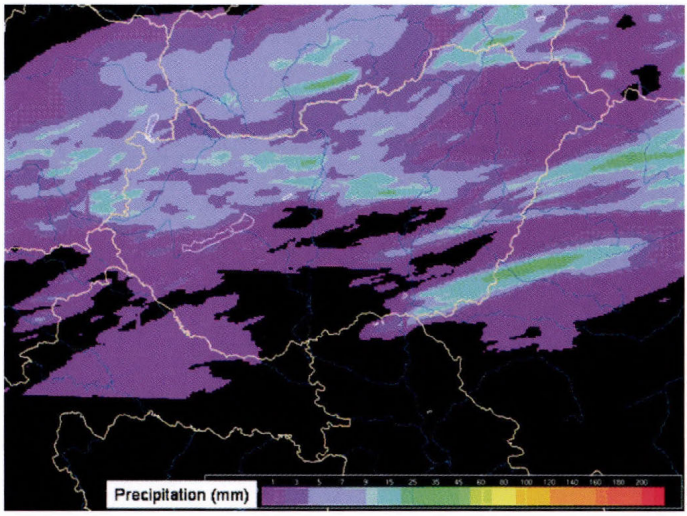

Fig. 9. 12-hour accumulated precipitation calculated by 1 minute interpolated radar images.

References

Bartholy, J. and *Pongrácz, R.*, 2005: Tendencies of extreme climate indices based on daily precipitation in the Carpathian Basin for the 20th century. *Időjárás 109*, 1–20.

Blöschl, G., Reszler, C. and *Komma, J.*, 2008: A spatially distributed flash flood forecasting model. *Environ. Modell. Softw. 23*, 464–478.

Bodolai, I., 1954: *Aerological and synoptical conditions of forming convective thunderstorms* (in Hungarian). Az OMI Kisebb Kiadványai 27, OMSZ, Budapest, 80 pp.

Bodolainé, J.E, 1980: *Using of radar measurements in short-range forecasting of precipitation* (in Hungarian) Az OMSZ Kisebb Kiadványai 48, OMSZ, Budapest, 79 pp.

Bodolainé, J.E., 1983: *Synoptical conditions of flood waves in the catchment of the Danube and Tisza* (in Hungarian). Az OMSZ Hivatalos Kiadányai 56, OMSZ, Budapest, 126 pp.

Bodolainé, J.E, Bodolai, I. and *Böjti, B.*, 1967: Macrosynoptical conditions for the formation of Slovenian squall lines and some properties of cold fronts with thunderstorm. *Időjárás 67*, 129–143.

Bodolainé, J.E. and *Homokiné, U.K.*, 1984: *Quantitative precipitation forecasts using the orographic precipitation enhancement* (in Hungarian). Az OMSZ Kisebb Kiadványai 57, OMSZ, Budapest, 45 pp.

Bodolainé, J.E. and *Tänczer, T.*, 1991: Instability line in a regional cyclone (in Hungarian). *Időjárás 95*, 178–195.

Bodolainé, J.E. and *Tänczer, T.*, 2003: *Mesoscale convective complexes producing flash floodwaves* (in Hungarian). Budapest, OMSZ, 184 pp.

Boncz, J., Kapovits, A., Pintér, F. and *Tänczer, T.*, 1987: A method for the complex analysis of synoptic weather radar and satellite data. *Időjárás 91*, 11–22.

Bonta, I. and *Takács, Á.*, 1988: *Construct of warning system for heavy rainfall in Hungary* (in Hungarian). Az OMSZ Kisebb Kiadványai 63, OMSZ, Budapest, 31 pp.

Browning, K.A., 1986: Conceptual Models of Precipitation Systems. *Weather Forecast. 1*, 23–41.

Caracena, F., Maddox, A.R., Hoxit, R.L., and *Chappell, C.F.*, 1979: Mesoanalysis of the Big Thompson Storm. *Mon. Weather Rev. 107*, 1–17.

Csonka, T. and *Kolláth, K.*, 2008: 'Transpannon monster", long-lived supercells on July 14, 2008 (in Hungarian). Published on the Internet: http://owww.met.hu/pages/bogacs20080714.php

Davis, R.S., 2001: Flash Flood Forecast and Detection Methods. In *Meteorological Monographs 28*, (ed: Doswell, C.A.), AMS, 481–525.

Déqué, M. and *Somot, S.*, 2008: Analysis of heavy precipitation for France using high resolution ALADIN RCM simulation. *Időjárás 112*, 179–190.

Dixon, M. and *Wiener, G.*, 1993. TITAN: Thunderstorm Identification, Tracking, Analysis and Nowcasting – A radar-based methodology. *J. Atmos. Ocean. Tech. 10*, 785–797.

Doswell, C.A. III, Brooks, H.E. and *Maddox, R.A.*, 1996: Flash flood forecasting: An ingredients-based methodology. *Weather Forecast. 11*, 560–581.

Geresdi, I., Horváth, Á., and *Mátyus, Á.*, 2004: Nowcasting of the precipitation type, Part II.: Forecast of thunderstorms and hailstone size. *Időjárás 108*, 33–50.

Götz, G. and *Bodolainé, J.E.*, 1963a: About mesosysnoptical forms (in Hungarian). *Időjárás 67*, 46–53.

Götz, G. and *Bodolainé, J.E.*, 1963b: Structures and analyses of instability lines (in Hungarian). Az OMI Kisebb Kiadványai 33, OMSZ, Budapest, 79 pp.

Hansen, E.M., Schreiner, L.C. and *Miller, J.F.*, 1982: *Application of probable maximum precipitation estimates – United States East of the 105th meridian.* Hydrometeorological Report 52, National Weather Service, NOAA, US Department of Commerce, Washington, DC., 168 pp.

Homokiné, U.K., 1999: Flood of River Tisza at autumn (in Hungarian). *Légkör 64(1)*, 2–6.

Homokiné, U. K., 2001: Flood in March in Transcarpathia (in Hungarian). *Légkör 66(2)*, 2–5.

Horváth, Á., Ács, F. and *Seres, A.T.*, 2008: Thunderstorm climatology analyses in Hungary using radar observations. *Időjárás 112*, 1–13.

Horváth, Á. and *Geresdi, I.* 2003: Severe Storms and Nowcasting in the Carpathian Basin. *Atmos. Res. 67–68*, 319–332.

Horváth, Á., Geresdi, I., Németh, P. and *Dombai, F.*,2007: The Constitution Day storm in Budapest: Case study of the August 20, 2006 severe storm. *Időjárás 111*, 41–63.

Kapovits, A., 1986: Hydrological aspect of using radar precipitation measurements (in Hungarian). *Vízügyi Közlemények 68.*, 486–499.

Kerényi, J. and *Putsay, M.*, 2005: Extreme flood monitoring in Romania and Hungary using Earth Observation Data, *Időjárás 109*, 205–216.

Kessler, E. and K.E. Wilk, 1968: Radar measurements of precipitation for hydrological purposes. Report 5, International Hydro. Decade. WMO, Geneva

Lombardo, F. and *Baldini, L.*: 2010: *Study on the rainfall dependence structure using radar and rain gauge data.* International Workshop Advances in Statistical hydrology, May 23–25 2010, Taormina, Italy

Maddox, R.A., 1979: A methodology for forecasting heavy convective precipitation and flash flooding. *National Weather Digest: Flood 4*(4), 30–42.

Maddox, R.A., 1980: Mesoscale convective complexes. *B. Am. Meteorol. Soc. 61*, 1374–1387.

Marshall, J.S. and *Palmer, W.M.*, 1948: The distribution of raindrops with size. *J. Meteorol. 5*, 165–166.

Mimikou, M.A. and *Baltas, E.A.*, 1996: Flood Forecasting Based on Radar Rainfall Measurements. *J.Water Res. Plan. Manage.* 122, 151–156.

Parker, M.D. and *Johnson, R. H.*, 2000: Organizational Modes of Midlatitude Mesoscale Convective Systems. *Month. Wea. Rev. 128*, 3413–3436.

Parker, M.D. and *Johnson, R.H.*, 2004: Structures and Dynamics of Quasi-2D Mesoscale Convective Systems. *J. Atmos. Sci. 61*, 545–567.

Rigo, T. and *Liasat, M.C.*, 2002: Analysis of convective structures that produce heavy rainfall events in Catalonia (NE of Spain), using meteorological radar. *Proc. ERAD*, 45–48.

Rossa, A.M., Cenzon, G., and *Monai, M.*, 2010: Quantitative comparison of radar QPE to rain gauges for the 26 September 2007 Venice Mestre flood. *Nat. Hazards Earth Syst. Sci. 10*, 371–378.

Smith, J.A., Baeck, M.L., Meierdiercks, K.L., Miller, A.J., and *Krajewski, W.F.*, 2007: Radar rainfall estimation for flash flood forecasting in small urban watersheds. *Adv. Water Res. 30*, 2087–2097.

Takács, Á., Girz, C., Tollerud, E., and *Kertész, S.*, 2000: New methods for severe precipitation warning for Hungary. *Időjárás 104*, 1–67.

Warner, T.T, Brandes, E.A, Sun, J., Yates, D.N., and *Mueller, C.K.*, 2000: Prediction of a flash flood in complex terrain. Part I: A comparison of rainfall estimates from radar, and very short range rainfall simulations from a dynamic model and an automated algorithmic system. *J. Appl. Meteorol. 39*, 797–814.

Wilson, J.W., and *Brandes, E.A, 1979*: Radar measurement of rainfall – a summary. *B. Am. Meteorol. Soc. 60*, 1048–1058.

Yates, D.N., Warner, T.T., and *Leavesley, G.H.*, 2000: Prediction of a flash flood in complex terrain. Part II: A comparison of flood discharge simulations using rainfall input from radar, a dynamic model, and an automated algorithmic system. *J. Appl. Meteor. 39*, 815–825.

IDŐJÁRÁS

Quarterly Journal of the Hungarian Meteorological Service
Vol. 116, No. 2, April–June 2012, pp. 93-107

Application of a novel photoacoustic instrument for ammonia concentration and flux monitoring above agricultural landscape – results of a field measurement campaign in Choryń, Poland

Andrea Pogány[1*], Tamás Weidinger[2], Zoltán Bozóki[3], Árpád Mohácsi[3], Jerzy Bieńkowski[4], Damian Józefczyk[4], Attila Eredics[5], Árpád Bordás[2], András Zénó Gyöngyösi[2], László Horváth[6], and **Gábor Szabó[1]**

[1]*Department of Optics and Quantum Electronics, University of Szeged, Dóm tér 9, 6720 Szeged, Hungary, E-mails: andrea@titan.physx.u-szeged.hu, gszabo@physx.u-szeged.hu*

[2]*Department of Meteorology, Eötvös Loránd University, Pázmány P. sétány 1/A, 1117 Budapest, Hungary, E-mails: weidi@ludens.elte.hu, zeno@nimbus.elte.hu, bordas.arpad@gmail.com*

[3]*Research Group on Laser Physics of the Hungarian Academy of Sciences, Dóm tér 9, 6720 Szeged, Hungary, E-mails: zbozoki@physx.u-szeged.hu, mohacsi@titan.physx.u-szeged.hu*

[4]*Institute for Agricultural and Forest Environment, PAS, Bukowska st. 19, Poznań, Poland, E-mail: bienkowjerzy@poczta.onet.pl*

[5]*Institute of Environmental and Earth Sciences, Faculty of Forestry, University of West Hungary, Cházár A. tér 1, 9400 Sopron, Hungary, E-mail: aeredics@yahoo.com*

[6]*Hungarian Meteorological Service, P.O. Box 39 H-1675, Budapest, Hungary; E-mail: horvath.l@met.hu*

[*]*Corresponding author*

(Manuscript received in final form January 19, 2012)

Abstract—A one-week field measurement campaign has been carried out on a winter wheat field nearby a cattle farm in Poland. The aim of the campaign was to demonstrate applicability of a recently developed photoacoustic ammonia monitoring instrument for environmental research purposes. The photoacoustic instrument was operated with three sampling lines, and a wet-chemical AMANDA instrument with one sampling inlet was used as a reference for ammonia concentration monitoring. In addition to the ammonia measurements, several meteorological parameters were measured with a micro-meteorological station. The campaign was started with instrument intercomparison when all inlets of the ammonia monitoring instruments were placed at the same point. Good agreement has been found between concentration data measured by the three channels of the photoacoustic instrument and the AMANDA, which proves reliability of the instruments. In the second part of the campaign, plume detection and flux measurement were carried out. During this period the photoacoustic instrument was placed 130 m east, the AMANDA instrument was placed 46 m northeast from the farm; and the photoacoustic instrument operated in gradient configuration, i.e., with the three sampling inlets placed at three different heights above canopy level. Background concentration was found to be around 2 $\mu g m^{-3}$, which is typical for agricultural landscapes. Concentrations up to 60 $\mu g m^{-3}$ were observed in case of wind blowing from the direction of the farm, and difference between concentrations measured at the two different locations around the farm varied according to wind direction, indicating changing position of the ammonia plume around the farm. Concentration gradients measured by the photoacoustic instrument during the campaign showed strong diurnal variation according to atmospheric stability. Ammonia fluxes calculated from the measured gradients were in the range of 0 to –90 $ng m^{-2} s^{-1}$, in good agreement with expectations.

Key-words: ammonia, photoacoustic spectroscopy, surface-atmosphere exchange flux, plume detection, agriculture

1. Introduction

Measuring ambient concentration and surface-atmosphere exchange of ammonia is an important problem in environmental science (*Sutton et al.,* 2009a). Ambient concentration of ammonia varies within a wide range: background concentration is typically a few $\mu g m^{-3}$, while concentrations up to several ten $mg m^{-3}$ might occur near emission sources. The most important emission source of ammonia is agriculture, and environmental impacts include acidification, eutrophication, and formation of secondary aerosol particles. During the past decades, ammonia as an air pollutant has been gaining increasing attention. Reasons for this increasing interest are increasing emission of ammonia as a result of increasing agricultural production, as well as success of previous environmental regulations on industrial air pollutants (e.g., sulfur-dioxide and nitrogen oxides). Furthermore, reduced sulfur-dioxide level decreases the rate of co-deposition of sulfur-dioxide and ammonia as well as the rate of conversion of gaseous NH_3 to ammonium (hydrogen) sulphate particles resulting in higher ambient ammonia concentration (*Flechard et al.*, 1999; *Fowler et al.*, 2001; *Erisman et al.*, 2001a). As environmental impacts of ammonia became clear, importance of regulations concerning emission of ammonia as well as

monitoring and modeling tasks were recognized (*Galloway et al.,* 2002; *Sutton et al.,* 2009b).

The first international agreement regulating ammonia emission was the Gothenburg Protocol of the UN Convention on Long Range Transboundary Air Pollution in Europe in 1999 (*Erisman et al.,* 2003). The Protocol determined emission ceilings for each participating country and required the annual reporting of national ammonia emissions. Therefore, measuring ammonia emissions became an important issue.

Since the most important source of ammonia is the agriculture, it originates mainly from areal sources, such as fertilized agricultural fields and animal farms, as a result of which quantifying emission (or deposition) of ammonia requires the application of micrometeorological methods or models.

Ammonia concentrations measured at different distances and directions from a concentrated source, such as an animal farm can be used to study the ammonia plume formed around the source. Plume detection together with dispersion modeling can be used to establish and verify emission factors and, thereby, estimate the amount of ammonia emitted by the source (*Faulkner et al.,* 2007; *Staebler et al.,* 2009; *Loubet et al.,* 2010).

Micrometeorological flux calculation methods are used to quantify ammonia emission from fertilized fields (*Milford et al.,* 2001, 2009; *Spirig et al.,* 2009), or deposition to areas surrounding point sources (*Fowler et al.,* 1998). Although, several instruments have been developed for ammonia concentration measurement (*Erisman et al.,* 2001b; *von Bobrutzki et al.,* 2010), their applicability for routine monitoring tasks, and especially for flux measurement is not trivial, due to high requirements regarding ease of operation, accuracy, and time resolution. At this time, gradient measurement using wet-chemical instruments (e.g., AMANDA instruments) is believed to be the most reliable, although it is a rather laborious method for measuring ammonia concentration and flux. The first wet-chemical ammonia analyzers were developed in the 1990s (*Wyers et al.,* 1993) and became the most widely used instruments for environmental ammonia monitoring by now. Wet-chemical instruments ensure detection limit around 0.1 $\mu g m^{-3}$ with time resolution of a few minutes and simultaneous concentration measurement at up to three channels. The gradient technique requires simultaneous concentration measurements at different heights above canopy. This technique has been used for quantifying trace gas fluxes since the 1930s (*Thornthwaite* and *Holzman*, 1939), as a result of which necessary correction algorithms and limitations of the applicability of the method are well established. Differences in concentrations measured at different heights within a few meters above canopy are typically 5–20% of the ambient concentration, which means a required precision of a few tenth $\mu g m^{-3}$ in case of elevated concentration in agricultural landscapes. Time resolution is not critical, measurement of 30–60 min concentration averages is appropriate for gradient measurements.

Previously, we have developed a novel photoacoustic instrument for environmental ammonia monitoring (*Pogány et al.*, 2009, 2010). In this paper we report the field application of this instrument near a cattle farm in an agricultural landscape and demonstrate that the instrument is suitable for on-line, automatic measurement of both ammonia concentration and flux around point sources; therefore, it is a useful tool for quantifying ammonia load caused by concentrated sources.

2. *Experimental*

2.1. Description of the field and instrumentation

The field campaign has been carried out near Choryń, Poland (52°02'N, 16°46'W, 80 m asl.), in an agricultural landscape with total area of 15,000 ha. The campaign lasted for one week in autumn, between 21 and 28, October 2008. Aerial photograph of the field is shown in *Fig 1.*

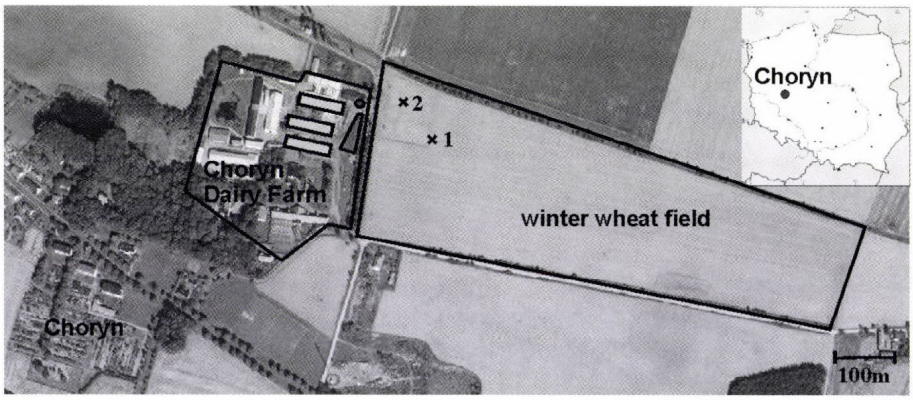

Fig. 1. Aerial photograph of the measurement sites. Light gray rectangles indicate farm buildings, dark grey frames indicate manure stack and slurry tank. Crosses show measurement sites 1 and 2, where the different instruments were installed (see in the text).

The Choryń Dairy Farm consists of three main buildings with 425 animals. Manure from the buildings is transported to an uncovered farmyard manure stack, while liquid fraction of cattle manure is stored in an uncovered slurry tank, both in a close vicinity of the farm buildings. Two measurement sites have been established in a winter wheat field with total area of 18 ha, at 130 m (site 1) and 46 m (site 2) distances from the cattle farm, as it is shown in *Fig. 1.*

A diode laser based photoacoustic instrument was used for measuring concentration and vertical concentration gradient of ammonia. Our previous results have proven that diode laser based photoacoustic spectroscopy is a reliable method for measuring gas concentration in field applications (*Bozóki et*

al., 2011), however, minimum detectable concentration with a simple diode laser based photoacoustic ammonia monitoring instrument (35 μgm^{-3}, *Huszár et al.,* 2008) is not sufficient for ambient ammonia concentration monitoring. Therefore, we supplemented the instrument with a pre-concentration unit, which resulted in an about 100-fold decrease in minimum detectable concentration (*Pogány et al.,* 2009). Furthermore, we have supplemented the instrument with two further sampling lines, which enables concentration measurement at three different sampling levels (*Pogány et al.,* 2010). Air sampling is carried out simultaneously through all sampling lines, while the subsequent concentration measurement is done one line after the other, using the same photoacoustic detector. The sampling lines are 3 m long Teflon tubes, with 8 mm inner diameter, and heated to ~50 °C to decrease adsorption of ammonia and water vapor in the sampling line. Teflon filters with 1 μm pore size in filter holders are placed at the inlets to prevent capture of aerosol particles in the pre-concentration units as well as to eliminate interference from ammonium containing particles. Vertical concentration gradient of ammonia can be measured by placing the three sampling inlets at three different heights above canopy, and ammonia flux can be calculated from the measured gradients. Time resolution of the instrument is 45 minutes that enables detection limit of 0.35 $\mu g m^{-3}$. Previously, the instrument was tested both for ammonia concentration (*von Bobrutzki et al.,* 2010) and flux (*Pogány et al.,* 2010) measurements.

An AMANDA system (Ammonia Measurement by ANnular Denuder sampling with on-line Analysis) purchased from ECN (Energy Research Centre of the Netherlands) was used as a reference instrument to measure ammonia concentration (*Wyers et al.,* 1993). The AMANDA instrument operated with one sampling inlet, 2 minutes time resolution and was calibrated daily with carefully prepared liquid samples.

Micrometeorological data were monitored by a meteorological station of four masts. Micrometeorological parameters for ammonia flux calculation were determined from data measured by an ultrasonic anemometer (METEK USA-1) placed at 2 m height on a separate mast. A microcomputer system was used for data acquisition at a rate of 10 Hz. Several further meteorological sensors were placed on the other three masts and in the soil; however, thorough analysis of all meteorological data is out of the scope of the current study. In this paper only a few data are shown to give an overview on the weather conditions during the experiment. The following meteorological data are shown in the present study: global radiation and net radiation (measured by Kipp & Zonen CNR1 net radiometer at 2 m height), air temperature and relative humidity (measured by a Vaisala HMP45 sensor from Campbell Scientific at 3.2 m height), soil temperature (measured by a 107-L thermistor from Campbell Scientific at 10 cm depth), wind speed and direction (measured by a Young wind monitor at 3.4 m height), and precipitation (measured by a Young tipping bucket rain gauge).

Data from the sensors were recorded by a Campbell CR23 datalogger every 10 minutes.

2.2. Measurement methods

The micrometeorological station and the photoacoustic instrument were operating throughout the whole campaign at site 1 (see *Fig. 1*). During the first part of the campaign as well as the last half day, the three inlets of the photoacoustic instrument were placed at the same height (1.2 m above canopy) to check precision of the instrument. Gradient measurements were carried out between 10 am on October 24 and 11 pm on October 27 at 0.5, 1.2, and 2.4 m heights above canopy.

During the first part of the campaign the AMANDA was also operating at site 1 and was moved to site 2 in the morning of October 25. The inlet of the AMANDA was placed at 1.2 m height at both sites.

Ammonia concentration data measured by the three channels of the photoacoustic instrument at the same height were compared, and precision of flux measurement was estimated on the basis of these data. Concentration data measured by the photoacoustic instrument and the AMANDA at the same site were also compared.

Ammonia concentrations measured by the two instruments at the two different sites were analyzed according to wind direction.

Ammonia fluxes were calculated from concentration data measured at three heights by the photoacoustic instrument using the gradient method (*Foken,* 2008), similarly to the method used in our previous work (*Pogány et al.,* 2010). In the followings, main steps of the applied flux calculation method are summarized.

Ammonia flux (F, in $\mu g\,m^{-2}\,s^{-1}$) was calculated as the product of friction velocity (u_*, in $m\,s^{-1}$) and dynamic concentration (c_*, in $\mu g\,m^{-3}$).

$$F = -u_* \cdot c_* . \tag{1}$$

Friction velocity was determined using the eddy covariance method, from vertical and horizontal wind velocity measured by the ultrasonic anemometer.

Dynamic concentration is calculated from concentrations measured at two different heights as:

$$c_* = \frac{\left[c(z_i) - c(z_j)\right]\kappa}{\ln\frac{z_i}{z_j} + \Psi(\zeta_i) - \Psi(\zeta_j)} , \tag{2}$$

where $c(z_i)$ and $c(z_j)$ are ammonia concentrations measured at z_i and z_j heights above canopy level, and □ is the von Kármán constant (0.4). □ is the universal function, i.e., a correction for atmospheric stability, and is a function of the dimensionless stability parameter ($\zeta = z / L$, where L is the Monin-Obukhov length). We used universal functions suggested by *Dyer* (1974), which is the most widely used correction in case of trace gas fluxes (*Weidinger et al.,* 2000).

Since we have measurement data from three heights, c_* was calculated for each sub-layer using concentrations measured at two heights (0.5–1.2 m, 1.2–2.4 m, and 0.5–2.4 m), and the average of the three values was used for ammonia flux calculation. For comparison, fluxes were also calculated for the individual sub-layers.

Raw data were filtered according to the following criteria. We did not calculate fluxes for periods with extraordinary stability, i.e., either $u < 0.8$ m s^{-1} or $|L| < 2.4$ m (corresponding to $|\zeta| > 1$ at 2.4 m height) due to limitations of the gradient method. Non-monotonic concentration profiles were also omitted from the calculations.

Precision of flux measurements was estimated by calculating "virtual ammonia flux" from concentration data measured at the same height. Virtual ammonia flux was calculated with the same method as real flux, supposing that the inlets are at 0.5, 1.2, and 2.4 m heights, however, they were at the same height. Average of the calculated virtual flux values should be zero, and standard deviation of the virtual ammonia flux gives the precision of flux measurements (*Pogány et al.,* 2010).

3. Results and discussion

3.1. Meteorological conditions

The weather during the campaign was cold with daily temperature maxima of 10–15 °C and minima around 0 °C. Relative humidity was high during the whole week, fog and dew formed during nighttime and one rain event occurred during the campaign, on October 22 (8.6 mm). Main micrometeorological parameters are shown in *Fig. 2*.

3.2. Instrument intercomparison

Fig. 3a shows the concentration readings of the three channels of the photoacoustic instrument for a one-day period, during which the inlets were placed at the same height. Difference of concentrations measured by the individual channels from the average concentration is depicted in *Fig. 3b*. Remarkably good agreement was found between the readings of the three channels.

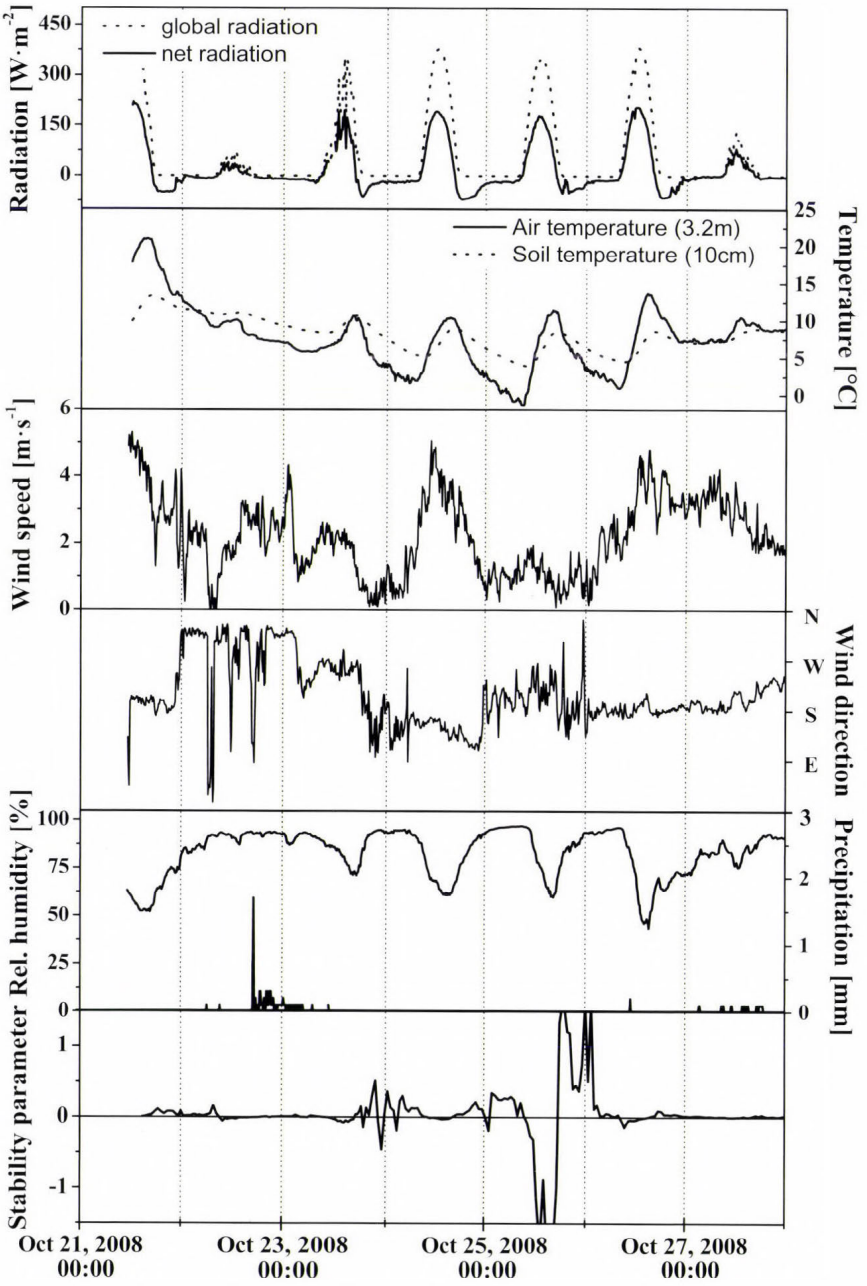

Fig. 2. Main meteorological parameters measured during the campaign (Note: ζ is calculated for 2.4 m height).

Average of the calculated virtual fluxes was found to be practically zero, i.e., smaller than the scatter of virtual flux, indicating that there is no systematic difference between the concentration readings of the three channels. Precision of flux measurements was found to be 15 $ng\,m^{-2}\,s^{-1}$, which is similar to the value determined during a similar flux measurement campaign with the same instrument (*Pogány et al.,* 2010). This value ensures precision better than 15% over fertilized agricultural fields, where typical ammonia fluxes range from 100 to several thousand $ng\,m^{-2}\,s^{-1}$.

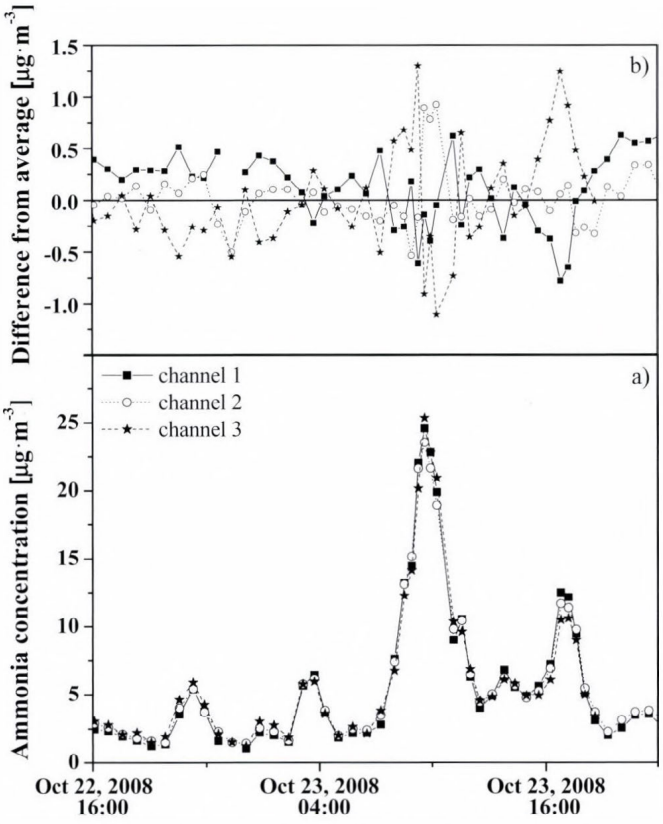

Fig. 3. Ammonia concentration measured at the same height by three channels of the photoacoustic instrument and deviation of the concentration reading of each channel from the average value.

Fig. 4 shows concentration data measured by the photoacoustic instrument and the AMANDA during the period when both instruments were operating at site 1. Closed symbols with solid line represent the average of the concentration readings of the three channels of the photoacoustic instrument, open symbols with dotted line represent concentration data measured by the AMANDA

averaged for the sampling periods of the photoacoustic instrument. The figure shows overall good agreement between the readings of the two instruments.

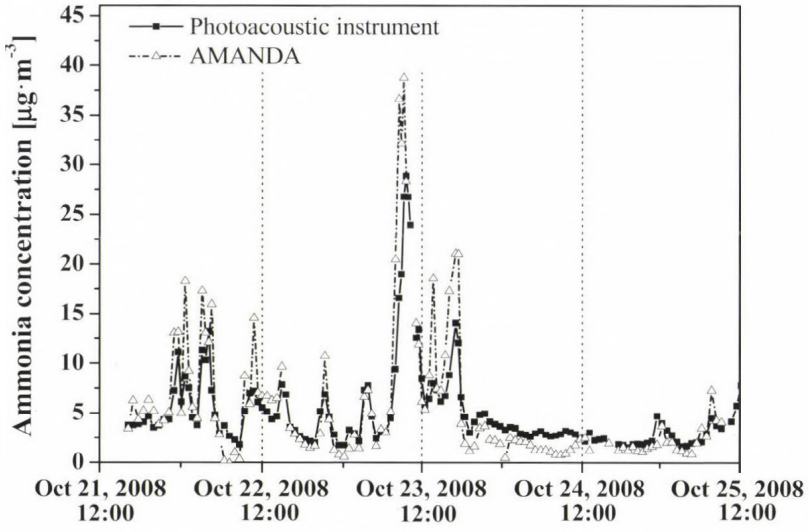

Fig. 4. Ammonia concentration measured by the photoacoustic instrument (closed squares and solid line) and by the AMANDA (open triangles and dotted line) at site 1 between October 21 and 25, 2008.

3.3. Plume detection

Fig. 5a shows ammonia concentration data measured by the photoacoustic instrument at site 1 and the AMANDA at site 2. *Fig. 5b* and *Fig. 5c* show wind direction and wind speed for the same period. During the first two days of the measurement, wind was not favorable for plume detection: on October 25, wind speed was very low, and afterwards southerly winds occurred, which caused the ammonia plume to form north of the farm, not in the direction of the instruments. During this period, only a few minor concentration peaks were observed indicating that the ammonia plume reached the AMANDA for a few short periods. Around midday on the October 27, wind direction changed to southwest and west, and differences in the measured concentration data clearly show the periods when only the AMANDA (October 27-28, southwesterly wind) or both instruments (in the morning October 28, westerly winds) were within the ammonia plume of the farm. Difference in the measured concentrations in case of westerly winds can be explained by the different distances of the two instruments from the farm.

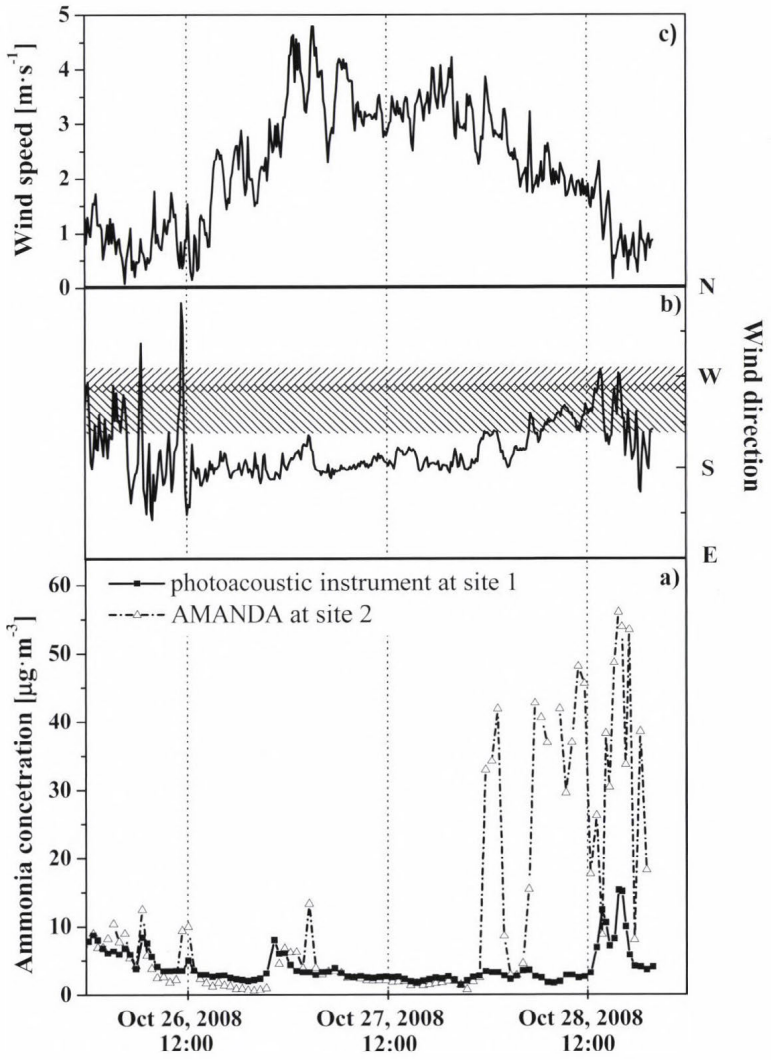

Fig 5. Ammonia concentration measured by the photoacoustic instrument at site 1 and by the AMANDA at site 2, together with wind direction and wind speed data. Shading indicates wind directions when the photoacoustic instrument (slope to the right) or the AMANDA (slope to the left) was within the ammonia plume of the cattle farm.

3.4. Flux measurements

Fig. 6 shows ammonia concentration data measured by the three channels of the photoacoustic instrument when the inlets were placed at three different heights.

Vertical gradient of ammonia shows very clear diurnal variation: differences between concentrations measured at the different heights were larger at night, and decreased to almost zero around midday both on the October 25 and 26, due to increased turbulence.

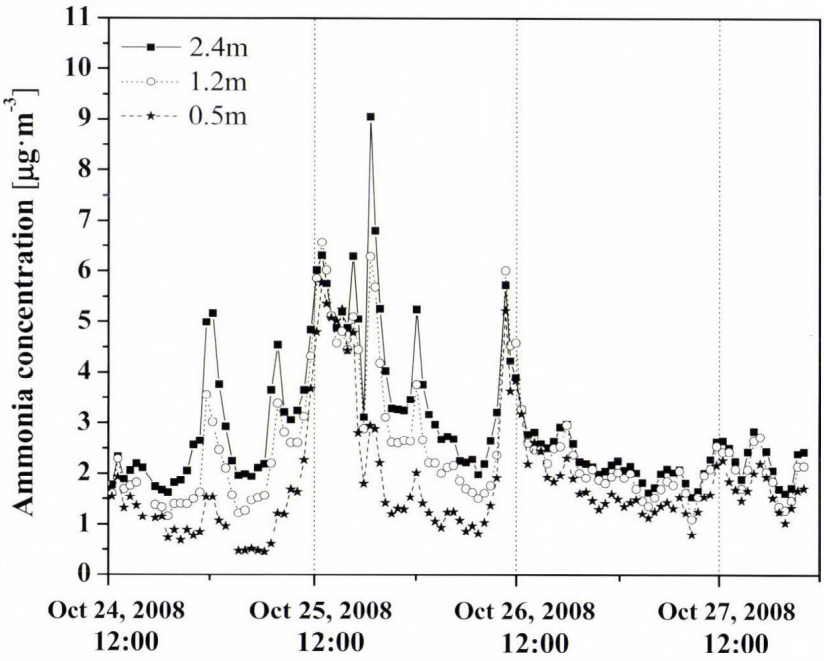

Fig. 6. Ammonia concentration measured by three channels of the photoacoustic instrument at 0.5, 1.2, and 2.4 m heights.

Fig. 7 shows the ammonia flux calculated from the concentration data depicted in *Fig. 6*. Altogether, 116 concentration gradient measurements were done with the sampling inlets placed at three different heights. 25 of these data were filtered out due to extreme stability conditions ($|\zeta|>1.5$, as it is shown in *Fig. 2*) or low wind speed on the October 25, while non-monotonic concentration profiles were the reason for omission in only 8 cases. Differences between fluxes calculated for the different sub-layers were in the 0–30 ng m^{-2} s^{-1} range.

The observed fluxes were negative in the range of 0 to -90 ng m^{-2} s^{-1} indicating ammonia deposition. Deposition of ammonia can be explained by elevated ammonia concentration caused by the farm, which exceeded the ammonia compensation point above the wheat field (*Asman,* 1998; *Fowler et al.,* 1998).

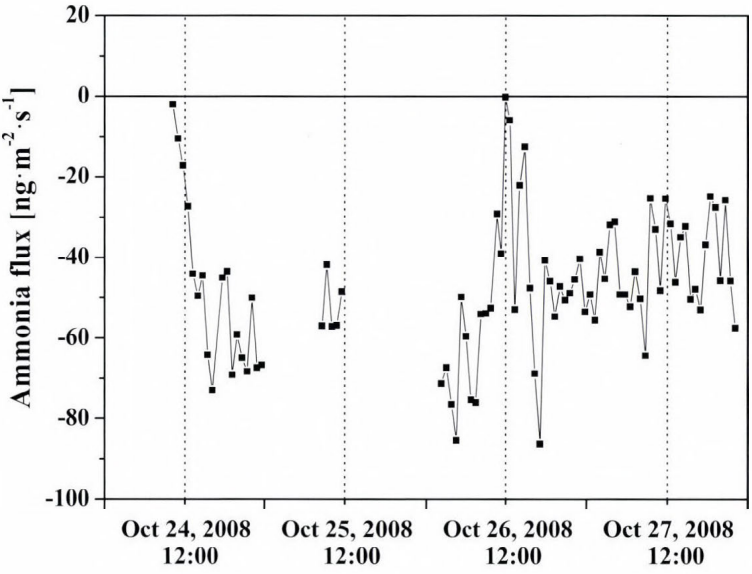

Fig. 7. Ammonia flux calculated from the concentration data shown in *Fig. 6.*

4. Conclusions

Results of the presented measurement campaign prove the applicability of our recently developed ammonia monitoring instrument in concentration and flux measurements over agricultural landscape. During the whole campaign, the photoacoustic instrument operated fully automatically and trouble-free, it required no maintenance, in contrast to the AMANDA instrument that requires frequent calibration and supply of chemicals. This fact proves that the photoacoustic instrument has the necessary robustness and it is easy to operate even under field conditions, therefore, fulfills technical requirements of environmental monitoring. Precision and time resolution of the instrument is proved to be suitable for field applications as well.

As far as the environmental impact of the studied emission source is concerned, measured data were found to agree with results of similar experiments. Concentration as well as deposition flux measured at 130 m distance from the farm was found to be slightly higher than the background value, similarly to results of an experiment around a poultry farm reported by *Fowler et al.* (1998).

Acknowledgements—We thank the Hungarian National Office for Research and Technology (NKFP3-00021/2005, and TUDAS-1-2006-0037), the OTKA foundation (Research and Technology

Innovation Fund, project number: CNK 78549), the European Social Fund (TÁMOP 4.2.1./B-09/1/KMR-2010-0003), COST action ES0804, NiNE Short Visit Grant No. 2417, and the NitroEurope EU 6th Framework Program "Energy, Environment and Sustainable Development, Global Change, Climate and Biodiversity; The nitrogen cycle and its influence on the European greenhouse gas balance NITROEUROPE IP" (2006–2011, Contract 017841) for financial support.
We thank *Mark Sutton* for initiating Hungarian-Polish scientific collaboration within the NitroEurope program, *Krzysztof Janku* for his help in organizing the campaign and setting up the instruments, and *Zoltán Istenes* for his help in designing the data acquisition system.

References

Asman, W.A.H., 1998: Factors influencing local dry deposition of gases with special reference to ammonia. *Atmos. Environ. 32*, 415–421.

von Bobrutzki, K., Braban, C.F., Famulari, D., Jones, S.K., Blackall, T., Smith, T.E.L., Blom, M., Coe, H., Gallagher, M., Ghalaieny, M., McGillen, M.R., Percival, C.J., Whitehead, J.D., Ellis, R., Murphy, J., Mohácsi, A., Pogány, A., Junninen, H., Rantanen, S., Sutton, M.A. and *Nemitz, E.*, 2010: Field inter-comparison of eleven atmospheric ammonia measurement techniques. *Atmos. Meas. Tech. 3*, 91–112.

Bozóki, Z., Pogány, A. and *Szabó, G.*, 2011: Photoacoustic instruments for practical applications: present, potentials and future challenges. *Appl. Spectrosc. Rev. 46*, 1–37.

Dyer, A. J., 1974: A review of flux-profile relationships. *Bound-Lay. Meteorol. 7*, 363–372.

Erisman, J.W., Hensen, A., Fowler, D., Flechard, C., Grüner, A., Spindler, G., Duyzer, J., Westsrate, H., Römer, F., Vonk, A. and *Jaarsveld, H.*, 2001a: Dry deposition monitoring in Europe. *Water Air Soil Poll. Focus 1*, 17–27.

Erisman, J.W., Otjes, R., Hensen, A., Jongejan, P., van den Bulk, P., Khlystov, A., Möls, H. and *Slanina, S.*, 2001b: Instrument development and application in studies and monitoring of ambient ammonia. *Atmos. Environ. 35*, 1913–1922.

Erisman, J.W., Grennfelt, P. and Sutton, M., 2003: The European perspective on nitrogen emission and deposition. Environ. Int.29, 311–325.

Faulkner, W.B., Powell, J.J., Lange, J.M., Shaw, B.W., Lacey, R.E. and *Parnell, C.B.*, 2007: Comparison of Dispersion Models for Ammonia Emissions from a Ground-Level Area Source. *Trans. ASABE. 50*, 2189–2197.

Foken, T., 2008: *Micrometeorology*. Springer Verlag ISBN 978-3-540 74666-9 308 pp.

Flechard, C.R., Fowler, D., Sutton, M.A. and *Cape, J.N.*, 1999: A dynamic chemical model of bi-directional ammonia exchange between semi-natural vegetation and the atmosphere. *Q. J. Roy. Meteorol. Soc. 125*, 2611–2641.

Fowler, D., Pitcairn, C.E.R., Sutton, M.A., Flechard, C., Loubet, B., Coyle, M. and *Munro, R.C.*, 1998: The mass budget of atmospheric ammonia in woodland within 1 km of livestock buildings. *Environ. Poll. 102 (S1)*, 343–348.

Fowler, D., Sutton, M.A., Flechard, C.R., Cape, J.N., Storeton-West, R., Coyle, M. and *Smith, R.I.*, 2001: The control of SO_2 dry deposition on to natural surfaces and its effects on regional deposition. *Water Air Soil Poll. Focus 1*, 39–48.

Galloway, J., Cowling, E., Erisman, J.W., Wisniewsky, J. and *Jordan, C.*, 2002: *Optimizing nitrogen management in food and energy production and environmental protection: contributed papers from the 2nd International Nitrogen Conference*, 14-18 October 2001, Potomac, Maryland, *USA*, Taylor & Francis, ISBN 90 265 1927 3, 1013 pp.

Huszár, H., Pogány, A., Bozóki, Z., Mohácsi, Á., Horváth, L. and *Szabó, G.*, 2008: Ammonia monitoring at ppb level using photoacoustic spectroscopy for environmental application. *Sensor. Actuator. B 134*, 1027–1033.

Loubet, B., Génermont, S., Ferrara, R., Bedos, C., Decuq, C., Personne, E., Fanucci, O., Durand, B., Rana, G. and *Cellier, P.*, 2010: An inverse model to estimate ammonia emissions from fields. *Eur. J. Soil Sci. Special Issue: Nitrogen and greenhouse gas exchange 61*, 793–805.

Milford, C., Theobald, M. R., Nemitz, E. and *Sutton, M. A.*, 2001: Dynamics of ammonia exchange in

response to cutting and fertilizing in an intensively-managed grassland. *Water Air Soil Poll. Focus 1,* 167–176.

Milford, C., Theobald, M.R., Nemitz, E. , Hargreaves, K.J., Horvath, L., Rásó, J., Dämmgen, U., Neftel, A., Jones, S.K., Hensen, A., Loubet, B., Cellier, P. and *Sutton, M.A.,* 2009: Ammonia fluxes in relation to cutting and fertilization of an intensively managed grassland derived from an inter-comparison of gradient measurements. *Biogeosciences 6,* 819–834.

Pogány, A., Mohácsi, Á., Varga, A., Bozóki, Z., Galbács, Z., Horváth, L. and *Szabó, G.,* 2009: A compact ammonia detector with sub-ppb accuracy using near-infrared photoacoustic spectroscopy and preconcentration sampling. *Environ. Sci. Tech. 43*, 826–830.

Pogány, A., Mohácsi, Á., Jones, S. K., Nemitz, E., Varga, A., Bozóki, Z., Galbács, Z., Weidinger, T., Horváth, L. and *Szabó, G.,* 2010: Evaluation of a diode laser based photoacoustic instrument combined with preconcentration sampling for measuring surface-atmosphere exchange of ammonia with the aerodynamic gradient method. *Atmos. Environ. 44,* 1490–1496.

Spirig, C., Flechard, C. R., Ammann, C. and *Neftel, A.,* 2009: The annual ammonia budget of fertilized cut grassland – Part 1: Micrometeorological flux measurements and emissions after slurry application. *Biogeosci. Discuss. 6,* 9583–9625.

Staebler, R.M., McGinn, S.M., Crenna, B.P., Flesch, T.K., Hayden, K.L. and *Li, S.-M.,* 2009: Three-dimensional characterization of the ammonia plume from a beef cattle feedlot. *Atmos. Environ. 43,* 6091–6099.

Sutton, M.A., Erisman, J.W, Dentener, F. and *Möller, D.,* 2009a: Ammonia in the environment: From ancient times to the present. *Environ. Poll. 156,* 583–604.

Sutton M.A., Reis, S. and *Baker, S.M.H.,* 2009b*: Atmospheric ammonia. Detecting emission changes and environmental impacts.* Springer Science, ISBN 978-1-40-20-9120-9. 461 pp.

Thornthwaite, C.W. and *Holzman, B.,* 1939: The determination of evaporation from land and water surfaces. *Month. Weather Rev. 67,* 4–11.

Weidinger, T., Pinto, J. and *Horváth, L.,* 2000: Effects of uncertainties in universal functions, roughness length, and displacement height on the calculation of surface layer fluxes. *Meteorol. Z. 9,* 139–154.

Wyers, G.P., Otjes, R.P. and *Slanina, J.,* 1993: A continuous flow denuder for the measurement of ambient concentration and surface-exchange fluxes of ammonia. *Atmos. Environ. 27A,* 2085–2090.

IDŐJÁRÁS

Quarterly Journal of the Hungarian Meteorological Service
Vol. 116, No. 2, April–June 2012, pp. 109-122

Microclimate simulation of climate change impacts in a maize canopy

Tímea Kocsis* and **Angéla Anda**

Department of Meteorology and Water Management,
University of Pannonia Georgikon Faculty,
P.O. Box 71, Keszthely H-8361, Hungary

Corresponding author; E-mail: timea.kocsis@gmail.com

(Manuscript received in final form January 5, 2012)

Abstract—Effects of possible climate modification on maize plant features have been evaluated by using the simulation model of *Goudriaan* for local climatic conditions and locally measured plant characteristics. Moderate climate modifications were hypothesized. According to the purpose of detecting local impacts of climate change, researches were made on the microclimate of maize canopies. In the energy transport of the plant stand, no shift has been experienced to the direction of the latent heat as it was expected because of the effect of warming up and decrease of precipitation. The changes of stomatal resistance and inside canopy air temperature suggested that the natural water supply will probably not cover the water demand of the plant, if the climate change is more intensive, therefore farmers must prepare to irrigated cultivation and to apply different agro-technical methods to save the water supplies of the ground.

Key-words: climate change, microclimate simulation model, maize, Keszthely, Hungary

1. Introduction

Climate change and variability may have an impact on the occurrence of food security hazards at various stages of the food chain, from primary production through to consumption (*Tirado et al.,* 2010). Worldwide agriculture has to face major changes in land use in the coming decades, and agriculture needs to meet rising claim with less resource while satisfying quality and environmental demands (*Stein* and *Goudriaan,* 2000). Agriculture is one of the fields that are highly affected by climate change also in Hungary (*Jolánkai,* 2010), therefore, researches in this field and developing adaptation strategies are very important. Prognostics of the impacts of climatic changes for the Carpathian Basin

(Hungary) in air temperature and precipitation in the range of 0.5–4°C global change were described by *Mika* (2002). The main statement of the scenarios is that the local weather would get warmer (1–5°C) and drier ((–40) – (–66) mm) in the first some decades of the global warming (*Mika,* 2002). *Bartholy et al.* (2004) estimated the regional effects of climate change at Lake Balaton – Sió Canal catchment area (where the experimental site of the researches is situated) by a stochastic-dynamic downscaling model using the ECHAM/GCM outputs. *Bartholy et al.* (2004) predict a decrease of 25–35% of precipitation amount in the summer half-year and 0–10% decline in the winter half-year at a climate corresponding to double CO_2 level. These statements were enhanced by *Bartholy et al.* (2008), *Szépszó* and *Horányi* (2008), and by the *Hungarian Meteorological Service* (2010) according to further regional climate model simulations.

Crop simulation models are often used to predict the impact of global atmospheric changes on food production (*Ewert et al.,* 2002). Plant canopies' role and their capability of modifying local microclimate has come into focus in the issue of adaptations to climate change. *Easterling et al.* (1997) provided an approximation of the potential for strategically positioned shelterbelt systems to reduce climate change-related stress on maize in the USA. *Guilioni et al.* (2000) examined the influence of temperature on plant's development rates and worked out a model that uses meteorological data to estimate the temperature of a maize apex. *Goudriaan* and *Zadoks* (1995) analyzed the combined effects of pests and diseases under changing climate by using modeling tools, because climatic change not only affects the potential yield levels, but it may also modify the effects of pests and diseases.

Fodor and *Pásztor* (2010) used the 4M crop simulation model to quantify some indices of the agro-ecological potential of Hungary and its future development under climate change. Their results indicate that the Hungarian agriculture cannot avoid the effects of climate change, and these effects will be mostly negative. The yields of the spring crop as maize, sunflower, etc. will decrease, while higher yields might be expected for the autumn crops. *Gaál* (2007) analyzed the modification of the climatic conditions of maize production in Hungary using HadCM3 and B2 SRES scenario for the periods of 2011–2020 and 2031–2040. The results concluded that with higher temperature, maize hybrids of 2–3 FAO group of longer vegetation period could be cultivated, but the limiting factor will be the precipitation.

Dióssy and *Anda* (2008) focused the attention on the impacts of drastic climate change on the energy consumers of maize canopy in Hungary. The energy distribution for sensible and latent heat fluxes of the applied scenarios were not significantly modified (*Dióssy* and *Anda*, 2009; *Anda* and *Dióssy,* 2010). *Dióssy* (2008) reports the effect of global warming on the inside air temperature of maize canopies. According to the degree of warming up, the air temperature in the canopy increased.

At the Agrometeorological Research Station of Keszthely, observations of the microclimate have been made for several decades. As field experiments are time consuming and expensive, another method is the use of crop growing models that can quantify the effects of management practices and environmental circumstances on crop growth and productivity (*Knörzer et al.,* 2011). At Keszthely for more than one decade, information was gained by using simulation model about crop microclimate that could rarely be registered earlier. Numerical models are often used to simulate the complex energy and mass transfer processes in soil-plant-atmosphere system (*Sauer* and *Norman*, 1995). In this study, the Crop Micrometeorological Simulation Model (CMSM) constructed by *Goudriaan* (1977) was applied. Using the earlier data of Keszthely station, and the downscaled information for the country and the watershed area of Lake Balaton, the aim was to simulate the impacts of some expected climatic conditions on the microclimate and the physiological processes of the maize stand.

2. Material and methods

2.1. The selected site and origin of input data

The inputs, both meteorological and plant features used in the simulations were collected at Keszthely Agrometeorological Research Station (46°44'N, 17°14' E, 114.2 m). The required above-canopy meteorological parameters are daily runs of air temperature, air humidity, wind speed, net radiation and/or incoming global radiation (*Stigter et al.,* 1977). Meteorological data were measured by a QLC-50 automatic climate station by 10 sec sampling time that was established in 1996. Hourly meteorological data were formed for the requirements of the model. Our sample day was an average day in July, when the plants were fully developed. The reference level of the model inputs was taken into account by calculated aerodynamic depths for every stage of plant development (*Goudriaan,* 1977). The roughness length and zero-plane displacement for maize was adapted from *Monteith* (1973). Wind speed was estimated at a reference level using combination of friction velocity and the logarithmic wind speed profile above the canopy (*Goudriaan,* 1977). In case of the wind speed, measurements were made at 10 meters above the ground.

Test plant, the mid-season maize hybrid Norma (FAO 450) has been sown and cultivated since the 1970s at a plant density of 7 plants m^{-2} on plots of 0.7 ha. The inputs of the model were site and plant specific parameters (plant height, leaf density in three layers), different soil characteristics (soil moisture content and physical properties), and hourly meteorological data from local measurements which were transformed from the standard observation level of 2 m above soil surface to the reference level required by the model (*Anda* and *Kocsis,* 2008). The height of reference level depends on actual plant development.

In the past 40 growing seasons, the leaf area and its density were measured in the field on the same 10 sample plants weekly, using an LI-3000A portable planimeter. The soil moisture content in the upper 1 m was also measured in the field gravimetrically every 10 days at 10 cm intervals. The actual soil water content was expressed in terms of soil water potential. The physical properties of the local Ramann type brown forest soil were determined at the beginning of the investigations.

2.2. The applied Crop Micrometeorological Simulation Model (CMSM)

Goudriaan's (1977) simulation model and its improved version (*Goudriaan* and *Van Laar,* 1994) follow the division of the radiation inside the canopy and its utilization in different energy-intensive processes (*Anda* and *Lőke,* 2003). The theoretical background of the Crop Micrometeorological Simulation Model (CMSM) is the physics of the energy-transfer and transport processes. CMSM is based on the traditions of model-developing work of Wageningen group (*Van Ittersum et al.,* 2003).

The productivity of crops is directly related to their capture of resources (water, light) and the efficiency with which they convert these physical resources into biological materials (*Yi et al.,* 2010). One part of the radiation energy that reaches the plants reflects, the second part penetrates into the stock, and the third part is fixed by the plant stand (*Jones,* 1983; *Anda* and *Lőke,* 2003). As the vertical structure of the plant stand is not homogeneous, the height of the plant is usually divided into different number of layers, the characteristics of which can be regarded as more or less homogeneous (multi-layer model). The resistances between air layers in the canopy are not neglected, and gradients in air properties inside the canopy are also taken into account (*Goudriaan,* 1989). The number of the layers can be influenced by the characteristics of the canopy, the aim, and the element to be examined (*Goudriaan,* 1977; *Anda et al.,* 2002). CMSM is a static model according to the air conditions and dynamic for the soil and plant data (*Hunkár,* 1990; *Páll et al.,* 1998; *Hunkár,* 2002). Exchange processes at the soil surface are important from a modeling perspective in that the soil surface is the interface between the soil and atmospheric systems (*Sauer* and *Norman,* 1995).

Within the parameters calculated by the model, sensible and latent heat fluxes, air temperature inside the canopy, plant temperature, stomatal resistance, and intensity of the photosynthesis were involved into our simulation examinations. The sensible and latent heat fluxues were described as *Bowen ratio* (β) that is the proportion of the sensible and latent heat fluxes. These parameters were presented on the border of the upper third of plant height in the study. This is the place of cob formation, where the intensity of physiological processes is the highest.

Model results were analyzed by *paired t-test* using *STATA 5.0* (1996) statistical program package in order to prove the significant deviations.

Scenarios were set up to simulate the effects of climate change on the maize stand. Carbon-dioxide concentration was raised of the intercellular spaces in accordance with the changes of the carbon-dioxide concentration of the atmosphere on the basis of the data of the literature (*Jackson et al.,* 1994).

In each layer there are energy sources and sinks. The intensity and direction of the source and loss of the different forms of energy must be determined. On the basis of detailed calculations, the model creates profiles for the meteorological elements inside the canopy.

The theory of the CMSM is the calculation of the radiation distribution among different environmental processes. The sensible heat flux (H_i) [J m^{-2}] in the *i*th layer is (*Goudriaan* and *Van Laar,* 1994):

$$H_i = \frac{(T_{L,i} - T_{a,i})\rho c_p}{r_{H,i}}, \tag{1}$$

where
ρc_p is the volumetric heat capacity of the air [J m^{-3} K^{-1}],
$T_{L,i}$ is the temperature of the plant [°C],
$T_{a,i}$ is the air temperature [°C], and
$r_{H,i}$ is the resistance against heat transmission [s m^{-1}].

The latent heat flux (λE_i) [J m^{-2}] in the *i*th layer can be calculated as follows (*Goudriaan* and *Van Laar,* 1994):

$$\lambda E_i = \frac{(e_{s,T_{L,i}} - e_{a,i})\rho c_p}{r_{V,i}\gamma}, \tag{2}$$

where
γ is the psychometric constant [mbar K^{-1}]
$e_{s,T_{L,i}}$ is the saturation water vapor pressure at actual plant temperature [mbar]
$e_{a,i}$ is the vapor pressure of the air [mbar]
$r_{V,i}$ is the resistance against the entrance of moisture into the layer [s m^{-1}].

Basis of the assumption of leaf resistance simulation is that mass transport processes – both water vapor and carbon-dioxide – occur via stomata, so that the ratio between their resistances is equal to the ratio between their diffusivities. In case of maize a linear relationship exists between net CO_2 assimilation and inverse leaf resistance at constant CO_2 concentration of substomatal cavity. This connection served to simulate the leaf resistance, since net CO_2 assimilation can be deducted precisely from the absorbed short wave radiation (*Goudriaan,* 1977). Exceeding the saturation point of CO_2 assimilation (200 J m^{-2} s^{-1} for sunny maize leaves), the leaf resistance approaches its minimum value (*Stigter*

et al., 1977). Rate of net CO_2 assimilation (F_n) [kg CO_2 m^{-2} s^{-1}] was found by an empirical representation of measured curves (*Van Laar* and *Penning de Vries,* 1972, *Goudriaan,* 1977):

$$F_n = (F_m - F_d)[1 - exp(-R_v \varepsilon / F_m)] + F_d, \quad (3)$$

where

F_m is the maximum rate of net CO_2 assimilation [kg CO_2 m^{-2} s^{-1}],
F_d is the net CO_2 assimilation in the dark respiration [kg CO_2 m^{-2} s^{-1}],
R_v is the absorbed visible radiation (per leaf area) [J m^{-2} s^{-1}], and
ε is the slope of the curve of F_n–R_v at low light intensities [kg CO_2 J^{-1}], or efficiency ($17.2 \cdot 10^{-9}$ kg CO_2 J^{-1} light in maize).

At calculation of F_m the influence of leaf age and ambient CO_2 concentration were simplified and their average values were applied. Dependence of leaf temperature was considered as a dependence on ambient air temperature. Dark respiration was at about –0.1 of F_m (*Goudriaan*, 1977). From the net CO_2 assimilation calculated by Eq. (3) the leaf resistance is calculated with:

$$F_n = \frac{1.83 \cdot 10^{-6}(C_e - C_r)}{1.66 r_{leaf} + 1.32 r_H}, \quad (4)$$

where

r_H is resistance against heat transmission [s m^{-1}],
1.66 is the ratio between diffusivities (for CO_2 and H_2O),
$1.83 \cdot 10^{-6}$ converts CO_2 concentration into kg CO_2 m^{-3} from ppmv at 20°C,
C_e is the external CO_2 concentration [ppmv],
C_r is assumed as 'regulatory' CO_2 concentration [ppmv], and
1.32 originates from calculation of boundary layer resistance for CO_2,

or

$$r_{leaf} = \frac{1.83 \cdot 10^{-6}(C_e - C_r)}{1.66 F_n} - 0.783\, r_H \quad [\text{s m}^{-1}], \quad (5)$$

where 0.783 is an empirical constant given in *Goudriaan* (1977).

After calculation of the sensible and latent heat, the estimation of the crop temperature in the *i*th layer ($T_{L,i}$) [°C] was as follows (*Goudriaan,* 1977):

$$T_{L,i} = T_{a,i} + (H_i - H_{i-1}) \frac{r_{H,i}}{\rho c_p}, \quad (6)$$

where

ρc_p is the volumetric heat capacity of the air [J m^{-3} K^{-1}],
$T_{a,I}$ is the air temperature [°C], and
$r_{H,I}$ is the resistance against heat transmission [s m^{-1}].

There is an analogy in calculation of canopy inside air temperature and crop temperature. When i=1, $T_{a,i-1}$ is the temperature from the reference level. The zero level (if i=1, i–1 is the level zero) is the place of the reference height.

Validation of the model outputs (crop temperature, leaf resistance, some elements of microclimate, photosynthesis) were carried out locally (*Anda* and *Lőke,* 2002, 2005; *Lőke*, 2004, *Anda et al.*, 1997) using RMSD (*Willmott,* 1982) and the model does not need further adaptation.

2.3. The applied scenarios

For the reason of climate change impact simulation in case of maize, scenarios that represent moderate climatic variations (compared to the model runs carried out by *Dióssy* and *Anda,* 2008) for Hungary were established. By most of the publications regarding local climate modifications, precipitation decrease is to be continued in the future. 25–35% decrease is expected in case of modelling doubled CO_2 concentration together with air temperature increase (1.3–2°C in summer) for Lake Balaton – Sió Canal catchment area, on the western part of Hungary, where Keszthely is situated (*Bartholy et al.,* 2004). The inputs of plant architecture, the size of the assimilatory surface and its density were chosen from the local measurements of the past four decades by using the principle of analogy. Plant data (LAI) of those seasons were used, when the air temperature and soil water content were similar in July as in the scenarios, respectively. In Scenario 1, continuous linear changes were supposed to be on the basis of the meteorological data of July between 1977 and 2006 at Keszthely. CO_2 concentration rise that should be pared to 0.6 °C temperature rise was 440 ppmv (*Mika,* 2007). In Scenarios 2 and 3, the atmospheric CO_2 concentration was increased to 760 ppmv (*Table 1*) with higher rise of the air temperature and decrease of the soil moisture.

Table 1. The applied scenarios

Scenario	Air temperature	Soil moisture	CO_2	LAI
Control	average in July	average soil moisture	380 ppmv	3.0
Scenario 1	+ 0.6 °C	– 10%	440 ppmv	2.8
Scenario 2	+ 1.3 °C	– 25%	760 ppmv	2.3
Scenario 3	+ 2.0 °C	– 35%	760 ppmv	2.0

3. Results

The incoming radiation, that is absorbed in a given crop layer after reflecting from the canopy or proceeding towards the soil, becomes the energy source of the heating processes (sensible heat flux), and evapotranspiration (latent energy flux). If there is no water restriction, evapotranspiration is the main energy consumer of the plant stand. The diurnal mean *Bowen ratio* is shown in *Fig. 1*, and the statistical analysis showed that significant deviation cannot be observed from the control run in any of the scenarios (*Table 2*).

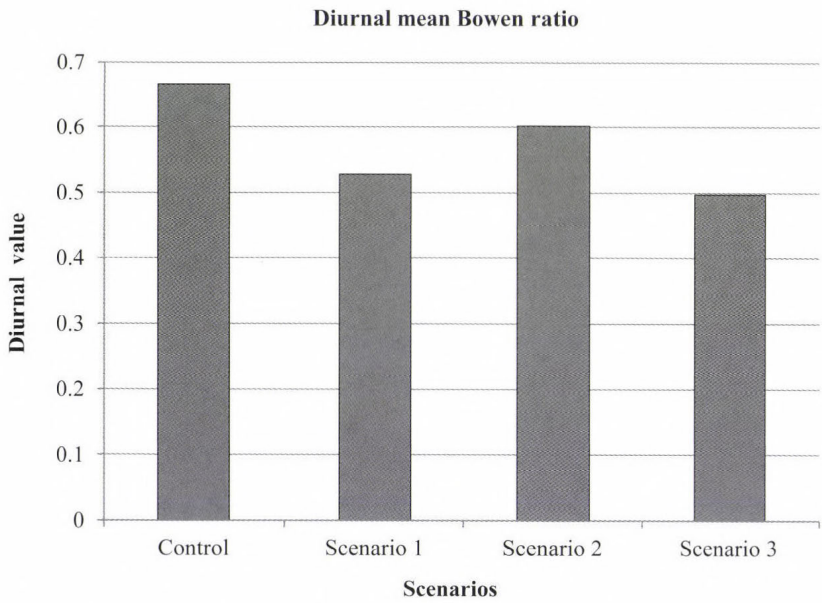

Fig. 1. Diurnal mean Bowen ratio.

Table 2. Results of the statistical analysis in case of the Bowen ratio

	Paired t-test	
	Mean (1–24 hours)	**p value**
Control	0.66	–
Scenario 1	0.53	0.21
Scenario 2	0.60	0.65
Scenario 3	0.50	0.13

The intensity of the photosynthesis and transpiration are influenced by the concentration of CO_2 because of its effect on the stomatal resistance. In order to get a higher yield, the plant must reach a balance between the as high as possible CO_2 amount that is needed for the photosynthesis, and gets into the leaves through the openings of the stomata, and the level of the amount of water that leaves the foliage which must be as low as possible in our climate. The two opposing processes are connected by the pores.

The stomatas can be regarded as closed when the stomatal resistance surpasses 2000 s m^{-1}. The stomatal resistance of the maize surpassed this value at night (between 8 pm and 7 am). On a daily average (between 8 am and 7 pm) the resistance rose by 16.76%, 61.55% and 69.1% in Scenarious 1, 2, and 3, respectively comparing them to the control run (*Fig. 2*). On the basis of statistical examinations, these deviations indicate significant changes.

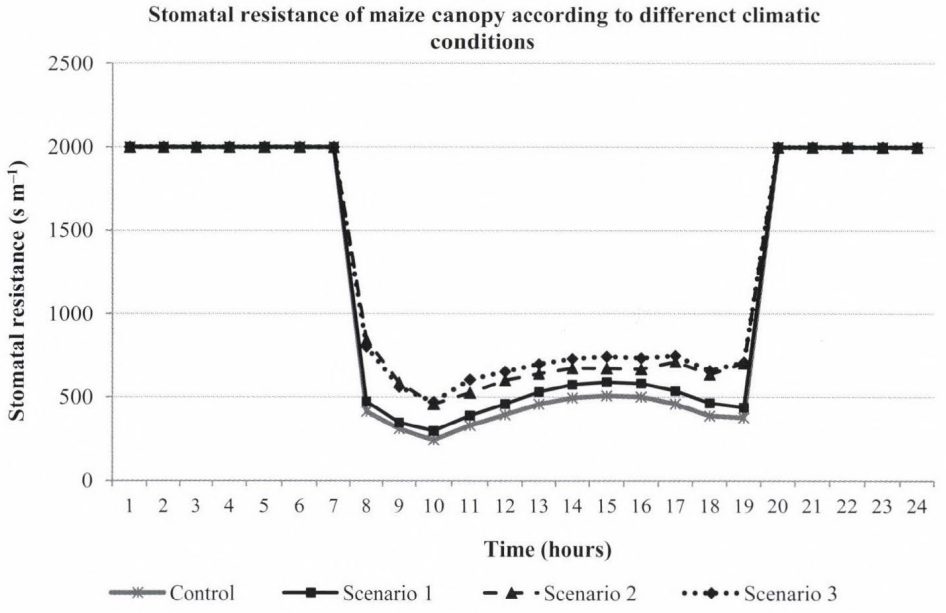

Fig. 2. Stomatal resistance of maize canopy according to different climatic conditions.

In the course of the production of organic matter, the process of photosynthesis uses carbon-dioxide from the surrounding air and water from the soil. The final benefit of the process is the difference between the amount of the organic matter created in the process of assimilation and used amount of

assimilates in the course of respiration (mainly at night). The intensity of the respiration (between 8 pm and 6 am) did not seem to be sensitive to climate change. The intensity of the photosynthesis, in the average of the values of day time, slightly decreased in the 1st and 3rd scenarios (*Table 3*), which indicates that the available carbon-dioxide (440 ppmv and 760 ppmv) could not compensate the reduction of precipitation (that was represented by ground water potential decrease in the model runs) and although the water consumption became more economical because of the narrowed stomatas, the amount of carbon-dioxide that got into the foliage was also restricted. In the 2nd scenario the 760 ppmv carbon-dioxide concentration could compensate the effects of the restriction of water supply and the intensity of photosynthesis increased. While in the 1st and 2nd scenarios the change of the intensity of photosynthesis indicates a significant deviation comparing to the control, the 3rd scenario does not show a significant modification (*Table 4*).

Table 3. Deviations between the control run and the scenarios for photosynthetic intensity

	Mean deviation from the control run in daytime hours (8–19 hours)
Scenario 1.	–2.99%
Scenario 2.	4.48%
Scenario 3.	–7.31%

Table 4. Results of the statistical analysis in case of the photosynthetic intensity

	Paired t-test	
	Mean (1–24 hours)	**p value**
Control	5.55E–07	–
Scenario 1.	5.36E–07	0.0174*
Scenario 2.	5.98E–07	0.0093*
Scenario 3.	5.26E–07	0.1954

*Significant difference if p is lower than 0.05.

In the Scenarious 2 and 3, the 24-hour average value of the inside canopy air temperature surpassed the additional air temperature rise while the average rise in the Scenario 1 was lower than the input temperature rise. The results of the plant temperature showed a higher rise in all scenarios than the rise of the ambient air temperature. In case of the average values of the daytime rise, the average growth in the cob level canopy temperature of all the three scenarios is

lower than the added temperature rise. The reason for this phenomena can be the self-shade of plants by day, and the leaves gave a special protection against sunshine, therefore, the inside canopy air temperature was more moderate than the temperature rise around it. In the case of the plant temperature, the average rise is almost the same or a little lower than the input temperature rise. The plant could keep its own temperature close to the temperature of the air surrounding it. Despite the decrease of the water supply and warming, the plant did not seem to suffer of heat-stress. The changes in all scenarios (regarding both temperature characteristics) show significant deviations (*Table 5* and *6*).

Table 5. Results of the statistical analysis in case of the inside canopy air temperature

	Paired t-test	
	Mean (1–24 hours)	**p value**
Control	21.56	–
Scenario 1	22.05	1.72E-03*
Scenario 2	23.14	3.28E-07*
Scenario 3	23.63	1.44E-08*

*Significant difference if p is lower than 0.05.

Table 6. Results of the statistical analysis in case of the crop temperature

	Paired t-test	
	Mean (1–24 hours)	**p value**
Control	20.75	–
Scenario 1	21.49	4.41E-07*
Scenario 2	22.65	2.68E-08*
Scenario 3	23.21	5.31E-10*

*Significant difference if p is lower than 0.05.

From the changes of the stomatal resistance and temperature of the air inside the canopy, it can be concluded that the natural water supply will not cover the water demand of the plant with the manifestation of the climate change, therefore, farmers must prepare for irrigation and application of agro-technical methods to save the water supplies of the ground. However, at the beginning of the climate change, the maize plant at Keszthely is able to compensate the unfavorable conditions and does not suffer damage when the water supply is moderately less.

4. Conclusions

Examining the microclimate of maize canopies it can be concluded, that in the energy transport of the plant stand no shift can be experienced to the direction of the latent heat as the effect of warming up and the decrease of precipitation. The increase of the stomatal resistance can be detected, while the intensity of the photosynthesis first increases, but when we assume stronger climate change, it decreases. Examining the changes of microclimatic elements, it can be concluded that besides the climate, the architecture of the plant stand has an important role as well. From the changes of the stomatal resistance and inside canopy air temperature it can be concluded that the natural water supply will probably not cover the water demand of the plant, if the climate change is more intensive, therefore, farmers must prepare to irrigation and to use different agro-technical practices to keep the water stores of the soil if they want to avoid yield loss.

Acknowledgements—This work was derived from the PhD thesis of *Timea Kocsis* who owes special thanks to *Prof. János Mika* and *Dr. Zoltán Varga* for their support.

References

Anda, A. and *Dióssy, L.*, 2010: Simulation in maize-water relations: case study for continental climate (Hungary). *Ecohydrology 3*, 487–496.

Anda, A. and *Kocsis, T.*, 2008: Impacts of atmospheric CO_2 enrichment on some elements of microclimate and physiology of locally grown maize. *Appl. Ecol. Environ. Res. 6,* 85–94.

Anda, A. and *Lőke, Zs.*, 2002: Stomatal resistance investigations in maize. *Acta Biol. Szegediensis 46,* 181–183.

Anda, A. and *Lőke, Zs.*, 2003: Parameters determining the evaporation of maize, calculation of stomatal resistance, plant temperature and photosynthetic intensity by simulation model. *Növénytermelés 52*, 351–363. (in Hungarian)

Anda, A. and *Lőke, Zs.*, 2005: Microclimate simulation in maize with two watering levels. *Időjárás 109*, 21–39.

Anda, A., Lőke, Zs., and *Sz. Kirkovits, M.*, 2002: Simulation of some parameters of plant water relation in maize. *J. Cent. Eur. Agric. 3*, 95–103. (in Hungarian)

Anda, A., Páll, J. and *Lőke, Zs.* 1997: Measurement of mean stomatal resistance in maize. Időjárás 101: 275–288.

Bartholy, J., Pongrácz, R., Matyasovszky, I., and Schlanger, V., 2004: Climate tendencies occurred in the 20th century and projected for the 21st century in Hungary. *AGRO-21 Füzetek 33*, 3–18. (in Hungarian)

Bartholy, J., Pongrácz, R., Gelybó, Gy., and *Szabó, P.*, 2008: Analysis of expected climate change in the Carpathian Basin using the PRUDENCE results. *Időjárás 112,* 249–264.

Dióssy, L., 2008: The influence of global climate change on air and soil temperatures in maize canopy. *Időjárás 112*, 125–139.

Dióssy, L., and *Anda, A.*, 2008: Energy Based Approach of Local Influence of Global Climate Change

in Maize Stand. *Cereal Res. Commun. 36,* 591–600.
Dióssy, L., and *Anda, A.,* 2009: Consequences of climate change on some maize characteristics in Hungary. *Időjárás 113*, 145–156.
Easterling, W. E., Hays, C. J., Easterling, M. M., and *Brandle J. R.,* 1997: Modelling the effect of shelterbelts on maize productivity under climate change: An application of the EPIC model. *Agr. Ecosys. Environ. 61,* 163–176.
Ewert, F., Rodriguez, D., Jamieson, P., Semenov, M.A., Mitchell, R.A.C., Goudriaan, J., Porter, J.R., Kimball, B.A., Pinter, P.J., Manderscheid, R., Weigel, H.J., Fangmeier, A., Fereres, E., and *Villalobos, F.,* 2002: Effect of elevated CO_2 and drought on wheat: testing crop simulation models for different experimental and climatic conditions. *Agr., Ecosys. Environ. 93*, 249–266.
Fodor, N., and *Pásztor, I.,* 2010: The agro–ecological potential of Hungary and its prospective development due to climate change. *Appl. Ecol. Environ. Res. 8,* 177–190.
Gaál, M., 2007: The modification of the climatic conditions of maize production according to B2 scenario. *AGRO-21 Füzetek 51*, 48–56. (in Hungarian)
Goudriaan, J., 1977: *Crop micrometeorology: a simulation study.* Simulation monographs, Pudoc, Wageningen.
Goudriaan, J., 1989: Simulation of micrometeorology of crops, some methods and their problems, and a few results. *Agr. Forest Meteorol. 47,* 239–258.
Goudriaan, J., and *Van Laar, H.H.,* 1994: Modelling Potential Crop Growth Processes. In *Current issues in Production Ecology, Vol. 2.,* Kluwer Academic Publishers, Netherlands.
Goudriaan, J., and *Zadoks, J.C.,* 1995: Global climate change: modelling the potential responses of agro-ecosystems with special reference to crop protection. *Environ. Pollut. 87*, 215–224.
Guilioni, L., Cellier, P., Ruget, F., Nicoullaud, B., and *Bonhomme, R.,* 2000. A model to estimate the temperature of a maize apex from meteorological data. *Agr. Forest Meteorol. 100,* 213–230.
Hungarian Meteorological Service, 2010: *Climate modelling activity, results*, OMSZ. (in Hungarian)
Hunkár, M., 1990: Simulation of microclimate of maize canopy. *Időjárás 94,* 221–229. (in Hungarian)
Hunkár, M., 2002: Moisture supply and microclimate-interactions with productivity potential. *Phys. Chem. Earth 27,* 1113–1117.
Jackson, R.B., Sala, O.E., Field, C.B., and *Mooney, H.A.,* 1994: CO_2 alters water use, carbon gain, and yield for dominant species in a natural grassland. *Oecologia 98,* 257–262.
Jolánkai, M., 2010: Agriculture, soil management and climate change. *Climate change and Hungary: mitigating the hazard and preparing for the impacts* (The VAHAVA Report), 38–45.
Jones H.G., 1983: *Plants and microclimate.* Cambridge University Press, Cambridge
Knörzer, H., Grözinger, H., Graeff-Hönninger, S., Hartung, K., Piepho, H.-P., and *Claupein, W.,* 2011: Integrating a simple shading algorithm into CERES-wheat and CERES-maize with particular regard to a changing microclimate within a relay-intercropping system. *Field Crop. Res. 121*, 274–285.
Lőke, Zs. 2004: Measurement and modelling average photosynthesis of maize. *J. Cent. Eur. Agr. 5,* 281–288. (In Hungarian)
Mika, J., 2002. About global climate change: from the point of view of a meteorologist. *Fizikai Szemle 52*, 258–268. (In Hungarian)
Monteith, J.L., 1973. *Principles of Environmental Physics.* Edward Arnold, London.
Páll, J., Anda, A. and Hunkár, M., 1998. Modelling microclimate of maize canopies with different water supplies. *Acta Geograph. Geolog. Meteorol. Debrecina 34*, 41–60 (in Hungarian)
Sauer, T.J., Norman, J.M., 1995: Simulated canopy microclimate using estimated below-canopy soil surface transfer coefficients. *Agr. Forest Meteorol. 75,* 135–160.
STATA 5.0, 1996: Stata Corporation LP Texas, USA. www.stata.com
Stein, A., Goudriaan, J., 2000: Spatial statistics for production ecology. *Agr. Ecosys. Environ. 81*, 1–3.
Stigter, C.J., Goudriaan, J., Bottemanne, F.A., Birnie, J., Lengkeek, J.G., and *Sibma, L.,* 1977: Experimental evaluation of a crop climate simulation model for Indian corn (Zea mays L.). *Agr. Meteorol. 18*, 163–186.
Szépszó, G. and *Horányi, A.,* 2008: Transient simulation of the REMO regional climate model and its evaluation over Hungary. *Időjárás 112,* 203–232.
Tirado, M.C., Clarke, R., Jaykus, L.A., McQuatters-Gollop, A., and *Frank, J.M.,* 2010: Climate change and food safety: A review. Food *Res. Int. 43,* 1745–1765.

Van Ittersum, M.K., Leffelaar, P.A., Van Keulen, H., Kropff, M.J., Bastiaans, L., and *Goudriaan, J.*, 2003: On approaches and applications of the Wageningen crop models. *Eur. J. Agron. 18*, 201–234.

Van Laar, H.H. and *Penning de Vries, F.W.T.* 1972: CO_2 assimilation light responce curves of leaves, some experimental data. *Vels. Inst. biol. scheik. Onderz. LandbGewassen* 62, Wageningen.

Willmott, C.J., 1982: Some comments on the evaluation of model performance. *Bull. Am. Meteorol. Soc.*, 1309–1313.

Yi, L., Shenjiao, Y., Shiqing, L., Xinping, C., and *Fang, C.*, 2010: Growth and development of maize (*Zea mays* L.) in response to different field water management practices: Resource capture and use efficiency. *Agr. Forest Meteorol. 150*, 606–613.

IDŐJÁRÁS

Quarterly Journal of the Hungarian Meteorological Service
Vol. 116, No. 2, April–June 2012, pp. 123-143

Assessing effect of time scale on the solar radiation sunshine duration relationship

Ji-Long Chen[1,2] and **Guo-Sheng Li**[1*]

[1]*Institute of Geographic Sciences and Natural Resources Research, Chinese Academy of Sciences, 100101 Beijing, China*

[2] *Graduate University of Chinese Academy of Sciences, 100039 Beijing, China*

[*]*Corresponding author; E-mail: ligscas@163.com*

(Manuscript received in final form September 12, 2011)

Abstract—Solar radiation is the principal and fundamental energy for many physical, chemical, and biological processes. Estimation of solar radiation from sunshine duration is common employed when no direct observation of solar radiation is available. Particularly, the *Ångström-Prescott* (A-P) model is widely used for its simplicity. This paper investigates the effect of time scale on the A-P parameters and the estimation accuracy using the data of 13 sites in Northeastern China. The results show that the A-P model can not be applied at annual, but less than seasonal time scale. Time scale effects the spatial variation of a and b parameters of the calibration curve, it has greater effect on parameter a than on b; while greater effect on temporal variation of b than that of a, and the differences of the parameters caused by time scales are generally large, however, the large differences of parameters do not result in significant difference of the estimation accuracy. Therefore, parameters at different time scales are interchangeable, the parameters calibrated at larger time scales can be applied to smaller time scales, and vice versa.

Key-words: solar radiation, estimation, *Ångström-Prescott* model, parameter, time scales

1. Introduction

Solar radiation is the principal and fundamental energy for many physical, chemical, and biological processes, and it is also an essential and important variable to many simulation models, such as agriculture, environment, hydrology, and ecology. However, in many cases, it is not readily available due to the cost and difficulty of maintenance and calibration of the measurement

equipment (*Hunt et al.*, 1998). Only a few meteorological stations measure solar radiation. For example, in USA, less than 1% of meteorological stations are recording solar radiation (*NCDC*, 1995; *Thorton* and *Running*, 1999). In China, more than 2000 stations have records of meteorological data, only 122 stations are recording solar radiation. The ratio of stations recording solar radiation to those recording temperature is about 1:500 around the world (*Thorton* and *Running*, 1999). Therefore, developing method to estimate solar radiation has been the focus of many studies.

Major methods including satellite-derived (*Frulla et al.*, 1988; *Pinker et al.*, 1995; *Olseth* and *Skartveit*, 2001; *Şenkal*, 2010), stochastic algorithm (*Richardson*, 1981; *Wilks* and *Wilby*, 1999; *Hansen*, 1999), empirical relationships (*Ångström*, 1924; *Prescott*, 1940; *Hargreaves*, 1981; *Bristow* and *Campbell*, 1984; *Hargreaves et al.*, 1985), interpolation (*Hay* and *Suckling*, 1979; *Rivington et al.*, 2006), and learning machine method (*Tymvios et al.*, 2005; *Cao et al.*, 2006; *Lam et al.*, 2008; *Jiang*, 2009; *Chen et al.*, 2011) have been developed for the purpose. Among them, the empirical relationship using other commonly measured meteorological data, such as sunshine duration, maximum and minimum temperatures, is attractive for its simplicity, efficiency, and lower data requirement. It is generally recognized that the sunshine-based methods outperform other meteorological variables models (*Iziomon* and *Mayer*, 2002; *Podestá et al.*, 2004; *Trnka et al.*, 2005), particularly the well-known *Ångström-Prescott* (A-P) model, proposed by *Ångström* (1924) and further modified by *Prescott* (1940), was widely used in different locations of the world (*Ångström*, 1924; *Prescott*, 1940; *Almorox* and *Hontoria*, 2004; *Liu et al.*, 2009). Several modifications to the A-P model have been proposed since it was developed (*Newland*, 1988; *Akinoglu* and *Ecevit*, 1990; *Ertekin* and *Yaldiz*, 2000). However, various comparative studies demonstrated that the modifications could not give significant improvement (*Iziomon* and *Mayer*, 2002; *Yorukoglu* and *Celik*, 2006; *Liu et al.*, 2009). As the result, the simple A-P model was preferred due to its greater simplicity and wider application.

A number of literatures focused on the studies of A-P model at monthly time scale (*Iziomon* and *Mayer*, 2002; *Almorox* and *Hontoria*, 2004; *Zhou et al.*, 2005), because the A-P model was initially developed using the monthly data; moreover, the author emphasized that the A-P model should be calibrated using the monthly data rather than the daily data (*Ångström*, 1956). Some literatures reported the studies at daily time scale (*Yorukoglu* and *Celik*, 2006), even at annual time scale (*Chen et al.*, 2006; *Liu et al.*, 2009), and showed that the parameters can be quite different in different places. Some of them noticed that the parameters changed with time scales (*Benson et al.*, 1984; *Ögelman et al.*, 1984), but they did not conclude the effect of the time scale. *Gueymard et al.* (1995) illustrated that the averaging time (time scale) is a critical factor in empirical and statistical models, stressed the importance of studying its effect,

and believed that the optimum averaging period for smoothing the data without significant loss of information remains unanswered. The effect of the time scale on relationship between solar radiation and sunshine duration remains unknown. Therefore, more investigation is necessary and important to clarify the effect of time scale on relationship between solar radiation and sunshine duration. The objectives of the current study are Eq.(1) to determine the A-P parameters at five time scales, namely, daily, half-monthly, monthly, seasonal and annual time scales (hereafter referred to as TS1, TS2, TS3, TS4, and TS5, respectively) in Northeastern China; Eq.(2) to investigate the effect of time scale on A-P parameters and estimation accuracy.

2. *Materials and method*

2.1. A-P model and calibration

The A-P model was proposed by *Ångström* (1924) and further modified by *Prescott* (1940). The original form of this model is:

$$\frac{Rs}{Ra} = a\frac{H}{Ho} + b \quad , \tag{1}$$

where Rs is daily actual global radiation [MJ m^{-2} d^{-1}], Ra is daily extra-terrestrial solar radiation [MJ m^{-2} d^{-1}], H is daily actual sunshine duration [h], Ho is daily potential sunshine duration [h], a and b are empirical parameters which are calibrated from regression analysis between H/Ho and Rs/Ra using the calibration data. The extra-terrestrial solar radiation and potential sunshine duration are calculated using the equations detailed by *Allen et al.* (1998).

$$Ra = 37.6d\left(\omega \sin\varphi \sin\delta + \cos\varphi \cos\delta \sin\omega\right), \tag{2}$$

$$d = 1 + 0.033\cos\left(\frac{2\pi}{365}n\right), \tag{3}$$

$$\delta = 0.4093\sin\left(\frac{2\pi}{365}n - 1.39\right), \tag{4}$$

$$\omega = \arccos\left(-\tan\varphi \tan\delta\right), \tag{5}$$

$$Ho = 24\omega / \pi \ , \tag{6}$$

where d is the correction of incoming solar radiation due to the changing distance between the Sun and the Earth, ω is the sunset hour angle [rad], φ is the latitude [rad], δ is the solar declination angle [rad], n is the number of the day of year starting from the first day of January.

2.2. Study area and site description

The current study focuses on Northeastern China (*Fig.1*), consisting of the three provinces of Liaoning, Jilin, and Heilongjiang and the four eastern prefectures of Inner Mongolia: Hulunbeier, Xinan, Tongliao, and Chifeng. The climate of the region has extreme seasonal contrasts, ranging from humid, almost tropical heat in the summer to windy, dry, and cold winter. The heartland of the region is the Northeast China Plain. It lies between the Greater and Lesser Khinggan and Changbai mountains, covering an area of 350 000 km^2. It is the main area of maize, millet and soybeans production in China, and hence the eco-environmental models and crop growth simulation are widely studied. However, only 13 meteorological stations provide solar radiation record. Moreover, no literature reported study on the solar radiation estimation for this region, and the information on the A-P model is limited.

A total of 13 stations with long-term available records of solar radiation are used in the present study (*Fig.1*). The mapping of stations roughly range from 38° to 52° latitude North, from 116° to 130° longitude East, and from 49 to 610 m altitude. *Table 1* shows the temporal period and the geographical information of the meteorological stations.

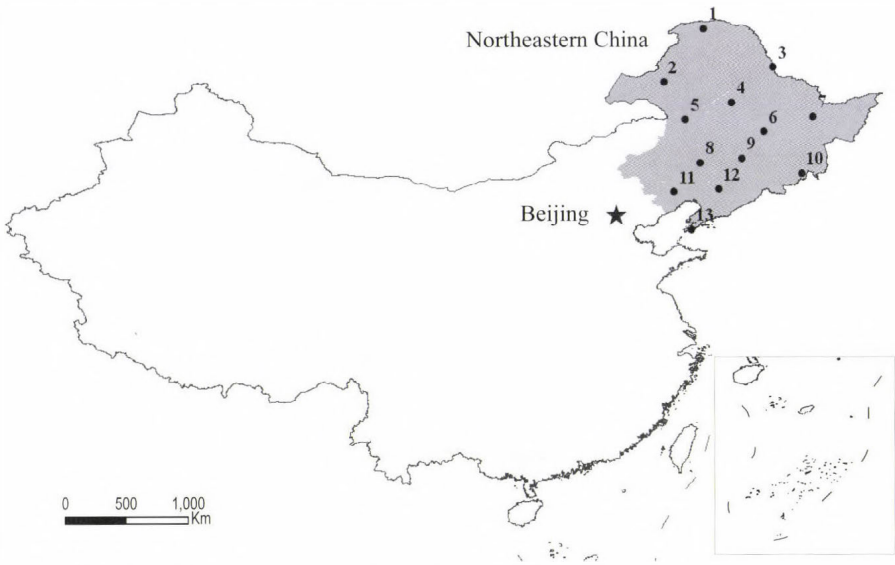

Fig.1. Location of the studied meteorological stations in Northeastern China (stations are numbered in compliance with *Table 1*).

2.3. Data collection and check

Daily actual global radiation and sunshine duration data of the study sites are used in the present study. The data were obtained from the National Meteorological Information Center (NMIC), China Meteorological Administration (CMA). The period of records ranges from 13 to 40 years covering the period between 1970 and 2009 (*Table 1*). Preliminary quality control tests were conducted by the suppliers. We further check the data according to the following criteria:

(a) For the daily data, records with missing data which were replaced by 32766, daily actual global radiation larger than the daily extra-terrestrial solar radiation, and actual sunshine duration larger than daily potential sunshine duration were removed from the data set.

(b) For half-month, we define days 1–15 as the first half month and day 16 through the end of the month as the latter half month. The half-monthly data is the average value of each day in the whole half-month. A half-month with more than 3 days of missing or faulty data in the same half-month was discarded.

(c) The monthly data is the average value of each day in the whole month. A month with more than 5 days of missing or faulty data in the same month was discarded.

(d) For season, we define March to May as spring, June to August as summer, September to November as autumn, December to February in the next year as winter. A season with more than 15 days of missing or faulty data in the same season, or 8 days of those in the same month was discarded.

(e) A year with more than 30 days of missing or faulty data, or 15 days of those in the same month, or 2 months with more than 10 days of missing or faulty data in the same month was discarded.

Two data sets are created for each time scale. About 75% of the total records are used for calibrating the parameters of A-P model, and the remainder for evaluating the model (*Table 1*). The investigation is operated at five time scales or averaging period, namely, daily (TS1), half-monthly (TS2), monthly (TS3), seasonal (TS4), and annual (TS5) time scales.

Table 1. Detailed information of the studied 13 stations in Northeastern China

Station ID	Station name	Latitude (N)	Longitude (E)	Altitude (m)	Calibration period	Validation period
1	Mohe	52.97	122.52	433.00	1997–2006	2007–2009
2	Hailaer	49.22	119.75	610.20	1972–1977 1982–2000	2001–2009
3	Heihe	50.25	127.45	166.40	1970–1999	2000–2009
4	Fuyu	47.80	124.48	162.70	1993–2004	2005–2009
5	Suolun	46.60	121.22	499.70	1992–2004	2005–2009
6	Haerbing	45.75	126.77	142.30	1970–1999	2000–2009
7	Jiamushi	46.82	130.28	81.20	1970–1978 1983–2000	2001–2009
8	Tongliao	43.60	122.27	178.70	1970–1999	2000–2009
9	ChangChun	43.90	125.22	236.80	1970–1981 1983–1999	2000–2009
10	Yanji	42.87	129.50	257.30	1970–1999	2000–2009
11	Chaoyang	41.55	120.45	169.90	1970–1999	2000–2009
12	Shengyang	41.73	123.52	49.00	1970–1999	2000–2009
13	Dalian	38.90	121.63	91.50	1970–1999	2000–2009

2.4. Data description

Fig. 2 shows the distribution of the averaged daily solar radiation (*Fig. 2*(a)) and sunshine duration (*Fig. 2*(b)) of the 13 sites in Northeastern China. Solar radiation and sunshine duration range from 4.53 to 21.73 MJ m^{-2} (averaged 13.26 MJ m^{-2}) and from 4.36 to 9.38 h (averaged 7.15 h), respectively. They generally have a similar tendency, with the maximum in July, and minimum in December. Pearson coefficient between solar radiation and sunshine duration is 0.92 ($p < 0.01$). Larger deviations of solar radiation and sunshine duration occur in April-September, which may be attributed to the large day-to-day fluctuation of the weather variables. Solar radiation shows larger variation than sunshine duration, with the *CV* of 40.68% and 16.87% for them, respectively, where *CV* is the ratio of standard deviation to arithmetic mean.

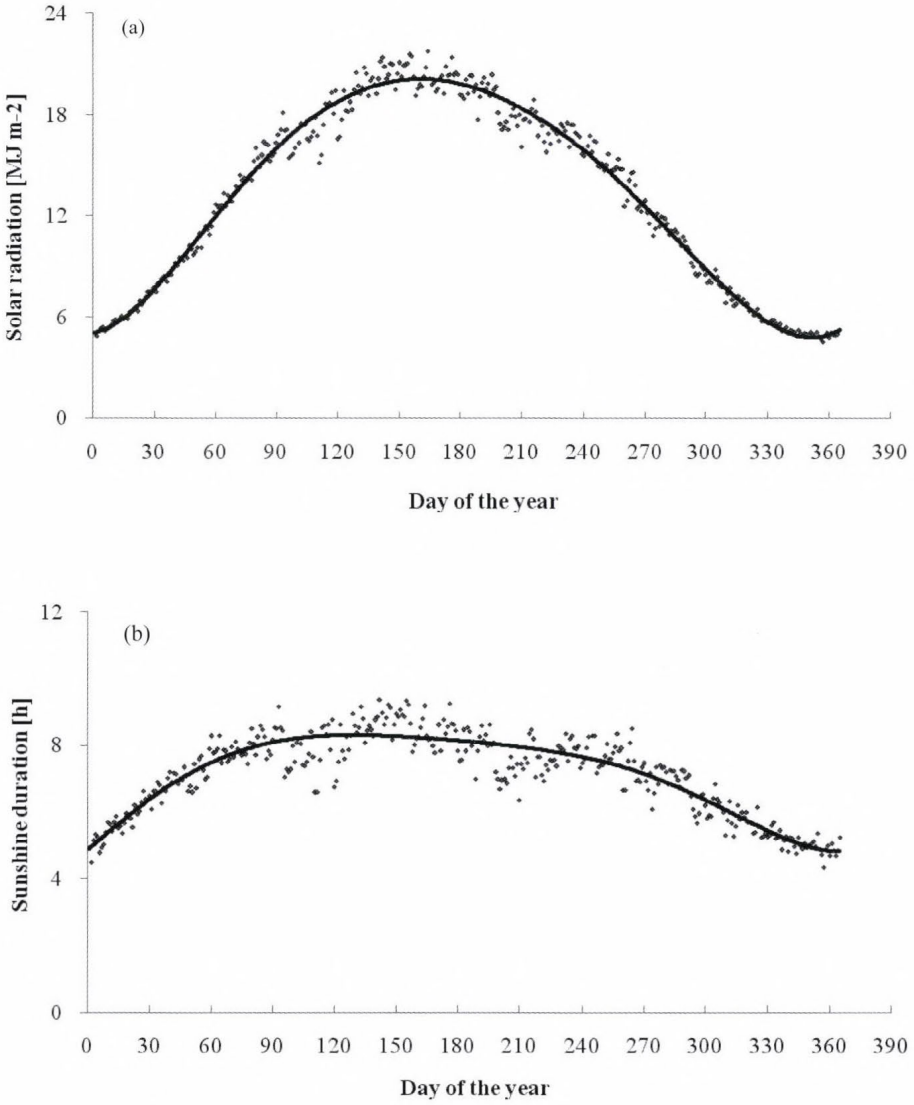

Fig.2. Distribution of the averaged daily solar radiation (a) and sunshine duration (b) of the 13 sites in Northeastern China.

2.5. Performance criteria

To assess the performance of the model, root mean square error (*RMSE*), relative root mean square error (*RRMSE*) [%] and coefficient of determination (R^2) are determined. R^2 is commonly calculated based on the calibration dataset

while *RMSE*, and *RRMSE* are based on the validation dataset. The metric R^2 varying from 0 to 1 is adopted to measure the fit of the model on calibration data, where the higher the value, better the fit. The *RMSE* provides information on the short term performance of the correlations by allowing a term by term comparison of the actual deviation between the estimated and measured values. The smaller the value, the better the model's performance. *RRMSE* is a dimensionless index allowing comparisons among a range of different model responses regardless of units. The value of *RRMSE* ranges from 0 to infinity. The smaller the *RRMSE*, the better is the model's performance. *RMSE* and *RRMSE* are calculated by the following equations:

$$RMSE = \sqrt{\frac{\sum_{i=1}^{n}(y_i - \hat{y}_i)^2}{n}}, \tag{7}$$

$$RRMSE = \frac{100}{\overline{y}}\sqrt{\frac{\sum_{i=1}^{n}(y_i - \hat{y}_i)^2}{n}}, \tag{8}$$

where n, y, $\hat{y}$, and $\overline{y}$ represent the number of testing data, the observed value, estimated value, and average value of the observation, respectively.

The metric *CV* calculated as ratio of standard deviation to arithmetic mean is adopted to measure the variation of the parameter. The higher the value, the larger the parameter's variation.

3. Results and discussion

3.1. Variations of A-P model parameters at five time scales

3.1.1. A-P model parameters calibrated at TS1

The calibrated parameters *a* and *b* at five time scales are summarized in *Table 2*. Using daily data (TS1), parameter *a* varies from 0.499 in Chaoyang to 0.606 in Heihe (averaged 0.545), *b* from 0.146 in Tongliao to 0.277 in Fuyu (averaged 0.196), and the sum of *a* and *b* (*a*+*b*) from 0.669 in Tongliao to 0.787 in Fuyu (averaged 0.741). Evidently, *a*+*b* are most stable with the *CV* of 4.89% followed by parameter a (*CV*=5.74%), while parameter *b* shows a larger variation with the *CV* of 21.44%.

Table 2. The parameters of A-P model calibrated at five time scales in the study area

Station	TS1				TS2				TS3			
	a	*b*	*a+b*	R^2	*a*	*b*	*a+b*	R^2	*a*	*b*	*a+b*	R^2
Mohe	0.538	0.241	0.779	0.757	0.600	0.206	0.806	0.567	0.627	0.190	0.817	0.483
Hailaer	0.518	0.252	0.770	0.725	0.518	0.252	0.770	0.522	0.517	0.253	0.769	0.445
Heihe	0.606	0.163	0.769	0.780	0.665	0.126	0.791	0.692	0.701	0.104	0.805	0.649
Fuyu	0.509	0.277	0.787	0.813	0.484	0.292	0.776	0.656	0.481	0.294	0.775	0.615
Suolun	0.551	0.232	0.783	0.743	0.483	0.276	0.759	0.473	0.463	0.288	0.752	0.404
Haerbing	0.532	0.192	0.724	0.721	0.484	0.220	0.705	0.524	0.439	0.247	0.686	0.403
Jiamushi	0.548	0.182	0.730	0.754	0.602	0.153	0.755	0.582	0.628	0.138	0.766	0.491
Tongliao	0.523	0.146	0.669	0.676	0.506	0.158	0.663	0.466	0.495	0.165	0.660	0.401
ChangChun	0.597	0.163	0.760	0.806	0.610	0.155	0.765	0.670	0.626	0.145	0.771	0.613
Yanji	0.550	0.183	0.733	0.788	0.473	0.223	0.697	0.540	0.447	0.237	0.684	0.455
Chaoyang	0.499	0.202	0.701	0.790	0.423	0.251	0.674	0.566	0.402	0.264	0.667	0.503
Shengyang	0.563	0.164	0.727	0.809	0.516	0.191	0.707	0.590	0.504	0.197	0.702	0.496
Dalian	0.556	0.152	0.708	0.720	0.499	0.188	0.687	0.555	0.503	0.186	0.690	0.480
Average	0.545	0.196	0.741	0.760	0.528	0.207	0.735	0.569	0.526	0.209	0.734	0.495
CV [%]	5.74	21.44	4.89	—	13.11	24.84	6.48	—	17.20	28.98	7.39	—

Table 2. (continued)

Station	TS4				TS5			
	a	*b*	*a+b*	R^2	*a*	*b*	*a+b*	R^2
Mohe	0.572	0.218	0.791	0.363	0.507	0.249	0.756	0.086
Hailaer	0.543	0.234	0.777	0.344	0.422	0.301	0.723	0.275
Heihe	0.725	0.088	0.813	0.587	0.973	-0.071	0.902	0.373
Fuyu	0.514	0.275	0.789	0.564	0.371	0.346	0.717	0.222
Suolun	0.452	0.296	0.748	0.355	0.028	0.554	0.582	0.001
Haerbing	0.370	0.286	0.656	0.364	0.040	0.475	0.515	0.001
Jiamushi	0.672	0.113	0.785	0.372	0.577	0.157	0.734	0.142
Tongliao	0.502	0.158	0.660	0.347	0.801	-0.050	0.751	0.187
ChangChun	0.654	0.127	0.781	0.533	0.284	0.340	0.624	0.055
Yanji	0.431	0.246	0.677	0.405	0.335	0.291	0.625	0.040
Chaoyang	0.371	0.284	0.655	0.443	-0.200	0.639	0.439	0.063
Shengyang	0.481	0.209	0.691	0.396	0.099	0.421	0.521	0.009
Dalian	0.436	0.228	0.664	0.393	0.294	0.317	0.611	0.027
Average	0.517	0.213	0.730	0.420	0.349	0.305	0.654	0.114
CV [%]	21.82	33.04	8.57	—	92.45	67.64	19.18	—

The values of R^2 vary from 0.676 to 0.813 (averaged 0.760). Although these values indicate that the simple linear equation gives goodness of fit on the calibration data set, other researchers have proposed several modifications by changing the order of *H/Ho*, such as, quadratic (*Akinoglu* and *Ecevit*, 1990), cubic (*Ertekin* and *Yaldiz*, 2000), and logarithmic models (*Ampratwum* and *Dorvlo*, 1999). In our work, we have used these functions to model the relation between *Rs/Ra* and *H/Ho*, however, they return quite similar values of R^2 to those of the simple linear A-P model within the same station. Several comparative studies also demonstrated that they returned almost identical values of R^2 and gave very similar accuracy (*Iziomon* and *Mayer*, 2002; *Almorox* and *Hontoria*, 2004; *Yorukoglu* and *Celik*, 2006). Therefore, there is no reason to choose a complex function to gain probably negligible accuracy at the cost of losing the simplicity and convenience of the simple A-P model. The goodness of fit also questions the restriction of A-P model calibration to monthly mean daily data (TS3) made by *Ångström* (1956).

3.1.2. A-P model parameters calibrated at TS2

There are many satellite imagine products data that scientists are using to study global change. Many products have been developed with Moderate Resolution Imaging Speetroradiometer (MODIS) data, these include 16-day composite images, such as the widely used MODIS Vegetation Index product. Together with these data, the 16-daily mean solar radiation is usually needed to parameterize or validate ecosystem process models and eco-environment simulation models. However, no literature has reported the study of A-P model at this time scales. In the present work, we calibrate the parameters and evaluate the performances of A-P model at half-monthly time scale (TS2), which differs little from the 16-day time scale, but does not result in significantly differences to the results. At this time scale, parameter a varies from 0.423 in Chaoyang to 0.665 in Heihe (averaged 0.528), b from 0.126 in Heihe to 0.292 in Fuyu (averaged 0.207), and $a+b$ from 0.663 in Tongliao to 0.806 in Mohe (averaged 0.735) (*Table 2*). The stability of the parameters is in order: $a+b$ (CV=6.48%) > a (CV=13.11%) > b (CV=24.84). R^2 varies from 0.466 to 0.692 (averaged 0.569). The values of R^2 indicate that A-P model gives goodness of fit, it therefore could be used to estimate solar radiation at this time scale.

3.1.3. A-P model parameters calibrated at TS3

Using the monthly mean daily data, parameter a varies from 0.402 in Chaoyang to 0.701 in Heihe (averaged 0.526), b from 0.104 in Heihe to 0.294 in Fuyu (averaged 0.209), and $a+b$ from 0.660 in Tongliao to 0.817 in Mohe (averaged 0.734), while R^2 varies from 0.401 to 0.649 (averaged 0.495). The A-P model was initially developed using the monthly mean daily data. More than 30 years later, the author stressed that the parameters of the model should be calibrated

from the monthly mean daily data rather than the daily data (*Ångström*, 1956). Consequently, a large amount of literatures reported the researches of the A-P model at TS3 (*Iziomon* and *Mayer*, 2002; *Almorox* and *Hontoria*, 2004; *Zhou et al.*, 2005). Another reason may be in that monthly mean daily data are more easily available than daily data. However, in the present work, better fits between Rs/Ra and H/H_0 are obtained at TS1 and TS2, as can be seen from *Table 2*, where the A-P model shows a 20.10%–83.80% (averaged 53.47%), and 6.54%–29.94% (averaged 14.97%) higher R^2 than those at TS3, respectively. Similar result was reported by *Tymvios et al.* (2005) who obtained higher R^2 of the A-P models established by using the daily data than that by monthly data of Athalassa. *Liu et al* (2009) also obtained a better fit between H/H_0 and Rs/Ra using daily data (TS1) than monthly mean daily data (TS3) of 29 stations in the Yellow River basin. These results again confirm our question of the restriction and suggest that it is unnecessary to restrict the A-P model calibration only to the monthly mean daily data.

3.1.4. A-P model parameters calibrated at TS4 and TS5

There is no any literature reported the study of A-P model using the seasonal mean daily (TS4) data. In the present work, the values of R^2 vary from 0.344 to 0.587(averaged 0.420), indicating that the A-P model retains goodness of fit and can be used at seasonal time scale. Parameter a vary from 0.370 in Haerbing to 0.725 in Heihe (averaged 0.517), b from 0.088 in Heihe to 0.296 in Suolun (averaged 0.213), and $a+b$ from 0.655 in Chaoyang to 0.813 in Heihe (averaged 0.730). Evidently, $a+b$ are much more stable (CV=8.57%) than parameter a (CV=21.82%) and b (CV=23.04%) individually.

The values of R^2 are very low at annual time scale (TS5), varying from 0.001 to 0.374 (averaged 0.114) is greater than 0.3only in Heihe (0.374), implying that the A-P model hardly explain the variation in solar radiation at TS5. The poor fit was also reported by *Chen et al.* (2006) who found that the fit was not improved by adding precipitation and air temperature data to the A-P equation. *Liu et al.* (2009) calibrated the A-P model using the hardly mean data from 13 sites in Yellow River basin. The returned R^2 varied from 0.02 to 0.61, it was greater than 0.5 at only two sites. Therefore, according to the analysis, the relation between solar radiation and sunshine duration can not be modeled by the A-P equation at hardly time scale, and the following discussion would be limited to the results fromTS1-TS4.

3.2. Analyses of effect of time scale on A-P model parameters

The spatial stability of parameters are dependent on time scale, as it can be seen from *Table 2*, where parameters at TS1 are the most stable with the CV of 5.74%, 21.44%, and 4.89% for a, b, and $a+b$, respectively, followed by those at

TS2 and TS3; while they show the largest spatial variations at TS4 with the *CV* of 21.82%, 33.04%, and 8.57%, respectively. Parameter *a* shows the largest differences of *CV* amongst different time scales, ranging from 4.09% between TS2 and TS3 to 16.08% between TS1 and TS4 (averaged 8.72%); while *a+b* shows small differences ranging from 0.91% between TS2 and TS3 to 3.68% between TS1 and TS4 (averaged 1.99%). These values indicate that time scale has greater effect on spatial variation of *a* than that of *b* and *a+b*.

There are significant correlations between the same parameters amongst different time scales, with the correlation coefficient $r>0.6$ and averaged r of 0.851 (*Table 3*). The most significant correlations are found between parameters at TS2 and TS3, with the r of 0.991 ($p<0.01$), 0.981 ($p<0.01$), and 0.991 ($p<0.01$) for *a*, *b*, and *a+b*, respectively. The correlations differ greatly among the parameters, *a+b* correlates most significantly amongst different time scales, with the $r>0.8$ ($p<0.01$) and averaged r of 0.917. These significant correlations indicate that the parameters at one time scale could be obtained from those at another time scale, and thus, the increase the availability of parameters without the need for calibration at all time scales.

Parameter *a* tends to decrease and *b* increase at larger time scales compared with those at smaller scale , as it can be seen in *Table 2*, where more than 61% of the stations have lower values of *a*, while higher *b* at larger time scales. The differences of the parameters caused by time scale are generally large, with 41% of the differences for *a* and 60% for *b* are greater than 10%. At some stations, this difference could be very large (e.g., Dalian, Chaoyang, Jamushi, Haerbing). Evidently, time scale has greater effect on temporal variation of *b* than that of *a*, with the differences ranging from 0.01% to 43.77% (averaged 9.99%) for *a* and from 0.09% to 61.74% (averaged 15.86%) for *b*. However, the differences of parameters *a* and *b* are always opposite as shown in *Fig. 3*, further confirming the stability of *a+b* with less variation at all spaces and time scales.

Table 3. Correlation efficient (r) between the parameters amongst different time scales

Time scale	Parameter	TS1			TS2			TS3			TS4		
		a	*b*	*a+b*	*a*	*b*	*a+b*	*a*	*b*	*a+b*	*a*	*b*	*a+b*
	a	1											
TS1	*b*	–0.544	1										
	a+b	0.234	0.689**	1									
	a	0.729**	–0.225	0.369	1								
TS2	*b*	–0.682*	0.807**	0.346	–0.726**	1							
	a+b	0.323	0.544	0.910**	0.670*	0.024	1						
	a	0.688**	–0.189	0.376	0.991**	–0.701**	0.684**	1					
TS3	*b*	–0.702**	0.702**	0.207	–0.821**	0.981**	–0.134	–0.813**	1				
	a+b	0.365	0.468	0.857**	0.737**	–0.076	0.991**	0.761**	–0.241	1			
	a	0.612*	–0.107	0.405	0.934**	–0.618*	0.692**	0.949**	–0.736**	0.762**	1		
TS4	*b*	–0.663*	0.601*	0.076	–0.850**	0.904**	–0.260	–0.849**	0.947**	–0.360	–0.868**	1	
	a+b	0.360	0.436	0.816**	0.732**	–0.100	0.957**	0.760**	–0.264	0.972**	0.830**	–0.444	1

* Significant at 0.05 significance level.
** Significant at 0.01 significance level.

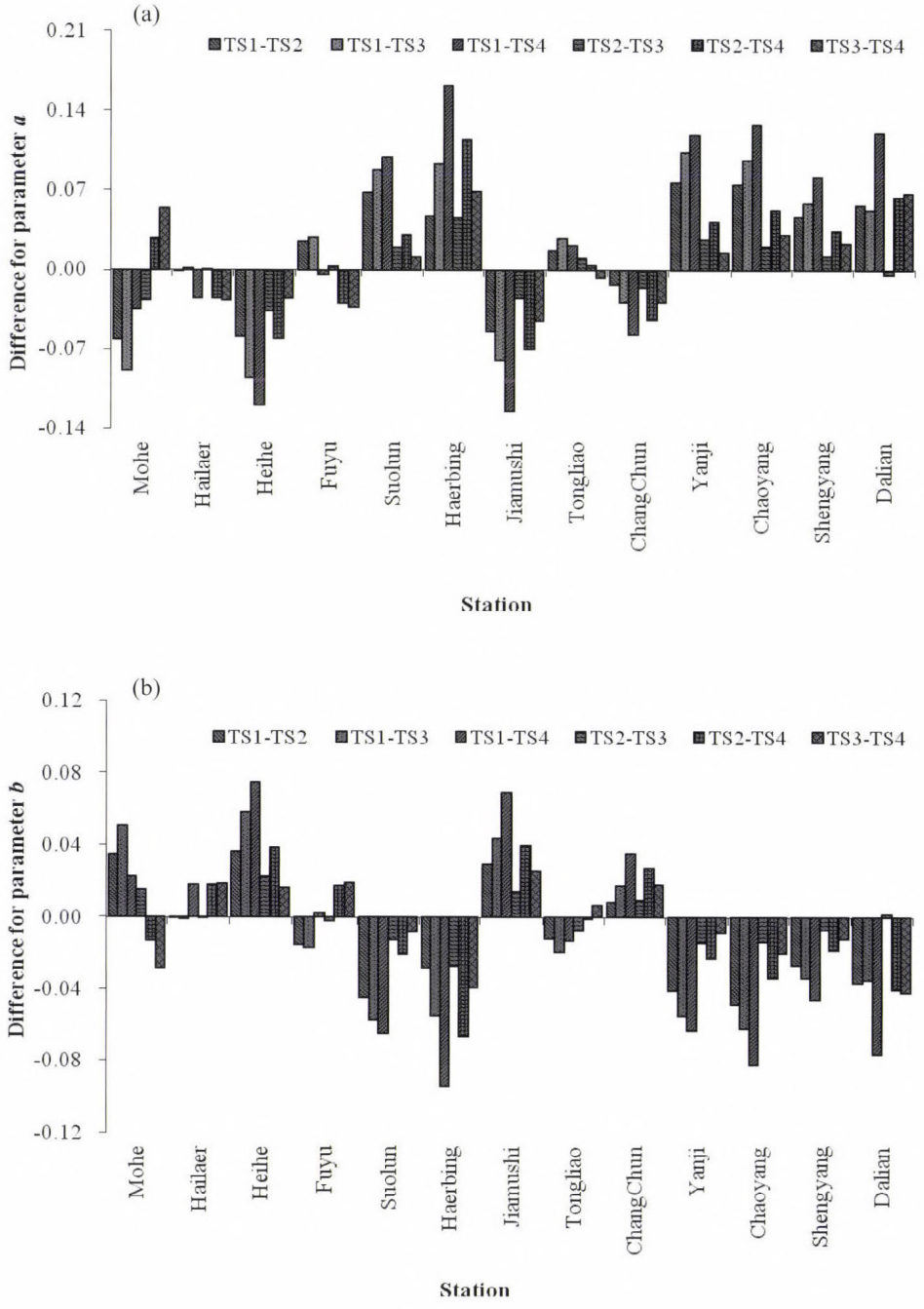

Fig.3. Difference of the parameter *a* (a) and *b* (b) among daily (TS1), half-monthly (TS2), monthly (TS3), and seasonal (TS4) time scales in the study area.

3.3. Comparison of the solar radiation estimation using parameters from different time scales

Conceptually, the calibrated parameters should only be used at the same time scale, namely, parameters calibrated from daily data should only be used to estimate daily solar radiation, while those calibrated at TS2, TS3, and TS4 should only be used at the corresponding time scales. It was also stated that the comparison in solar radiation at different scales can only be made possible when the estimation is in the same time scale. However, in many cases, no observation of meteorological data is available at some time scales, making the calibration difficult. To solve this problem, two possible alternatives may be considered, one is to use the values recommended by other authors who conducted the similar work. For example, *Ångström* suggested values of 0.2 and 0.5, and *Prescott* suggested 0.22 and 0.54 for the parameters a and b (*Prescott*, 1940), respectively; *Page* (1961) gave the corresponding values of 0.23 and 0.48, which was believed to be applicable anywhere in the world. However, lots of literatures reported the parameters for different places and showed that they varied from location to location, namely, they are site-dependent.

Another alternative is to directly use parameters calibrated at other time scales, for example, using the parameters at TS3 to estimate solar radiation at TS1, TS2, and TS4. This has never been done before but actually is of potential importance for practical applications, since monthly data are widely available. Therefore, in our work, an attempt is made to estimate solar radiation using the parameters calibrated at other different time scales, and the performances are summarized in *Tables 4–7*.

3.3.1. Estimating daily solar radiation using the parameters calibrated at all time scales

The A-P model gives good performances when using the parameters calibrated at TS1–TS4 to estimate the daily solar radiation, with the $RMSE < 2.7$ MJ m^{-2} (averaged 2.002 MJ m^{-2}) and $RRMSE < 20\%$ (averaged 15.01%) (*Table 4*). The estimation using parameters at TS1 is overall the best, with the lowest averaged *RMSE* of 1.949 MJ m^{-2} and *RRMSE* of 14.61%. However, it is noted that it is only slightly better than those using the parameters at TS2–TS4, with nearly identical averaged *RMSE* and *RMSE* of those at TS2–TS4 (*RMSE* of 1.978, 2.01, 2.068 MJ m^{-2}; *RRMSE* of 14.83%, 15.07%, 15.52%, respectively).

These values again prove that the A-P model can be used to estimate daily solar radiation with a good performance; furthermore, it implies that the parameters calibrated at TS2, TS3, and TS4 can replace those at TS1 in daily solar radiation estimation, suggesting that the parameters calibrated at larger time scale can be applied to smaller time scale.

Table 4. Root mean square error (*RMSE*) and relative root mean square error (*RRMSE*) of estimation daily solar radiation by A-P model using the parameters calibrated at all time scales.

Station	RMSE [MJ m^{-2}]				RRMSE [%]			
	TS1	TS2	TS3	TS4	TS1	TS2	TS3	TS4
Mohe	1.712	1.654	1.674	1.644	14.09	13.62	13.78	13.53
Hailaer	2.303	2.303	2.302	2.326	17.37	17.37	17.37	17.55
Heihe	1.636	1.809	1.969	2.019	12.70	14.04	15.29	15.67
Fuyu	1.871	1.917	1.923	1.867	13.30	13.62	13.67	13.27
Suolun	1.795	1.890	1.918	1.931	12.30	12.95	13.15	13.23
Haerbing	1.728	1.691	1.756	2.014	13.70	13.41	13.92	15.97
Jiamushi	1.489	1.575	1.592	1.671	11.85	12.53	12.66	13.29
Tongliao	2.615	2.591	2.579	2.611	18.41	18.24	18.16	18.39
ChangChun	1.906	1.920	1.946	2.020	14.26	14.37	14.56	15.11
Yanji	1.663	1.782	1.852	1.862	12.91	13.83	14.38	14.46
Chaoyang	2.516	2.549	2.591	2.678	18.43	18.67	18.98	19.62
Shengyang	2.240	2.176	2.174	2.195	16.80	16.32	16.30	16.46
Dalian	1.860	1.865	1.857	2.051	13.75	13.79	13.73	15.17
Average	1.949	1.978	2.010	2.068	14.61	14.83	15.07	15.52

3.1.2. Estimating half-monthly and monthly mean solar radiation using the parameters calibrated at all time scales

When estimating half-monthly and monthly mean solar radiation using the parameters calibrated at TS1–TS4, the A-P model also performs well, with the *RMSE* < 2.1 MJ m^{-2} (averaged 1.073 MJ m^{-2}) and *RRMSE* < 15% (averaged 8.01%) (*Table 5*), as well as *RMSE* < 2 MJ m^{-2} (averaged 0.990 J m^{-2}) and *RRMSE* < 14% (averaged 7.38%) (*Table 6*), respectively. The estimation of half-monthly solar radiation using parameters at TS2 is slightly better than that using parameters at TS1, TS3, and TS4, as it can been see from *Table 5*, where the differences for *RMSE* are less than 1%, and only in Jiamushi is greater than 0.1 MJ m^{-2}. Similar result is also found in the estimation of monthly solar radiation (*Table 6*), with the differences for *RMSE* and *RRMSE* less than 0.1 MJ m^{-2} and 1%, respectively.

These results indicate that the parameters calibrated at TS1, TS3, and TS4 can replace those at TS2 in half-monthly solar radiation estimation, and parameters calibrated at TS1, TS2, and TS4 can replace those at TS3 in monthly solar radiation estimation, not only suggesting that the parameters calibrated at a smaller time scale can be applied to larger time scales, but also again confirming that the parameters calibrated at a larger time scale can be applied to smaller time scales. Namely, the parameters at different time scales are interchangeable.

Table 5. Root mean square error (*RMSE*) and relative root mean square error (*RRMSE*) of estimation of half-monthly mean solar radiation by A-P model using the parameters calibrated at all time scales.

Station	RMSE [MJ m^{-2}]				RRMSE [%]			
	TS1	TS2	TS3	TS4	TS1	TS2	TS3	TS4
Mohe	0.822	0.751	0.737	0.736	6.77	6.18	6.07	6.06
Hailaer	1.577	1.577	1.576	1.606	11.90	11.90	11.89	12.12
Heihe	0.758	0.793	0.838	0.879	5.88	6.16	6.51	6.82
Fuyu	1.018	1.018	1.018	1.021	7.23	7.24	7.24	7.25
Suolun	0.881	0.946	0.978	1.004	6.04	6.49	6.71	6.88
Haerbing	0.799	0.748	0.740	0.804	6.34	5.93	5.87	6.38
Jiamushi	0.658	0.682	0.714	0.797	5.23	5.42	5.68	6.34
Tongliao	2.044	2.016	1.999	2.042	14.40	14.20	14.08	14.38
ChangChun	0.842	0.857	0.879	0.929	6.30	6.41	6.58	6.95
Yanji	0.702	0.698	0.726	0.748	5.45	5.42	5.64	5.81
Chaoyang	1.786	1.727	1.721	1.719	13.08	12.65	12.60	12.59
Shengyang	1.259	1.163	1.144	1.131	9.44	8.72	8.58	8.48
Dalian	0.813	0.783	0.778	0.831	6.01	5.80	5.75	6.15
Average	1.074	1.058	1.065	1.096	8.01	7.89	7.94	8.17

Table 6. Root mean square error (*RMSE*) and relative root mean square error (*RRMSE*) of estimation of monthly mean solar radiation by A-P model using the parameters calibrated at all time scales.

Station	RMSE [MJ m^{-2}]				RRMSE [%]			
	TS1	TS2	TS3	TS4	TS1	TS2	TS3	TS4
Mohe	0.753	0.675	0.653	0.662	6.20	5.57	5.38	5.46
Hailaer	1.526	1.526	1.525	1.557	11.52	11.52	11.51	11.76
Heihe	0.685	0.702	0.731	0.760	5.32	5.46	5.68	5.90
Fuyu	0.960	0.960	0.960	0.962	6.82	6.83	6.82	6.84
Suolun	0.783	0.869	0.902	0.929	5.37	5.96	6.19	6.37
Haerbing	0.717	0.668	0.654	0.693	5.69	5.30	5.19	5.50
Jiamushi	0.593	0.614	0.641	0.711	4.72	4.89	5.11	5.66
Tongliao	1.984	1.958	1.942	1.985	13.99	13.80	13.69	13.99
ChangChun	0.717	0.727	0.743	0.780	5.37	5.44	5.57	5.84
Yanji	0.623	0.617	0.637	0.653	4.84	4.79	4.95	5.08
Chaoyang	1.708	1.650	1.642	1.636	12.51	12.09	12.03	11.99
Shengyang	1.183	1.088	1.068	1.052	8.87	8.16	8.01	7.89
Dalian	0.709	0.670	0.664	0.698	5.25	4.96	4.91	5.16
Average	0.995	0.979	0.982	1.006	7.42	7.29	7.31	7.50

The *RMSE* and *RRMSE* for estimation of half-monthly and monthly solar radiation are much lower than those for estimation of daily solar radiation, implying that after the data smoothing by half-monthly or monthly averaging process, most of the instrumental random errors and day-to-day fluctuation of the data are removed. Therefore, if each day within the averaging lag takes the same values of the corresponding time scale mean daily solar radiation, it would not match the day-to-day variation of solar radiation. *Liu et al.* (2009) found that the *RMSE* increased greatly if the monthly mean daily solar radiation estimated at TS3 was directly used as the daily solar radiation approximation. *Gueymard et al.* (1995) stressed the importance of studying the effect of the averaging time (time scale), and believed that the optimum averaging period for smoothing the data remain unanswered. According to our analysis, the optimum averaging period should be less than 15 days, so that most of the instrumental random errors are removed without significant loss of information of the data. It would be significant to investigate further to determine the optimum lag, but it is beyond the objective of this study.

Table 7. Root mean square error (*RMSE*) and relative root mean square error (*RRMSE*) of estimation of seasonal mean solar radiation by A-P model using the parameters calibrated at all time scales.

Station	RMSE [MJ m^{-2}]				RRMSE [%]			
	TS1	TS2	TS3	TS4	TS1	TS2	TS3	TS4
Mohe	0.316	0.254	0.237	0.216	2.47	1.99	1.85	1.69
Hailaer	1.389	1.389	1.388	1.413	10.37	10.37	10.36	10.55
Heihe	0.550	0.556	0.568	0.581	4.23	4.27	4.37	4.47
Fuyu	0.788	0.801	0.801	0.788	5.48	5.57	5.57	5.48
Suolun	0.644	0.753	0.786	0.812	4.32	5.06	5.28	5.45
Haerbing	0.600	0.551	0.529	0.547	4.71	4.32	4.15	4.29
Jiamushi	0.486	0.498	0.516	0.562	3.83	3.92	4.06	4.43
Tongliao	1.861	1.836	1.820	1.863	13.01	12.83	12.72	13.02
ChangChun	0.515	0.520	0.531	0.556	3.82	3.86	3.94	4.13
Yanji	0.516	0.463	0.457	0.457	3.97	3.56	3.52	3.52
Chaoyang	1.605	1.557	1.551	1.545	11.67	11.32	11.28	11.23
Shengyang	1.105	1.039	1.014	0.990	7.95	7.47	7.29	7.12
Dalian	0.566	0.512	0.505	0.544	4.02	3.63	3.58	3.86
Average	0.842	0.825	0.823	0.837	6.14	6.01	6.00	6.09

3.3.3. Estimating seasonal mean solar radiation using the parameters calibrated at all time scales

When estimating seasonal mean daily solar radiation using the parameters calibrated at TS1-TS4, the A-P model retains good performances, with the $RMSE < 1.9$ MJ m^{-2} (averaged 0.833 MJ m^{-2}) and $RRMSE < 13\%$ (averaged 6.07%). The *RMSE* and *RRMSE* are much lower than those at TS1-TS3 due to the data smoothing by seasonal averaging process. Similarly, no significant difference of *RMSE* and *RRMSE* resulted by time scales is found, as it can be seen in *Table 7*, where only the differences for *RMSE* in Shengyang and Suolun are greater than 0.1 MJ m^{-2}, and only that for *RRMSE* in Suolun is greater than 1%. These results indicate that the parameters calibrated at TS1, TS2, and TS3 can replace those at TS4 in the estimation of seasonal solar radiation, again proving that the parameters calibrated at a smaller time scale can be applied to larger time scales.

4. Conclusion

Solar radiation is the principal and fundamental energy for many physical, chemical, and biological processes. Estimation of solar radiation from sunshine duration is common employed when no direct observation of solar radiation is available. Particularly, the *Ångström-Prescott* model is widely used for its simplicity. This paper investigates the effect of time scale on the *Ångström-Prescott* parameters and the estimation accuracy in Northeastern China. The relation between solar radiation and sunshine duration can not be modeled by the *Ångström-Prescott* equation at annual time scale, but less than seasonal time scales. Time scale effects the spatial variation of parameters, it has greater effect on parameter *a* than on *b*, and larger spatial variation are presented at larger time scales. Parameter *a* tends to decrease and *b* increase at larger time scales, and the differences of the parameters caused by time scale are generally large, with 41% of the differences for *a* and 60% for *b* are greater than 10%. Evidently, time scale has greater effect on temporal variation of *b* than that of *a*. However, the large differences of parameters caused by time scale do not result in significant difference of the estimation accuracy, estimation using the parameters from other time scales give the most identical performances with that using the parameters from itself time scale, therefore, parameters at different time scales are interchangeable, the parameters calibrated at larger time scales can be applied to smaller time scales, and vice versa.

Acknowledgments—The work was supported by the Geological Survey program of China Geological Survey (GZH201200503) and Special Fund for Land and Resources Research in the Public Interest (201111023). We thank the National Meteorological Information Center, China Meteorological Administration for providing the long-term data records. Many thanks go to the anonymous reviewers for the comments on the manuscript.

References

Akinoglu, B.G. and *Ecevit, A.*, 1990: Construction of a quadratic model using modified Ångström coefficients to estimate global solar radiation. *Sol. Energy* 45, 85–92.

Allen, R.G., Pereira, L.S., Raes, D., and *Smith, M.*, 1998: Crop evapotranspiration. Guidelines for computing crop water requirements. *FAO Irrigation and Drainage paper 56*. Rome.

Almorox, J. and *Hontoria, C.*, 2004: Global solar radiation estimation using sunshine duration in Spain. *Energ. Convers. Manage 45*, 1529–1535.

Ampratwum, D.B. and *Dorvlo, A.S.S.*, 1999: Estimation of solar radiation from the number of sunshine hours. *Appl. Energ. 62*, 161–167.

Ångström, A., 1924: Solar and terrestrial radiation. *Q. J. Roy. Meteor. Soc. 50*, 121–126.

Ångström, A., 1956: On the computation of global radiation from records of sunshine. *Ark. Geof. 2*, 471–479.

Benson, R.B., Paris, M.V., Sherry, J.E., and *Justus, C.G.*, 1984: Estimation of daily and monthly direct, diffuse and global solar radiation from sunshine duration measurements, *Sol. Energy 32*, 523–535.

Bristow, K.L. and *Campbell, G.S.*, 1984: On the relationship between incoming solar radiation and daily maximum and minimum temperature. *Agr. Forest Meteorol. 31*, 159–166.

Cao, J.C. and *Cao, S.H.*, 2006: Study of forecasting solar irradiance using neural networks with preprocessing sample data by wavelet analysis. *Energy 31*, 3435–3445.

Chen, J.L., Liu, H.B., Wu, W., and *Xie, D.T.*, 2011: Estimation of monthly solar radiation from measured temperatures using support vector machines-A case study, *Renew. Energ. 36*, 413–420.

Chen, R.S., Kang, E.S., Ji, X.B., Yang, J.P., and *Zhang, Z.H.*, 2006: Trends of the global radiation and sunshine hours in 1961–1998 and their relationships in China, *Energ. Convers. Manage 47*, 2859–2866.

Ertekin, C. and *Yaldiz, O.*, 2000: Comparison of some existing models for estimating global solar radiation for Antalya (Turkey), *Energ. Convers. Manage. 41*, 30–31.

Frulla, L.A., Gagliardini, D.A., Grossi G.H., Lopardo, R., and *Tarpley, J.D.*, 1988: Incident solar radiation on Argentina from the geostationary satellite GOES: comparison with ground measurements, *Sol. Energy 41*, 61–69.

Gueymard, C., Jidra, P., and *Eatrada, C.V.*, 1995: A critical look at recent interpretations of the Ångström approach and its future in global solar irradiation prediction, *Sol. Energy 54*, 357–363.

Hansen, J.W., 1999: Stochastic daily solar irradiance for biological modeling applications, *Agr. Forest Meteorol. 94*, 53–63.

Hargreaves, G.H., 1981: Responding to tropical climates. In *The 1980–81 food and climate review, the food and climate forum*. Boulder (Colo): Aspen Institute for Humanistic Studies, 29–32.

Hargreaves, G.L., Hargreaves, G.H., and *Riley, J.P.*, 1985: Irrigation water requirement for Senegal River Basin. *J. Irrig. Drain E-ASCE 111*, 265–275.

Hay, J.E. and *Suckling, P.W.*, 1979: An assessment of the net-works for measuring and modelling solar radiation in British Columbia and adjacent areas of western Canada. *Can. Geogr. 23*, 222–238.

Hunt, L.A., Kuchar, L., and *Swanton, C.J.*, 1998: Estimation of solar radiation for use in crop modelling. *Agr. Forest Meteorol. 91*, 293–300.

Iziomon, M.G. and *Mayer, H.*, 2002: Assessment of some global solar radiation parameterizations. *J. Atmos. Sol.-Terr. Phy. 64*, 1631–1643.

Jiang, Y.G., 2009: Computation of monthly mean daily global solar radiation in China using artificial neural networks and comparison with other empirical models. *Energy 34*, 1276–1283.

Lam, J.C., Wan, K.K.W., and *Yang, L.*, 2008: Solar radiation modeling using ANNs for different climates in China. *Energ. Convers. Manage. 49*, 1080–1090.

Liu, X.Y., Mei, X.R., Li, Y.Z., Zhang, Y.Q., and *Wang, Q.S.*, 2009: Calibration of the Ångström-Prescott coefficients (a, b) under different time scales and their impacts in estimating global solar radiation in the Yellow River basin. *Agr. Forest Meteorol.149*, 697–710.

NCDC (National Climatic Data Center), 1995: *Cooperative summary of the day, dataset TD 3200*. U.S. Department of Commerce, National Oceanographic and Atmospheric Administration, National Climatic Data Center, Asheville, NC.

Newland, F.J., 1988: A study of solar radiation models for the coastal region of South China. *Sol. Energy 31*, 227–235.

Ögelman, H., Ecevit, A., and *Tasdemiroglu, E.*, 1984: A new method for estimating solar radiation from bright sunshine data. *Sol. Energy 33*, 619–625.

Olseth, A. and *Skartveit, A.*, 2001: Solar irradiance, sunshine duration and daylight illuminance derived from METEOSAT data for some European sites. *Theor. Appl. Climatol. 69*, 239–252.

Page, J.K., 1961: The estimation of monthly mean values of daily total short wave radiation on vertical and inclined surface from sunshine records for latitudes 40N–40S. *Proceedings of UN Conference on New Sources of Energy, 4*, 378–390.

Pinker, R.T., Frouin, R., and *Li, Z.*, 1995: A review of satellite methods to derive shortwave irradiance. *Remote Sens. Environ. 51*, 108–124.

Podestá, G.P., Núñez, L., Villanueva, C.A., and *Skansi, M.A.*, 2004: Estimating daily solar radiation in the Argentine Pampas. *Agr. Forest Meteorol. 123*, 41–53.

Prescott, J.A., 1940: Evaporation from a water surface in relation to solar radiation. *T. Roy. Soc. South Aust. 64*, 114–118.

Richardson, C.W., 1981: Stochastic simulation of daily precipitation, temperature, and solar radiation. *Water Resour. Res. 17*, 182–190.

Rivington, M., Matthews, K.B., Bellocchi, G., and *Buchan, K.*, 2006: Evaluating uncertainty introduced to process-based simulation model estimates by alternative sources of meteorological data. *Agr. Syst. 88*, 451–471.

Şenkal, O., 2010: Modeling of solar radiation using remote sensing and artificial neural network in Turkey. *Energy 35*, 4795–4801.

Thorton, P.E. and *Running, S.W.*, 1999: An improved algorithm for estimating daily solar radiation from measurements of temperature, humidity, and precipitation. *Agr. Forest Meteorol.* 93, 211–228.

Trnka, M., Zalud, Z., Eitzinger, J., and *Dubrovský, M.*, 2005: Global solar radiation in Central European lowlands estimated by various empirical formulae, *Agr. Forest Meteorol. 131*, 54–76.

Tymvios, F.S., Jacovides, C.P., Michaelides, S.C., and *Scouteli, C.*, 2005: Comparative study of Ångström's and artificial neural network's methodologies in estimating global solar radiation. *Sol. Energy 78*, 752–762.

Wilks, D.S. and *Wilby, R.L.*, 1999: The weather generation game: a review of stochastic weather models. *Prog. Phys. Geogr. 23*, 329–357.

Yorukoglu, M. and *Celik, A.N.*, 2006: A critical review on the estimation of daily global solar radiation from sunshine duration. *Energ. Convers. Manage. 47*, 2441–2450.

Zhou, J., Wu, Y., and *Yan, G.*, 2005: General formula for estimation of monthly average daily global solar radiation in China. *Energ. Convers. Manage. 46*, 257–268.

IDŐJÁRÁS

Quarterly Journal of the Hungarian Meteorological Service
Vol. 116, No. 2, April–June 2012, pp. 145-169

Influence of carbon-dioxide concentration on human well-being and intensity of mental work

László Kajtár and **Levente Herczeg***

Department of Building Service Engineering and Process Engineering
Budapest University of Technology and Economics
Műegyetem rkp. 3, H-1111, Budapest

*Corresponding author E-mail: herczeg@epgep.bme.hu

(Manuscript received in final form December 19, 2011)

Abstract—In the frame of experiments carried out at the Department of Building Service Engineering and Process Engineering of Budapest University of Technology and Economics BUTE the impact of CO_2 concentration in the air was examined. Subjects' well-being was evaluated by the aid of subjective scales, physiological variables were recorded, and subjects' mental performance was measured by a standard test. Results obtained in the experiments show that subjects evaluated air quality is less acceptable, more unpleasant, and became more exhausted when the CO_2 concentration increased up to 3000 ppm. 3000 ppm CO_2 concentration in the air proved to be less advantageous for mental performance than 600 ppm. Several physiological measures show that a mental task requires a greater effort from the subjects when the CO_2 concentration in the air reaches 3000 ppm. It was shown that human well-being as well as the capacity to concentrate attention are declining when subjects spend 2 to 3 hours in a closed space with 3000 ppm or higher CO_2 concentration in the air.

Standards accurately prescribe the values of fresh air, breathing, and inside air quality assuring the health protection at workplaces.

We examined the level of carbon-dioxide concentration above which the efficiency of mental work and the human well-being significantly declines.

Key-words: air quality, carbon-dioxide, IAQ assessment, measurement technique, mental work

1. Introduction

The comfort in closed spaces is usually understood as thermal, air quality, acoustical, and illumination engineering comfort. The office plays a special role in providing adequate comfort as workers spend a longer time in closed spaces performing intellectual work. In the air-conditioning of comfort spaces, the primary task is to provide a pleasant indoor microclimate for the people staying in the room. In addition to thermal comfort, air quality is also regulated by international requirements and standards. In the occupied zone, a sufficient amount of fresh air of appropriate quality must be provided for the people staying in the room. Hungarian technical regulations do not fully cover these aspects yet, hence the complaints frequently heard from employees working in air-conditioned spaces are the air has an unpleasant 'smell', they experience 'lack of air' or perhaps have headaches. Among pollutants, carbon-dioxide, a by-product of the human metabolism, is regarded as one of the key factors. The carbon-dioxide content of exhaled air is higher than that of the outdoor air, leading to an increase in the carbon-dioxide concentration in the closed space. CO_2 concentration influences human well-being. In closed spaces the allowed CO_2 concentration may be ensured by supplying the adequate amount of fresh air. The exact volume of fresh air varies in Hungarian and international literature, ranging from 20 to 120 m^3/person. This is also a matter of economic efficiency as the volume flow of fresh air has an impact on the energy use of the air conditioning system (*Kajtár et al.*, 2001; *Kajtár* and *Hrustinszky*, 2002, 2003)

The fundamentals of the science of indoor air quality (IAQ) were laid down by Professor *Fanger* at the Danish Technical University. *Max von Pettenkoffer*, who published his research results in a medical journal in Munich in 1858, can be called the pioneer of IAQ. Using the CO_2 concentration in comfort spaces, his research focused on defining the average carbon-dioxide level below which human well-being is still ensured.

Further research conducted in the subject always investigated the joint impact of several factors influencing air quality, therefore the impact of carbon-dioxide on its own could not be determined.

We conducted studies concerning the impact of CO_2 on mental performance and well-being, at the same time determining the necessary fresh air demand.

2. Practical implications

In the present investigation, the influence of CO_2 concentration on human well-being and efficiency of mental work has been evaluated. These issues arise from time to time in connection with office work and the air-conditioning of office

buildings. It is very important to find the optimal balance between the biological requirements of office employees concerning fresh air on the one hand and economic efficiency on the other hand. A reduction in fresh air supply is required according to the arguments for profitability, whereas an increase of fresh air supply is needed when subjects' well-being is taken into consideration.

Table 1 shows the highest allowed CO_2 concentration in closed places provided by Hungarian and international standards and prescriptions.

Table 1. Maximum allowed CO_2 concentration in closed places

No.	Standards and prescriptions	Allowed CO_2 concentration [ppm]
	Comfort spaces	
1.	*MSZ 04.135/1-1982	1400.0
2.	MSZ 21875-2-1991	1066.6
3.	**DIN 1946/2 single office	900.0
4.	DIN 1946/2 landscaped office	733.3
5.	MSZ CR 1752 "A" cat.	860.0
6.	MSZ CR 1752 "B" cat.	1060.0
7.	MSZ CR 1752 "C" cat.	1590.0
	Workplaces	
8.	***TRGS 900	5000.0
9.	MSZ 21461 1-2	4830.0

*MSZ: Hungarian Standard
**DIN: Deutsches Institut für Normung
***TRGS: Technische Regeln für Gefahrstoffe

The above table indicates that the standards and prescriptions have not touched upon a wide range of CO_2 concentration from 1590 ppm to 4830 ppm. The aim of our research was to examine the influence of CO_2 concentration on human well-being and mental effort between 600 and 5000 ppm that was pointed in *Fig. 1.*

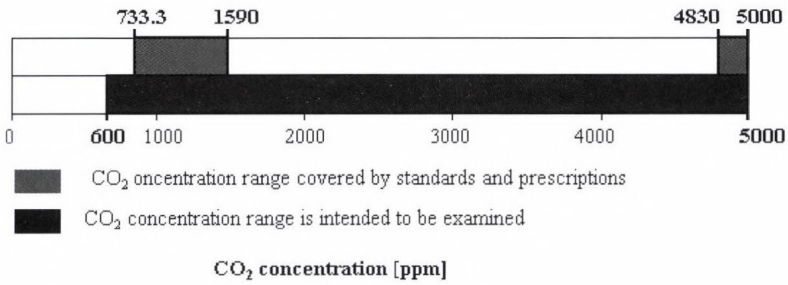

Fig. 1. The aim of our research.

The influence of CO_2 concentration on humans could be specified by means of examination of subjective comfort parameters and such objective parameters which were measured on humans and of performing experiments on subjects. The measuring-room that was built in Indoor Air Quality Laboratory of Department of Building Service Engineering and Process Engineering of BUTE were chosen for carrying out the experiments. Only this room could provide us that other air-polluting material did not influence the results of the measurements and subjects could stay in full thermal and air quality comfort during the measurements.

After finishing and evaluating the measurements, a maximum CO_2 concentration could be determined, under which there could not be any observable change in the human well-being and mental effort.

3. Methods

In the framework of our research, we investigated the impact of carbon-dioxide concentration on well-being and performance in the office. In the laboratory measurements we set the following CO_2 concentrations: 600, 1500, 2500, 3000, 4000, and 5000 ppm. The laboratory measuring room contained two carbon-dioxide sources: two main measuring subjects and carbon-dioxide, suitable for inhaling, fed from a bottle. The circuit diagram for the laboratory measurements is shown in *Fig. 2*.

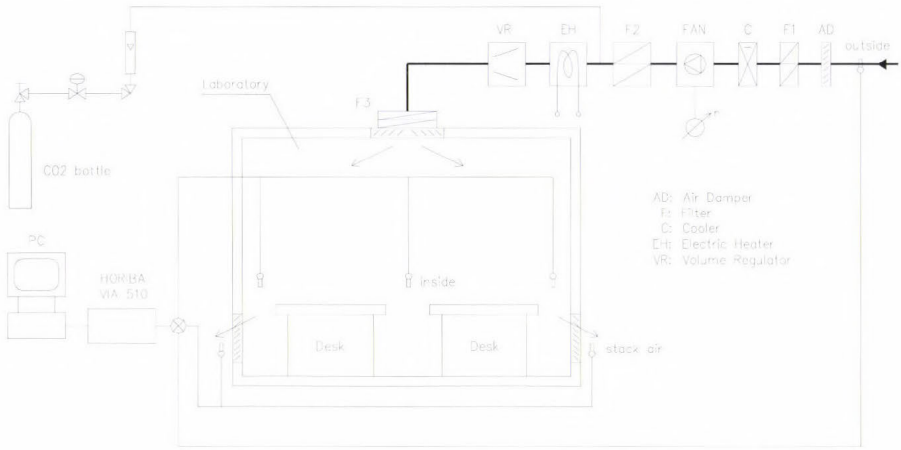

Fig. 2. Circuit diagram of the laboratory measurements.

The carbon-dioxide was fed into the measuring room mixed with 120 m^3/h fresh air. During the measurements, the carbon-dioxide concentration had to be kept at a constant level, therefore, the feeding valve had to be set accordingly. The share of carbon-dioxide sources is contained in *Table 2*. The carbon-dioxide concentration of outdoor air was 360 ppm.

Table 2. Carbon-dioxide sources in the measuring room

Measuring room CO_2 concentration [ppm]	Source of carbon-dioxide		Share human/total [%]
	Total [ppm]	Human [ppm]	
600	240	240	100.0
1500	1140	240	21.0
2500	2140	240	11.2
3000	2640	240	9.1
4000	3640	240	6.6
5000	4640	240	5.2

Carbon-dioxide fed from the bottle, was a gas of 99.995 V% cleanness, suitable for inhaling. Owing to their slight share, other pollutants in the carbon-dioxide gas ($O_2 \leq 25$ vpm, $N_2 \leq 25$ vpm, $HC \leq 1$ vpm, $CO \leq 1$ vpm, $H_2O < 5$ vpm) did not influence the results of the measurements. The pressure reducer and other armatures did not pollute the carbon-dioxide gas as their use is permitted in case of a gas of greater cleanness (99.998 V%).

In the present paper, two series of experiments are presented:

1. series of experiments carried out in 2001,
2. series of experiments carried out in 2002.

Both series of experiments were conducted in a laboratory constructed for the above purposes in the Department of Building Service Engineering and Process Engineering of the Budapest University of Technology and Economics. Inodorous air of appropriate, cleanliness, thermal comfort, as well as appropriate acoustic conditions have to be ensured in the laboratory.

In order to meet the requirements concerning air quality, the laboratory was built using specific low emitting building materials generally used in operating rooms, with practically no emission of contaminant substances.

To produce fresh air supply of the required cleanliness, a two-step filtration has been applied (G4 and F7). Air ducts as well as the filter unit at the second step of filtration were made from rust-proof steel plates.

During the various investigations in the laboratory, a high ventilation rate prevents the indoor air from becoming stale. Overpressure has been induced to prevent the influx of contaminating substances from outside (*Kajtár* and *Hrustinszky*, 2002, 2003).

Main data of the laboratory outlined above:

Floor area:	2.1×3.3 m $= 6.9$ m^2
Inside height:	2.5 m
Volume:	17.3 m^3
Volume flow of supply air:	1 000 m^3/h (maximum)
Ventilation rate:	57.8 l/h (maximum)
Filters:	G3, F7.

During experiments, a HORIBA VIA 510 infrared gas analyzer has been used. Main technical parameters of the instrument:

- Measuring range: 0–1 000 ppm, 0–2 500 ppm, 0–6 000 ppm, 0–10 000 ppm
- Measuring accuracy: ± 1.0%. Measurements were carried out by the aid of two parallel infrared rays. Automatic data collection was carried out by a data-collector developed by us. In this way data were stored and processed by a PC.

To measure comfort parameters, the following instruments were used:

- thermal comfort PMV meter: Thermal Comfort Meter 1212,
- air temperature and humidity meter: TESTO Testotor 175 Logger,
- wall surface temperature meter: TESTO Quicktemp 824-2,
- acoustics meter: ROLINE RO-1350 Sound Level Meter.

Instruments used to record physiological data:

- ISAX instrument,
- blood pressure monitor: wrist model,
- skin surface temperature meter: TESTO T2.

3.2. Subjects and procedures

In the laboratory measurements, a pleasant thermal, acoustic, and illumination technology comfort was provided to ensure that human well-being is only impacted by air quality (carbon-dioxide gas).

A pleasant thermal comfort was ensured for all live subjects by regulating the air temperature and individually selecting the clothing. The sound level in the measuring room was 36.6–37.0 dB(A).

The set carbon-dioxide concentrations were unknown to the subjects.

The number of subjects was defined through an empirical way (*Wyon* and *Bánhidi*, 2003), consequently 10 subjects were enough because significant differences could be found among the results.

3.2.1. First series of experiments

Ten subjects participated in the study (5 males and 5 females, mean age = 22.5 years). Each subject participated in four experimental sessions with different pre-set CO_2 concentrations (600, 1500, 2500, and 5000 ppm). Sessions succeeded each other in the following manner: session 1 (1500 ppm CO_2), session 2 (2500 ppm), session 3 (600 ppm), session 4 (5000 ppm). Each session consisted of 2×70 minutes mental work periods. The mental work involved the reading of a text manipulated for this purpose and the search for typographic errors. Performance of subjects was characterized by the number of rows read by the subjects (quantity aspect), and the percentage of misspelled words found by them (quality aspect). Prior to and following the work periods, questionnaires were to be filled in for evaluating subjective comfort and well-being, as well as physiological tests were carried out and measurements of skin temperature were taken.

3.2.2. Second series of experiments

The same measuring stand was used as in the 1st set of experiments. Ten subjects participated in the study (4 males and 6 females, mean age $= 21.3 \pm 1.5$ years). Each subject participated in 4 experimental sessions with different pre-set CO_2 concentrations (600, 1500, 3000, and 4000 ppm). Sessions succeeded each other in the following manner: session 1 (1500 ppm CO_2), session 2 (3000 ppm), session 3 (600 ppm), session 4 (4000 ppm). Two sessions (with 1500 and 4000 ppm CO_2 concentration) consisted of 2×70 minutes mental work periods. Two sessions (with 3000 and 600 ppm CO_2 concentration) consisted of 3×70 minutes mental work periods. Subjects had to perform a mental work slightly different from the mental work performed in the 1st series of experiments. Prior to and following the work

periods questionnaires were to be filled in for evaluating subjective comfort and well-being, as well as physiological tests were carried out and measures of skin temperature were taken.

The exposure time was longer only for two levels of CO_2 (600 and 3000 ppm). Periods with corresponding exposure time were compared. The measuring stand was the same as in the first session (*Fig. 1*).

3.3. Measurement of objective microclimatic characteristics

The following objective microclimatic parameters were examined:

- Measurements of CO_2 concentration were carried out with the aid of a HORIBA VIA 510 infrared gas analyzer for which the department has developed a data collector to be connected to a computer. Measurements were carried out during the entire experimental session with 30s sampling intervals.
- PMV (predicted mean vote) and PPD (predicted percentage of dissatisfied) values are objective measurements concerning thermal comfort which were conducted with a PMV meter. Data were read every 70 min in a work period.
- Temperature of the supply air, as well as temperature of exhaust air were measured with two temperature data collectors. Temperature and relative humidity in the occupied zone were also measured with the aid of a temperature and humidity data collector. Measurements were carried out during the entire experimental session, with 30s sampling intervals.
- Surface temperature of the four side walls of the floor and the ceiling was measured using a laser surface thermometer. Sampling was done at the start of the session, before the breaks, and at the end of the session.

3.4. Evaluation of subjective comfort

The following parameters were examined in the evaluation of subjective comfort:

- *Fanger scale*: subjects had to report whether they find air quality acceptable or unacceptable by marking +1 (clearly acceptable) and –1 (clearly unacceptable) on a scale (*Fanger* and *Wargocki*, 2002).
- *Hedonic scale*: subjects' comfort was measured in the range of pleasant (5) and unbearable (1) (*Fanger* and *Wargocki*, 2002).
- *Air Quality scale*: analogue scale for evaluation of freshness of the air. The endpoints of the scale were fresh and very unpleasant sensation.
- In the examination of human well-being changes in subjects' freshness, tiredness and concentration were surveyed.

The above measurements were carried out in each session at the beginning, at the end, and in the breaks between the 70 minutes working periods. These way questionnaires were filled in three times during sessions in the first series of experiments. In the second series of experiments, questionnaires were filled in three times during session 1 (1500 ppm CO_2) and session 4 (4000 ppm CO_2) consisting of two working periods, while during sessions consisting of three working periods (session 2 with 3000 ppm CO_2, and session 3 with 600 ppm CO_2), measurements were carried out four times.

The following measurements were carried out at the beginning and end of each session:

- Subjective evaluation of surface temperature of human skin: subjective thermal comfort was recorded with the help of a 7-grade scale (very hot: 3; pleasant: 0; very cold: –3) at 5 different points: forehead, nose, chest, right hand, and left hand.
- Subjective evaluation of general thermal comfort: subjects' thermal comfort was examined using an analogue scale.

3.5. Study of objective physiological parameters for humans

The following physiological and psycho-physiological parameters were measured and computed: systolic blood pressure (SBP), diastolic blood pressure (DBP), pulse rate, skin temperature.

During each session, SBP, DBP, and pulse rate have been taken at the beginning and end of the session, as well as in the pause between 2 reading periods by the aid of a wrist digital sphygmomanometer. The surface temperature of the human skin was measured with a surface thermometer at the beginning and end of the sessions (measured points: forehead, nose, chest, and both hands).

Heart periods (HP) or RR-intervals were collected continuously during sessions (HP is the time elapsed between 2 subsequent R waves of the ECG, this practically means time elapsed between adjacent heart beats). The variation of HP-s is largely determined by a balance between levels of activity of the cardiac sympathetic and parasympathetic nerves. Spectral analysis of heart period variance (HPV) allows the contributions of these autonomic nerves to be isolated providing insight into the actual balance of the activity of autonomic nerves. It has been shown (*Hyndman et al.*, 1971; *Luczak* and *Laurig* 1973; *Mulder* and *van der Meulen*, 1973; *Sayers*, 1971, 1973; *Womack*, 1971; *Akselrod et al.*, 1981, 1985;) that short-term (time-scale of seconds to minutes) fluctuations in heart periods is concentrated in several principal peaks (low-frequency (LF), mid-frequency (MF), and high-frequency (HF) components of HPV). The HF component of HPV is the so called respiratory component of HPV, it reflects the respiratory rate and it is

influenced by the volume of respiration. HF component is mediated solely by the vagus nerve, while MF component of HPV is mediated jointly by sympathetic nerves and n. vagus (*Akselrod*, 1988; *Akselrod et al.*, 1981, 1985; *Lombardi et al.*, 1987; *Pagani et al.*, 1986; *Pomeranz et al.*, 1985; *Weise et al.*, 1987). Thus, the relative power of these spectral components as well as the ratio of MF and HF components can be used to monitor the actual balance of autonomic nerves (*Lombardi et al.*, 1987; *Pagani et al.*, 1986). For more about spectral analysis of HPV see the reviews by *Láng* and *Szilágyi* (1991), *Eckberg et al.* (1997).

A number of studies has shown that increasing mental load causes a decrease in heart rate variance (*Luczak* and *Laurig*, 1973; *Mulder* and *van der Meulen*, 1973). *Sayers* (1971, 1973) found that consistent changes occur in the heart period spectrum especially in the band from 50 to 150 mHz. According to *Mulder et al.* (1973), the mid-frequency band of HPV (70–140 mHz) appeared to be more sensitive to mental workload than total variance or respiratory fluctuations.

It is believed that mental load (when the task requires explicit effort) operates like a defense reaction. The defense reaction is characterized by a decrease in sensitivity of the baroreflex which results in a decrease of HRV, because changes in the blood pressure will be less reflected in changes in HR. Defense reaction involves suppression of the vagal component of the reflex (*Mulder*, 1980).

Spectral analysis of heart period variance (HPV) is extensively used as a mental effort monitor in the field of ergonomics and psychophysiology (*Itoh et al.*, 1989; *Izsó* and *Láng*, 2000; *Izsó*, 2001; *Mulder*, 1980; *Mulder et al.*, 2000).

It was hypothesized that in unfavorable environmental conditions, such as higher concentration of CO_2 in the air, mental task might request more mental effort.

To assess the actual balance of the autonomic nervous system on the basis of spectral analysis of heart period variance (HPV), an integrated system (ISAX) has been developed and validated (*Láng* and *Horváth*, 1994; *Láng et al.*, 1994, 1997).

It consists of:

- a portable , easy to use equipment for 24-hour ambulatory measurement and storage of heart period (HP) beat by beat and, optionally, other bio-signals, plus
- a user-friendly software package for spectral analysis (autoregressive model) of the stored data in a single personal computer, algorithms to evaluate parameters of the significant spectral components of the power spectra of HPV, and plain text table output for further statistical purposes (*Láng et al.*, 1998).

The acquisition module is a small (300g) portable plastic box that can be mounted on the patient by a clip, and connected to the sensors. The ambulatory

recorded data are stored in the built in NVRAM. Two channels serve the purposes of event-marking in order to be able to identify data sequences recorded in special conditions. The recorded data are read and processed by a host computer. Processing of RR-interval series by the ISAX program consists of steps as follows: RR-interval series are interpolated for the sampling procedure (1 Hz). RR-interval time functions are displayed for interactive selection of appropriate analysis frame. A sufficiently long stationary and representative part of the RR-interval function is selected for spectral analysis. The RR-interval function marked for analysis is converted into zero-mean process. An all-pole auto-regressive model is fitted to the data set (*Akaike*, 1969; *Itakura* and *Saito*, 1969) using a modified Burg algorithm (*Gray et al.*, 1980). More compact characteristics of spectral peaks (such as central frequencies and bandwidths) are computed from the numerically determined poles of the synthesis model.

For compatibility with the conventional analysis methods, sub-band powers (low-, mid-, and high-frequency) are calculated by integrating the spectra over sub-band boundaries specified. Using default, the software calculates the spectral power (ms^2) of heart period variability for predetermined frequency ranges [low-frequency range: 10 mHz–70 mHz (LF); mid- frequency range: 70 mHz–150 mHz (MF); high-frequency range:150 mHz–450 mHz (HF)] (*Láng et al.*, 1998). In the recent study the following non-spectral and spectral parameters were computed for further statistical analysis: RR-interval mean (ms) (mean of the analysis frame), MF-power (ms^2), HF-power (ms^2) of the HPV spectrum. Relative powers were expressed in normalized units by dividing each component by the sum of their powers (sum = HF-power + MF-power). Thus, HF-relative = HF-power/sum, MF-relative = MF-power/sum.

One of the problems of spectral analysis is the issue of non-stationarity of the time series to be analyzed. In ISAX program this problem has been attacked by an approach called by *Mulder* (1988) spectral profile method. Spectral computations are carried out on short time segments (20–60 seconds.) By shifting such segments over the time series to be analyzed, and by introducing a certain overlap (90% or more), series of spectral values are obtained. Spectral power of a selected frequency band versus time is the so-called "spectral profile" of this frequency band (*Izsó* and *Láng*, 2000).

3.6. Statistical analysis

Statistical analysis on the above variables was performed using SPSS 10.00 for Windows program package. Differences between sessions, as well as changes appearing during the same session (differences between measurements of the same session) were revealed using analysis of variance with repeated measurements and

appropriate contrasts. Differences were considered significant when $p < 0.05$. More about analysis of variance see in Appendices (*Ferguson*, 1988; *Rosenthal* and *Roskov*, 1987; *SPSS Advanced Statistics 7.0 update*, 1996).

The repeated measures procedure provides analysis of variance when the same measurement is made several times on each subject or case. In repeated measures analysis, all dependent variables represent different measurements of the same variable for different values (or levels) of a within-subjects factor (*SPSS Advanced Statistics 7.0 update*, 1996).

In our case, all dependent variables represent different measurements of the same variable for different levels of CO_2 concentration in the air.

4. Results and discussion

4.1. Results of the first series of experiments

Results of the first series of experiments described in section 3.2. are discussed in this section. Concentrations of CO_2 were set at 600, 1500, 2500, and 5000 ppm.

4.1.1. Results concerning evaluation of subjective comfort

When comparing corresponding measurements of different sessions using the *Fanger scale* the analysis of variance revealed significant differences between sessions with 600 and 5000 ppm CO_2 already at the beginning of the sessions: subjects evaluated air quality less acceptable during the session with 5000 than with 600 ppm CO_2. Between sessions with 5000 and 1500 ppm CO_2 a significant difference appeared only at the end of sessions, that is after 140 minutes: subjects evaluated air quality less acceptable during the session with 5000 than with 1500 ppm CO_2 (*Fig. 3*).

Similar results were found with the *Air Quality scale.*

In the case of *Hedonic scale* subjects evaluated air with 600 and 1500 ppm CO_2 significantly less unpleasant than air with 5000 ppm CO_2.

Concerning *freshness, tiredness* scales difference between the first and the last measurements of the same session was the greatest in the case of session with 5000 ppm CO_2, showing that subjects became the most exhausted in this session. In this respect the difference between session, with 5000 and 600 ppm CO_2 concentration reached the level of significance.

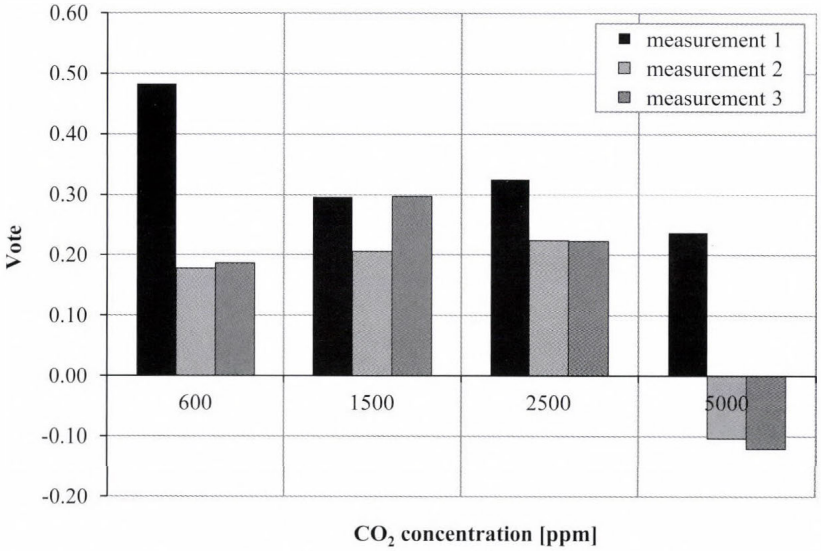

Fig. 3. Results of measurements with *Fanger scale* (acceptable {+1}, unacceptable {-1}). Measurement 1, 2, and 3 were carried out in each sessions at the beginning, before the breaks, and at the end of each session, respectively.

Fig. 4 shows the results of measurement on the tiredness scale.

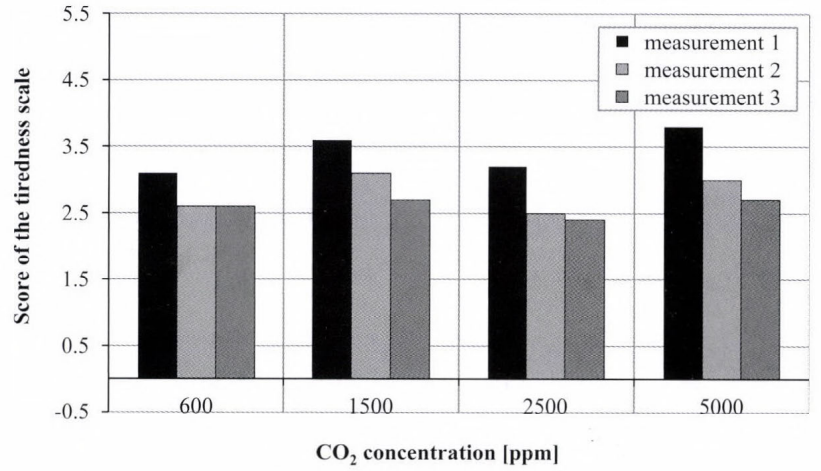

Fig. 4. Results of measurements with tiredness scale. Measurement 1, 2, and 3 were carried out in each sessions at the beginning, before the breaks, and at the end of each session, respectively.

4.1.2. Results concerning mental workload

Subjects' performance characterized by the number of rows read during the session (quantity aspect), as well as the percentage of mistakes found by the subjects (quality aspect of performance) was not significantly impacted by the degree of CO_2 concentration.

4.1.3. Results concerning physiological parameters

Heart rate (pulse rate) showed a decreasing tendency during each session. This is usually the case when subjects are sitting quietly for hours, the mental task does not require a high mental effort, and the temperature of the air does not increase substantially. The degree of this decrease of the heart rate (difference between measurements at the beginning and end of the same session) was significantly less expressed in the case of session with 5000 ppm CO_2 concentration as compared with sessions with lower CO_2 concentration. Changes of the heart rate within sessions (difference between the heart rates observed at the end (measurement 3) and beginning (measurement 1) of the same session) are illustrated by *Fig. 5.*

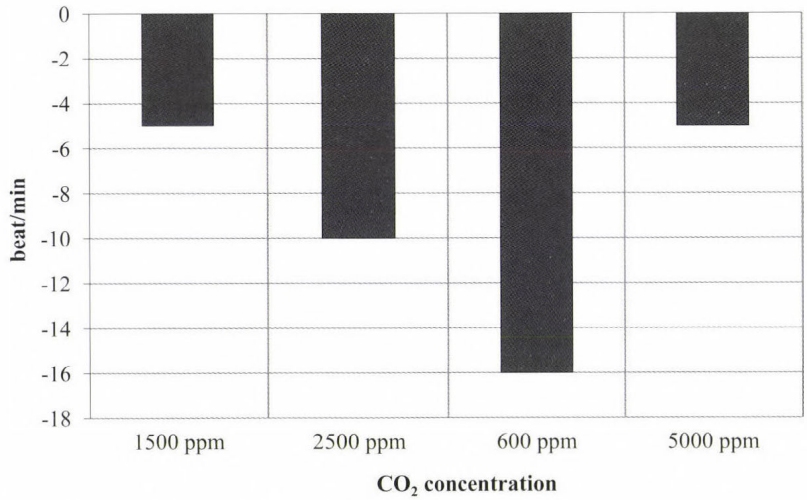

Fig. 5. Changes of the heart rate during the same session.

The analysis of variance revealed a small but significant increase of the *diastolic blood pressure (DBP)* during the session with 5000 ppm CO_2 concentration. Concerning the degree of DBP changes within sessions (difference between measurements at the beginning and end of the same session), sessions with

600 and 5000 ppm CO_2 concentration were significantly different from each other. Increase of DBP usually is caused by the increase of total peripheral resistance due to constriction of blood-vessels (vasoconstriction). It may be supposed that 5000 ppm CO_2 concentration in the air slightly raised the vasoconstrictor tone of subjects.

Fig. 6 illustrates the changes of DBP within sessions (difference between the DBP values observed at the end (measurement 3) and beginning (measurement 1) of the same session).

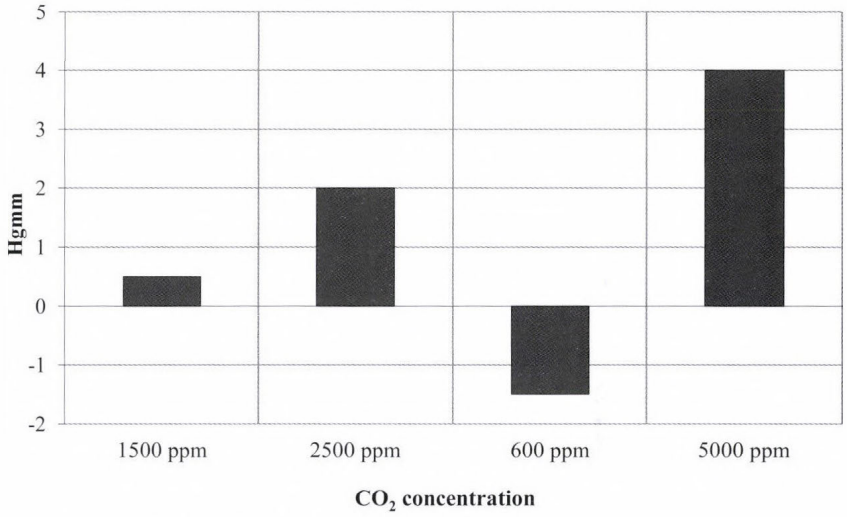

Fig. 6. Changes of DBP within sessions.

By the aid of the ISAX system, it was revealed that the respiratory frequency and the volume of respiration of the majority of subjects were higher in the session with 5000 ppm CO_2 concentration than in the session with 600 ppm. *Fig. 7* shows that the HF component of HPV was significantly higher in the session with 5000 ppm CO_2 concentration than in the session with 600 ppm CO_2 concentration.

In the case of subjects who became very exhausted according to the *freshness, tiredness* scales in the session with 5000 ppm CO_2 concentration but did not show any decrease in mental performance, the HPV analysis revealed a higher mental effort during mental load. As it was mentioned in Section 3 the suppression of MF component of HPV reflects the mental effort invested by the subjects. Thus, it

might be concluded that in the case of the above subjects the mental task might require more mental effort in unfavorable environmental conditions such as higher concentration of CO_2 in the air.

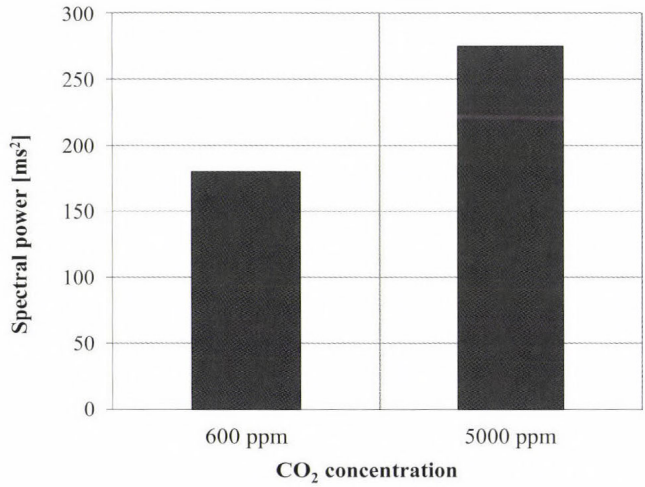

Fig. 7. Spectral power of the HF component (respiratory component) of HPV.

Similary to the measurements of skin temperature and the subjective evaluation of surface temperature and general thermal comfort, the analysis of variance did not reveal significant differences between sessions with different CO_2 concentrations.

4.1.4. Summary of results obtained in the first series of experiments

Significant differences were obtained concerning subjective evaluation of air quality and human well-being between work periods with 600 and 5000 ppm CO_2 concentration, showing a decline of well-being when CO_2 concentration in the air reaches 5000 ppm. At the same time, no significant differences were found concerning mental performance between work periods at different CO_2 concentrations. HPV analysis (MF component) revealed, however, that a mental task required more mental effort under 5000 ppm CO_2 as compared to 600 ppm. Moreover, the respiratory component of HPV reflected an increase in respiratory volume and respiratory frequency at 5000 ppm CO_2 concentration.

4.2. Results of the second series of experiments

Results of the second series of experiments described in Section 3.2. are discussed in this section. Concentrations of CO_2 were set at 600, 1500, 3000, and 4000 ppm.

4.2.1.Results concerning evaluation of subjective comfort

The analysis of variance with repeated measurements using the *Fanger scale* revealed significant differences between measurements of the same session. Subjects evaluated air quality less acceptable at the end than at the beginning of the same session. In the case of session with 600 ppm CO_2, subjects evaluated air quality less acceptable only after the second working period, while subjects' well-being already declined following the first 70-minute working period during other sessions.
Using the *Air Quality scale, s*imilar results were found as in the case of *Fanger scale.* At the same time, there were differences between the sessions. When comparing corresponding measurements of different sessions using the *Fanger scale* the analysis of variance showed that significant differences appeared between sessions only following the second working period, that is after 140 minutes. Subjects evaluated air with 3000 and 4000 ppm CO_2 significantly less acceptable than air with 600 ppm CO_2. Air with 1500 ppm CO_2 concentration was judged as significantly more acceptable than air with 4000 ppm CO_2. In the case of sessions with 600 and 3000 ppm CO_2, three 70-minute working periods were used. After the third working period (210 minutes) air was denoted significantly less acceptable during session with 3000 ppm CO_2 as compared to session with 600 ppm CO_2 (as it was the case already after 140 minutes). *Fig. 8* shows the results of measurements with the *Fanger scale.*

Using *Air Quality scale* similar results were found as in the case of the *Fanger scale*, with the only advantage, that after 140 minutes air with 1500 ppm CO_2 concentration was judged as significantly fresher than air with 3000 ppm. *Fig. 9* shows the results of measurements with the *Air Quality scale.*
The analyses of variance performed on scores on *freshness, tiredness,* and *concentration* scales revealed significant differences between measurements of the same session in the case of sessions with higher CO_2 concentration than 600 ppm, showing that subjects get more tired, became less fresh, and their capability to focus their attention was declining in the course of the session. Concerning scores on *freshness* and *tiredness* scales, when comparing corresponding measurements of different sessions, the analysis of variance showed that significant differences appeared between sessions with 600 and 3000 ppm CO_2 concentration only following the third working period, that is after 210 minutes. Subjects became more exhausted at the end of session with 3000 ppm than at the end of session with 600 ppm CO_2 concentration.

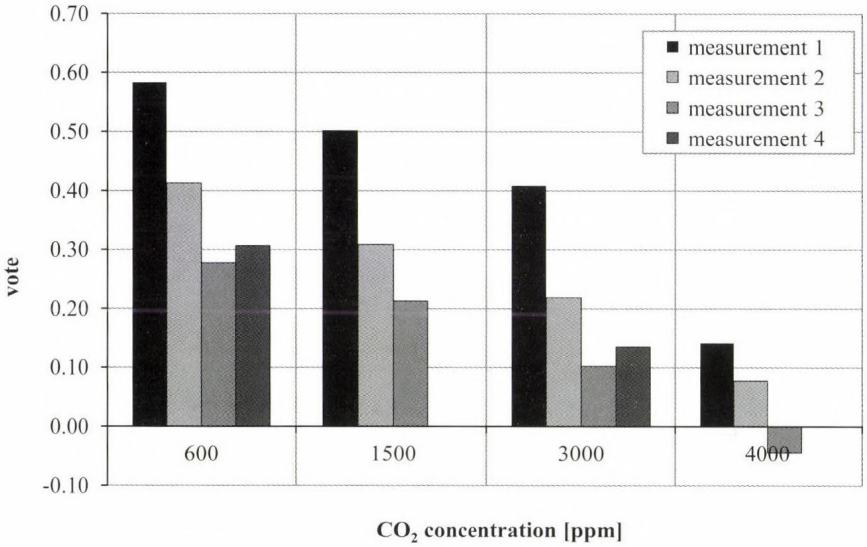

Fig. 8. Results of measurements with Fanger scale (acceptable {+1}, unacceptable {-1}). Measurement 1, 2, 3, and 4 were carried out in each sessions at the beginning, before the breaks, and at the end of each session, respectively.

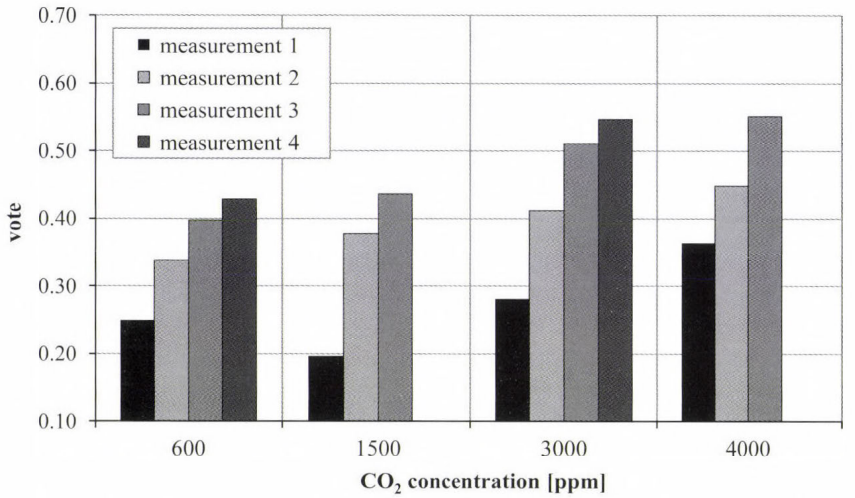

Fig. 9. Results of measurement, with *Air Quality scale* (fresh {0}, very unpleasant sensation {+1}). Measurement 1, 2, 3, and 4 were carried out in each sessions at the beginning, before the breaks, and at the end of each session, respectively.

4.2.2. Results concerning mental workload

As it was mentioned in Section 3, a different text was used in the second series of experiments. In the first series, neither the number of rows read by the subjects, nor the percentage of mistakes found by the subjects were influenced by the degree of CO_2 concentration. Therefore, we decided to use a more difficult text in the second series of experiments.

Subjects' performance characterized by the number of rows read during the session (quantity aspect) was not significantly impacted by the degree of CO_2 concentration. Concerning this variable, the *time effect* (learning) was found: subjects' performance related to the quantity of read rows increased from the first to the last session. The quality aspect of performance (percentage of mistakes found by the subjects), however, proved to be more sensitive to the concentration of CO_2. The analysis of variance revealed that during the second 70-minute working period, the percentage of mistakes found by the subjects was significantly higher in session with 600 ppm CO_2 than in the corresponding working period of session with 4000 ppm CO_2 concentration. Moreover, during the third 70-minute working period of session with 600 ppm CO_2, the percentage of mistakes found by the subjects was almost significantly higher than in the corresponding period of session with 3000 ppm CO_2 concentration. In this case, the number of rows read by the subjects in the session with 600 ppm CO_2 also exceeded the number of rows read in the corresponding period of session with 3000 CO_2 concentration. That means that the third working period with 600 ppm CO_2 proved to be more advantageous for both aspects of mental performance than 3000 ppm CO_2 concentration (*Fig. 10*).

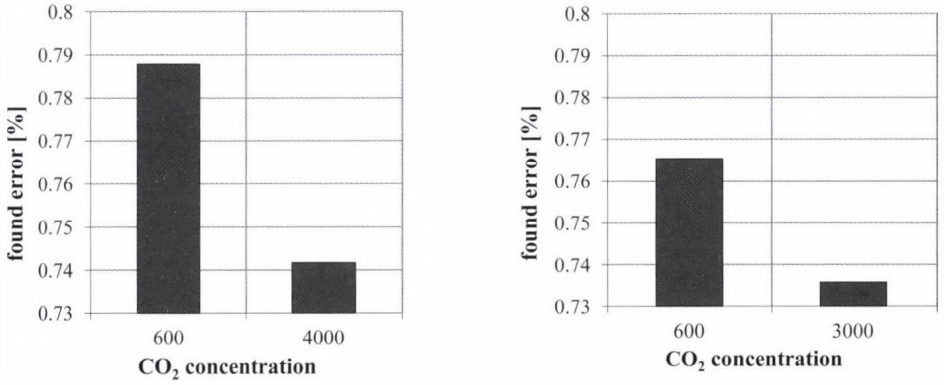

Fig. 10. Influence of CO_2 concentration on percentage of errors found by subjects in the second(left) and third(right) 70-minute working periods.

The quality aspect of mental work expresses the ability to concentrate attention. It seems that human well-being as well as the capacity to concentrate attention decline when CO_2 concentration increases up to 3000 ppm.

4.2.3. Results concerning physiological parameters

The analysis of variance did not reveal any significant effect of CO_2 concentration in air (in the range of 600 to 4000 ppm) on the systolic blood pressure (SBP), and diastolic blood pressure (DBP). In these experiments, these parameters were not sensitive enough to show the impact of CO_2 concentration in air under 4000 ppm. For this reason, in the analysis of physiological parameters we preferred to use the ISAX system, which is based on measuring heart period parameters.

The analysis of variance revealed that heart periods (HP) (time elapsed between two heart beats) increased during each session from the beginning to the end. This means that the pulse rate decreased from the beginning to the end of each session. This is a typical phenomenon when subjects are sitting quietly for hours. Concentration of CO_2 had no impact on the HP. Absolute and relative values of MF (mid-frequency component) of heart period variability (HPV) are used to measure mental effort requested by the task. The less the value of the MF component, the more pronounced the effort invested by the subjects along the mental tasks. As it was mentioned in Section 3., MF component of HPV was proposed to be used as an objective psycho-physiological measure of actual mental effort invested by the subjects (*Mulder*, 1980; *Izsó* and *Láng*, 2000; *Izsó*, 2001).

As a tendency, the lowest values of the MF component could be seen during the session with 4000 ppm CO_2, while the highest values of MF component were obtained in the session with 600 ppm CO_2. Concerning HF component, just the contrary was the case. HF component reflects the frequency of respiration and might reflect the volume of respiration. A significant difference was revealed between sessions with 600 and 4000 ppm CO_2 by the analysis of variance performed on the MF/HF ratio, as well as on relative values of MF and HF components. Increase of HF component indicates increased volume of respiration in sessions with 4000 ppm CO_2 concentration. Decrease of MF component and MF/HF ratio indicates more effort invested by the subject in sessions with 4000 ppm CO_2 concentration. This is in accordance with the declining ability to concentrate attention in sessions with 4000 ppm CO_2 as shown by the scores on *freshness* and *tiredness* scales as well as by the decrease of mental performance.

Figs. 11 and *12* show that the relative value of MF of each subject reaches a higher value in sessions with 600 ppm than in sessions with 4000 ppm CO_2.

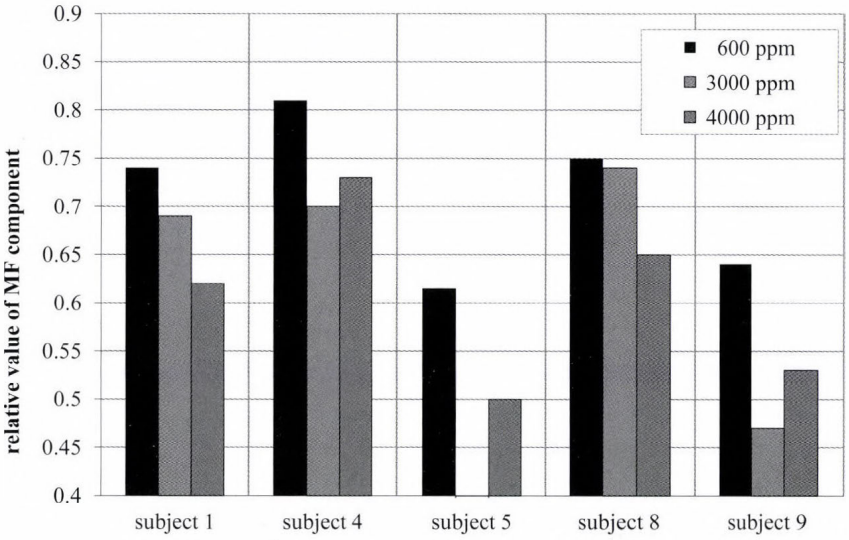

Fig. 11. Impact of CO_2 concentration on the relative value of MF component of HPV in 5 subjects.

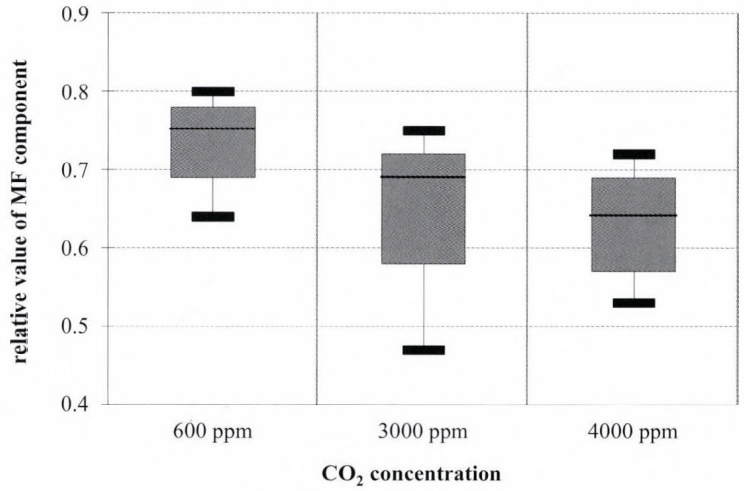

Fig. 12. The relative value of MF component of HPV in sessions with different CO_2 concentration.

Concerning measurements of skin temperature and the subjective evaluation of surface temperature and general thermal comfort, the analysis of variance did not reveal significant differences between sessions with different CO_2 concentration.

4.2.4. Summary of results obtained in the second series of experiments

Significant differences were obtained concerning subjective evaluation of air quality and human well-being between work periods with 600 and 4000 ppm CO_2 concentration after 140 minutes. After 210 minutes, significant differences appeared between work periods with 600 and 3000 ppm CO_2 concentration showing a decline in human well-being in closed spaces with 3000 ppm CO_2 concentration in the air. The same was true for results concerning mental workload: during the second 70-minute working period, the percentage of mistakes found by the subjects was significantly higher in sessions with 600 ppm CO_2 than in the corresponding working period of sessions with 4000 ppm CO_2 concentration. Concerning the third 70-minute working period, sessions with 600 ppm CO_2 proved to be more advantageous for both aspects (quantity and quality aspects) of mental performance than 3000 ppm CO_2 concentration. These results are in accordance with the objective psycho-physiological measurements of actual mental effort derived from HPV spectra.

5. Summary and conclusions

A specific laboratory and measuring stand was constructed to investigate the impact of CO_2 concentration in the air on human well-being and office work intensity, and to determine the necessary fresh air demand. Air of appropriate cleanliness, thermal comfort, as well as appropriate acoustic conditions were ensured in the laboratory.

Objective microclimatic characteristics were measured during experimental sessions. Two series of experiments were conducted with different pre-set CO_2 concentrations in the air.

Various standard scales were used in the evaluation of subjective comfort concerning air quality and human well-being changes indicating the subjects' freshness, tiredness, and concentration. Subjects participating in the investigations were performing a mental task in order to measure their mental effort and efficiency. In addition, objective physiological variables were measured. Data were processed and statistically analyzed. Experience gained from the first series of experiments was taken into consideration when designing the second series of experiments.

It was shown that subjects evaluated air quality less acceptable, more unpleasant, and they became more exhausted when CO_2 concentration increased up to 3000 ppm. 3000 ppm CO_2 concentration in the air proved to be less advantageous for mental performance than 600 ppm. Several physiological measures (spectral components of HPV) show that the mental task required more effort from the subjects when CO_2 concentration in the air reached 3000 ppm.

It was shown that human well-being as well as the capacity to concentrate attention decline when subjects spend 2–3 hours in a closed space with 3000 ppm or higher CO_2 concentration in the air.

Aknowledgements—This study was carried out in the frame of the 'Insurance of indoor air quality in climatized places, required indoor air quality and evaluation method of climate systems' project (T 029451) and received financial support from the Hungarian Scientific Research Fund.

Appendix

The analysis of variance is used to test the significance of the differences between the means of a number of different samples. The null hypothesis is formulated that the samples are drawn from populations having the same mean. Assuming that the treatments applied are having no effect, some variations are expected between means, due to sampling fluctuation. If the variation cannot reasonably attributed to sampling error, we reject the null hypothesis and accept the alternative hypothesis that the treatments applied are having an effect. With only two means, this approach leads to the same result as the obtained from the *t* test for the significance of the difference between means of two samples. If the variation between means is not small and of such magnitude that it could arise in random sampling in less than 1 or 5 per cent of cases, then the evidence is sufficient to warrant rejection of the null hypothesis and acceptance of the alternative hypothesis that the variation differs in yield. The problem of testing the significance of differences between a number of means results from experiments designed to study the variation. For this, the *F* ratio is calculated (S_b^2 / S_w^2) and referred to the table of *F*.

If the probability of obtaining the observed *F* value is small (less than 0.05 or 0.1), the null hypothesis is rejected.

Following the application of an *F* test, a meaningful interpretation of the data may require a comparison of pairs of means. These differences between some pairs may be significant, while other differences may not be. A number of alternative methods exist for making such comparisons (*Ferguson*, 1988).

Contrasts are the significance tests of focused questions. By a focused test (as opposed to an omnibus test), we mean any statistical test that addresses precise questions, as in any 1 *df F* test or *t* test. Omnibus tests, on the other hand, are tests

of significance that address diffuse (or unfocus) questions, as in F test with numerator $df > 1$. Contrasts allow us to answer planned comparisons instead of the overall analysis of variance (*Rosenthal* and *Rosnow*, 1987). In our case series, pairwise comparisons were performed between treatment means.

Contrasts are used to test the differences among the levels of a factor (in our case the factor is the CO_2 concentration in the air). Contrast types used in the study were: simple contrast (compares the mean of each level to the mean of the first or last category of the reference) and repeated contrast, which compares the mean of each level (except the last) to the mean of the subsequent level (*SPSS Advanced Statistics 7.0 update*, 1996).

References

Akaike, H., 1969: Fitting autoregressive models for prediction. *Ann. Inst. Statist. Math. 21*, 243–247.

Akselrod, S., 1988: Spectral analysis of fluctuations in cardiovascular parameters: a quantitative tool for the investigation of autonomic control. *Trends Pharmacol. Sci. 9*, 6–9.

Akselrod, S., Gordon, D., Madwed, J.B., Snidman, N.C., Shannon, D.C., and *Cohen, R.J.*, 1985: Hemodynamic regulation: investigation by spectral analysis. *Am. J. Physiology 249*, H867–H875.

Akselrod, S., Gordon, D., Ubel, F.D., Shannon, D.C., and *Cohen, R.J.*, 1981: Power spectrum analysis of heart rate fluctuations: A quantitative probe of beat-to-beat cardiovascular control. *Science 213*, 220–222.

Eckberg, D.L., Grossman, P., Kaufmann, P.G., Malik, M., Nagaraja, H.N., Porges, S.W., Saul J.P., Stone, P.H. and *van der Molen, M.W.*, 1997: Heart rate variability: Origins, methods, and interpretive caveats. *Psychophysiology 34*, 623–648.

Fanger, P.O. and Wargocki, P., 2002: Increased office productivity through improved indoor air quality. *Proceedings of Fifth International HVAC&R Technology Symposium, Istanbul, 29 April – 1 May (CD-ROM).*

Ferguson, G.A.,1988: Statistical Analysis in Psychology and Education. The Guilford Press, New York.

Gray, A.H., Wong, D.Y., 1980: The Burg Algorithm for LPC Speech Analysis Synthesis. *IEEE Trans. Tr. ASSP. 28*, 609–615.

Hyndman, B.W., Kitney, R.I., and *Sayers, B.McA.*, 1971: Spontaneous rhythms in physiological control systems. *Nature 233*, 339.

Itakura, F., Saito, S., 1969: Speech Analyzis Synthesis Systems based on the Partial Autocorrelation Coefficient. *Acoust. Soc. of Japan Meating.*

Itoh,Y., Hayashi, Y., Tsukui, I., Saito, S., 1989: Heart rate variability and subjective mental workload in flight task. In *Work with Computers: Organizational, Management, Stress and Health aspects* (eds.: *Smith* and *Salvany*). Elsevier Science Publishers B V. Amsterdam.

Izsó, L., 2001: Developing evaluation Methodologies for Human-Computer Interaction. *Delft University Press*, 2600 MG Delft, The Nederlands.

Izsó, L. and *Láng, E.*, 2000: Heart period variability as a mental effort monitor in Human Computer Interaction. *Behav. Inf. Technol. 19*, 297–306.

Kajtár, L., Erdősi, I., and Bakó-Biró, Zs., 2001: Thermal and Air Quality comfort in the Hungarian Office Buildings. *Proceedings of the Second NSF International Conference on Indoor Air Health. Miami Beach, USA, 270–278 p.*

Kajtár, L. and Hrustinszky, T., 2002: Measurements of Indoor Air Quality and Emission of Indoor Materials. *Proceedings of the third conference on mechanical engineering, Budapest, Hungary*, 362–366.

Kajtár, L. and Hrustinszky, T., 2003*:* Investigation of indoor air quality and emission of indoor used materials in Hungary. *7th International Conference Healthy Buildings, Singapore, Proc. 3. 752–757.*

Láng, E. and *Szilágyi, N.,*1991: Significance and assessment of autonomic indices in cardiovascular reactions. *Acta Physiol. Hung. 78*, 241–260.

Láng, E. and *Horváth, Gy.,* 1994: Integrated System for Ambulatory Cardio-respiratory data acquisition and Spectral analysis (ISAX). *User's manual.* Budapest.

Láng, E., Horváth, G., and *Slezsák, I.,*1997: Integrated system for ambulatory cardio-respiratory data acquisition and spectral analysis. *World Congress of Medical Physics and Biomedical Engineering*, Nice 14–19 September, *Medical and Biological Engineering and Computing 5, Suppl.*, 118.

*Láng, E., Bánhidi, L., Antalovits, M., Izsó, L., Mitsányi, A., Zsuffa, A., Magyar, Z., Horváth, Gy., Slezsák, I., Majoros, A., Dombi, I.,*and *Molnár, L.,* 1994: A complex psychophysiological method to assess environmental effects (-temperature, illumination, sound -) on objective and subjective parameters of humans in simulated work setting. *"Healthy Buildings'94". Proceedings of the 3rd International Conference,* Budapest, Hungary, 22–25. August, 799–803.

Láng, E., Caminal, P., Horváth, G., Jané, R., Vallverdu, M., Slezsák, I., and *Bayés de Luna, A.,*1998: Spectral analysis of heart period variance (HPV) - a tool to stratify risk following myocardial infarction. *J. Med. Eng. Technol. 22*, 248–256.

Lombardi, F., Sandrone, G., Pernpruner, S., Sala, R., Garimoldi, M., Cerutti, S., Baselli, G., Pagani, M., and *Malliani, A.*, 1987: Heart rate variability as an index of sympathovagal interaction after acute myocardial infarction. *Am. J. Cardiology 60*, 1239–1245

Luczak, H. and *Laurig, W.,* 1973: Analysis of heart rate variability. *Ergonomics, 16,* 85–97.

Mulder, G., 1980: "The heart of mental effort", Ph.D. Thesis, University of Groningen.

Mulder, L.J.M., 1988: Assessment of cardiovascular reactivity by means of spectral analysis. Ph.D. Thesis, University of Groningen.

Mulder, G. and *Mulder-Hajonides van der Meulen, W.R.E.H.,* 1973: Mental load and the measurement of heart rate variability. *Ergonomics 16*, 69–83.

Mulder, G., Mulder L.J.M., Meijman T.F., Veldman. J.B.P., and *van Roon, A.M.,* 2000: A psychophysiological approach to working conditions. In (Eds.) *Engineering Psychophysiology* (eds.: *R.W. Backs* and *W. Boucsein*) Lawrence Erlbaum Associates, Publishers, Mahwah, 139–159.

Pagani, M., Lombardi, F., Guzzetti, S., Rimoldi, O., Sandrone, G., Malfatto, G., Dell'Orto, S., Piccaluga, E., Turiel, M., Baselli, G., Cerutti, S. and *Malliani, A.,* 1986: Power spectral analysis of heart rate and arterial pressure variabilities as a marker of sympathovagal interaction in man and conscious dog. *Circ. Res., 59*, 178–193.

Pettenkoffer, M. v., 1858: Über den Luftweschel in Wohngebauden. Literarisch-Artistische Anstalt der J.G. Gottaschen Buchhandlung. München.

Pomeranz, B., Macaulay, R.J.B., Caudill, M.A., Kutz, I., Adam, D., Gordon, D., Kilborn, K.M., Barger, A.C., Shannon, D.C., Cohen, R.J. and *Benson, H.,* 1985: Assessment of autonomic functions in humans by heart rate spectral analysis. *Am. J. Physiol. 248;* H151–H153

Rosenthal, R. and Rosnow, R., 1987: Contrast Analysis. Cambridge University Press.Cambridge.

Sayers, B. McA., 1971: The analysis of cardiac interbeat interval sequences and the effect of mental work load. *Proceedings of the Royal Society for Medicine 64*, 707–710.

Sayers, B. McA., 1973: Analysis of heart rate variability. *Ergonomics 16*, 17–32.

SPSS Advanced Statistics 7.0 update, 1996:. Library of Congress Catalog Card Number 95–072794.

Weise, F., Heydenreich, F. and *Runge, U.,* 1987: Contributions of sympathetic and vagal mechanisms to the genesis of heart rate fluctuations during orthostatic load: a spectral analysis. *J. Auton. Nerv. Syst. 21*, 127–134.

Womack, B.F., 1971: The analysis of respiratory sinus arrhythmia using spectral analysis and digital filtering. *IEEE Trans. Biomed. Eng. 18*, 399–409.

Wyon, D.P., and Bánhidi, L., 2003: The Question of Model Size in the Research of the Indoor Environment Effects. *(in Hungarian) Magyar Épületgépészet 52 (12),* 9–10.

BOOK REVIEW

B. Cushman-Roisin and *J.-M. Beckers*: **Introduction to Geophysical Fluid Dynamics - Physical and Numerical Aspects** (second edition). Academic Press, 2011, 828 pages, 22 chapters.

Almost twenty years after the praiseful first edition, Academic Press published the enlarged and updated new edition of the Introduction to Geophysical Fluid Dynamics. B. Cushman-Roisin, the author of the first edition was joined by J.-M. Beckers as coauthor. The aim of the book is to introduce readers, first of all students and scientists in the fields of dynamical meteorology and physical oceanography, to the principles governing air and water flow on large terrestrial scales and to the basic numerical methods and simple models by which these flows can be simulated.

The book is organized into five parts. The introductory part reviews the fundamentals of fluid motion and geophysical flows, as well as diffusion and advection processes. The next two parts are devoted to the effects of rotation and stratification, respectively. Geostrophic flows, vorticity dynamics, Ekman layers, barotropic waves, and barotropic instability are described, turbulence in stratified fluids and internal waves are analyzed. The fourth part is dedicated to the combined effects of rotation and stratification, which play a very important role in the simulation of geophysical fluid processes. The final part is focused on the general circulation of the atmosphere and ocean, equatorial dynamics, and data assimilation. The authors close with a recapitulation of the elements of fluid mechanics, wave kinematics, and a survey of numerical schemes in the appendix.

Extending the content of the first edition with subjects such as turbulence closure techniques and data assimilation, and supplementing it with numerical topics, the text is written easy to understand. Each part is divided into well-organized chapters which conclude with short biographic notes of notable scientists putting science into a historical perspective. The chapters are accompanied by a set of analytical problems and numerical exercises. Useful Matlab codes necessary for some of the numerical exercises are available on the publisher's website related to the book. Unfortunately, the numerical solutions of the analytical problems are not provided. Contrary to the first edition, short descriptions of the suggested laboratory demonstrations are left out. It is very laudable that during the preparation of the book, the actual manuscript was attainable on B. Cushman-Roisin's website.

Outshining the first edition, the authors cover a broad range of topics providing an introduction to the physical principles of geophysical fluid mechanics and computational methods necessary for numerical modeling. This is an excellent textbook, the pearl of GFD literature.

Á. Bordás

INSTRUCTIONS TO AUTHORS OF *IDŐJÁRÁS*

The purpose of the journal is to publish papers in any field of meteorology and atmosphere related scientific areas. These may be

- research papers on new results of scientific investigations,
- critical review articles summarizing the current state of art of a certain topic,
- short contributions dealing with a particular question.

Some issues contain "News" and "Book review", therefore, such contributions are also welcome. The papers must be in American English and should be checked by a native speaker if necessary.

Authors are requested to send their manuscripts to

Editor-in Chief of IDŐJÁRÁS
P.O. Box 38, H-1525 Budapest, Hungary
E-mail: journal.idojaras@met.hu

including all illustrations. MS Word format is preferred in electronic submission. Papers will then be reviewed normally by two independent referees, who remain unidentified for the author(s). The Editor-in-Chief will inform the author(s) whether or not the paper is acceptable for publication, and what modifications, if any, are necessary.

Please, follow the order given below when typing manuscripts.

Title page: should consist of the title, the name(s) of the author(s), their affiliation(s) including full postal and e-mail address(es). In case of more than one author, the corresponding author must be identified.

Abstract: should contain the purpose, the applied data and methods as well as the basic conclusion(s) of the paper.

Key-words: must be included (from 5 to 10) to help to classify the topic.

Text: has to be typed in single spacing on an A4 size paper using 14 pt Times New Roman font if possible. Use of S.I. units are expected, and the use of negative exponent is preferred to fractional sign. Mathematical formulae are expected to be as simple as possible and numbered in parentheses at the right margin.

All publications cited in the text should be presented in the *list of references*, arranged in alphabetical order. For an article: name(s) of author(s) in Italics, year, title of article, name of journal, volume, number (the latter two in Italics) and pages. E.g., *Nathan, K.K.,* 1986: A note on the relationship between photo-synthetically active radiation and cloud amount. *Időjárás 90,* 10-13. For a book: name(s) of author(s), year, title of the book (all in Italics except the year), publisher and place of publication. E.g., *Junge, C.E.,* 1963: *Air Chemistry and Radioactivity.* Academic Press, New York and London. Reference in the text should contain the name(s) of the author(s) in Italics and year of publication. E.g., in the case of one author: *Miller* (1989); in the case of two authors: *Gamov* and *Cleveland* (1973); and if there are more than two authors: *Smith et al.* (1990). If the name of the author cannot be fitted into the text: *(Miller,* 1989); etc. When referring papers published in the same year by the same author, letters a, b, c, etc. should follow the year of publication.

Tables should be marked by Arabic numbers and printed in separate sheets with their numbers and legends given below them. Avoid too lengthy or complicated tables, or tables duplicating results given in other form in the manuscript (e.g., graphs).

Figures should also be marked with Arabic numbers and printed in black and white or color (under special arrangement) in separate sheets with their numbers and captions given below them. JPG, TIF, GIF, BMP or PNG formats should be used for electronic artwork submission.

Reprints: authors receive 30 reprints free of charge. Additional reprints may be ordered at the authors' expense when sending back the proofs to the Editorial Office.

More information for authors is available: journal.idojaras@met.hu

Published by the Hungarian Meteorological Service

Budapest, Hungary

INDEX 26 361

HU ISSN 0324-6329

IDŐJÁRÁS

QUARTERLY JOURNAL
OF THE HUNGARIAN METEOROLOGICAL SERVICE

Special Issue: Recent Challenges in Agrometeorology in Hungary

Guest Editors: **Angéla Anda** and **Sándor Szalai**

CONTENTS

****

http://www.met.hu/Journal-Idojaras.php

VOL. 116 * NO. 3 * JULY – SEPTEMBER 2012

IDŐJÁRÁS

Quarterly Journal of the Hungarian Meteorological Service

Editorial Office: Kitaibel P.u. 1, H-1024 Budapest, Hungary
P.O. Box 38, H-1525 Budapest, Hungary
E-mail: journal.idojaras@met.hu
Fax: (36-1) 346-4669

Indexed and abstracted in Science Citation Index Expanded™ and Journal Citation Reports/Science Edition
Covered in the abstract and citation database SCOPUS®

Subscription by

mail: IDŐJÁRÁS, P.O. Box 38, H-1525 Budapest, Hungary
E-mail: journal.idojaras@met.hu

Editorial

Recent Challenges in Agrometeorology in Hungary

Climate of Hungary is favorable for agricultural production. Any kind of agricultural productions (intensive, extensive, ecological, horticulture, etc.) needs detailed climatological, meteorological, especially agrometeorological information. Hungary had a high level agrometeorology, both theoretically and experimentally, before the change around 1990. In the first half of 90s, the strong decrease in the agriculture affected the development of the agrometeorology as well. Experimental poligons and departments were closed and experts left the branch. Recognizing the changing internal and external conditions, agriculture has an upwings in Hungary recently, both small and medium enterprises and large companies. Unfortunately, the lost expertise, information, and data bases cannot be reproduced as fast, as the production increases and it would be required. Feeling the demands of the users, the Meteorological Scientific Committee of the Hungarian Academy of Sciences (MSC HAS) decided to dedicate the annually organized Meteorological Scientific Days to agrometeorology in 2011. The disantageous situation of agrometeorology urged the organisers to invite more than usual foreigner lecturer to the connected conference. During the organizational work, a good picture has been evolved on the status of the present agrometeorology in Hungary. Benefits and gaps were detected the research level at individual topics according to the international results became more clear. The picture has positive features: many results have been archived despite of the individual, project-by-project development. Experts and/or research groups follow the main international directions on their field of interest. From the other side, there are many gaps, and some investigations are far from the international level, mostly because of the low level of resources both personally and financially. This volume contents only a small part of the presentations, but could give a first guess on some developments in the country. Many lessons have been learned. First, despite of the mosaic development of the discipline, a lot of results have been archived. This is because of the external requests, the needs of users for agrometeorological information. This leads to the second point: agrometeorology needs more support, not only from the users, but on state level, where higher level coordination is possible, and this necessity is the third lesson. Unfortunately, neither of the research groups have enough resources for a continuously high-level, wide range research production. This would be possible only by more stable supporting systems and better organization structures.

We strongly believe, that by the common efforts of the stakeholder groups, especially the groups of scientific and policy decision makers will lead the development of the Hungarian agrometeorology to get international position similarly to the past, and this publication is a small, but substantial step in this direction.

Angéla Anda and *Sándor Szalai*
Guest Editors

IDŐJÁRÁS

Quarterly Journal of the Hungarian Meteorological Service
Vol. 116, No. 3, July–September 2012, pp. 173–194

Evaluating the performance of stochastic distribution models for European beech at low-elevation xeric limits

Ervin Rasztovits[1*], Norbert Móricz[1], Imre Berki[1], Elisabeth Pötzelsberger[2], Csaba Mátyás[1]

[1]*Institute of Environmental and Earth Sciences, University of West Hungary, Bajcsy-Zs. u. 4, H-9400 Sopron, Hungary*

[2]*Institute of Silviculture, Department of Forest- and Soil Sciences, University of Natural Resources and Applied Life Sciences Vienna, Peter Jordan str. 82, A-1190 Wien, Austria*

**Corresponding author E-mail: raszto@emk.nyme.hu*

(Manuscript received in final form April 10, 2012)

Abstract—Projection for future climate conditions is an increasingly popular application of distribution modeling. However, good performance of a model under current climate does not guarantee similar performance under future climate, particularly where prediction is outside the range of environmental conditions on which the original model was set up. The objective of this study was to model the habitat suitability for beech forests during three terms (2025, 2050, and 2100) in the 21st century in Hungary using species distribution models (SDMs).

Six out of the eight methods were unsuited for predicting climate change effects on the future distribution of beech. This underlines that predictions for conservation and management issues should be based on multimodel assessments. Spatial inconsistency appeared mainly in regions, where beech is situated close to its distributional range limit (xeric limit). This suggests that the basic theoretical assumption of species distribution models may not hold at the trailing edge.

Key-words: beech, Hungary, climate change, xeric limit, Ellenberg's climate quotient

1. Introduction

Fagus sylvatica L. is one of the dominant tree species in central European temperate forests with high physiological tolerance and competitiveness

(*Ellenberg et al.*, 1992). Drought sensitivity is assumed to be a key factor limiting growth and distribution of beech close to its lower distributional limit (xeric limit) (*Mátyás et al.*, 2009) in southern and south-eastern Europe (*Backes* and *Leuschner,* 2000).

Several studies suggested a decline in beech regeneration (*Rennenberg et al.*, 2004*; Penuelas et al.*, 2007) or extensive beech dieback (*Berki et al.*, 2009*; Czúcz et al.*, 2010*; Kramer et al.*, 2010*; Lindner et al.*, 2010) under increasingly adverse climatic conditions (*Gálos et al.*, 2007). Consequently, modeling the vitality response of beech to predicted changes of climate is a critical issue (*Franke* and *Köstner,* 2007; *Mátyás,* 2009).

For management and conservation issues (*Hannah et al.*, 2002), species distribution models (SDMs) have been extensively used. SDMs derive the species' environmental envelope from the observed conditions at the localities where it is currently known to occur. They can be evaluated for their ability to predict current distributions, but it is not tested whether models that are successful in predicting current distributions are equally powerful in predicting distributions under different climates. Studies comparing modeling algorithms are now common (*Segurado* and *Araujo,* 2004; *Elith et al.*, 2006; *Tsoar et al.*, 2007), but *Thuiller et al.* (2004) have pointed out the problem of strong variation between SDM predictions for future distributions. SDMs are 'statistical' models without specific ecological knowledge, they do not describe 'cause and effect' between model parameters and response (*Guisan* and *Zimmermann*, 2000; *Pearson* and *Dawson,* 2003; *Kearney* and *Porter,* 2004).

In this study, we compared and evaluated the results of eight SDMs for beech (*Fagus sylvatica* L.). Beech is considered a climate sensitive species, which is uniquely vulnerable in south-eastern Europe and, therefore, well suited for modeling. Another advantage is that compared to other tree species in Hungary, its populations are in a relatively undisturbed condition as they were rarely regenerated artificially, and the species' reproductive material was not subject to commercial relocations (*Mátyás et al.*, 2010). Modeling focused on its distribution in Hungary, since here the retreat of the species is imminent. This ecologically and climatically specific area has been largely neglected by European studies (*Jump et al.*, 2009; *Lindner et al.*, 2010; *Mátyás*, 2010).

We address the following questions:

1. Which SDM can best describe the present distribution of beech in Hungary?
2. What are the projections for the potential future distribution of beech using SDMs?

To answer the research questions we modeled the current and potential future distribution of beech in Hungary using SDMs, and compared the performance of the different methods.

2. *Material and methods*

There are many environmental niche modeling packages available; for example, MaxEnt (*Phillips et al.,* 2006), GARP (*Stockwell* and *Peters,* 1999), ModEco (*Guo* and *Liu,* 2010), BIOMOD (*Thuiller et al.,* 2009), and Openmodeller (*Munoz et al.,* 2009).

The primary reason to choose ModEco (*Guo* and *Liu,* 2010) was that it contains models for dealing with presence-only and presence/absence data. Additional advantages of ModEco are tools for feature analysis, and model performance evaluation, as well as an accuracy assessment tool. As ModEco incorporates several modeling methods, the training, analyses, and assessments can be carried out on the same platform supporting consistent comparisons.

A disadvantage of the platform is that a trained model needs new environmental surfaces for climate change predictions, which slows down the process (*Fig. 1*).

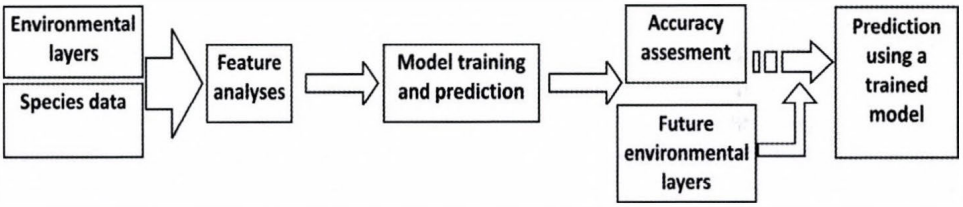

Fig. 1. General workflow of the modeling process.

2.1. *Environmental variables*

96 different environmental predictor surface maps were used as input, all with a spatial resolution of 0.0083 (appr. 1×1 km). Environmental variables were selected according to their relevance to tree survival and growth. Climatic variables were taken as surrogates for variables having more direct physiological roles in limiting the ability of plants to survive.

Although the main environmental data used were climate data, soil and geomorphological factors were also included. Soil texture and moisture regimes are indirect variables considered as surrogates for soil type, with direct impacts on nutrient and water availability for plant growth (*Austin* and *Smith, 1989*). Geomorphological factors were used as surrogates for sites in non-zonal positions.

2.2. *Soil data*

Three soil variables (soil texture, soil moisture regime, and genetic soil type – *AGROTOPO*, 2002) and three topographical factors (mean altitude, slope, and dominant orientation) were applied.

2.3. Climatic data

The dataset included monthly maximum, minimum, and mean temperatures, and monthly precipitation (48 variables in total); and a set of 19 climate-derived variables obtained from the "worldclim" database (*Hijmans et al.*, 2005).

2.4. Bioclimatic indices

12 bioclimatic factors (23 variables in total) computed from minimum and maximum monthly averaged temperatures and monthly precipitations were used (*Table 1.*). These bioclimatic predictors are: thermicity index (*Rivas-Martínez*, 1996), ombrothermic indices (*Rivas-Martínez,* 1990), de Martonne aridity index (*de Martonne,* 1942), Ellenberg quotients (*Ellenberg,* 1986; *Ellenberg*, 1996), monthly potential evapotranspiration (*Thornthwaite,* 1948), Box moisture index of precipitation/evapotranspiration (*Box,* 1981), continentality indices (*Gorczinski*, 1920; *Emberger*, 1930), forest aridity index (*Führer*, 2010; *Führer et al.,* 2011), and beech tolerance index (*Berki et. al,* 2009).

2.5. Species data

Species data for the habitat modeling were derived from the Hungarian Forest Inventory database provided by the Central Agricultural Office. The database incorporates every forest subcompartment containing beech. (A tree species is registered in a forest subcompartment, if the mixture ratio of the given tree species exceeds the 5% threshold limit.) These subcompartments were considered in the model as "true - presence" observation points (in total 11,332 subcompartments). For the presence-absence methods, "pseudo-absence" points were created randomly throughout the country with a buffer zone of 1000 m around the presence points. The size of the buffer zone was determined according to the spatial resolution of the environmental layers. The amount of pseudo-absence points was equal to the number of the presence points. As the environmental data were given in a 1×1 km grid, distribution maps were also converted to a raster format with the same resolution.

At this point it should be emphasized, that forests in Hungary are managed forest, and therefore, the presence/absence of beech is human influenced.

2.6. Future climate

The downscaled "Climate Limited Area Modeling" (CLM) regional climate model was applied for simulation of future vitality condition of beech using the A1B scenario (mean of two runs) with a grid size of 0.2 for the period 2000–2100 (*Keuler et al.*, 2009). Downscaling to regional level requires some assumptions, e.g., GCM biases are small at boundary locations or regional

dynamics are non-linear and add uncertainty or biases or both due to detailed parameterizations (*Wu et al.*, 2005)).

CLM model data were corrected using the delta change approach (*Hay et al.*, 2000), based on the mean deviation of the observed and simulated variables between 1960 and 2000 for each grid box. Corrected long-term averages from monthly air temperature and precipitation were derived by kriging interpolation considering the elevation for the periods 2011–2040, 2036–2065, and 2066–2095.

Table 1. Bioclimatic variables

Bioclimatic predictors	Formula or reference
Beech tolerance index (BTI)	$= (0.2P_3+0.5P_4+P_5+P_6+P_7+0.8P_8) / T_{6-8}$
Box moisture index (BMI)	= P/PET
Continentality index (CONTINENTY)	$= T_{max}-T_{min}$
De Martonne aridity index (DMI)	$= [(P/T+10)+12p/(t+10)]/2$
Ellenberg index (EQ)	$= (T_{max}/P)1000$
Forest Aridity Index (FAI)	$= 100(T_{7-8})/(P_{5-7}+P_{7-8})$
Gorczinski's continentality index (GCT)	$= ((1.7A)/(\sin L)) - 20.4$
Modified Ellenberg index (EQm)	$= (T_{max}/P_{veg})\ 1000$
Ombrothermic index (Io)	$= (P_p/T_p)10$
Ombrothermic index of the summer quarter (Iosq)	$= (P_{6-8}/T_{6-8})/10$
Thermicity index (It)	$= (T + m + M)10$
Thornthwaite's formula (PET)	$= 16N_m\left(\frac{10\bar{T}_i}{I}\right)^a, \quad I = \sum i_m = \sum\left(\frac{\bar{T}_i}{5}\right)^{1.5}$ $a = 6.7*10^{-7}*I^3 - 7.7*10^{-5}*I^2 + 1.8*10^{-2}*I + 0.49$

T_{max}: mean temperature of the hottest month [°C]
T_{min}: mean temperature of the coldest month [°C]
P: annual precipitation [mm]
T: mean annual temperature [°C]
P_i: precipitation sum of the given month [mm]
P_{ii}: precipitation sum of the given months [mm]
T_{ii}: mean temperature of the given months [°C]
p: precipitation of the driest month [mm]
t: mean temperature of the driest month [°C]
PET: annual accumulated potential evapotranspiration calculated by the Thornthwaite equation [mm]
A: mean annual air temperature amplitude [°C]
L: latitude of the site [absolute value]
P_{veg}: precipitation sum of the vegetation period [mm]
P_p: Yearly Positive Precipitation [mm] (total average precipitation of those months whose average temperature is higher than 0°C)
T_p: Yearly Positive Temperature [°C] (sum of the monthly average temperature of those months whose average temperature is higher than 0°C)
m: average minimum temperature of the coldest month of the year [°C]
M: average maximum temperature of the coldest month of the year [°C]
N_m: monthly adjustment factor related to hours of daylight [–]
I: heat index for the year [–]

2.7. *Modeling algorithms*

We evaluated and compared the following eight methods: "presence-only" methods such as BioClim (*Nix*, 1986; *Busby*, 1991), Domain (*Carpenter et al.*, 1993), and one-class support vector machine (SVM) (*Vapnik*, 1995); „presence-absence" classification methods such as generalized linear model (GLM), artificial neural network using back-propagation algorithm (BP-ANN, *Maravelias et al.*, 2003), maximum likelihood classification (*Richards* and *Jia,* 1999), maximum entropy (MAXENT, *Phillips et al.*, 2006), and classification tree (CTree, *Breiman et al.*, 1984).

2.8. *Accuracy assessment*

Cross-validation accuracy, area under the receiver operator curve (AUC), receiver operating characteristic (ROC), error matrix and maximum kappa values were used to assess the accuracy of presence/absence-based models (*Wiley et al.*, 2003; *Elith et al.*, 2006). For presence-only models, the above mentioned measures are not applicable, therefore, the true positive rate (TPR) vs. the factional prediction area (FPA) as a proxy for true positive rate vs. false positive rate, and the area under TPR vs. FPA were used (*Guo et al.*, 2005; *Phillips et al.*, 2006).

2.9. *Factor analyses*

Factor importance analysis was carried out to examine the contributions of different environmental factors (with-only and without a specific environmental factor) to the overall classification accuracy of SDMs, based on the kappa values (*Forman*, 2003). This importance analysis is designed to evaluate the change of classification accuracy of the model (*Phillips*, 2006).

Some models (i.e., Maximum likelihood, Domain) are sensitive to the number of the predictors therefore, the reduction of environmental factors was essential in some cases. Redundant environmental layers were identified via pairwise correlations. Variables with a correlation higher than 0.8 were considered redundant. Between any two redundant variables, those related to climate extremes were preferred.

3. Results

3.1. Performance of presence-only methods

3.1.1. Potential current distribution

Presence-only methods showed marked variation in modeling success. Although *TPR* was very similar, the predicted area varied a lot among the models. Using the accuracy measures of presence-only data, the one-class SVM performed better (*TPR*: 0.794) for predicting current distribution than BioClim and Domain, but the predicted area was also greater. If we also consider the specifically generated pseudo-absence points during the assessment and penalize the false negative predictions by using the *ROC* score (true positive rate vs. true negative rate), Domain showed the best performance (*Table 2*).

Table 2. Parameters and statistical performance of presence-only methods for predicting potential current distribution of beech in Hungary

Models	Parameters	Number of layers	True positive rate (TPR)	Predicted area	*TPR* vs. predicted area	*ROC*
BioClim	percentile: 96%	88	0.708	1.004	0.8924	0.898
Domain	similarity: 0.995	64	0.765	0.987	0.7264	**0.933**
One-class SVM	Nu:0.064 Gamma: 27.6	65	**0.794**	**1.318**	**0.9046**	0.909

There were significant regional differences between the modeled potential and the actual distribution. While BioClim, the simplest climate envelope model, predicted in total almost the observed suitable area, there still were regional biases. BioClim notably overpredicted in the Southwest (Zala county, south from Szombathely) and Northeast (Cserhát, north from the Mátra Mountains), but also a smaller patch north form the lake Balaton (Balaton-felvidék) was predicted as suitable for beech. BioClim systematically excluded the marginal sites (Mátra, Bükk, Zemplén, Kőszeg, Sopron, and Börzsöny Mountains, Mura Valley) and also failed in the Őrség and Aggtelek Karst. One-class SVM performed regionally similarly to BioClim, only the magnitude of the overprediction was greater. Domain predicted very precisely the current distribution of beech, almost all observation point were enclosed in the potential area (*Fig. 2–3*).

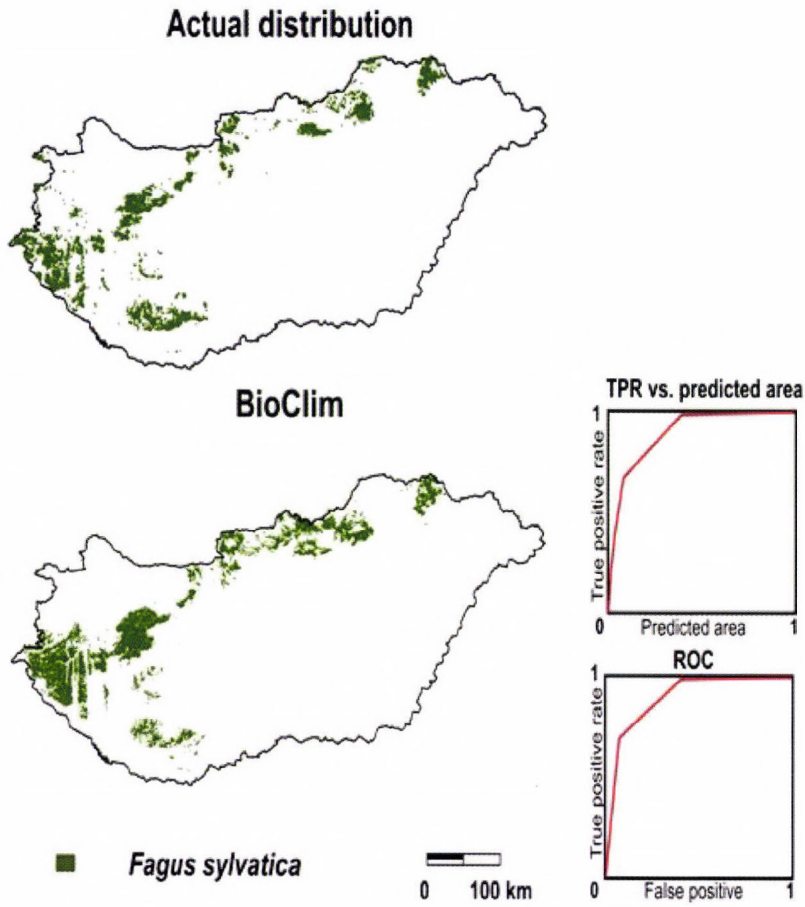

Fig. 2. Actual distribution and potential current distribution modeled by BioClim and the related operating curves. Green color represents observed localities of beech in the first map and areas modeled as suitable in the potential maps.

3.1.2. Future distribution

While the presence-only methods performed fairly well describing the current distribution of beech, all three methods were unsuited for predicting climate change impacts. BioClim and Domain removed all beech even for the near future (2011–2040), while one-class SVM predicted potential occurrence only for regions under sub-Mediterranean and subcontinental influences.

Prediction with Domain and BioClim was only possible when the number of the environmental predictors was strongly reduced.

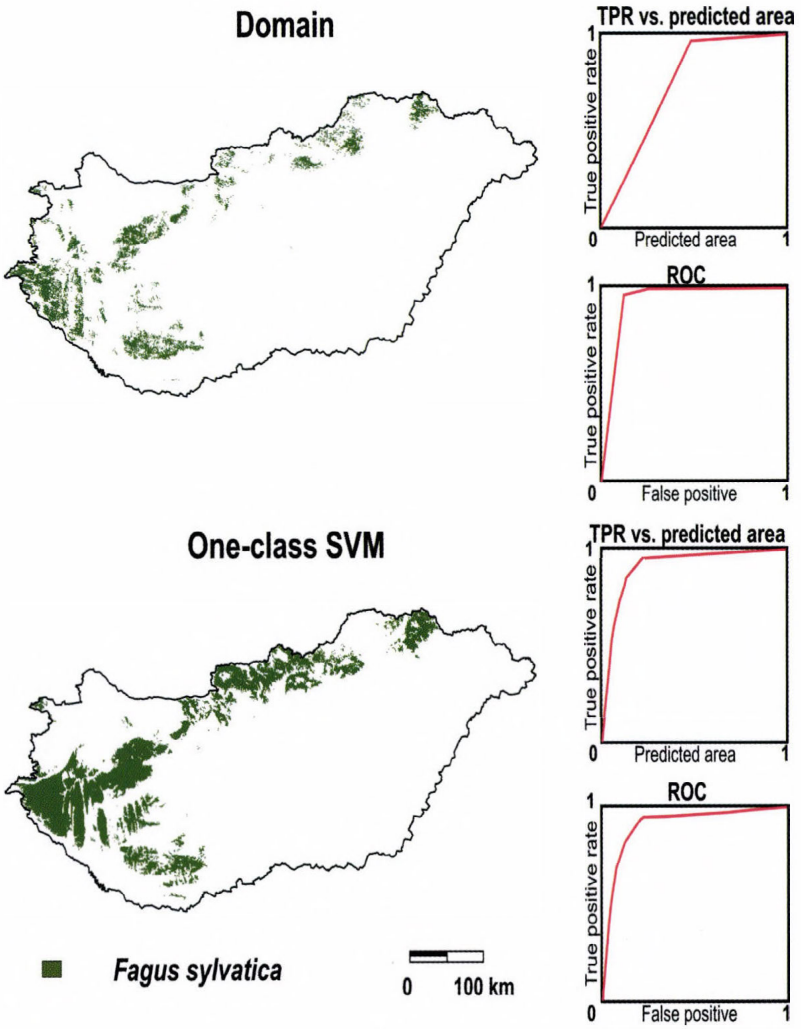

Fig. 3. Potential current distribution modeled by Domain and one-class SVM and the related operating curves. Green color represents areas modeled as suitable for beech.

3.2. Performance of presence/absence classification methods

3.2.1. Potential current distribution

Presence/absence classification methods outperformed presence-only models, the TPR and also the kappa score was higher in all cases (*Table 3*).

Table 3. Parameters and statistical performance of presence/absence models

Model	**Parameters**	**True positive rate (*TPR*)**	**Predicted area**	**Kappa index**
Artificial neural network with backpropagation (BP-ANN)	Momentum: 0.3 Learning rate: 0.1	0.9425	1.2096	**0.8336**
Classification tree (CTree)	Number of trails: 10 Window size: 20 Pruning confidence level: 0.25	0.9493	1.3196	**0.8431**
General linear model (GLM)	Link function type: LOGIT Threshold: 0.426	0.9592	1.6237	0.8174
Maximum entropy (MAXENT)	Omission rate: 0.05	0.9395	1.4362	0.8145
Maximum likelihood (MLC)	No parameter required	0.9415	1.5205	0.8076

MAXENT, MLC, and GLM performed relatively poorly, only GLM had high TPR (0.959), which was due to its strong overprediction of the species area (1.623). CTree and BP-ANN methods performed significantly better than the other models. The high *TPR*, the smaller predicted potential area, and the high kappa score indicated that these models are able to capture non-linear responses and can handle interactions between the variables.

Visually, the CTree model created a more dispersed potential area, while the BP-ANN model produced a less fragmented distribution with more distinct boundaries (*Fig. 4*).

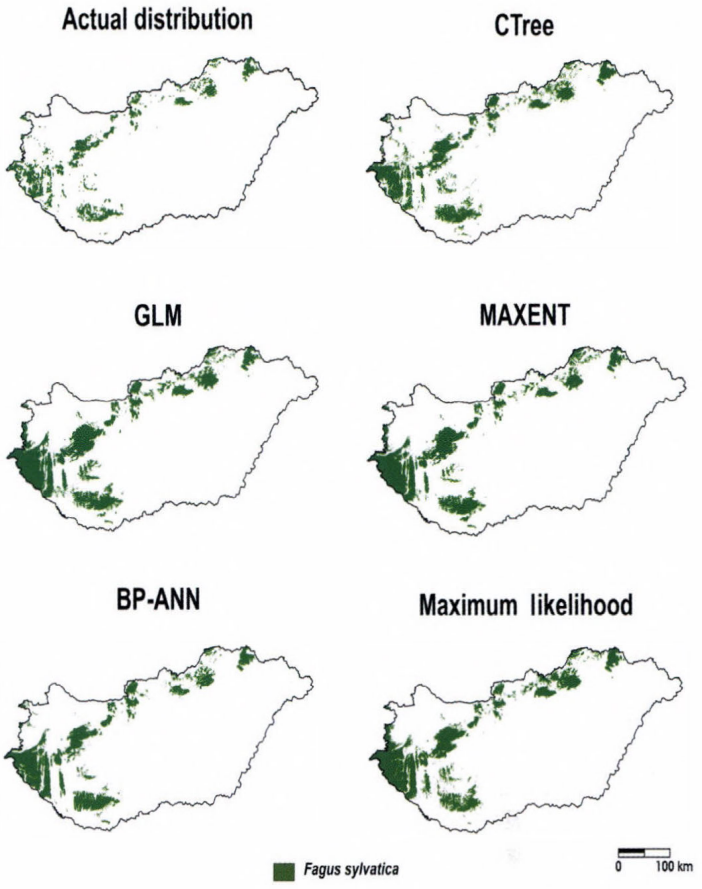

Fig. 4. Actual distribution and potential current distribution modeled by BP-ANN, CTree, GLM, MAXENT, and Maximum likelihood methods. Green color represents observed localities of beech in the top left map and areas modeled as suitable in the potential maps.

3.2.2. Future distribution

The Maximum likelihood method predicted complete extinction of beech for the whole country for the period 2011–2040. GLM overpredicted the distribution of beech in the near future, and marked regions as potential area, which are already out of the current distribution range. MAXENT predicted a considerable dieback even for the near future removing more than 91.6% of the current stands.

BP-ANN predicted almost no reduction in the potential area for the period 2011–2040 and a very slight (8.0%) for 2036–2065. A considerable shrinkage (56.8%) of the potential area was predicted only to the end of this century, which results that 45.2% of the current stands will be out of the potential area. Regionally, the most serious decrease was predicted for the sub-Mediterranean region in the Southwest.

CTree predicted a more pronounced shrinkage in all regions of Hungary by losing 37.3%, 67.5%, and 74.7%, respectively (*Fig. 5*).

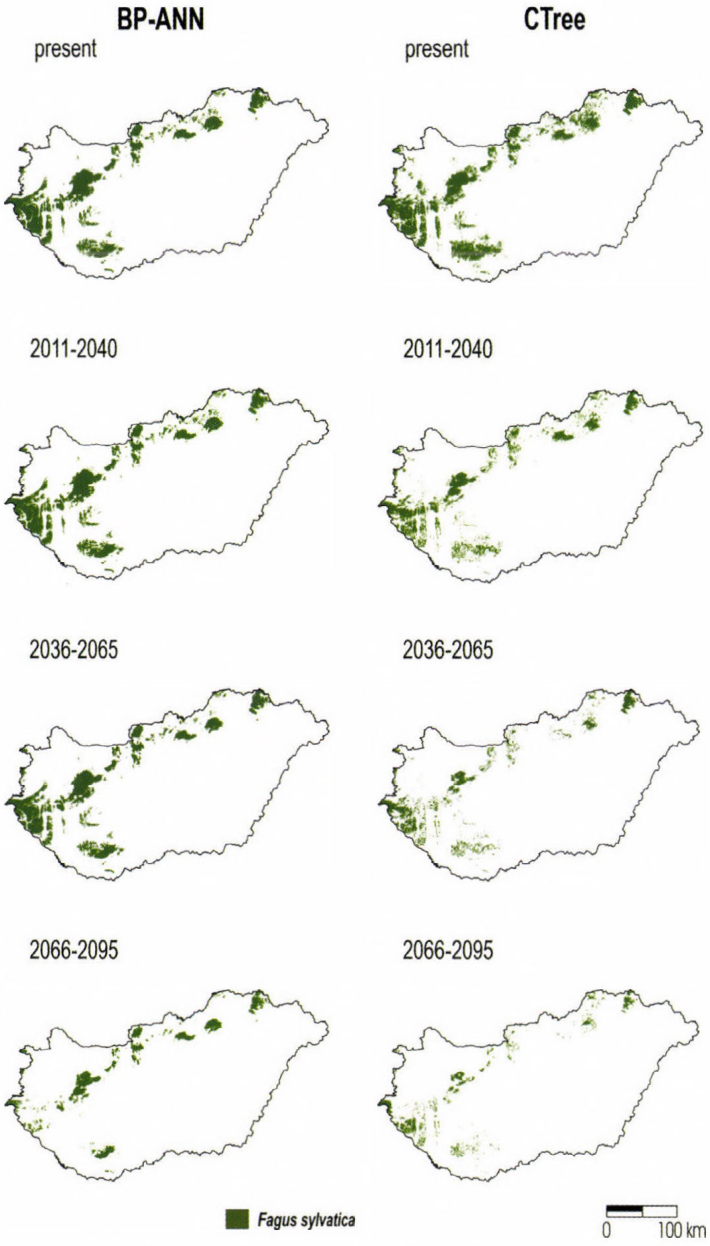

Fig. 5. Potential distribution modeled by BP-ANN and CTree for present and future conditions (2011–2040, 2036–2065, and 2066–2095, respectively). Green color represents areas modeled as suitable for beech during the given periods.

3.3. Factor importance analysis

Factor importance analysis is algorithm-sensitive, but among the environmental variables, the maximum temperature of May and the modified Ellenberg quotient appeared repeatedly as the most influential predictor. In addition, maximum temperatures of summer and precipitation of late summer played a significant role in determining the presence of beech (*Table 4*).

A climate quotient to characterize the humidity conditions of beech and oak forests was first suggested by *Ellenberg* (1986). He defined the climate quotient *EQ* as the quotient of the mean air temperature of the long-term hottest month per year and the annual precipitation sum. Later this quotient was changed to include a definition of the forest's growing period *(EQm)*, taking into account only the precipitation of the growing season (*Ellenberg, 1996*). This climate quotient has been successfully applied to separate areas dominated by beech from areas of boreal or thermophilic species (*Schlüter, 1968; Hofmann, 1968; Jensen et al., 2004; Czúcz et al., 2010*). *EQ* has been also used to evaluate sites of mixed beech-oak stands for studies of carbon and water relations (*Franke* and *Köstner, 2007*).

Table 4. The overall classification accuracy of the models and the most predictive five factors with their related kappa values resulting from the factor importance analyses. The repeatedly occurring predictors are in bold

Rank	Models							
	BioClim		**One-Class SVM**		**CTree**		**GLM**	
	Predictor	**kappa**	**Predictor**	**kappa**	**Predictor**	**kappa**	**Predictor**	**kappa**
	overall	0.611	overall	0.788	overall	0.843	overall	0.817
1.	**EQm**	0.570	**EQm**	0.533	**Tmax_05**	0.717	**Tmax_05**	0.708
2.	**Tmax_05**	0.565	Prec_09	0.511	Tmax_06	0.707	Tmax_06	0.697
3.	BMI	0.555	**Tmax_05**	0.491	Tmax_08	0.704	Tmax_07	0.673
4.	Prec_09	0.544	Tmax_08	0.544	Tmax_04	0.704	**EQm**	0.670
5.	IO	0.534	Prec_08	0.451	**EQm**	0.673	Tmean_05	0.664

4. Discussion

Overall, the BP-ANN method showed the highest model performance, whereas similarity- and ordination-based models (DOMAIN, BioClim, one-class SVM) showed the lowest performances by predicting the potential future distribution of beech. While some authors (e.g., *Mastrorillo et al.,* 1997; *Pearson et al.,* 2002) also consider BP-ANN to be advantageous to model species occurrences, these observations are not supported by other studies, where BP-ANN showed overall performances comparable to GLM (*Manel et al.,* 1999). Other studies also showed that similarity and ordination-based methods perform less well than

advanced techniques, namely CTree and BP-ANN (*Elith* and *Burgman,* 2002). Since these studies did not always use the same parameterization, they are, however, not fully comparable.

4.1. Actual and potential current distribution

BioClim treats the environmental data values at the locations of species occurrence as multiple one-tailed percentile distributions. It creates hyperboxes to include a given percentile for each variable so that, for example, the fifth percentile is treated the same as the 95th percentile. This results in an approach in which locations with extreme conditions (wettest – driest, hottest – coldest, etc.) are considered as outliers. This is the reason, why BioClim obviously failed at the top of the mountains in the Northwest (coldest sites of Börzsöny, Mátra, Bükk, and Zemplén Mountains) and at low elevation sites in Zala (Mura Valley).

Domain is a similarity based model, which uses the Gower distance method to classify the suitability of any new sites. The more variables are incorporated, the more accurate is the similarity assessment of a new site. The calculation was very time consuming, but resulted in a very precise prediction with a high accuracy rate.

BioClim uses only hyperboxes to contain the presence data. Thus this model is often unsuitable for other forms of data that have irregular distributions in feature space. Therefore, one-class SVM was also applied. One-class SVMs seek to find an optimal hypersphere which contains all or most of the training points, at the same time tightly constraining the presence data in feature space. Originally, SVMs are designed for 2-class problems (separating two types of data) and optimized for working with low number of predictors. The relatively high number of the environmental variables produced a very complex distribution pattern which resulted in greater overprediction.

Although CTree has clear advantages over classic climate envelope methods, certain disadvantages emerged. CTree appeared to be very sensitive to the number of predictors. Even small changes produced highly divergent results. The dispersed potential map of CTree could be a sign of overfitting, which means, that the model is too specific (unbalance of specificity and sensitivity).

Except Domain, all models predicted larger potential area than the current distribution. The systematic overprediction of the models might be explained mainly by the following factors:

Human interaction: After the post-glacial recolonization, a general reduction of the distribution of tree species occurred as a result of deforestation and land use change. Due to the low-altitude occurrence of beech in the Southwest, beech forests were often transformed through human land use (plough-land, populated places). In the mountainous areas, human impact on beech forests has been traditionally low (cold and moist areas are unsuitable for

agriculture), however, the low-elevation beech forests were often converted into oak forests (pasture).

Lack of soil data: Beech can be found on a wide scale of soil types from acidic to calcareous. However, beech is not able to tolerate quick changes of dry and wet soil conditions. Although, soil data were considered in the study, fine-scale soil information for forests was not available. Therefore, some models (BioClim, one-class SVM, GLM) assessed the macroclimate as suitable for beech in the west part Hungary. Nevertheless, its occurrence is often hindered by reduced aeration or unfavorable physical and textural characteristics of the soil.

Competition and other biotic interactions: Competition is an important mechanism that is absent from SDMs. Competitive tree species as predictors were not included in this work. Even if applying occurrence data of competitive species could enhance model performance by predicting current potential distribution, such reliable information is not available for the future (future distribution of competitors). We hypothesized that the occurrence of competitive tree species could be surrogated by applying a wide range of environmental predictors during the modeling.

Beside competition, other biotic interactions should be also considered, such as facilitation, pollination, herbivory, or symbiosis. However, databases for these factors do not exist.

Extreme events: Most SDMs are calibrated under the assumption that range margins are formulated by climatic means. The association of range margin and climatic mean may not hold when climatic extremes occur with a skewed frequency distribution, thus, predictions based on climatic means alone could overestimate ranges. The inclusion of real extreme measures could be especially important along the trailing edge (xeric limit) of the distribution (*Zimmermann et al.,* 2009).

4.2. Future potential distribution

The mathematical properties of the models can help to explain the differences in their predictive performance. The most important reason for the underprediction of BioClim is that the model is very sensitive to the occurrence of variables that are outside of what was observed as the current climate, even if this is not truly a limiting factor (*Tsoar et al.,* 2007). In Domain, all occurrence points are treated separately and, unlike in the other models, there is no generalization (creation of response functions). Domain is, therefore, very sensitive to the occurrence of new combinations of the environmental predictors, and this negatively affects its predictive ability. One-class SVMs are able to represent very irregular data distribution shapes without making assumption on the probability density of the data (*Tax* and *Duin,* 2002), which allowed better performance during prediction.

Presence-absence classification models seemed to be able to predict species distributions better under current and novel combinations of climate than

presence-only methods. GLM performed relatively poorly due to the lack of flexibility (*Austin,* 2002). MAXENT uses an exponential model for probabilities, and gave very large predicted values for environmental conditions outside the range present in the training set (*Phillips et al.,* 2006). CTree provided the best statistical performance describing the current distribution among all models, although the predictions for the future showed regional inconsistency, especially in the Southwest and Northeast. The relatively good predictive performance of CTree could be explained by the ability of finding interactions and hierarchical relations among environmental variables (*Hastie* and *Tibshirani,* 1990; *Austin,* 2002).

BP-ANN significantly outperformed CTree in the domain of predicting the future potential distribution of beech. Although BP-ANN performed slightly poorer than CTree by predicting the current potential distribution, the predictions for the future were more realistic without regional inconsistency. The larger predicted area and the distinct boundaries in the future potential maps of BP-ANN indicated that the generalization ability of BP-ANN was clearly superior to that of CTree. One possible explanation for the difference in the predictive performance is that complex features that are constructed allow non axis-parallel and nonlinear decision boundaries.

The results of this investigation provide clear support to the preference for neural networks in at least this type of bio-informatics problems.

4.3. Regional differences

Model accuracy can be measured not only on the country scale (overall model performance), but also at a finer (regional) scale. Accuracy measures like *TPR*, *AUC*, Kappa values and predicted area can be assessed also across different forest regions. The regional analyses of the model performance enable the assessment of SDMs under different climatical/ecological conditions.

Hungary stretches across three climate regions. Southwest Hungary is under strong Mediterranean influence, northwest Hungary is subatlantic, while the north-eastern part is more continental. The soil and hydrological conditions that sustain the forest vary greatly. As a result, Hungary features 6 main forest regions and 54 forest regions, each supporting characteristic tree species and forest types.

The breakdown of the accuracy measures for forest regions indicated that false negative rates (overprediction) of the BP-ANN and CTree model were higher in Mecsek Mountains, Göcsej Hills, Őrség, east Zala Hills, Marcali Ridge, and west Zselic than the overall false negative rate by predicting the current potential distribution (*Fig. 6*). Beech in the above mentioned forest regions reaches its lower xeric distribution limit (trailing edge). The Mecsek Mountains, east Zala Hills and west Zselic were already affected with large-scale beech decline after 2003,(*Lakatos* and *Molnár*, 2009).

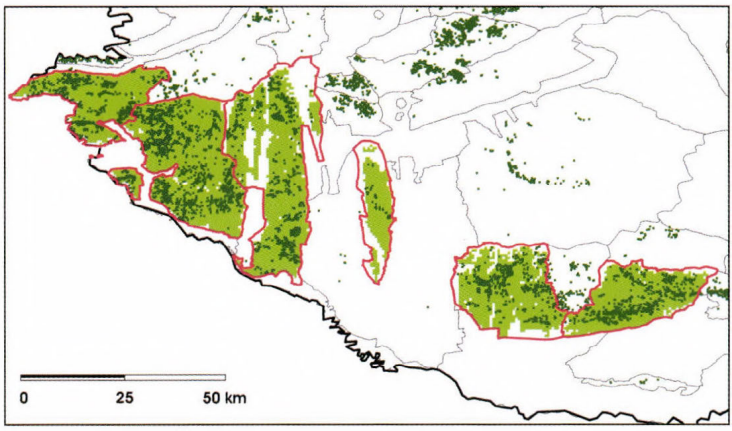

Fig. 6. Beech dominated forest regions (indicated with red contours) in southwest Hungary with high false negative values (overprediction) during the simulations under current climate conditions with the BP-ANN model. The potential area predicted by the BP-ANN method is colored with light green, observed localities with beech occurrence are indicated with dark green.

False negatives typically are due to the violation of the fundamental equilibrium assumption of static models (*Guisan* and *Zimmermann,* 2000). Accordingly, in the present study they suggest that beech at its trailing edge is not in equilibrium with the climate characterized by long-term means.

After the extreme dry and hot 2003, widespread beech decline was observed in several forest regions where beech reaches its lower distributional limit. This suggests that range margins of beech in Hungary are formulated by short-term dry periods – rather than by long-term climatic means.

4.4. Correlates of beech distribution

Beech trees show a rapid increase of radial increment from mid-May to July as soon as leaf expansion starts. Until the end of June 30–70% of annual growth is achieved (*Lebaube et al.,* 2000, *Bouriaud et al.,* 2003). In conclusion, beech appears particularly sensitive to weather conditions at the beginning of the growing season.

The factor importance analysis ranked the maximum temperature of spring and early summer and the modified Ellenberg quotient among the most influential factors. Our results, underlining the importance of May-June weather conditions in the presence of beech, are coherent with results obtained from dendrochronological analyses (*Lebourgeois et al.,* 2005; *Di Filippo et al.,* 2007).

Using climatic predictors, only the current distribution of beech could be easily predicted under optimal conditions, but models failed in the Southwest and Northeast. Including soil data and continentality indices improved model

performance in these regions. This suggests that soil conditions could play an important role in determining the presence of beech at the edge of its distribution range.

An example of better prediction accuracy improved by the addition of soil parameters can be seen in *Fig. 7.*

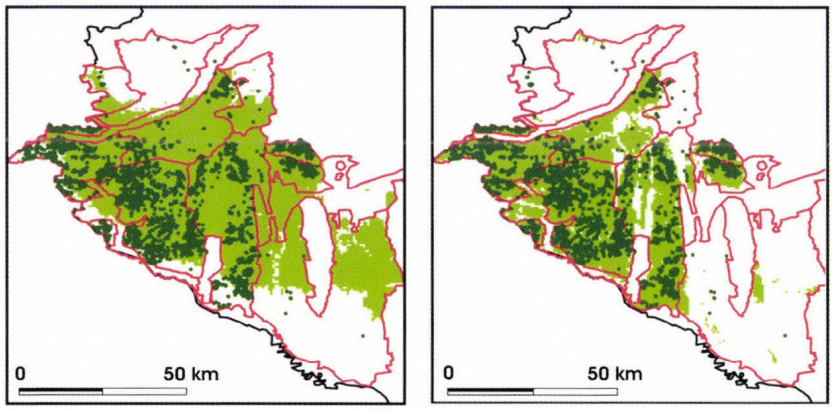

Fig. 7. Predicted potential distribution of beech by the BP-ANN method in southwest Hungary using climate predictors only (left) and using climate, soil, and geomorphological predictors (right). Forest regions are indicated with red.

5. Conclusions

The aim of this study was to test the performance of species distribution models predicting the potential future distribution of beech (*Fagus sylvatica* L.) near to the xeric limit in Hungary. To achieve this aim eight different stochastic algorithms were compared and evaluated.

Most of the species distribution models performed fair or good description of the current distribution of beech, but machine learning methods like classification trees and artificial neural networks with backpropagation algorithm, generally outperformed the established ones. Six out of the eight methods were unsuited for predicting climate change effects on the future distribution of beech. This confirms that a good model performance in predicting the current distribution does not guarantee success in predicting distribution under different climates. The relative failure of some methods underlines that predictions for conservation and management issues should be based on multimodel assessments.

Even machine learning methods like artificial neural networks with backpropagation algorithm failed in regions where beech reaches its distributional limit. The results of the present study suggest that:

- beech in Hungary at its trailing edge (xeric limit) is not in equilibrium with the climate and
- range margins of beech in Hungary are formulated by short-term dry periods rather than long-term climatic means.

The factor importance analysis of the species distribution models ranked the maximum temperature of May and the modified Ellenberg quotient repeatedly as the most influential predictors. In addition, maximum temperatures of summer and precipitation of late summer played a significant role in determining the presence of beech. The ranking suggests that the distribution of beech in Hungary is determined mainly by the maximum temperatures during springtime and it is secondly related to precipitation.

Acknowledgments—This research was funded by the Austrian-Hungarian Transboundary Cooperation 2007-2013 ("FaKlim" project - L00044) and by National Research and Development Agency ("TALENTUM" project - TÁMOP 4.2.2.B-10/1-2010-0018).

References

AGROTOPO, 2002: AGROTOPO database of RISSAC, HAS, Budapest.

Austin, M.P., 2002: Spatial prediction of species distribution: an interface between ecological theory and statistical modeling. *Ecol. Model. 157*, 101–118.

Austin, M.P. and *Smith, T.M.*, 1989: A new model for the continuum concept. *Vegetatio 83*, 35-47.

Backes, K. and *Leuschner, C.*, 2000: Leaf water relations of competitive *Fagus sylvatica* and *Quercus petraea* trees during 4 years differing in soil drought. *Canadian J. Forest Res. 30*, 335–346.

Berki, I., Rasztovits, E., Móricz, N. and *Mátyás, Cs.*, 2009: Determination of the drought tolerance limit of beech forests and forecasting their future distribution in Hungary. *Cereal Res. Commun. 37*, 613–616.

Bouriaud, O., Bréda, N., Le Mogúedec G. and *Nepveu, G.*, 2003 :Modeling variability of wood density in beech as affected by ring age, radial growth and climate. *Trees 18*, 264–276.

Box, E.O., 1981: Predicting physiognomic vegetation types with climate variables. *Vegetatio 45*, 127–139.

Breiman, L., Friedman, J.H., Olshen, R.A. and *Stone, C.J.*, 1984: *Classification and regression trees*. Chapman & Hall, New York.

Busby, J.R., 1991: BIOCLIM: a bioclimate analysis and prediction system. *Plant Prot. Quart. 6*, 8–9.

Carpenter, G., Gillison, A.N. and *Winter, J.*, 1993: Domain - a flexible modeling procedure for mapping potential distributions of plants and animals. *Biodivers. Conserv. 2*, 667–680.

Czúcz, B., Gálhidy, L. and *Mátyás, Cs.*, 2010: Limiting climating factors and potential future distribution of beech (*Fagus sylvatica* L.) and sessile oak (*Quercus* petraea (Mattuscha) Liebl.) forests near their low altitude - xeric limit in Central Europe. *Ann. Forest Sci.* 68(1), 99–108.

Di Filippo, A., Biondi, F., Cufar, K., De Luis, M., Grabner, M., Maugeri, M., Presutti Saba, E., Schirone, B. and *Piovesan, G.*, 2007: Bioclimatology of beech (*Fagus sylvatica* L.) in the Eastern Alps: spatial and altitudinal climatic signals identified through a tree-ring network. *J. Biogeogr. 34*, 1873–1892.

Elith, J. and *Burgman, M.A.*, 2002: Predictions and their validation: rare plants in the Central Highlands, Victoria, Australia. In: *Predicting Species Occurrences: Issues of Accuracy and Scale* (eds *Scott, J.M., Heglund, P.J., Morrison, M.L., Raphael, M.G., Wall, W.A.* and *Samson, F.B.*). Island Press, Covelo, CA, 303–314.

Elith, J., Graham, C.H., Anderson, R.P., Dudik, M., Ferrier, S., Guisan, A., Hijmans, R.J., Huettmann, J.R., Lehmann, A., Li, J., Lucia, G., Lohmann, L.G., Loiselle, B.A., Manion, G., Moritz, C.,

Nakamura, M., Nakazawa, Y., Overton, J.M.C., Peterson, A.T., Phillips, S.J., Richardson, K.S., Scachetti-Pereira, R., Schapire, R.E., Soberón, J., Williams, S., Wisz, M.S. and *Zimmermann, N.E.*, 2006: Novel methods improve prediction of species' distributions from occurrence data. *Ecography 29*, 129–151.

Ellenberg, H., 1986: *Vegetation Mitteleuropas mit den Alpen*. 4th Edition. Fischer, Stuttgart, Germany.

Ellenberg. H., 1996: *Vegetation Mitteleuropas mit den Alpen in ökologischer, dynamischer und historischer Sicht*. Eugen Ulmer, Stuttgart.

Ellenberg, H., Weber, H.E., Düll, R., Wirth, V. and *Werner, W.*, 1992: *Zeigerwerte von Pflanzen in Mitteleuropa*. Goltze, Göttingen, Germany.

Emberger, L. 1930: Sur une formule applicable en géographie botanique. *Comptes Rendus de l'Academie des Sciences de Paris 19*,389–390.

Forman, G. 2003: An extensive empirical study of feature selection metrics for text classification. *J. Mach. Learn. Res. 3*, 1289–1305.

Franke, J. and *Köstner, B.*, 2007: Effects of recent climate trends on the distribution of potential natural vegetation in Central Germany. *Int. J. Biometeorol.52*, 139–147.

Führer, E., 2010: A fák növekedése és a klíma, *„KLÍMA-21" Füzetek 61*, 98–107.

Führer, E., Horváth, L., Jagodics, A., Machon, A. and *Szabados, I.*, 2011: Application of a new aridity index in Hungarian forestry practice. *Időjárás, 115*, 205–216.

Gálos, B., Lorenz, Ph., Jacob, D., 2007: Will dry events occure more often in Hungary in the future? *Environ. Res. Let. 2*, 034006.

Gorczinski, W., 1920: Sur le calcul du degré de continentalisme et son application dans la climatologie. *Geografiska Annaler 2*, 324–331.

Guisan, A. and *Zimmermann, N.E*, 2000: Predictive habitat distribution models in ecology. *Ecol. Model. 135*, 147–186.

Guo, Q., Kelly, M. and *Graham, C.H.*, 2005: Support vector machines for predicting distribution of Sudden Oak Death in California. *Ecol. Model. 182*, 75–90.

Guo, Q. and *Liu, Y.*, 2010: ModEco: An integrated software package for ecological niche modeling. *Ecography 33*, 637–642.

Hannah, L., Midgley, G.F. and *Millar, D.*, 2002: Climate change-integrated conservation strategies. *Global Ecol. Biogeogr. 11*, 485–495.

Hastie, T.J. and *Tibshirani, R.* 1990: *Generalized additive models*. Chapman & Hall, London, UK.

Hay, L.E., Wilby, R.L. and *Leavesley, G.H.*, 2000: A comparison of delta change and downscaled GCM scenarios for three mountainous basins in the United States. *J. Am. Water Res. Ass. 36*, 387–398.

Hijmans, R.J., Cameron, S.E., Parra, J.L., Jones, P.G. and *Jarvis, A.*, 2005: Very high resolution interpolated climate surfaces for global land areas. *Int. J. Climatol. 25*, 1965–1978.

Hofmann, W., 1968: Vitalität der Rotbuche und Klima in Mainfranken. *Feddes Report 78*, 135–137.

Jensen, L.U., Lawesson, J.E., Balslev, H. and *Forchhammer, M.C.* 2004: Predicting the distribution of Carpinus betulus in Denmark with Ellenberg's Climate Quotient. *Nordic J.Botany 23*, 57–67.

Jump, A., Mátyás, Cs. and *Penuelas, J.*, 2009: The paradox of altitude for latitude comparisons in species range retractions. *Trends Ecol. Evol. 24*, 694–700.

Kearney, M. and *Porter, W.P.* 2004: Mapping the fundamental niche: physiology, climate, and the distribution of a nocturnal lizard. *Ecology 85*, 3119–3131.

Keuler, K., Lautenschlager, M., Wunram, C., Keup-Thiel, E., Schubert, M., Will, A,, Rockel, B., and *Boehm, U.* 2009: Climate Simulation with CLM, Scenario A1B run no.1, Data Stream 2: European region MPI-M/MaD. *World Data Center for Climate*. [online 23 October 2011] URL: http://dx.doi.org/DOI:10.1594/WDCC/CLM_A1B_1_D2

Kramer, K., Degen, B., Buschbom, J., Hickler, T., Thuiller, W., Sykes, M.T. and *de Winter, W.*, 2010: Modeling exploration of the future of European beech (*Fagus sylvatica L.*) under climate change - Range abundance genetic diversity and adaptive response. *Forest Ecol. Manag. 259*, 2213–2222.

Lakatos, F. and *Molnár, M.*, 2009: Mass mortality of beech on Southwest Hungary. *Acta Silvatica et Lignaria Hungarica 5*: 75–82.

Lebaube, S., Le Goff, N., Ottorini, JM., Granier, A., 2000: Carbon balance and tree growth in a *Fagus sylvatica* stand. *Ann. Forest Sci. 57*, 49–61.

Lebourgeois, F., Bréda, N., Ulrich, E. and *Granier, A.* 2005: Climate-tree-growth relationships of European beech (*Fagus sylvatica* L.) in the French permanent plot network (Renecofor). *Trees–Struct. Funct. 19*, 385–401.

Lindner, M., Maroschek, M., Netherer, S., Kremer, A., Barbati, A,, Garcia-Gonzalo, J., Seidl, R., Delzon, S., Corona, P., Kolstrom, M., Lexer, M.J. and *Marchetti, M.*, 2010: Climate change impacts adaptive capacity and vulnerability of European forest ecosystems. *Forest Ecol. Manag. 259*, 698–709.

Manel, S., Dias, J.M. and *Ormerod, S.*, 1999: Comparing discriminant analysis, neural networks and logistic regression for predicting species distribution: a case study with a Himalayan river bird. *Ecol. Model. 120*, 337–47.

Maravelias, C.D., Haralabous, J. and *Papaconstantinou, C.*, 2003: "Predicting demersal fish species distributions in the mediterranean sea using artificial neural networks", *Marine Ecol.-Progr. Ser. 255*, 249–258.

Martonne, D.E., 1942: Nouvelle carte mondiale de l'indice d'aridite. *Ann. Geographie 51*, 242–250.

Mastrorillo, S., Lek, S., Dauba, F. and *Belaud, A.*, 1997: The use of artificial neural networks to predict the presence of smallbodied fish in a river. *Freshwater Biol. 38*, 237–246.

Mátyás, Cs., 2009: Ecological challenges of climate change in Europe's continental drought-threatened Southeast. In *Regional aspects of climate-terrestrial-hydrologic interactions in non-boreal Eastern Europe* (eds.: *Groisman, P.Y.* and *Ivanov, S.V.*) NATO Science Series Springer Verl., 35–46.

Mátyás, Cs., Vendramin, G.G. and *Fady, B.*, 2009: Forests at the limit: evolutionary-genetic consequences of environmental changes at the receding (xeric) edge of distribution. *Ann. Forest Sci. 66*, 800–809.

Mátyás, Cs., (2010): Forecasts needed for retreating forests (Opinion). *Nature 464*, 1271.

Mátyás, Cs., Berki, I., Czúcz, B., Gálos, B., Móricz, N. and *Rasztovits, E.*, 2010: Future of Beech in Southeast Europe from the Perspective of Evolutionary Ecology. *Acta Silvatica et Lignaria Hungarica 6*, 91–110.

Munoz, M.E.S., Giovanni, R.D., Siqueira, M.F., Sutton, T., Brewer, P., Pereira, R.S., Canhos, D.A.L., Canhos, and *V.P.*, 2009: Open Modeller: a generic approach to species' potential distribution modeling. *Geoinformatica,* doi: 10.1007/s10707–009–0090–7.

Nix, H.A., 1986: A biogeographic analysis of Australian elapid snakes in R. Longmore, ed. Atlas of elapid snakes of Australia. *Government Publishing Service*. Canberra, Australian.

Pearson, R.G. and *Dawson, T.E.*, 2003: Predicting the impacts of climate change on the distribution of species: are bioclimatic envelope models useful? *Global Ecol. Biogeogr. 12*, 361–371.

Pearson, R.G., Dawson, T.E., Berry, P.M. and *Harrison, P.A.*, 2002: SPECIES: a spatial evaluation of climate impact on the envelope of species. *Ecol. Model. 154*, 289–300.

Penuelas, J., Ogaya, R., Boada, M. and *Jump, A.S.*, 2007: Migration invasion and decline changes in recruitment and forest structure in a warming-linked shift of European beech forest in Catalonia (NE Spain). *Ecography 30*, 829–837.

Phillips, S., 2006: Maxent software for species habitat modeling. [online 25 October 2011] URL: http://www.cs.princeton.edu/~schapire/maxent/.

Phillips, S.J., Anderson, R., and *Schapire, R.E.*, 2006: Maximum entropy modeling of species geographic distributions. *Ecol. Model. 190*, 231–259.

Rennenberg, H., Seiler, W., Matyssek, R., Gessler, A., and *Kreuzwieser, J.*, 2004: Die Buche (*Fagus sylvatica* L.) - ein Waldbaum ohne Zukunft im südlichen Mitteleuropa? *Allg. Forst Jagdztg 175*, 210–224.

Richards, J.A. and *Jia, X.*, 1999: *Remote Sensing Digital Image Analysis. An Introduction*, Third edition. Springer. Berlin. Germany.

Rivas-Martínez, S., 1990: Bioclimatic belts of West Europe (relations between bioclimate and plant ecosystems). *Proc. Eur. School Climate Nat. Hazards Course* (Arles, 1990). Strasbourg. 225–246.

Rivas-Martínez, S., 1996: Classificacion bioclimatica della tierra. *Folia Botanica Matrietensis 16*: 1–25.

Schlüter, H., 1968: Zur systematischen und räumlichen Gliederung des Carpinion in Mittelthüringen. *Feddes Repert 77*, 117–141.

Segurado, P. and *Araújo, M.B.*, 2004: An evaluation of methods for modeling species distributions. *J. Biogeogr. 31*, 1555–1568.

Stockwell, D., Peters, D., 1999: The GARP modeling system: problems and solutions to automated spatial prediction. *Int. J. Geographic. Inform. Sci. 13*, 143–158.

Tax, D.M.J. and *Duin, R.P.W.*, 2002: Uniform object generation for optimizing one-class classifiers. *J. Mach. Learn. Res. 2*, 155–173.

Thornthwaite, W.C., 1948: An approach toward a rational classification of climate. *Geogr.Rev. 38*, 55–103.

Thuiller, W., Araujo, M.B. and *Pearson, R.G.*, 2004: Biodiversity conservation - uncertainty in predictions of extinction risk. *Nature 430*, 34.

Thuiller, W., Lafourcade, B., Engler, R. and *Araújo, M.B.*, 2009: BIOMOD - A platform for ensemble forecasting of species distributions. *Ecography 32*, 369–373.

Tsoar, A., Allouche, O., Steinitz, O., Rotem, D. and *Kadmon, R.*, 2007: A comparative evaluation of presence-only methods for modeling species distribution. *Divers. Distrib. 13*, 397–405.

Vapnik, V., 1995: *The Nature of Statistical Learning Theory*. Springer-Verlag. New York. USA.

Wiley, E.O., McNyset, K.M., Peterson, A.T., Robins, C.R. and *Stewart, A.M.*, 2003: Niche modeling and geographic range predictions in the marine environment using a machine-learning algorithm. *Oceanography 16*, 120–127.

Wu, W., Lynch A.H. and *Rivers, A.* 2005: Estimating the Uncertainty in a Regional Climate Model Related to Initial and Lateral Boundary Conditions. *J. Clim.18*, 917–933.

Zimmermann, N.E., Yoccoz, N.G., Edwards, T.C., Meier, E.S., and *Thuiller, W*, 2009: Climatic extremes improve predictions of spatial patterns of tree species. *Proceedings of the National Academy of Sciences of the United States of America, USA 106*: 19723–19728.

IDŐJÁRÁS

Quarterly Journal of the Hungarian Meteorological Service
Vol. 116, No. 3, July–September 2012, pp. 195-209

Application of phenological observations in agrometeorological models and climate change research

Márta Hunkár[1]*, Enikő Vincze[2], Ildikó Szenyán[2], Zoltán Dunkel[2]

[1] *Department of Economical Methodology*
University of Pannonia, Georgikon Faculty,
P.O.B.71, H-8360 Keszthely, Hungary

[2]*Hungarian Meteorological Service,*
P.O.B. 38, H-1525 Budapest, Hungary

**Corresponding author; E-mail: hunkar@georgikon.hu*

(Manuscript received in final form April 24, 2012)

Abstract—This paper intends to give a brief overview on the different approaches existing in plant phenological studies. The history of plant phenological observations in Europe and Hungary shows that the aim of the observations turned from the pure scientific interest to the application in agricultural practice, and recently, to climatic studies. Modeling of phenological development is demonstrated via examples for wheat and maize. The analysis of historical data has got new horizons by the international efforts done by COST Actions. New perspectives in observations of vegetation are remote sensing data. Vegetation indices like normalized difference vegetation index (NDVI) and enhanced vegetation index (EVI) are also used for tracking the seasonal development of plants, and they give opportunity to analyze the year by year change.

Key-words: phenology, observational network, climate change, NDVI, EVI.

1. Introduction

Vegetation dynamics like growth, reproduction, and winter rest, competition for nutrients, water, and light are strongly influenced and determined by climate variables. Even in case of unchanged climate we can find big differences year by year in the start of life period simply as a result of different weather situation. A change in climate will result in a change of these dynamics. Phenology is the study of the timing of recurrent biological processes such as budburst, flowering, flight activity of insect, bird nesting, fruit ripening, and leaf fall. That

is the scientific discipline, which is able to link vegetation dynamics with climate variables. The identified and recorded events are the so-called phenophases.

Phenological observations have long history, but the aim of observations has changed from scientific interest to practical applications, from local to global characterization of climate and biosphere interactions. The methodology of the observation could be different according to the relevant aims. It is important to know the time of the phenological phases for organizing agricultural works as well as the plant protection. Time by time organizing observational networks on national and international levels has got remarkable attentiveness, nevertheless, long-term data series are rather rare. Computerized crop simulation models contain phenological submodels since the potential biomass production is affected by the actual phenological phases. Examples of phenological models are presented for maize and wheat phenological development. Recently, in climate change studies phenology became interesting again, and great efforts have been done to collect old data series from large geographical area. The new possibilities for monitoring the vegetation on large spatial and temporal scale are remote sensing. Using vegetation indices like normalized difference vegetation index (NDVI) or enhanced vegetation index (EVI) makes possible to track phenological development of the vegetation on the scale of "landscape phenology" which differs from the traditional morphological characterization of individual plants.

2. Brief history of plant phenological observations

The scientific father of observations of periodical phenomena of plants and animals was *Carl Linné* (1707–1778). Besides his taxonomical works, he observed and recorded the timing of occurrence of birds, flowering of plants, and gave a calendar of nature for Scandinavia.

In the middle of the nineteenth century, two remarkable scientists in Belgium continued a long debate about the aims and methods of observations of periodical phenomena. *Demarrée* and *Rutishauser* (2011) give a detailed description of the correspondence between *Adolphe Quetelet* (1796–1874) and *Charles Morren* (1807–1858). *Quetelet* was physicist and astronomer. He was the founder of the Royal Observatory of Brussels and served as the Permanent Secretary of the Academy of Sciences, Brussels. He initiated a program of systematic observations of periodical phenomena of the vegetation and animal kingdoms in 1841. *Morren* was a professor of botany at the University of Liège and fellow of the Academy of Sciences, Brussels. According to *Quetelet*'s view, only few plants and animals should be observed but at the same time, on a large geographical area. This is very similar to the methods of meteorological observations. *Morren* argued this "too simple" approach and suggested

recording the date of occurrence of phenological events. Finally, the discipline of phenology derives from *Morren*'s theory: the goal which proposes the association of the observation of the periodical phenomena is to know "the manifestation of life ruled by the time." (*Morren*, 1843).

In Hungary, *Pál Kitaibel* (1757–1817) was the first natural scientist who systematically observed flowering time of plants and explained the differences with climatic reasons. He intended to map flowering times of several agricultural plants; therefore, a circular letter was issued to collect data. Unfortunately, only few response arrived, and therefore, the mapping was not successful (*Both*, 2009).

The relationship of plant phenology and climate was obvious from the beginning; therefore, the observational program of National Meteorological Institutes organized in the middle of the nineteenth century contained also plant phenological observations. Meteorological yearbooks between the years 1871 and 1885 published by the Royal Hungarian Institute for Meteorology and Geomagnetism contain records from 57 locations for 200 plants (not all the plants from each location). Later, in 1910, the Hungarian Geographical Society and in 1934, the Research Institute for Forestry organized observational networks for plant phenological observations.

Organizing and especially maintaining an observational network is not an easy task. There is a need for competent observers and persistent work.

In 1935, the decision of the Agricultural Meteorological Committee of the International Meteorological Organization stated that the same species of plants should be observed in phenological studies everywhere, and that the different stages of development (phitophasis) should be determined uniformly. As *Réthly* (1936) wrote: systematic phenological observations have been carried on for a long time in Hungary by the State Foresters, and have provided much valuable data. The author therefore requests the Hungarian foresters to work according to the above lines in the future.

The collected observations were non-systematic either in space or time. *Dunay* (1984) gave a detailed description on the history of the time by time reorganization of phenological observation network in the Hungarian Meteorological Service. The next starting date of a phenological network maintained by the Meteorological Institute is 1951. The institute prepared the "Guidelines for phenological observations". The guidelines described the phases of 75 growing wild plants. The pictures of the guidelines were drawn by *Ms. Vera Csapody*, the famous Hungarian artist and botanist.

The newly established network mainly focused on plants growing wildly. The observation posts of the network were the precipitation stations of the institute. The agricultural plants were observed in 13 places in the agricultural research institutes and in species trial stations. The network was renewed in 1961, when new posts were organized instead of the closed stations. Using the gained experience, a detailed phenological observation program was worked

out, and a new guideline, "Guideline for phenological observation of cultivated plants" was issued. The reorganized network had 80 observation stations. The number of observed cultivated plants was 34. Among others, many cereals, rough fodder, cereal fodder, industrial crops, vegetables, and fruits were monitored. Each station observed those species which had importance in their region. Some of the stations observed the phenological phases of cultivated plants; other stations had to monitor fruits or vegetables. The observation program was not restricted to the phenophases only, but it was extended to recording of the agricultural works, the general condition of the plants, and any damage.

The set of the observed growing wild plants were revised, and according to the international practice, the program was renewed again with 36 species. The network monitored 10 treespecies, 10 shrubs, and 16 grass species. Increasing the number of the stations, the phenological network consisted of 120 wildly growing and 80 cultivated plants observations. The Agrometeorological Division submitted a reconstruction plan in 1975 to add plus 33 natural and 236 cultivated plants stations to the network. Within the network, a rapid reporting smaller network was planned with only 30 stations. Taking into consideration the operative demand, a crucial change was carried out in the organization and data transfer system of the network. Instead of professional staff members of the standard meteorological network, the specialists of the MEM-NAK, the Hungarian Plant Protection and Agrochemistry Organization of the Ministry of Agriculture, were recruited into the phenological observation network. Much less mistake was found in the professional agronomist's observations. The base of the data transfer was the national telex system. In the 80s it was the most rapid and effective tool in the telecommunication. Unfortunately, the observation of natural vegetation was minimized, but the observation of few "signaling plant" was maintained. Few of them was a good sign of the start of the spring, others have got some economic importance. The new network started its work in 1983 cooperating with the MEM-NAK. This network continued its activity until 2000 when the OMSZ, the Hungarian Meteorological Service closed it because of financial reasons.

According to the international networks, the International Phenological Gardens (IPG) are a European and individual network within the Phenology Study Group of the International Society of Biometeorology. The network was founded in 1957 by *F. Schnelle* and *E. Volkert*. The current network ranges across 28 latitudes from Scandinavia to Macedonia and across 37 longitudes from Ireland to Finland in the north and from Portugal to Macedonia in the south. It consists of 89 gardens in 19 European countries. The philosophy of this network is quite different than the Hungarian's one. In all gardens, genetically identical trees and shrubs are planted in order to make large-scale comparisons among the timing of different developmental stages of plants. Recently, the coordination of this network belongs to the Humbolt University of Berlin (*Chmielewski*, 1996).

Among the most important and recent phenological activities at international level, there is the youngest phenological network of the United States. After two years of preparatory period, in 2007 it started its activities based mainly on volunteer observers (*Betancourt et al.*, 2007).

3. Phenological research work

The use of phenological observations is manifold. For scientific investigations, for planning and consulting tasks as well as in daily practice, phenological data are required. Examples for the application of phenological data are investigations of the impact of climate changes on plants, calibration of remotely sensed data, use of these data in yield-, growth-, or hydrological models, determination of regions with high frost-risks for fruit-tree growing, and the monitoring of environmental changes. Since the end of the 1980s, the demand for phenological observations increased substantially. Mainly, the rise in air temperature in the previous decades and the clear phenological response by plants led to this increased interest in phenological data.

3.1. Phenology in crop models

The ability to estimate the time required for a crop to pass through its various stages of development to maturity is useful in at least one other important way - it assists greatly in estimating crop yield. The history of phenological modeling goes back at least as far as 1735. It was then that *Reaumur* (1735) suggested that the time required for plants to complete a phase of their development could be more accurately estimated from temperature sums than from calendar days. Although there are many variations of the original concept, most methods of estimating phenological development still use this relatively simple approach.

Phenological modeling inevitably involves mathematical equations that express the rate of change in life stage as a function of environmental variables, such as temperature, humidity, photoperiod, and radiation. These equations are usually the product of regression analyses of experimental data (*Shaykewich*, 1995).

The models can be different according to:

- the phenophases taken into consideration,
- environmental variables (temperature, day-length, vernalization, etc.),
- the form of functions describing the effect of the environmental variables (linear, non-linear),
- the structure of the model (additive, multiplicative).

The models are always plant specific. They contain several plant specific parameters which can be different even for the different varieties.

Example 1: In the CERES-Maize model (*Jones* and *Kiniry*, 1986), phenological development is calculated as a function of growing degree days or daily thermal time (*DTT*) with a base temperature of 8 °C. The maize phenological phases used in the model are described in *Table 1*. The model assumes that the rate of development increases linearly above the base temperature up to 34 °C and then decreases linearly to zero as temperature increases from 34 to 44 °C. Similarly, rates of leaf initiation and leaf-tip appearance are assumed to change linearly in these two ranges of temperature. Photoperiodic induction is assumed to decrease with increasing photoperiod for photoperiods longer than12.5 hours. The number of days of tassel initiation delay for each hour increase in photoperiod is assumed to be a constant for any given photoperiod-sensitive cultivar. The total number of leaves is determined from the number of leaf primordia initiated between seedling emergence and tassel initiation. Date of tassel initiation is determined using both *DTT* with a base temperature of 8 °C and photoperiod. Silking or end of leaf growth is determined from total leaf number and the rate of leaf-tip appearance.

Table 1. Phenological phases used in CERES-Maize model.
(Source: *Jones* and *Kiniry*, 1986)

Phase No.	Description
1.	Seedling emergence to end of juvenile phase
2.	End of juvenile phase to tassel initiation (photoperiod-sensitive phase)
3.	Tassel initiation to silking
4.	Silking to beginning of effective grain-filling period (lag phase)
5.	Effective grain-filling period
6.	End of effective grain-filling period to physiological maturity (black layer)
7.	Before sowing (fallow)
8.	Sowing to germination
9.	Germination to seedling emergence

Example 2: Wheat phenological model of *Wang* and *Engel* (1998) is a multiplicative non-linear model. The first step in using the WE model is to calculate the daily rate of plant development (r). There are two main developmental stages: vegetative phase from emergence until anthesis and reproductive phase from anthesis until physiological maturity. The developmental stage (DS) is then calculated by accumulating the daily development rate values (i.e., at a 1 day time step, $DS=\Sigma r$). Other developmental stages in the vegetative phase are 0.4 at spikelet initiation, 0.8 at late booting, and 0.88 at awns first visible.

The model equationfor the vegetative phase is

$$r = R_{max,v} f(T) f(P) f(V), \tag{1}$$

while for the reproductive phase it is

$$r = R_{max,r} f(T), \tag{2}$$

where r is the daily development rate (per day), $R_{max,v}$ and $R_{max,r}$ are the maximum development rate (per day) in the vegetative and reproductive phases, and $f(T)$, $f(P)$, and $f(V)$ are temperature, photoperiod, and vernalization response functions, varying from 0 to 1.
The temperature response function is

$$f(T) = \frac{2(T - T_{min})^{\alpha}(T_{opt} - T_{min})^{\alpha} - (T - T_{min})^{2\alpha}}{(T_{opt} - T_{min})^{2\alpha}}, \tag{3}$$

$$\alpha = \frac{ln\,2}{ln[(T_{max} - T_{min})/(T_{opt} - T_{min})]}, \tag{4}$$

where T_{min}, T_{opt}, and T_{max} are the cardinal temperatures for development (minimum, optimum, and maximum), and T is the mean daily temperature calculated from the 24 h temperature.
For the vegetative phase, T_{min}, T_{opt}, and T_{max} were 0 °C, 24 °C, and 35 °C, and for the reproductive phase they were 8 °C, 29 °C, and 40 °C, respectively (*Xue et al.*, 2004).

The photoperiod response function is

$$f(P) = 1 - e^{-\omega(P - P_c)}, \tag{5}$$

where P is the actual photoperiod (h), P_c the critical photoperiod (h) below which no development occurs, and ω is a cultivar specific photoperiod sensitivity coefficient [h^{-1} g]. Values of P_c and of ω are variety specific.
The vernalization response function:

$$f(V) = min\{1; max[0; (V_n - V_{nb})/(V_{nd} - V_{nb})]\}, \tag{6}$$

where V_n is the effective vernalization days, V_{nd} is the number of effective vernalization days for the plant to be fully vernalized, and V_{nb} is the minimum effective vernalization days, i.e. development begins only after a minimum value of V_{nb} has been reached (*Weir et al.*, 1984).
The functions max and min in Eq. (6) represent the maximum and minimum values in a string of numbers, respectively. The effective vernalization days, V_n, is calculated from sowing as

$$V_n = \sum fv_n(T), \tag{7}$$

where $fv_n(T)$ is the daily vernalization rate (per day), calculated using Eqs. (3) and (4) with the cardinal temperatures for vernalization ($T_{\min,vn}$, $T_{\text{opt},vn}$, and $T_{\max,vn}$) being −1.3, 4.9, and 15.7 °C (*Porter* and *Gawith*, 1999). Both V_{nb} and V_{nd} are cultivar dependent.

These types of plant phenological models are always plant specific. Parameterization of the model is possible on experimental plots or in growth chambers. Whenever you want to develop phenological model for a native plant (especially for trees and shrubs), you should use long-time data series and the physiological parameters should be estimated on statistical ways.

3.2. Phenology in climate change studies

In the 1990s, the interest in phenological research and thus, the demand for phenological observations has increased substantially. Mainly, rising air temperatures in recent decades and the clear phenological response of plants and animals to this increase have caused the growing interest. Many studies have shown that the timing of life cycle events is able to provide a good indicator for climate change impacts (*Schwartz,* 1994; *Menzel et al.*, 2006; *Chmielewski* and *Rötzer,* 2001, 2002). The timing of phenological phases depends on numerous environmental conditions: temperature, precipitation, soil type, soil moisture, and insolation. However, in mid- and high latitudes, with vegetation-rest (dormancy) in winter and active growing period in summer, air temperature has the greatest influence on phenology (*Fitter et al.*, 1995; *Sparks et al.*, 2000; *Chmielewski et al.*, 2005). A comprehensive understanding of species phenological responses to global warming will require observations that are both long-term and spatially extensive. Long-term data series deriving from the same place are rare. One of these rarities is the data series of cherry tree flowering in Kyoto, Japan (*Aono* and *Kazui*, 2008), in which the first records came from the ninth centuries. In England, phenological events of various plants and animals observed since the 18th century have been reported as Marsham's phenological data series (*Margary*, 1926). In Geneva, Switzerland, the leafing date of the chestnut tree has been observed since 1808, and these records have been used to show climatic warming since the early 19th century (*Defila* and *Clot*, 2001). In

Hungary, there is unique series of St. George Day's wine shoot book in Kőszeg, in which every year since 1740 wine shoot captures notes and drawings are included. The work is still continuing, so more than 205 years of data series available (*Kiss*, 2009; *Kiss et al.*, 2011).

Monitoring phenological phases is carried out in many European countries. Each country has its own database, in some cases still on paper, mostly on databank-systems, going back to the 1950s in many cases.

After a period of reduction of the density of phenological networks and even cancelling all national observations in some countries in the 1980s, new interest in phenology grew in the following decade due to the new interest in climate change issues. In 2004, a new COST (European Cooperation in the Field of Scientific and Technical Research) Action was launched on European level. The basic idea of the Action was as a starting point to build a reference data set of selected species and phases that have been observed in European countries over a common reference period of at least one decade but preferably longer, using the BBCH code which was applied on phenophases observed in different countries by the German Weather Service. The project ended in 2009. According to the final report of COST 725 (*Koch et al.*, 2009) using 125,000 observational series of 542 plant and 19 animal species in 21 European countries for the period 1971–2000, the aggregation of the time series revealed a strong signal across Europe of changing spring and summer phenology: spring and summer exhibited a clear advance by 2.5 days/decade in Europe. Mean autumn trends were close to zero, but suggested more of a delay when the average trend per country was examined (1.3 days/decade). The patterns of observed changes in spring (leafing, flowering, and animal phases) were spatially consistent and matched measured national warming across 19 European countries; thus, the phenological evidence quantitatively mirrors a regional climate warming. The COST 725 results assessed the possible lack of evidence at a continental scale as 20%, since about 80% of spring/summer phases were found to be advancing.

In the IPCC AR4 WG II report (*Parry et al.*, 2007), the COST 725 study is one of the major contributions for the assessment of observed changes and responses in natural and managed systems. As a continuation, the chair of COST 725 submitted a 5 years project proposal PEP 725 (Pan European Phenological database), which was accepted by EUMETNET and launched in 2010. COST 725/PEP 725 is also being one of the leading partners of the new GEO-task: Global Phenology Data. Together with the USA National Phenology Network and the University of Milwaukee, COST 725/PEP 725 will coordinate the collection of in-situ phenology observations and expand existing observing networks, identify and generate satellite-derived phenological/temporal metrics, and test models for describing the phenological characteristics of natural and modified ecosystems. Changes in vegetation phenology impact biodiversity, net primary productivity, species distribution, albedo, biomass, and ultimately, the global climate.

4. Phenology from the space

The guides for plant phenological observations give detailed descriptions about morphology of different phenophases concerning to individual plants. This method is applicable in phenological gardens, where plants are the same or planted in the same place year by year, and they are monitored day by day. If a larger area of plant stands should be characterized by the phenological stages, difficulties arise because of the variability of individuals. In this case the percentage of plants having that specific phase should be estimated. This is a significant source of bias.

Remote sensing phenology, the use of satellites to track phenological events can complement ground observation networks. Satellites provide a unique perspective of the planet and allow for regular, even daily, monitoring of the entire global land surface.

Because the most frequently used satellite sensors for monitoring phenological events have relatively large "footprints" on the land surface, they gather data about entire ecosystems or regions rather than individual species. Remote sensing phenology can reveal broad-scale phenological trends that would be difficult, if not impossible, to detect from the ground. Moreover, because data collection by satellite sensors can be standardized, the data are reliably objective. Obviously, remote sensing data are not the traditional phenological phases but they are reflectance (ρ) in different spectral channels. The status of the vegetation is in close connection with its reflectance, especially in the near infrared and red spectra; therefore, the normalized difference vegetation index, (NDVI) has often used to characterize the vegetation status (*Reed et al.*, 1994):

$$NDVI = \frac{\rho_{nir} - \rho_{red}}{\rho_{nir} + \rho_{red}}. \tag{8}$$

Analyzing the seasonal curve of NDVI, the time of onset and the end of the vegetation season can be taken when NDVI reaches a threshold value (0.3) (*White et al.*, 2009; *Botta et al.*, 2000; *Jolly et al.*, 2005).

A bit more sophisticated the enhancedvegetation index (EVI) has an advantage over NDVI, because EVI includes a blue band, which allows residual atmospheric contamination and weight to be taken into account, compensating for the variable soil background reflectance (*Liu* and *Huete*, 1995; *Huete et al.*, 2002; *Churkina et al.*, 2005).

$$EVI = G \times \frac{\rho_{nir}/\rho_{red} - 1}{\rho_{nir}/\rho_{red} + \left(C_1 - C_2 \times \rho_{blue}/\rho_{red}\right) + L/\rho_{red}}, \tag{9}$$

where L is a soil adjustment factor, and C_1 and C_2 are coefficients used to correct aerosol scattering in the red band by the use of the blue band. ρ_{blue}, ρ_{red}, and ρ_{nir} represent reflectance at the blue (0.45–0.52μm), red (0.6–0.7μm), and near-infrared (NIR) wavelengths (0.7–1.1μm), respectively. In general, G=2.5, C_1=6.0, C_2=7.5, and L=1.

Temporal variation in EVI data are modeled using piecewise sigmoidal models. Each growth cycle is modeled using two sigmoidal functions: one for the growth phase, one for the senescence phase. To identify phenological transition dates, the rate of change in the curvature of the fitted logistic models is used. Specifically, transition dates correspond to the times at which the rate of change in curvature in the EVI data exhibits local minima or maxima. For each growth cycle, four phenological transition dates are recorded based on the approach described above. The corresponding phenological transition dates are defined as the onset of greenness increase, the onset of greenness maximum, the onset of greenness decrease, and the onset of greenness minimum.

Both NDVI and EVI data are available from MODIS placed at Terra and Aqua satellites. Data are provided by NASA Land Processes Distributed Active Archive Center (*NASA LP DAAC,* 2011). Our future plan is analyzing EVI data for different regions of Hungary for the last ten years. The EVI data on June 26, 2011 is shown in *Fig. 1* for Hungary. For a selected area of 5 × 5 km around Szenna (46°18.47'N, 17°43.95'E), time series from April to August, 2011 of EVI is presented in *Fig. 2*. The average seasonal curve for one pixel selected from the area mentioned above using data from 2003–2011 is shown in *Fig. 3*.

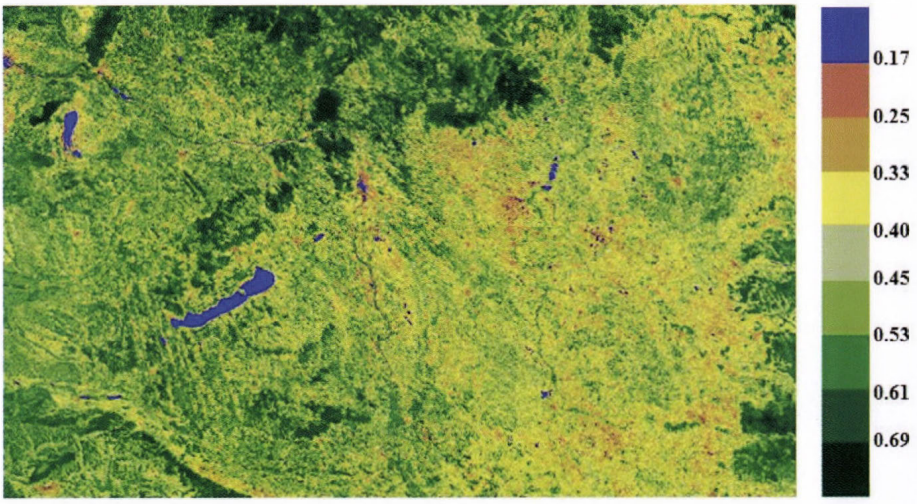

Fig. 1. Enhanced vegetation index (EVI) for the area of Hungary on June 26, 2011. Larger EVI indicates more developed vegetation.

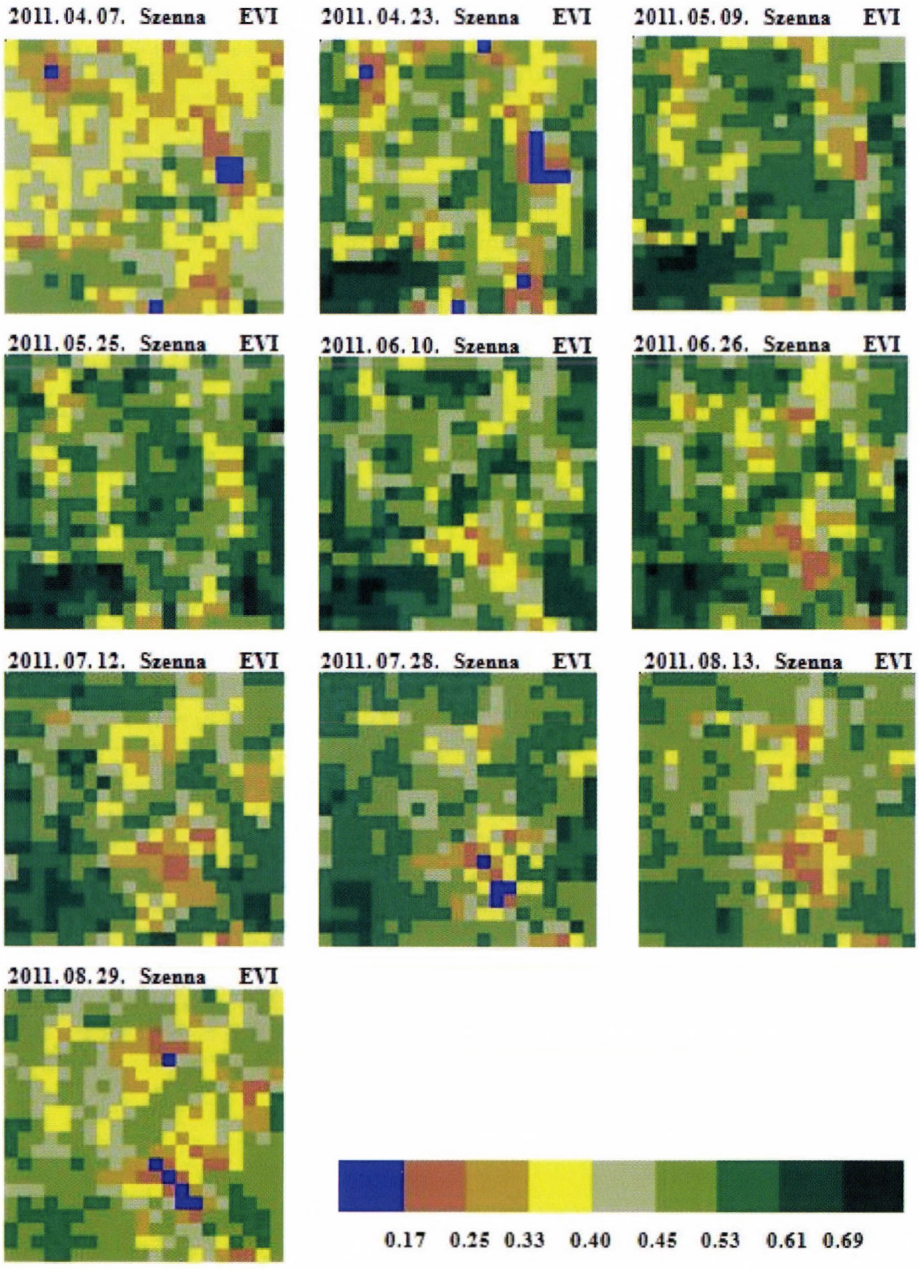

Fig. 2. Seasonal development of vegetation in a selected area according to EVI. The site of observations is a 5 km x 5 km area around Szenna (46°18.47'N, 17°43.95'E) between April and August, 2011.

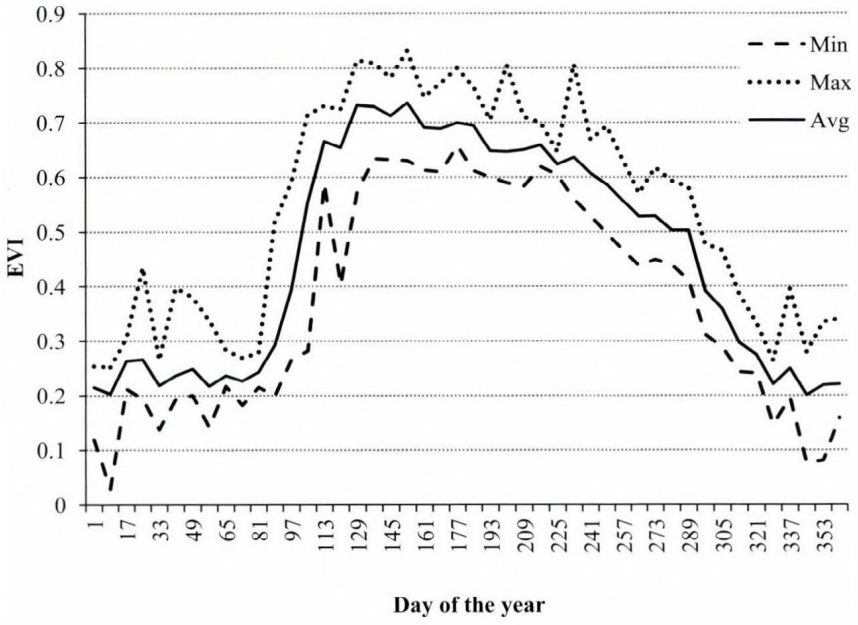

Fig. 3. Seasonal curve of EVI averaged for the years 2003–2011 for a selected pixel.

5. Conclusion

In the last two decades, climate change became a prevailing scientific paradigm, therefore, relating areas like phenology has been refocused. Searching for old phenological records, developing phenological models and new observation techniques applicable to track responses of vegetation to changing environment, and revealing interrelationships between biosphere and atmosphere are interesting tasks. New projects have been launched worldwide both on national and international levels to study plant and animal phenology. Reorganization of observation networks and collecting data is a big deal again. Remote sensing techniques offer new opportunities for comprehensive evaluation of processes taking place in biosphere.

Acknowledgement—The research project is supported by OTKA 81972.

References

Aono, Y., Kazui, K., 2008: Phenological data series of cherry tree flowering in Kyoto, Japan, and its application to reconstruction of springtime temperatures since the 9th century. *Int. J. Climatol. 28,* 905–914.

Betancourt, J.L., Schwartz, M.D., Breshears, D.D., Brewer, C.A., Frazer, G., Gross, J.E., Mazer, S.J., Reed, B.C. and *Wilson, B.E.*, 2007: Evolving plans for the USA National Phenology Network, *Eos. Trans. AGU 88(19)*, 211.

Both, M., 2009: Work of Kitaibel Pál in Geosciences, particular description of land use in the Carpathian basin. *PhD Thesis, University of Miskolc,*(in Hungarian), http://phd.lib.uni-miskolc.hu/jadox/portal/browser.psml.

Botta, A., Viovy, N., Ciais, P., 2000: A global prognostic scheme of leaf onset using satellite data. *Glob. Change Biol. 6*, 709–725.

Chmielewski, F.M., 1996: The international phenological gardens across Europe. Present state and perspectives. *Phenol. Seasonality 1*, 19–23

Chmielewski, F.M., Rötzer, T. 2001: Responses of tree phenology to climate change across Europe. *Agr. Forest Meteorol. 108,* 101–112.

Chmielewski, F.M., Rötzer, T., 2002: Annual and spatial variability of the beginning of the growing season in Europe in relation to air temperature changes. *Clim. Res. 19,* 257–264.

Chmielewski, F.M., Müller, A., Küchler, W., 2005: Possible impacts of climate change on natural vegetation in Saxony (Germany). *Int. J. Biometeorol. 50*, 96–104.

*Churkina, G., Schimel, D.*and *Braswell, B.H.*, 2005: Spatial analysis of growing season length control over net ecosystem exchange. *Glob. Change Biol. 11*, 1777–1787.

Defila, C., Clot, B., 2001: Phytophenological trends in Switzerland. *Int. J. Biometeorol. 45*, 203–207.

Demarée, G.R., Rutishauser, T., 2011: From "Periodical Observations" to Anthochronology" and "Phenology" – the scientific debate between Adolphe Quetelet and Charles Morren on the origin of the word "Phenology". *Int. J. Biometeorol. 55*, 753–761.

Dunay, S., 1984: Plant phenological observations in Hungary *Légkör 29*, 2–9 (in Hungarian).

Fitter, A.H., Fitter, R.S.R., Harris, I.T.B., Williamson, M.H., 1995: Relationships between first flowering date and temperature in the flora of locality in central England. *Func. Ecol. 9*, 55–60.

Huete, A.R., Didan, K., Miura, T., Rodriguez, E.P. , Gao, X., and *Ferreira, L.G.*, 2002: Overview of the radiometric and biophysical performance of the MODIS vegetation indices, *Remote Sens. Environ. 83,* 195–213.

Jolly, W.M., Nemani, R., and *Running, S.W.*, 2005: A generalized bioclimatic index to predict foliar phenology in response to climate. *Glob. Change Biol. 11*, 619–632.

Jones, C.A. and *Kiniry, J.R.*, 1986: Ceres-Maize: a simulation model for maize growth and development. Texas A&M University Press, College Station, TX. p194.

Kiss, A., 2009: Historical climatology in Hungary: Role of documentary evidence in the study of past climates and hydrometeorological extremes. *Időjárás 113,* 315–339.

Kiss, A., Wilson, R. and *Bariska, I.*, 2011: An experimental 392-year documentary-based multi-proxy (vine and grain) reconstruction of May-July temperatures for Kőszeg, West-Hungary. *Int. J. Biometeorol., 55*, 595–611.

Koch, E., Donelly, A., Lipa, W., Menzel, A. and *Nekovář, J.* (eds.) 2009: Final Scientific Report of COST 725 -Establishing a European data platform for climatological applications. EUR 23922, p.88. http://proclimweb.scnat.ch/portal/ressources/937.pdf.

Liu, H.Q. and *Huete, A.*, 1995: A feedback based modification of the NDVI to minimize canopy background and atmospheric noise. *IEEE Trans. on Geosci. Remote Sens. 33*, 814–814.

Margary, I.D., 1926: The marsham phenological record in Norfolk, 1736–1925, and some others. *Quart. J. Roy. Met. Soc. 52*, 27–54.

Menzel, A., Sparks, T.H., Estrella, N., Koch, E., Aasa, A., Ahas, R., Alm-Kübler, K., Bissolli, P., Braslavská, O., Briede, A., Chmielewski, F.M., Crepinsek, Z., Curnel, Y., Dahl, Å., Defila, C., Donnelly, A., Filella, Y., Jatczak, K., Måge, F., and *Mestre, A.*: 2006. European phenological response to climate change matches the warming pattern. *Glob. Change Biol. 12*, 1969–1976.

Morren, C., 1843: *Fleurs éphémères*. Librairie encyclopédique de Périchon, Bruxelles, 439–440.

NASA LP DAAC, 2011*:* https://lpdaac.usgs.gov/get_data (15.11.2011).

Parry, M.L., Canziani, O.F., Palutikof, J.P., van der Linden, P.J., and *Hanson, C.E. (eds),* 2007: Contribution of Working Group II to the Fourth Assessment Report of the Intergovernmental Panel on Climate Change. Cambridge University Press, Cambridge.

Porter, J.R. and *Gawith, M.*, 1999: Temperatures and the growth and development of wheat: a review. *Eur. J. Agron. 10*, 23–36.

Reaumur, R.A.F., 1735: Thermetric observations made at Paris during the year 1735, compared to those made below the equator on the Isle of Mauritius, at Algiers and on a few American islands. *Acad. Sci. Memoirs.* Acad. Sci. Paris. 545.

Reed, B.C., Brown, J.F., VanderZee, D. Loveland, T.R., Merchant, J.W., and *Ohlen, D.O,* 1994: Measuring phenological variability from satellite imagery. *J. Veg. Sci. 5,* 703–714.

Réthly, A., 1936: Hungary's participation in the international study of phenology. *Erdészeti Lapok. 75,* 1029–1038 (in Hungarian).

Schwartz, M.D. 1994: Monitoring global change with phenology: the case of the spring green wave. *Int. J. Biometeorol. 38,* 18–22.

Shaykewich, C.F., 1995: An appraisal of cereal crop phenology modelling. *Can. J. Plant Sci. 75,* 329–341.

Sparks, T.H., Jeffree, E.P., Jeffree, C.E., 2000: An examination of the relationship between flowering times and temperature at the national scale using long-term phenological records from the UK. *Int. J. Biometeorol. 44,* 82–87.

Wang, E.L and *Engel, T.*, 1998: Simulation of phenological development of wheat crops. *Agr. Syst. 58,* 1–24.

Weir, A.H., Bragg, P.L., Porter, J.R. and *Rayner, J.H.,* 1984: A winter wheat crop simulation model without water and nutrient limitations. *J. Agric. Sci. 102,* 371–382.

White, M.A., de Beurs, K.M., Didan, K., Inouye, D.W., Richardson, A., and *Jensen, O.P.,* 2009: Intercomparison, interpretation, and assessment of spring phenology in North America estimated from remote sensing for 1982–2006. *Glob. Change Biol. 15,* 2335–2359.

Xue, Q., Weiss, A. and *Baezinger, P.S.*, 2004: Predicting phenological development in winter wheat. *Clim. Res. 25,* 243–252.

IDŐJÁRÁS

Quarterly Journal of the Hungarian Meteorological Service
Vol. 116, No. 3, July–September 2012, pp. 211-220

Impact of precipitation on yield quantity and quality of wheat and maize crops

Csaba Gyuricza[1*], István Balla[1], Ákos Tarnawa[1], Ferenc H. Nyárai[1], Katalin Kassai[1], Zsolt Szentpétery[2] and Márton Jolánkai[1-3]

[1] *Crop Production Institute,*
Szent István University
Páter Károly utca 1, H-2100 Gödöllő, Hungary

[2] *Institute of Management and System Engineering,*
Szent István University
Páter Károly utca 1, H-2100 Gödöllő, Hungary

[3] *Agronomy Research Group,*
Hungarian Academy of Sciences–Szent István University,
Páter Károly utca 1, H-2100 Gödöllő, Hungary

**Corresponding authorE-mail: gyuricza.csaba@mkk.szie.hu*

(Manuscript received in final form April 26, 2012)

Abstract—Yield samples of winter wheat *Triticum aestivum* L. and maize *Zea mays* L. taken from consecutive series of crop years at the Nagygombos experimental field of the Szent István University have been evaluated. Impact of precipitation on yield quantity and quality was studied. In case of wheat protein, wet gluten, farinographic value, and Hagberg sedimentation, while in case of maize, protein, starch, oil, and fibre content were examined.

Yield performance of wheat and maize varieties has been highly variable regarding crop years. Wheat was less affected by precipitation in general, however, extremely high precipitation as well as drought caused yield depression. Water demand of yield formation was in accordance with that of C3 – C4 physiological patterns. Yield quality was highly influenced by different crop years. In case of wheat, wet gluten content proved to be a most stable characteristic. Protein, farinographic values, and Hagberg sedimentation figures were more variable in relation with the precipitation of crop years. Yield quantity of maize crop proved to be more variable than quality parameters. Protein values were smaller, and starch values higher in rainy years. Other parameters, like oil and fibre have shown no consequent changes that could be related to the amount of annual precipitation.

Key-words: Precipitation impacts, grain crops, yield, grain quality.

1. Introduction

Water availability profoundly influences all physiological processes of plant life. Water transport of individual plants as well as water budget of the crop site determine growth and development, and finally, quality.

Crop water use, consumptive use, and evapotranspiration are terms used interchangeably to describe the water consumed by a crop. This water is mainly used for physiological processes; a negligible amount is retained by the crop for growth. Water requirements for crops depend mainly on environmental conditions. Plants use water for cooling purposes, and the driving force of this process is prevailing weather conditions. Different crops have different water use requirements, under the same weather conditions (*Várallyay,* 2008; *Pepó,* 2010). Crops will transpire water at the maximum rate when the soil water is at field capacity. When soil moisture decreases, crops have to exert greater forces (energy) to extract water from the soil. Usually, the transpiration rate does not decrease significantly until the soil moisture falls below 50 percent of available water capacity.

Information regarding seasonal crop water requirements are crucial for planning crop species planting especially during drought years. For example, in Hungary, the seasonal water use of maize crop is 550 mm, while wheat crops use some 400. These water requirements are net crop water use or the amount a crop will use (not counting water losses such as deep percolation and runoff) in an average year, given soil moisture levels do not fall below critical levels. Under ideal conditions, this net water requirement is reduced by the effective rain (*Muchová* and *Fazekašová,* 2010; *Führer et al.,* 2011; *Pásztorová et al.,* 2011).

Availability of water is a major stress in relation with yield quality and quantity performance of winter wheat. Cereals represent a most plausible source of human alimentation in the world. Wheat provides a basic staple for mankind. This crop is one of the most important cereals in Hungary with a high economic value. Utility, market, and alimentation values of the crop are highly affected by climatic conditions, annual weather performances, as well as soil moisture conditions (*Ács et al.*, 2008; *Koltai et al.*, 2008; *Skalová et al,* 2008; *Várallyay,* 2008). The aim of wheat production is twofold; to provide quantity and quality. Milling and baking quality of wheat is mainly determined by the genetic basis, however, it can be influenced by management techniques (*Pollhamer,* 1981; *Nagy* and *Jan*, 2006; *Varga et al.*, 2007; *Vida et al.,* 1996). The aim of this study was to determine the role of water availability impacts on wheat quantity and quality. Since main quality indicators – protein, farinographic value, gluten content, Hagberg falling number for wheat, as well as protein, starch, oil, and fibre for maize – have a rather diverse manifestation, there is a need to gain more information concerning the behavior of them.

2. *Materials and methods*

In long term field trials, a wide range of high milling and baking quality winter wheat *Triticum aestivum* L. varieties were examined under identical agronomic conditions during a 15 years period in the experimental years of 1996–2010, and high starch maize (*Zea mays* L.) hybrids were tested in a 9 years period of 2002–2010. The small plot trials were run at the Nagygombos experimental field of the Szent István University, Crop Production Institute, Hungary. Soil type of the experimental field is chernozem (calciustoll). Annual precipitation of the experimental site belongs to the 550–600 mm belt of the northern edges of the Great Plain in a 40 years average, 1961–2000 (*Fig. 1*), while the average depth of groundwater varies between 2 to 3 meters (*Fig. 2*).

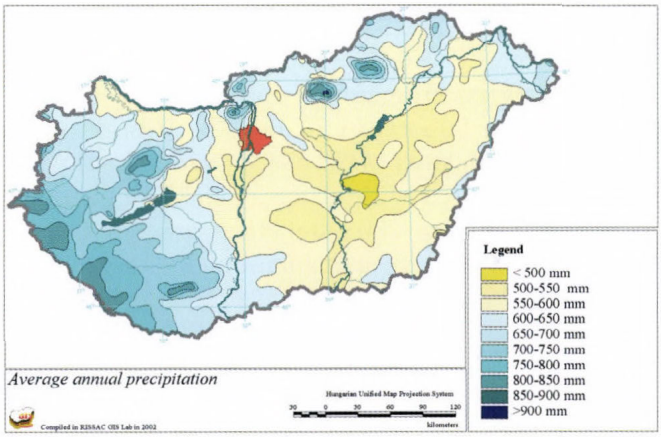

Fig. 1. Spatial distribution of average annual precipitation in Hungary (Source: RISSAC, 2002).

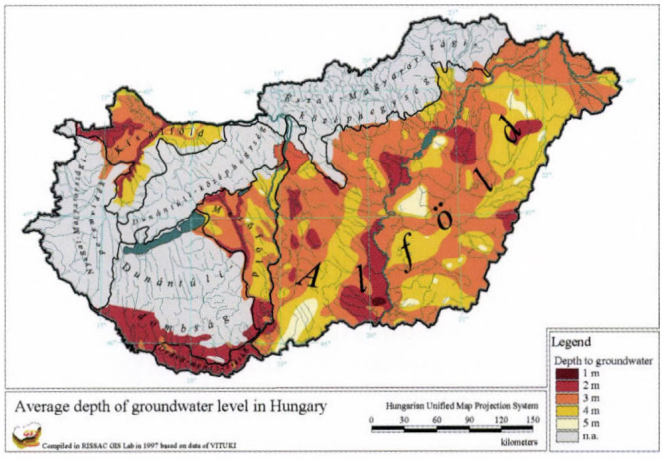

Fig. 2. Average depth of groundwater level in Hungary (Source: RISSAC, 1997).

Experiments were conducted in split-plot design with four replications. The size of each plot was 10 m^2. Plots were sown and harvested by plot machines (standard Wintersteiger cereal and maize specific experimental plot machinery series). Various identical agronomic treatments were applied to plots. Plant protection and plant nutrition applications were done in single and combined treatments. All plots were sown with identical series of wheat varieties and maize hybrids for studying their performance in relation with agronomic impacts. Regarding water availability impacts, experimental mean values of respective treatments and homogenized bulk yield samples were used only. Precipitation records have been evaluated in relation with yield quantity and quality. Wheat grain quality parameters like protein, farinographic value, wet gluten content, and Hagberg falling number results were processed, as well as maize quality parameters: protein, starch, oil, and fibre content. According to the specific harvest conditions of 1999 and 2010 crop years, Hagberg figures were not applicable. In case of maize trials, oil values have been analyzed from 2006 only. Quality characteristics were processed at the Research Laboratory of the SIU Crop Production Institute, according to Hungarian standards (*MSZ 6383,* 1998). Grain yield samples and quality figures were correlated with water availability parameters. Analyses were done by Microsoft Office 2003 statistical programmes with respect to the methodology of phenotypic crop adaptation (*Eberhart* and *Russell,* 1966; *Finlay* and *Wilkinson,* 1963; *Hohls,* 1995).

3. Results and discussion

Annual amounts of precipitation and winter wheat yields have been examined in a 15 years time range, while that of maize in a 9 years period at the Nagygombos experimental field of the Szent István University, Gödöllő. *Tables 1* and *2* illustrate the annual changes of yield and precipitation mean values. Yields have been correlated with water availability.

Yield figures were in accordance with annual precipitation patterns with an exception of some years when the distribution was irregular, eg., in 1999, when 837 mm rainfall, one of the highests in the period examined was recorded, however, a severely drought spring was followed by an extreme moist summer obstructing yield formation and ripening, as well as harvest. Also, the year 2010 with the ever highest annual precipitation, 847 mm measured at the experimetal site resulted in poor yield performance for both wheat and maize crops due long periods of water logging. Apart from these two years, annual precipitation was in accordance with the water consumption of the respective crop species and their C3 and C4 physiological patterns.

Table 1. Annual precipitation, yield and quality figures of a winter wheat trial (Nagygombos, 1996–2010)

Year	Precipitation, [mm]*	Yield [tha^{-1}]	Protein, [%]	Farinographic value	Wet gluten [%]	Hagberg Falling No
1996	544	4.08	15.8	89.7	37.8	339
1997	407	2.88	13.2	50.4	30.5	213
1998	725	6.21	11.5	70.7	27.4	278
1999	837	2.87	14.3	47.4	32.2	–
2000	344	3.32	11.6	44.4	28.3	188
2001	706	5.28	12.0	51.6	27.5	295
2002	426	4.34	17.2	62.4	38.4	362
2003	442	3.47	17.6	63.3	36.8	370
2004	463	6.06	15.3	58.8	29.9	296
2005	705	5.72	14.3	50.9	30.1	282
2006	593	7.11	15.4	54.8	33.7	346
2007	545	5.21	18.1	62.6	38.8	420
2008	612	7.82	13.2	54.1	28.8	349
2009	623	6.55	12.2	58.3	32.7	293
2010	847	3.87	14.5	–	32.3	–

*Source: OMSZ

Table 2. Annual precipitation, yield, and quality figures of a maize trial (Nagygombos, 2002–2010)

Year	Precipitation* [mm]	Yield [tha^{-1}]	Protein, [%]	Starch [%]	Oil [%]	Fibre [%]
2002	426	5.44	9.2	63.5	–	4.4
2003	442	4.12	7.63	72.2	–	4.35
2004	463	5.60	8.43	68.8	–	4.87
2005	705	5.22	7.1	74.5	–	3.96
2006	593	7.40	6.7	74.1	4.6	3.84
2007	545	8.24	8.5	65.8	4.7	5.8
2008	612	6.28	7.9	64.3	4.6	3.4
2009	623	7.34	6.8	63.3	4.2	2.1
2010	847	4.09	8.2	70.5	4.4	–

*Source: OMSZ

Quality manifestation of winter wheat yields have been impacted by annual precipitation in general in accordance with previous reports (*Klupács et al.*, 2010; *Pepó,* 2010). *Table 1* provides a summary of changes in yield

quality characteristics. Apart from grain yields, protein, farinographic value, wet gluten, and Hagberg falling number records have also been evaluated all along the experiment. Yield figures were in accordance with annual amounts of precipitation with two exceptions regarding the 1999 and 2010 crop years.

Wet gluten content of grain samples proved to be a most stable quality characteristic. Annual changes of protein figures were significant. Farninographic values and Hagberg falling number figures were affected by precipitation. In some dry years like 2002 and 2003, baking quality was far better than in moist years, however, it was escorted by low yield figures as well. The manifestation of the Hagberg falling number was due to the rain conditions of the harvest and post-harvest periods. Re-moistening of ripen dry grain may result in alterations of the α-amylase activity, thus, it may have an impact on rheological characteristics of dough.

Results of maize experiments are summarized in *Table 2*. Yield quantity of maize crop proved to be more variable than quality parameters. Protein values were smaller, and starch values higher in rainy years. Oil values have shown no major changes. Fibre content values in certain crop years were randomly changing, however, no systematic trends could be observed.

4. Conclusions

Water availability can be considered as a basic factor related to yield quality and quantity performance of grain crops. In an agronomic long term trial run at the Szent István University's Nagygombos experimental site, the impact of water availability on wheat and maize crops have been evaluated. Correlation tables are presented in *Tables 3* and *4*. Various crop years have had different impacts on crop yield quantity. Yield figures were not in correlation with annual precipitation in general. However, with an exception of two years of extremely high precipitation, yield figures were in accordance with that the annual precipitation. Moisture availability had diverse influence on quality manifestation. High precipitation has often resulted in poorer quality, especially gluten and Hagberg values have been affected by that. Protein and gluten values proved to be the most stable quality characteristics in this study. Drought stress reducing the amount of yield has induced quality improvement in a few cases. Maize yields were more variable than that of wheat. Maize quality parameters proved to be more stable than yield figures except for fibre content values (*Fig. 3*). In *Fig. 3*, maize yields and quality parameters are displayed on a 9 years basis, while wheat yields and quality parameters are displayed on a 15 years basis. Both yields are clustered into three groups representing dry (<500 mm), normal (500–700 mm), and moist (>700 mm) crop years, and the range of stability is expressed in % of respective X value deviations.

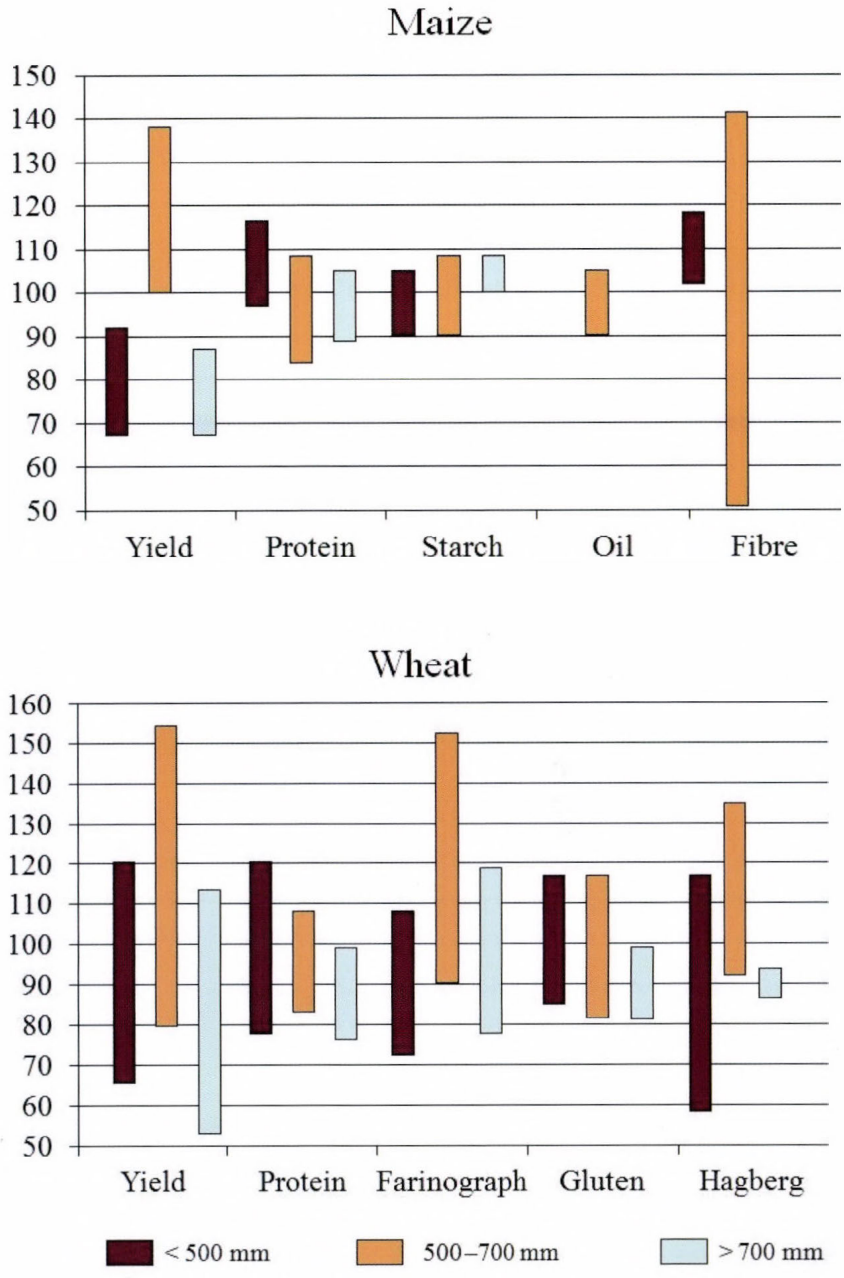

Fig. 3. Stability of yields and quality parameters of maize and wheat crops. (Nagygombos, 2002–2010; 1996–2010)

Table 3. Correlation figures of winter wheat trial. (Nagygombos, 1996–2010)

Correlation r value	Year	Precipitation [mm]	Yield [tha^{-1}]	Protein [%]	Farinographic value	Wet gluten [%]	Hagberg Falling No
Year	1	0.254	0.526	0.168	–0.268	0.084	0.449
Precipitation [mm]	0.254	1	0.180	–0.244	–0.044	–0.249	0.178
Yield [tha^{-1}]	0.526	0.180	1	–0.165	0.058	–0.246	0.308
Protein [%]	0.168	–0.244	–0.165	1	0.359	0.874	0.778
Farino-graphic value	–0.268	–0.044	0.058	0.359	1	0.513	0.453
Wet gluten [%]	0.084	–0.249	–0.246	0.875	0.513	1	0.716
Hagberg Falling No	0.449	0.178	0.308	0.778	0.453	0.716	1

Regression coefficient	Year	Precipitation [mm]	Yield [tha^{-1}]	Protein [%]	Farinographic value	Wet gluten [%]	Hagberg Falling No
Year	1	0.007	1.493	0.348	–0.098	0.095	0.029
Precipitation [mm]	8.807	1	17.69	–17.50	–0.547	–9.710	0.348
Yield [tha^{-1}]	0.185	0.002	1	–0.121	0.008	–0.097	0.007
Protein [%]	0.081	–0.003	–0.227	1	0.070	0.475	0.028
Farino-graphic value	–0.733	–0.004	0.415	1.833	1	1.425	0.081
Wet gluten [%]	0.075	–0.006	–0.619	1.610	0.185	1	0.048
Hagberg Falling No	6.786	0.091	12.82	21.28	2.530	10.65	1

There have been two parameters in this study with less chance to observe; once the soil impacts on water availability, since the trials were designed in a *ceteris paribus* agronomic layout. The other is the varietal differences between wheat cultivars and maize hybrids. These fields are to be evaluated in further studies.

Table 4. Correlation figures of maize trial (Nagygombos, 2002–2010)

Correlation r value	Year	Precipitation [mm]	Yield [tha^{-1}]	Protein [%]	Starch [%]	Oil [%]	Fibre [%]
Year	1	0.795	0.270	–0.331	–0.166	–0.712	–0.489
Precipitation [mm]	0.795	1	–0.131	–0.355	0.269	–0.448	–0.478
Yield [tha^{-1}]	0.270	–0.131	1	–0.223	–0.363	0.316	–0.024
Protein [%]	–0.331	–0.355	–0.223	1	–0.463	0.456	0.644
Starch [%]	–0.166	0.269	–0.363	–0.463	1	0.263	0.169
Oil [%]	–0.711	–0.448	0.316	0.456	0.263	1	0.858
Fibre [%]	–0.489	–0.478	–0.024	0.645	0.169	0.856	1

Regression coefficient	Year	Precipitation [mm]	Yield [tha^{-1}]	Protein [%]	Starch [%]	Oil [%]	Fibre [%]
Year	1	0.016	0.505	–1.072	–0.101	–5.625	–1.107
Precipitation [mm]	39.42	1	–12.13	–56.84	8.117	–263.1	–44.07
Yield [tha^{-1}]	0.144	–0.001	1	–0.385	–0.118	2.531	–0.031
Protein [%]	–0.103	–0.002	–0.129	1	–0.087	1.875	0.532
Starch [%]	–0.273	0.009	–1.117	–2.461	1	6.000	0.742
Oil [%]	–0.090	–0.001	0.039	0.111	0.012	1	0.124
Fibre [%]	–0.216	–0.006	–0.019	0.782	0.039	5.936	1

Acknowledgements—Authors are indebted regarding support received from NKTH and from the HAS.

References

Ács, F., Horváth, Á. and *Breuer, H.*, 2008: The role of soil in variations of the weather. *Agrokémia és Talajta. 57,* 225–238.

Eberhart, S.A. and *Russell, W.A.*, 1966: Stability parameters for comparing varieties. *Crop Sci. 6,* 36–40.

Finlay, K.W. and *Wilkinson, G.N.*, 1963: The analysis of adaptation in a plant breeding program. *Australian J.f Agric. Res. 14,* 742–754.

Führer, E., Horváth, L., Jagodics, A., Machon, A., and *Szabados, I.*, 2011: Application of a new aridity index in Hungarian Forestry practice. *Időjárás 115,* 205–216.

Hohls, T., 1995: Analysis of genotype environment interactions. *South African J. Sci. 91,* 121–124.

Klupács, H., Tarnawa, Á., Balla, I., and *Jolánkai, M.*, 2010: Impact of water availability on winter wheat (*Triticum aestivum* L.) yield characteristics. *Agrokémia és Talajtan 59,* 151–156.

Koltai, G., Milics, G., Neményi, M., Nagy, V., and *Rajkai, K.*, 2008: Plant water supply of layered alluvial soils under different weather conditions. *Cereal Res. Commun. 36, Suppl.* 167–171.

MSZ 6383,1998: 824/2000/EK Grain quality standards, Hungary.

Muchová, D. and *Fazekašová, D.*, 2010: The contribution of variety mixture utilization for enhancing the resilience of agro-ecosystems. *Növénytermelés 59, Suppl.* 509–512. (in Hungarian)

Nagy, V. and *Ján, H.*, 2006: Method to estimate the critical soil water content of limited availability for plants. *Biologia. 61. Suppl. 19.* 289–293.

Pásztorová M., Skalová J., Vitková J. 2011: Analisys of impact of management on groundwater level of abrod wetland. *Növénytermelés. 60. Suppl.* 361–364. (in Hungarian)

Pepó P. 2010: Adaptive capacity of wheat (Triticum aestivum L.) and maize (Zea mays L.) crop models to ecological conditions. *Növénytermelés. 59. Suppl.* 325–328. (in Hungarian)

Pollhamer, E. 1981: *A búza és a liszt minősége. (Quality of wheat and flour).* Mezőgazdasági Kiadó, Budapest. (in Hungarian)

Skalová, J. and Jaros, B., 2008: Soil water regime assessment in Morava basin. *Cereal Res. Commun. 36, Suppl.* 243–246.

Várallyay, G., 2008: Extreme soil moisture regime as limiting factor of the plants' water uptake. *Cereal Res. Commun. 36, Suppl.* 3–6.

Varga, B., Svečnjak, Z., Jurković, Z., and *Pospišil M.*, 2007: Quality responses of winter wheat cultivars to nitrogen and fungicide applications in Croatia. *Acta Agron. Hun., 55,* 37–48.

Vida, Gy., Bedő, Z. and *Jolánkai, M.*, 1996: Agronómiai kezeléskombinációk őszi búzafajták sütőipari minőségére gyakorolt hatásának elemzése főkomponens-analízissel. (Impacts of various agronomic methods on baking quality of wheat evaluated with factor analysis). *Növénytermelés 45,* 453–462. (in Hungarian)

IDŐJÁRÁS

Quarterly Journal of the Hungarian Meteorological Service
Vol. 116, No. 3, July–September 2012, pp. 221–236

Impact of atmospheric black carbon on some members of the heat and water balances

Angela Anda

University of Pannonia, Georgikon Faculty
Department of Meteorology and Water Management
P. O. Box 71, Keszthely H-8361, Hungary
E-mail: anda-a@georgikon.hu; anda@keszthelynet.hu

(Manuscript received in final form February 10, 2012)

Abstract—Impact of atmospheric black carbon (BC) on albedo, evapotranspiration, and growing characters of field grown maize was investigated at Keszthely, Hungary, over the 2010–2011 growing seasons. Chemically "pure" black carbon was used in weekly pollution (3 g m^{-2}). Low doses simulated the effect of particulates derived from vehicle exhaust and abrasion of tyres. Albedo of crop stand (0.3 ha/treatment) was measured with CMA-11-type pyranometers every 6 seconds. Maize grown in Thornthwaite-type compensation evapotranspirometers was included in the study. Dry matter yield of maize cob was determined in the end of the growing season.

Surprisingly, BC did not influence significantly the phenological phases and length of the crop year. Due to wet weather in 2010, seasonal water loss of BC treated maize increased only with 4%. Amount of seasonal total evapotranspiration of polluted crops was about threefold higher in dry 2011. The mean albedo of polluted canopy declined in both seasons. The surplus energy retention of BC polluted crops increased the canopy surface temperature of about 0.5–1.5 °C in midday hours, independently of the studied year. Significant yield loss in BC polluted maize stands was observed only in rainfed canopy. The production loss of dusted maize amounted 8.7% and 19.8%, in 2010 and 2011, respectively. Extra water of evapotranspirometers prevented yield drop-out of soot polluted plants. In arid years, BC had more severe impacts on maize characteristics and yield.

Key-words: black carbon, albedo, evapotranspiration, canopy temperature, dry matter, yield, maize

1. Introduction

Size and composition of atmospheric particulate matters (PM) are greatly variable. The class of particles having grain size of 2.5–10 μm is the coarse fraction. They are emitted to the air directly mainly from natural sources (earth crust, volcano eruption, deflation, erosion, etc). The fine fraction comprises particles below 2.5 μm. Fine fraction is forming by chemical and physical processes in the atmosphere. In the air of Budapest, the number of fine particles is higher (100,000/ml) than that of the coarse class (below 100/ml) after *Salma* and *Ocskay* (2006). The black carbon content is only about a few percent in the coarse fraction, while it may reach the 20% in the fine one. Diesel-exhaust particle may be elemental carbon up to 20–40% (*Balmes,* 2010). Soot has also been derived from incomplete burning (fossil fuels, biomass, etc.) as well as from industrial processes. Vehicle tyres are also sources of black carbon.

In EU standard, we are allowed to exceed the daily suspended particulate matter limitation of 50 $\mu g/m^3$ 30 times per year (WHO, 2000; *Krzyzanowski et al.*, 2005). Unfortunately, already in the course of February, we often overstep this threshold at Hungary (examples are the years 2009 and 2010). This is due to the aged carriage park and the weather conditions in Hungarian winter.

Global scale influence of black carbon (BC), changing the radiative properties of the atmosphere (nucleation of clouds) and cryosphere (melting of ice cover) was published among others by IPCC (2007) or *Giere* and *Querol* (2010). The effect of soot on human health (*Behndig et al.*, 2011) and on some soil properties (*Hammes et al.*, 2008; *Nguyen et al.*, 2009; *Lorenz et al.*, 2010) are also well investigated. Studies on health impacts of particulates show an increased number of hospital admissions from chronic obstructive pulmonary disease, asthma, and other respiratory diseases (*Postma et al.*, 2011).

The importance of albedo modifications are widely studied in different observation levels. The local level contains relationship between crop life (physiological processes) and solar radiation. *Betts et al.* (2007) published that the global surface temperature change owing to vegetation changes is mainly due to the surface albedo changes. Land-use change in the past, involving variation from natural vegetation of relatively low albedo to arable crop growing with higher albedo has suppressed surface temperatures (*Monteith* and *Unsworth*, 1990). In an arable region of small size, *Matthews et al.* (2003) determined a 0.17°C cooling in response to 0.03–0.09 increase in albedo. In field level, *Ridgwell et al.* (2009) simulated more intense, 1 °C cooling in summertime surface temperature when increasing the albedo with 0.04.

Due to difference in crop stand morphology, significant variability exists not only between crop species, but among varieties of the same plant. The maximum of albedo modification due to crop varieties may reach the value of 0.04 (*Hatfield* and *Carlson*, 1979; *Febrero et al.*, 1998). One of the possible reasons of albedo variability within crop species may be the existence of wax or

other leaf structural differences. Not only the crop species but the density of maize may impact the albedo. In thin maize stands (40,000 ha^{-1}), the decrease in albedo was significant, sometimes being as high as 8–10% when compared to dense canopy (100,000 ha^{-1}) with the same species (*Anda* and *Loke*, 2005).

Until now it remains unknown, how and to what extent the soot deposition effects the crop life. The aim of our investigation is to discuss the relationship between maize physiological properties and soot deriving from vehicle exhaust and tyres. A reproducible field trial was conducted, that is not extended in pollution studies even now. Despite that two decades have been passing, we still aimed the "stage of reproducible exposure experiment" that has not yet advanced (*Olszyk et al.*, 1989) in contaminated crops grown in the open air.

2. Material and methods

Field experiment was conducted to study the impact of black carbon on some maize crop characteristics and canopy microclimate. The place of the study was the Agrometeorological Research Station of Keszthely (46°45'N, 17°14'E, 102 m above sea level), during the vegetation periods of 2010 and 2011. The prevailing genetic soil type is the Ramann type brown forest soil with a mean bulk density of 1.46 $Mg\,m^{-3}$ in the top 1 m of the profile. The available water capacity is 150 $mm\,m^{-1}$. A Swiss-bred maize hybrid, Sperlona (FAO 340), was sown in the field using a plant density of 70,000 plants per hectare. A part of the crops was grown under rainfed conditions, while the others in growing chambers of Thornthwaite-type compensation evapotranspirometers (ET). This latter part of the experiment supplied a treatment of "ad libitum" watering level. The size of the evapotranspirometer's growing chamber was 2×2 m in area, and 1 m in depth. They were filled with a soil monolith from the surrounding field, layered as in the natural state. Dimension of field plots differed from ET chambers, due to the needs of radiation (albedo) measurements. The area of rainfed plots reached 0.3 ha.

Except of unlimited watering of evapotranspirometers, the usual agronomic procedures (plant protection, weed control) recommended for the place by the local staff of the University of Agricultural Sciences, Keszthely, were applied.

The black carbon applied by the Hankook Tyre Company (Dunaújváros, Hungary) to improve the wear resistance of tyres was used as contaminant. More than half of the soot grains are below 18.8 μm, and 90% of the total soot quantity is below 50.6 μm (*Fig. 1*). The black carbon is chemically "pure", i.e., it is free of other contaminants (heavy metals, etc.), so the reproducibility of the experiment is not problematic, unlike that of tests on other atmospheric air pollutants. Relatively small doses were applied (3 $g\,m^{-2}$), but they were repeated at weekly intervals. Due to lack of local information, in determination of applied dose, the extreme amounts of dust sediments published to vegetation surface

during the growing season (*Prusty et al.*, 2005; *Freer-Smith et al.*, 2005), and the soot content of local road dust (*Salma* and *Ocskay*, 2006) were taken into account. The published road dust depositions included the background pollution. A motorized sprayer of SP 415 type was used to pollute the crops. The instrument acted as a pulverizer (dry application of BC).

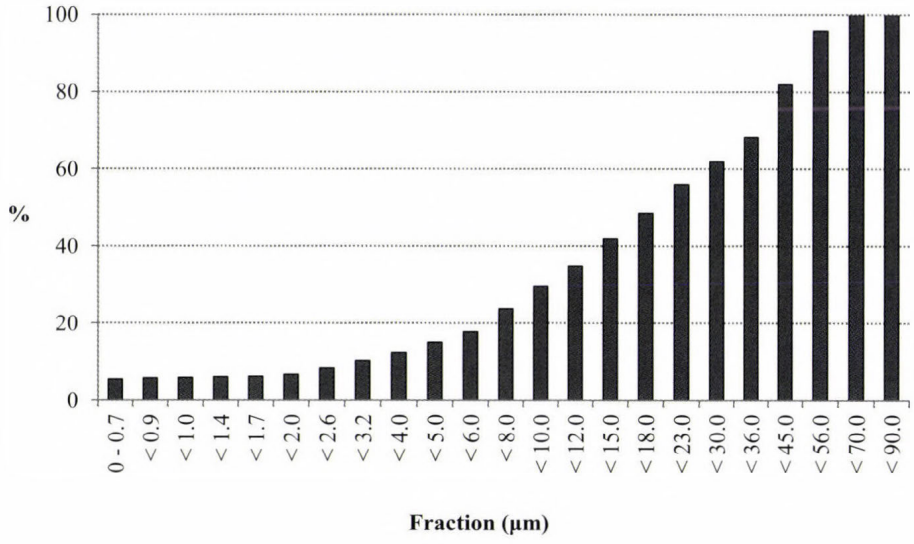

Fig. 1. Cumulative curve of the size distribution of black carbon.

Pyranometers of the CMA-11 type (Kipp & Zonen, Vaisala) were installed on columns of adjustable height in the centre of the 0.3 ha plots designated for albedo measurements. The height of the sensors was raised each week as the plants grew, so that they were always at least 1.5 m above the canopy. Data were collected using a Logbox SD (Kipp & Zonen, Vaisala) datalogger in the form of 10-minute means of samples taken every 6 seconds. Either these 10-minute means or the hourly or daily means calculated from them were used for the analysis.

Canopy temperature was measured by infrared thermometer of RAYNGER II. RTL type (Raytek., Santa Cruz, Calif. USA) with 2 ° field of view and an 8–14 µm waveband filter. For sample takings, the thermometer was hand-held about 1 m above the canopy at an oblique angle three, four or five times per reading at midday (from 12:00 to 3:00 p.m.). After canopy closure, temperature readings were taken daily in clear-sky and calm weather conditions. The emissivity was set to 0.96.

The grain yield was measured in plants from the 10 m^2 at the center area of each plot. In case of ET, the whole growing area of the chambers (4 m^2) was included in yield analysis. The samples were oven dried at 60 °C to a constant weight for 5–7 days and then weighed.

Meteorological data were obtained from the local QLC-50 automatic climate station.

Due to the fixed nature of evapotranspirometers, the experiment was laid out in a block design with four replications, while the dry plots were arranged in a randomized complete block design. The non-irrigated plots, also used for solar radiation measurements, had an area of 0.3 ha. Data analysis was performed using the STATA 5.0 computer package (STATA 5.0, 1996). The t-test was used to determine significant differences between the dry matter yields of polluted and control plants and of rainfed and ET-grown plants. In time series analysis, two-tailed t-test was applied. The significant level was settled to 5% ($P<0.05$).

3. Results and discussions

3.1. Crop and weather characteristics in the seasons

In 2010, the seasonal and monthly mean temperatures were in good correspondence with the long-term mean with the exception of July. In July, mean air temperature was 1.8 °C higher than the 1901–2000 average. Mean air temperature was 1.1 °C higher than the climatic norm in the season of 2011. The only exceptional month in 2011 was also July, when the air temperature was close to the average. The growing season of 2010 was substantially wetter than the mean, having 38% higher rainfall sum than the average over many years (*Fig. 2*). May, August, and September received more than double amount of rainfall. In July, however, the precipitation dropped off the long-term mean, the air temperature was high. Oppositely to the previous summer, the growing season of 2011 was extremely dry (the driest season from the beginning of weather observations at Keszthely). The amount of rainfall hardly exceeded the half of the long-term average (51%).

In spite of the variable weather of the two studied summers, the black carbon did not influence either the duration of the vegetation period or the length of phenological phases irrespective to water supplies.

Like a tendency, a moderate increase in the final height of dusted crops (about 20–40 cm) was measured independently on water level or season. This positive modification might be attributed to warming effect of black carbon, mainly during the cooler periods of the crop year, at the beginning of the growing season. In spring, higher air temperature may increase the intensity of photosynthesis producing more photosynthate used in the course of crop growing. The warming impact of soot was detected in the surface temperature of polluted crops.

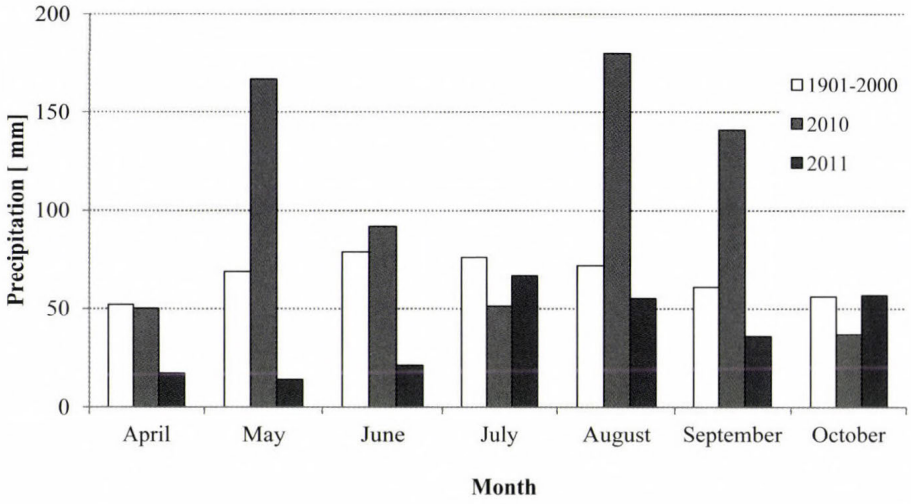

Fig. 2. Monthly sums of precipitation at Keszthely. The values were compared to the climate norm (1901–2000).

The excessive rainfall in 2010 approximated the assimilatory surface sizes of different treatments. Irrespectively to the extra water supply, the seasonal mean of leaf area index (LAI) in the plots was close to that of measured in the ET chamber (data not shown). In 2011, the warmer spring and early summer moderately increased the size of LAI comparing to the results of the previous year (*Figs. 3a* and *b*). Later on, drought of 2011 generated an intense leaf shriveling, and finally the yearly mean assimilatory surfaces were similar in the two studied seasons. Deviations in seasonal mean value of LAI between the two studied years were below 5% with the exception of non-irrigated control (6.8%).

In the wet summer of 2010, the yearly mean LAI of polluted maize remained unchanged. The black carbon was only drawn out the leaf withering in ET chambers. In polluted ET the green leaves lasted a week longer. The drying off of polluted crops in ET began a week later that increased the withering of dusted maize. It was excluded from the length of the growing season as it acted after full ripe of maize. In 2011, the seasonal mean LAI of polluted crops increased with 14.8 ($P<0.05$) and 11.4% ($P<0.05$) in non-irrigated control and ET, respectively. In rainy weather the rain might wash out the pollutant from the leaf surface on a larger extent. At about 15–20% of the dust has been removed by rain in our observation. The washing out was also modeled in laboratory, before conducting the field trial.

One of the most important plant characteristics is the season long-integrator, the yield. We expressed it in terms of ear dry matter (DM) production. The excessive water supply in ET could not amount the grain DM production probably due to rainy summer in 2010. In the next season,

the "ad libitum watering" of ET significantly rose the maize yield with 13% comparing to the production of non-irrigated control plots ($P<0.01$). This is in accordance with earlier local investigations (*Anda*, 2001).

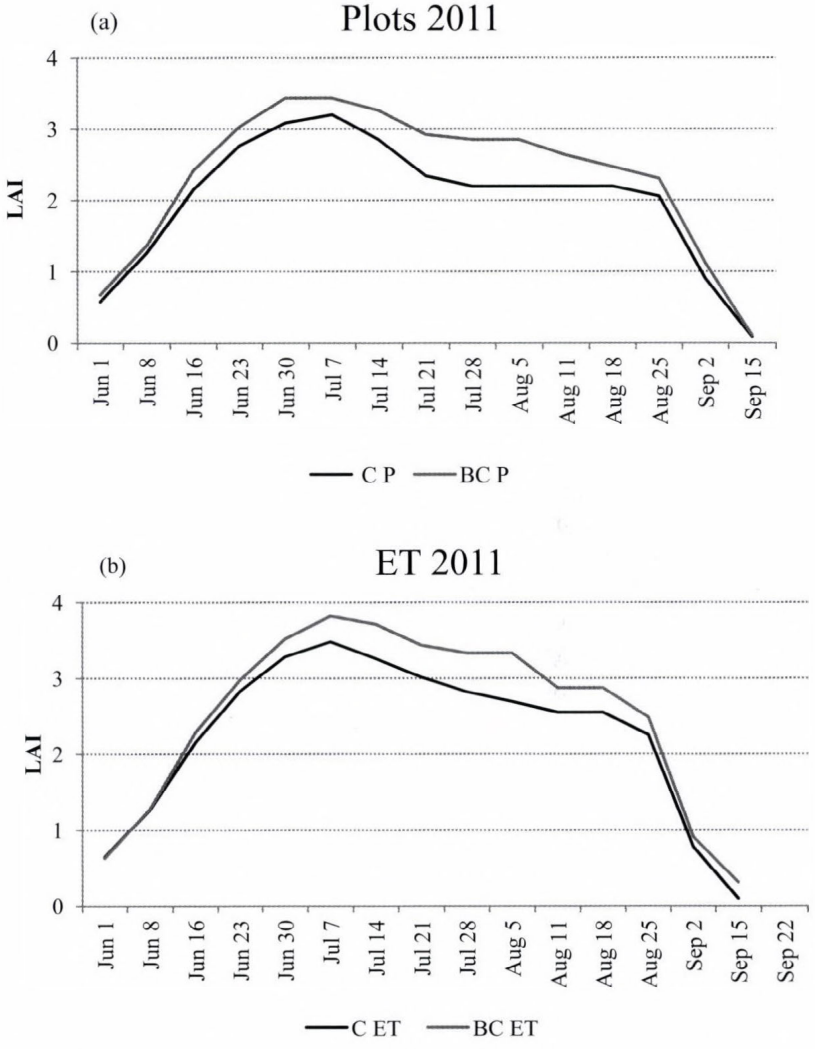

Fig. 3(a) and (b). Seasonal variation in weekly LAI of plots (P) and ET growing chambers (ET). C and BC stands for control and polluted treatments, respectively.

The black carbon pollution significantly declined the grain DM of maize grown in the rainfed plots. The yield loss was close to 9% ($P<0.05$) in 2010, while yield depression doubled ($P<0.05$) during the dry 2011. The same was not

observed in dusted ET. A moderate, but not significant deterioration of DM production, including the grain DM of maize grown in the ET chambers was obtained. Finally, the surplus water of ET chambers reduced the yield loss of polluted grain maize irrespectively of variable weather conditions of the two seasons.

3.2. A few members of the heat and water balances

3.2.1 Reflection coefficient, the albedo (a)

Incoming solar radiation is partly reflected from the canopy, partly transmitted to the crop stand, and partly absorbed by the crops. The fraction of incoming short wave solar radiation that is reflected from the surface is called albedo. The albedo is the measure of lost radiation energy from the canopy surface.

In earlier studies, the mean albedo of maize is placed somewhere between 0.18 and 0.22 (*Davies* and *Idso*, 1979; *Hatfield* and *Carlson*, 1979; *Oke*, 1987; *Campbell* and *Norman*, 1998). In the two seasons investigation, after canopy closure, the mean albedo was 0.17 in the control canopy. The highest daily mean values of 0.21 and 0.20 (2010 and 2011) were measured in July, while the minimum albedo (0.11) was found in the end of September, when the crops were completely dried. The black carbon significantly decreased the seasonal mean albedo with about 0.03.

The size of albedo depends on surface characteristics – mainly the color and roughness – and on sun elevation. The black carbon makes the crop color darker declining the size of its albedo. Averaged over the whole measuring period, the mean albedo of polluted maize was 17.5% and 21.7% lower ($P<0.05$) in 2010 and 2011, respectively, than the albedo of control maize *(Fig. 4)*. Soot pollution resulted in a decline in the albedo leaded to higher energy retention of polluted crops. This amount of energy might be high enough to modify the physiological processes as well as crop microclimate.

Over the observations, the greatest deviation in daily mean albedo found for the wax ripe period was 30% in the polluted crop stand. At the beginning of the vegetative period, mainly until canopy closure, alteration in mean albedo of polluted crops fell well below 10%.

Shape of albedo's diurnal variation followed the regular one; while the greatest values were measured at low solar angles (afternoon hours), the minimum albedo was obtained at high elevation (*Fig. 5*). Irrespectively of treatment, the variability of albedo is more pronounced for the morning and afternoon hours. The sample day of *Fig. 5* contains twenty-minute averages of albedo for July 21, 2010. This day was extremely hot with extra strong insolation and high temperatures. The variability in the shape of albedo's curve was the most compensated in the course of cloudless days. These observations were also valid for the season of 2011.

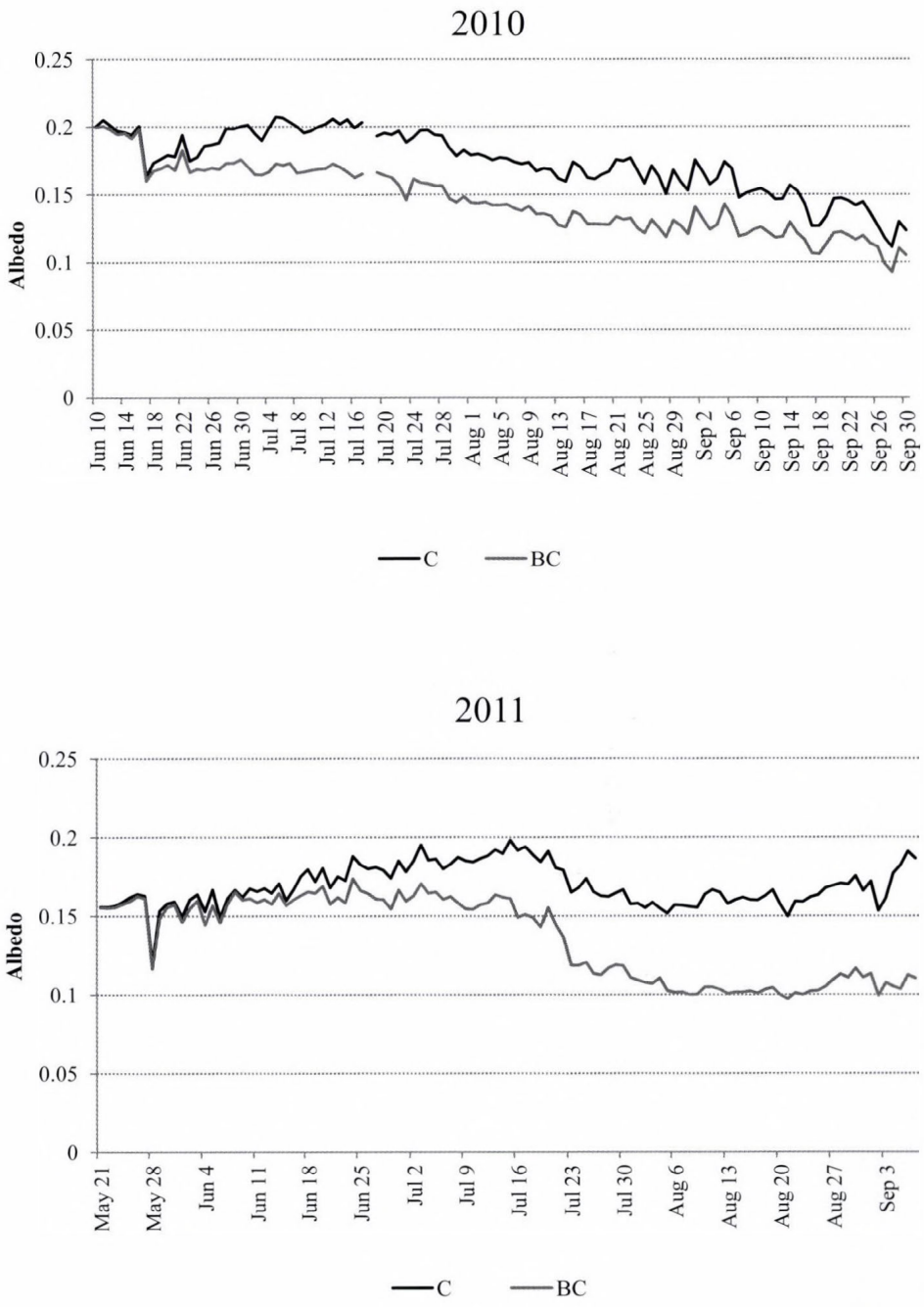

Fig. 4. Daily means of albedo during 2010 and 2011. C and BC denotes control and polluted crop stands, respectively.

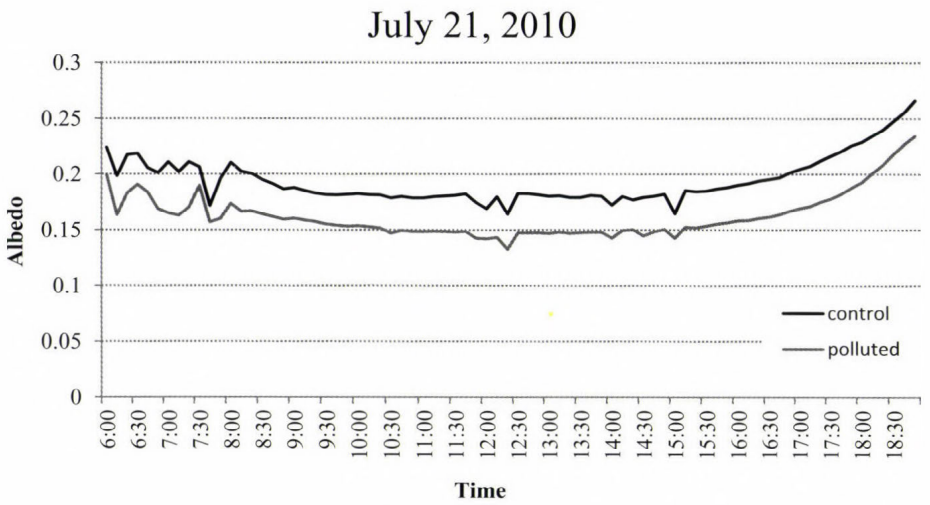

Fig. 5. Diurnal variation in the albedo of maize. Black and grey lines represent the albedo of control and polluted crops, respectively.

Irrespectively to studied summer, daily variation in the albedo's difference due to pollution remained the same as in the control at about in the half of the sample days. In the other half of the days, more pronounced soot impact on albedo was found at low solar elevation reaching values of 0.05–0.09 (*Fig. 6*). Equalized differences can be clearly detected at high insolation.

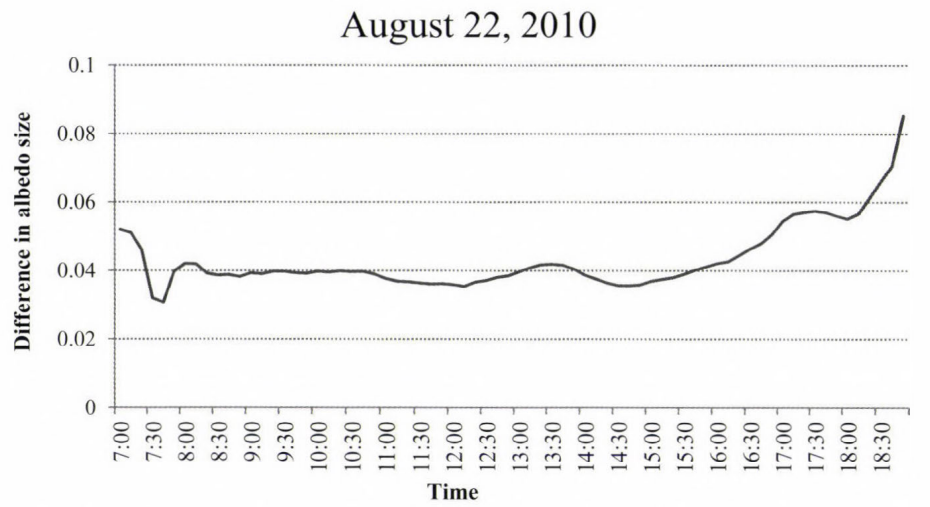

Fig. 6. Differences (contol data - polluted data) in the twenty-minute mean of albedo on August 22, 2010.

3.2.2. Maize evapotranspiration

For maize in ET, the seasonal totals of evapotranspiration were 403.7 and 572.1 mm in 2010 and 2011, respectively. Increment in water loss of the arid season was 34.5% ($P<0.01$). Soot pollution also rose the evapotranspiration of maize. In the wet season of 2010, only slight difference was observed (3.9%). The impact of black carbon increased by 9.6% during the arid 2011. Analyzing the evapotranspiration on daily basis showed that differences between treatments were consistent in time with and without pollution. The top water uses were 7.0 and 7.9 mm day^{-1} in control and polluted maize, respectively on July 19, 2010. The maximum water losses were 8.8 and 10 mm day^{-1} in the middle of July, 2011.

Variability in evapotranspiration is influenced by atmospheric and plant (biological) factors. The solar radiation and transpiration surface size (LAI) are the most important governor factors of plant water losses. Analyzing the evapotranspiration relationships, radiation properties were characterized by albedo, crop features were taken into account by transpiration surface size in the polluted and control treatments separately (*Figs. 7* and *8*). Data collected after canopy closure was included in the study, since information from the early vegetative period deteriorated the relationship between the variables. The number of observation pairs was 81. The observed relationship agreed well in both seasons, this is why the data of 2010 are presented only.

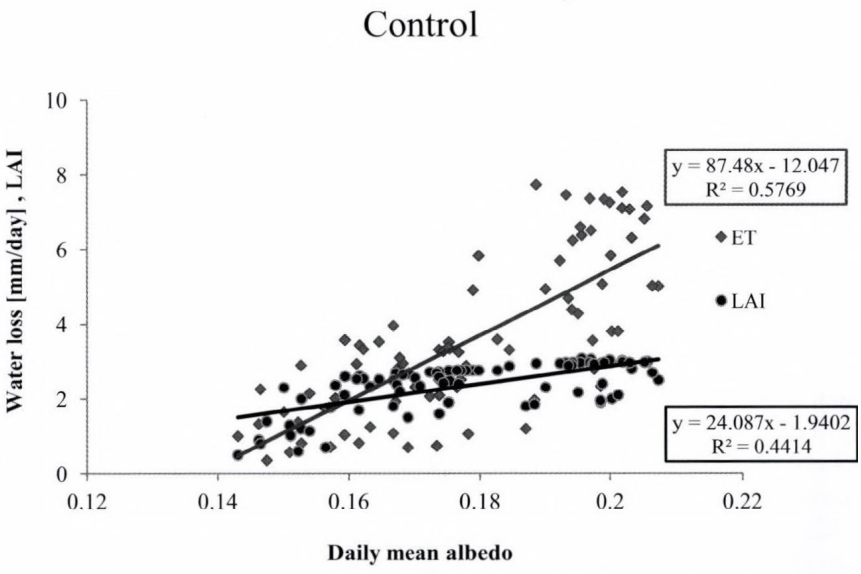

Fig. 7. Impact of albedo on evapotranspiration and leaf area index in control canopy. The number of measurements was 81.

Linear relationship exists between daily mean albedo and evapotranspiration of both treatments. Low water losses were measured in the end of the season when albedo also declined. After canopy closure (the end of June), growth in albedo results almost the same increment in crop water losses, irrespectively to the soot pollution. The reason of this surprising relationship is probably due to the drying off of leaves during the last third of the vegetation period. Withering opens the canopy, declines both transpiration and albedo. There was hardly enough difference in line interception between control and polluted treatments.

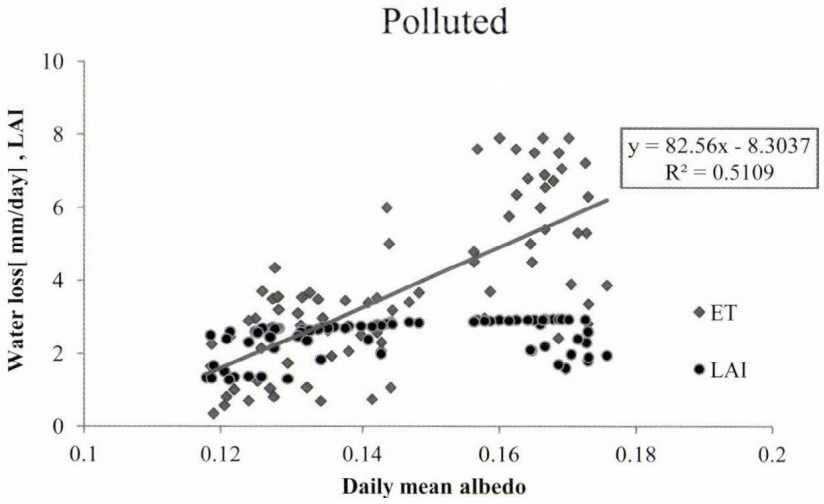

Fig. 8. Impact of albedo on evapotranspiration and leaf area index in polluted canopy. The number of measurements was 81.

The albedo-LAI relation was weaker than the albedo-water loss relation both treatments. In the control maize, linear relationship in albedo and evapotranspiration surface size may be acceptable, but not in case of polluted crops. Albedo of maize with BC was independent of the transpiration surface size after canopy closure. *Oguntunde* and *van de Giesen* (2004) found closer connection between albedo and LAI (correlation coefficient 0.970) in maize for the whole vegetation period. Only the linear shape of relationship agreed with earlier results (albedo data of open canopy are excluded from the study).

For a long while we know that temperature determines the plant growth and particularly development rates. *Warrington* and *Kanemasu* (1983) published that leaf initiation, leaf appearance and elongation are strongly related to temperature in maize. From the thermal time concept, strong correlation is assumed between air and crop temperatures (*Jackson*, 1982). Canopy temperature gave the best results in growth predictions when compared to soil

and air temperatures (*Jamieson et al.*, 1995). In spite of the arising error, when extreme humidity and cloudiness mask canopy temperature differences with respect to the temperature differences in the air, the surface temperature is widely applied also in semi-humid regions (*Bajwa* and *Vories*, 2007).

The direction of change in canopy surface temperature resulted from black carbon pollution was irrespective to water supply. The size of change in non-irrigated crops exceeded the temperatures of crops grown in ET. As a rule, difference in crop temperatures between control and polluted plants in ET dropped at about half of those measured in the non-irrigated control plots. As the direction of soot impact on canopy surface temperature was independent of the seasons, detailed discussion is given for 2010 only. In 2011, the size of seasonal mean temperature change in ET resulted from pollution was almost the same as measured in the earlier season. In non-irrigated polluted control plots, more intense crop temperature modification was observed, and the increment in the seasonal mean of polluted maize reached the 1.6 °C (data not shown).

Altogether, 13 days were suitable for canopy temperature measurements in the wet growing season of 2010. We could only take one and two samples in June and August, respectively. In July, when monthly mean temperature was 1.8 °C higher than the climate norm, the crop temperatures were also extremely high, similarly to the larger part of the season in 2011. In spite of the extra water supply in ET, crop temperatures exceeded 31–32 °C three times during July. (The number of these occasions was the same in rainfed plots.) High crop temperatures in 2010, exceeding air temperatures, could not have been the result of water deficiency, but can be attributed to the influence of heat stress. The precipitation might be quite sufficient to supply the maize water need even in the rainfed plots. Finally, soot increased with 0.97 °C the seasonal mean of crop temperature observed at solar noon. Due to the same crop temperature change in ET and control treatments, the impact of BC measured in control is presented (*Fig. 9*). The same data for 2011 was 1.6 °C.

4. Conclusions

With the exception of leaf withering, maize polluted with low doses of BC ($3\ g\ m^{-2}\ week^{-1}$) produced similar development (length and appearance of phenological phases). The polluted crops retained their green leaves a week longer in wet 2010. Like a tendency, the final crop height increased with 0.2–0.4 m in both seasons. It is important to mention, that this increment was not proved statistically.

The albedo of a crop stand is a key regulator in atmospheric circulation and plays an important role in mechanistic accounting of many ecological processes (*Oguntunde* and *van de Giesen*, 2004). The authors found that the albedo is avaluable input in agricultural practice as well as in different types of modeling

(crop production models, eco-hydrological models, regional weather and climate models). Soot pollution significantly declined the mean albedo with about 0.03 after canopy closure. This value meant 17.5% and 21.8% higher energy retention of polluted crops in 2010 and 2011, respectively. A portion of the higher energy retention increased the midday canopy temperatures of dusted maize irrespectively to the season characteristics. In a global climate model, decreasing cropland albedo by 0.04 drives a more than 1 °C warming in summertime surface air temperatures in a wide latitudinal band spanning North America and Eurasia (*Betts et al.*, 2007). These findings are close to our field observations. *Ridgwell et al.* (2009) published more moderate temperature variations; albedo increments of 0.04 and 0.08 produced only 0.11 °C and 0.21 °C surface cooling, respectively.

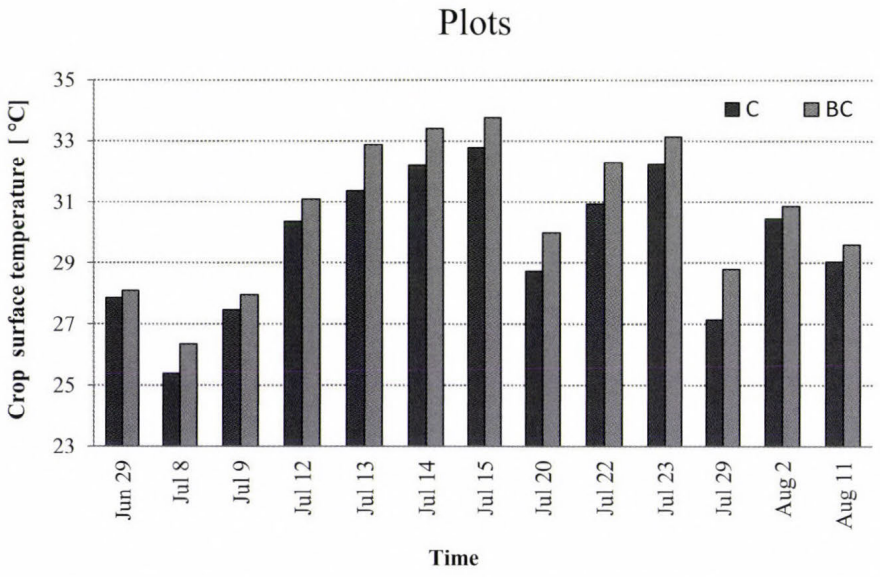

Fig. 9. Canopy surface temperatures measured at solar noon on clear-sky conditions during 2010.

The impact of BC on maize seasonal water loss was reasonable over the wet growing season of 2010. This might have been due to ample precipitation of the summer. Oppositely to 2010, the growth in seasonal water loss of polluted maize increased until 11% in the arid 2011. The physiologically desired crop temperature in ET was achieved with more intense transpiration during 2011 than in 2010.

After canopy closure, a linear relationship exists between daily water loss and albedo even in BC polluted crops. Linear connection between LAI and albedo is acceptable only in case of control maize. In polluted maize stand, the change in albedo seems to be independent on green leaf area size in maize after canopy closure.

Reasonable yield decline was measured in polluted maize plots irrespectively of season's weather. In polluted rainfed plots, the drop-out of DM grain yields were 9% and 20% in the two consecutive seasons. Irrespectively to the weather, the extra water supply in ET decreased the yield loss of polluted maize. The irrigation may be the proper tool to cope the negative impacts of atmospheric origin black carbon pollution.

Acknowledgement—The financial and infrastructural support of the State of Hungary and the European Union in the frame of the TÁMOP-4.2.2/B-10/1-2010-0025 project is gratefully acknowledged.

References

Anda, A., 2001: Micro-meteorological observations and modification of canopy microclimate. DSc Thesis Budapest Hungary. (In Hungarian).

Anda, A. and *Loke, Zs.*, 2005: Radiation balance components of maize hybrids grown at various plant densities. *J. Agron. Crop Sci. 191*, 202–209.

Bajwa, S. and *Vories, E.*, 2007: Spatial analysis of cotton canopy responses to irrigation in a moderately humid area. *Irrig. Sci. 25*, 429–441.

Balmes J. R., 2010: How does diesel exhaust impact asthma? *Thorax 66*, 4–6.

Behndig, A. F., Larsson, N., Brown J. L., Stenfors, N., Helleday, R., Duggan, S. T., Dove R. E., Wilson S. J., Sandstrom,T., Kelly F. J., Mudway, I. S., Blomberg, A., 2011. Proinflammatory doses of diesel exhaust in healthy subjects fail to elicit equivalent or augmented airway inflammation in subjects with asthma. *Thorax 66*,12-19.

Betts, R.A., Faloon, P.D., Goldewijk, K.K., and *Ramankutty, N.*, 2007: Biogeophysical effects of land use on climate: Model simulation of radiative forcing and large-scale temperature change. *Agr. Forest Met. 142*, 216–233.

Campbell, G.S., and *Norman J.M.*, 1998: An introduction to environmental biophysics. 2nd edition. Springer, New York, NY, USA.

Davies, J.A. and *Idso S.B.*, 1979: Estimating the surface radiation balance and its components. In *Modifications of the aerial environment of crops* (eds.:*Barfield, B.J., Gerber J.F.*),. ASAE St. Joseph, MO, USA, 183–210.

Febrero, A., Fernandez, S., Molina-Cano, J., and *Araus, J.*, 1998: Yield, carbon isotope discrimination, canopy reflectance and cuticular conductance of barley isolines of differing glaucousness. *J. Exp. Bot. 49*, 1575–1581.

Freer-Smith, P.H., Beckett, K.P., and *Taylor, G.*, 2005: Deposition velocities to Sorbus aria, Acer campestre, Populus deltoidesxtrichocarpa, Pinus nigra and Cupressocyparis leylandii for coarse, fine and ultra-fine particles in the urban environment. *Environ. Poll. 133*, 157–167.

Giere R. and *Querol X.*, 2010: Solid Particulate Matter in the Atmosphere. *Elements Mineral. Soc. America 6*, 215 – 222.

Hammes, K., Torn, M.S., Lapenas, A.G., and *Schmidt, M.W.I.*, 2008: Centennial black carbon turnover in a Russian steppe soil. *Biogeosciences 5*, 1339–1350.

Hatfield, J.L. and *Carlson, R.E.*, 1979: Light quality distributions and spectral albedo of 3 maize canopies. *Agric. Met. 20*, 215–226.

IPCC, 2007: Summary for Policymakers. In: Climate Change (eds.: *Solomon, S., Qin, D., Manning, M., Chen, Z., Marquis, M., Averyt, K.B., Tignor, H.L., Miller, G*) The Physical Science Basis. Contribution of Working Group I to the Fourth Assessment Report of the Intergovernmental Panel on Climate Change, Cambridge University Press, Cambridge, Available online: www.ipcc.ch.

Jackson, R.D., 1982: Canopy temperature and Crop Water Stress. *Advances Irrig. 1*, 43–85.

Jamieson, P.D., Brooking, I.R., Porter, J.R., and *Wilson, D.R.,* 1995: Prediction of leaf appearance in wheat: a question of temperature. *Field Crop Res. 41*, 35–44.

Krzyzanowski, M., Kuna-Dibbert, B., Schneider, J. (eds) 2005. Health effects of transport-related air pollution. WHO Regional Office, Copenhagen, (ISBN 92-890-1373-7) http://www.euro.who.int/__data/assets/pdf_file/0006/74715/E86650.pdf.

Lorenz, K., Lal, R. and *Jiménez, J.J.,* 2010: Characterization of soil organic matter and black carbon in dry tropical forests of Costa Rica. *Geoderma 158*, 315–321.

Matthews, H.D., Weaver, A.J., Eby, M., and *Meissner, K.J.,* 2003: Radiative forcing of climate by historical land cover change. *Geophys. Res. Letter 30*: 1055.

Monteith, J.L. and *Unsworth, M.,* 1990: Principles of Environmental Physics. Edward Arnold Publ., London.

Nguyen B.T., Lehmann C.J. Kinyangi C.J. Smernik C.R. Riha S.J. Mark C. and *Engelhard H.,* 2009: Long-term black carbon dynamics in cultivated soil. *Biogeochemistry 92,* 163–176.

Oguntunde P.G. and *van de Giesen N.,* 2004: Crop growth and development effects on surface albedo for maize and cowpea fields in Ghana, West Africa. *Int. J. Biomet. 49*, 106–112.

Oke, T.R., 1987: Boundary layer climates. Routledge, New York, USA.

Olszyk, D.M., Bytnerowicz, A. and *Takemoto, B.K.,* 1989: Photochemical oxidant pollution and vegetation: Effects of mixtures of gases, fog and particles. *Environ. Poll. 61,* 11–29.

Postma, D.S., Kerkhof, M., Boezen, H.M. and *Koppelman, G.H.*, 2011: Asthma and Chronic Obstructive Pulmonary Disease: Common Genes, Common Environments? *Am. J. Respir. Crit. Care Med. 183*, 1588–1594.

Prusty, B.A.K., Mishra, P.C., and *Azeez, P.A.,* 2005: Dust accumulation and leaf pigment content in vegetation near the national highway at Sambalpur, Orissa, India. *Ecotox. Environ. Saf. 60*, 228–235.

Ridgwell, A., Singarayer, J.S., Hetherington, A.M. and *Valdes P.J.,* 2009: Tackling Regional Climate Change By Leaf Albedo Bio-geoengineering. *Curr. Biol. 19*, 1–5.

Salma I. and *Ocskay R.,* 2006: Budapest: a dusty and colourless city? *Természet világa 137*(3), 1–6. (In Hungarian).

STATA 5.0 1996: Stata Corporation LP Texas, USA, www.stata.com.

Warrington, I.J. and *Kanemasu, E.T.,* 1983: Corn growth response to temperature and photoperiod. *Agron. J. 75*, 749–75.

WHO (World Health Organisation), 2000: In: Air Quality Guidelines for Europe. *WHO Regional Publications, European Series, 91*. WHO, Copenhagen.

INSTRUCTIONS TO AUTHORS OF *IDŐJÁRÁS*

The purpose of the journal is to publish papers in any field of meteorology and atmosphere related scientific areas. These may be

- research papers on new results of scientific investigations,
- critical review articles summarizing the current state of art of a certain topic,
- short contributions dealing with a particular question.

Some issues contain "News" and "Book review", therefore, such contributions are also welcome. The papers must be in American English and should be checked by a native speaker if necessary.

Authors are requested to send their manuscripts to

Editor-in Chief of IDŐJÁRÁS
P.O. Box 38, H-1525 Budapest, Hungary
E-mail: journal.idojaras@met.hu

including all illustrations. MS Word format is preferred in electronic submission. Papers will then be reviewed normally by two independent referees, who remain unidentified for the author(s). The Editor-in-Chief will inform the author(s) whether or not the paper is acceptable for publication, and what modifications, if any, are necessary.

Please, follow the order given below when typing manuscripts.

Title page: should consist of the title, the name(s) of the author(s), their affiliation(s) including full postal and e-mail address(es). In case of more than one author, the corresponding author must be identified.

Abstract: should contain the purpose, the applied data and methods as well as the basic conclusion(s) of the paper.

Key-words: must be included (from 5 to 10) to help to classify the topic.

Text: has to be typed in single spacing on an A4 size paper using 14 pt Times New Roman font if possible. Use of S.I. units are expected, and the use of negative exponent is preferred to fractional sign. Mathematical formulae are expected to be as simple as possible and numbered in parentheses at the right margin.

All publications cited in the text should be presented in the *list of references*, arranged in alphabetical order. For an article: name(s) of author(s) in Italics, year, title of article, name of journal, volume, number (the latter two in Italics) and pages. E.g., *Nathan, K.K.,* 1986: A note on the relationship between photo-synthetically active radiation and cloud amount. *Időjárás 90,* 10-13. For a book: name(s) of author(s), year, title of the book (all in Italics except the year), publisher and place of publication. E.g., *Junge, C.E.,* 1963: *Air Chemistry and Radioactivity.* Academic Press, New York and London. Reference in the text should contain the name(s) of the author(s) in Italics and year of publication. E.g., in the case of one author: *Miller* (1989); in the case of two authors: *Gamov* and *Cleveland* (1973); and if there are more than two authors: *Smith et al.* (1990). If the name of the author cannot be fitted into the text: *(Miller,* 1989); etc. When referring papers published in the same year by the same author, letters a, b, c, etc. should follow the year of publication.

Tables should be marked by Arabic numbers and printed in separate sheets with their numbers and legends given below them. Avoid too lengthy or complicated tables, or tables duplicating results given in other form in the manuscript (e.g., graphs).

Figures should also be marked with Arabic numbers and printed in black and white or color (under special arrangement) in separate sheets with their numbers and captions given below them. JPG, TIF, GIF, BMP or PNG formats should be used for electronic artwork submission.

Reprints: authors receive 30 reprints free of charge. Additional reprints may be ordered at the authors' expense when sending back the proofs to the Editorial Office.

More information for authors is available: journal.idojaras@met.hu

Published by the Hungarian Meteorological Service

Budapest, Hungary

INDEX 26 361

HU ISSN 0324-6329

IDŐJÁRÁS

QUARTERLY JOURNAL
OF THE HUNGARIAN METEOROLOGICAL SERVICE

CONTENTS

****

http://www.met.hu/Journal-Idojaras.php

VOL. 116 * NO. 4 * OCTOBER – DECEMBER 2012

IDŐJÁRÁS

Quarterly Journal of the Hungarian Meteorological Service

Editorial Office: Kitaibel P.u. 1, H-1024 Budapest, Hungary
P.O. Box 38, H-1525 Budapest, Hungary
E-mail: journal.idojaras@met.hu
Fax: (36-1) 346-4669

Indexed and abstracted in Science Citation Index Expanded™ and Journal Citation Reports/Science Edition
Covered in the abstract and citation database SCOPUS®

Subscription by

mail: IDŐJÁRÁS, P.O. Box 38, H-1525 Budapest, Hungary
E-mail: journal.idojaras@met.hu

IDŐJÁRÁS

Quarterly Journal of the Hungarian Meteorological Service
Vol. 116, No. 4, October–December 2012, pp. 237–251

Environmental modeling using graphical processing unit with CUDA

Róbert Mészáros[1], **Ferenc Molnár Jr.**[2], **Ferenc Izsák**[3], **Tibor Kovács**[4], **Péter Dombovári**[5], **Ákos Steierlein**[1], **Roland Nagy**[1], and **István Lagzi**[6]*

[1] *Department of Meteorology, Eötvös Loránd University, Pázmány Péter sétány 1/A, H-1117 Budapest, Hungary*

[2] *Department of Physics, Applied Physics and Astronomy, Rensselaer Polytechnic Institute, 110 Eighth Street, Troy,12180-New York, USA*

[3] *Department of Applied Analysis and Computational Mathematics, Eötvös Loránd University, Pázmány Péter sétány 1/A, H-1117 Budapest, Hungary*

[4] *Institute of Radiochemistry and Radioecology, University of Pannonia, Egyetem u. 10, H-8200 Veszprém, Hungary*

[5] *Department of Radiation Protection, Nuclear Power Plant of Paks, P.O.Box. 71, H-7031 Paks, Hungary*

[6] *Department of Physics, Budapest University of Technology and Economics, Műegyetem rkp. 3, H-1111 Budapest, Hungary*

**Corresponding author E-mail: istvanlagzi@gmail.com*

(Manuscript received in final form May 14, 2012)

Abstract—Modeling transport and deposition processes of toxic materials in the atmosphere is one of the most challenging environmental tasks. These numerical simulations with dispersion models are very time consuming, therefore, their acceleration is extremely important. One possible, effective solution for increasing the computational time can be the parallelization of the source codes. At the same time, the technological improvement of graphics hardware created a possibility to use desktop video cards to solve numerically intensive tasks. In this study, we present a new and powerful parallel computing structure for solving different environmental model simulations using the graphics processing units (GPUs) with CUDA (compute unified device architecture). Two different types of dispersion models were developed and applied based on this

technology: a stochastic Lagrangian particle model and an Eulerian model. We present and discuss the results and advantages of both methods. A Lagrangian particle model was applied to simulate the transport of radioactive pollutants from a point source after a hypothetical accidental release at local scale. In addition, an Eulerian model was used to simulate sulfur dioxide transport and transformation in the troposphere at regional scale. Moreover, in both cases, CPU and GPU computational times were also compared. We can achieve typical acceleration values in the order of 80–120 times in case of Lagrangian model and 30–40 times in case of Eulerian model using this new parallel computational framework compared to CPU using a single-threaded implementation. Next to the obvious advantages, the barriers of this new method are also discussed in this study.

Key-words: environmental modeling; accidental release; air pollution; CUDA; GPU computing

1. Introduction

Protecting the environment and developing new green technologies are among the most important issues of the society that should be addressed in this century. Computer aided models already assist many aspects of our everyday life as well as our future, and are important drivers of our decisions. Their presence in environmental sciences continuously serves the society in short term practical decisions, e.g., through weather forecasts (*Csima* and *Horányi*, 2008) or air pollution modeling (*Leelőssy et al.*, 2011; *Mészáros et al.*, 2011) as well as in concluding global consequences affecting several generations, e.g., modeling and simulation of climate change and their impacts on global and regional environment (*Bartholy et al.*, 2008; *Torma et al.*, 2008). It is well-known that environmental model simulations must have a high degree of accuracy and must be achieved faster than in real time to be of use in decision support (*Lagzi et al.*, 2004; *Mészáros et al.*, 2010). In the past few years, the graphics processing unit (GPU) has became a powerful tool for parallel computing and both performance and capabilities of GPUs have increased noticeably (e.g., *Stone et al.*, 2007; *Liu et al.*, 2008; *Preis et al.*, 2009; *Block et al.*, 2010; *Komatitsch et al.*, 2010; *Preis*, 2011). NVIDIA created a parallel computing framework, the so-called compute unified device architecture (CUDA) to utilize this performance and simplify programming of general purpose computations (NVIDIA, 2011).

We have developed applications of GPU using CUDA framework for environmental studies serving as a basement for decision-making strategies. A stochastic Lagrangian model was developed on CUDA to estimate the transport and transformation of the radionuclides from a single point source during hypothetical accidental releases. With the Lagrangian particle model (*Molnár et al.*, 2010) the dispersion of radionuclides was simulated in a 30 km radius circle around the Paks Nuclear Power Plant (Hungary). This advanced computational platform is used by the Paks NPP as a part of the nuclear safety system called TREX (Transport–Exchange) model (*Mészáros et al.*, 2010, *Molnár et al.*, 2011). Our other environmental application of GPU with CUDA was the

simulation of the atmospheric dispersion and transformation of sulfur dioxide using an Eulerian modeling system.

In this study, we present the efficiency and barriers of calculations on GPU in case of environmental tasks, compared the advantages of this new technique during the applications of Lagrangian and Eulerian modeling methods.

2. CUDA

The parallel computing model of CUDA is fundamentally different from previous parallel computers. Supercomputer architectures, clusters, and grids share the property that each node is responsible only for one, or a few number of threads (sequence of instructions), and generally, they may execute different computations. In contrast, a CUDA program defines thousands of threads for a single GPU, all of which are executing the same computation (the kernel function) on different data elements. These threads are lightweight in the sense that they only coordinate the distribution of the computational work to the physical computing units. Threads are grouped into blocks, which are always executed by a single multiprocessor. However, a GPU usually contains several multiprocessors, allowing many blocks (and threads within) to run simultaneously. On the level of multiprocessors, the threads of a block are executed in a time-sliced way in small batches called *warps*; different blocks are scheduled one after another on available multiprocessors. This scheduling and executing procedure takes place at every kernel launch, but gives practically zero overhead.

The two-level of splitting a computation into blocks, and further into threads is not arbitrary. Threads within a single block can synchronize their execution using a barrier, and they may share data via the common *shared memory* (*Fig. 1*). However, threads from different blocks cannot communicate with each other directly, because the order of block allocation and execution on multiprocessors is arbitrarily decided by the GPU. The only guaranteed barrier between executions of blocks is the completion of a kernel function: a new kernel is not launched until all blocks from the previous kernel launch are finished.

There are many memory resources available, optimized for various purposes on the video card. The most important is the *global memory*, which is essentially the large RAM available on the video card (*Fig. 1*). It can be accessed by any threads at any time, and it is responsibility of the programmer to avoid writing the same address at the same time. This is where the main data of the computation is located. From here, threads read the data, process it, and write back the results during a kernel execution. Further, there are cached memory areas, which provide read-only data for the threads. These are optimized for a specific reading pattern, e.g., the *constant memory* is optimized

to provide data to all threads at the same time, the *texture memory* is optimized to provide interpolated sampling of 2D or 3D data in a localized region for threads of the same block (*Fig. 1*). All of these memory areas are accessible from the host (the CPU-part of the program).

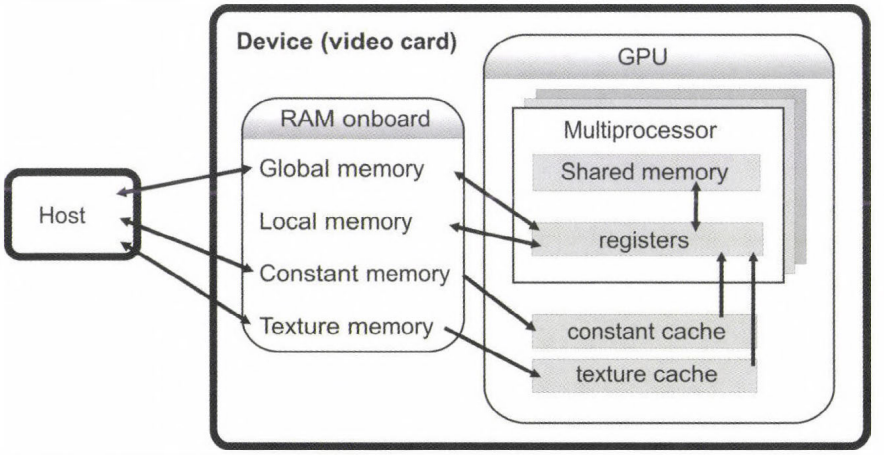

Fig. 1. The structure of a video card.

In order to create optimal CUDA applications, one needs to understand the proper usage and limitations of resources, and follow development guidelines, which are detailed in the programming guide of CUDA (*NVIDIA CUDA Programming Guide*). Here we only provided a brief overview of the most important features that will be explicitly mentioned in our applications.

3. Models

3.1. Lagrangian particle model

A stochastic Lagrangian particle model was developed for simulating accidental release of radionuclides on local scale. This model type has an advantage on local scale simulations, because it can handle steep gradient of emitted species near a point source (*Bartnicki et al.*, 2003; *Lepicard et al.*, 2004; *Molnár et al.*, 2010). In the Lagrangian model, individual particles are released from a point source in each time step. Each particle represents a given mass or activity, and they can be moved in space by advection (wind field) and turbulent diffusion, they can transform to other species (by radioactive decay), and particles can be removed from the atmosphere to the surface via dry and wet deposition pathways. This means that the model is continuous in space and discontinuous

in time. In this model, the advection is deterministic, but the effect of the turbulent diffusion is stochastic. The new spatial position of the particles can be calculated by the following equations:

$$X_i^{new} = X_i^{old} + v_i^{adv}\Delta t + \tilde{x}_i, \tag{1}$$

where X_i^{new} and X_i^{old} are the spatial coordinates of particles after and before the time step, respectively. v_i^{adv} is the ith coordinate of the wind velocity vector, Δt is the time step (10 s in the model simulation). The last term in the Eq. (1) ($\tilde{x}_i$) describes the effect of stochastic, turbulent processes, and i denotes the spatial dimension (i = 1, 2, 3). The stochastic term is calculated by

$$\tilde{x}_i = (rand)\sqrt{2K_i\Delta t}\,. \tag{2}$$

Random numbers (*rand*) with normal distribution (with mean 0.0 and variance 1.0) were generated using Mersenne Twister random number generator and Box-Muller transformation. K_i is the turbulent diffusion coefficient in each direction. For horizontal dispersion a constant value was used ($K_x = K_y = 100\ \mathrm{m^2 s^{-1}}$). Vertical diffusion coefficient (K_z) depends on the height, and it was calculated using the Monin–Obuhov similarity theory.

Released radioactive particles can decay and deposit by dry and wet pathways. The probability that individual particles during a time step Δt will decay or deposit can be estimated by the following relation:

$$p = 1 - e^{-k\Delta t}, \tag{3}$$

where k is either the radioactive decay constant or wet or dry deposition constant. These constants depend on the chemical nature of the toxic species. During dry deposition, particles can deposit below the mixing layer height. Wet deposition occurs only in case of precipitation.

Implementing a single-threaded CPU version of the model is straightforward. Assuming that the emission profile (the amount of emitted particles in every time step) for all species and the maximum number of particles released during the simulation are known, activities or masses can be a priori assigned to the particles. The maximum number of particles is the dominant variable that affects simulation time and precision. It is limited only by available memory. In every iteration, the main steps for every particle are the same: interpolating (sampling) meteorological data obtained from a numerical weather prediction model in x, y, z, and time dimensions using linear

interpolation, calculating the turbulent diffusion coefficient, moving the particle by the wind, then by turbulent diffusion, and finally testing for dry and wet depositions. Particles may become inactive, meaning they are no longer moved by wind or turbulent diffusion, when the particle is deposited or it reaches the predefined boundaries of the simulated area. Activities or masses of particles were summarized on a rectangular grid for visualization and further statistical evaluation.

In the parallelized CUDA version of the program, we utilize the various memory types available. Meteorological data are loaded into three-dimensional textures, to utilize the hardware-implemented trilinear interpolation. Since the meteorological data are four-dimensional (3 space and 1 time), an extra interpolation step is necessary. Using texture memory is also useful because the plume usually propagates in a specific direction, giving the required spatial locality for the texture cache to work efficiently. Physical constants of the isotopes are loaded to constant memory. Shared memory is used for caching the particle data (position, state information). The data is loaded from global memory to shared memory when a kernel starts, and written back at the end, if data was modified.

The calculations in each time step are done by two kernel functions. First step is generating random numbers, using the Mersenne Twister random number generator. A large buffer (on the GPU) is used to store the numbers, because the random number generator works more efficiently if large amount of numbers is asked for at once. The second step is the main kernel. Each thread is responsible for updating the status of a single particle. First, particle information and random numbers are loaded from global memory to shared memory. Second step is sampling the meteorological data, interpolating in vertical direction, and calculating the turbulent diffusion coefficient using the Monin–Obukhov similarity theory. These results are stored in shared memory. Next step is moving the particles by wind field and turbulent diffusion, and testing for radioactive decay and deposition. This step uses the interpolated outputs of weather prediction model and the random numbers for calculation of turbulent motion, radioactive decay, and stochastic deposition. The final step is writing the changed particle information back to global memory.

3.2. Eulerian model – solving reaction-advection-diffusion equations

Solving reaction-advection-diffusion equations fits to the architecture of CUDA as well. The atmospheric reaction-advection-diffusion equation can be written in the following form:

$$\frac{\partial c}{\partial t} = -\nabla(\vec{u}c) + K\nabla^2 c + R + E - D, \tag{4}$$

where c is the concentration of the chemical species, $\vec{u}$ is the 3D wind velocity, K is the turbulent diffusion coefficient, R is the reaction term, which usually contains non-linear functions, E is the emission term, and D is the deposition term, which usually contains the effect of the dry and wet deposition processes. Solving diffusion-advection equations to describe the spread and/or transformation of air pollutants is a very time consuming computational task. The numerical simulations must be obviously achieved faster than in real time in order to use them in decision support. A feasible way is the parallelization of the source code using supercomputers, clusters, GRID, or GPU (*Martin et al.*, 1999; *Alexandrov et al.*, 2004; *Lovas et al.*, 2004).

During our simulations, a standard "method of line" technique was used to solve Eq. (4). The "method of lines" technique has two consecutive steps, the first is a spatial discretization of the partial differential equations followed by a temporal integration of the produced ordinary differential equations with an upwind approximation to provide a stable solution.

Our Eulerian model has 32 horizontal layers and each layer contains 96×90 equidistant grid cells (this mesh covers the central part of Europe). No-flux (Neumann) boundary condition was applied for chemical species at the boundary of the computational domain. Meteorological data (wind field, surface temperature, cloud coverage, relative humidity, mixing layer height) were obtained from the ALADIN limited area weather prediction model operated at the Hungarian Meteorological Service. The model calculates the energy balance and the Monin–Obukhov length from which the vertical turbulent diffusion coefficient can be estimated. The vertical turbulent diffusion coefficient plays an important role in the vertical mixing of pollutants. Therefore, its parameterization is one of the most important tasks in the air pollution modeling. However, it should be noted that the contribution of the horizontal turbulence to the mass transport of pollutants comparing to the effect of the advection is negligible. Horizontally, the transport is mostly governed by the wind field.

In the CUDA implementation, concentrations of the species in a simulation can be stored in global memory on the device. We can assign computation of the next time level to a kernel function, assigning threads to compute individual grid points. The rectangular space represented by the grid points can easily be split to smaller parts, which can be assigned to blocks. Shared memory within a block utilized in the approximation of the spatial derivatives, because this computation requires data which belongs to neighboring grid points (and threads). Physical constants and other parameters of a simulation can be stored in the constant memory.

The communication between threads, required by the computation of spatial derivatives, gives a challenging optimization task. Access to the shared memory must be coordinated by barrier synchronization, and for optimal execution, the bank structure of the shared memory must be

considered as well. Further, in order to provide communication between spatially neighboring blocks, a layer of grid points must overlap between the blocks. This gives non-contiguous memory addressing of grid points in the threads of blocks, which causes a significant performance drop on the first generation of CUDA devices. A sophisticated solution (*Molnár et al.*, 2011) is required to maintain optimal performance. Nevertheless, the coordination and communication between threads gives a significant (but unavoidable) overhead to the computations.

4. Results

Since the particles (in fact particle packages) are independent in the Lagrangian model, there is no communication, and therefore, no synchronization is necessary between threads. This allows us to split the computation arbitrarily on a very fine-grained level, specifically, in a way to best fit to the capabilities of the GPU. Additionally, the trilinear interpolation provided by the hardware significantly reduces the amount of computation needed per particle, while this is a necessary computation on the CPU. These factors lead to about 80–120 times speedup on a first-generation device (GeForce 8800GTX) and about 100–140 times speedup on a second-generation device (GeForce GTX 275) compared to the single-threaded CPU computation (on a 2.33 GHz Core 2 CPU). This means, for example, that in case of an accidental release, a Lagrangian particle model simulation takes 2 hours on CPU, but it decreases to only 1 minute using GPU.

Fig. 2 shows an example of the plume structure and the deposited amount of the I-131 isotope originated from the Paks Nuclear Power Plant in a hypothetical accidental release. For this simulation the stochastic Lagrangian particle model was used. In the figure, the structures of a radioactive plume in a homogeneous wind field at different wind velocities are presented. It can be noticed that a Lagrangian particle model can also be used at low wind velocity, where the traditional Eulerian or Gaussian models cannot handle the extremely steep concentration gradient of chemical species near the point source. This low wind speed causes unpredictable plume profile in Gaussian models and numerical instability in Eulerian models near the source due to the high concentration gradients. Therefore, this approach can be successfully used to describe the air pollution transport from a single, but strong emission source even in regional scale.

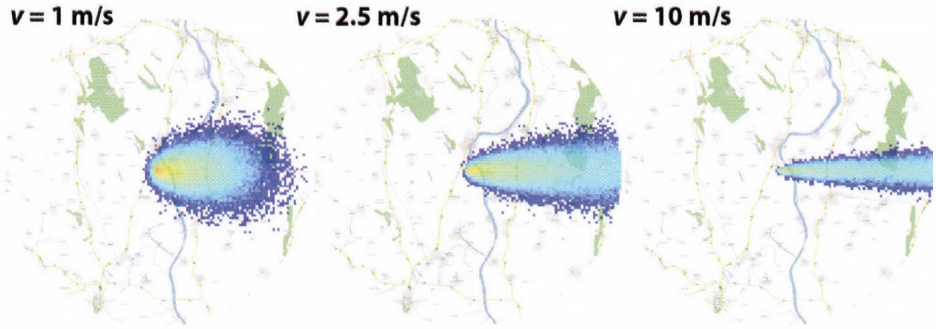

Fig. 2. Accidental release of I-131 isotope at the Paks Nuclear Power Plant using a stochastic Largangian particle model at different wind velocities.

At the same time, in regional scale, the Eulerian models could be more appropriate tools for dispersion simulations, as they can more easily handle the 3D meteorological fields on a previously defined grid. To illustrate the capacity and power of Eulerian models, we developed a model, which can calculate the spread and chemical transformation of air pollutants in the atmosphere. Here, we present the results of model simulations for sulfur dioxide (SO_2) emitted from area sources. Emission inventory of the European Monitoring and Evaluation Programme (EMEP) for SO_2 was used and converted from the EMEP to the model grid (*Fig. 3*), and we supposed a continuous emission rate in the simulations. The exact heights of the emission sources are unknown, therefore, we assumed that the emitted amount of SO_2 was distributed evenly in the model layers in the lower 100 m. A simple, first order chemical reaction was considered to describe the transformation of SO_2 to sulfate aerosol ($R = -k_r c$; $k_r = 1.083 \times 10^{-5}$ s^{-1}) (*Luria et al.*, 2001; *Woo et al.*, 2003), and dry deposition was also considered as a first order chemical reaction ($D = k_{dry} c$; $k_{dry} = 6.38 \times 10^{-4}$ s^{-1}). A homogeneous initial condition was used in the domain with $[SO_2]_0 = 0.01$ mg/m^3.

Fig. 4 shows the spatial distribution of the SO_2 in the surface layer (first layer) over the central part of Europe in daytime and night. We can see higher concentration near strong emitting sources (south Poland, Romania), which is a trivial consequence of the SO_2 dispersion and chemical transformation. However, we can clearly see that the average concentration in the surface layer is higher at daytime than at night. This is attributed to the fact that the height of the mixing layer is much smaller at nighttime than in daytime because of the lack of irradiation, therefore, a large part of the emitted SO_2 remains above the mixing layer at night.

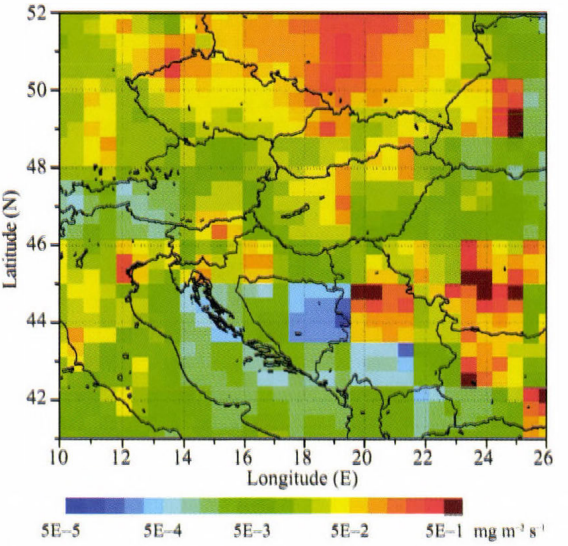

Fig. 3. EMEP Emission inventory of sulfur dioxide used in the Eulerian model.

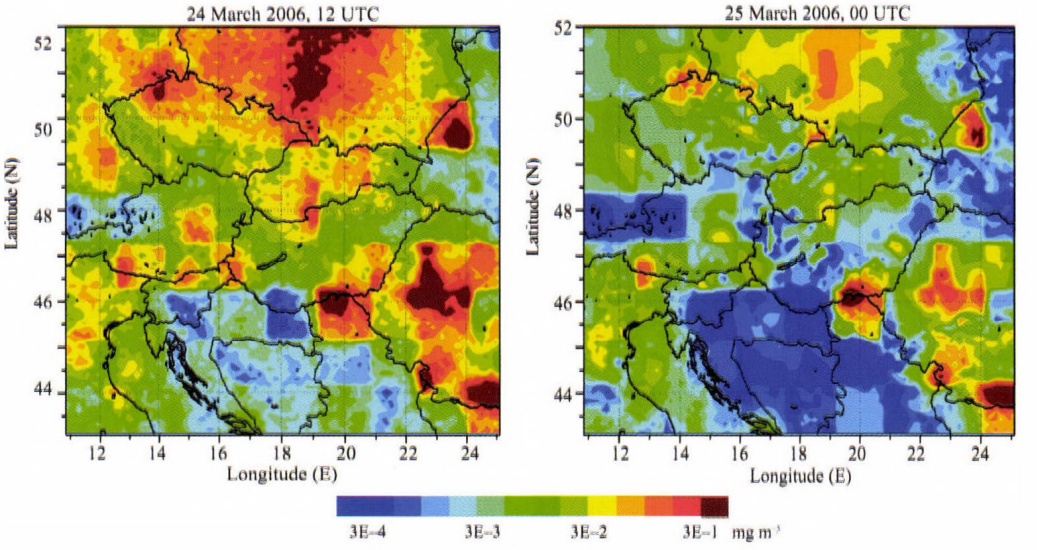

Fig. 4. Concentration of sulfur dioxide in the surface layer on March 24, 2006, at 12 UTC and March 25, at 00 UTC.

An important aspect of a model development is the validation of the model results against the field measurements. *Fig. 5* shows the modeled SO_2 concentration and the observed one at an EMEP monitoring station in Illmitz. The calculated concentration values are in a good accordance with the observed concentrations. Moreover, the Eulerian model could also capture the temporal variation of the SO_2.

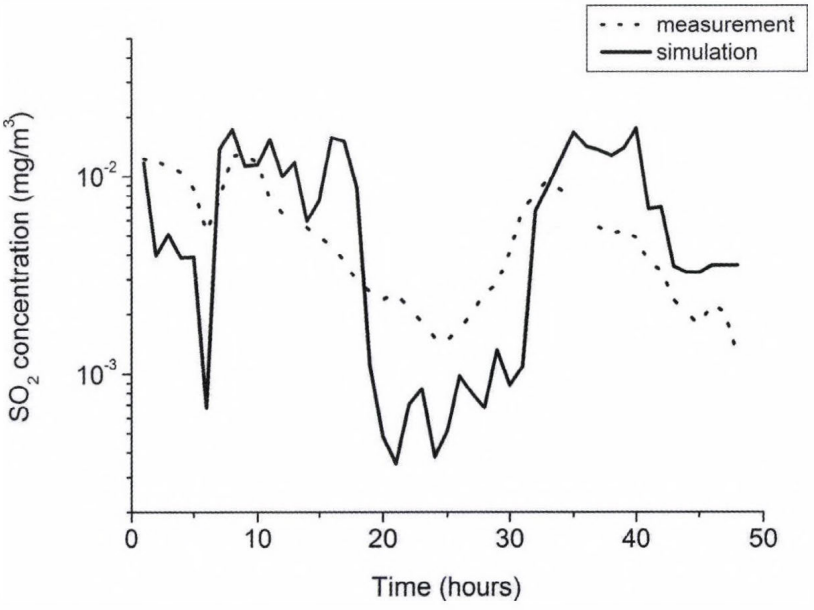

Fig. 5. Measured and modeled concentration of sulfur dioxide in the surface layer at Illmitz EMEP monitoring station (47° 46'N, 16° 46'E). Simulation started on March 24, 2006, at 00 UTC.

The application of GPU in case of Eulerian model was also investigated. We can achieve speedups up to 20–25 times on first-generation devices (GeForce 8800GTX) and 30–40 times on second-generation devices (GeForce GTX 275) compared to the single-threaded CPU implementation (2.33 GHz Core 2 CPU). We should emphasize, however, that this model is fundamentally different from the Lagrangian model; this is essentially a PDE solver using finite difference method, while the Lagrangian model is more like a Monte-Carlo-type simulation. The speedups alone should not be used to compare these models, because we need different amounts of computation to reach the same quality of results.

5. *Conclusions*

In this paper we showed and discussed the capability of two types of models, Lagrangian and Eulerian. Most of the models used in environmental protection and air quality management fall into these two categories. Therefore, it is important to know the real advantages and drawbacks of the applied models. From results presented in this study, we can clearly see that if we estimate the dispersion of pollutants from a strong point source in local scale, a Lagrangian particle model should inevitably be used. This model has the main advantage that the positions of each particle are continuous functions in space. This can overcome the problem of steep concentration gradients arising near a point source, and the Lagrangian particle model can be used even in case of extremely low wind speed, where other models (Gaussian, Eulerian) simply fail and they cannot provide a stable and/or realistic solution. On the other hand, the main problem with this approach is that each particle represents a given mass or activity (in case of radionuclides), therefore, it is very hard to obtain a continuous physical quantity, like concentration with small number of particles, and increasing this number results in an increase in computational time. Using Lagrangian particle model to simulate the transport of air pollutants from multi-emission sources is practically impossible because of huge computational task. However, this task is really suitable for Eulerian models, and they can easily provide and calculate continuous quantities. Eulerian models can be predominantly used to calculate the transport of chemical species from multi-emission sources. In this framework, the chemical reactions occurring between chemical species can be easily handled, because the chemical rate can be calculated from concentrations, which are prognostic variables in Eulerian models. Modeling of the chemical interactions between particles in Lagrangian models is very challenging task, and it involves consideration of the stochastic nature of chemical reactions. In conclusion, the model should always be chosen to a given air pollution problem to provide accurate and cost-efficient solution. Development of such cost-efficient strategies requires very accurate calculations, and numerical simulations need a huge computational effort.

There are numerous solutions to address this issue. Parallelization of the models and using supercomputers, clusters, or grid systems to solve problems is a common technique. These systems are built by connecting numerous processors, either by some sort of direct link or by a network connection. Several computing centers can be connected to each other by the Internet, thus creating grids. We investigated a new parallel computational framework to solve environmental related problems using graphical processing unit. We developed a stochastic Lagrangian particle model and an Eulerian model on CUDA to estimate the transport and transformation of the radionuclides from a single point source during hypothetical accidental releases. Our results show that parallel implementation achieves typical acceleration values in the order of a

hundred times in case of Lagrangian model and tens of times in case of Eulerian model compared to CPU using a single-threaded implementation on a regular desktop computer (*Fig. 6*). The relatively high speedup with no additional costs to maintain this parallel architecture could result in a wide usage of GPU for diversified environmental applications in the near future.

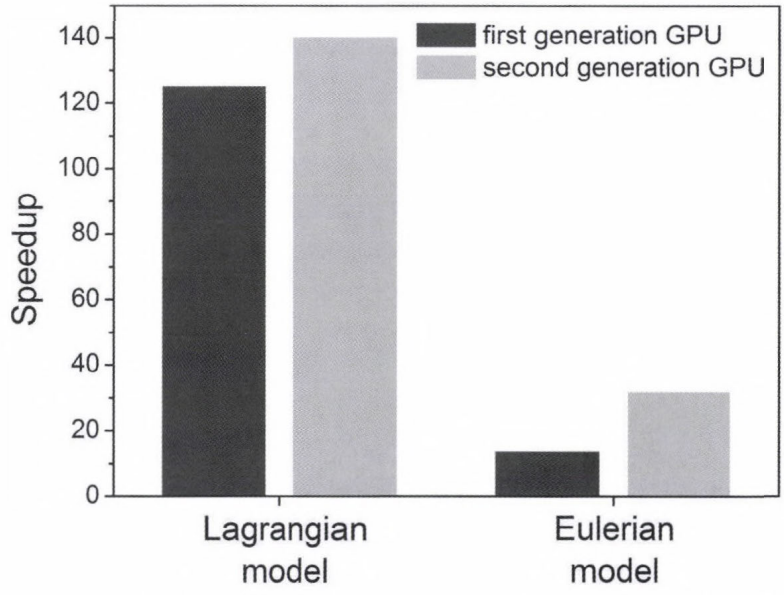

Fig. 6. Speedup of different applications on first and second generation CUDA-capable video cards (GeForce 8800 GTX and GeForce GTX 275, respectively) compared to CPU (2.33 GHz Core 2).

We should also mention some important aspects of this technology. In the past years, as this technology has developed, many papers have been published (for as review see *Lee et al.*, 2010), and it seems that the "speedup" gained over general CPU solutions has become the measure of CUDA technology. However, one must be very careful to interpret such results correctly. There are numerous parameters that formulate the final performance gain over the CPU, such as the GPU type, clock frequency, number of CUDA cores, amount of memory, speed of memory on the video card, CPU type, CPU clock, host memory amount and speed, and most importantly, the implementation of the algorithm itself. These together make it almost impossible to predict a given computational speedup when ported to CUDA. Some of the published works show speedups of several hundred times (*Lee et al.*, 2010). This is never the "magical" power of CUDA, it is always the result of the unoptimized CPU code which serves as the basis of comparison. Paper published by *Lee et al.* (2010) carries important information:

you can achieve great optimizations on CPU if you have enough experience and expertise, bringing down the relative performance gain of GPU solutions. This can be close to what you could expect by looking at the raw hardware performance of CPUs and GPUs. However, the amount of computational and programming knowledge required to do so, is usually so large, that only computer scientists of specific fields can afford to learn them. This is why CUDA has gained much popularity among scientists from different fields: with relatively limited (but still advanced) knowledge of CPU and GPU programming, the CUDA solution is much faster than the CPU solution. This is the main advantage of CUDA (together with its cost-effectiveness).

We believe that using GPU – as a new computational tool – will revolutionize the environmental computing and can provide a new, cost–efficient, and effective technique in environmental protection. This system can be effectively used, and hence, the most profitable it would be in simulation of an accidental release of hazardous materials from industrial facilities (e.g., nuclear power plants). The recent accident at the Fukushima Nuclear Power Plant highlights the importance of predicting accidental release of toxic materials (*Bolsunovsky* and *Dementyev*, 2011; *Leelőssy et al.*, 2011; *Manolopoulou et al.*, 2011; *Sinclair et al.*, 2011). Implementing a model using this easy-to-maintain and cost-efficient computational framework in all facilities storing hazardous materials would be realistic and could help to decrease environmental consequences of possible future accidents.

Acknowledgments—Authors acknowledge the financial support of the Hungarian Research Found (OTKA K81933, K81975, K104666, NK100296, and PD 104441) and the European Union and the European Social Fund (TÁMOP 4.2.1./B-09/KMR-2010-0003).

References

Alexandrov, V.N., Owczarz, W., Thomson, P.G. and *Zlatev, Z.*, 2004: Parallel runs of a large air pollution model on a grid of Sun computers. *Math. Comput. Simulat.*, *65*, 557–577.

Bartholy, J., Pongrácz, R., Gelybó, G. and *Szabó, P.*, 2008: Analysis of expected climate change in the Carpathian Basin using the PRUDENCE results. *Időjárás*, *112*, 249–264.

Bartnicki, J., Saltbones, J. and *Foss, A.*, 2003: Performance of the SNAP model in an ENSEMBLE exercise of simulating real-time dispersion from a nuclear accident. *Int. J. Environ. Pollut. 20*, 1–6, 22–32.

Bolsunovsky, A. and *Dementyev, D.*, 2011: Evidence of the radioactive fallout in the center of Asia (Russia) following the Fukushima nuclear accident. *J. Environ. Radioact.*, doi:10.1016/j.jenvrad.2011.06.007.

Block, B., Virnau, P. and *Preis, T.*, 2010: Multi-GPU accelerated multi-spin Monte Carlo simulations of the 2D Ising model. *Comput. Phys. Commun. 181*, 1549–1556.

Csima, G. and *Horányi, A.*, 2008: Validation of the ALADIN-Climate regional climate model at the Hungarian Meteorological Service. *Időjárás 112*, 155–177.

Komatitsch, D., Erlebacher, G., Goddeke, D. and *Michea, D.*, 2010: High-order finite-element seismic wave propagation modeling with MPI on a large GPU cluster. *J. Comput. Phys. 229*, 7692–7714.

Lagzi, I., Kármán, D., Turányi, T., Tomlin, A.S. and *Haszpra, L.*, 2004: Simulation of the dispersion of nuclear contamination using an adaptive Eulerian grid model, *J. Environ. Radioactiv. 75*, 59–82.

Lee, V.W., Kim, C., Chhugani, J., Deisher, M., Kim, D., Nguyen, A.D., Satish, N., Smelyanskiy, M., Chennupaty, S., Hammarlund, P., Singhal, R. and *Dubey, P.*, 2010: Debunking the 100X GPU vs. CPU myth: an evaluation of throughput computing on CPU and GPU. In: ISCA '10 Proceedings of the 37th annual international symposium on Computer architecture, ACM New York, NY, USA, 451–460.

Leelőssy, Á., Mészáros, R. and *Lagzi, I.*, 2011: Short and long term dispersion patterns of radionuclides in the atmosphere around the Fukushima Nuclear Power Plant, *J. Environ. Radioactiv. 102*, 1117–1121.

Lepicard, S., Heling, R. and *Maderich, V.*, 2004: POSEIDON/RODOS models for radiological assessment of marine environment after accidental releases: application to coastal areas of the Baltic, Black and North Seas. *J. Environ. Radioactiv. 72*, 153–161.

Liu, W., Schmidt, B., Voss, G. and *Müller-Wittig, W.*, 2008: Accelerating molecular dynamics simulations using Graphics Processing Units with CUDA. *Comput. Phys. Commun. 179*, 634–641.

Lovas, R., Kacsuk, P., Lagzi, I. and *Turányi, T.*, 2004: Unified development solution for cluster and Grid computing and its application in chemistry. *Lect. Notes Comp. Sc. 3044*, 226–235.

Luria, M., Imhoff, RE., Valente, RJ., Parkhurst, W.J., and *Tanner, R.L.*, 2001: Rates of conversion of sulfur dioxide to sulfate in a scrubbed power plant plume. *J. Air Waste Manag. Assoc. 51*, 1408–1413.

Mészáros, R., Vincze, Cs. and *Lagzi, I.*, 2010: Simulation of accidental release using a coupled transport (TREX) and numerical weather prediction (ALADIN) model. *Időjárás 114*, 101–120.

Mészáros, R., Leelőssy, Á., Vincze, Cs., Szűcs, M., Kovács, T. and *Lagzi. I.*, 2011: Estimation of the dispersion of an accidental release of radionuclides and toxic materials based on weather type classification *Theor. Appl. Climatol.* DOI: 10.1007/s00704-011-0482-0

Manolopoulou, M., Vagena, E., Stoulos, S., Ioannidou, A. and *Papastefanou, C.*, 2011: Radioiodine and radiocesium in Thessaloniki, Northern Greece due to the Fukushima nuclear accident. *J. Environ. Radioact. 102*, 796–797.

Martin, M., Oberson, O., Chopard, B., Mueller, F. and *Clappier, A.*, 1999: Atmospheric pollution transport: the parallelization of a transport & chemistry code. *Atmos. Environ. 33*, 1853–1860.

Molnár, F., Szakály, T., Mészáros, R. and *Lagzi, I.*, 2010: Air pollution modelling using a Graphics Processing Unit with CUDA. *Comput. Phys. Commun. 181*, 105–112.

Molnár, F., Izsák, F., Mészáros, R. and *Lagzi, I.*, 2011: Simulation of reaction-diffusion processes in three dimensions using CUDA. *Chemometr. Intell. Lab. 108*, 76–85.

NVIDIA CUDA Programming guide, NVIDIA corporation
http://developer.download.nvidia.com/compute/cuda/2_1/toolkit/docs/NVIDIA_CUDA_Programming_Guide_2.1.pdf.

Preis, T., Virnau, P., Paul, W. and *Schneider, J.J.*, 2009: GPU accelerated Monte Carlo simulation of the 2D and 3D Ising model. *J. Comput. Phys. 228*, 4468–4477.

Preis, T., 2011: GPU-computing in econophysics and statistical physics. *Eur. Phys. J.- Spec. Top. 194*, 87–119.

Sinclair, L.E., Seywerd, H.C.J., Fortin, R., Carson, J.M., Saull, P.R.B., Coyle, M.J., Van Brabant, R.A., Buckle, J.L., Desjardins, S.M. and *Hall, R.M.*, 2011: Aerial measurement of radioxenon concentration off the west coast of Vancouver Island following the Fukushima reactor accident. *J. Environ. Radioact.*, Doi:10.1016/j.jenvrad.2011.06.008.

Stone, J.E., Phillips, J.C., Freddolino, P.L., Hardy, D.J., Trabuco, L.G. and *Schulten, K.*, 2007: Accelerating molecular modeling applications with graphics processors. *J. Comput. Chem. 28*, 2618–2640.

Torma, C., Bartholy, J., Pongrácz, R., Barcza, Z., Coppola, E. and *Giorgi, F.*, 2008: Adaptation of the RegCM3 climate model for the Carpathian Basin. *Időjárás 112*, 233–247.

Woo, J.-H., Baek, J.M., Kim, J.-W., Carmichael, G.R., N. Thongbooncho, N., Kim, S.T., An, J.H., 2003: Development of a multi-resolution emission inventory and its impact on sulfur distribution for Northeast Asia. *Water Air Soil Pollut. 148*, 259–278.

IDŐJÁRÁS

Quarterly Journal of the Hungarian Meteorological Service
Vol. 116, No. 4, October–December 2012, pp. 253–280

Numerical study of the impact of the changes in the tropospheric temperature profile on the microphysics, dynamics and precipitation of mid-latitude summer continental convective clouds

Angelina Brandiyska[1], **Rumjana Mitzeva**[2]*, **Boryana Tsenova**[3], and **John Latham**[4,5]

[1] *Geophysical Institute, Acad. Bonchev str, Bl. 3, 1113 Sofia, Bulgaria*
imdnme@gmail.com

[2] *Faculty of Physics, University of Sofia, James Bourchier blv, 1164 Sofia, Bulgaria*
rumypm@phys.uni-sofia.bg

[3] *National Institute of Meteorology and Hydrology,*
66 Tsarigradsko chausse, 1784 Sofia,Bulgaria,
boryana.tsenova@meteo.bg

[4] *MMM Division, NCAR, 3450 Mitchell Lane, Boulder, 80301 Colorado, USA,*

[5] *SEAES, University of Manchester, Manchester, M13 9PL,UK*
latham@ucar.edu

**Corresponding author*

(Manuscript received in final form October 25, 2012)

Abstract—This paper investigates the effect of the expected changes of tropospheric temperature profile on the dynamical and microphysical characteristics of individual summertime convective storms and on the processes of precipitation development in these storms. Two dynamically different clouds (a 'big' and a 'small' one) were simulated with the Regional Atmospheric Modeling System (RAMS v6.0). The differences between simulations of the clouds, developed in a present-day and in a modified environment are discussed. Macro- and microphysical evolution is examined in detail, and the changes in precipitation intensity and total rainfall volume are explained physically as a consequence of the temperature increase in the upper troposphere. Results show that the warming leads to a decrease of precipitation in the 'small' cloud case, while in the 'big' cloud case, warming leads to the increase of precipitation. The detailed analysis reveals that the main reason for the opposite direction of the impact of the projected tropospheric changes on different sized clouds lies in the ice phase evolution.

Key-words: climate warming, convective cloud, numerical model, RAMS

1. Introduction

In the scientific community, it is expected that the projected global warming will give rise to greater frequency and severity of extreme precipitation events, as stated in the Report of the Intergovernmental Panel on Climate Change (IPCC, 2007), based on studies such as *Semenov* and *Bengtsson*, 2002; *Kharin* and *Zwiers*, 2005; *Meehl et al.*, 2006 and others. *Trenberth et al.*, 2003 studied different methods of assessing the impact of various thermodynamical factors on precipitation, and concluded that the increased moisture content as a result of climate warming would have a significant impact on precipitation amount and intensity. As extreme precipitation relates to increases in moisture content and due to the nonlinearities involved with the Clausius-Clapeyron relationship, for a given increase of temperature, the projected increase of extreme precipitation is more pronounced than the mean precipitation increase (*Allen* and *Ingram*, 2002). In mid-latitude continental regions, summertime precipitation falls mainly from convective clouds with a great vertical extent, often supplemented by lightning, hail, floods. Obviously, changes in extreme local weather events are connected to the airmass properties – changes occurring in temperature and humidity, their vertical profiles or concentration and size of aerosols. *McCaul et al.* (2005), using RAMS model, examined the sensitivity of supercell storms to environmental temperature by changing only the temperature at the lifting condensation level with convective available potential temperature and other parameters being fixed. Their simulations indicate that in the limit of their assumptions, the updraft speed and precipitation efficiency are higher at a colder environment, while the peak precipitation rate in a warmer environment is comparable to that in colder environment. Numerical simulations of *Takemi* (2010), by Advanced Research WRF model reveal the dependence of the precipitation intensity in mesoscale convective systems on the temperature lapse rate. In the frame of their model simulations they found that with the increase of the lapse rate the mean precipitation intensity increases and the maximum precipitation intensity decreases. They stress on the need for diagnosis of stability in climate simulations and the need to investigate further the effects of cloud microphysics on the production of precipitation in a given temperature environment. To clarify this question, preliminary investigations on the impact of change in temperature and humidity profiles on microphysical characteristics of convective storms and on the processes of precipitation development would be of use. In *Mitzeva et al.* (2008) the influence of global warming on convective cloud dynamics and microphysics is investigated with a 1.5 D cloud model and compared with the influence of the pollution represented by CCN concentration. Their results show that in warmer profile temperature more vigorous cloud form, with larger cloud, rain water, and ice content.

In the present study, the impact of changes in tropospheric temperature and humidity profiles on individual summertime convective continental cloud

development and precipitation is investigated. Numerical simulations are performed with RAMS (regional atmospheric modeling system) and changes of temperature and humidity are imposed on a reference sounding. Two clouds were simulated which are formed with the same meteorological conditions, but triggered by different sized thermal bubbles. The simulated clouds dynamical evolution, hydrometeor mixing ratios, and resulting precipitation are evaluated in detail. The analysis focuses on clarifying the changes in the process of formation of precipitation, with emphasis on the ice phase process. The present study is a first step for testing whether and how temperature profile changes would affect convective clouds development without pretending to be sufficient for the drawing of general conclusions.

2. Cloud model

The model used in the present study is the Regional Atmospheric Model System (RAMS v.6.0), which is developed by the Colorado State University and is widely used as a research tool for numerical studies of thunderstorms (*Pielke et al.*, 1992; *Cotton et al.*, 2003). It combines the capabilities of different types of atmospheric models, from mesoscale to large eddy simulations. RAMS is a 3-dimensional non-hydrostatic cloud resolving atmospheric model. It includes equations and parameterizations for a wide range of physical processes, as it is designed as a comprehensive meteorological modeling system: advection, diffusion, turbulence, radiation, and large-scale precipitation; it also includes a land surface model and a bulk microphysics scheme for resolved clouds and precipitation. Spatial resolution can vary from hundreds of meters to hundreds of kilometers and the time-step can be fixed or varying, user-defined, or automatically calculated by the model.

The two-moment bulk microphysics scheme in RAMS predicts both mass mixing ratio and number concentration of hydrometeor species thus allowing the mean diameter of hydrometeors to evolve. (*Meyers et al.*, 1997). CCN number concentration is defined in the beginning of the run and it is kept constant during the simulations. The size distribution of aerosols is included indirectly through the shape of the cloud droplet spectrum. Cloud droplet as well as other hydrometeor spectra are approximated by a gamma function, which depends on prognosed mean radius and number concentration, and it has a fixed shape.

Sensitivity studies (e.g., *Demott et al.*, 1994; *Van den Heever et al.*, 2006; *Phillips et al.,* 2007, and others) show that nucleation processes are fundamental microphysics processes that must be routinely included in cloud schemes to capture the lifecycle of convective clouds. For the present simulations, since we focus on the impact of the temperature profile changes on cloud formation and development by simulating idealized convective clouds, CCN concentration and

gamma shape parameters for different hydrometeor species are selected in an appropriate way to represent microphysical conditions typical for mid-latitude continental climate.

In the model, seven species of hydrometeors are categorized: cloud droplets, rain, pristine ice, snow, aggregates, graupel, and hail. Cloud droplets and pristine ice nucleate from vapor and may convert into other categories after they grow. Together, pristine ice and snow categories represent a bimodal distribution of ice crystals. Graupel has higher density than snow but still consists mostly of ice and can carry only a small percentage of liquid. If the percentage of liquid is higher than 30%, the ice particle is considered as hail – the highest density hydrometeor formed by freezing of raindrops, riming or partial melting of graupel. The fall speeds of the hydrometeors vary depending on diameter and category. Note, that the definitions of graupel and hail categories in the model emphasize their composition and density rather than their method of formation. Thus, a melting graupel particle will increase its liquid fraction and density, and it will be categorized as hail.

Apart from nucleation, vapor deposition, riming, and melting, coalescence is also taken into account by using pre-calculated look-up tables that contain approximate solutions of the stochastic collection equation. The two-moment scheme also includes breakup of raindrops (formulated into the collection efficiency), diagnosis of pristine ice and snow habit dependent on temperature and saturation, evaporation and melting of each species. Details of microphysical parameterization can be found in *Meyers et al.*, (1997).

3. Numerical simulations

In the present study, in order to lower the computational expense of the experiments, some of the schemes in the model are switched off (short-wave and long-wave radiation, soil model). They do not have significant influence on processes of such space and time scales like single convective storms. The microphysics parameters are selected in a way to represent an urban region with a mid-latitude continental climate. The hydrometeor shape-parameters as well as other initialization parameters are shown in *Table 1*. The time step is automatically calculated by the model, depending on the resolution.

The model domain dimensions are 30 × 30 × 15.5 km consisting of 50 × 50 × 60 points with 600 m grid spacing in a Lambert conformal projection. It covers the area of Sofia City with center point latitude/longitude of 42.65 N/23.38 E. The topography is simplified to a flat surface with elevation of 595 m above sea level. The vertical coordinate is terrain-following sigma coordinate with level thickness ΔZ increasing from 30 m at ground level to 300 m in the free troposphere with a stretch ratio of 1.25. Initial conditions (at the surface) are horizontally homogeneous and are taken from the aerological sounding

measurement in Sofia on 14 July 2006 – a day when a (moderate) thunderstorm was observed, or from the modified sounding.

Table 1. Forcing conditions of the numerical simulations

Parameter	Value
Horizontal resolution	600m
Vertical resolution at z=0m	30m
Vertical resolution above z=2000m	300m
Large time step	4s
Small time step	1s
CCN number	$1.0*10^9$ #/m^3
gamma shape parameter, cloud droplets	3.0
gamma shape parameter, raindrops	2.0
gamma shape parameter, pristine crystals	1.5
gamma shape parameter, snow	2.0
gamma shape parameter, aggregates	2.0
gamma shape parameter, graupel	2.0
gamma shape parameter, hail	2.0
Thermal bubble amplitude (ΔT)	2K
Thermal bubble relative humidity ratio	1.2
Thermal bubble horizontal size	3km; 4.2km
Thermal bubble vertical size	1.1km; 1.7km

Boundary conditions are open. Simulations were carried out for one hour starting at 12:00 UTC. A real sounding was used in order to assure that the environmental conditions chosen for model simulation are adequate for thunderstorm formation, rather than to simulate the real thunderstorm that developed over Sofia. Clouds were initiated by introducing a warm moist bubble at the surface. The so called "thermal bubble" had 2 K temperature excess and 20% higher relative humidity compared to the environmental air. By varying the thermal bubble's horizontal and vertical dimensions, two convective clouds were simulated – cloud A, simulated with initial bubble size of $4.2 \times 4.2 \times 1.7$ km and cloud B, simulated with initial bubble size of $3 \times 3 \times 1.7$ km. Thus, our study is an idealized modeling study. As a result of an appropriate choice of the initial conditions, two typical (for mid-latitude) single summer continental precipitating clouds were simulated. Hereafter, we will call them 'big' and 'small', because one (cloud A) is bigger than the other (cloud B). The 'control simulation' is the simulation carried out with the original sounding from July 14, 2006, for cloud A (simulated with the larger thermal bubble) and for cloud B (simulated with the smaller thermal bubble). The modifications of the temperature profile used in the present study (*Fig. 1*) are based on IPCC,

2007 and *Santer et al.*, (2003). IPCC climate projections predict an increase of global mean surface temperature from 2 to 6 °C till the end of the 21th century. The investigations of *Santer et al.*, (2003) reveal that temperature changes with height depend on latitude and the temperature increase in the upper troposphere for the mid-latitudes is about 1.5 times greater than the surface temperature with maximum around 300 mb. Due to the very limited studies and no clear trend in relative humidity (*Elliot* and *Angell*, 1997) in our simulations the dew-point temperature profile was modified to keep the relative humidity in accordance to the original sounding, i.e., the relative humidity was not modified.

The control simulation (with the original sounding) is hereafter denoted as ΔT=0 and the simulations with two modified profiles are denoted as ΔT=3 and ΔT=5 respectively, where the numbers 3 and 5 refer to the surface temperature increase in degrees Celsius. The original sounding is shown in Fig.1a and the modification of temperature profile is shown in *Fig. 1b*. The relative humidity is not modified among the runs.

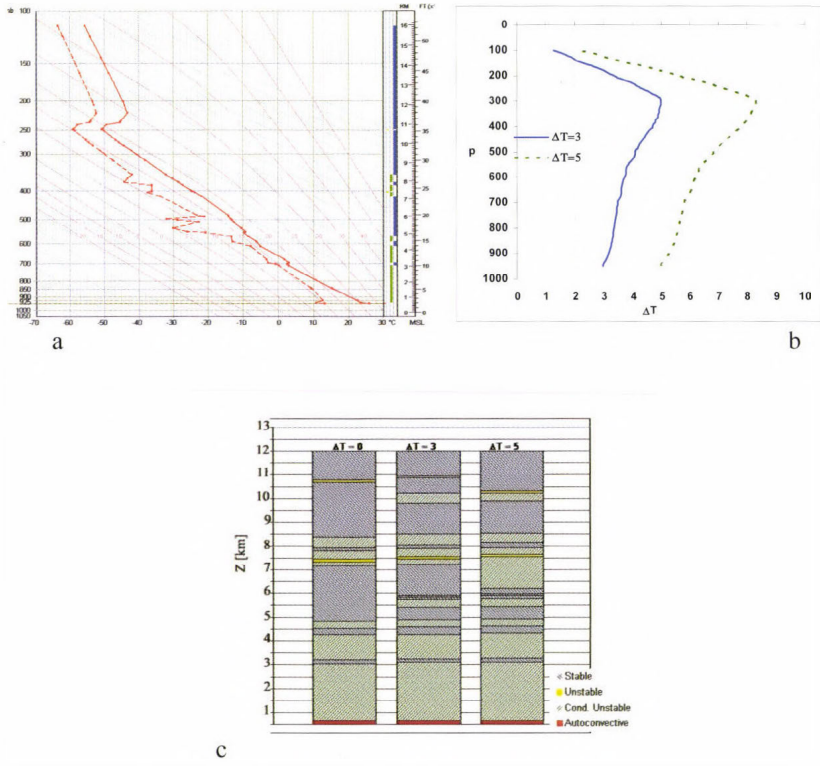

Fig. 1. a) Aerological sounding from 14 July 2006; b) increase of temperature ΔT used for the simulations of global warming; c) atmospheric stability for the simulated cases with ΔT=0, ΔT=3, ΔT=5, Z is in km ASL.

The original sounding is characterized by alternating moist conditionally unstable and stable layers (*Fig. 1c*), evaluated using the temperature lapse rate. The instability increases above 5.3 km in ΔT=3 and ΔT=5. This tendency is most pronounced in the layers between 6.1 km and 7.2 km in ΔT=5. In the original sounding, the zero isotherm is located at 3.6 km. The modifications lead to its upward displacement, at 4.1 km for ΔT=3 and 4.6 km for ΔT=5, respectively. The temperature interval where homogeneous freezing occurs is also shifted upward in the warmer environment. The 40 °C isotherm in the original sounding is at 9.4 km AGL above ground level, while for ΔT=3 it is at 10 km AGL and for ΔT=5 - at 10.3 km AGL. Due to the assumption that the relative humidity is kept constant with the warming, the condensation level is almost at the same altitude (around 1.7 km AGL). However, the temperature at cloud base (even at the same altitude) is higher with the warming modification.

4. Results

The results are presented in the following manner. First, we consider the dynamical and microphysical characteristics of cloud A ('big' cloud), simulated with the reference sounding. After that, the same characteristics of simulations ΔT=3 and ΔT=5 are analyzed, pointing to the differences between them and the control one. The analysis of cloud B ('small' cloud) is presented in the same way.

Cloud A simulated with the reference sounding has a maximum cloud top height of 12 km above ground level (AGL) and maximum updraft speed of 24 m/s. Its anvil is well above the level of maximum heating in warming scenarios. The smaller cloud (cloud B) simulated with the reference sounding has maximum cloud top at 10 km AGL and maximum updraft speed of 18 m/s.

4.1. Cloud A

4.1.1. Macro- and microphysical evolution of the control cloud

Condensation starts at 9 min model time (MT) at 1726 m above ground level (AGL), at temperature 14.2 °C. The cloud grows during the following 12 minutes (*Fig. 2*) and at 21 min MT the cloud top reaches the tropopause (10.7 km AGL). During the rapid growth stage (18–21 min), two maximums of the vertical velocity are visible in *Fig. 3*. At 18 min MT, these maximums can be seen at ~5 km AGL (21 m/s) and at ~7 km AGL (24 m/s), respectively. The sounding instability and high moisture (*Fig. 1*) provide the energy needed to accelerate the updraft. The level of the maximum water mixing ratio (*Fig. 2*) coincides with the level of the first updraft velocity maximum (*Fig. 3*). A slight decrease in velocity at 18 min MT is seen between 5 and 6 km in *Fig. 3*, due to the

dry and stable environment. The analyses reveal that above 6 km AGL (–14 °C), intensive freezing occurs and the updraft speed increases again. Between 18 and 21 min MT the cloud top reaches the layer above 7 km AGL where the moisture increases (*Fig. 1*) and the environment is unstable. The main reason for the increase of updraft velocity above 9 km AGL (*Fig. 3*) is the latent heat released by homogeneous freezing.

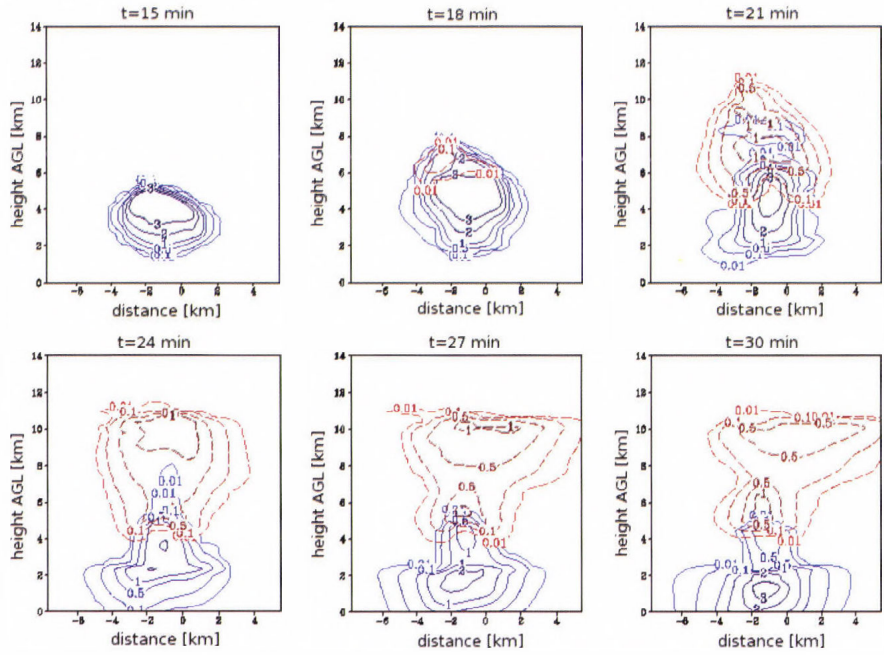

Fig. 2. Cloud A: sum of rain and cloud water mixing ratios (solid) and sum of pristine ice, snow, and aggregates mixing ratios (dashed) in the control simulation (ΔT=0)

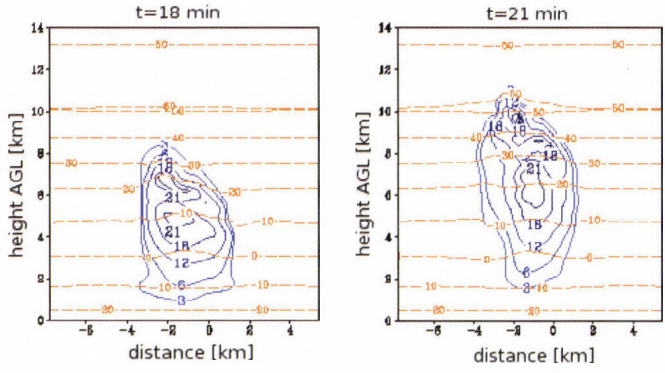

Fig. 3. Cloud A: updraft velocity (solid) and temperature (dashed) at 18 and 21 min model times in the control simulation (ΔT=0).

When the simulated cloud reaches the tropopause (at about 21 min MT), it stops moving upwards and an anvil begins to spread (*Fig. 2*). At this time the cloud is in a mature stage, precipitation reaches the ground (*Fig. 2* bottom panel), and the updraft core start to decay (not shown here).

When the simulated cloud reaches the tropopause (at about 24 min MT) it stops moving upwards and an anvil begins to spread (*Fig. 2*). At this time the cloud is in a mature stage and some of precipitation reaches the ground (*Fig. 2* bottom panel).

The first ice particles form between 15 and 18 min MT at 5.5 km AGL (see *Fig. 2*), where the in-cloud temperature is about –12°C. Afterwards, the mixing ratio of all ice species increases (*Fig. 2* and *Fig. 4*). Around 21 and 27 min MT, the maximum values of mixing ratio of hail and graupel, respectively, are reached (*Fig. 4*, *Table 2a*). At 27 min the updraft starts to weaken and part of graupel and hail particles fall down, melt, and transform to rain drops. As a result, graupel and hail mixing ratios in the simulated cloud A (*Fig. 4*) decrease. After 33 min MT the cloud–starts to dissipate. The precipitation intensity simulated by the model with reference sounding maximum (in space and time) is 66.18 mm/hr, and the maximum accumulated precipitation (in space) is 10.25 l/m^2. The total rainfall volume yield (total volume of liquid water fallen on the ground) is 1.98×10^6 m^3.

4.1.2. Effect of warming – comparison between simulations with modified soundings and the control run.

As it can be seen from *Fig. 1*, the increase in atmospheric temperature as a result of the projected regional climate change is expected to be the largest at 300 hPa. Below 4 km ASL (~650 hPa), in warmer environment, the lapse rate is slightly lower, and convection will be suppressed, while above 9 km (300 hPa) there is an increase of the lapse rate and stability decreases. Due to the assumption that the relative humidity is not changed, specific humidity increases where temperature increases. Increased humidity means increased reservoir of water and the associated latent energy, so there is a potential for intensification of cloud dynamics. Intensive storms (with strong updraft) usually reach the 300 hPa level which in our simulation is at 8900 m AGL.

Another important consequence of warming is the upward displacement of the zero isotherm (from 3.6 km in ΔT=0, to 4.1 km in ΔT=3 and 4.6 km in ΔT=5), which affects the formation and development of ice particles in the simulated clouds. Additionally, the cloud base in ΔT=3 is at 17.5 °C, while in ΔT=5 it is at 19.7 °C, or respectively, it is about 3.3 and 5.5 °C warmer than the control cloud base. Together with the zero isotherm upward displacement, the increase of the cloud base temperature due to the warming (and the keeping of the relative humidity unchanged) leads to an extension of the region with temperature higher than 0°C in the simulated 'warming' clouds in ΔT=3 and ΔT=5.

Table 2a. Maximum (in space and time) values for cloud, rain, pristine, snow, aggregates, graupel, hail mixing ratio [g/kg] for simulated "big" cloud

	Cloud	Rain	Pristine	Snow	Aggregate	Graupel	Hail
ΔT=0	6.39	4.09	0.59	0.67	1.14	2.5	7.14
ΔT=3	6.55	4.81	1.04	0.64	1.15	2.4	9.35
ΔT=5	6.78	7.93	1.42	0.69	1.37	2.23	11.04

Table 2b. Integrated (space and time) values for cloud; rain, pristine, snow, and aggregates; graupel and hail mixing ratios [g/kg] for simulated "big" cloud

	Cloud	Rain	Pristine+Snow+Aggregates	Graupel+Hail
ΔT=0	5758	9933	12766	33497
ΔT=3	6062	12696	17041	32558
ΔT=5	6163	14999	18335	28668

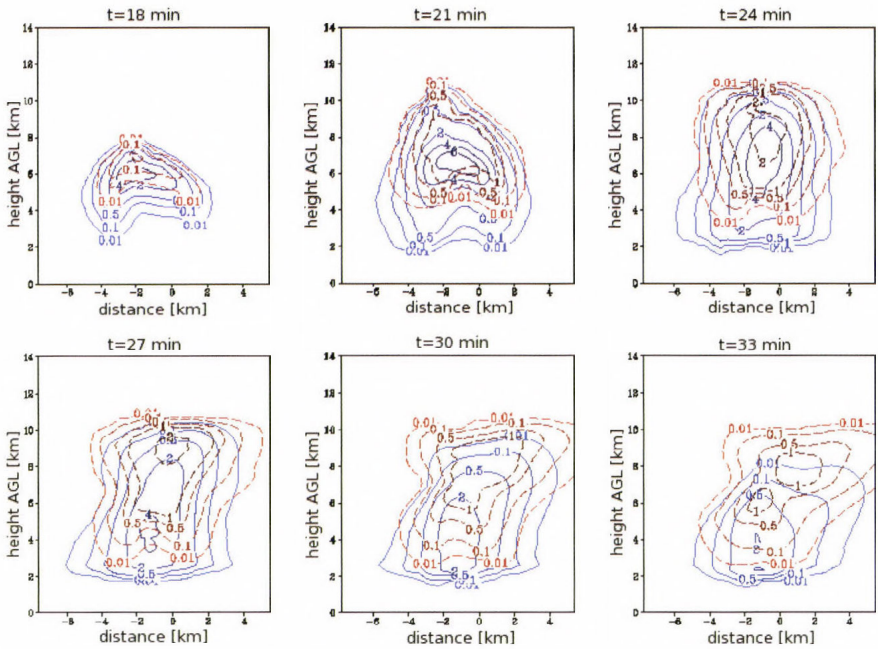

Fig .4. Cloud A: hail (solid) and graupel (dashed) mixing ratios from 18 to 33 min model time in the control simulation (ΔT=0).

The results presented in *Table 2a* show that maximum values of cloud water and aggregates mixing ratio only slightly increase with warming, while there is a significant increase in maximum values of pristine ice, rain, and hail mixing ratios. The warming leads to the increase of space and time integrated mixing ratio of liquid hydrometeors and of small ice particles and to the decrease of the sum of graupel and hail mixing ratio (*Table 2b*). An idea for changes of the evolution of space integrated mixing ratios as a result of warming gives *Figs. 5a – 5d.* The effect of warming on space integrated cloud water mixing ratio is not well pronounced (*Fig. 5a*), while a significant increase of space integrated rain water mixing ratio until 30 min MT is visible in *Fig. 5b* for warmer cases. After 22 min MT, the sum of space integrated ice, snow and aggregates mixing ratios also increases with warming (*Fig. 5c*). The decrease in sum of space integrated graupel and hail mixing ratios (*Fig. 5d*) can be explained by melting of graupel and hail in the warmer environment, which contributes to the increase of rain water mixing ratio.

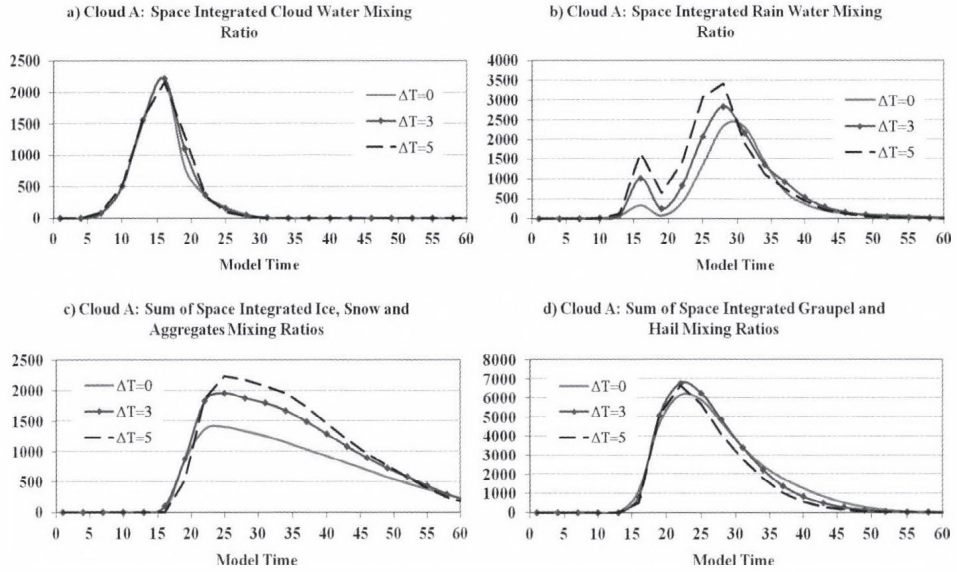

Fig. 5. Cloud A: temporal evolution of a) space integrated cloud water; b) space integrated rain water; c) sum of space integrated ice, snow and aggregates; d) sum of space integrated graupel and hail mixing ratios in g/kg as a function of model time MT in min for ΔT=0, 3, 5.

The top of the control cloud reaches 300 hPa (8.9 km AGL) at 18 min MT. After 18 min MT, the updraft velocity and the processes of formation and

growth of ice particles are intensified and the cloud top rises fast, due to the homogeneous freezing that occurs between –30 °C and –50 °C in the model. The analyses reveal that the clouds simulated with ΔT=3 and ΔT=5 experience similar stages of development to the control cloud (ΔT=0). There are only slight differences in cloud top height (*Fig. 6*) and location and intensity of updraft core (*Fig. 7*). From *Fig. 7* one can see that at 18 min MT, the updraft velocities are almost identical in ΔT=0, ΔT=3, and ΔT=5.

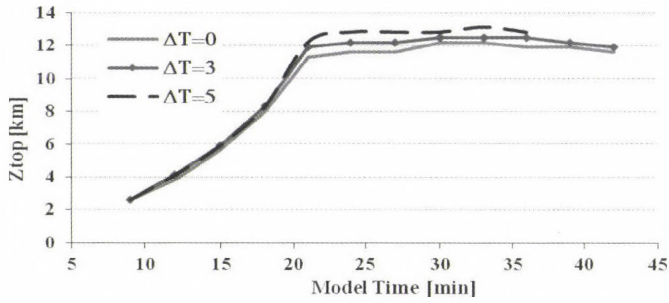

Fig. 6. Cloud A: cloud top height as a function of time for ΔT=0, 3, 5.

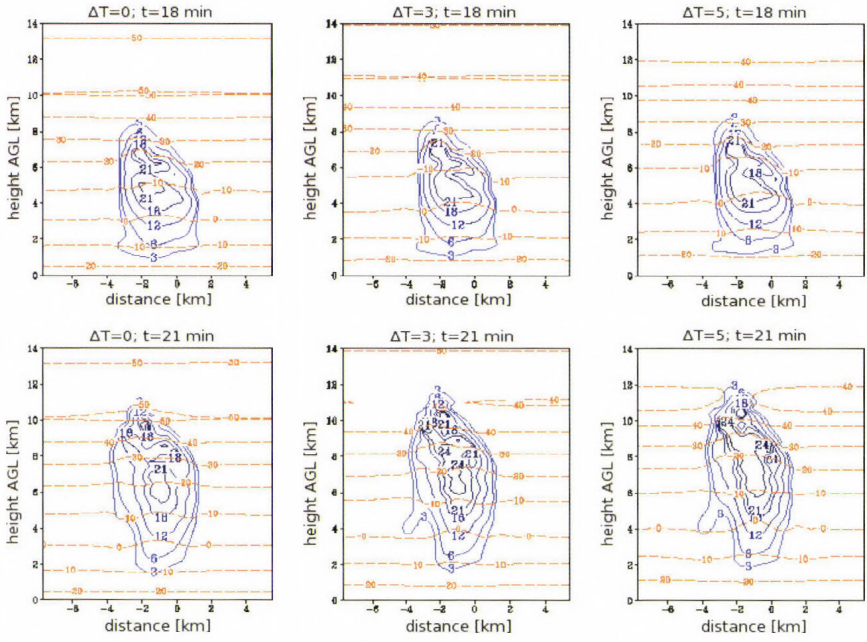

Fig. 7. Cloud A: updraft velocity (solid) and temperature (dashed) at 18 min MT (top panel) and 21 min MT (bottom panel) for ΔT=0, 3, 5 (left, middle, and right panel, respectively).

In the warmer environment, the updraft velocity in the lower parts of simulated clouds has slightly lower values due to slightly lower lapse rates at heights below 4 km. Later, above 4 km, the updraft velocity in the warming cases is larger due to the released latent heat from the frozen water during the formation of hail particles. The top panel of *Fig. 9* shows that the hail mixing ratio increases with warming. Ice crystal particles (*Fig. 8a*, top panel) form a few minutes earlier in the control run than in the clouds, simulated with ΔT=3 and ΔT=5. The reason for the earlier formation of ice particles at lower altitude in ΔT=0 is the lower temperature in the original sounding. At 21 min MT, all three clouds have passed the –40 °C isotherm which is at higher altitudes (9.3, 9.9, and 10.3 km AGL, respectively for the control run, ΔT=3, and ΔT=5) in warming cases. The updraft velocity in the latter case is highest, showing very intensive growth (*Fig. 7*). This corresponds to the thermodynamic effect of the increased lapse rate above 9 km AGL in warming cases. Another reason for the increase of the updraft velocity in the "big" cloud developed in the warmer environment is the higher water mixing ratio at higher levels in these cases (*Fig. 8a*, top panel). Liquid water, once frozen, leads to the increase of the ice mixing ratio (*Fig. 8a* , bottom panel) above –30 °C and the release of more latent heat. A strong maximum of 33 m/s is seen (*Fig. 7*) in ΔT=5 case (compared to 24 m/s in the control cloud and 30 m/s in ΔT=3).

From *Figs. 8* and *9* it is visible that the higher liquid water and higher ice mixing ratio (*Fig. 8a*) in the warmer environment lead to higher hail mixing ratio (*Fig. 9a*, top panel). At 24 min MT, the hail mixing ratio in the layer between 5 and 10 km is almost double in ΔT=5 compared to ΔT=0. The analyses show that in cases ΔT=3 and ΔT=5, the hail particles have larger liquid fraction, higher density, and larger fall velocity, so they fall earlier to lower levels in comparison with ΔT=0. Precipitation for all three simulations begins at about 21 min MT and stops at 50 min MT (*Fig. 10*). Melted hail particles contribute to the earlier occurrence of the maximum precipitation rate in the warming cases – 30 min MT in ΔT=5, compared to 33 min in ΔT=0. Precipitation rate, accumulated precipitation, and total rainfall volume increase in the warm simulations (*Table 3*). The peak precipitation rate in ΔT=5 is almost twice as high as in ΔT= 0.

Table 3. Peaks of rainfall rate, accumulated (for 50 min MT) rainfall, and accumulated total rainfall volume yield from cloud A ("big" cloud)

	Peak precipitation rate [mm/h]	**Peak accumulated precipitation [l/m^2]**	**Total rainfall volume [m^3]**
ΔT=0	66.18	10.25	1.98 10^6
ΔT=3	71.71	11.40	2.23 10^8
ΔT=5	112.24	12.75	2.42 10^8

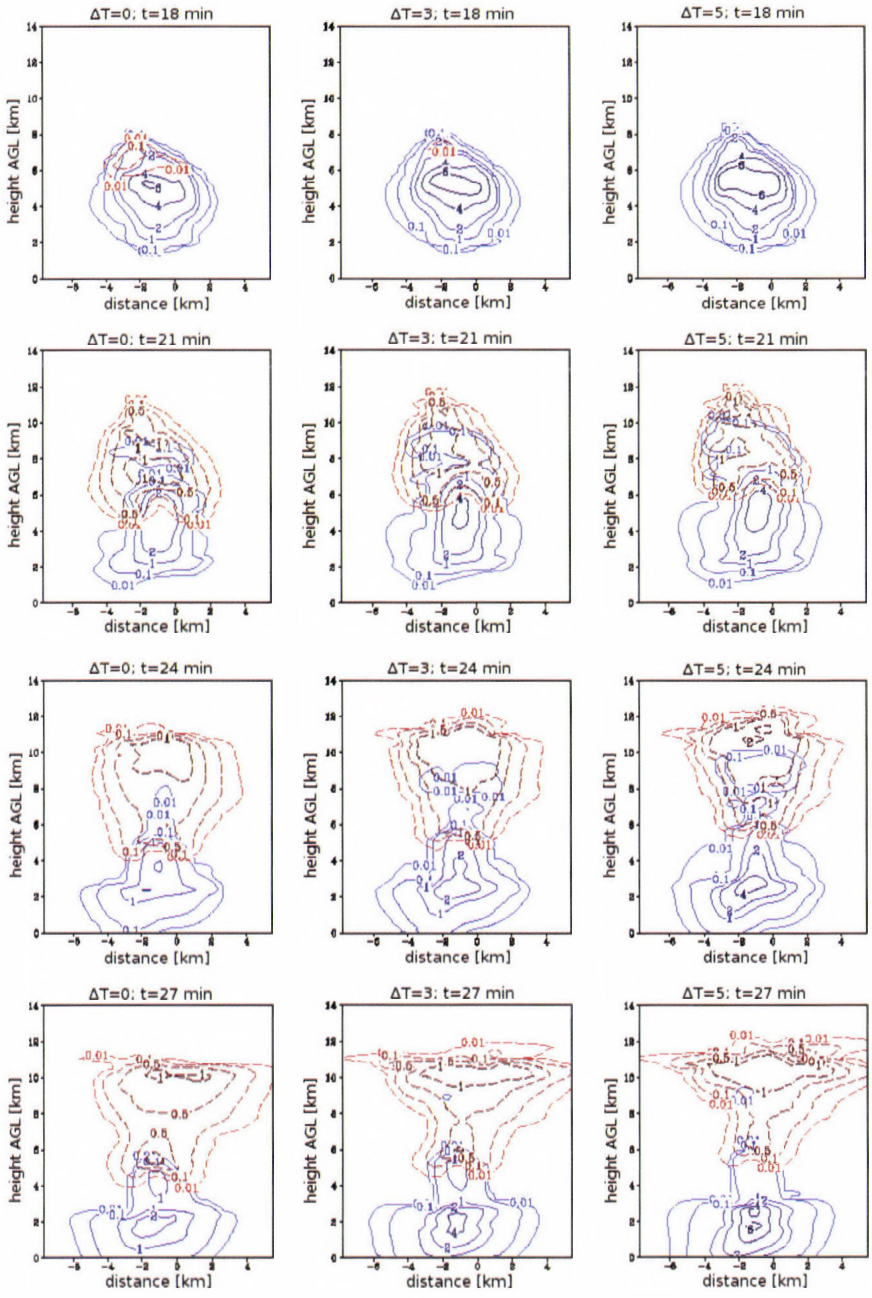

Fig. 8. Cloud A: sum of rain and cloud water mixing ratios (solid) and sum of pristine ice, snow, and aggregates mixing ratios (dashed) at 18 min MT, 21 min MT, 24 min MT, and 27 min MT (from top to bottom panel) for ΔT=0, 3, 5 (left, middle, and right panel, respectively).

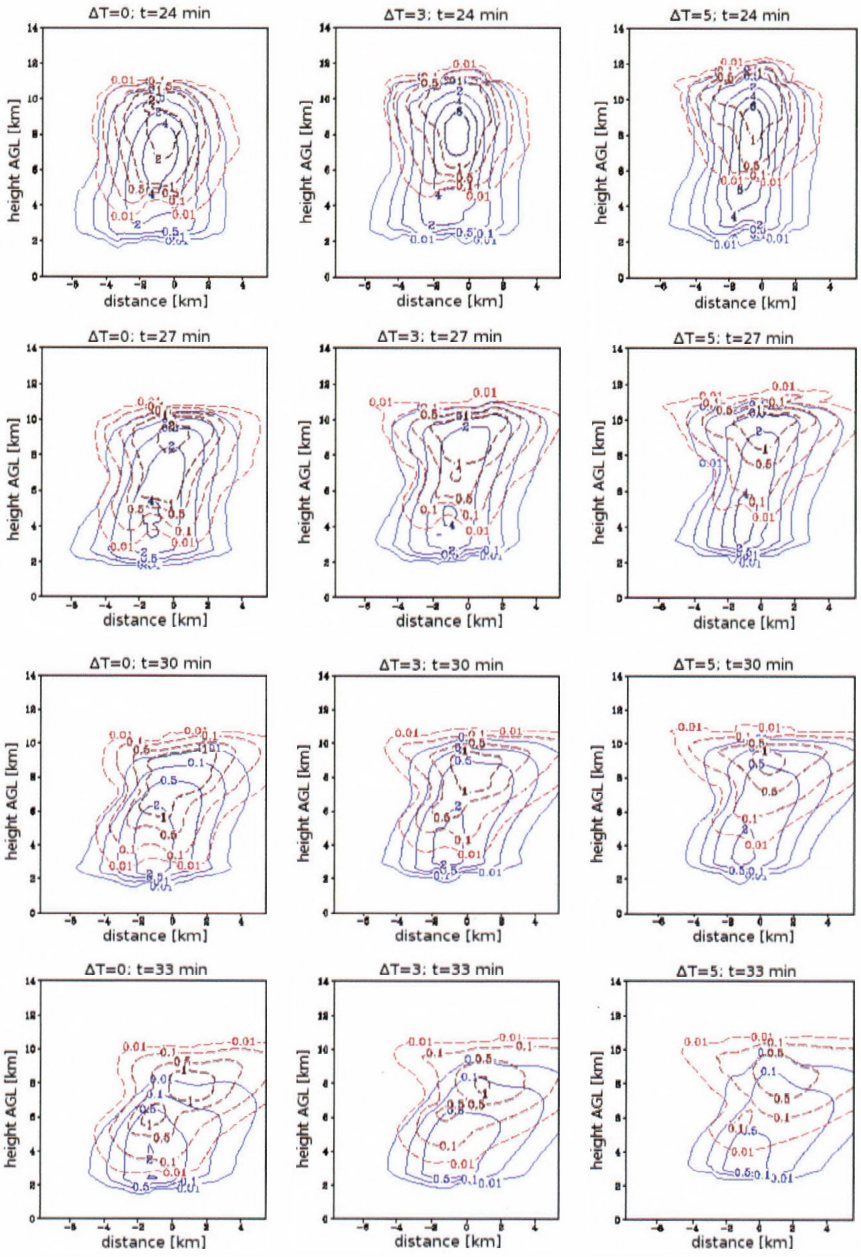

Fig. 9. Cloud A: hail (solid) and graupel (dashed) mixing ratios at 24 min MT, 27 min MT, 30 min MT, and 33 min MT (from top to bottom panel) for ΔT=0, 3, 5 (left, middle, and right panel, respectively).

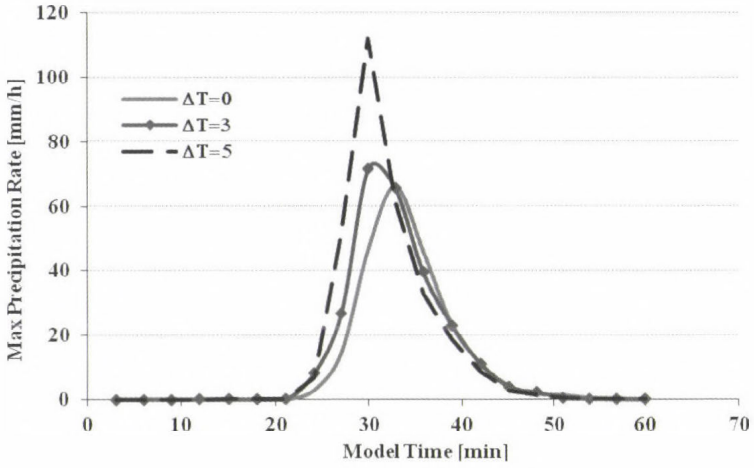

Fig. 10. Cloud A: peak rainfall rate as a function of time for ΔT=0, 3, 5.

4.2. Cloud B

Cloud B is the 'small' cumulonimbus that develops in the same environment as cloud A, but it is initiated with a smaller thermal bubble (see *Table 1*).

4.2.1. Macro- and microphysical evolution of the control cloud

Similarly to cloud A, cloud development begins at 9 min MT, and the cloud base height is at 1726 m AGL (14.16 °C). During the next 15 min, the cloud top rises at a rate of 10 m/s until 24 min MT and at 27 min MT it reaches its maximum height of 9.5 km AGL, where the temperature in the environment is –41 °C (*Figs. 12*, and *15*). The maximum updraft velocity (18 m/s) is reached at ~5 km AGL at 24 min MT (*Fig. 12*). After 24 min MT, the updraft velocity starts to decrease and after 30 min MT, the downdrafts prevail. Then the simulated cloud B begins to dissipate, and precipitation falls on the ground.

Ice formation (*Fig. 11*) starts after 18 min MT at an altitude above 4 km (about –5 °C). The formation of hail and graupel starts at the same time and altitude (*Fig. 13*). Maximum mixing ratios of hail and graupel are reached at 21 and 24 min MT, respectively (*Fig. 13* and *Table 4a*).

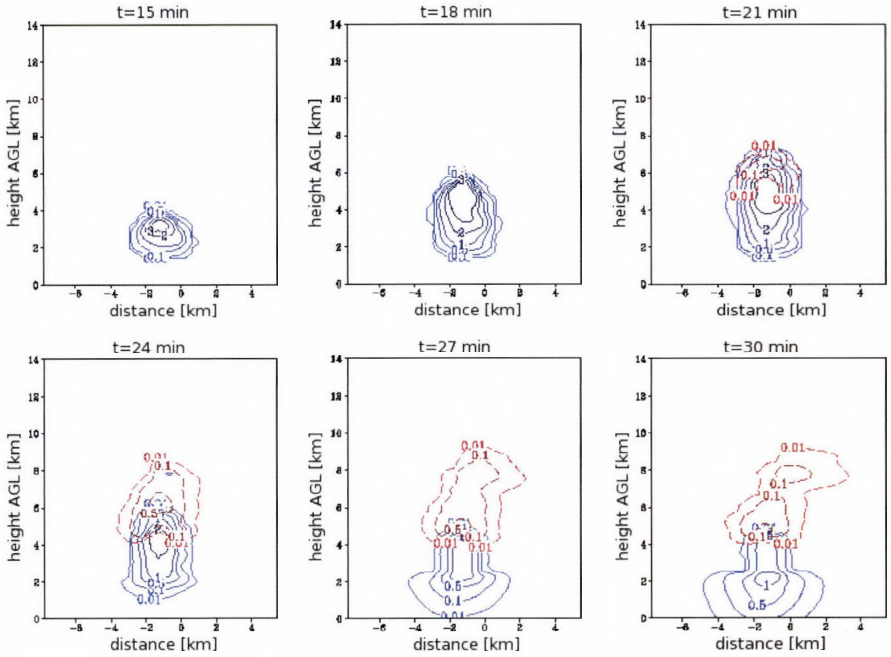

Fig. 11. Cloud B: sum of rain and cloud water mixing ratios (solid) and sum of pristine ice, snow, and aggregates mixing ratios (dashed) in the control simulation (ΔT=0).

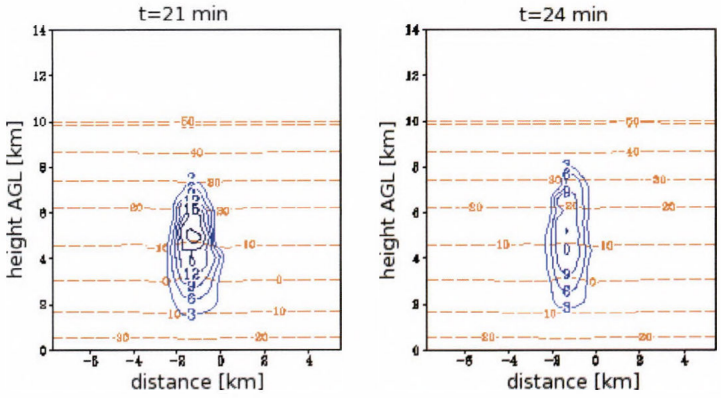

Fig. 12. Cloud B: updraft velocity (solid) and temperature (dashed) at 21 and 24 min model times in the control simulation (ΔT=0).

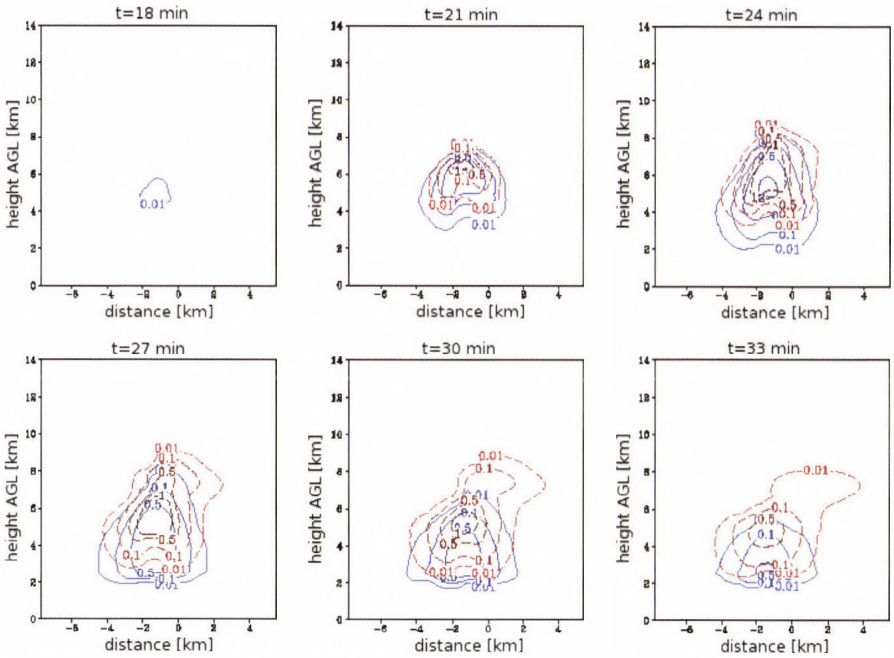

Fig. 13. Cloud B: hail (solid) and graupel (dashed) mixing ratios from 18 to 33 min model times in the control simulation (ΔT=0).

Table 4a. Maximum (in space and time) values for cloud, rain, pristine, snow, aggregates, graupel, hail mixing ratio [g/kg] for cloud B formed in different environmental conditions

	Cloud	**Rain**	**Pristine**	**Snow**	**Aggregate**	**Graupel**	**Hail**
ΔT=0	5.37	1.51	0.14	0.4	0.71	2.32	2.81
ΔT=3	5.43	1.47	0.08	0.51	0.55	1.62	3.58
ΔT=5	5.26	1.81	0.1	0.37	0.76	1.17	3.38

Table 4b. Integrated (space and time) values for cloud and rain water; pristine, snow and aggregates; graupel and hail mixing ratios [g/kg] for cloud B formed in different environmental conditions

	Cloud	**Rain**	**Pristine+Snow+Aggregates**	**Graupel+Hail**
ΔT=0	1743	1544	549.39	3895.28
ΔT=3	1542	1387	272.97	1810.96
ΔT=5	1372	1223	107.08	954.11

The lifecycle of this cloud is different from that of cloud A. There is less vigorous convection and less condensation takes place, so the cloud grows smaller and the mixing ratios of all hydrometeors are lower. Their size (not shown here) and fall velocity are also lower.

The simulated maximum (*Table 5*) precipitation intensity of space and time is 16.77 mm/hr and the peak accumulated precipitation is 2.25 l/m^2. The total rainfall volume yield is $0.253 \cdot 10^6$ m^3, which is ten times less than the rainfall volume yield in cloud A.

Table 5. Peaks of rainfall rate, accumulated (for 50 min MT) rainfall and accumulated total rainfall volume yield for Cloud B ("small" cloud)

	Peak precipitation rate [mm/h]	**Peak accumulated precipitation [l/m^2]**	**Total rainfall volume [m^3]**
ΔT=0	16.77	2.25	$0.25\ 10^6$
ΔT=3	15.01	1.65	$0.19\ 10^6$
ΔT=5	12.85	1.24	$0.14\ 10^6$

4.2.2. Effect of warming – comparison between the modified simulations and the control run.

From *Fig. 14* it can be seen, that cloud top heights of simulated "small" clouds in warmer environment are a few hundred meters lower than the cloud top height of control cloud B, although the maximum heights are reached at the same time, 27 min MT. However, the analyses reveals that the control run reaches temperatures around –42 °C, while the warming cases ΔT=3 and ΔT=5 reach –37 °C and –30 °C, respectively.

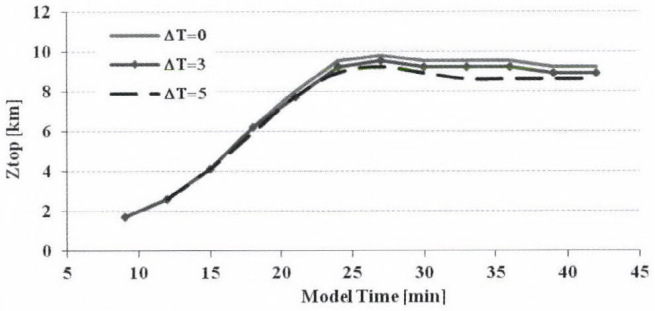

Fig. 14. Cloud B: cloud top height for cloud B as a function of time for ΔT=0, 3, 5.

Results presented in *Table 4a* show that there is no well defined tendency in the changes of maximum values of mixing ratios of the hydrometeors as a result of warming, while the integrated (in space and time) mixing ratios of solid hydrometeors are significantly lower (see column 3 and 4 of *Table 4b*) at higher environmental temperatures. The warming also leads to the decrease of both cloud (column 1 in *Table 4b*) and rain (column 2 in *Table 4b*) mixing ratios integrated in space and time. The evolution of space integrated mixing ratios (*Fig. 15*) reveals that the space integrated rain water mixing ratio in the clouds simulated with warmer environment is higher until 27 min MT, and after that it is lower in comparison to the space integrated rain water mixing ratio in the control cloud.

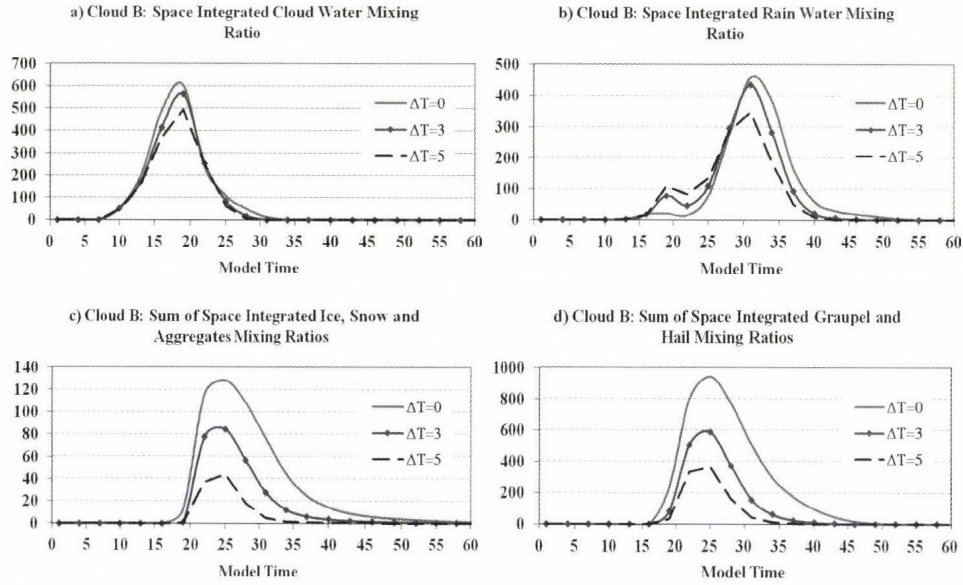

Fig. 15. Cloud B: temporal evolution of a) space integrated cloud water; b) space integrated rain water; c) sum of space integrated ice, snow, and aggregates; d) sum of space integrated graupel and hail mixing ratios in g/kg as a function of model time MT (in min) for ΔT=0, 3, 5.

Plots of the vertical velocity for 21 and 24 min MT (*Fig. 16*) show that the values of the maximum vertical velocity are almost the same, however, it is slightly decreasing and located at lower altitudes with the warming. In the three simulated clouds there is almost no difference in updraft velocities below 5 km, while above 5 km in the warming cases the updraft velocity is lower. In the upper parts of clouds in ΔT=3 and ΔT=5, compared to the control one, there is a smaller amount of freezing water due to the higher temperature. Furthermore,

the clouds denoted with ΔT=3 and ΔT=5 do not reach the level of ~40 °C where intensive homogeneous freezing occurs. Since freezing provides latent heat to accelerate the updraft, this leads to lower values of updraft velocity, despite the decreased stability.

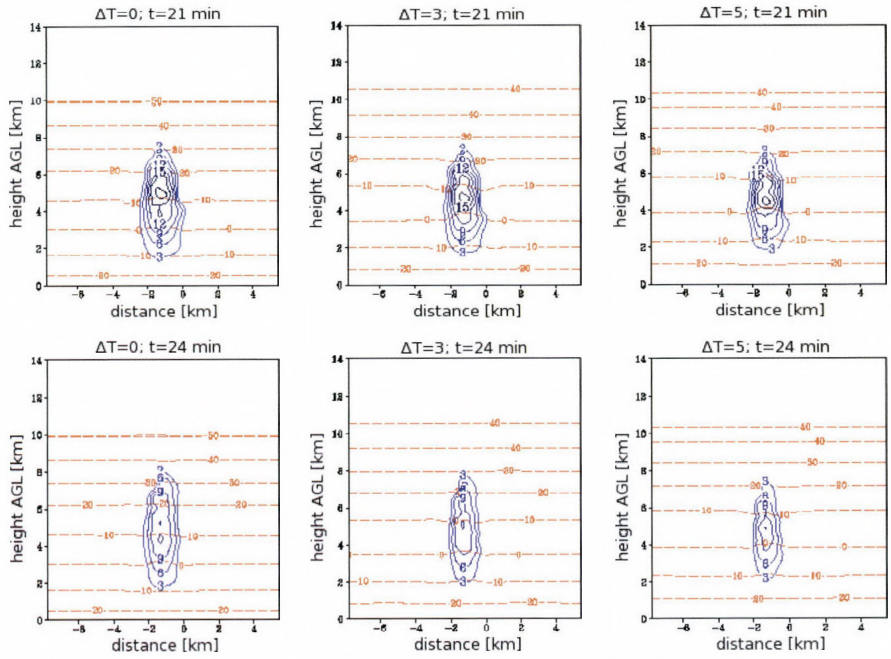

Fig. 16. Cloud B: updraft velocity (solid) and temperature (dashed) at 21 and 24 min model times for ΔT =0, 3, 5.

The analysis of mixing ratio of hydrometeors in vertical cross section at different moments of time (*Figs. 17* and *18*) shows that in clouds developed in a warmer environment the total liquid water mixing ratio is slightly higher than in the simulated ΔT=0 cloud, while due to higher temperatures, the values of ice (the sum of pristine, snow, and aggregates) and graupel mixing ratio (*Fig. 18*) are lower compared to the control cloud. There is higher rain water mixing ratio in warming cases (*Fig. 17*). The more detailed analysis shows, that in ΔT=0 at 21 min MT, ice starts to form at 5–7 km by freezing of cloud and rain drops, while in ΔT=5 there is still no ice. Coagulation of drops with graupel and hail in ΔT=0 further contributes to the decrease of the liquid water mixing ratio at these altitudes. On the other hand, in ΔT=5 the mixing ratios of cloud and rain water

continue to increase. After the formation of ice in ΔT=5 (see bottom panel of *Fig. 17*), the rain mixing ratio also starts to decrease. Hail mixing ratio increases in ΔT=3 compared to ΔT=0 and decreases in ΔT=5 compared to ΔT=3. The increase in hail mixing ratio in ΔT=3 and ΔT=5 is accompanied by an increase of hail liquid fraction (not shown here). The reason for that can be found in the definition of hail as a higher density hydrometeor than graupel that can carry a larger fraction of liquid water. The sources for hail particles are coalescence between solid and liquid particles (when water freezes slowly) or partial melting of graupel, and the sinks are shedding and melting into rain. In warming cases, due to the increased temperature, water droplets colliding with an ice particle freeze slower, thus increasing the ice particle density and leading to the formation of hail rather than graupel. This could be a reasonable explanation for the fact that the hail mixing ratio increases in ΔT=3. Obviously, in warming cases more hail particles grow in wet regime. In ΔT=5 hail, particles carry a larger fraction of liquid, have higher density and consequently a higher fall velocity, so more hail particles fall to levels having positive temperature and melt to form rain. This can be the reason for the decrease of maximum hail mixing ratio in ΔT=5 compared to ΔT=3. These speculations are supported by the results presented in *Fig. 17*, where plots of the sum of cloud and rain and the sum of pristine, snow, and aggregates are shown, and in *Fig. 18*, where graupel and hail mixing ratios are shown. From *Fig. 17* it is evident that ice starts to form later in warming cases compared to the control run. At 27 min MT, the difference in microphysical development can be seen – the control cloud still has lots of ice in its upper part, a slightly lowered liquid water mixing ratio and some graupel and hail close to cloud base (*Fig. 18*), while ΔT=5 has lost much of its ice mixing ratio above 5 km and has more hail close to cloud base, compared to ΔT=0 and ΔT=3. The melting of ice is visible in *Fig. 18* where hail mixing ratios for 24 min MT are high in all three clouds, but later it decreases faster in warming cases, and there is almost no ice in ΔT=5 at 33 min. From the same figure it can be seen that during the mature stage (27–33 min), the hail mixing ratio close to cloud base slightly decreases in the warm simulations, while graupel mixing ratio decreases significantly.

These differences in the clouds' microphysical evolution lead to differences in precipitation. In ΔT=5 at 24 min, large amount of liquid water is "found" in the layer between 4–6 km, consisting mostly of raindrops, and it decreases sharply at 27 min (*Fig. 17*). At 33 min MT, there is a low amount of graupel and hail in ΔT=5 compared to ΔT=0, while the liquid mixing ratio in the clouds (not shown here) has similar values. Precipitation starts at the same MT for the three clouds (*Fig. 19*), but it is less intensive in warming cases. Despite the increased reservoir of water vapor in the warmer atmosphere, the precipitation (intensity and total volume) is lower than the precipitation from the control cloud (see *Table 5*, *Fig. 19*) The peak in the ΔT=5 case is earlier than ΔT=0. The decrease in total rainfall volume is 25% for "ΔT=3" and another 25% for ΔT=5 compared to ΔT=3.

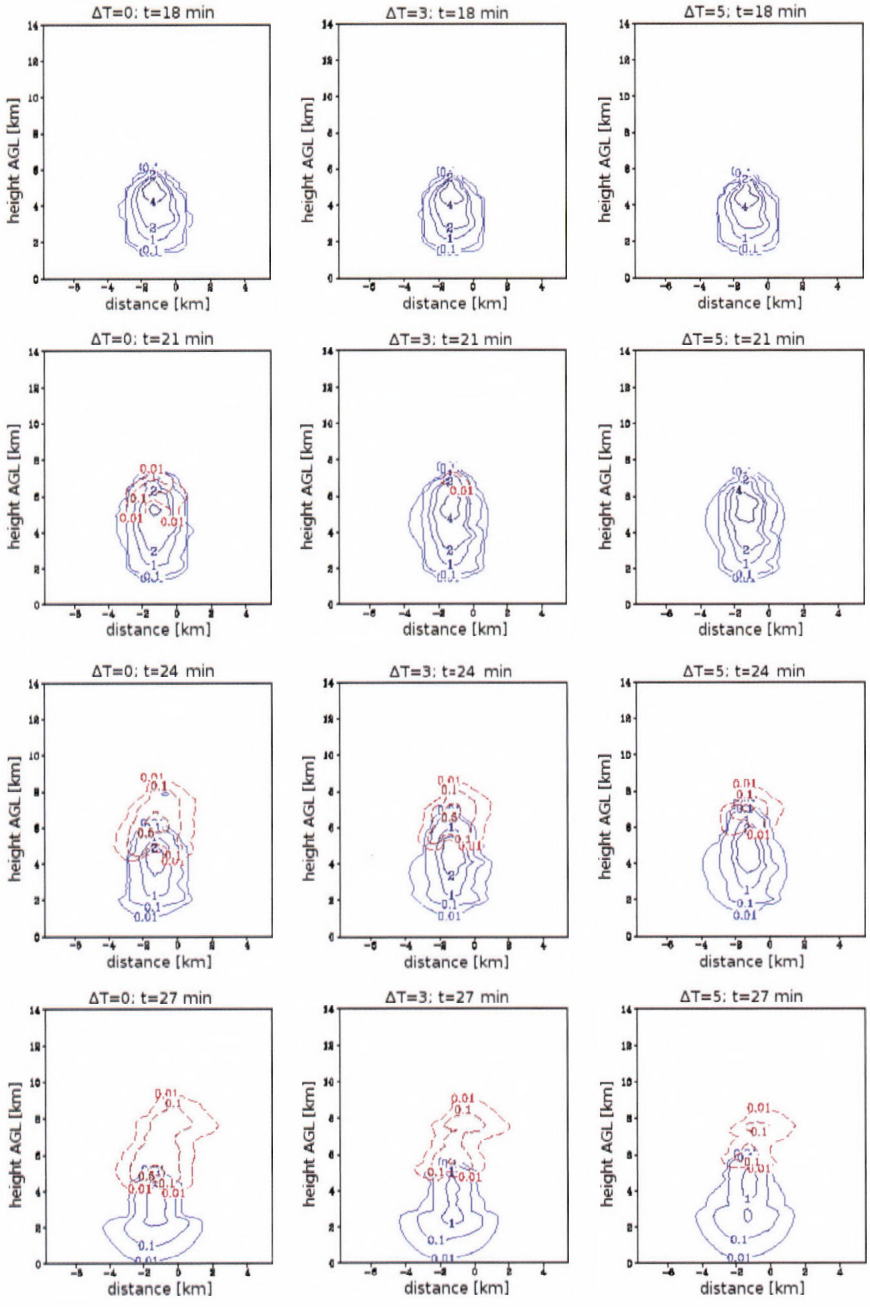

Fig. 17. Cloud B: sum of rain and cloud water mixing ratios (solid) and sum of pristine ice, snow, and aggregates mixing ratios (dashed) at 18 min MT, 21 min MT, 24 min MT, and 27 min MT (from top to bottom panel) for ΔT=0, 3, 5 (left, middle, and right panel, respectively).

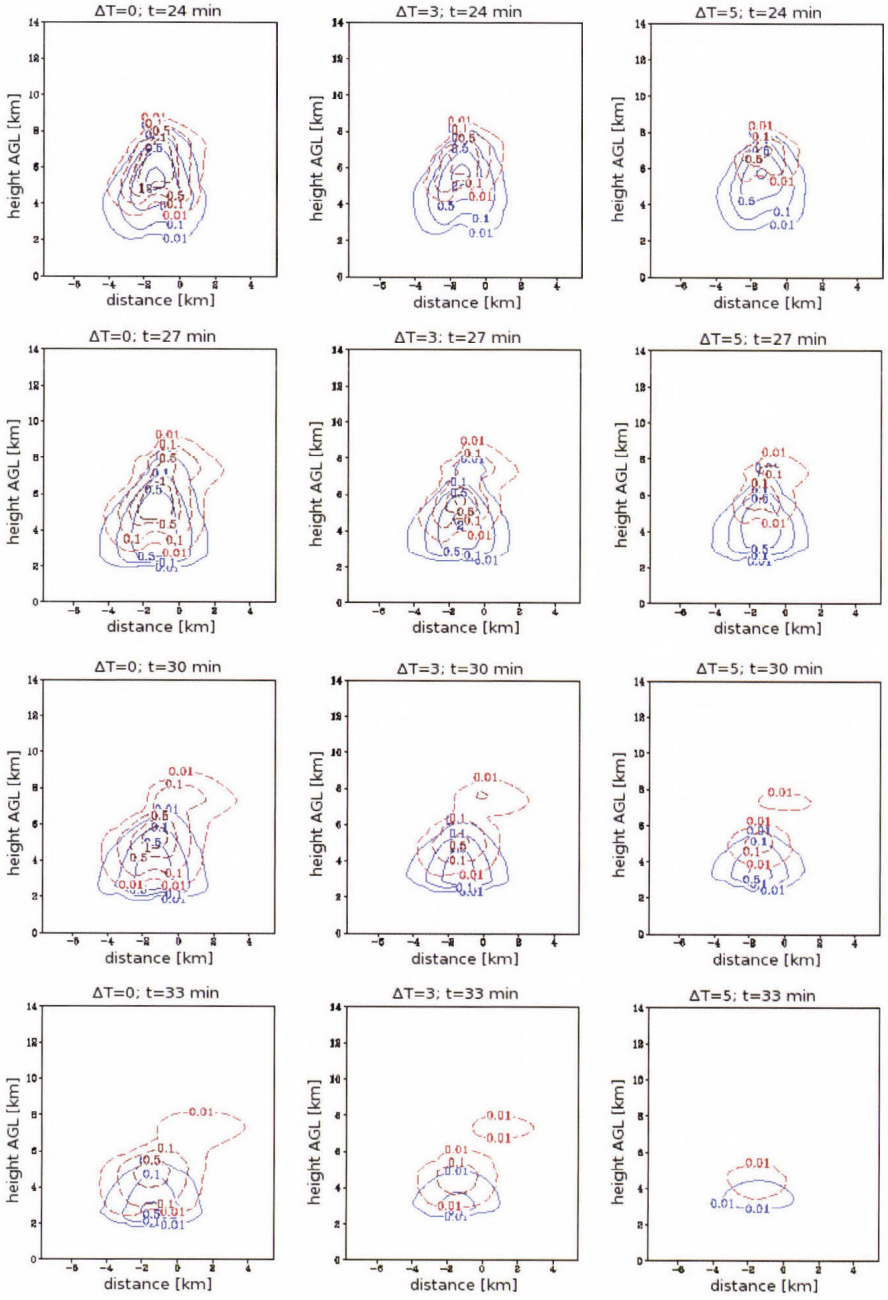

Fig. 18. Cloud B: hail (solid) and graupel (dashed) mixing ratios at 24 min MT, 27 min MT, 30 min MT, and 33 min MT (from top to bottom panel) for ΔT=0, 3, 5 (left, middle, and right panel, respectively).

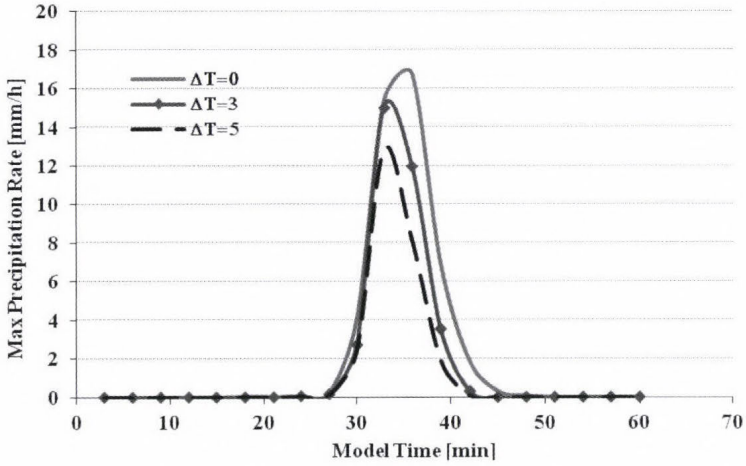

Fig. 19. Cloud B: peak rainfall rate as a function of time for ΔT=0, 3, 5.

5. Conclusions

In the present study, the impact of projected changes of the temperature and humidity profiles in the mid-latitude troposphere (IPCC, 2007) on the development and precipitation from summertime convective clouds is investigated. One typical sounding from Sofia is selected, and two scenarios of projected changes, according to IPCC, 2007, are imposed on this sounding. Two clouds with different dynamics are simulated, identified here as a 'big' one and a 'small' one.

The results can be summarized in the following way for the clouds developed in a warming environment – in comparison with the "control" clouds. For both clouds ('big' and 'small'):

- Sum of space and time integrated mixing ratios of graupel and hail decreases.
- Precipitation intensity has a more rapid increase in the beginning and its maximum occurs earlier.

Big cloud (A):

- Liquid water mixing ratio increases.
- Small ice particles (pristine, snow, and aggregates) mixing ratios increase.
- The updrafts are more intensive.

- Accumulated precipitation and total rainfall volume are higher.

Small cloud (B):

- Liquid water mixing ratio decreases.
- Small ice particles (pristine, snow, and aggregates) mixing ratios decrease.
- The updrafts are more intensive in lower levels and suppressed at higher levels of the cloud.
- Accumulated precipitation and total rainfall volume are significantly lower.

Results show that there are two sides of the expected pattern of change in the thermodynamic structure of the troposphere – it leads to the suppression of cloud dynamics and reduction of precipitation in the "small" cloud and to the intensification of the updraft and increase of precipitation in the "big" cloud. Our study analyzes the reasons for the contrary impact of climate warming depending on cloud intensity. For both types of cloud ("big" and "small"), the projected warming leads to higher values of liquid mixing ratio in low cloud layers and a delay in freezing, which takes place higher in the cloud. The study demonstrates that when the forcing conditions are strong enough ("big" cloud) for the cloud to reach levels with low temperatures, especially where homogeneous freezing occurs, more latent heat is released due to the freezing of a larger quantity of liquid water in warmer cases. This leads to higher content of ice particles and cloud intensification – increase of cloud updraft and cloud top. The quantity of ice precipitation particles increases and adds to the amount of liquid precipitation after melting. In these cases, the projected warming amplifies precipitation rate, accumulated precipitation, and total rainfall volume. In the cases with weaker forcing conditions ("small" cloud), when the cloud does not have enough energy to rise to higher levels (especially the level of homogeneous freezing), in a warming environment, less liquid water freezes, leading to the occurrence of a smaller quantity of ice precipitation particles inside the cloud, which in turns leads to the decrease of contribution of ice particles to the liquid precipitation. Thus, the decrease of precipitation rate, accumulated precipitation, and total rainfall volume in the "small" clouds at the increase of environmental temperature can be explained by the decrease of mixing ratios of liquid and solid precipitating particles at ΔT =3 and ΔT =5 in comparison with ΔT =0.

Results indicate the importance of the ice phase evolution in the formation of precipitation in continental mid-latitude convective clouds. Within the limitations of the model used in this study, one can conclude that in a warming environment intensive storms will have enhanced power, so they will create greater damage. On the other hand, warming can also lead to droughts by

suppressing the development of smaller cumuli. Since the present work is based on only one case study, we have to stress that different conclusions might emanate from further modeling runs encompassing wide ranges of meteorological conditions and combinations of other climate change factors. The thermodynamic forcing, investigated in the present paper, acts in the same direction as the forcing created from increasing aerosol concentrations, as explained by the conceptual model of *Rosenfeld et al.* (2008), so it is a challenging question how convective clouds and precipitation will change when those two factors work together.

It is also worth mentioning that the scenario tested in the present study is based on the concept of constant relative humidity. If the moisture above the continents is not enough and the relative humidity decreases, probably the effect of the thermodynamic changes in the environment air on convective clouds microphysics, dynamics, and precipitation would be reduced.

Furthermore, since the evaporation from the surface and the interactions between adjacent clouds are also important, real cases with larger domains and more than one cloud or even whole mesoscale systems should be simulated, in order to investigate the potential impact of climate warming on mid-latitude convective precipitation.

Acknowledgements —The present work is partially supported by EC through FP6 project ACCENT (GOCE-CT-2002-500337), the NATO SfP – ESP.EAP.SFPP 981393, and the Science Foundation of Sofia University (grant 153/2009).

References

Allen, M.R. and *Ingram, W.J.*, 2002: Constraints on future changes in climate and the hydrologic cycle. *Nature 419*, 224–232.

Cotton, W., Pielke Sr, R., Walko, R., Liston, G,. Trembecack, C., Jiang, H., McAnelly, R., Harrington, J., Nicholls, M., Carrio, G., McFadden, J., 2003: 'RAMS 2001: Current status and future directions', *Meteorol. Atmos. Phys. 82*, 5–29.

Demott, P.J., Meyers, M.P., and *Cotton, W.R.*, 1994: Parameterization and impact of ice initiation processes relevant to numerical model simulation of cirrus clouds. *J. Atmos. Sci. 51*, 77–90.

Elliot, W.P. and *Angell, J.K.*, 1997: Variations of cloudness, precipitable water, and relative humidity over the United States;1973-1993, *Geophys. Res. Lett.*, *24*, 41–44.

IPCC, 2007: Climate Change 2007: Report of the Intergovernmental Panel on Climate Change, *Cambridge University Press*, 921.

Kharin, V.V. and *Zwiers, F.W.*, 2005: Estimating extremes in transient climate change simulations. *J. Clim. 18*, 1156–1173.

McCaul Jr., E.W., Cohen, C., Kirkpatric, C., 2005: The sensitivity of simulated storm structure, intensity and precipitation efficiency to environmental temperature, *Mon. Weather Re.133*, 3015–3037.

Meyers, M., Walko, R., Harrington, J.,and *Cotton, W.*,1997: New RAMS cloud microphysics parametrization. Part II: The two-moment scheme. *Atmos. Res. 45*, 3–39.

Meehl, G.A., Washington, W. M, Santer, B.D., Collins, W.D., Arblaster, J.M., Hu, A., Lawrence, D.M., Teng, H., Buja, L.E., and Strand, W.G., 2006: Climate Change Projections for the Twenty-First Century and Climate Change Commitment in the CCSM3. *J. Climate 19*, 2597–2616.

Mitzeva, R., Tsenova, B., Todorova, A., and *Latham, J.*,2008: Comparative modeling study of the impact of aerosols and climate changes on microphysics and dynamics of mixed-phase convective clouds. *15th International Conference of Clouds and Precipitation, Cancun-Mexico*, July 7–13, 2008.

Philips, V.T.J., Donner, L.J., and *Garner S.T.*, 2007: Nucleation processes in deep convection simulated by a cloud-system resolving model with double moment bulk microphysics. *J. Atmos. Sci. 64*, 738–761.

Pielke, R.A., Cotton, W., Walko, R., Tremback, C.J., Lyons, W.A., Grasso, L.D., Nicholls, M.E., 1992: A Comprehensive Meteorological Modeling System RAMS. *Meteorol. Atmos. Phys. 49*, 69–91.

Rosenfeld, D., Lohman, U., Raga, O'Dowd, G., Kulmala, M., Fussi, S., Reissell, A., and *Andreae, M*, 2008: Flood or drought: How do aerosols affect precipitation, *Science*, *321*, 1309–1313.

Santer, B.D, Sausen, R., Wigley, T M.L., Boyle, J S., Rao, A., Doutriaux, K., Hansen, C., Meehl, J.E., Roeckner, G.A., Ruedy, E., Schmidt, R., G., and *Taylor, K.E.*, 2003: Behaviour of tropopause height and atmospheric temperature in models, reanalyses and observations. Decadal changes, *J. Geophys. Res. 108*, D1, 4001.

Semenov, V.A. and *Bengtsson, L.*, 2002: Secular trends in daily precipitation characteristics: greenhouse gas simulation with a coupled AOGCM. *Clim. Dyn. 19*, 123–140.

Takemi T., 2010: Dependence of the precipitation intensity in mesoscale convective systems to temperature lapse rate. *Atmos. Res. 96*, 273–285.

Trenberth K, Dai, A., Rasmussen, R., and *Parsons, D.*, 2003: The changing character of precipitation. *B.Am.Meteorol.Soc. 84*, 1205–1217.

Van den Heever, S.C., Carrio, G.G., Cotton, W.R., Demott, P.J., and *Prenni, A.J.*, 2006: Impacts of nucleating aerosols on Florida Storms. Part I: Mesoscale simulations. *J. Atmos. Sci.* 63, 1752–1775.

IDŐJÁRÁS

Quarterly Journal of the Hungarian Meteorological Service
Vol. 116, No. 4, October–December 2012, pp. 281–295

Spatial and temporal evolution of drought conditions at various time scales in the Czech Republic during growing period

Vera Potop[1]*, **Constanţa Boroneanţ**[2], **Martin Možný**[3], **Petr Štěpánek**[4], and **Petr Skalák**[4]

[1]*Czech University of Life Sciences Prague, Faculty of Agrobiology, Food and Natural Resources, Department of Agroecology and Biometeorology, Kamycka 129, 165 21 Prague 6 – Suchdol, Czech Republic*

[2]*Center for Climate Change, Geography Department, University Rovira I Virgili, Campus Terres de l'Ebre, Av. Remolins 13-15, 43500 Tortosa, Spain*

[3]*Czech Hydrometeorological Institute, Na Šabatce 2050/17 143 06 Prague 412-Komořany, Czech Republic*

[4]*Global Change Research Centre AS CR, Bědila 986/4a, 603 00 Brno, Czech Republic*

**Corresponding author E-mail: potop@af.czu.cz*

(Manuscript received in final form April 24, 2012)

Abstract—This paper analyzes the characteristics of spatial evolution of the standardized precipitation evapotranspiration index (SPEI) at various time scales during the growing period (April-September) over the Czech Republic. The SPEI was calculated from monthly records of mean temperature and precipitation totals measured at a dense network of 184 climatological stations for the period 1961–2010. Using various lags, 1, 3, 6, 12, and 24 months. The drought at these time scales is relevant for agricultural, hydrological, and socio-economic impacts, respectively. The study refers to the warm season of the year (from April to September). The principal modes of variability of the SPEI calculated at these five time scales were identified by using the empirical orthogonal functions (EOF) analysis. The explained variance of the leading EOF ranges between 71 and 61% as the time scale for calculating the SPEI increases from 1 to 24 months. The explained variance of EOF2 and EOF3 ranges between 5 and 9%, and 4 and 6%, respectively, as the SPEI is calculated for 1–24 months. With a few exceptions at stations at the highest altitudes, the spatial coefficients of the EOF1 for all SPEI time scales have the same sign over the country´s territory. Based on the spatial distribution of

the spatial coefficients of EOF2 and EOF3, at all SPEI time scales we have identified three climatically homogenous regions, corresponding to the altitudes below 400 m, between 401 and 700 m, and above 700 m. This regionalization corresponds to some extend to that which was previously used in other studies. These three regions reflect different land use types corresponding to: (i) mostly intensive agriculture, (ii) less intensive agriculture, and (iii) limited agricultural production and mostly forested, respectively. For these three regions, the frequency distribution of the SPEI values in 7 classes of drought category (%) were calculated based on station records for each region. The normal conditions represent around 65% out of the total values of SPEI for all time scales, in all three regions, while moderate drought and moderate wet conditions are almost equally distributed around 10.5%. As the SPEI time scale increases, the difference between the percentages of extremely dry and extremely wet conditions changes on average from 0.2% (SPEI 1-month) to 4% (SPEI 24-month).

Key-words: standardized precipitation evapotranspiration index, frequency distribution, empirical orthogonal function, Czech Republic.

1. Introduction

Drought indices associated with specific time-scales are useful tools for monitoring and management of drought. For quantifying the drought conditions, *Vicente-Serrano et al.* (2010) have developed a new drought index – the standardized precipitation evapotranspiration index (SPEI) based on precipitation and potential evapotranspiration (PET). The SPEI combines the sensitivity of the Palmer drought severity index (PDSI) to changes in evaporative demand (related to temperature fluctuations and trends) with the multi-temporal nature of the Standardized Precipitation Index (SPI). The various time scales provided by the SPEI can be related to different drought types in a region. Short time scales show a high relationship with variations of soil moisture, which determine water availability for vegetation and agriculture, while water resources in reservoirs are related to longer time scales (*Dai*, 2011; *Vicente-Serrano et al.,* 2011).

In previous studies (*Potop et al.*, 2011, 2012), drought was extensively analyzed by comparing results from the most advanced drought indices (e.g., SPI and SPEI), which take into account the role of antecedent conditions in quantifying drought severity in the lowland regions of the Czech Republic. Decadal trend in the drought extent detected by the SPEI are apparent, however, with higher values of drought incidences in the 1940s, early 1950s, and 1990s, and with fewer drought episodes in the 1910s, 1930s, and 1980s. These episodes coincide with the secular drought evolution recorded in the central part of Europe (*Brázdil et al.*, 2009; *Dai*, 2011). Consequently, SPEI and SPI showed large differences in the evolution drought severity during decades with the lowest summer negative temperature anomalies combined with the lowest precipitation (cold and dry; the first two decades of the 20th century), the highest summer positive temperature anomalies (the end of the 20th century), both high spring positive temperature and precipitation anomalies (warm and

wet; the beginning of the 20th century), and the lowest deficit of water balance (1947, 2003, 1994, 1983, and 1933) (*Potop et al.*, 2012). On the other hand, similarities between two indices were reported during the decades with high fluctuations of positive spring temperature and lower precipitation (warm and dry; 1950s, 1990s, and 2000s); extremely long sunshine durations (155% of the normal amount in extremely dry June of 2006 and August 2003, up to twice the norm for April of 2007 and 2009, in the reference period of 1961–1990); and consecutive dry days. Therefore, the role of temperature was evident in summer drought episodes which depend on the intensity and duration of temperature anomalies, generating a higher water demand by potential evapotranspiration at the end of the last century.

New detailed results on the temporal evolution of the SPEI at various time-scales and the impact of drought on vegetable crops were discussed and presented in broader climatological and European contexts in, e.g., *Potop* and *Možný* (2011a, 2011b), *Potop* and *Soukup* (2011). However, more in-depth analysis is required to explore the vulnerability to drought in the context of climate change based on a denser station network to better representation of various climate conditions across the Czech Republic (*Potop et al.* 2012a; *Potop et al.* 2012b).

The present study aims at the analysis of the spatial evolution of the SPEI at various time scales during the warm period (April-September) over the Czech Republic. To this aim, the principal modes of variability of SPEI are examined based on data from a dense network of climatological stations in the Czech Republic during the period of 1961–2010 in order to reveal the regional characteristics of drought variability. Frequency distribution of SPEI values over the three regions in 7 classes of drought category (%) at time scales of 1, 3, 6, 12, and 24 months, and the spectral analysis of the series of the SPEI ≤ -1 were also analyzed.

2. Data and methods

The SPEI was calculated from monthly records of mean temperature and precipitation totals using a dense network of 184 climatological stations from the Czech Republic for the period of 1961–2010. The selected stations as input dataset in calculation of the SPEI are uniformly covering the Czech Republic. Station elevations range between 158 and 1490 m above sea level (*Fig. 1*). The selected stations represent various climate conditions both in lowland and highland regions and reflect the differences between the maritime and continental weather regimes which manifest across the Czech Republic. Monthly series of temperature and precipitation were taken from the Czech Hydrometeorological Institute (CHMI) CLIDATA database. Measured data were subjected to quality control, gap filling, and homogenization by means of

ProClimDB and AnClim software (*Štěpánek,* 2010*)*. The approach of quality control of daily and monthly temperature and precipitation series combines several methodologies such as differences of neighbor stations comparison, comparison with "expected" values calculated by means of geostatistical methods, etc. Interpolation, where needed, was carried out applying an approach adopted at CHMI. It is based on local linear regression (dependence of given meteorological element on altitude) and universal kriging interpolation, and inverse distance weighting methods (*Šercl* and *Lett,* 2002). The homogeneity of monthly precipitation and temperature series was tested using the Alexandersson's SNHT, bivariate test, and Vincent methods (*Štěpánek et al.,* 2009; *Štěpánek,* 2010*)*.

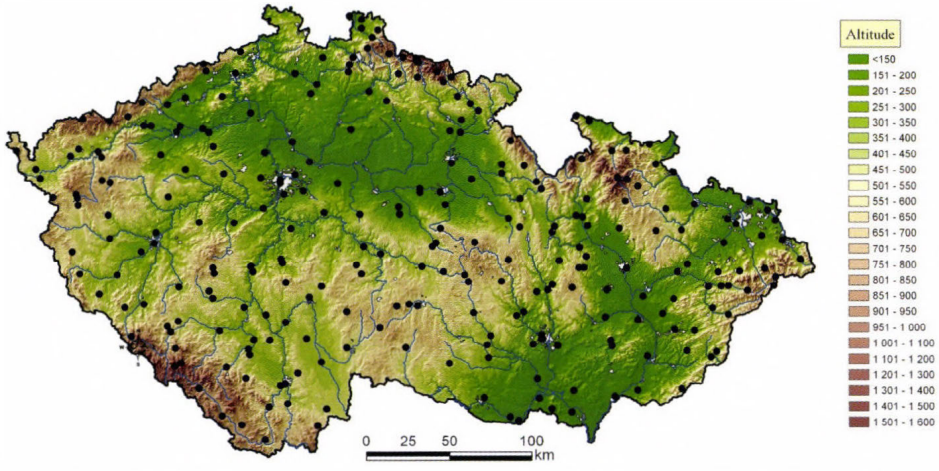

Fig. 1. Location of stations used for the calculation of the SPEI drought index in the Czech Republic.

For the SPEI calculations, the algorithm developed by *Vicente-Serrano et al.* (2010) was used. The SPEI is based on a monthly climatic water balance (precipitation (*P*) minus potential evapotranspiration (*PET*)). *PET* is calculated using the method of *Thornthwaite* (1948). The documentation and executable files for SPEI calculation are freely available at http://digital.csic.es/handle/10261/10002. A batch script was created and used for optimizing the calculation of the SPEI for the 184 stations and five accumulated periods: 1, 3, 6, 12, and 24 months. The SPEI was calculated for each month of the year, but this study refers only to the warm season of the year (from April to September). The drought at these time scales is relevant for agricultural (1-, 3-, and 6-month), hydrological (12-month), and socio-economic

impacts (24-month), respectively. A drought episode was defined as a continuous period of months when the SPEI values were less than –1, while values between –0.99 and 0.99 were considered as normal conditions. Drought categories according to the SPEI are presented in *Table 1*.

Table 1. Drought categories according to the SPEI

SPEI	Drought category	Probability
≥ 2.00	Extreme wet	0.02
1.50 – 1.99	Severe wet	0.06
1.49 – 1.00	Moderate wet	0.10
0.99 – (–0.99)	Normal	0.65
(–1.00) – (–1.49)	Moderate drought	0.10
(–1.50) – (–1.99)	Severe drought	0.05
≤ (–2.00)	Extreme drought	0.02

Taking into consideration the climatic characteristics in the Czech Republic such as the degree of continentality and the diversity of physico-geographic conditions (topography, soil type), the evaluation of drought was carried out in more details for the selected climatic regions. To identify the principal modes of variability of the SPEI at the various time scales, the empirical orthogonal functions (EOF) have been calculated over the territory of the Czech Republic. This approach has been widely used to explore regional patterns of the drought over Europe and various regions of the world (*Dai*, 2011). Based on the patterns of the spatial coefficients of the EOF2 and EOF3 of the SPEI at the considered time scales, we have identified three regions, corresponding to the altitudes below 400 m, between 401 and 700 m, and above 700 m. They correspond, to some extend, to a previous regionalization used in other studies (*Quitt,* 1971*; Tolasz et al.* 2007; *Trnka et al.* 2009*)*. These regions correspond to different land use types with mostly intensive agriculture, less intensive agriculture, and mostly forested with limited agricultural production, respectively. Moreover, these regions also correspond to the climatic classification according to *Quitt* (1971), where three main climatic regions (warm, moderate warm, and cold) were defined on the basis of 14 climatic characteristics [annual number of warm, frost, and ice days, number of overcast and clear days, number of days with snow cover, number of days with precipitation of 1 mm or more, mean air temperature in January, April, July, and October, sum of precipitation in warm (April-September) and cold (October-March) periods of year, as well as the number of days with mean temperature 10 °C and more]. For each station, the SPEI values were analyzed in order to assess the frequency distribution and the drought severity during the warm period of the year in the given regions.

The following analysis was carried out to assess the regional drought characteristics over the Czech Republic:

(1) numerical values of the SPEI at five accumulated periods (1, 3, 6, 12 and 24 months) calculated for each station, which then allowed to evaluate the drought conditions both for entire territory of the Czech Republic and the selected climatic regions;
(2) averaged number of drought episodes (SPEI ≤ -1) during the growing season at various time scales for three SPEI series: (1) at each station, (2) at each climatic region, and (3) at the entire country territory;
(3) averaged number of drought episodes (SPEI ≤ -1) counted during the growing season at various SPEI time scales both for country level and each of the three climatic regions; and
(4) frequency distribution of monthly SPEI values in 7 classes of drought category (%) at five accumulated periods for the above mentioned SPEI series.

3. Results and discussion

3.1. The principal modes of variability of the SPEI

For each station, the monthly series of the SPEI were averaged over six months of the warm season (from April to September). These SPEI series at five accumulated periods (1, 3, 6, 12, and 24 months) were used for the empirical orthogonal functions (EOF) analysis in order to identify the characteristics of drought variability over the territory of the Czech Republic. The patterns of the three leading EOFs of the SPEI are very similar for all of the five accumulated periods. *Figs. 2 a,b,* and *c* show, as example, the spatial patterns of the three leading modes of variability of the SPEI calculated at 6-month lag and averaged over the warm season (from April to September). The spatial coefficients of the EOF1, with few exceptions, have the same sign over the country (*Fig. 2a*). The time series of the principal component (PC1) coefficients shows the temporal evolution of the EOF1 pattern, identifying the dry and wet years, and the intensity of its anomalies in terms of the standard deviation of the PC1 time series (*Fig. 3*). The periods with consecutive dry warm season were 1967–1969, 1981–1983, 1988–1994, and 1998–2000. The year 2003 was the driest during the period of 1961–2010 according to the PC1 of the SPEI at the 6-month accumulation period. The explained variance of the EOF1 ranges between 71 and 61% as the time scale of the accumulated period for calculation of the SPEI increases from 1 month to 24 months (*Table 2*). The pattern of the spatial coefficients of the EOF2 roughly separates the lowland and highland regions (*Fig. 2b*). The explained variance of the EOF2 and EOF3 ranges from 5 to 9% and 4 to 6%, respectively, as the SPEI is calculated for 1–24 months. The spatial

distribution of the EOF2 for all time scales of the SPEI corresponds, to some extend, to the regionalization previously used in other studies (*Tolasz et al.* 2007; *Trnka et al,* 2009) which identified three climatically homogeneous regions, corresponding to the altitudes below 400 m, between 401 and 700 m, and above 700 m (*Fig. 1* and *Fig. 2*). This station classification according to the altitude was further used in this study to assess the spatial and temporal drought characteristics over the Czech Republic.

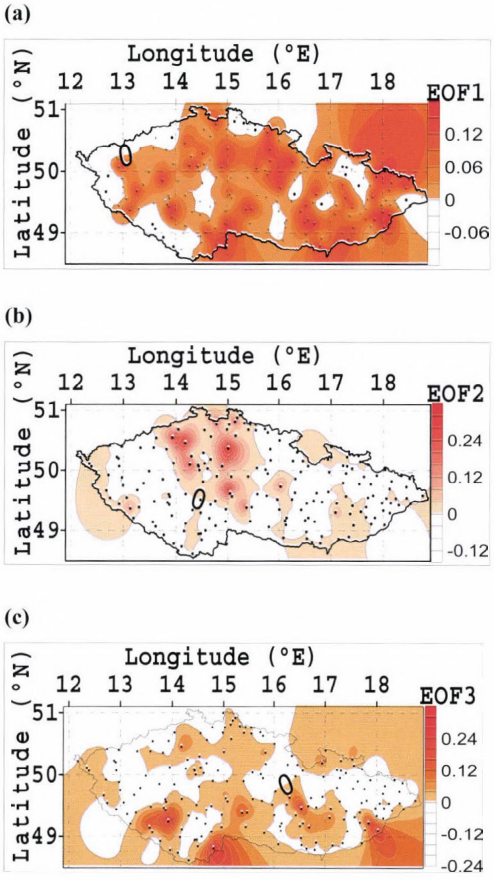

Fig. 2a, b, c,. Spatial patterns of the three leading modes of variability from an EOF of average SPEI values during the warm season (Apr-Sept) over the Czech Republic (1961–2010) at time scale of 6-month.

Table 2. Explained variance of the leading EOFs of averaged SPEI (April-September) over the Czech Republic, 1961–2010

	Explained variance (%)				
	SPEI-1	**SPEI-3**	**SPEI-6**	**SPEI-12**	**SPEI-24**
EOF1	71.68	70.03	69.14	64.46	61.49
EOF2	5.68	6.31	7.33	8.44	9.35
EOF3	4.36	4.12	4.65	5.32	6.05

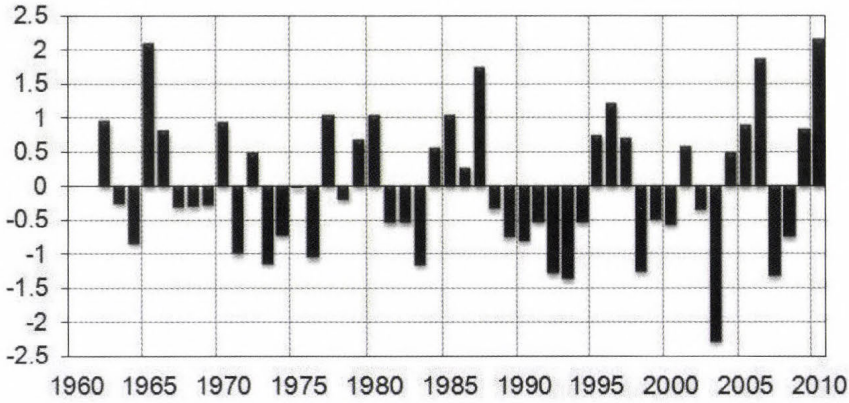

Fig. 3. Standard deviation of principal components (PC1) of SPEI series at 6 months during the warm season (Apr-Sept) over the Czech Republic (1961–2010).

3.2. Frequency distribution of the SPEI values

In this subsection, drought occurrences are analyzed on the basis of frequency distribution of the SPEI values in 7 classes (see *Table 1*). The frequency distribution was calculated as the ratio between the number of occurrences in each SPEI category and the total number of events counted for all stations in a given region for a given time scale (1, 3, 6, 12, and 24 months). The aim here is to identify the areas with high drought frequency detected by the SPEI during the growing season (i.e., April-September). The occurrences in varying drought categories at multiple scales are also analyzed on a regional basis inside the three main climatic regions: warm, moderate warm, and cold (*Quitt,* 1971). For these three regions, the frequency distribution of the SPEI values were calculated based on station records inside each region.

In the *Table 3*, percentage of drought occurrences is expressed in 7 classes of drought categories (%) at time scales of 1, 3, 6, 12, and 24 months for the period of 1961–2010. Normal conditions represent around 65% out of the total

values of SPEI for all times scales, in all three regions, while moderate drought and moderate wet conditions are almost equally distributed at around 10.5%. As the SPEI time scale increases, the difference between the percentages of extremely dry and extremely wet conditions changes on average from 0.2% (SPEI 1-month) to 4% (SPEI 24-month). As it is shown in *Table 3*, the frequency of extreme moisture conditions occurrence (the SPEI values outside ±2) shows a slight tendency toward dry conditions, especially at long time-scales (12 and 24 months).

Table 3. Frequency distribution of monthly SPEI values in 7 classes of drought category (%) at time scales of 1, 3, 6, 12, and 24 months averaged per regions

Region	Extreme drought	Severe drought	Moderate drought	Normal	Moderate wet	Severe wet	Extreme wet
				SPEI-1			
I	2.10	5.37	10.13	64.66	10.22	5.59	1.93
II	2.24	4.71	10.53	64.52	10.56	5.61	1.83
III	1.92	5.06	10.20	65.39	10.24	5.26	1.92
				SPEI-3			
I	2.17	5.57	9.92	65.15	9.70	5.48	2.01
II	1.94	5.53	10.20	65.19	10.13	4.96	2.05
III	1.62	5.64	10.47	64.91	10.62	4.94	1.80
				SPEI-6			
I	2.85	4.83	9.87	64.90	9.96	6.01	1.58
II	2.64	4.86	10.42	64.71	10.24	5.59	1.53
III	2.56	4.39	10.38	65.47	10.08	5.65	1.47
				SPEI-12			
I	3.71	5.67	10.33	62.58	10.70	5.54	1.46
II	3.54	5.36	10.30	63.02	10.91	5.49	1.38
III	3.09	5.55	10.35	63.36	11.09	5.61	0.95
				SPEI-24			
I	5.27	5.89	11.09	60.26	10.42	5.91	1.16
II	5.18	5.4	11.02	60.53	11.33	5.44	1.10
III	4.98	4.95	10.98	61.92	11.36	5.02	0.77

I : altitudes below 400 m,
II : altitudes between 401, and 700 m
III: altitudes above 700 m.

The results of the SPEI values for each station and the corresponding drought categories were mapped using a Surfer program. The Surfer program allows us to generate calculated data points (184 of station observations) on a regular spaced grid. We used the grid to generate the contour map (gridding by

Kriging interpolation technique) of the spatial frequency distribution of moderate, severe, and extreme drought at 1, 3, 6, 12, and 24 months time scales (*Fig. 4*). The spatial interpolation of SPEI values ranges from the longitude of 12.2°E to18.8°E and the latitude of 48.6°N to 51.0°N. The lowest and highest grid points in the dataset have the elevation of 158 and 1490 m, respectively, with 1332 m elevation range (*Table 4*).

Table 4. Frequency distribution of moderate, severe, and extreme drought (%) occurrences during the warm period of the year at different time scales. It is spatially averaged over all stations (λ=12.2°E - 18.8°E; φ=48.6°N - 51.0°N, h=158 1490 m a.s.l.)

	Coordinates			SPEI-1	SPEI-3	SPEI-6	SPEI-12	SPEI-24
	λ° *E*	φ° *N*	h, m					
Moderate drought								
Mean	15.5	49.7	450	10.3	10.1	10.2	10.3	11.1
Minimum	12.2	48.6	158	6.7	6.3	5.7	5.0	4.0
Maximum	18.8	51.0	1490	15.7	14.7	15.0	15.3	17.0
Range	6.6	2.4	1332	9.0	8.3	9.3	10.3	13.0
Severe drought								
Mean	15.5	49.7	450	5.1	5.6	4.8	5.5	5.6
Minimum	12.2	48.6	158	2.7	2.3	1.7	2.3	2.3
Maximum	18.8	51.0	1490	8.7	10.3	8.7	8.7	8.7
Range	6.6	2.4	1332	6.0	8.0	7.0	6.3	6.3
Extreme drought								
Mean	15.5	49.7	450	2.1	2.0	2.7	3.6	5.2
Minimum	12.2	48.6	158	0.7	0.3	1.0	2.0	4.0
Maximum	18.8	51.0	1490	3.7	3.7	5.0	5.7	8.0
Range	6.6	2.4	1332	3.0	3.3	4.0	3.7	4.0

These maps show that the shortest time scales (1 and 3 months) produce clear spatial patterns for the drought frequency. In other words, great percentage of frequency distribution of moderate, severe, and extreme drought occurrences at 1, 3, and 6 months (associated with meteorological and agricultural drought) were identified in regions with relatively low precipitation and high potential evapotranspiration (region I with mostly intensive agriculture, corresponding to the altitudes below 400 m).

The spatial analysis of the SPEI values with **moderate drought** occurrences during the growing period indicates that they tend to occur in the rain shadow of the Ore Mountains, in the south-eastern, south-western, and central parts of Elbe lowland at 1–3 months time-scales. Regions with elevations above 600 m are characterized by the lowest frequencies (lower than 9%) at the

same time scales (left panel of *Fig. 4*). The spatial distribution of frequencies of moderate drought ranges between 6.3% and 15.7% (*Table 4*). The maximum frequencies of moderate drought (15.7% occurrences) are shown in region I (stations situated in lowland region below 400 m a.s.l.). As the time-scale increases from 6 to 12 months, no major changes are observed for maximum frequencies (reached 15.3% at SPEI-12), rather a shift in the low drought occurrences toward the Bohemian Upland region is detected. At 24-month time scale, the moderate droughts occur more frequently and cover more than 60% of the country territory. Their spatial occurence varies between 4% and 17%.

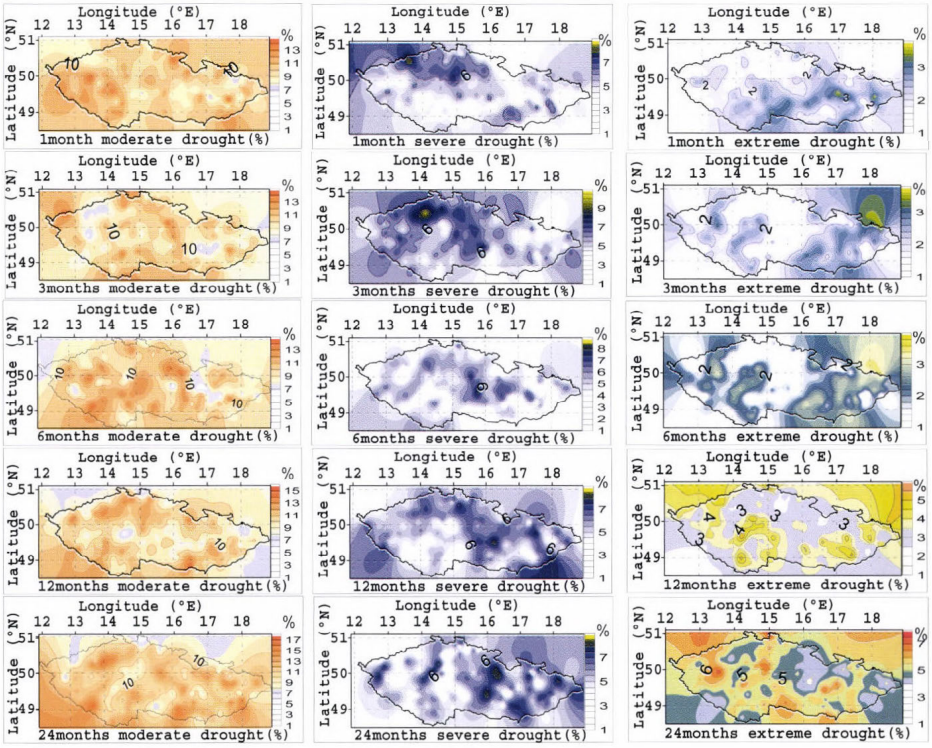

Fig. 4. Frequency distribution of SPEI values in moderate (left panel), severe (central panel), and extreme (right panel) drought categories (%) at time scales of 1, 3, 6, 12, and 24 months averaged for 50 years (1961–2010).

The occurrence of the **severe droughts** at shorter time-scales (1–3 months) was identified within the regions with the highest drought risk in the Czech Republic. According to the SPEI values, we found that high frequency of severe drought occurrences was detected in the following regions: lowlands of the Elbe river valley, central Bohemia, southern Moravia, and lowlands of southeastern

and southern Bohemia (central panel of *Fig. 4*). The same results obtained by different drought indices are highlighted in other studies (*Tolasz et al.* 2007; *Potop et al.* 2008; *Trnka et al.* 2009; *Potop et al.* 2010; *Možný et al.* 2012; *Potop et al.* 2011). These maps show the spatial distribution of severe drought which shifts from short-term (1 month, meteorological drought) and medium-term (3 and 6 months, agricultural drought) to long-term droughts (12 and 24 months, hydrological drought). Severe meteorological drought (SPEI at 1 month) identified first in the north-western Bohemia and southern Moravia have then extended at longer time scales in Elbe lowland and south-eastern areas. Not significant differences are shown in the spatial distribution of severe drought occurrences as the time scale for calculation of SPEI was increased (*Table 4*). The maximum frequency of severe drought occurrences ranges between 8.7% and 10%, while on average at country level it is 5.5%.

As for the **extreme droughts,** regional differences in its occurrence are observed when increasing the SPEI time-scales (right panel of *Fig. 4*). The areas affected by extreme drought evolve gradually, and the regions turn to be affected by higher frequency of extreme drought from shorter time-scales (meteorological drought) to longer time-scales (hydrological drought). The resulted maps show more spatial variability in frequency of drought at 12 and 24 months than for shorter time scales. In general, the SPEI at the 24 months time-scale indicates the more complex patterns of extreme drought frequency (right panel of *Fig. 4*). The highest percentage of extreme drought occurrences is 3.7% at short-term scale (SPE-1), whereas at medium-term (SPEI-3 and SPEI-6 months) and long-term (SPEI-12, SPEI-24) the drought ranges from 5.7 to 8.0%. The frequency of extreme drought is the lowest or missing at stations with altitude more than 1000 m (0.3%).

3.3. Spectral analysis

The periodograms via fast fourier transform spectral techniques were also applied to search for significant periodicities in the time series of the SPEI≤–1 (moderate to extreme drought) averaged for the six months of the growing season (April-September). *Table 5* presents the results of the spectral analysis: the peak frequency and the length of cycles exceeding the 95% confidence level at various time-scales. The frequency is calculated as the number of cycles per time unit (where each observation is treated as one unit of time). The results of the peak frequency and the length of cycle in spectral analysis calculated for the three regions have been analyzed. Thus, at 1 month SPEI, the peak frequency of 0.41 (the number of units of time necessary to complete one full cycle) corresponds to a 2.5-year drought occurrence in the region I, while in the region II and region III the frequency of 0.34 corresponds to the occurrence of drought in every 3 years. This means that frequent meteorological drought events from moderate to severe in the SPEI-1 series are observed in every 2.5 years in the

region I that is considered the warmest and driest area in the country, while in the regions II and III the frequency of meteorological drought slightly decreased (*Table 5*). A clear peak frequency and cycle length of 3-month and 6-month (corresponding to agricultural drought) was 0.20 standing for the drought occurence in every 5 years in all regions. The same result was reported in previous studies (*Potop et al.*, 2008; *Potop et al.*, 2010) which combine the three drought indices as a tool for the identification of the drought frequency in the Czech Republic. At the time-scale of 12-month (hydrological drought), the frequency peak was 0.11 corresponding to a drought occurrence period of 9.4 years. As the results in *Table 5* show, at time scale of 24-month (the largest socio-economic impact) there is a well-defined regional drought frequency pattern. In the region with the altitudes below 400 m, the frequency peak of drought was 0.13 corresponding to a period of drought occurrence of 7.6 years, while in the regions with altitudes between 401 and 700 m and above 700 m the frequency peaks were at 0.11 and 0.06, standing for the occurrence of drought in every 9.4 and 15.3 years, respectively (*Table 5*).

Table 5. Spectral analysis of SPEI≤-1 series (at 95% confidence level) at time-scales 1, 3, 6, 12, and 24 months (1961–2010) per regions

	SPEI-1	SPEI-3	SPEI-6	SPEI-12	SPEI-24
I: the altitudes below 400 m					
Peak of frequency, %	0.41	0.20	0.20	0.11	0.13
Length of cycle, years	2.50	5.00	5.00	9.40	7.60
II: the altitudes between 401 and 700 m					
Peak of frequency, %	0.34	0.20	0.20	0.11	0.11
Length of cycle, years	3.0	5.0	5.0	9.4	9.40
III: the altitudes above 700 m					
Peak of frequency, %	0.34	0.20	0.22	0.11	0.06
Length of cycle, years	3.0	5.0	5.00	9.40	15.30

4. Conclusions

In this study, the characteristics of drought over the Czech Republic at various time-scales during the growing season (April-September) were analyzed. The drought was quantified with the standardized precipitation evapotranspiration index (SPEI) at 184 climatological stations during the period of 1961–2010. The main results can be summarized as follows:

(a) In order to identify the drought variability over the territory of Czech Republic the empirical orthogonal functions (EOF) approach was used.

According to spatial distribution of coefficients of the EOF2, three drought homogeneous regions were distinguished, corresponding to the altitudes below 400 m, between 401 and 700 m, andabove 700 m: the lowlands and the high altitude regions.

(b) Regarding the drought time scales, most parts of lowlands and partially of highland regions are vulnerable to moderate agricultural drought during growing season. For the entire period of study, the vulnerability of extreme agricultural drought is low. However, the evolution of agricultural drought in the second half of the 20th century and the first decade of the 21st century showed increasing frequency that has been reinforced by long dry periods in the 1990s and 2000s. The drought during these periods was associated with high temperature anomalies (i.e., more than 2.5 °C). Consequently, the SPEI has the ability to detect the reinforcement of drought severity due to the temperature increasing during the 1990s and 2000s.

(c) The occurrences of various drought time-scales and severity categories show distinct patterns. The maximum frequencies of **moderate and severe drought** were identified at stations situated in lowland regions below 400 m. High number of severe meteorological and agricultural drought events also occured in the southern Moravia, the north-western Bohemian areas, the south-eastern areas, and in the Elbe lowland. In other words, the majority of the historical droughts occurred in the regions corresponding to the altitudes below 400 m and between 401 and 700 m. The highest percentage of **extreme drought** occurrences was 3.7% at short-term scale, whereas the highest percentage of medium-term and long-term droughts ranges from 5.7 to 8.0%. The frequency of extreme drought is the lowest in the region with stations with altitude higher than 1000 m (0.3%).

(d) The short-term drought (meteorological drought) and mid-term drought (impacting agricultural production) occur at the whole territory of the country approximately in every three and five years, respectively. The long-term drought (impacting the water system) can occur in every nine years in all of the regions.

Acknowledgements: The research on drought conditions in the Czech Republic was supported by S grant of MSMT CR and projects OC10010, 6046070901, CzechGlobe – Centre for Global Climate Change Impacts Studies, Reg. No. CZ.1.05/1.1.00/02.0073. The authors would like to thank Sergio M. Vicente-Serrano (Instituto Pirenaico de Ecologia-CSIC, Zaragoza, Spain) for providing the detailed algorithm to calculate the SPEI.

References

Brázdil, R., Trnka, M., Dobrovolný, P., Chroma, K., Hlavinka, P. and *Žalud, Z.*, 2009: Variability of droughts in the Czech Republic, 1881-2006. *Theor. Appl. Climatol. 97*, 297–315.

Dai, A., 2011: Characteristics and trends in various forms of the Palmer Drought Severity Index during 1900–2008. *J. Geophys.Res.116*, D12115.

Možný, M., Trnka, M., Žalud, Z., Hlavinka, P., Nekovař, J., Potop, V. and *Virag, M.*, 2012: Use of a soil moisture network for drought monitoring in the Czech Republic. *Theor. Appl. Climatol.* 107, 99–111.

Potop, V., Türkott, L. and *Kožnarová, V.*, 2008: Spatiotemporal characteristics of drought in Czechia. *Sci. Agr. Bohemica 39*, 258–268.

Potop, V., Türkott, L., Kožnarová, V. and *Možný, M.*, 2010: Drought episodes in the Czech Republic and their potential effects in agriculture. *Theor. Appl. Climatol. 99*, 373–388.

Potop, V. and *Možný, M.*, 2011a: The application a new drought index - standardized precipitation evapotranspiration index in the Czech Republic. In: *Mikroklima a mezoklima krajinných struktur a antropogenních prostředí.*(eds*: Středová, H., Rožnovský, J., Litschmann, T), Skalní mlýn*, 2. – 4.2. 2011. (CD).

Potop, V. and *Možný, M.*, 2011b: Examination of the effect of evapotranspiration as an output parameter in SPEI drought index in Central Bohemian region. In: Bioclimate: Source and Limit of Social Development, International Scientific Conference, (eds: Šiška, B., Hauptvogl, M., Eliašová, M.) 6–9. September 2011, Topoľčianky, Slovakia. (CD).

Potop, V. and *Soukup J.*, 2011: Assessing risk of dry episodes during growing seasons of vegetable crops in Polabí, Czech Republic. In: *1st Climate Change, Economic Development, Environment and People Conference.* 14-16 September, 2011, Novi Sad, Serbia.

Potop, V., Soukup, J., and *Možný, M.*, 2011: Drought at various time-scales for secular lowland climatologically stations in the Czech Republic. *Meteorologické Zpravy 64*, 177–188.

Potop, V., Možný, M., and *Soukup, J.*, 2012: Drought at various time scales in the lowland regions and their impact on vegetable crops in the Czech Republic. *Agric. Forest Meteorol. 156*, 121–133.

Potop, V., Boroneanț, C., Možný, M., Štěpánek, P. and *Skalák, P.*, 2012a: Observed evolution of drought episodes assessed with the Standardized Precipitation Evapotranspiration Index (SPEI) over the Czech Republic. In: *EGU General Assembly 2012. Geophysical Research Abstracts Vol. 14, EGU2012-7681*, 2012, 22–27 April, Vienna.

Potop, V., Boroneanț, C., Štěpánek, P., Skalák, P. and *Možný, M.*, 2012b: Projected changes in the evolution of drought assessed with the SPEI over the Czech Republic. In: *EGU General Assembly 2012. Geophysical Research Abstracts Vol. 14, EGU2012-7681,* 2012, 22–27 April, Vienna.

Quitt, E., 1971: Climatic regions of Czechoslovakia. *Studia Geographica, sv. 16. Brno: Czechoslovak Academy of Science – Institute of Geography. 79.*

Šercl, P. and *Lett, P., 2002:* Výpočet rastru srážek v prostředí GIS (s využitím ArcView Spatial Analyst). *Uživatelská příručka verze 2.0.1,* ČHMÚ, OPV, Praha.

Štěpánek, P., 2010: ProClimDB – software for processing climatological datasets. CHMI, regional office Brno. http://www.climahom.eu/ProcData.html.

Štěpánek, P., Zahradníček, P. and *Skalák, P.*, 2009: Data quality control and homogenization of air temperature and precipitation series in the area of the Czech Republic in the period 1961–2007. *Adv. Sci. Res. 3*, 23–26.

Thornthwaite, C.W., 1948: An approach toward a rational classification of climate. Geogr Rev. 38, 55–94.

Tolasz, R., (ed), 2007: Atlas podnebí Česká. Climate Atlas of Czechia. ČHMÚ, Univerzita Palackého v Olomouci, Praha-Olomouc, 254.

Trnka, M., Dubrovský, M., Svoboda, M.D., Semeradová, D., Hayes, M.J., Žalud, Z. and *Wilhite. D.A.*, 2009: Developing a regional drought climatology for the Czech Republic for 1961–2000. *Int J Climatol 29*, 863–883.

Vicente-Serrano, S.M., Beguería, S. and *López-Moreno, J.I.*, 2010: A Multi-scalar drought index sensitive to global warming: The Standardized Precipitation Evapotranspiration Index – SPEI. *J. Climate 23*, 1696–1718.

Vicente-Serrano, S.M., Beguería, S. and *López-Moreno, J.I.*, 2011: Comment on "Characteristic and trends in various forms on the Palmer Drought Severity Index (PDSI) during 1900-2008" by Aiguo Dai. *J. Geograph. Res.116*, D19112.

IDŐJÁRÁS

Quarterly Journal of the Hungarian Meteorological Service
Vol. 116, No. 4, October–December 2012, pp. 297–321

Comprehensive assessment of climate change policies and measures in Hungary: concerns and tasks in an underestimated challenge

Sándor Molnár[1]* and **Márk Molnár**[2]

[1] *Szent István University, Faculty of Mechanical Engineering, Institute of Mathematics and Informatics, Páter K. u.1,H- 2103 Gödöllő,Hungary*

[2] *Szent István University, Faculty of Economics and Business Management, Institute of Economic Sciences, Páter K. u.1,H- 2103 Gödöllő,Hungary*

**Corresponding author E-mail: Molnar.Sandor@gek.szie.hu*

(Manuscript received in final form Oktober 15, 2012)

Abstract—Parties included in Annex I to the UNFCCC are requested to submit national communications to the Secretariat. This report strives to present a review of the results of the 5th National Communication (NC5) of Hungary with respect to the relevant provisions of the Convention and Article 8 of the Kyoto Protocol.

Key-words: greenhouse gas emissions, inventory, projections, National Communication

1. Introduction

For Hungary, the Convention entered into force on May 25, 1994 and the Kyoto Protocol on February 16, 2005. Under the Kyoto Protocol, Hungary committed itself to reducing its net greenhouse gas (GHG) emissions by 6 percent compared with the average level for the period 1985–1987 (base year) during the first commitment period from 2008 to 2012.

Hungary's 5th National Communication (NC5) complies in general with the UNFCCC Guidelines for the preparation of national communications, and

Hungary considered most of the recommendations provided in the report on the in-depth review of the 4th National Communication (NC4) of Hungary.

The NC5 covers all of the sections required by the UNFCCC reporting guidelines and most of the supplementary information required under Article 7, paragraph 2, of the Kyoto Protocol, except for information on supplementarity relating to the mechanisms pursuant to Articles 6, 12, and 17 of the Kyoto Protocol (see Section 2). The NC5 does not include information required by the UNFCCC reporting guidelines on steps undertaken to limit or reduce GHG emissions from aviation and marine bunkers and on international activities relating to systematic observations, including Global Climate Observing System (GCOS) activities.

2. Assessment of the current situation

In its NC5, Hungary has provided an overall description of the national circumstances and has elaborated on the framework legislation and key policy documents on climate change. Information has been provided on the government structure, population, geography, climate, settlement structure and building stock, economy and relevant economic sectors. However, while national circumstances were well described in the NC5, the analysis of how these national circumstances and changes affect GHG emissions and removals in Hungary could be further enhanced.

The main drivers of emission trends in Hungary include overall restructuring and reducing the levels of economic activity, and restructuring of primary energy supply, since Hungary undertook a transition from a centrally planned economy to a market based economy that has taken place in the 1990s. Since 1995, the economy has grown, with associated small growth in energy consumption, while GHG emissions have remained relatively stable and have decreased even further since 2005. The transparency of future national communications can be further enhanced by providing more information on the changes in sectoral emissions (e.g., transport, energy, industrial, and agricultural emissions) and the relationship between sectoral emissions and changes in activity, and on how the national circumstances are driving these changes. *Table 1* summaries the relevant indicators of emissions and removals for Hungary.

The Hungarian Meteorological Service (together with the Forestry Directorate of the Central Agricultural Office and the Forest Research Institute) is responsible for the national GHG inventory. Climate change policy is underpinned by the National Climate Change Strategy 2008–2025 (NCCS), and a significant proportion of the PaMs are implemented at the national level. The implementation of climate change policy is set out in the National Climate Change Programme.

*Table 1.*Indicators relevant to greenhouse gas emissions and removals for Hungary

	1990	1995	2000	2005	2008	Change[a] 1990–2000 (%)	Change 2000–2008 (%)	Change[a] 1990–2008 (%)
Population (million)	10.4	10.3	10.2	10.1	10.0	–1.5	–1.7	–3.2
GDP (USD 2 000 billion using PPP)	115.1	102.1	123.7	152.2	160.8	7.5	30.0	39.8
TPES (Mtoe)	28.7	25.9	25.0	27.6	26.5	–12.8	5.9	–7.7
GDP per capita (USD 2 000 thousand using PPP)	11.1	9.9	12.1	15.1	16.0	9.2	32.2	44.4
TPES per capita (toe)	2.8	2.5	2.4	2.7	2.6	–11.4	7.7	–4.7
GHG emissions without LULUCF (Tg CO_2 eq)	114.5[a]	78.7	77.1	79.8	73.1	–32.7	–5.1	–36.1
GHG emissions with LULUCF (Tg CO_2 eq)	112.3[a]	71.9	75.9	75.3	68.6	–32.5	–9.5	–38.9
CO_2 emissions per capita (Mg)	8.2	5.9	5.7	6.0	5.6	–30.0	–2.3	–31.6
CO_2 emissions per GDP unit (kg per 2 000 USD using PPP)	0.7	0.6	0.5	0.4	0.4	–35.9	–15.4	–45.8
GHG emissions per capita (Mg CO_2 eq)	11.0	7.6	7.5	7.9	7.3	–30.3	–3.5	–32.7
GHG emissions per GDP unit (kg CO_2 eq per 2 000 USD using PPP)	1.0	0.8	0.6	0.5	0.5	–36.2	–27.0	–53.4

Abbreviations: GDP = gross domestic product, GHG = greenhouse gas, LULUCF = land use, land-use change and forestry, PPP = purchasing power parity, TPES = total primary energy supply.

Sources: (1) GHG emissions data: Hungary's 2010 greenhouse gas inventory submission; (2) Population, GDP and TPES data: International Energy Agency.

Note: The ratios per capita and per GDP unit are calculated relative to GHG emissions without LULUCF; the ratios are calculated using the exact (not rounded) values and may therefore differ from a ratio calculated with the rounded numbers provided in the table.

[a] For emissions, base year data are used instead of 1990 data, whereas GDP, TPES, and population data are for 1990, which may lead to some inconsistency in the calculation of GHG emissions per capita and per GDP unit.

GHG emission trends are provided for the period 1985–2007. This information is consistent with the 2009 national GHG inventory submission. Total GHG emissions excluding emissions and removals from land use, land-use change, and forestry (LULUCF) decreased by 36.1 percent between the base year and 2008, whereas total GHG emissions including net emissions or removals from LULUCF decreased by 38.9 percent. This was mainly attributed to CO_2 emissions, which decreased by 33.8 percent over this period. Emissions of methane (CH_4) also decreased by 28.5 percent, while emissions of nitrous oxide (N_2O) decreased by 56.9 percent. Most of these decreases were experienced during the years 1987–1995 (trends for 1987–1995: CO_2 27.3 percent, CH_4 21.3 percent, N_2O 56.0 percent, and total GHGs 31.1 percent). Emissions of F-gases accounted for about 0.30 percent of total GHG emissions

in 1995 and 1.28 percent in 2008. Total GHG emissions have decreased, mostly due to GHG emission reductions in industry (manufacturing industry and industrial processes), agriculture, and energy use in the sector "others" (residential and commercial sectors), driven chiefly by a decline in industrial output, restructuring and associated energy use, and agricultural production. During the same period that emissions from transport grew substantially, those from waste also increased. *Table 2* provides an overview of GHG emissions by sector from the base year to 2008.

Table 2. Greenhouse gas emissions by sector in Hungary, 1990–2008

	GHG emissions (Tg CO_2 eq)							Change (%)		Shares[a] by sector (%)	
Sector	**BY**	**1990**	**1995**	**2000**	**2005**	**2007**	**2008**	**BY [a] –2008**	**2007 –2008**	**BY**	**2008**
1. Energy	82.9	70.5	60.8	57.8	59.8	56.7	55.5	–33.1	–2.1	72.3	75.9
A1. Energy industries	27.3	22.2	23.9	23.6	18.8	20.6	19.7	–27.8	–4.3	23.8	26.9
A2. Manufacturing industries and construction	20.1	15.0	11.0	8.5	8.7	7.2	7.0	–65.4	–3.7	17.6	9.5
A3. Transport	7.8	8.2	7.0	8.8	12.2	12.8	12.9	65.7	0.4	6.8	17.6
A4.–A5. Other	25.0	22.7	16.4	14.5	17.9	13.9	13.8	–44.7	–0.5	21.8	18.9
B. Fugitive emissions	2.7	2.4	2.5	2.5	2.2	2.2	2.1	–21.7	–1.1	2.4	2.9
2. Industrial processes	10.9	8.9	5.5	6.3	7.0	6.0	4.7	–56.5	–20.6	9.5	6.5
3. Solvent and other product use	0.3	0.2	0.2	0.2	0.4	0.4	0.4	42.8	11.0	0.2	0.6
4. Agriculture	17.5	14.5	8.7	9.1	8.8	8.9	8.8	–49.8	–1.4	15.3	12.0
5. LULUCF	–2.3	–2.9	–6.8	–1.2	–4.6	–2.9	–4.5	100.8	57.0	–2.0	–6.2
6. Waste	3.0	3.3	3.5	3.7	3.9	3.8	3.7	25.3	–1.6	2.6	5.1
7. Other	NA	NA	NA	NA	NA	NA	NA	NA	NA	NA	NA
GHG total with LULUCF	**112.3**	**94.4**	**71.9**	**75.9**	**75.3**	**72.8**	**68.6**	**–38.9**	**–5.8**	**NA**	**NA**
GHG total without LULUCF	**114.5**	**97.4**	**78.7**	**77.1**	**79.8**	**75.7**	**73.1**	**–36.1**	**–3.4**	**100.0**	**100.0**

Abbreviations: BY = base year, GHG = greenhouse gas, LULUCF = land use, land-use change and forestry, NA= not applicable.

Note: The changes in emissions and the shares by sector are calculated using the exact (not rounded) values and may therefore differ from values calculated with the rounded numbers provided in the table.

[a] The shares of sectors are calculated relative to GHG emissions without LULUCF; for the LULUCF sector, the negative values indicate the share of GHG emissions that was offset by GHG removals through LULUCF.

After the sharp decline in emissions during the period 1987–1995, Hungary's GHG emissions remained relatively stable until 2005 against the backdrop of stable economic growth. This suggests a decoupling of economic growth from the GHG emissions for that period. During the last three years

between 2008 and 2009, Hungary's emissions decreased even further, by 8.4 percent, mainly due to a decrease in energy consumption, the extreme mild winter in 2007, and modernization in the chemical industry. Transparency of the reporting on GHG emission trends could be improved by providing additional information on sector-specific trends and relevant drivers.

3. Policies and measures

The key framework for climate and energy policy is the NCCS 2008–2025. The National Climate Change Programme (NCCP) gives effect to the implementation of the strategy, and the progress made in implementing the NCCS is reviewed every two years. The NCCS attaches priority to meeting the objectives of the EU directives and international conventions related to climate change that lead to a lower carbon economy, avoid adverse, ecological and social economic effects, and promote awareness of climate change.

Hungary expects to meet its Kyoto Protocol emission reduction target without any further measures. In accordance with the 'without measures' scenario, Hungary expects its emissions to be 11.8 percent below the base year level compared to the Kyoto target of 6 percent below the base year level. Hungary joined the EU ETS in 2005. Most emissions allowances are allocated freely during 2008–2012; however, from 2012, the quantity of free allowances will decrease by 17.4 percent compared to the average annual total quantity of allowances currently issued by EU member States.

Improvements to the energy efficiency of the residential sector have provided the most cost-effective and biggest impact on reducing GHG emissions in Hungary. The Hungarian residential sector is dominated by large pre-fabricated apartment blocks built prior to the 1990s with low thermal efficiency, heated by district heating, and commonly fueled by oil and coal. Emissions from this sector decreased by 64 percent in 2008 compared to the base year level due to energy-efficiency improvements and the shift from coal to gas in the residential sector. In the 1990s and 2000s, policies to improve energy efficiency in the residential sector were strengthened and their benefits, in terms of improving air quality and human health and providing employment opportunities during the recession, were recognized.

The NC5 provided estimates of the effects of PaMs by sector and by gas for most sectors except for the agriculture, industrial processes, and waste sectors. Reduction in agriculture emissions would predominantly be from N_2O.

Limited information is available on the implementation costs of PaMs. Retrofitting and improving the energy efficiency of the building stock has largely been funded through the Green Investment Scheme (GIS) with finance raised from the sale of assigned amount units (AAUs). Hungary has invested 7.5 billion Hungarian forints (HUF) from the GIS into retrofitting and improving the

energy efficiency of the building stock. Hungary anticipates using the GIS further to fund investment in renewable energy supply.

Hungary has no PaMs in the agriculture sector that could potentially increase emissions through a growth in the output of livestock and cropping. None of the PaMs in the agricultural sector directly addressed GHG emission reduction. Further, the potential effects can hardly be quantified so that no precise information is available on the effects of PaMs on agriculture emission. *Table 3* provides a summary of the reported information on the PaMs of Hungary.

*Table 3.*Summary of information on policies and measures

Major policies and measures	**Examples/comments**
Policy framework and cross-sectoral measures	
National Climate Change Strategy (NCCS)	National framework for making climate change related decisions. The National Climate Change Programme is adopted every two years to implement the NCCS
Emissions trading	European Union emissions trading scheme (EU ETS) from 2005. The existing installations have been allocated an average of 26.1 Mt of CO_2 emission allowances per year during the period 2008–2012. About 13.1 Mt are reserved for new entrants during this period
Policies and measures by sector	
Energy	
National Energy Efficiency Action Plan (NEEAP)	The NEEAP spans from 2007 to 2013 and encompasses a number of national energy-saving programmes and measures, including the Energy Saving Credit Fund and the Energy Certificate
Promotion of renewable energy sources	The Renewable Energy Strategy (RES) includes feed-in-tariffs for renewables and waste, and certificates of origin for RES electricity. It also supports various projects, including those promoting biomass, biogas, geothermal energy, and small-scale wind turbines
	In line with the EU renewable energy directive, the renewables target is set to be 13 percent by 2020, which translates to 96 PJ based on a post-economic recession projection of energy supply
Energy-efficiency improvements	The Hungarian Energy Efficiency Strategy and Action Plan designates the following areas for policy intervention: residential buildings, institutional buildings, energy transformation, traffic and transport, architecture, and typical energy consumption product groups that may have a more significant influence on the volume of energy needs
	Energy efficiency in housing, funded through the Green Investment Scheme (GIS)
	Energy efficiency in communal residences, which includes the upgrading of district heating systems and the conversion from coal to gas
Combined heat and power generation	Obligatory takeover of electricity produced through combined heat and power
Nuclear power	Refurbishment and extension of existing capacity (6–10 Mt CO_2 eq)

Major policies and measures	Examples/comments
Transport	
Renewable transport target	Target of 10% renewable transport through biofuels and electric motives (including passenger cars)
Road pricing	Tolls for heavy vehicles
Industrial processes	
Joint implementation	Project implemented to eliminate almost all N_2O emissions from nitric acid production
Fluorinated gases	Hungary is implementing the EU directive on F-gases
Agriculture	
New Hungary Rural Development Strategic Plan	Increase of energy plantations and energy forests
	EU nitrates directive
	Modernization of agriculture livestock production, crop production and machinery
	Financial support for improved environmental management and animal management
Forestry	
Afforestation	Grants for afforestation
	Restrictions on deforestation: any deforestation must be offset with equal or greater afforestation elsewhere
	Emphasis on natural regeneration and the return to the natural state wherever possible
Waste	
	Waste prevention (including hazardous waste) and packaging reduction, as mandated by the EU
	Landfill gas flaring or capture if economically viable
	Upgrading waste incineration in Budapest, employing heat used for electricity and district heating
	Reduction of landfill sites and rehabilitation of old sites

Note: The greenhouse gas emission reduction estimates given for some measures (in parentheses) are reductions in CO_2 or CO_2 eq for the year 2020.

3.1. Policy framework and cross-sectoral measures

The current climate change policy is elaborated in the NCCS 2008–2025. The NCCS sets out the overall strategy for Hungary to address climate change, including mitigation and adaptation, as well as the communication of climate change. The NCCS was to be reviewed after two years and then every five years. However, the 2010 review was deferred to 2011 because of a substantive government restructuring and the preparation for the presidency of the EU

during the first half of 2011. The NCCP implements the climate change measures, outlined in the NCCS and is reviewed every two years, and a new two-year programme is produced.

Hungary's 2020 pledged emissions reduction target compared to 1990 levels is a reduction of 16 –25 percent if the EU target is 20 percent, or a reduction of 27–34 percent if the EU target is 30 percent. The target for 2050 is a reduction of 80 percent, and Hungary's vision for 2050 will be further elaborated in the revised NCCS during 2011. The higher end of the less stringent target (16–25 percent) is commensurate with the 'with measures' projected reduction relative to 1990 of 26 percent, and the higher end of the more stringent target (27–34 percent) is commensurate with the projected reduction in emissions under the 'with additional measures' projection for 2020 relative to 1990. Hungary could be expected to meet the less stringent target with existing measures and the more stringent target with additional measures. Hungary has not reported on how it intends to make use of forestry removals to meet its 2020 and 2050 targets.

Under the EU directive on energy efficiency, Hungary is to improve energy efficiency by 20 percent between 2008 and 2020 in the non-EU ETS trading sector. The energy efficiency allocation plan is yet to enter into force. EU directive 2009/28/EK sets a renewable energy target for Hungary's primary energy supply of 13 percent by 2020.

Hungary complies with the climate change related directives of the EU; Hungary is planning to implement the EU directive on F-gases. Under the EU renewable energy target directive (2009/29/EK), Hungary's target is to meet 13 percent of total primary energy demand from renewable sources. The target, in absolute terms, equates to 96 PJ (13 percent of total projected energy supply in 2020 of 740 PJ) by 2020 and was lowered to take into consideration lower-than-expected energy demand in 2020 due to the recent global financial recession. The transport sector's target is to meet 10 percent of its energy demand from renewable sources, including biofuels and the electrification of road and rail transport. In addition, energy efficiency is to be improved by 20 percent between 2008 and 2020 in the non-EU ETS trading sector. The energy efficiency allocation plan is yet to enter into force.

3.2. Policies and measures in the energy sector

Between the base year and 2008, GHG emissions from the energy sector decreased by 33.1 percent (27,392.9 Gg CO_2 eq), mainly driven by reductions in energy demand in manufacturing industries and construction (–65.4 percent or –13,154.6 Gg CO_2 eq), and in the residential sector (–45.8 percent or –7,643.4 Gg CO_2 eq). Between the base year and 1993, Hungary's economic activity was substantially reduced during the transition to a market-based economy, causing the large reduction in emissions from manufacturing

industries and construction. Emissions from the residential and commercial sectors were reduced by the shift from coal-fired to natural gas in heating plants and improvements in the thermal efficiency of the residential and commercial sectors.

The share of fossil-based fuel consumption in Hungary's energy supply declined from 1990 to 2007 due to changes in economic activity. Between 1990 and 2007, coal consumption decreased by 60 percent (from 186.4 to 74.2 PJ), oil consumption decreased by 57 percent (from 80.9 to 35.1 PJ), and gas consumption decreased by 47 percent (from 159.6 to 83.9 PJ). Over the same period, nuclear power increased by 7 percent (from 149.7 to 160 PJ), and renewables are estimated to have increased by 65 percent (from 18.5 to 30.6 PJ). Hungary also intends to make use of geothermal heat for district heating.

Nuclear power provided almost 40 percent of Hungary's electricity supply in 2007. Hungary has implemented a parliamentary decree to extend the lifetime of the existing nuclear power plant and to increase the capacity of each of the four units from 440 MW to 500 MW. The refurbishment will ensure that at least 40 percent of future electricity needs are met from nuclear power. Depending on the assumed fuel mix for generation, the refurbishment of the nuclear power plant will reduce Hungary's GHG emissions by 6–10 Mt CO_2 eq annually.

Renewable energy sources. The renewable energy target has been set using energy projections made since the onset of the global recession, as expectations of future energy demand are now lower than projected before the recession. Preliminary sectoral targets to achieve this aggregate target are divided as follows: 14.3 percent for heating and cooling, 13.8 percent for power generation, and 10 percent for transport. Hungary has not yet determined how the renewable target will be financed but expects to make use of GIS funds.

Energy efficiency. Hungary has successfully reduced GHG emissions in the energy sector by increasing the energy efficiency of buildings, and the estimates suggest that there is still scope for further improvement. Buildings in need of thermal efficiency improvements are firstly graded for their thermal efficiency. The building owners finance the improvements to their building and the building is then graded again for thermal efficiency. A grant of up to 60 percent is paid for successful improvements. Larger grants may be paid if the upgrade exceeds expectations and a higher grade is achieved. Funding for the programme is provided from the GIS. The returns, in terms of energy savings to the programme, are high. From an initial investment of HUF 3.3 billion, the energy savings are estimated to be HUF 30 billion. The benefits of the scheme appear large and could possibly occur under 'business as usual'. There is a need for Hungary to continue to re-evaluate the scheme in order to ensure that the improvements do not occur under 'business as usual', and because the benefits of the scheme are likely to diminish over time as energy efficiency is improved.

Residential and commercial sectors. Emissions from the residential and commercial sectors have decreased from 16.7 Mt CO_2 eq to 9.1 Mt CO_2 eq

between the base year and 2008. The reduction is largely due to improvements in energy efficiency and the shift from coal-fired heating to gas as well as improvements to the thermal efficiency of pre-1992 residential and commercial buildings. Other PaMs for the residential sector include: voluntary measures and awareness-raising campaigns, including labelling of appliances and household boilers; and financial incentives for the replacement of refrigerators and freezers with more efficient appliances. Buildings in Hungary are required to have energy rating certificates prior to sale.

Transport sector. In contrast to the other sectors where emissions declined, emissions from the transport sector increased by 65.7 percent during the period 1990 –2008. This reflects changes in lifestyle and a major shift from public transport to private cars. The transport fleet underwent significant modernization during the 1990s and up to 2004, from an old car fleet with a high proportion of 2-stroke engines to modern vehicles meeting EU emissions standards. However, the average age of the cars increased from 10.5 years to 11.7 years between 2004 and 2008, largely due to financial difficulties preventing individuals from financing new vehicles. Hungary's road infrastructure is still expanding in order to catch up with the level of road infrastructure in more developed EU countries. Hungary applies a differentiated road tax on purchases of motor vehicles (irrespective of age) graduated on emissions standards, which is in inverse relationship to the vehicle emissions standard. Environmental testing for smoky vehicles was previously annual for cars older than four years. In recent years, each has to go through a mechanical test every second year, however, this includes environmental testing too. Compliance with vehicle testing is still strictly enforced, but with less frequency, which is more cost effective for the vehicle owners.

Hungary has a 10 percent domestic reduction target for emissions from transport relative to projected transport emissions in 2020. Much of the emissions reduction is expected to be made through the renewables transport target. Other transport policies include: the improved integration of public transport systems; park and ride systems; the modernization of the transport fleet; and tolls on heavy vehicles. Existing measures in the transport sector are expected to reduce transport emissions by 7 percent relative to projected transport emissions in 2020. How the remaining 3 percent emissions reduction will be achieved remains unclear. Hopefully, the introduction of more stringent emission standards, and the EU-wide regulation on decreasing the GHG emissions (caps) of a producer's car fleet will help to close the gap.

Hungary is land-locked but can use the Danube River for some international shipping. Currently, there are no Hungarian flagged ships engaged in international shipping on the Danube River. Shipping on the Danube River is largely unscheduled and informal, over which Hungary has no specific jurisdiction. Historically, Hungary has used the Danube River for freight transportation and believes that an opportunity exists to use the river for freight transport, again with a view to reducing road freight emissions

Industrial sector. The focus of PaMs in the industrial sector is on improving energy efficiency through financial support programmes, energy audits, and voluntary programmes. Funding is available through financial assistance on a grant basis provided by the EU programme, Poland and Hungary: Assistance for Restructuring their Economies (PHARE). Funds have been set aside to increase renewable energy and reduce energy loss in energy carriers. Beneficiaries also include municipalities, private and municipality-owned companies. The technologies are mainly efficient street lighting, small-scale combined heat and power systems, improvements of production processes, and – to a lesser extent – projects involving renewable energies.

Financial incentives in the form of grants are also available under the efficient energy consumption instrument to reduce energy consumption in buildings and to modernize district heating and buildings for small- and medium-sized enterprises. Large energy consumers are required by law to employ an energy manager and to report on energy consumption and efforts being implemented to improve energy efficiency. Reporting of PaMs in the industrial sector could be improved by separating out the activities related to the non-industrial sector (e.g., improving the efficiency of street lighting) and wherever several PaMs target one activity (e.g., improving boiler efficiency).

3.3. Policies and measures in other sectors

Between the base year and 2008, GHG emissions from industrial processes (including solvent and other product use), agriculture, and waste decreased by 44.2 percent (14,013 Gg CO_2 eq), mainly driven by reductions in emissions from agriculture and industrial processes. The trend in GHG emissions from industrial processes (including solvents and other product use) showed a notable decrease of 54.0 percent (or 6,039 Gg CO_2 eq). The decrease in emissions from agriculture was of the same range, 49.8 percent (or 8,728 Gg CO_2 eq). In contrast, emissions from the waste sector increased by 25.3 percent (753 Gg CO_2 eq).

Industrial processes. The decrease in GHG emissions from the industrial processes sector (including solvents and other product use) between the base year and 2008 was mainly driven by reductions in economic activity and the closing down of some industrial facilities following Hungary's transition to a market economy. A joint implementation project also contributed to a reduction of N_2O emissions from nitric acid production by 1,423 Gg CO_2 eq between 2006 and 2008.

Agriculture. Between the base year and 2008, the decrease in GHG emissions from the agriculture sector was mainly driven by reductions in agriculture activity following Hungary's transition to a market economy (*Kovács-Székely* and *Szalai*, 2009). Total emission reductions due to agriculture measures were reported to be 1,244.56 Gg CO_2 eq by the year 2020; however, information on

the effect of agriculture policies was not provided separately for N_2O and CH_4 emissions. Most of the abatement in agricultural emissions was expected to come from reduced emissions of N_2O driven by the implementation of the EU nitrates directive. The focus of the implementation of this directive in Hungary is on improved farming practices.

Most of the reduction in agriculture emissions would be from N_2O from protein forage optimization and derived nitrogen (N) excretion reductions. The N excretion reductions are driven by EU directives and implemented through improved farming practices. PaMs were modeled jointly to correctly account for the overlap (or double counting) between policies.

Other PaMs in the agriculture sector focus on the modernization of farming systems, financial support for improved environmental practices, and afforestation on agricultural land.

LULUCF. The LULUCF sector was a net removal of 4,515 Gg CO_2 eq in Hungary in 2008, and the net GHG removal increased by 2,267 Gg CO_2 eq from the base year. The trend was mainly driven by afforestation policies. Information on policies to effect LULUCF activities under Article 3, paragraphs 3 and 4, of the Kyoto Protocol was not provided in the NC5.

Hungary has implemented a new Forestry Act of 2009 replacing the 1996 Forestry Act. The emphasis of forestry policy in Hungary is on the promotion of afforestation. In accordance with this policy, any deforestation (settlements and highways) must be compensated by an equivalent or greater amount of afforestation elsewhere. Deforestation for agriculture and over-thinning is not permitted. Forests must be allowed to regenerate to the most natural state possible wherever applicable. Until 2004, funding for afforestation was provided by the Hungarian Government but now the EU provides funding for most of the afforestation activities. Within the agri-environmental programme, 44,000 ha have been approved for afforestation, and the total area for afforestation under the programme (69,000 ha) appears feasible. The effects of PaMs in the forestry sector which were reported in the re-submission of the 2010 annual inventory on November 8, 2010 are as follows: removals in 2008 totaled 1.16 Mt CO_2 from afforestation and reforestation activities and 2.8 Mt CO_2 from forest management activities under Article 3, paragraph 4.

Waste management. Between the base year and 2008, GHG emissions from the waste sector increased by 25.3 percent (or 753 Gg CO_2 eq). Information on the effects of policies on the waste sector by gas has not been provided. The key policy to reduce waste and waste emissions is implemented in the context of the EU waste management directive and is under transposition into domestic legislation. The directive focuses on waste prevention and minimization, separation, reuse, and recycling. This includes the prevention of hazardous waste and the reduction of the amount of packaging.

The number of solid waste disposal sites across Hungary was approximately 2,600 in year 2002 of which only 1,000 sites operated. Between

2002 and 15 July 2009 their number decreased to 75, out of which the number of municipal solid waste disposal sites dropped from approximately 150 to 57. Closed sites are rehabilitated and checked to ensure that there is no wastewater leaching. Landfill sites are assessed for landfill gas capacity. Sites determined to have a positive economic value of landfill gas use landfill capture, otherwise the gases are flared. Whether the gas is captured or flared depends on the economic assessment. One waste management facility in Budapest has been retrofitted and the waste is burned for district heating and electricity generation.

4. Projections and the total effect of policies and measures, and supplementarity relating to the Kyoto Protocol mechanisms

4.1. Projections overview, methodology, and key assumptions

Hungary submitted three scenarios in its NC5, with 2005 as the starting year: (a) a 'without measures' (WOM) scenario, also called the 'baseline' scenario, which is presented as a theoretical trend line for comparison under the assumption of 'frozen technology' (no efficiency improvements in the power sector and energy demand, and no increase in the renewables share), while activities change; (b) a 'with measures' (WM) scenario (called 'with existing measures' in the NC5), which includes the effects of full implementation of existing and adopted measures, as well as the assumption that renewables targets will be met according to the base case in the Renewable Energy Strategy (RES) (an 11–13 percent renewables share of total primary energy consumption by 2020); and (c) a 'with additional measures' (WAM) scenario, which assumes that renewables targets will be met according to the more ambitious scenario defined in the RES (a 13 –15 percent renewables share of total primary energy consumption by 2020), and that other planned and possible new measures will be implemented, in addition to the ones already included in the WM scenario. This scenario also envisages that the EU ETS (covering power and heating plants, oil refineries, and production installations in industry) will continue until 2020 with a carbon price of EUR 24 –30/t, while the non-EU ETS sector (covering households, transport, waste, agriculture, and services) will achieve a 10 percent reduction in emissions.

The methodology used for preparing projections is well described in the NC5. Different approaches are used in different sectors. For most sectors (energy, waste, transport, industry, households, and the tertiary sector) the HUNMIT model is used. HUNMIT is a modeling framework that uses a bottom-up approach to estimate the demand of useful energy (i.e., energy for lighting and heating), rather than projecting energy demand based on fuel use. Input factors to the model are the population forecast, fuel prices, demand for electricity, and industrial and district heating. The model works out the most cost-effective fuel mix for the whole energy system. The HUNMIT model can

assess multiple policies simultaneously, thus ensuring that abatement estimates are not double counted. For LULUCF (forestry), a carbon accounting model called CASMOFOR is used, which takes into account the afforestation rate (total area in ha/year), site fertility, and species composition (slow- versus fast-growing species). For the agriculture sector, projections are based on work undertaken by the Agricultural Economics Research Institute (AERI), which uses several models: (1) the HUSIM model for developing major macro indicators; (2) the FARM-T model to analyze structural changes in agriculture; and (3) the MICROSIM model for farm-level forecasts on the farms which could become bankrupt.

The NC5 presents key assumptions on GDP growth, fuel prices, power production, emission factors for electricity generation, population, waste disposal, number of kilometres traveled by passenger cars, and the thermal efficiency of fossil plants for the years 2010, 2015, and 2020 in tabular format. Assumptions on the carbon price up to the year 2020 are also given in the text. Assumed changes in the activity rate in preparing projections are given in an appendix to the NC5 as five-year averages (2005–2010, 2010–2015, 2015–2020 and 2020–2025) for the following subcategories: different power plants in power generation and heat production; different subsectors in industry; housing stock and appliances used in households; building stock and appliances used in the tertiary sector; and waste management. Assumptions on GDP and population are similar to those in the NC4. Assumptions and, accordingly, projections do not take into account the recent economic crisis.

The sensitivity of the results using different input parameters is discussed in the NC5. The main parameters that have been considered are discount rates, energy prices, and CO_2 emission factors for electricity. The impact of a variation in these parameters on the projected GHG emissions is discussed in the NC5 only qualitatively, and no resulting numbers/uncertainty ranges are provided.

4.2. Results of projections

Hungary's base year emissions were fixed at 115.4 Mt CO_2 eq during the initial review. Hungary's quantified emission reduction commitment is 94 percent. This yields a target of 108.5 Mt CO_2 eq annual emissions for the Kyoto Protocol first commitment period (2008–2012). Hungary is on track to overreach this target by domestic efforts alone. In 2008, Hungary's total aggregated GHG emissions were 36.6 percent below base year levels, and 32.6 percent below the Kyoto Protocol target. The 'with measures' projections indicate that Hungary's GHG emissions will be 31.8 percent below the Kyoto Protocol target in 2010. Activities under Article 3, paragraphs 3 and 4, of the Kyoto Protocol are expected to provide further annual emission reductions and relevant removal units of 3.8 Mt CO_2 eq in 2010.

Table 4 summarises the projected emissions. Under the 'with measures' scenario, between the base year and 2010, CO_2 emissions are expected to decrease by 36.2 percent, CH_4 emissions by 17.3 percent, N_2O emissions by 47.6 percent, while F-gases are expected to increase by 203 percent.

Table 4. Summary of greenhouse gas emission projections for Hungary

	Greenhouse gas emissions (Tg CO_2 eq per year)	**Changes in relation to base year level (%)**	**Changes in relation to 1990 level (%)**
Inventory data 1990 [a]	97.365	–15.63	0.00
Inventory data 2008 [a]	73.139	–36.62	–24.88
Kyoto Protocol base year[b]	115.397	0.00	18.52
Kyoto Protocol target[b]	108.473	–6.00	11.41
'Without measures' projections for 2010[c]	85.915	–25.55	–11.76
'With measures' projections for 2010[c]	73.949	–35.92	–24.05
'With additional measures' projections for 2010[c]	73.489	–36.32	–24.52
'Without measures' projections for 2020[c]	100.865	–12.59	3.59
'With measures' projections for 2020[c]	73.276	–36.50	–24.74
'With additional measures' projections for 2020[c]	66.562	–42.32	–31.64

Sources: [a] Hungary's 2010 greenhouse gas (GHG) inventory submission; the emissions are without land use, land-use change and forestry (LULUCF).
[b] Based on the initial review report contained in document FCCC/IRR/2007/HUN.
[c] Hungary's 5th National Communication.

Beyond the first commitment period of the Kyoto Protocol, according to the 'with measures' projections, between 2005 and 2020 total CO_2 emissions will decrease by 3.8 percent, CH_4 emissions will increase by 3.7 percent, N_2O emissions will increase by 9.8 percent, and F-gases are expected to increase by 15.5 percent. Under the 'with measures' scenario, the relative contribution to the total GHG emissions (in CO_2 eq) in 2010 is 74 percent for CO_2, decreasing to 72 percent in 2020; 11 percent for CH_4 in 2010, increasing to 12 percent in 2020; 14 percent for N_2O in 2010, increasing to 15 percent in 2020; and 1 percent for F-gases in 2010 and 2020. The past and forecasted emission trends are shown in *Fig. 1.*

The effects of the recent global recession was considered on the short term by setting activity rate changes between 2005 and 2010 to a very low level (stagnation).

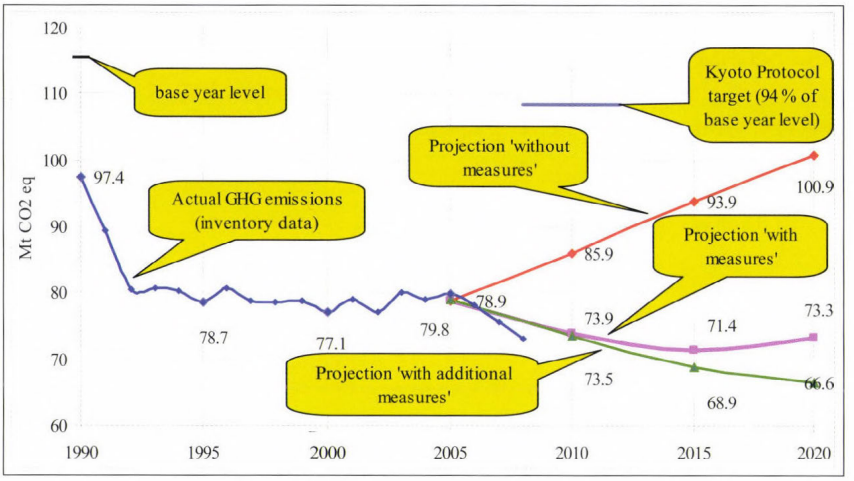

Sources: (1) Data for the years 1990–2008: Hungary's 2010 greenhouse gas inventory submission; the emissions are without land use, land-use change and forestry (LULUCF). (2) Data for the years 2005–2020: Hungary's 5th National Communication; the emissions are without LULUCF.

Fig. 1. Greenhouse gas emission projections.

Hungary has a conditional objective with regards to emission reductions up to 2020, defined in the NCCS: in the case of an EU emissions reduction target of 20 percent, Hungary would commit to a 16–25 percent reduction by 2020, compared to 1990 levels, and if the EU emissions reduction target is 30 percent, Hungary would commit to a 27–34 percent reduction by 2020. Based on Hungary's 1990 emissions figures in the latest NIR of 97.4 Mt CO_2 eq, these commitments would translate to an emissions target of 73.0–81.8 Mt CO_2 eq (for an EU target of –20 percent) or 64.3– 71.1 Mt CO_2 eq (for an EU target of –30 percent). The less ambitious commitment would be met under the current 'with measures' scenario, if all PaMs included in this scenario deliver emission reductions according to the expectations. The more ambitious commitment would be met under the 'with additional measures' scenario.

4.3. Total effect of policies and measures

In the NC5, Hungary presents the estimated and expected total effect of implemented and adopted PaMs in accordance with the 'with measures' definition, compared with a situation without such PaMs. Information is presented in terms of GHG emissions avoided or sequestered (on a CO_2 eq basis) in 2010, 2015, and 2020. It also presents relevant information on factors and activities for each sector for the years 2005–2020/2025.

Hungary reported that the total estimated effect of adopted and implemented PaMs is 10.7 Mt CO_2 eq in 2010, 18.2 Mt CO_2 eq in 2015, and

24.1 Mt CO_2 eq in 2020. According to the information reported in the NC5, the RES will deliver by far the largest emission reductions, followed by the EU ETS and the NEEAP. Within the NEEAP measures, PaMs in the industrial sector will deliver the largest emission reductions, followed by measures in the tertiary and household sectors. The most effective PaMs and drivers behind GHG emission reductions are described in Section 2. *Table 5* provides an overview of the total effect of PaMs as reported by Hungary.

Under the 'with measures' scenario, the power supply sector is the main source of emissions in 2005, contributing 27 percent of total GHG emissions, followed by industry with 18 percent. The contribution of the power supply sector to total GHG emissions decreases constantly until 2020, both in absolute and relative terms. In 2020, the power sector is expected to contribute 19 percent of total emissions. In contrast, transport emissions are constantly rising, and by 2020 the transport sector will replace power supply as the largest contributor of GHG emissions, with a 22 percent share of total GHG emissions. The relative contribution from the agriculture sector also increases constantly, from 12 percent in 2005 to 16 percent in 2020.

In absolute terms, under the 'with measures' scenario, the main reduction between 2005 and 2020 is expected to take place in the power supply sector, by 7.8 Mt CO_2 eq. Emissions in the transport sector are expected to increase in the same period by 3.6 Mt CO_2 eq, and in the agriculture sector by 2.0 Mt CO_2 eq. A reduction of 2.7 Mt CO_2 eq is expected in the industry sector between 2005 and 2020.

Table 5. Projected effects of planned, implemented, and adopted policies and measures in 2010 and 2020

Sector	Effect of implemented and adopted measures (Tg CO_2 eq)	Relative value (% of base year emissions)	Effect including planned measures (Tg CO_2 eq)	Relative value (% of base year emissions)	Effect of implemented and adopted measures (Tg CO_2 eq)	Relative value (% of base year emissions)	Effect including planned measures (Tg CO_2 eq)	Relative value (% of base year emissions)
	2010				2020			
NEEAP								
household	0.297	0.26	0.383	0.33	1.343	1.16	2.274	1.97
tertiary	0.375	0.32	0.424	0.37	1.504	1.30	2.210	1.92
industrial	0.502	0.44	0.693	0.60	2.236	1.94	3.996	3.46
transport	0.080	0.07	0.134	0.12	0.361	0.31	0.771	0.67
intersectoral	0.004	0.00	0.004	0.00	0.020	0.02	0.026	0.02
NEEAP total	1.258	1.09	1.638	1.42	5.464	4.73	9.277	8.04
RES	6.710	5.81	7.378	6.39	11.391	9.87	15.223	13.19
EU ETS	2.778	2.41	2.778	2.41	4.583	5.41	6.248	5.41
Total	**10.746**	**9.31**	**11.794**	**10.22**	**21.438**	**18.58**	**30.748**	**26.65**

Source: Hungary's 5th National Communication.

Abbreviations: EU ETS = European Union emissions trading scheme, NEEAP = National Energy Efficiency Action Plan, RES = Renewable Energy Strategy.

5. *Vulnerability assessment, climate change impacts, and adaptation measures*

In its NC5, Hungary has provided the required information on the expected impacts of climate change in the country and on adaptation options. Regional climate scenarios, using the REMO, NCAR RegCM, and ALADIN-Climate models for the Carpathian Basin, were provided for the years 2021–2040. The scenarios point to: a significant rise in temperature in all seasons; a decrease in the number of frost days; an increase in the number of days with heat alert; and an insignificant change in annual and seasonal precipitation. In June 2003, the Ministry for Environment and Water (KvVM) and the Hungarian Academy of Sciences (MTA) launched a joint research project entitled "Global climate changes, Hungarian impacts and responses", which recently became known as the VAHAVA project. Based on the modeling studies and activities as part of this project (*Bozó et al*, 2010a), Hungary's climate change impacts can generally be described as moderate, with an increasing probability of more severe impacts due to climate change. Agriculture, forestry, and human health are the sectors most likely to be affected (*Csete et al.*, 2012). Hungary's NCCS 2008–2025 sets out Hungary's long-term climate change policy direction. Adaptation is recognized as a key pillar of the policy, which will see its prominence increased in the revised NCCS due in 2011. *Table 6* summarizes the information on vulnerability and adaptation to climate change presented in the NC5.

The key vulnerabilities due to climate change for Hungary are attributed to water resource management (*Kovács et al.*, 2010). Increased surface temperature and heat, and a decrease in precipitation would have a direct impact on hydrology, leading to reduced water availability and the drying of soils. At the other extreme, increased frequency and intensity of precipitation can lead to floods, the inundation of low-lying areas, and hydromorphological changes (*Tanos et al.*, 2011). The NC5 did not demonstrate any rigorous assessments specific to Hungary; most information was adopted for the local situation. However, the VAHAVA study contained more specific examples which could have been included in the NC5. Such targeted information should be included in future national communications.

The NC5 recognizes the critical role of adaptation on a timely basis and examines the climate–security nexus in the critical areas of ecosystems, agriculture and forest management, infrastructure and water management. Particular issues arising out of the urban heat problem (i.e., the heat effect due to urbanization) are highlighted, given that Hungary's urban population is forecasted to rise to 80 percent of the total population in a few years. The importance of adaptation in the above areas is described, and possible adaptation measures to deal with the likely impacts of climate change are outlined. Many of the adaptation measures are generic responses to impacts as contained in the literature (*Szenteleki et al.*, 2012). There is scope for more targeted, localized

responses, which Hungary should include in its future national communications (*Kis-Kovács et al.*, 2011).

Table 6. Summary of information on vulnerability and adaptation to climate change

Vulnerable area	Examples/comments/adaptation measures reported
Agriculture and food security	*Vulnerability:* The vulnerability of the agriculture sector is estimated to be high *Adaptation:* The use of appropriate land use and cultivation, irrigation and relevant technologies are possible adaptation measures. Studies of the relationship between climatic variables and species and the agronomic characteristics of crops will underpin adaptation measures
Biodiversity and natural ecosystems	*Vulnerability:* Natural habitats and biodiversity are likely to be negatively impacted. The availability of water was recognized as a key driver. The social and economic services rely on healthy ecosystems *Adaptation:* More data and studies are needed to estimate specific climate change impacts on horticulture and other ecosystems
Drought	*Vulnerability:* The modelling results point to extremes of rainfall, with reduced amounts in some regions *Adaptation:* The use of technologies in specific sectors are possible adaptation measures
Forests	*Vulnerability:* Forests are also recognized as being vulnerable to water availability and temperature *Adaptation:* The use of technology and further studies on the behaviour of species in response to changes in climatic variables are suggested
Human health	*Vulnerability:* An increase in temperature would lead to an increase in the number of days with heat alert. This has implications on human health, especially among Hungary's ageing population *Adaptation:* No specific measures are mentioned
Infrastructure and economy	*Vulnerability:* This is recognized as a major security issue *Adaptation:* The need for further assessment of the effects of climate change on key infrastructure, such as roads, drainage and storage facilities, is recognized. The ability to respond to these challenges, through a risk-based approach, needs to be strengthened
Water resources	*Vulnerability:* This is a key sector that is vulnerable to the extreme situations of excess and reduced water availability as well as quality. It would affect many sectors, such as agriculture, forestry, health, and ecosystems *Adaptation:* The assessment and monitoring of water reserves, policies on water usage and flood control are possible adaptation measures

Vulnerability and impacts need to be based on solid scientific analysis and assessment. These in turn should form the basis of priority adaptation strategies and measures. Hungary should improve the linkages between the sections reporting on the scenarios, vulnerability, and adaptation in its future national communications.

6. Research and systematic observation

Hungary has provided information on its actions relating to research and systematic observation, mainly in relation to domestic activities. There is, however, a lack of details on international activities, including the World Climate Programme, the International Geosphere–Biosphere Programme (IGBP), the GCOS, and the IPCC. Hungary has not provided a summary of information on World Meteorological Organization (WMO) programmes and subprogrammes such as World Weather Watch (WWW), Global Atmosphere Watch (GAW), Global Observation System (GOS), GCOS, Global Ocean Observation System (GOOS), and Global Terrestrial Observing System (GTOS) activities. In addition, the NC5 does not reflect the action taken to support related capacity-building in developing countries. The lack of information in Hungary's NC5 on the observational networks, data management, QC, and data exchange is noticable. While this information was provided by the Hungarian Meteorological Service, Hungary should include this information explicitly in its future national communications.

The VAHAVA project, carried out by the Hungarian Academy of Sciences, provides the scientific and technical basis for the NCCS. The NCCP outlines a comprehensive list of research activities, including collaboration at the EU and international levels. The modeling work is carried out as a joint activity between the Hungarian Meteorological Service and the Department of Meteorology at Eötvös Loránd University (*Bozó*, 2011). The international research activities are currently limited to EU countries, and Hungary has not reported on any other international research collaboration.

Funding for climate change research stems mainly from EU sources, as part of the cooperation programme under the 7th Research Framework Programme. The National Office for Research and Technology also provides funds for climate change research under the Liveable and Sustainable Environment, and the Defence and Security Research subprogrammes. The national research efforts appear to be well coordinated and supported through the active participation of the Hungarian Academy of Sciences, the Hungarian Meteorological Service, and national universities and research institutions. As part of the VAHAVA project, the periodical *AGRO-21* has been developed, consisting of 18 volumes focusing on climate change and the required responses, covering almost all the main economic and social sectors, such as nature conservation, water management, agriculture, forestry, rural development, transport, energy, environmental health, settlements, and insurance. The largest positive result of this research project has been raising the awareness of the public to the importance of preparing for the adaptation to and mitigation of climate change and its impacts (*Bozó et al*, 2010b). However, Hungary has not reported on any initiatives to support capacity-building or research and development in developing countries.

The bulk of the observational activities are carried out by the Hungarian Meteorological Service and the Department of Meteorology at Eötvös Loránd University. Hungary, as a member of the European Organization for the Exploitation of Meteorological Satellites (EUMETSAT), participates in satellite observation networks. Hungarian institutions have also participated in several international research efforts on carbon balance projects such as CarboEurope-IP, Carbon-Pro, and COST Action 725. Hungary was also part of the Adam Project 2006–09, implemented by the University of East Anglia (United Kingdom of Great Britain and Northern Ireland) involving around 19 countries undertaking adaptation and mitigation projects.

6.1. Education, training, and public awareness

In the NC5, Hungary has provided information on its actions relating to education, training, and public awareness at three levels of action: environmental education; publicly available environmental education; and strengthening the role of the media in raising awareness. A comprehensive list of courses and programmes offered by Hungarian colleges and universities is provided in the NC5, which underlines the diversity of climate change related studies; collaborative programmes with institutions in Greece, Sweden, and the United Kingdom have been set up.

The NC5 outlined the governmental support for education programmes and training related to climate change. Various organizations and professional bodies such as the Energy Centre, the Hungarian Green Building Council, and the Association for Sustainable Economies carry out regular workshops and conferences on climate change and sustainable development. In its NC5, Hungary has not reported on any joint training programmes or capacity-building activities with developing countries. Such information should be present in future national communications.

A large and diverse range of activities to raise public awareness are highlighted in the NC5. These have been actively supported by non-governmental organizations (NGOs), churches, and business councils. The Hungarian Government organized a Climate Road Show in 2008 aimed at raising awareness of climate change throughout the country. A government-administered website – Liveable Environment (http://www.elhetokornyezet.hu)– is also dedicated to raising public awareness. Hungary used the opportunity provided through the EU-funded You Control Climate Change campaign to raise awareness about global climate change. International NGOs, such as Greenpeace and the World Wildlife Fund (WWF), have been active at global forums such as the Road to Copenhagen, and Earth Hour. Civil society in Hungary appears to be well organized and supported in its public awareness and advocacy campaigns. A survey conducted by the NGOs showed a high level of public awareness of climate change issues, although the behavioral change activities at the domestic level are often dictated by economic considerations.

7. *Conclusions and recommendations*

Hungary's emissions for 2008 were estimated to be 36.1 percent below its base year level excluding LULUCF and 38.9 percent below including LULUCF. Emissions decreases were driven by a downturn in the economy, fuel switching to less carbon-intensive fuels, and a restructuring of the economy.

Hungary presents GHG projections for the years 2010, 2015, and 2020, using 2005 as the starting point for the projections. Three scenarios are included: the baseline ('without measures') scenario; the 'with measures' scenario (called 'with existing measures' in the NC5); and the 'with additional measures' scenario. The projected reductions in GHG emissions under the baseline scenario, in relation to the base year, and under the 'with measures' and 'with additional measures' scenarios, are 25.6, 35.9, and 36.3 percent, respectively, for 2010. Thus, the projections indicate that Hungary can meet its Kyoto Protocol target (which is a 6 percent reduction), even under the baseline scenario with the domestic policies currently in place. Moreover, GHG emissions are not expected to exceed the Kyoto Protocol target even by 2020.

The National Climate Change Strategy 2008–2025 and the promotion of energy efficiency and renewable energy are among the most important PaMs in reducing GHG emissions. The benefits of the energy efficiency PaMs in Hungary appear to be high relative to the cost and could possibly occur under a 'business as usual' scenario. It is, therefore, important for Hungary to continue to re-evaluate the energy efficiency measures in place in order to ensure that the improvements would be additional to what could occur under 'business as usual', given that the benefits of the scheme are likely to diminish over time as the energy efficiency of the housing stock is improved.

Mitigating emissions from transport is the most challenging part of the overall mitigation strategy for Hungary. Under the PaMs currently in place, Hungary expects to reduce transport emissions by only 7 percent between 2005 and 2020. Additional PaMs need to be put in place in order to reach the national target of at least a 10 percent reduction in emissions from the transport sector. Further, options to support measures to achieve the renewable energy supply target in Hungary of 13 percent by 2020 need to be explored, given that no PaMs have been implemented yet to meet this target. The introduction of more stringent emission standards, and the EU-wide regulation on decreasing the GHG-emissions (caps) of a producer's car fleet will help to close the gap.

The key vulnerabilities are attributed to water resource management, which will be impacted by extremes of precipitation and temperature increase. Climate change impacts are expected to be visible in other sectors as well, including agriculture, forestry, biodiversity, and health. Various adaptation measures are explored as potential responses to these impacts.

Hungary has actions relating to research and systematic observation, and has effectively addressed its domestic activities. There are references to its

international activities, including the World Climate Programme, the IGBP, the GCOS, and the IPCC. Hungary contributes effectively to EU observation efforts and participates in a number of carbon monitoring projects. There is a growing emphasis on research activities on climate change and its impacts under the guidance of the Hungarian Academy of Sciences and various universities. There is also a substantial emphasis on integrating climate change education into formal programmes at the primary, secondary, and tertiary levels.

Several recommendations can be formulated related to the completeness and transparency of Hungary's reporting under the Convention and its Kyoto Protocol. The key recommendations are that, in its future national communications, Hungary includes information on:

a. The effects of PaMs on GHG emissions for all sectors and gases, especially for the agriculture, waste, and industrial processes sectors;
b. The steps undertaken to limit or reduce GHG emissions from aviation and marine bunkers;
c. The use of the mechanisms under Articles 6, 12 and 17 of the Kyoto Protocol and their supplementarity to domestic action.

It is recommended that Hungary undertakes a number of improvements regarding transparency and completeness of reporting as follows:

d. Provide a clearer link throughout the national communication between national circumstances, the GHG emissions profile and emission trends, and PaMs;
e. Provide more details on the climate change governance structure and explain how PaMs are implemented by municipal governments, in particular how central government can affect climate policies at the municipality levels given that municipalities have competencies over policy issues at those levels;
f. Provide more detailed information on how EU-directed policies are implemented in Hungary and their impact on emissions;
g. Provide a best estimate of the projected effects of the EU ETS in the PaMs chapter, and explain any overlap with existing PaMs;
h. Provide information on activities under Article 3, paragraphs 3 and 4, of the Kyoto Protocol;
i. Provide further information on its activities in the area of research, and data gathering, in particular on the collaboration with developing countries and other international agencies/organizations;
j. Provide further information on international activities relating to systematic observations, including GCOS activities;
k. Enhance the linkages between the sections on research, modeling, vulnerability assessments, and adaptation measures;

l. Provide further information on the minimization of adverse effects and impacts in accordance with Article 2, paragraph 3, and Article 3, paragraph 14, of the Kyoto Protocol;

m. Provide projections of the following indirect GHGs: carbon monoxide (CO), nitrogen oxides (NOX), non-methane volatile organic compounds (NMVOCs), and sulfur dioxide (SO2).

n. Provide strengths and weaknesses of modeling environments used for emission forecasting.

Acknowledgements—The authors would like to express their gratitude for the support of the TÁMOP-4.2.1.B-11/2/KMR-2011-0003 project titled "Az oktatás és kutatás színvonalának emelése a Szent István Egyetemen".

References

"Guidelines for the preparation of national communications by Parties included in Annex I to the Convention, Part II: UNFCCC reporting guidelines on national communications". FCCC/CP/1999/7. Available at <http://unfccc.int/resource/docs/cop5/07.pdf>.

"Guidelines for the preparation of national communications by Parties included in Annex I to the Convention, Part I: UNFCCC reporting guidelines on annual inventories". FCCC/CP/1999/7. Available at <http://unfccc.int/resource/docs/cop5/07.pdf>.

FCCC/SBI/2007/INF.6. Compilation and synthesis of fourth national communications. Available at <http://unfccc.int/resource/docs/2007/sbi/eng/inf06.pdf>.

FCCC/SBI/2007/INF.7. Compilation and synthesis of supplementary information incorporated in fourth national communications submitted in accordance with Article 7, paragraph 2, of the Kyoto Protocol. Available at <http://unfccc.int/resource/docs/2007/ sbi/eng/inf07.pdf>.

FCCC/ARR/2009/HUN. Report of the individual review of the greenhouse gas inventory of Hungary submitted in 2009. Available at <http://unfccc.int/national_reports/annex_i_ghg_inventories/national_inventories_submissions/items/4771.php>.

FCCC/IDR.4/HUN. Report on the in-depth review of the fourth national communication of Hungary. Available at <http://unfccc.int/resource/docs/2006/idr/hun04.pdf>.

4th national communication of Hungary. Available at <http://unfccc.int/resource/docs/natc/hunnc4.pdf>.

2009 GHG inventory submission of Hungary. Available at <http://unfccc.int/national_reports/annex_i_ghg_inventories/national_inventories_submissions/items/4771.php>.

2010 GHG inventory submission of Hungary. Available at <http://unfccc.int/national_reports/annex_i_ghg_inventories/national_inventories_submissions/items/5270.php>.

VAHAVA project (Change (VÁltozás) Impact (HAtás) Response (VÁlasz) – Joint scientific cooperation of the Hungarian Ministry for the Environment and Water (KvVM) and the Hungarian Academy of Sciences (MTA), 2003–2006.

National Climate Change Strategy (NCCS), 2008–2025, Ministry for the Environment and Water and the Hungarian Academy of Sciences.

Bozó, L., 2011: Hungarian National Report on IAMAS 2007–2010: Activities at the Hungarian Meteorological Service. *Acta Geodaetica et geopjysica Hungarica 46*, 215–231.

Bozó, L., Horváth, Á., Zsikla, Á., Hadvári, M., and *Kovács, A.,* 2010a: Szélsőséges meteorológiai helyzetek 2010. május-júniusban. *Klíma-21 Füzetek 16*, 7–15. (In Hungarian)

Bozó, L., Horváth, L., Láng, I., and *Vári, A.* (eds.), 2010b: *Környezeti Jövőkép – Környezet- és Klímabiztonság*. (Köztestületi Stratégiai Programok), Magyar Tudományos Akadémia, Budapest. (In Hungarian)

Csete, M. and *Horváth L.*, 2012: Sustainability and Green Development in Urban Policies and Strategies. *Appl. Ecol. Environ.Res. 10*, 185–194.

Kis-Kovács, G., Bozó, L., Lovas, K., Nagy, E., and *Tarczay, K.*, 2011: Adalékok az üvegház-hatású gázok antropogén kibocsátásának és elnyelésének vizsgálatához Magyarországon. In *Sebezhetőség és adaptáció, A reziliencia esélyei.* (eds.: *Tamás, P.* and *Bulla, M.*). MTA Szociológiai Kutatóintézet, Budapest, 305–314. (In Hungarian)

Kovács-Székely, I. and *Szalai, J.*, 2009: The impact of climate change on production conditions of Hungarian agriculture, especially on shallow groundwater supply.. *Proceedings of BBS*, ISBN 978-963-06-8171-1, 79–96.

Kovács, J., Kiszely-Peres, B., Szalai, J., and *Kovácsné Székely, I.*, 2010: Periodicity in shallow groundwater level fluctuation time series on the Trans-Tisza Region, Hungary. *Acta Geographica Ac Geologica Et Meteorologica Debrecina 4–5*, 65–70.

Szenteleki, K., Horváth, L., and *Ladányi, M.*, 2012: Climate Risk and Climate Analogies in Hungarian Viticulture. *International proceedings of chemical, biological and environmental engineering 28*, 250–254.

Tanos, P., Kovács, J., Kovácsné Székely, I., and *Hatvani, I.G.*, 2011: Exploratory data analysis on the Upper-Tisza section using single and multivariate data analysis methods. *Cent. Eur. Geol. 54*, 345–356.

IDŐJÁRÁS

Quarterly Journal of the Hungarian Meteorological Service
Vol. 116, No. 4, October–December 2012, pp. 323–335

Response of summer rainfalls in Pakistan to dust aerosols in an atmospheric general circulation model

Rashed Mahmood[1,2,3]* and **Shuanglin Li**[1]

[1]*Nansen-Zhu International Research Centre (NZC), Institute of Atmospheric Physics (IAP), 100029 Beijing China*

[2]*Graduate University of the Chinese Academy of Sciences (GUCAS), 100029 Beijing China*

[3]*Department of Meteorology, COMSATS Institute of Information Technology (CIIT), 44000 Islamabad Pakistan*

**Corresponding author E-mail: rashed@mail.iap.ac.cn*

(Manuscript received in final form August 29, 2012)

Abstract—Satellite data indicate that the dust concentration over Pakistan and its surrounding regions is substantially large especially in summer season when southwesterly winds actively bring additional dust (apart from local deserts) from eastern Africa and the Arabian Peninsula. To assess the potential response of summer rainfalls in Pakistan for dust concentrations, in this study we use an atmospheric general circulation model with prescribed sea surface temperatures and elucidate that the contribution of dust in modulating summer precipitation can be substantial with mainly positive responses over northern and southern Pakistan while negligibly small negative response over the central region. The anomalous results for dust aerosols in the model are calculated as the difference between two types of ensemble sensitive experiments with one ensemble simulation including dust while in the other ensemble the dust is removed over a selected domain. The maximum amount of enhanced rainfall is about 0.7 mm/day which is approximately 10% of the summer season rainfall in northern Pakistan. Such anomalous amplification in rainfall is realized through the advection of moist static energy into land regions of Pakistan as well as the additional supply of moisture from the Bay of Bengal and the Arabian Sea.

Key-words: dust aerosols, rainfall in Pakistan, south Asian monsoon, total ozone mapping spectrometer aerosol index (TOMS-AI), Arabian Sea

1. Introduction

Dust aerosols can play a significant role in modulating global and regional climates, primarily through absorbing and, to some extent, scattering of solar radiations (*Miller* and *Tegen*, 1998; *Andreae et al.*, 2005). The absorption of radiations in the atmosphere implicates changes in vertical profiles of atmospheric temperatures with heating in lower to middle troposphere while cooling near surface (*Hui et al.*, 2008). This reorganization of energy can modify the stability of the atmosphere, and thus, can potentially augment regional climate conditions (*Perlwitz* and *Miller*, 2010; *Hui et al.*, 2008). Therefore, understanding the role of dust aerosol in regional and global climate can be intriguing and has been one of the major focus points for research in climate science studies (e.g., *Tegen* and *Fung*, 1996; *Miller* and *Tegen*, 1998; *Miller et al.*, 2004; *Andreae et al.*, 2005; *Engelstaedter* and *Washington*, 2007; *Hui et al.*, 2008; *Perlwitz* and *Miller*, 2010).

Most of the dust aerosols instigate into the atmosphere through soil erosion driven by winds (*Miller et al.*, 2004). These aerosols can travel thousands of kilometers from their source regions depending on particle size and the prevailing atmospheric conditions (*Perlwitz* and *Miller*, 2010; *Engelstaedter* and *Washington*, 2007). Satellite data, such as total ozone mapping spectrometer (TOMS) aerosol index (AI) (*Torres et al.*, 1998; *Prospero et al.*, 2002), provides opportunities for visualizing large scale absorbing aerosol (mainly dust and black carbon) transport from vast deserts of Africa and Asia towards remote locations (*Fig. 1*). A considerable amount of dust is transported towards Arabian Sea and southern Pakistan through southwesterly boreal summer monsoonal winds (wind vectors in *Fig. 1*). In Pakistan, dust is not only transported from remote locations, but also the local deserts (such as Thar, Thal, and Cholistan) contribute to the total concentrations. Thus, the potential influence of dust aerosols on regional climate of Pakistan can be expected given the large concentrations therein and surrounding areas as well. These considerate motivate the present study in which we used an atmospheric general circulation model (AM2) from the National Oceanic and Atmospheric Administration's (NOAA) Geophysical Fluid Dynamics Laboratory (GFDL) (Anderson et al., 2004), to investigate the contribution of dust aerosols in regional summer climate of Pakistan.

2. Model basics

The AM2 model has been used frequently in many previous studies (e.g., *Anderson et al.*, 2004; *Randles* and *Ramaswamy*, 2008, 2010; *Ming* and *Ramaswamy*, 2009, 2011; *Mahmood* and *Li*, 2011, 2012; *Bollasina et al.*, 2011), and thus, it needs not to be fully discussed here in order to avoid repetition. Therefore, only the most important components that are helpful in understating

the results of current study would be discussed. For detailed and comprehensive information on physical parameterizations, readers may consult *Anderson et al.* (2004). The model is based on the finite-volume dynamical core of *Lin* (2004), with horizontal resolution of 2° latitude × 2.5° longitude and 24 levels in vertical with top at about 3 hPa. The model incorporates the scheme of *Freidenreich* and *Ramaswamy* (1999) for shortwave radiation algorithms with some modifications made by *Anderson et al.* (2004) to optimize computational efficiency. This scheme considers absorption by several greenhouse gases along with molecular scattering, and absorption and scattering by clouds and aerosols. The longwave radiation scheme is based on an improved version of simplified exchange approximation (*Schwarzkopf* and *Ramaswamy*, 1999) where aerosols and clouds are treated as absorbers, while the scheme considers absorption and emissions from several greenhouse gases.

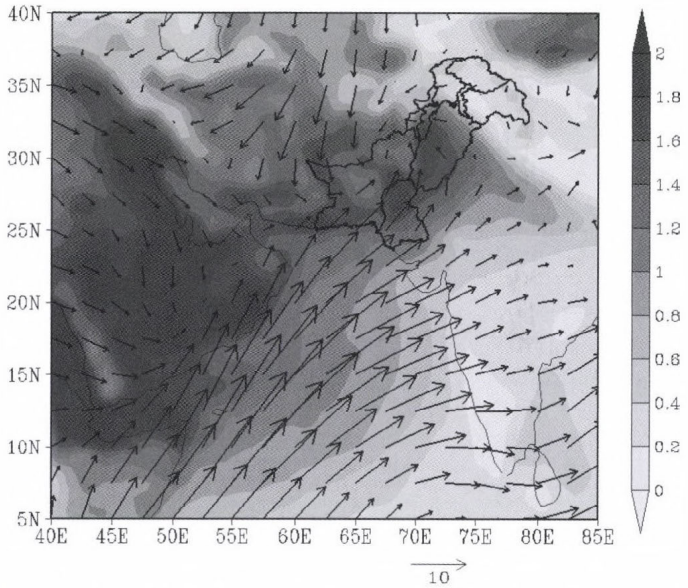

Fig. 1. TOMS-AI climatology (1979-1992) for Jun-Jul-Aug (JJA): climatological winds at 1000 hPa level (1961-1990) for the month of July from NCEP data. Reference wind vector is shown below the figure. Bold black polygons represent geographical location of Pakistan.

The aerosol climatologies, used as inputs in AM2, are calculated offline using a separate chemical transport model known as Model of Ozone and Related Chemical Tracers (MOZART) Version 2 (*Horowitz et al.*, 2003), which is driven by meteorological parameters. The dust aerosol climatology is

simulated in MOZART with meteorological parameters obtained from NCEP/NCAR reanalysis (*Kalnay et al.*, 1996), and dust sources specified from *Ginoux et al.* (2001).

Note that dust is assumed to be of natural origin and kept constant throughout the simulation period with climatological seasonal cycle in AM2 model (*Ginoux et al.*, 2006), therefore, our study is not concerned with "climate change" phenomenon as studied for post/pre industrial simulations in case of anthropogenic aerosol induced radiative forcing. Instead, this study is designed to evaluate the possible contribution of dust aerosols to the "routine" summer climate of Pakistan.

Two kinds of ensemble simulations (with each ensemble having five members) were performed by including/excluding dust in simulations. In the first experiment (i.e., control ensemble), the dust is included in all five simulations of the ensemble, while in the second experiment (i.e., sensitive experiment), the dust over a regional domain comprising eastern Africa and Asia (i.e. 0°-50°N, 25°E-130°E) is removed from simulations. The sea surface temperatures are prescribed according to the observed seasonal cycles. The multiple members of each ensemble were designed with similar characteristics except a slight change in their initial times. The model is integrated for 21 years starting from January 1980 to December 2000. The influence of dust on climate is isolated here by subtracting the sensitive experiment from control experiment (i.e. control-sensitive) for the last 20 years of model simulations.

3. Results and discussions

Fig. 2 shows column burden of dust for summer season. Comparing with *Fig. 1*, the spatial features of model simulated dust burden appears to be qualitatively in agreement with TOMS-AI. For example, the largest burdens over eastern and southern Arabian Peninsula and southern Pakistan correspond well with strongest AI values. Similarly, the dust from Taklamakan desert in western China is well captured by the model. However, the regions south of Himalayan Mountains show little correspondence with TOMS-AI. This is because in this study we only show the burdens for dust aerosols, while the TOMS-AI product includes contributions both from dust and black carbon. The later has high concentration near Himalayan Mountains (*Sahu et al.*, 2008). Therefore, the dust simulation in model can be considered reasonable, though the model biases are expected in common with many previous modeling studies (*Ginoux et al.*, 2006). Important to note is the extension of dust from Middle East and Arabian Peninsula towards southern Pakistan both in summer and spring seasons (spring season is not shown here), which can influence the behavior of summer monsoons in Pakistan as discussed next in this section.

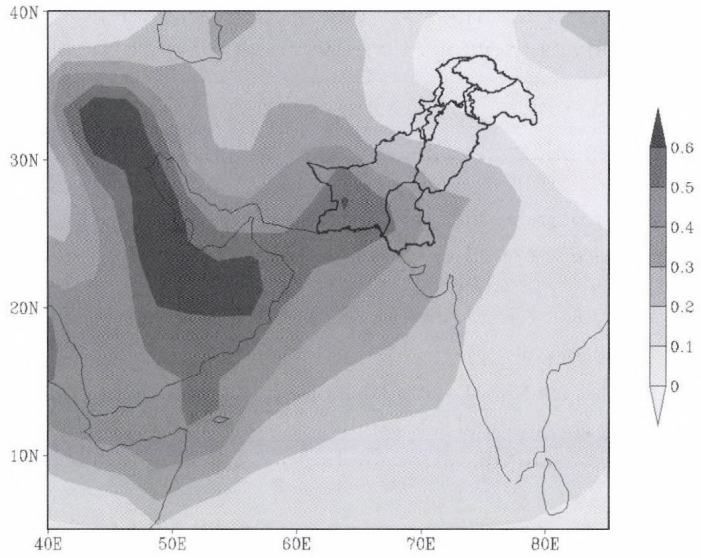

Fig. 2. Modeled column burden of dust aerosols for JJA. Unit: g/m^2

A substantial increase in clear sky shortwave radiative heating induced by dust over the longitudes of Pakistan can be seen visually in *Fig. 3*. The maximum heating region (about 0.5 K/day) lies between 900 and 800 hPa levels, while relatively less heating appear near the surface which is in agreement with previous conclusions that the dust aerosols absorb solar radiations in the lower troposphere, and hence, reduce the amounts reaching the surface (*Miller* and *Tegen*, 1998). Further, consistently with dust burdens, the heating is strongest over southern regions while less prominent near northern areas. Despite, even for the northern part, the magnitude is considerable with values reaching up to 0.35 K/day. Since the dust absorbs radiations in the lower troposphere, the anomalous changes in near surface air temperature over most of the highest dust concentration regions is negative (*Fig. 4*). The statistically significant (at 90% confidence level) negative temperature anomalies prevail over the maximum dust loading regions, i.e., southern Arabian Peninsula and Pakistan, while positive responses appear over China, especially the Tibetan Plateau, where dust loading were assumed to be small in the model (*Fig. 2*). Similarly, in most parts of the central Asian region the temperature changes are negative but statistically insignificant. These temperature changes are in line with the proposed mechanisms in that dust absorbs solar radiations in the atmosphere leaving fewer radiations reaching the surface (*Miller* and *Tegen*, 1998). However, some exceptions also exist, e.g., Taklamakan desert (about ~40N in western China) where small positive but less significant anomalies are found, although dust concentration is considerable in this region (*Figs. 1* and *2*). This implies that the strong cooling, especially over Pakistan with maximum values reaching up

to –0.7 K, may have been exaggerated by circulation changes such as horizontal and vertical dry advection of cooler air akin to elevated heat pump theorem proposed by *Lau et al.* (2006), however model biases, of course, may persist and cannot be ruled out for such anomalous changes.

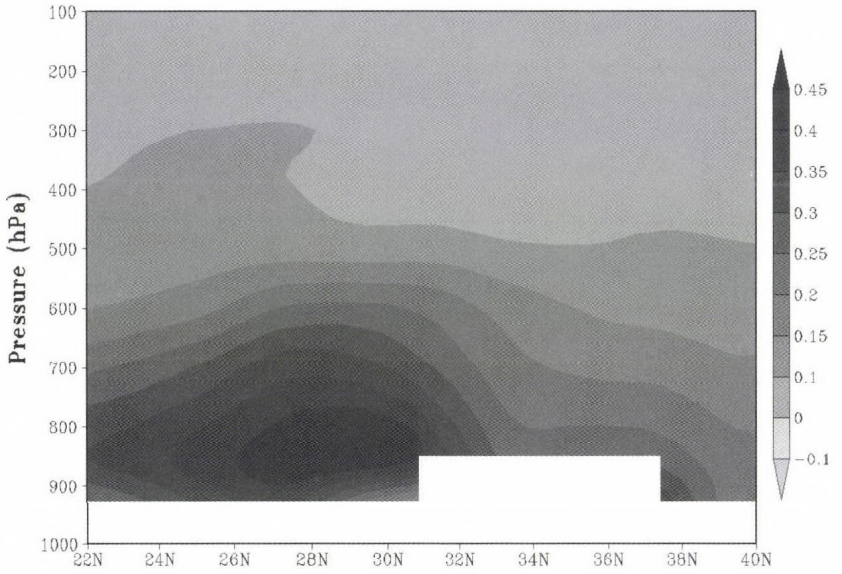

Fig. 3. Vertical cross section of clear-sky shortwave heating anomaly longitudinally averaged over Pakistan (60°E-75°E). White color is caused by the elevated topography. Unit: K/day

More important for the major considerate of the current study are changes in precipitation and circulation associated with dust aerosol (*Figs. 5, 6* and *7*) along with possible potential mechanisms as shown in *Fig. 8*. *Fig. 5* represents the anomalous precipitation changes over Pakistan. Significant positive rainfalls can be seen over the northern part of the country, especially over northern Punjab and parts of Azad Kashmir and Khyber Pakhtunkhwa provinces (which is approximately the climatologically mean location of summer rainfalls in Pakistan). Similarly, changes in rainfall are also significant over lower Sindh and Balochistan provinces, especially in coastal areas with maximum values approaching 0.7 mm/day, while negligibly small negative response occur over the central regions. This shows that, on average, the dust aerosols can induce a surplus of 10% to the seasonal rainfalls in Pakistan, where the observed summer season rainfall rate is about 7 mm/day (*Webster et al.*, 2011). Thus, the dust aerosols can have a significant contribution to the overall behavior of summer monsoon rainfalls in Pakistan.

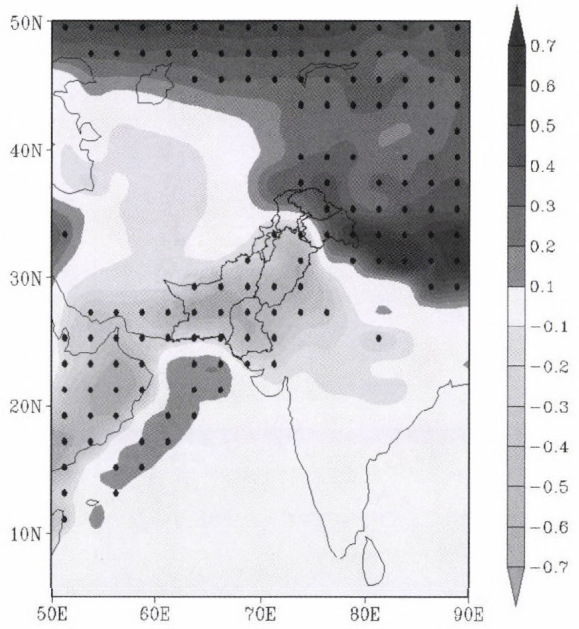

Fig. 4. Anomalous changes in near surface temperature (at 2m). Black dots represent the grid point values which are statistically significant at 90% confidence level. Unit: K.

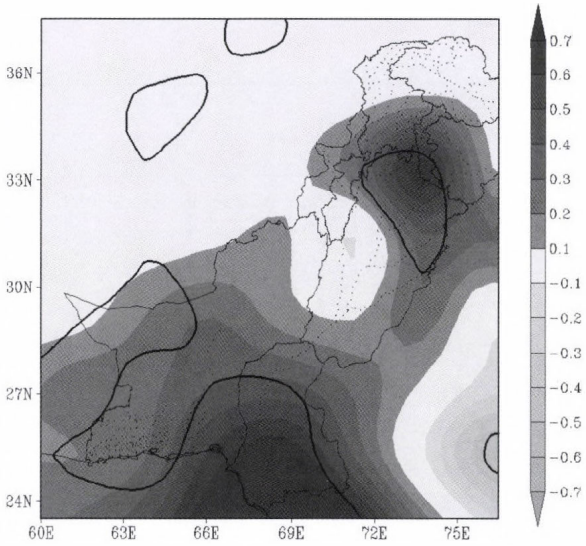

Fig. 5. Anomalous changes in precipitation (unit: mm/day). Thick black contour represents the values which are statistically significant at 90% confidence level. Thin dotted lines represent the Indus River and its major tributaries.

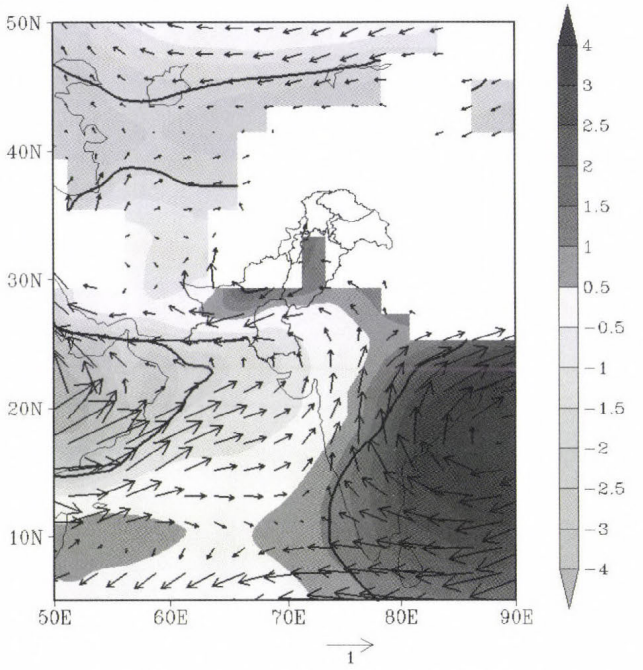

Fig. 6: Circulation anomalies at 850 hPa level; shading represents geopotential height (unit: gpm) and vectors represent wind (unit: m/s). Thick black contour represents height values which are statistical significant at 90% confidence level. White regions are caused by the elevated topography.

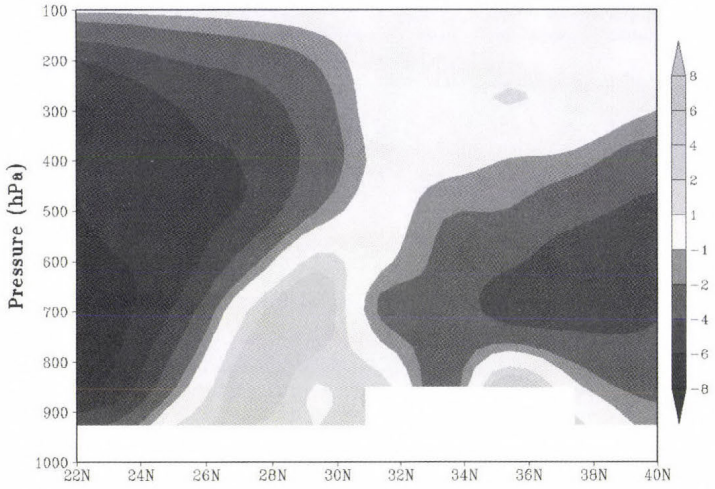

Fig. 7: Anomalous changes in vertical pressure velocity averaged over Pakistan (60°E-75°E) (negative values represent ascent). Unit: 10^{-3} Pa/s..

The corresponding changes in near surface (at 850 hPa level) geopotential height and winds are shown in *Fig. 6*. Strong dipole-like height anomalies prevail in northern Indian Ocean with significantly positive response over the Bay of Bengal and an extended low over Arabian Sea including southern Pakistan. Significant negative height anomalies also appear over central Asia and China. This distribution of height anomalies, especially stronger high pressure over Bay of Bengal, disperses moist winds from Bay of Bengal and also the Arabian Sea towards Pakistan as shown by the vectors in *Fig. 6*. The most favorable dynamics for enhanced rainfall in Pakistan in this case can be attributed to the strong anticyclonic circulations over Bay of Bengal which enhances the advection of anomalous winds with magnitudes up to 1 m/s towards northern Pakistan. Interestingly, for central Pakistan, where the rainfall response is negative, there exists a small positive height center which appears to deflect wind towards southern Pakistan implying further the consistency between precipitation and circulation anomalies.

The tri-polar precipitation anomalies over Pakistan (i.e., wetness over north/south regions and small dryness over central areas) can further be explored by analyzing the vertical velocity as shown in *Fig. 7*. Two ascending branches of anomalous vertical velocity can be seen near the coastal area (the stronger one), and the northern part implying strong convective activity taking place in these regions. These ascending motions are accompanied by a small descending branch in central Pakistan implying small dryness in this region (*Fig. 5*).

Wang et al. (2009) highlighted the importance of perturbation in moist static energy as a response to anthropogenic aerosol forcing, and argued that the changes in sub-cloud layer moist static energy can represent not only the northward migration of south Asian monsoons but also the strength of convection during the monsoon season. To see whether similar interpretations can be made for the current simulations, we calculated vertically integrated (1000–100 hPa) moist static energy (VMSE for short) as shown in *Fig. 8a*. Consistent with *Wang et al.* (2009), the VMSE is enhanced over Pakistan with a clear extension towards northern areas. The strongest anomaly in VMSE is, of course, near the southern moisture source region that is the northern Arabian Sea.

Finally, we calculated vertically integrated moisture flux (*Zhu* and *Newell*, 1998) to assess further the dust induced wet conditions in Pakistan (*Fig. 8b*). As shown by the figure, the moisture supply is enhanced towards Pakistan from three source regions, namely Bay of Bengal, eastern Arabian Sea, and the Persian Gulf. The strongest moisture flux is from Bay of Bengal and eastern Arabian Sea that travels along the foothills of Himalayas and finally converges over Pakistan.

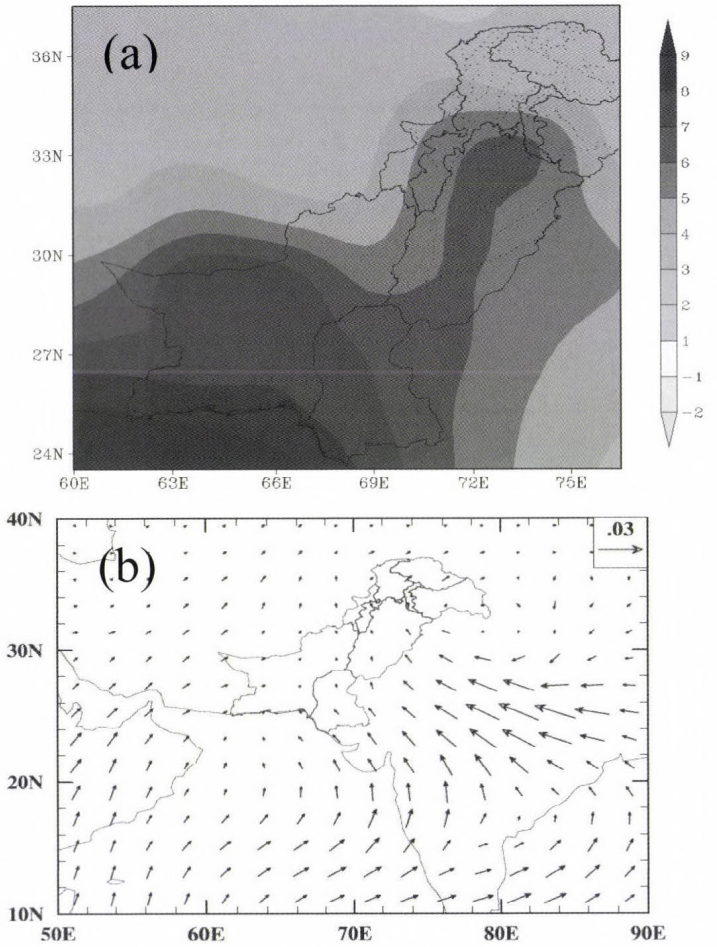

Fig. 8. Vertically integrated (1000-100 hPa) anomalous changes in (a) moist static energy (unit: 10^3 kJ/kg) and (b) moisture transport (unit: kg/ms). Reference vector for moisture transport is shown in upper right corner of (b).

4. Summary and remarks

In this study we investigate, using an atmospheric general circulation model AM2, the potential influence of Afro-Asian dust on regional summer climate of Pakistan. Two sets of ensemble simulations with and without dust aerosols were carried out to isolate the possible influence. Significant enhancement of rainfall over Pakistan was seen with maximum amount of anomalous rainfall reaching up to 0.7 mm/day. These modeled changes in precipitation are about 10% of the total observed summer rainfall in northern Pakistan (*Webster et al.*, 2011). The

anomalous circulation pattern show that a strong high over Bay of Bengal and a low pressure over the Arabian Peninsula/northern Arabian Sea including central Asia force the moister lower level winds towards northern Pakistan, some of which is deflected back to the southern coastal region and Arabian Sea.

The strong advection of moisture from the Arabian Sea and Bay of Bengal is further confirmed by the anomalous vertically integrated moisture transport towards Pakistan. Furthermore, the dust induced anomalous response was also observed by changes in VMSE which appeared to extend from northern Arabian Sea towards northern Pakistan. *Wang et al.* (2009) also found similar changes in (lower tropospheric) moist static energy over land regions of northwest subcontinent for anthropogenic aerosols using a different general circulation model. Thus, the collective affect of natural (e.g., dust) and anthropogenic aerosols may further exacerbate the above discussed rainfalls patterns. However, to explore the combined effects of natural plus anthropogenic aerosols on summer climate in Pakistan is beyond the scope of this study.

Further caveats of the study are the prescribed SSTs and missing indirect aerosol affects. Similarly, ground based observations of dust emission, transport, and overall concentrations in Pakistan are unfortunately not available. Thus, though the results from model simulations can be valuable, especially for studying aerosol influence on climate for which models are the primary diagnostic tools, they still need to be confirmed by ground based observations to make concrete conclusions. That the model results indicate significant change in circulations and precipitation over Pakistan in response to dust aerosols, which implies that we need to establish a network of ground based dust observations to fully grasp the interaction between strong dust concentrations and the relevant climate response in Pakistan. Therefore, further research is warranted, especially using ground based observations and multi-model simulations, to make conclusions more solid.

Acknowledgements—This study was supported by the Knowledge Innovation Program of the Chinese Academy of Sciences (Grant No. KZCX2-YW-Q11-03). The TOMS level 2 and 3 data sets are processed by NASA/Goddard Space Flight Center's Ozone Processing Team (OPT), we thankfully acknowledge them for making the data sets publically available.

References

Anderson, J.L., Balaji, V., Broccoli A.J., Cooke, W.F., Delworth, T.L., Dixon, K.W., Donner, L.J., Dunne, K.A., Freidenreich, S.M., Garner, S.T., Gudgel, R.G., Gordon, C.T., Held, I.M., Hemler, R.S., Horowitz, L.W., Klein, S.A., Knutson, T.R., Kushner, P.J., Langenhost, A.R., Lau, N.-C., Liang, Z., Malyshev, S.L., Milly, P.C.D., Nath, M.J., Ploshay, J.J., Ramaswamy, V., Schwarzkopf, M.D., Shevliakova, E., Sirutis, J.J., Soden, B.J., Stern, W.F., Thompson, L.A., Wilson, R.J., Wittenberg, A.T., and *Wyman, B.L.,* 2004: The new global atmosphere and land model AM2-LM2: Evaluation with prescribed SST simulations. *J. Climate 17*, 4641–4673.

Andreae, M.O., Jones, C.D. and *Cox, P.M.,* 2005: Strong present-day aerosol cooling implies a hot future. *Nature 435*, 1187–1190.

Bollasina, M.A., Ming, Y. and *Ramaswamy, V.,* 2011: Anthropogenic aerosols and the weakening of the south Asian summer monsoon. *Science 334*, 502–505.

Engelstaedter, S., and *Washington, R.,* 2007: Atmospheric controls on the annual cycle of North African dust. *J. Geophys. Res. 112*, D03103.

Freidenreich, S.M., and *V. Ramaswamy*, 1999: A new multiple-band solar radiative parameterization for general circulation models, *J. Geophys. Res. 104*, 31389–31409.

Ginoux, P., Chin, M., Tegan, I., Prospero, J.M., Holben, B., Dubovik, O., and *Lin, S.-J.,* 2001: Sources and distribution of dust aerosols simulated with GOCART model, *J. Geophys. Res. 106*, 20255–20273.

Ginoux, P., Horowitz, L.W., Ramaswamy, V., Geogdzhayev, I.V., Holben, B.N., Stenchikov, G., and *Tie, X.,* 2006: Evaluation of aerosol distribution and optical depth in the Geophysical Fluid Dynamics Laboratory coupled model CM2.1 for present climate. *J. Geophys. Res. 111*, D22210.

Horowitz, L.W., Walters, S., Mauzerall, D.L., Emmons, L.K., Rasch, P.J., Granier, C., Tie, X., Lamarque, J.-F., Schultz, M.G., Tyndall, G.S., Orlando, J.J., and *Brasseur, G.P.,* 2003: A global simulation of tropospheric ozone and related tracers: Description and evaluation of MOZART, version 2. *J. Geophys. Res. 108 (D24)*, 4784.

Hui, W.J., Cook, B.I., Ravi, S., Fuentes J.D., and *D'Odorico, P.,* 2008: Dust-rainfall feedbacks in the West African Sahel. *Water Resour. Res. 44*, W05202.

Kalnay, E., Kanamitsu, M.,Kistler, R., Collins, W., Deaven, D., Gandin, L., Iredell, M., Saha, S., White, G., Woollen, G., Zhu, Y., Chelliah, M., Ebisuzaki, W., Higgins, W., Janowiak, J., Mo, K.C., Ropelewski, C., Wang, J., Leetma, A., Reynolds, R., Jenne, R., and *Joseph, D.,* 1996: The NCEP/NCAR 40-year reanalysis project, *Bull. Amer. Meteor. Soc. 77*, 437–470.

Lau, K., Kim, M.K. and *Kim, K.M.,* 2006: Asian summer monsoon anomalies induced by aerosol direct forcing: the role of the Tibetan Plateau. *Clim. Dynam. 26*, 855–864.

Lin, S-J., 2004: A ''vertically Lagrangian'' finite-volume dynamical core for global models. *Mon. Weather Rev. 132*, 2293–2307.

Mahmood, R., and *Li, S.,* 2011: Modeled influence of East Asian black carbon on Inter-decadal shifts in East China summer rainfall. *Atmos. Oceanic Sci. Lett. 4*, 349–355.

Mahmood, R., and *Li, S.*, 2012: Delay in the onset of south Asian summer monsoon induced by local black carbon in an AGCM. *Theor. Appl. Climatol.* DOI 10.1007/s00704-012-0681-3.

Miller, R.L., and *Tegen, I.,* 1998: Climate response to soil dust aerosols, *J. Climate 11*, 3247–3267.

Miller, R.L., Tegen, I., and *Perlwitz, J.,* 2004: Surface radiative forcing by soil dust aerosols and the hydrologic cycle. *J. Geophys. Res. 109*, D04203.

Ming, Y., and *Ramaswamy, V.,* 2009: Nonlinear climate and hydrological responses to aerosol effects. *J. Climate 22*, 1329–1339.

Ming, Y., and *Ramaswamy, V.,* 2011: A model based investigation of aerosol-induced changes in tropical circulation. *J. Climate 24*, 5125–5133.

Perlwitz, J., and *Miller, R.L.,* 2010: Cloud cover increase with increasing aerosol absorptivity: A counterexample to the conventional semidirect aerosol effect. *J. Geophys. Res. 115*, D08203.

Prospero, J.M., Ginoux, P., Torres, O., Nicholson, S.E., and *Gill, T.E.,* 2002: Environmental characterization of global sources of atmospheric soil dust identified with the Nimbus 7 Total Ozone Mapping Spectrometer (TOMS) absorbing aerosol products. *Rev. Geophys. 40*, 1002.

Randles, C.A., and *Ramaswamy, V.,* 2008: Absorbing aerosols over Asia: A Geophysical Fluid Dynamics Laboratory general circulation model sensitivity study of model response to aerosol optical depth and aerosol absorption. *J. Geophys. Res. 113*, D21203.

Randles, C.A., and *Ramaswamy, V.,* 2010: Direct and semi-direct impacts of absorbing biomass burning aerosol on the climate of southern Africa: a Geophysical Fluid Dynamics Laboratory GCM sensitivity study.*Atmos. Chem. Phys. 10*, 9819–9831.

Sahu, S.K., Beig, G. and *Sharma, C.,* 2008: Decadal growth of black carbon emissions in India. *Geophys. Res. Lett. 35*, L02807.

Schwarzkopf, M.D., and *Ramaswamy, V.,* 1999: Radiative effects of CH4, N2O, halocarbons and the foreign-broadened H2O continuum: A GCM experiment. *J. Geophys. Res. 104*, 9467–9488.

Tegen, I., Lacis, A.A. and *Fung, I.,* 1996: The influence on climate forcing of mineral aerosols from disturbed soils, *Nature 308*, 419–422.

Torres, O., Bhartia, P.K., Herman, J.R., Ahmad, Z., and *Geason, J.,* 1998: Derivation of aerosol properties from satellite measurements of backscattered ultraviolet radiation: Theoretical bases. *J. Geophys. Res. 103(D14)*, 17099–17110.

Wang, C., Kim, D., Ekman, A.M.L., Barth, M.C., and *Rasch, P.J.,* 2009: Impact of anthropogenic aerosols on Indian summer monsoon. *Geophys. Res. Lett. 36*, L21704.

Webster, P.J., Toma, V.E. and *Kim, H.-M.,* 2011: Were the 2010 Pakistan floods predictable?. *Geophys. Res. Lett. 38*, L04806.

Zhu, Y. and *Newell, R.E.,* 1998: A proposed algorithm for moisture fluxes from atmospheric rivers, *Mon. Weather Rev. 126*, 725–735.

IDŐJÁRÁS

VOLUME 116 * 2012

BUDAPEST, HUNGARY

AUTHOR INDEX

TABLE OF CONTENTS

I. Papers

II. Book review

SUBJECT INDEX

T

U

V

W

X

Y

INSTRUCTIONS TO AUTHORS OF *IDŐJÁRÁS*

The purpose of the journal is to publish papers in any field of meteorology and atmosphere related scientific areas. These may be

- research papers on new results of scientific investigations,
- critical review articles summarizing the current state of art of a certain topic,
- short contributions dealing with a particular question.

Some issues contain "News" and "Book review", therefore, such contributions are also welcome. The papers must be in American English and should be checked by a native speaker if necessary.

Authors are requested to send their manuscripts to

Editor-in Chief of IDŐJÁRÁS
P.O. Box 38, H-1525 Budapest, Hungary
E-mail: journal.idojaras@met.hu

including all illustrations. MS Word format is preferred in electronic submission. Papers will then be reviewed normally by two independent referees, who remain unidentified for the author(s). The Editor-in-Chief will inform the author(s) whether or not the paper is acceptable for publication, and what modifications, if any, are necessary.

Please, follow the order given below when typing manuscripts.

Title page: should consist of the title, the name(s) of the author(s), their affiliation(s) including full postal and e-mail address(es). In case of more than one author, the corresponding author must be identified.

Abstract: should contain the purpose, the applied data and methods as well as the basic conclusion(s) of the paper.

Key-words: must be included (from 5 to 10) to help to classify the topic.

Text: has to be typed in single spacing on an A4 size paper using 14 pt Times New Roman font if possible. Use of S.I. units are expected, and the use of negative exponent is preferred to fractional sign. Mathematical formulae are expected to be as simple as possible and numbered in parentheses at the right margin.

All publications cited in the text should be presented in the *list of references*, arranged in alphabetical order. For an article: name(s) of author(s) in Italics, year, title of article, name of journal, volume, number (the latter two in Italics) and pages. E.g., *Nathan, K.K.,* 1986: A note on the relationship between photo-synthetically active radiation and cloud amount. *Időjárás 90,* 10-13. For a book: name(s) of author(s), year, title of the book (all in Italics except the year), publisher and place of publication. E.g., *Junge, C.E.,* 1963: *Air Chemistry and Radioactivity.* Academic Press, New York and London. Reference in the text should contain the name(s) of the author(s) in Italics and year of publication. E.g., in the case of one author: *Miller* (1989); in the case of two authors: *Gamov* and *Cleveland* (1973); and if there are more than two authors: *Smith et al.* (1990). If the name of the author cannot be fitted into the text: *(Miller,* 1989); etc. When referring papers published in the same year by the same author, letters a, b, c, etc. should follow the year of publication.

Tables should be marked by Arabic numbers and printed in separate sheets with their numbers and legends given below them. Avoid too lengthy or complicated tables, or tables duplicating results given in other form in the manuscript (e.g., graphs).

Figures should also be marked with Arabic numbers and printed in black and white or color (under special arrangement) in separate sheets with their numbers and captions given below them. JPG, TIF, GIF, BMP or PNG formats should be used for electronic artwork submission.

Reprints: authors receive 30 reprints free of charge. Additional reprints may be ordered at the authors' expense when sending back the proofs to the Editorial Office.

More information for authors is available: journal.idojaras@met.hu

Published by the Hungarian Meteorological Service

Budapest, Hungary

INDEX 26 361

HU ISSN 0324-6329